ATMOSPHERE, IONOSPHERE, SAFETY



Kaliningrad
2025

UDK 550.51
BBK 552.44
A92

A92 **Atmosphere, ionosphere, safety** / edited by O.P. Borchevkina, M.G. Golubkov. — Kaliningrad, 2025. — 284 p.
ISBN 978-5-6042044-9-8

Proceedings of International Conference "Atmosphere, ionosphere, safety" (AIS-2025) include materials reports on: (1) — response analysis of the atmosphere — ionosphere to natural and manmade processes, various causes related geophysical phenomena and evaluate possible consequences of their effects on the human system and process; (2) — to study the possibility of monitoring and finding ways to reduce risk. Scientists from different countries and regions of Russia participated in the conference. Attention was given to questions interconnected with modern nanotechnology and environmental protection. Knowledge of the factors influencing the atmosphere and ionosphere can use them to monitor natural disasters and to establish the appropriate methods on this basis.

The content of the reports is of interest for research and students specializing in physics and chemistry of the atmosphere and ionosphere.

ISBN 978-5-6042044-9-8
9 785604 204498

UDK 550.51
BBK 552.44

ATMOSPHERE-IONOSPHERE COUPLING

CLIMATE CHANGES IN STRATOSPHERE AND MESOSPHERE IN OBSERVATIONAL AND MODELING DATA

Pavel N. Vargin[1,2,3], Sergey V. Kostrykin[4,5], Andrey V. Koval[3,6], Eugene V. Rozanov[3,7], Eugene M. Volodin[4], Sergey P. Smyshlyev[6], Igor I. Mokhov[2], and Vladimir I. Perminov[2]

[1]Central Aerological Observatory, Moscow region, Russia
[2]Obukhov Institute of Atmospheric Physics of the Russian Academy of Science, Moscow, Russia
[3]Atmospheric Physics Department, Saint Petersburg University, Saint Petersburg, Russia
[4]Marchuk Institute of Numerical Mathematics of the Russian Academy of Science, Moscow, Russia
[5]Yu. A. Izrael Institute of Global Climate and Ecology, Moscow, Russia
[6]Department of Science, Technology and Innovation of Russian State Hydrometeorological University, Saint Petersburg, Russia
[7]Physikalisch-Meteorologisches Observatorium Davos / World Radiation Center (PMOD/WRC), Davos, Switzerland

The increase in greenhouse gas (GHG) concentrations leads to a decrease in the temperature of the stratosphere, which increases with altitude. This cooling of stratosphere is confirmed by observational data (satellite, lidar, spectrographic, etc.) over the past 45-50 years.

Climate models reproduce this temperature decrease. The rate of decrease in stratospheric temperature in the coming decades will depend on scenarios for the growth of GHG concentrations and will affect the circulation and chemical composition of the stratosphere.

According to estimates from model calculations (including INMCM6, CCM SOCOLv4), stratospheric temperature decrease and residual meridional circulation (RMC) changes lead to enhancement of the zonal mean zonal wind of the high latitudinal lower–middle stratosphere during the 21 century (stronger under the severe GHG emission scenario).

The stratospheric temperature decrease in certain years in the spring period in the second half of the 21 century may lead to an increase in the stratospheric polar vortex in the Arctic, which may create conditions for severe destruction of the ozone layer comparable with observed in the spring of 2011 but weaker than in the spring of 2020 when the record ozone loss was observed. However, overall, ozone content at high latitudes will increase and at equatorial latitudes will decrease during the 21st century. Interestingly, although satellite data already show a decline in ozone-depleting compounds, estimates of total ozone trends from observations and reanalysis data show divergent trends in mid- and high latitudes over the past 40 years.

The other expected changes of chemical composition of the stratosphere include increase of water vapour: particularly in the Arctic lower stratosphere in March up to 10% and 20% is expected under the moderate (SSP2–4.5) and severe (SSP5–8.5) scenarios respectively according to CCM SOCOLv4 experiments. Probably, a more pronounced stratospheric water vapour positive trend under the severe scenario is related to stronger tropospheric water vapor influx into the stratosphere and enhanced production from CH_4 oxidation.

In addition to changes in the ozone layer and water vapor, model calculations show an increase in nitric acid (HNO_3) concentrations in the 21 century. Known HNO_3 plays an important role in main processes related to ozone depletion in the polar lower stratosphere. HNO_3 ensemble mean changes in

the Arctic lower stratosphere particularly in March (when strongest ozone loss observed) throughout the 21st century in the SOCOLv4 simulations are characterized by a positive significant trend under both moderate and severe scenarios.

Model estimates show that the Arctic stratospheric polar vortex is expected to shift eastward toward northern Eurasia. Possible weakening or strengthening of the stratospheric polar vortex in the Arctic is associated with strengthening of the propagation of wave activity upward or to lower latitudes respectively.

Sudden stratospheric warming (SSW) events are the most striking manifestation of the interannual variability of the polar stratosphere, which affect the whole atmosphere and the ozone layer. Model estimates have not revealed a tendency for the frequency change of major SSWs in the Arctic during the 21st century. However, these calculations retain significant inter-model differences and there is uncertainty associated with the definition of the major SSW events, since some minor SSWs can have a very strong influence on the circulation of the Arctic stratosphere and hence on the ozone layer (as for instance in January 2015).

In the mesosphere the cooling is also observed, but various observations are not fully consistent, maybe partially due to insufficient length of the data series used. It is suggested that observational data sets longer than two solar cycles are necessary to obtain a reliable long-term trend. Analysis of SABER satellite data shows that trends might significantly vary with local time and height in the whole height range of 30–110 km. Possibly that with a longer data series available the differences would be smaller. The SABER data also shows a contraction of the mesosphere (and lower thermosphere) over the period of 2002 and 2019 (the year of the most recent solar minimum) due to a combination of a decline in the intensity of the 11-year solar cycle and increasing CO_2.

Analysis of spectral observations of the hydroxyl airglow (reflecting the thermal state of the mesopause region) at the Zvenigorod Science Station, Obukhov Institute of Atmospheric Physics (56°N, 37°E) over the period since 1957 up to the present (one of the longest period among all known observations) shows a strong cooling (−0.53 +/-0.34 K / yr) until the 1970s and its slowdown to −0.14 +/- 0.03 K/yr thereafter. It is assumed that the reasons for the temperature trend, in addition to the growth of GHG, the main of which is CO_2, may be long-term changes in the dynamics of the upper atmosphere.

This investigation was performed with the financial support of Russian Science Foundation (grant № 25-47-00122).

1. Abalos, M., Calvo N., Benito-Barca S., Garny H., et al. The Brewer–Dobson circulation in CMIP6 // *Atmos. Chem. Phys*. 2021. V. 21. P. 13571–13591. DOI: 10.5194/acp-21-13571-2021.
2. Ayarzagüena, B., Charlton-Perez A. J., Butler A. H., Hitchcock P., et al. Uncertainty in the response of SSWs and stratosphere-troposphere coupling to quadrupled CO_2 concentrations in CMIP6 models // *J. Geophys. Res.* 2020. V, 125. Is. 6. ID e2019JD032345. DOI: 10.1029/2019JD032345.
3. Baldwin M., Birner T., Brasseur G., Burrows J. et al. 100 Years of progress in understanding the stratosphere and mesosphere // *Meteorol. Monogr.* 2019. V. 59. P. 27.1–27.62. DOI: 10.1175/AMSMONOGRAPHS-D-19-0003.1.
4. Dalin P., Perminov V., Pertsev N., Romejko V. Updated long-term trends in mesopause temperature, airglow emissions, and noctilucent clouds // *J. Geophys. Res. Atmos*. 2020. V. 125. Is. 5. P. e2019JD030814. DOI: 10.1029/2019JD030814.
5. Friedel M., Chiodo G., Sukhodolov T., Keeble J. et al. Weakening of springtime Arctic ozone depletion with climate change // *Atmos. Chem. Phys*., 2023. V.23. Is. 17. P. 10235-10254. DOI: 10.5194/acp-23-10235-2023.
6. Garcia, R., Yue J., Russell J. M. III. Middle atmosphere temperature trends in the XX and XXI centuries simulated with the Whole Atmosphere Community Climate Model (WACCM) // *J. Geophys. Res.* 2019. V. 124. P. 7984-7993. DOI: 10.1029/2019JA026909.

7. Huang F. T., Mayr H. G. Temperature decadal trends, and their relation to diurnal variations in the lower thermosphere, stratosphere, and mesosphere, based on measurements from SABER on TIMED // *Ann. Geophys*., 2021. V. 39. Is. 2. P. 327-339. DOI: 10.5194/angeo-39-327-2021.
8. Karpechko A., Afargan-Gerstman H., Butler A.H., Domeisen D. I. V., et al. Northern hemisphere stratosphere-troposphere circulation change in CMIP6 models: 1. Inter-model spread and scenario sensitivity // *J. Geophys. Res.* 2022. V. 127. Is. 18. ID e2022JD036992. DOI: 10.1029/2022JD036992.
9. Karagodin-Doyennel A., Rozanov E., Sukhodolov T., Egorova T., Sedlacek J., Peter T. The future ozone trends in changing climate simulated with SOCOLv4 // *EGUsphere*. 2022. V. 23. Is. 8. P. 4801-4817. DOI: 10.5194/acp-23-4801-2023.
10. Laštovicka J. Progress in investigating long-term trends in the mesosphere, thermosphere, and ionosphere // Atmos. Chem. Phys. 2024. V. 23. Is. 10. P. 5783-5800. DOI: 10.5194/acp-23-5783-2023.
11. Mlynczak M.G., Hunt L.A., Garcia R.R., Harvey L.V., et al. Cooling and contraction of the mesosphere and lower thermosphere from 2002 to 2021 // *J. Geophys. Res.* 2022.V. 127. Is. 22. ID e2022JD036767. DOI: 10.1029/2022JD036767.
12. Mokhov I.I., Perminov V.I., Fomina I.A. Temperature changes in the mesopause region during climate change in recent decades (1960−2024) // *Bull. of Lomonosov Moscow State Un-ty*. 2024. V. 79. No 5. P. 634-644. DOI:10.3103/S0027134924701984.
13. Pedatella N., Chau J. L., Schmidt H., Goncharenko L. P., et al. How sudden stratospheric warming affects the whole atmosphere // *EOS, Trans. Amer. Geophys. Union*, 2018. DOI: 10.1029/2018EO092441.
14. Perminov V. I., Semenov A. I., Pertsev N. N., et al. Multi-year behavior of the midnight OH* temperature according to observations at Zvenigorod over 2000–2016 // *Adv. Space Res.* 2018. V. 61. Is. 7. P. 1901-1908. DOI: 10.1016/j.asr.2017.07.020.
15. Sivakandan M., Peters D., Entzian G. Long-term oscillations and trends of the mesosphere derived from 60 Years of standard phase-heights measurements over Europe: An update // *J. Atmos. Sol.-Terr. Phys*. 2024. V. 261. Atr No 106274. DOI: 10.1016/j.jastp.2024.106274.
16. Steiner A., Ladstädter F., Randel W. J., Maycock A. C. et al., Observed Temperature Changes in the Troposphere and Stratosphere from 1979 to 2018 // *J. Climate*, 2020. V. 33. Is. 19. P. 8165–8194. DOI: 10.1175/JCLI-D-19-0998.1.
17. Vargin P.N., Kostrykin S.V., Rakushina E.V., et al. Investigation of variability of Spring Breakup dates and Arctic stratospheric polar vortex parameters in modeling and reanalysis data // *Izv. Atmos. Ocean. Phys.* 2020. V. 56. No 5. P. 526-539. DOI: 10.1134/S0001433820050114.
18. Vargin P.N., Kostrykin S.V., Volodin E.M., et al. Arctic stratosphere circulation changes in XXI century in simulations of INM CM5 // *Atmosphere*. 2022. V. 13 No 1. P. 25. DOI:10.3390/atmos13010025.
19. Vargin P., Kostrykin S., Koval A., et al. Arctic stratosphere changes in the 21st century in the Earth system model SOCOLv4 // Front. Earth Science, 2023. V. 11. P. 1214418. DOI:10.3389/feart.2023.1214418.
20. von der Gathen, Kivi R., Wohltmann I. et al. Climate change favours large seasonal loss of Arctic ozone // *Nat. Commun.* 2021.V/ 12/ P. 3886. DOI: 10.1038/s41467-021-24089-6.
21. Venkat Ratnam M., Raj A.S.T., Qianet L. Long-term trends in the low-latitude middle atmosphere temperature and winds: Observations and WACCM-X model simulations // *J. Geophys. Res. Space.* 2019. V. 124. Is. 8. P. 7320-7331. DOI: 10.1029/2019JA026928.

THE INFLUENCE OF CLOUDS ON THE ATMOSPHERIC CONDUCTIVITY

Valery V. Denisenko[1,2] and Eugene V. Rozanov[3,4]

[1]Institute of Computational Modelling of the Russian Academy of Sciences Siberian Branch, Krasnoyarsk, Academgorodok, Russia
[2]Kaliningrad Branch of Pushkov Institute of Terrestrial Magnetism, Ionosphere and Radio Wave Propagation, Russian Academy of Sciences, Kaliningrad, Russia
[3]St. Petersburg State University, Laboratory of the Ozone Layer and Upper Atmosphere Research, St. Petersburg, Petrodvorets, Russia
[4]Physikalisch-Meteorologisches Observatorium and World Radiation Center, Davos, Switzerland

When studying large-scale currents in the atmosphere flowing from the ionosphere to the ground, the ionosphere and the Earth's surface can be considered as the ideal conductors with good accuracy. These currents are determined by the ground-ionosphere voltage and the spatial distribution of the conductivity in the atmosphere. It is possible to reduce the spatial distribution of conductivity to the distribution in longitude and latitude of the conductivity of the atmospheric columns. By integrating the conductance over the entire surface of the Earth, we obtain the total conductance of the atmosphere. Inside clouds, air conductivity decreases due to the ion attachment to water drops. Based on the available data on a decrease in local conductivity within individual clouds, we analyze the effect of cloud density in latitude, longitude, and height on the geographical distribution of the conductance and the total conductance of the atmosphere.

In our general model [1] we treat the atmosphere, ionosphere, and magnetosphere as a single conductor. The basic equations for the steady state electric field **E** and current density **j** are Faraday's law, the charge conservation law, and Ohm's law with conductivity tensor that is a scalar σ in the lower atmosphere. For the electric potential V, ($\mathbf{E} = -\,grad\,V$) the system of the equations is reduced to the current continuity equation

$$-\mathrm{div}(\sigma\,\mathrm{grad}\,V) = 0. \qquad (1)$$

We use the geographical coordinates φ, λ. The height h is calculated from the mean sea level, which is defined in the World Geodetic System WGS 84. The height of the Earth's surface above mean sea level is acquired from (http://www.ngdc.noaa.gov/mgg/topo/globe.html).

At horizontal scales of the order and more than 100 km, a one-dimensional model corresponding to the verticality of atmospheric currents can be used. Then the conductivity σ and potential V depend only on the height h, and therefore the boundary value problem of electric current continuity is reduced to solving a one-dimensional problem over h. We neglect sphericity, and the one-dimensional problem (1) takes the following form

$$-\frac{d}{dh}\left(\sigma(h)\frac{dV(h)}{dh}\right) = 0, \;\; V|_{h=h_I} = V_0, \;\; V|_{h=h_0} = 0, \qquad (2)$$

where, strictly speaking, the functions $V(h)$ and $\sigma(h)$ must have indices φ, λ, since they are specific at each point with coordinates φ, λ, but for brevity we do not write these indices, h_0 denotes the height $h_g(\varphi, \lambda)$ of the Earth's surface at the point under consideration, h_I is the height at which the ionospheric conductor begins, which we consider an ideal one. The rise of the upper boundary h_I of the atmospheric conductor above 30 km in known empirical models of air conductivity increases the resistance of the atmospheric column by only 0.5%. This can be ignored, and therefore we set $h_I = 30$ km.

The solution for the problem (2) gives the vertical electric field strength $E(h) = -dV(h)/dh$ and the current density $j = -\sigma(h)\, dV(h)/dh$. The current density does not vary with height and therefore is a function only of the coordinates φ, λ. The latter circumstance makes it possible to reduce the solution for problem (2) to height integration

$$V_0 = -j(\varphi, \lambda) \int_{h_0}^{h_I} dh/\sigma(h) = -j(\varphi, \lambda)\, R(\varphi, \lambda), \quad (3)$$

where $R(\varphi, \lambda)$ is the resistance of an atmospheric column having a cross-section of 1 m^2. In our model, if cloudiness is not considered, it is determined only by the height of the surface h_0 which has an uniform value for marine areas. From this equation, the value of $j(\varphi, \lambda)$, and the electric field strength, including the field near the ground E_0, are obtained. We introduce the notation σ_0 for the conductivity near the ground. The electric field strength near the ground is

$$E_0 = -V_0/(R\sigma_0). \quad (4)$$

For the electric field strength and current density near the ground, a vertical column of air is equivalent to a homogeneous column with constant conductivity σ_0 and thickness:

$$H = R\sigma_0. \quad (5)$$

This parameter H is naturally called the thickness of a homogeneous atmospheric conductor above the surface point under consideration [1]. It is a characteristic height scale of conductivity growth.

The inverse of $R(\varphi, \lambda)$ value, $\Sigma(\varphi, \lambda) = 1/R(\varphi, \lambda)$, is the conductance of an atmospheric column. The integral of $\Sigma(\varphi, \lambda)$ over the entire surface of the Earth gives the conductance of the atmosphere as a whole Σ_{tot}. The inverse value is the resistance of the global atmospheric conductor R_{tot} and the total return current of GEC

$$I = V_0/R_{tot}. \quad (6)$$

Because of (4)-(6)

$$E_0 = R_{tot}(I/H). \quad (7)$$

In the steady state case, I is the value of not only the current that discharges the capacitor ground-ionosphere but also equals to the charging current. The last one describes the total generator of GEC and so it is the main parameter, while V_0 is the result of the ionospheric charge accumulation till the value V_0 that makes the discharging current equal to the charging one. So when we discuss GEC as a whole it is adequate to use (7) in which just I is given.

In our model of altitude conductivity distributions, the atmospheric column resistances for low-lying land and sea are $9.5 \cdot 10^{16}$ Ohms and $5.9 \cdot 10^{16}$ Ohms, respectively. Our simplified model does not distinguish different types of ground: sand, forest, snow, and others. It gives three times lower value for ground in comparison with sea. It means that just a decrease in conductivity due to dust is more important in our approach. So it is natural to simulate ice on the sea surface as ground as well as snow or ice on land. Daily global sea ice concentration distributions are presented in the Copernicus Marine data-base (https://data.marine.copernicus.eu/products).

The conductivity of atmospheric air is mainly determined by ions, which are formed by cosmic rays with additional ionization by radon near the ground. The equilibrium ion concentrations are determined by the balance of ionization and recombination processes. In the presence of water droplets that absorb ions falling on them, the number of ions in the air decreases. If ions of the same sign stick mainly to the droplets, the droplets become charged and contribute to the conduction current, as well as to the external current caused, for example, by the settling of droplets in the gravitational field of the Earth. The mobility of droplets is many orders of magnitude less than the mobility of ions, and therefore their contribution to the conduction current can be neglected, and the conductivity due to ions decreases in proportion to the decrease in their concentration. It was shown in [2] that a five-fold decrease in the air conductivity inside the cloud is characteristic; sometimes a 10-fold decrease was considered typical. To account for different cloud densities, which can vary from 0 to 1 (often expressed as a percentage), we use the following formula for converting conductivity σ to $\tilde{\sigma}$:

$$\tilde{\sigma}(\varphi,\lambda,h) = \sigma(\varphi,\lambda,h)/(1+4c(\varphi,\lambda,h)).$$

That is, in the absence of clouds, the conductivity does not change, but with full clouds, it decreases by 5 times.

The average characteristics of the cloudiness field for two-hour intervals for the whole of 2009 were calculated using the SOCOLv4 Earth system model [3] as part of a project comparing chemistry-climate models. The boundary conditions necessary for calculations determining the state of the atmosphere were borrowed from the recommendations for the "D1" scenario (https://cpb-eu-w2.wpmucdn.com/blogs.reading.ac.uk/dist/7/201/files/2020/09/CCMI-2022_REF-D1_proposal_20200921.pdf) proposed to the participants of the CCMI-2022 project. Cloud calculations are performed in the physical process module of the ECHAM6, an integral part of the SOCOLv4 model, presented in detail in [4]. Using calculated values of temperature, humidity, and other physical parameters of the atmospheric state, the module calculates the characteristics of clouds of various types, including the proportion of the cloud layer in all cells of the model. In this paper, therefore, calculated three-dimensional (longitude, latitude, altitude) fields of the cloud amount are used. In addition, the model also provides a two-dimensional (longitude, latitude) total cloud amount $C(\varphi,\lambda)$, which is calculated using a vertical cloud profile, considering the degree of cloud coverage of each grid cell as it is visible from space.

The values of the total atmospheric resistance R_{tot} for 365 days of 2009 with a two-hour interval were obtained. For each moment UT, averaging was performed for an interval ± 0.5 of each integer value m, m is the time since the beginning of the year in months. If thunderstorm generators introduce a constant current I into the ionosphere during the year, then the total (total over the Earth) return current would be equal to the same constant due to the stationarity of the process. Therefore, the potential difference in the ground-ionosphere $V_0 = R_{tot}I$ (6) would vary proportionally to R_{tot}. Due to the determination of the thickness of a homogeneous atmospheric conductor H, the electric field strength at the Earth's surface is $E_0 = -V_0/H$. For the fair-weather field above the sea following (7) E_0^{sea} is proportional to R_{tot}. The value $H_{sea} = 2$ km is obtained for the used conductivity model.

The calculated average value for 2009 is $< R_{tot} >= 136.2$ Ohms. Assuming an average value over the sea $< E_0 >= 130$ V/m, we obtain the average value $< V_0 >=< E_0 > H_{sea} = 260$ kV, and the constant GEC current $I =< V_0 >< R_{tot} >^{-1}= 1.9$ kA. These values are typical for the GEC [5]. Using the relation (7) and the constancy of the fraction in parentheses, from the received R_{tot} variations during the year, we move on to the proportional variation of the fair-weather field over the sea:

$$\delta E_0 = E_0 - < E_0 >= -(R_{tot} - < R_{tot} >)(I/H).$$

Figure 1 shows as an example the global distribution of atmospheric conductance $\Sigma(\varphi,\lambda)$ at 18 UT on February 1, 2009, based on considering topography, clouds, and floating ice. Its integral over the entire area of the Earth is Σ_{tot}=7.4 mS, that means R_{tot} =135 Ohms. Without clouds Σ_{tot}=8.8 mS, that means R_{tot} =114 Ohms. This means that at this point in time, the cloudiness has increased the total resistance of the atmosphere by 18%. It could be expected. The surprise is that this increase has such small variations during a year, only $\pm$2.5% if every two hours interval during a year is studied or even only $\pm$1% after monthly averaging of these values obtained for the same moment of UT. Because of (7) the fair-weather electric field strength above sea E_0^{sea} is proportional to R_{tot} when generators of GEC are not varied. So this 2% is negligible in comparison with variations $\pm$25% of E_0^{sea} presented by the Carnegie diagram in [1].

It is shown by the actual simulation that cloudiness reduces the total conductance of the atmosphere by about 20%. Its variations during the day and year are so small that the model fair-weather electric field varies only by 2% due to cloudiness. It is an order of magnitude less than the usual variations of the fair-weather electric field strength.

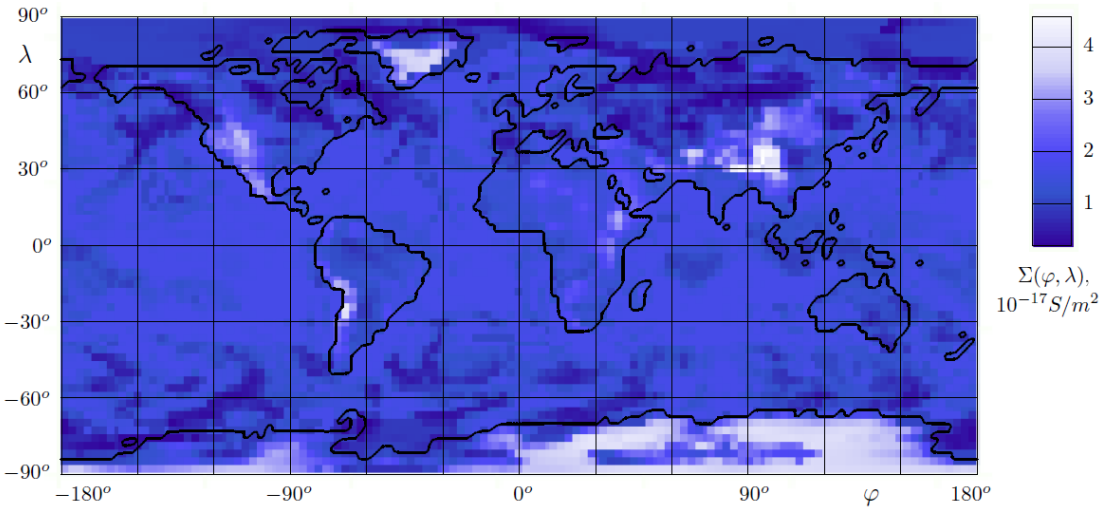


FIGURE 1. Global distribution of atmospheric conductance $\Sigma(\varphi, \lambda)$ at 18 UT on Feb. 1, 2009.

The constructed model of atmospheric conductance makes it possible to find global distributions of the return currents that transfer charge from the ionosphere to the ground in the frame of the Global electric circuit.

This work is supported by the Krasnoyarsk Mathematical Center and financed by the Ministry of Science and Higher Education of the Russian Federation in the framework of the establishment and development of regional Centers for Mathematics Research and Education (Agreement No. 075-02-2025-1606).

1. Denisenko V.V. Rycroft M.J. Seasonal Dependence of the Equatorial Electrojets Generated by Thunderstorms. // *Advances in Space Research.* 2024. V. 73. No. 7. P. 3464-3471. DOI: 10.1016/j.asr.2023.08.017.
2. Harrison R.G., Nicoll K.A., Mareev E., Slyunyaev N., Rycroft M.J. Extensive layer clouds in the global electric circuit: their effects on vertical charge distribution and storage. // *Proceedings of the Royal Society A.* 2020. V. 476, 20190758. DOI: 10.1098/rspa.2019.0758.
3. Sukhodolov T., Egorova T., Stenke A., Ball W.T., Brodowsky C., Chiodo G., Feinberg A., Friedel M., Karagodin-Doyennel A., Peter T., Sedlacek. J., Vattioni S., Rozanov E. Atmosphere-Ocean-Aerosol-Chemistry-Climate Model SOCOLv4.0: description and evaluation. // *Geoscientific Model Development.* 2021. V. 14, P. 5525-5560. DOI: 10.5194/gmd-14-5525-2021.
4. Stevens B., Giorgetta M.A., Esch M., Mauritsen T., Crueger T., Rast S., Salzmann M., Schmidt H., Bader J., Block K., Brokopf R., Fast I., Kinne S., Kornblueh L., Lohmann U., Pincus R., Reichler T., Roeckner E. The atmospheric component of the MPI-M Earth System Model: ECHAM6. // *Journal of Advances in Modeling Earth Systems.* 2013. V. 5, P. 146-172. DOI: 10.1002/jame.20015.
5. Mareev E.A. Achievements and prospects of the global electric circuit. // *Physics-Uspekhi.* 2010. V. 53. P. 504–534. DOI: 10.3367/UFNr.0180.201005h.0527.

INFLUENCE OF SOLAR AND GEOMAGNETIC ACTIVITY ON TEMPERATURE STRATIFICATION OF THE MIDDLE ATMOSPHERE

Semen V. Nikolashkin, Semen V. Titov, Uigulan N. Evseev and Nikolay E. Sidorov

Yu.G. Shafer Institute of Cosmophysical Research and Aeronomy SB RAS, Yakutsk, Russian Federation

Solar activity acts as a kind of "trigger" that gives impetus to the development of various instabilities in the upper atmosphere and ionosphere. Under the influence of plasma irregularities, UV and X-ray flashes in the upper and middle atmosphere, the compositional balance is disturbed - disturbances of the ionized component of the atmosphere and the associated formation of atomic oxygen, nitrogen oxides, ozone, changes in temperature stratification, and aerosol formation lead to the appearance of turbulent irregularities in the atmospheric circulation. It has been established that this effect has an ambiguous effect on the dynamics of the atmosphere [1, 2], depending on local features of the global circulation. In winter, the stationary pattern of the global atmospheric circulation is regularly disturbed, especially in the Northern Hemisphere [3]. Quasi-stationary formations associated with the appearance of standing planetary waves caused by the passage of the average flow through the orographic irregularities of the underlying surface appear. The interaction of moving planetary waves with them leads to a strong disturbance of the circumpolar vortex and can cause impressive increases in the temperature of the polar stratosphere - the so-called sudden stratospheric warmings [4]. On the other hand, the presence of orographic inhomogeneities suggests the existence of regional features of planetary wave dissipation [5]. The fundamental property of planetary waves is that when propagating from the lower atmosphere to the overlying layers, they transfer energy and momentum. Dissipating at the heights of the middle atmosphere and thermosphere, these waves transfer energy and momentum to the environment, thereby affecting the thermal balance and zonal-average circulation of the atmosphere. Aerosols can also influence the formation of climate and atmospheric dynamics, changing the chemical composition of the atmosphere, its transparency (for example, the eruption of El Chichon and Pinatubo volcanoes). Powerful solar flares can also cause the formation of aerosols and clouds [6, 7].

To study the dependence of the lower thermosphere temperature on the solar activity level, we used data obtained during 1979–2020 at the IKFIA optical observatory in Maimaga (63N; 129.9E) on the photographic and photoelectric Fabry-Perot interferometers in the night lower thermosphere by measuring the temperature from the Doppler broadening of the 557.7 nm [OI] line profile, the maximum intensity of which is localized at an altitude of 97±2 km [8]. Observations were carried out in autumn, winter and spring from October to March. Based on the obtained data array, average winter temperatures of the lower thermosphere were calculated, assuming that temperatures obtained from October to March can be considered winter temperatures. Night temperatures observed during visible forms of polar auroras were excluded from consideration. Figure 1a, b shows a comparison of the temperature of the lower thermosphere with the daily sum of the Kp-index, where the points indicating the average values of the nighttime temperature of the 557.7 nm emission correspond to more than 40 temperature values. The average daily temperature values and the daily sum of the Kp-index are tied to the middle of the night.

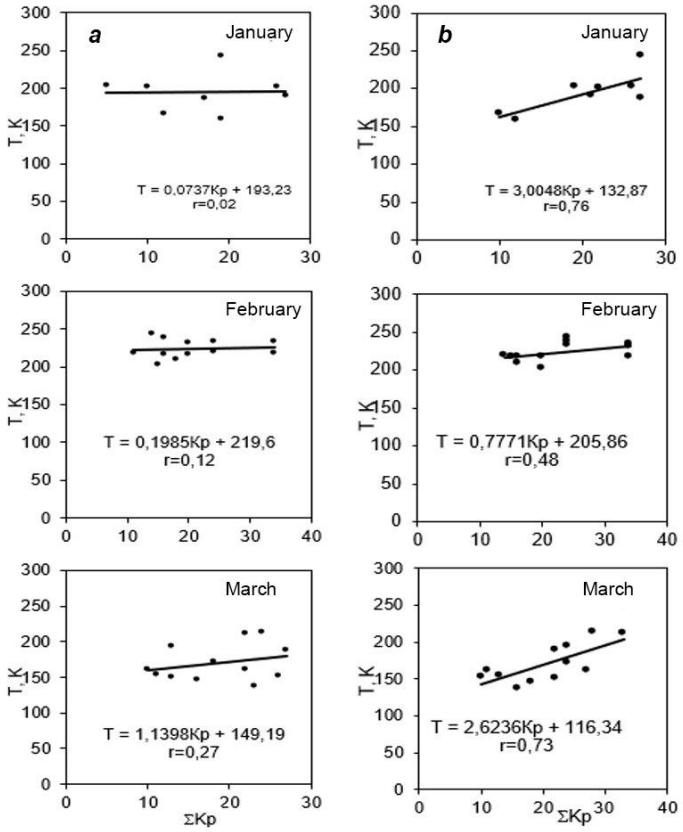


FIGURE 1. Dependence of the temperature of the lower thermosphere on geomagnetic activity (ΣKp). Straight lines are regression lines using the least squares method. The graphs show the regression equations. a – temperature and Kp index without shift; b – temperatures are shifted back by 2 days relative to Kp.

As can be seen from Figure 1a, there is no clear correlation between temperature and geomagnetic activity. But when the temperatures shift back 2–3 days relative to the daily sum of the Kp-index, there is a great similarity in the variations of the Doppler temperature and the sum of the Kp-index (Figure 1b). Thus, we can confidently say that there is some connection between the Doppler temperature and the Kp-indices. This behavior of the relationship between temperature and geomagnetic activity, shown in Figure 1, can be explained by the effect of the "aftereffect" of a magnetic storm [9-11], which is a consequence of the transfer of activated air masses that arose in the auroral zone from the high latitude region to the equatorial region.

In [12], an estimate was made of the number of oxygen atoms arising directly as a result of the effect of the corpuscular flow on the ionic composition of the lower thermosphere, and a calculation was made of the redistribution of recombination heat by altitude as a result of diffusion processes.

The reactions of dissociative recombination of molecular ions O_2^+ and NO^+ produce oxygen, the amount of which depends on the power of the polar auroras. It is natural to assume that the amount of additionally released heat depends on the concentration of atomic oxygen in the lower thermosphere; the more oxygen atoms are stored in the activated volume of air at h=90–100 km, the more intense will be the influx of heat into this region of the atmosphere. The transfer of the activated air mass in the lower thermosphere will be accompanied by a change in the concentration of chemically active gases both as a result of diffusion and as a result of chemical processes. In the case of exothermic reactions, these changes are accompanied by the release of thermal energy. One of such reactions can be considered the release of heat during the exothermic recombination of atomic oxygen in triple collision reactions [12]. One of the most important phenomena that determines variations in one or another atmospheric parameter across the planet, including meteorological parameters, is the so-called quasi-biennial oscillations (QBO). It has now been established that QBO phases to one degree or another affect the entire planetary atmospheric dynamics, including the polar regions and the upper layers of the atmosphere [5,13,14].

To determine the relationship between the temperature T557.7 of the lower thermosphere and the F10.7 index, all temperature values were averaged during the night and grouped by seasons (winter, spring, autumn) separately for the eastern and western phases of the QBO. Data on the QBO phases are

taken from [15], as well as the new NOAA/ESRL QBO indices (https://www.esrl.noaa.gov/psd/data/correlation/qbo.data).

For each season and a specific QBO phase, the average long-term values of temperature *Tc* were found. Then, the average seasonal values of temperature *Tc* were subtracted from the initial average nighttime values of temperatures *Ti* for each season and a specific QBO phase. The resulting differences $\Delta T_i = T_i - T_c$ were divided into groups corresponding to the values of the F10.7 index equal to 60–80, 80–100 to 240–260 sfu. After that, the average ($\Delta \overline{T}$) and standard deviations were calculated in each group. Figure 2 shows the results of comparison of temperatures $T_{557.7}$, T_{OH}, T_{30}, and index F10.7 for the western and eastern phases of QBO. It also shows the regression lines calculated using the well-known formula:

$$T(F_{10,7}) = T_{60} + b \quad (F_{10,7} - 60),$$

where T_{60} is the temperature in calm conditions (F10.7<60), F10.7 is the average daily value of the solar activity index, changing in the range 60≤F10.7≤260, *b* - is the regression coefficient.

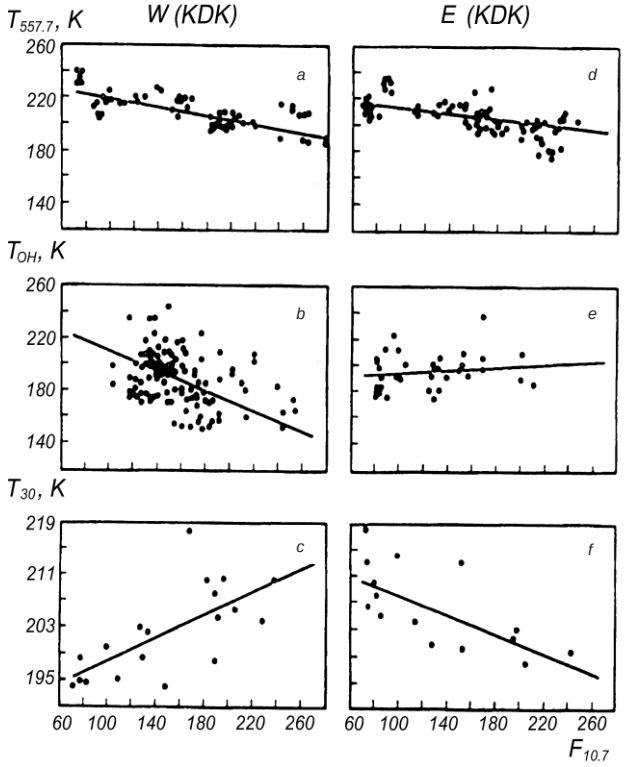


FIGURE 2. Comparison of temperatures $T_{557.7}$, T_{OH}, T_{30} with index F10.7 in the western and eastern phases of the QDC (solid lines – linear regression)

The numerical values of the coefficients included in the equation, the correlation r and their confidence probability p for the western and eastern phases of the QBO in the stratosphere, mesopause and lower thermosphere are given in the table 1. Here, the letter n denotes the number of average daily values of the stratosphere temperature and the average nighttime temperatures of the mesopause and lower thermosphere. It is evident that in the western phase of the QBO, a positive correlation is observed between the temperature and the F10.7 index in the stratosphere and a negative one in the mesopause and lower thermosphere. The anticorrelation is expressed more strongly in the mesopause than in the lower thermosphere. During the eastern phase of the QBO, the correlation in the stratosphere changes to the opposite; in the mesopause, a very weak positive correlation is observed; in the lower thermosphere, the correlation changes little, i.e., it remains negative.

TABLE 1. Numerical values of the regression coefficients *T60*, *b*, correlation *r* and confidence probability *p* at different altitude levels in the western and eastern phases of the QBO

Temperature	QBO	*n*	T_{60}, K	*b*, K/$F_{10,7}$	*r*	*p*
T_{30}	W	1121	194,5 (±3,7)	0,08 (±0,022)	0,682	0,577
	E	885	211,0 (±2,5)	–0,07 (±0,017)	–0,748	0,981
T_{OH}	W	117	226,6 (±18,6)	–0,391 (±0,117)	–0,861	0,961
	E	35	192,1 (±16,3)	0,053 (±0,135)	0,278	0,963
$T_{557,7}$	W	67	225,2 (±9,1)	–0,159 (±0,054)	–0,826	0,976
	E	77	217,2 (±8,8)	–0,101 (±0,058)	–0,652	0,980

The complex wave pattern obtained in this realistic simulation demonstrates the need to improve the existing parametrizations of atmospheric waves or develop new approaches to take these waves into account in numerical models. And it will also provide characteristics of the source of meteorological disturbance, which can be used in large-scale models of the upper atmosphere.

This investigation was performed with the financial support by State assignment № 122011700172-2.

1. Morozova A.L., Pudovkin M.I. Climate of Central Europe in the 16th-20th centuries and secular variations in solar activity // *Geomagnetism and Aeronomy*. 2000. V. 40. No. 6. P. 68-75.
2. Tinsley B.A., Heelis R.A. Correlations of atmospheric dynamics with solar activity evidence for a connection via the solar wind, atmospheric electricity, and cloud microphysics // *J. Geophys. Res. Atmospheres*. 1993. V. 98. Is. D6. P. 10375-10384. DOI:10.1029/93JD00627.
3. Labitzke K. Sunspots, the QBO and stratospheric temperature in the North polar region // Geophys. Res. Lett. 1987. V.14. Is. 5. P. 535-537. DOI: 10.1029/GL014i005p00535.
4. Matsuno T. A. A dynamical model of the stratospheric sudden warming // *J. Atmos. Sci*. 1971. V. 28. Is. 8 P.1479-1494. DOI: 10.1175/1520-0469(1971)028<1479:ADMOTS>2.0.CO;2.
5. Zarubin A. S., Pogoreltsev A. I. Planetary waves in the winter stratosphere of the Northern Hemisphere based on observational data from the COSMIC experiment // Scientific Notes of the Russian State Hydrometeorological University. 2012. No. 26. P. 91–99.
6. Kukoleva A. A., Kononova N. K., Krivolutsky A. A. Manifestation of the solar activity cycle in the circulation characteristics of the lower atmosphere of the Northern Hemisphere // *Geomagn. Aeronom*. 2018. V. 58. No. 6. P. 775–783. DOI: 10.1134/S0016793218060087.
7. Skryabin N. G. Possible physicochemical amplifying mechanism of solar-terrestrial relations. // Preprint IKFIA SB USSR AS. Yakutsk. 1980.
8. Ignat'ev V.M., Nikolashkin S.V., Yugov V.A., etc. A high-luminosity Fabry-Perot spectrometer // *Instruments and experimental equipment*. 1998. Vol. 41. No. 4. P. 544.
9. Shefov N.N. Non-corpuscular nature of ionospheric warming occurring at mid-latitudes after geomagnetic storms // Aurorae and night airglow. Moscow: Sovetskoye Radio. 1978. No .27. P. 36–44.
10. Ramakrishna S., Seshamani R. Mesospheric Temperature Response to Variations in Geomagnetic Activity // *Planet.Space Sci*. 1973. V.21. P.1447–1453. DOI: 10.1016/0032-0633(73)90235-3.
11. Mayr H.G., Volland H. Composition waves in the thermosphere // *J. Geophys. Res*. 1976. V.81. P. 671–676. DOI: 10.1029/JA081i004p00671.
12. Büttner E.K., Dmitrieva L.K. On the distribution of atomic oxygen in the winter polar mesosphere // Geomagnetism and Aeronomy. 1968. V.8. N. 4. P.688–696.
13. Shefov N.N., Relations between the Hydroxyl Emission of the Upper Atmosphere and Stratospheric Warming // Gerlands Beitr. Geophys. 1973. V. 82. P. 111–114.
14. Chanin M.L. A Review of the 11-year solar cycle, the QBO, and atmosphere relationship // In: J. Lastovichka (Ed.) Middle Atmosphere Program, Handbook for MAP, ICSU SCOSTEP. 1989. V. 29. P. 1. P. 27–30.
15. Labitzke K. A Note from Working Group 5.1 – DECADAL (Decadal Atmospheric Variation Project) // Solar – Terrestrial Energy Program. 1994. V.4. N6. P. 1–2.

IONOSPHERE BETWEEN MESO– AND TURBOPAUSE: IDEAS, EXPERIMENTS, NEW RESULTS

Nataliya V. Bakhmetieva, Gennady I. Grigoriev, Ilia N. Zhemiakov, Elena E. Kalinina, and Aleksandr A. Lisov

Radiophysical Research Institute Nizhny Novgorod State University, Nizhny Novgorod, Russia

The work is devoted to the studies of the Earth's mesosphere and lower thermosphere in the altitude range of 50–130 km. This dynamic region of the atmosphere includes the mesopause, which is characterized by a minimum of the temperature of the neutral component, and the turbopause as the altitude at which turbulent mixing of gas components is replaced by their diffusion separation. At the same time, these altitudes of the ionosphere are occupied by the D-region (50–90 km) and the E-region (90–150 km). A large number of atmospheric and ionospheric phenomena occur in this altitude range.

The paper presents the results of a study of the characteristics of the neutral and ionized components of this region of the atmosphere. In order to study this part of the Earth's atmosphere and the phenomena occurring in it, the NIRFI UNN has developed and included into the practice of ionospheric research a method based on the controlled impact on the ionospheric plasma of powerful HF radio emission from the SURA heating facility (56.1°N; 46.1°E) with the creation of artificial periodic irregularities (APIs) of the ionospheric plasma. Scattering of probe radio waves on the APIs allows us to study the state of the mesosphere and lower thermosphere in different heliogeophysical conditions and determine the most important characteristics of the neutral and ionized components of the atmosphere [1].

Fig. 1 demonstrates variations in the amplitude of the scattered signal at the stage of relaxation of irregularities at sunset and sunrise at altitudes of 60–120 km. Variations in the scattered signal show stratification of the E-region, sunset-sunrise asymmetry of the D-region. Atomic oxygen at altitudes of 78–85 km prevents the API formation, resulting in the cessation of them [1, 2]. This allows us to determine the lower limit of the appearance of atomic oxygen in different ionospheric conditions.

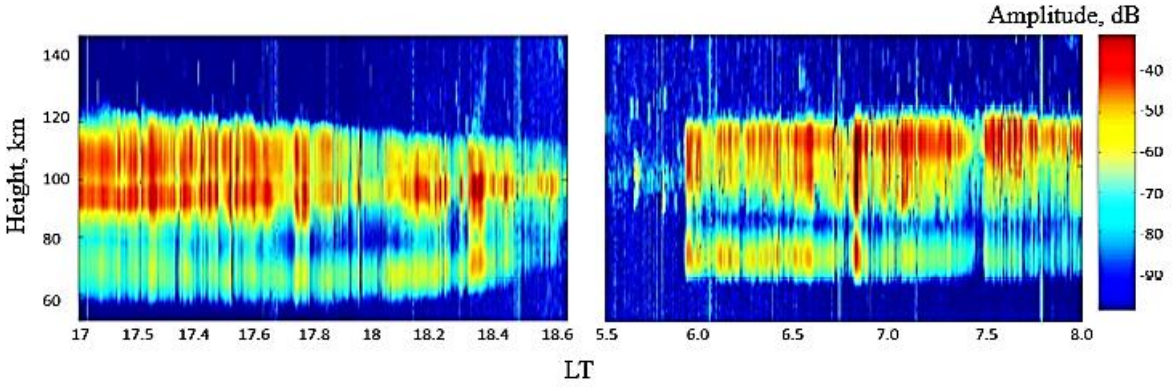


FIGURE 1. Amplitude of the API scattered signal versus height and time in the mesosphere and lower thermosphere at sunset on September 24, 2024 and sunrise on September 25, 2024.

The region of the mesosphere and lower thermosphere is characterized by developed dynamics, which is manifested in variations of parameters of the ionized and neutral components and the in stratification of the D- and E-regions. Dynamic phenomena are especially strong on days of disturbances in the ionosphere, for example, associated with a solar eclipse. The API method observed similar stratification in the E-region, including the sporadic E layer (E_s). An example of the layered structure of

the D- and E-regions is shown in Fig. 2. Probably, such stratification is caused by the interference of signals scattered by API, sporadic E layers and natural large-scale ionospheric irregularities [1].

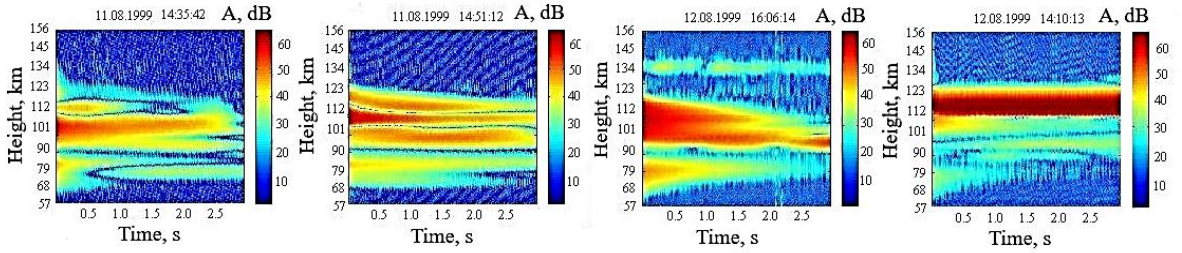


FIGURE 2. Time-height-intensity plot of the API scattered signal, including the period of the solar eclipse on July 11, 1999 and the next day July 12, 1999. These are examples of the complex structure of the D- and E-regions and the stratification of the sporadic E layer.

The velocity of vertical plasma motion at altitudes of 50–130 km coincides with the velocity of the neutral component [3]. Fig. 3 shows an example of velocity variations for two days in September 2024. Here, the measured velocity values are averaged over a 5-minute time interval with an altitude step of 1.4 km. Significant differences in velocity variations in magnitude and direction can be seen on different days (positive velocity values correspond to downward motion). Fig. 3 shows periodic velocity variations caused by the propagation of acoustic-gravity waves. The altitude gradient of the desired sign of velocity ensures the formation of a sporadic E layer.

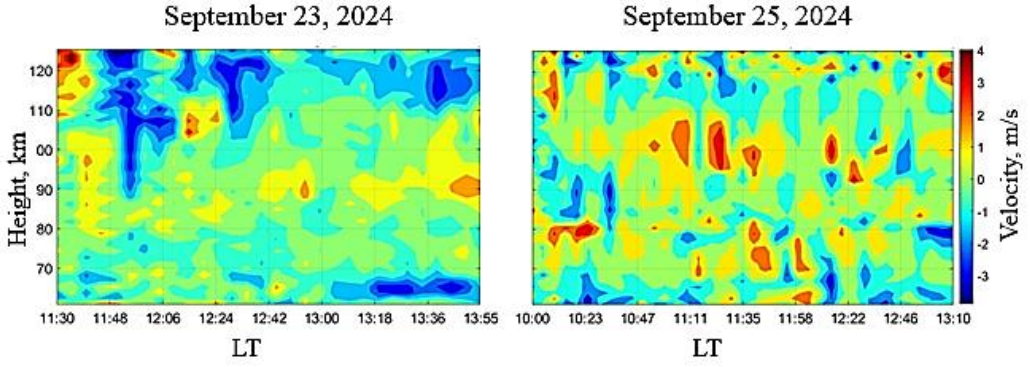


FIGURE 3. The height-time dependence of the vertical velocity during daylight hours on September 23, 2024 and on September 25, 2024.

Turbulence has a great influence on the state of the mesosphere and lower thermosphere [1–4]. An example of altitude variations of turbulent velocity below the turbopause level is shown in Fig. 4.

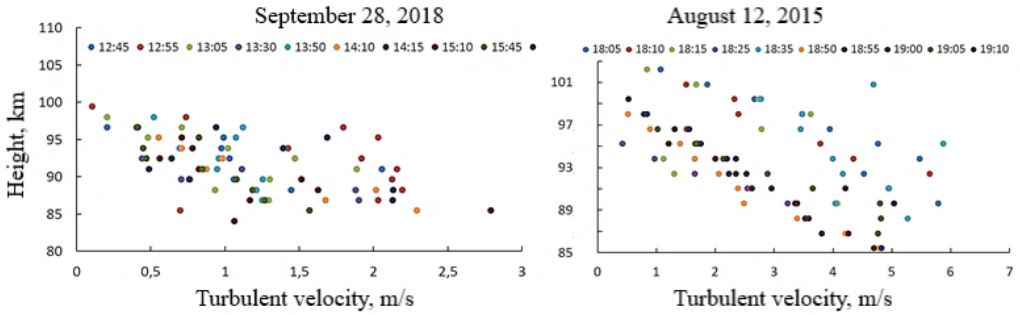


FIGURE 4. The turbulent velocity versus height on August 12, 2015 and September 28, 2018 below the turbopause level. It can see the turbulent velocity can reach 3–4 m/s, increasing up to 5–7 m/s at certain times, that is, a value close to the regular vertical velocity of the environment.

It was found that turbulent velocity decreases with altitude, approaching zero at the turbopause heights. It can reach 5–7 m/s at the mesopause level. In magnitude, turbulent velocity is comparable to the velocity of regular vertical movement of the environment. As a result, anomalies of the neutral component temperature appear, caused by a complex dynamic regime at altitudes between the meso- and turbopause levels. An example of time variations of the turbopause level is shown in Fig. 5.

The turbopause level can vary greatly over time. Fig. 5 shows wave-like changes in the turbopause level from 87 km to 108 km. The low values of the turbopause level in some cases mean that the diffusion separation of gases can begin below the usual heights, and the meso- and turbopause levels can converge in height.

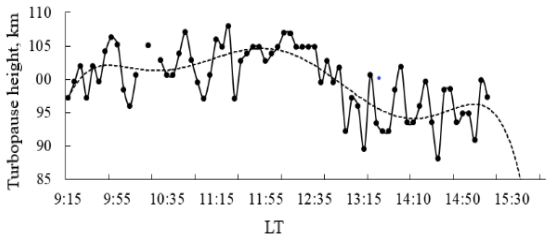


FIGURE 5. The time variations of the turbopause level on October 26, 2018.

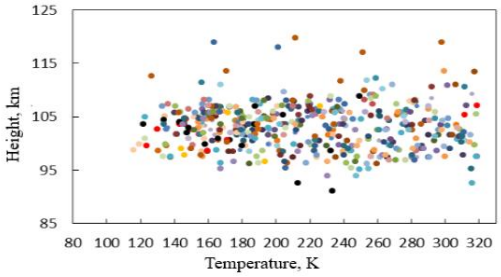


FIGURE 6. Neutral temperature and density on October 25, 2022

The most important characteristic of the atmosphere is the temperature of the neutral component. The API method allows it to be determined, as a rule, in the altitude range of 90–130 km. A limitation of the method is the need to exclude the influence of atmospheric turbulence and the sporadic E layer [5]. Figure 6 shows temperature variations over 7 hours of observations at altitudes of 90–120 km. Typically, at these altitudes, the temperature experiences deep variations, changing from 120 to 320 K.

The dependence of temperature on altitude has a complex form (Fig. 7). Local minima and maxima of temperature are observed. Measurements over many years have shown that sometimes a local minimum appears at altitudes of 88–90 km, which is close to the level of the traditional mesopause. In other cases, it is located at altitudes of 100–105 km. This may probably confirm the hypothesis of the two-level nature of the mesopause [6].

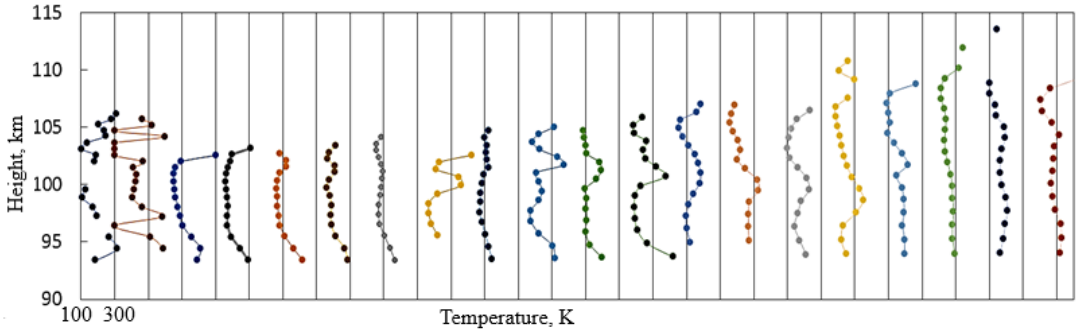


FIGURE 7. Height-temperature profiles for October 24, 2024 from 05:30 to 11:00, including sunrise.

Complex studies of the ionosphere by the API method clearly showed the large variability of the ionosphere at the heights of the mesosphere and lower thermosphere, including the turbopause level, turbulent velocity, the velocity of vertical regular motion, and the temperature of the neutral component. The major influence of atmospheric waves and turbulence on the mesosphere and lower thermosphere has been convincingly confirmed. It was found that turbulent motions along with regular vertical transfer make a large contribution to the dynamics of the lower ionosphere. The turbulent velocity, which is

several m/s, is comparable in magnitude with the velocity of plasma regular vertical motion. The turbopause level is usually in the altitude range of 90–110 km and is subject to both rapid and slow variations, sometimes decreasing to a height close to the mesopause.

This investigation was performed with the financial support of the Russian Science Foundation under grant No. 15-27-00031.

1. Belikovich V.V., Benediktov E.A., Tolmacheva A.V., Bakhmet'eva N.V. *Ionospheric Research by Means of Artificial Periodic Irregularities* – Copernicus GmbH, 2002. Katlenburg-Lindau, Germany, 160 pp.
2. Bakhmetieva N.V., Grigoriev G.I. Study of the Mesosphere and Lower Thermosphere by the Method of Creating Artificial Periodic Irregularities of the Ionospheric Plasma // *Atmosphere.* 2022. Vol. 13. No. 9. P. 1346. https://doi.org/10.3390/atmos13091346.
3. Brunelli B.E., Namgaladze A.A. *Physics of the ionosphere*. M.: Nauka, 1988. 528 p. (In Russian).
4. Lehmacher G.A., Scott T.D., Larsen M. F., Bilén S.G.,Croskey C. L., Mitchell J.D., Rapp M., Lübken F.-J., Collins R.L. The Turbopause experiment: atmospheric stability and turbulent structure spanning the turbopause altitude // *Ann. Geophys*. 2011. V. 29. No.12. P. 2327–2339. https://doi.org/10.5194/angeo-29-2327-2011.
5. Bakhmetieva N.V., Grigoriev G.I., Zhemyakov I.N., Kalinina E.E. Artificial Periodic Irregularities and Temperature of the Lower Thermosphere // *Atmosphere*. 2023.V. 14. No 5. P. 846. DOI: 10.3390/atmos14050846.
6. Vlasov M.N., Kelley M.C. Eddy turbulence, the double mesopause, and the double layer of atomic oxygen // *Ann. Geophys*. 2012. V. 30. P.251–258. DOI: 10.5194/angeo-30-251-2012.

VARIATIONS OF ATMOSPHERIC PLANETARY WAVES UNDER CONDITIONS OF DIFFERENT COMBINATIONS OF NATURAL TROPICAL OSCILLATIONS

Kseniia A. Didenko[1,2], Andrey V. Koval[2,3], Tatiana S. Ermakova[2,3], and Aleksey S. Fadeev[2]

[1]Space weather prediction center, Pushkov Institute of Terrestrial Magnetism, Ionosphere, and Radio Wave Propagation (IZMIRAN), Troitsk, Moscow, Russia
[2]Department of Atmospheric Physics, Saint Petersburg University, St. Petersburg, Russia
[3]Department of Meteorological Forecasts, Russian State Hydrometeorological University, St. Petersburg, Russia

A series of numerical experiments to study the impact of the Quasi-Biennial Oscillation phase of the zonal wind in the equatorial stratosphere (QBO) and the El Niño-Southern Oscillation (ENSO) on stationary and westward travelling planetary waves (PWs) with different zonal wave numbers and periods were performed. The simulation was carried out for boreal winter conditions using the general circulation model of the middle and upper atmosphere (MUAM). MUAM allows taking into account various boundary and background conditions when modeling the general circulation of the atmosphere [1]. Numerical modeling allowed us to carry out idealized experiment, without imposition of other atmospheric processes capable to cause erroneous results, which cannot be conducted using reanalysis measurements. Stationary PWs (SPWs) with zonal wave numbers $m = 1$ and $m = 2$ were studied, as well

as westward travelling PWs with periods of about 5-, 10-days with m = 1 and 4-,7-days with m = 2, determined according to the classification proposed by Longuet-Higgins [2].

To account the QBO in the MUAM a nudge is used, i.e. zonally averaged zonal wind fields are stepwise pushed to observations. Since the model is not able to self-consistently reproduce QBO in the stratosphere, the background and initial distributions of hydrodynamic fields, which are considered for years with different phases of QBO are set in the model. These distributions are calculated from data sets consonant with a certain phase of the QBO. Two data sets of 10 years each were obtained using the method of decomposing meteorological fields into empirical orthogonal functions (EOF) for the easterly and westerly phases of the QBO. For this work one of the latest versions of the MUAM was used, including parameterizations of atmospheric heating rates caused by the release of latent heat, which take into account both diurnal and longitude oscillations and dependence on the El Niño-Southern oscillation phase ENSO. Years corresponding to the warm El Niño phase and the cold La Niña phase were selected based on a multivariate index – MEI. Using the table of available MEI values, 5 years were selected for the conditions of the each of two ENSO phases. Temperature and geopotential fields from these two data sets were averaged and used as initial conditions in the MUAM.

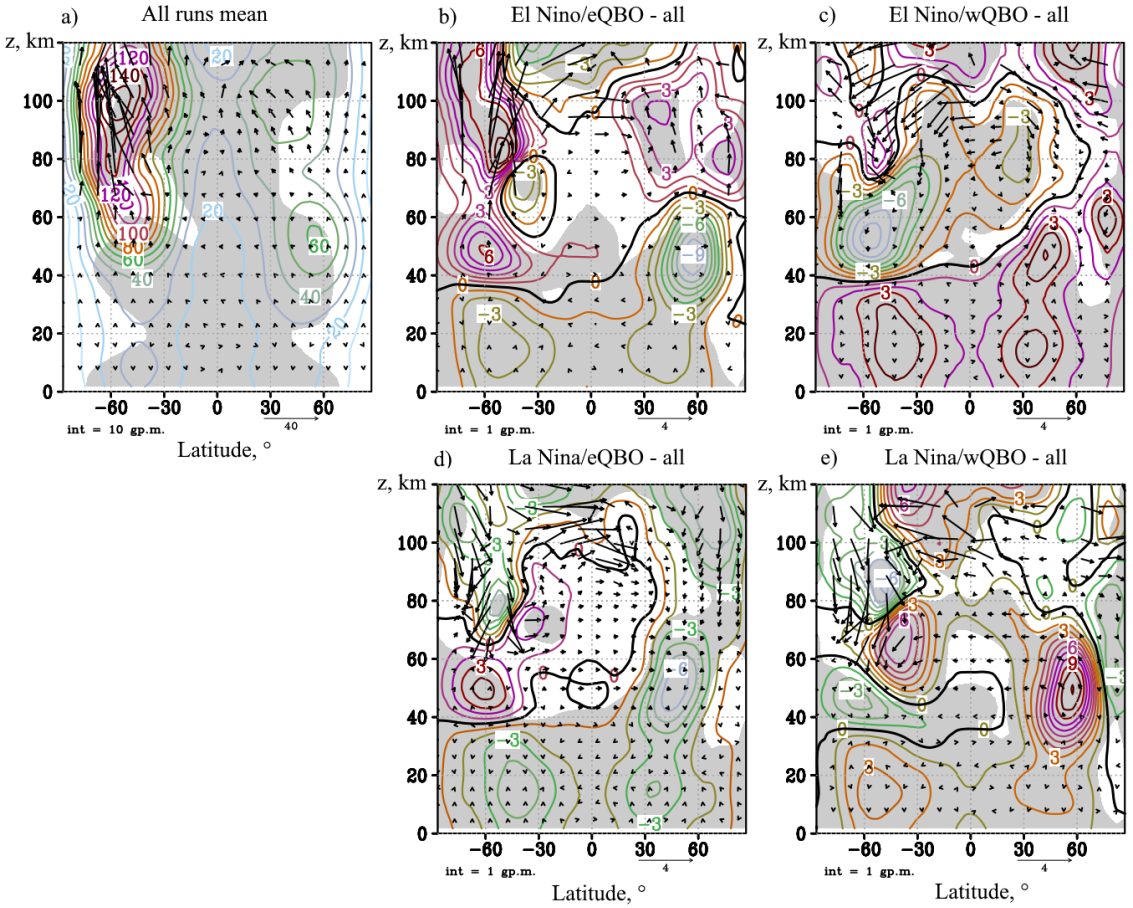


FIGURE 1. Amplitudes of the geopotential height variations (m) caused by westward travelling atmospheric PW with τ = 5 days, m = 1 (contours), EP flux in $e^{z/70}$ m^2/s^2 with multiplied vertical component by 200 (arrows) and waveguide (gray background) averaged over January–February and all MUAM simulations – a). Respective amplitude (contours) and EP flux (arrows) increments due to change of ENSO/QBO phase, 95% statistical significance (gray background) averaged over January–February and MUAM simulations under El Niño/eQBO, El Niño/wQBO, La Niña/eQBO, and La Niña/wQBO – b), c), d), and e), respectively. Intervals between contours are indicated in the left bottom corner of each plot.

To study the structures and wave activity fluxes of the SPW and westward travelling PWs under the various conditions related to the different phase combinations of tropical oscillations, the fields of hydrometeorological parameters modeled by the MUAM were used. 4 ensembles containing of 10 solutions ("runs") each were obtained, corresponding to 4 combinations of QBO and ENSO phases: El Niño/eQBO (easterly phase of QBO), El Niño/wQBO (westerly phase of QBO), La Niña/eQBO and La Niña/wQBO. For example, Figure 1 shows the calculation results for the westward travelling PW with a zonal wave number $m = 1$ and period of 5 day for January-February. Similar results were obtained for SPW1 and SPW2 (stationary planetary waves with zonal wave numbers of 1 and 2, respectively), as well as the westward travelling PW with a zonal wave number $m = 1$ and period of 10 day; with a zonal wave number $m = 2$, periods of 4 and 7 days (not presented).

Fig.1 look as follows: in the panels a) the values of the amplitudes of the corresponding PW (contours), their waveguide or regions with a positive refractive index n^2 that shows the regions of PW propagation [3, 4] (gray areas) and the vectors of the EP fluxes [5] (arrows) averaged over all 40 runs are shown, i.e. the model mean climatic values; panels b) show deviations of the amplitudes (contours) and of the EP flux vectors (arrows) of the corresponding PW in the combination of El Niño/eQBO from the model mean climatic value; panels c) – the same as on b), but under the combination of El Niño/wQBO; panels d) – the same as on b), but under the combination of La Niña/eQBO; on panels e) - the same as on b), but under the combination of La Niña/wQBO. For all deviations from the model mean climatic values 95% statistical significance was obtained and presented in panels b)-e) of Fig. 1 by gray areas and based on the Student's paired t-criterion, calculated from 40 paired values (10 model runs × 4 time subintervals) [6].

In the study of atmospheric waves and wave processes special attention is being paid to the MLT (mesosphere-lower thermosphere) region. As can be seen from panels a) of Fig. 1, interruption of PW waveguide is mainly observed in this region. The same situation is detected for the waveguides of the other waves both stationary and westward travelling. Despite this, in the MLT area waves still dominate wind and temperature regimes, and consequently, the study of their parameters in this layer is necessary to analyze the influence of PW sources and PW propagation in the lower and upper atmospheric layers.

The results of modeling under conditions of various QBO and ENSO combinations for the MLT region show similar statistically significant increases of the amplitudes of SPW1 and SPW2 under El Niño phase, regardless of the QBO phase. SPW amplitudes and wave activity fluxes under La Niña conditions vary differently, leading to more substantial contribution of the QBO phase to these changes. The variability of westward travelling PW in the MLT region is much more complex and is influenced by both ENSO and QBO phases. For example, the 5-day PW amplitudes variability in the Southern Hemisphere is mainly due to the ENSO phase, and in the Northern Hemisphere this variability is individual in each combination – Fig. 1. In turn, in structurally similar 10- ($m = 1$) and 7- ($m = 2$) day PWs, there are no statistically significant considerable amplitude increments at La Niña/eQBO. Amplitudes of 10- and 7-day PWs increase under El Niño/eQBO. The attenuation of these PW amplitudes in the MLT region is determined by the QBO phase and is observed under its westerly phase. The statistically significant variability of the 4-day PW amplitudes is subject to the QBO phase, i.e., the amplitude increases under the eQBO and decreases under the wQBO.

The results obtained show that natural tropical oscillations having origin in low latitudes impact significantly on the structure of planetary waves and their wave activity fluxes not only in the regions of their climatic maxima, but also in the entire middle atmosphere and thermosphere of both hemispheres. At the same time, unlike many other studies where the influence of QBO and ENSO on atmospheric waves is evaluated separately, this work shows that the maximum statistically significant increments of PW amplitudes and wave activity fluxes can be registered under a certain combination of QBO and ENSO phases. Further investigation of the structures, characteristics and propagation of PWs under the development of various oscillations is of great practical importance for describing the

formation mechanisms of atmospheric circulation anomalies, which in turn lead to variability of tropospheric processes associated with temperature and wind anomalies for example in the Asia-Pacific Region.

This investigation was performed with the financial support of the Russian Science Foundation (grant #25-47-00122).

1. Pogoreltsev A.I. Generation of normal atmospheric modes by stratospheric vacillations // *Izvestiya Atmos. Ocean. Phys.* 2007. V. 43. No 4. P. 423-435. DOI: 10.1134/S0001433807040044.
2. Longuet-Higgins M.S. The eigenfunctions of Laplace's tidal equation over a sphere // *Philos. Trans. R. Soc. Lond.* 1968. V. 262. P. 511-607. DOI: 10.1098/rsta.1968.0003.
3. Matsuno T. Vertical propagation of stationary planetary waves in the winter Northern Hemisphere // *J. Atmos. Sci.* 1970. V. 27. No 6. P. 871-883. DOI: 10.1175/1520-0469(1970)027<0871:VPOSPW>2.0.CO;2.
4. Albers J.R., McCormack J.P., Nathan T.R. Stratospheric ozone and the morphology of the northern hemisphere planetary waveguide // *J. Geophys. Res. Atmos.* 2013. V. 118. P. 563-576. DOI:10.1029/2012JD017937.
5. D. G. Andrews, J. R. Holton, and C. B. Leovy, *Middle Atmosphere Dynamics*, Academic Press, 1987.
6. Koval A.V. Statistically significant estimates of influence of solar activity on planetary waves. In the middle atmosphere of the northern hemisphere as derived from MUAM model data // *J. Atmos. Solar.-Terr. Phys.* 2019.V. 5. No 4. P. 53-59. DOI: 10.12737/stp-54201907.

EFFECTS OF SUDDEN STRATOSPHERIC WARMINGS ON AIRGLOW EMISSION LAYERS OVER SIBERIA

Olga S. Zorkaltseva[1], Andrei V. Saunkin[1], Roman V. Vasilyev[1] and Galina A. Gavrilyeva[2]

[1]Institute of Solar-Terrestrial Physics, Siberian Branch of the Russian Academy of Sciences, Irkutsk, Russia
[2]Institute of Cosmophysical Research and Aeronomy, Siberian Branch of the Russian Academy of Sciences, Yakutsk, Russia

Airglow, a natural atmospheric phenomenon, occurs at altitudes above 70 km due to the dissociation, ionization, and excitation of atmospheric gases under the influence of solar electromagnetic and corpuscular radiation. The study of airglow layers falls within the scope of aeronomy, a field that bridges atmospheric chemistry and physics [1]. Over time, research has expanded from understanding the spectral composition and morphology of airglow to using it for atmospheric diagnostics. Today, the study of airglow remains important for addressing global challenges such as climate change, space weather, and vertical coupling in atmosphere [2].

The intensity and structure of airglow layers are influenced by various factors, including solar activity and geomagnetic storms. Other significant factors include interactions with artificial and natural space objects such as meteors, spacecraft and seismic activity [3]. Sudden stratospheric warming SSWs are among the most remarkable dynamical events in the physical climate system. Triggered by the breaking of planetary waves propagating upward from the troposphere, these events are characterized by a rapid and substantial temperature increase and, in extreme cases, a reversal of the climatological westerly zonal-mean zonal winds associated with the stratospheric polar night jet [4]. SSWs are a

significant driver of upper-atmospheric changes, inducing pronounced warming in the stratosphere, cooling in the mesosphere, and the generation of atmospheric gravity waves.

This study investigates the effects of SSW events on variations in the intensity of atomic oxygen 557.7 nm (O) and hydroxyl (OH) airglow emissions, as well as on temperature changes in these airglow layers. The analysis is based on both ground-based and satellite observations. Ground-based data were obtained using an infrared spectrograph at the Maimaga Optical Observatory (63°N, 129.5°E) and a Fabry–Perot interferometer at the Tory Geophysical Observatory (52°N, 103°E). Satellite data were sourced from the SABER radiometer aboard the TIMED platform. To determine the timing of sudden stratospheric warming events, we analyzed ERA5 reanalysis data, specifically the zonal mean air temperature along 80°N (T) and zonal mean zonal wind at 60°N (U) at a 10 hPa pressure level, using a 2.5° × 2.5° spatial grid. SSWs can be classified as either minor or major events [4]. In this study, we focus on major SSWs, defined as events involving a reversal of the zonal-mean zonal wind at 60°N latitude. The onset date of an SSW event was defined as the day with a rapid temperature increase exceeding 5 K/day, while the termination date was defined as the day when easterly winds reverted to westerly. The central SSW date was identified as the day of maximum temperature at 10 hPa [4, 5].

To assess the influence of SSWs on the airglow layers of hydroxyl (OH) and atomic oxygen (O), we applied a composite analysis. For this purpose, data from the FPI, the infrared spectrograph, and the SABER radiometer were averaged relative to the day of maximum SSW intensity, spanning a range of ±15 days from this central date. This approach, commonly referred to as superposed epoch analysis (or composite analysis), allowed us to identify systematic changes in airglow parameters during the SSW events. Composite graphs of temperature variations were created using ground-based observations (unfortunately, the graphs for ground-based instruments are not shown due to the publication volume limitation), averaged relative to the reference date of maximum SSW activity over a ±15-day range. Day 0 is the day of maximum SSW's temperature.

Based on SABER data, the airglow layers of atomic oxygen and hydroxyl are clearly identifiable in the VER profiles. The 557.7 nm oxygen airglow layer spans altitudes of 85–100 km, with its maximum intensity occurring at approximately 95 km (Fig. 1, left). The hydroxyl airglow layer spans altitudes of 78–95 km, with its maximum intensity at around 85 km (Fig. 1, right).

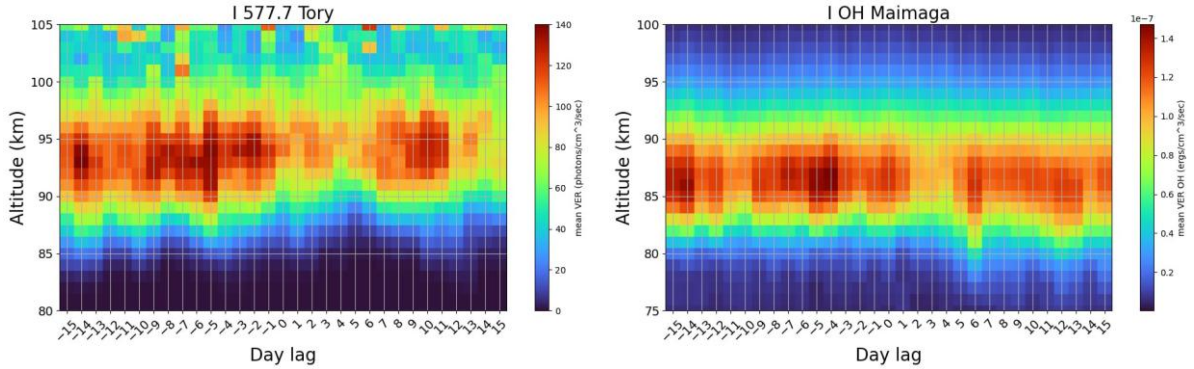


FIGURE 1. Composite cross-section of the emission intensity of atomic O at Tory and OH Maimaga by SABER data.

Prior to the SSW, elevated VER values are observed for both the oxygen and hydroxyl layers. On the day of maximum SSW's temperature (Day 0) and for 5–7 days afterward, a decrease in VER values and a thinning of the airglow layers are observed. The layers begin to recover approximately 5–7 days after the SSWs event.

The temperature behavior reveals distinct features associated with the SSWs (Fig. 2). A decrease in mesosphere temperature and simultaneous warming in the stratosphere are observed during the period from Day -3 to Day +12 relative to the SSWs maximum. This pattern aligns with the typical duration of

an SSWs, which averages about three weeks [5]. On Day 0, mesosphere warming is evident; however, the cold mesopause region expands downward, creating a noticeable vertical shift. Notably, these temperature characteristics are observed at both Siberian observatories, despite their considerable geographic separation, suggesting a regional consistency in the atmospheric response to SSW events. The geographic positioning of the observatories provides additional context for these observations. The Tory observatory, located further south than Maimaga, consistently records higher baseline temperatures in cross-sections. However, during SSWs, the temperature anomalies or the atmospheric response to the event are more pronounced over the Maimaga observatory, highlighting its sensitivity to SSWs dynamics. The stratosphere (below 50 km) warms more significantly before the central date of the SSW over Maimaga (Fig.2) and cools more substantially afterward compared to Tory. In contrast, temperature anomalies in the mesosphere become comparable over both observatories.

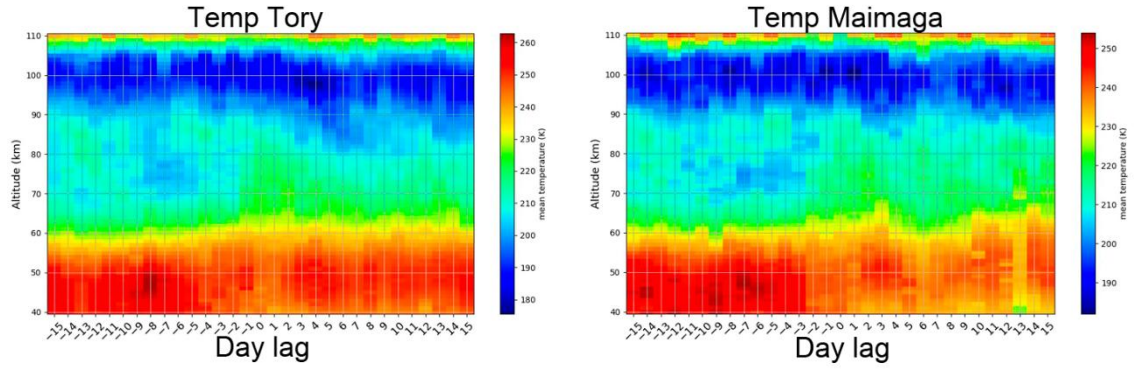


FIGURE 2. Composite cross-section of the temperature at Tory (left) and Maimaga (right) by SABER data.

To better understand the vertical structure, we calculated the average vertical profiles of temperature and VER for the altitude range of 85–100 km above Tory and 78–95 km above Maimaga. Additionally, we identified the maximum height at which the VER occurs, providing insights into the altitude-dependent response of the airglow layers during the SSW events.

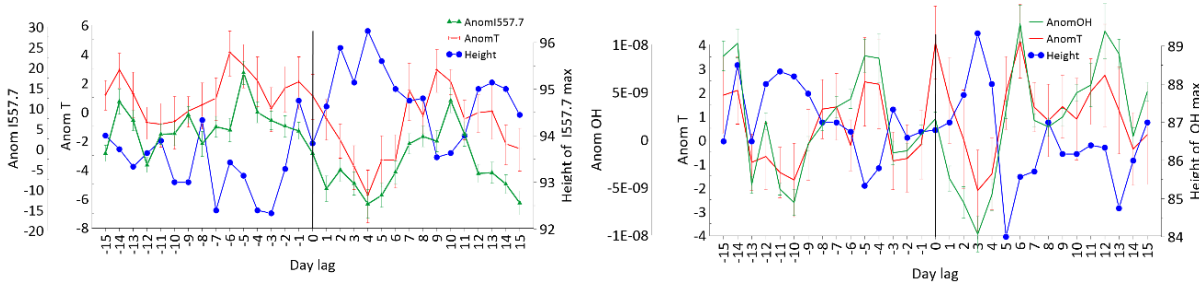


FIGURE 3. Composite variation of the temperature anomalies, VER anomalies, height of VER maximum at Tory (left) average from 85 to 100 km and Maimaga (right) average from 78 to 95 km by SABER data.

Figure 3 demonstrates a strong positive correlation between temperature and the VER, as well as a negative correlation between the maximum height of the airglow layers and both temperature and VER. During SSW events, large-amplitude planetary waves are known to propagate into the upper atmosphere from the stratosphere, altering circulation patterns and modifying the filtering of gravity waves. The alternating anomaly structure observed in cross-sections (Fig. 2-3) suggests adiabatic processes. Prior to Day 0 of the SSWs, there appears to be compression (increased density) in the stratosphere, rarefaction (decreased pressure) in the mesosphere, and compression in the thermosphere. After the

SSWs, these dynamics are reversed. This suggests that temperature variations in the mesosphere and thermosphere are likely driven by adiabatic cooling or heating, depending on stratospheric dynamics.

The observed increase in temperature and VER, accompanied by a decrease in the maximum height of the airglow layers (Fig.3), aligns with the concept of adiabatic compression. Conversely, the maximum height of the airglow layers occurs around Day +3 to +4 after the SSWs peak (Day 0), coinciding with the lowest temperature and intensity values. This reflects adiabatic expansion, where the temperature decreases and, according to the Barth mechanism, the VER diminishes. The alternating structure of temperature anomalies can be attributed to the weakening of the meridional component of the residual mean circulation (RMC), as discussed in studies such as Laskar [6] and Bal [7]. This, in turn, alters the vertical component of the RMC: a weakened descending branch below the mesopause contributes to adiabatic cooling, while a strengthened branch above the mesopause leads to adiabatic heating [8].

This investigation was performed with the financial support by the Russian Science Foundation, Project no. 22-77-10008 "Studies of large-scale events in the lower and middle atmosphere and estimate of their local influence at the heights of the mesosphere-lower thermosphere".

1. Brasseur G., Solomon S. Aeronomy of the Middle Atmosphere Chemistry and Physics of the Stratosphere and Mesosphere // *Third ed., Dordrecht: Springer*. 2005, pp.1–51.
2. Khomich V. Y., Semenov A. I., Shefov N. N. Airglow as an indicator of upper atmospheric structure and dynamics // *Springer Science & Business Media*. 2008. pp.661–703.
3. Mikhalev A. V. Manifestation of solar activity and dynamics of the atmosphere in variations of 577.7 and 630.0 nm atmospheric emissions in solar cycle 24 // *Solnechno-Zemnaya Fizika*. 2020. V. 6. Iss. 3. P. 81–85. DOI: 10.12737/szf-63202011.
4. Butler A. H., Seidel D. J., Hardiman S. C., Butchart N., Birner T., Match A. Defining Sudden Stratospheric Warmings // *Bull. Amer. Meteor. Soc.* 2015. V. 96. Is. 11. P. 1913-1928. DOI: 10.1175/BAMS-D-13-00173.1.
5. Zorkaltseva O. S., Vasilyev R.V. Stratospheric influence on MLT over mid-latitudes in winter by Fabry-Perot interferometer data // *Ann. Geophys.* 2021. V. 39. Is. 1. P. 267–276. DOI:10.5194/angeo-39-267-2021.
6. Laskar F., McCormack I., Chau J.P., Pallamraju J.L., Hoffmann D.P., Singh R.P. Interhemispheric Meridional Circulation During Sudden Stratospheric Warming // *J. of Geophysical Research: Space Physics*. 2019. V. 124. Is. 8. P. 7112-7122. DOI:10.1029/2018JA026424.
7. Bal S., Schimanke S., Spangehl T., Cubasch U. Enhanced residual mean circulation during the evolution of split type sudden stratospheric warming in observations and model simulations // J. Earth Syst. Sci. 2018. V. 127. Is. 68. DOI: 10.1007/s12040-018-0972-x.
8. Koval A.V., Chen W., Didenko K.A., Ermakova T.S., Gavrilov N.M., Pogoreltsev A.I., Toptunova O.N., Wei K., Yarusova A.N., Zarubin A.S. Modelling the residual mean meridional circulation at different stages of sudden stratospheric warming events // *Ann. Geophys*. 2021. V.39. Is. 2. P. 357-368. DOI: 10.5194/angeo-39-357-2021.

THE INFLUENCE OF ATMOSPHERIC FACTORS ON THE CONDITIONS OF PROPAGATION OF VLF SIGNALS

Iliya A. Ryakhovsky[1,2], Olga P. Borchevkina[1] and Jury V. Poklad[1]

[1]Kaliningrad Branch of Pushkov Institute of Terrestrial Magnetism, Ionosphere and Radio Wave Propagation, Russian Academy of Sciences, Kaliningrad, Russian Federation
[2]Sadovsky Institute of Geospheres Dynamics, Russian Academy of Sciences, Moscow, Russian Federation

Numerous geophysical processes affecting the state and dynamics of the lower ionosphere also have a significant impact on the propagation of electromagnetic waves in the very low frequency range (VLF, 3–30 kHz). Signals in this range are capable of traveling vast distances in a waveguide formed by the Earth's surface and the lower ionosphere with minimal energy loss, while demonstrating high sensitivity to any changes in the D-region (60–90 km). Due to this feature, the analysis of variations in the amplitude and phase of VLF signals allows for both qualitative and quantitative assessment of the processes occurring in the lower ionosphere. Thus, monitoring VLF signals is one of the most effective methods for remote sensing of the lower ionosphere.

To monitor the state and dynamics of the lower ionosphere, the Ulyanovka Observatory in the Kaliningrad Region has been continuously recording the amplitude and phase of VLF transmitter signals located around the world since June 2021. Figure 1 shows the layout of the receiver of the Ulyanovka observatory in the Kaliningrad region and the VLF transmitters GQD (22.1 kHz), GBZ (19.6 kHz) and NAA (24 kHz).

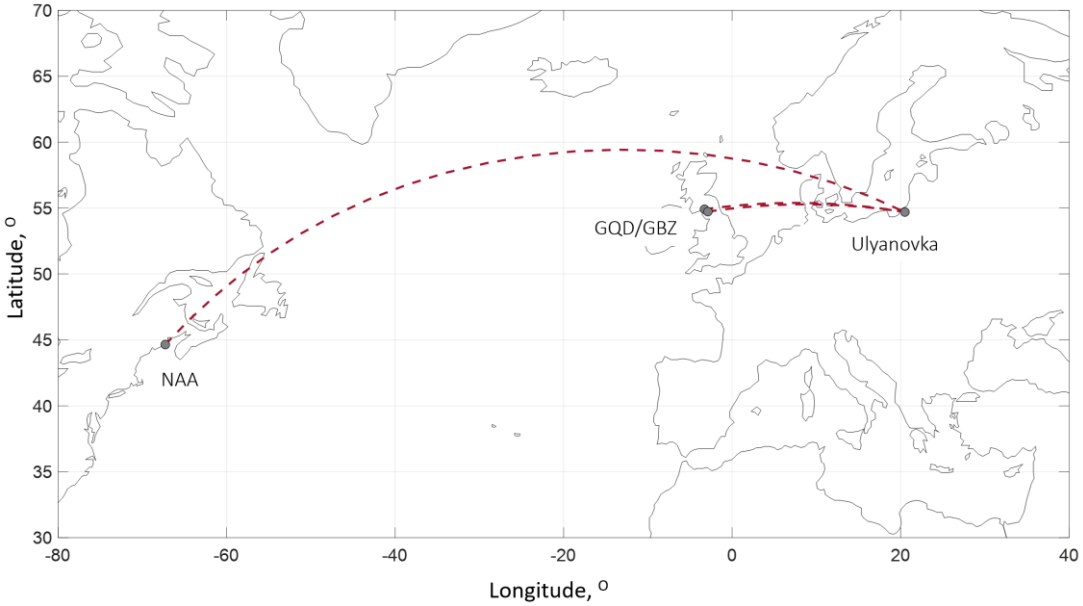


FIGURE 1. Scheme of the receiver of the Ulyanovka observatory in the Kaliningrad region and the VLF transmitters GQD (22.1 kHz), GBZ (19.6 kHz) and NAA (24 kHz).

Between 14 and 22 February 2022, northwestern Europe experienced a series of powerful storms – Dudley, Eunice and Franklin – which struck almost simultaneously [1]. To assess the impact of these storms on the propagation of very low frequency (VLF) signals, signal amplitude data from the GQD (22.1 kHz), GBZ (19.6 kHz) and NAA (24 kHz) transmitters were analyzed. The results of the GQD signal analysis are presented in Figure 2.

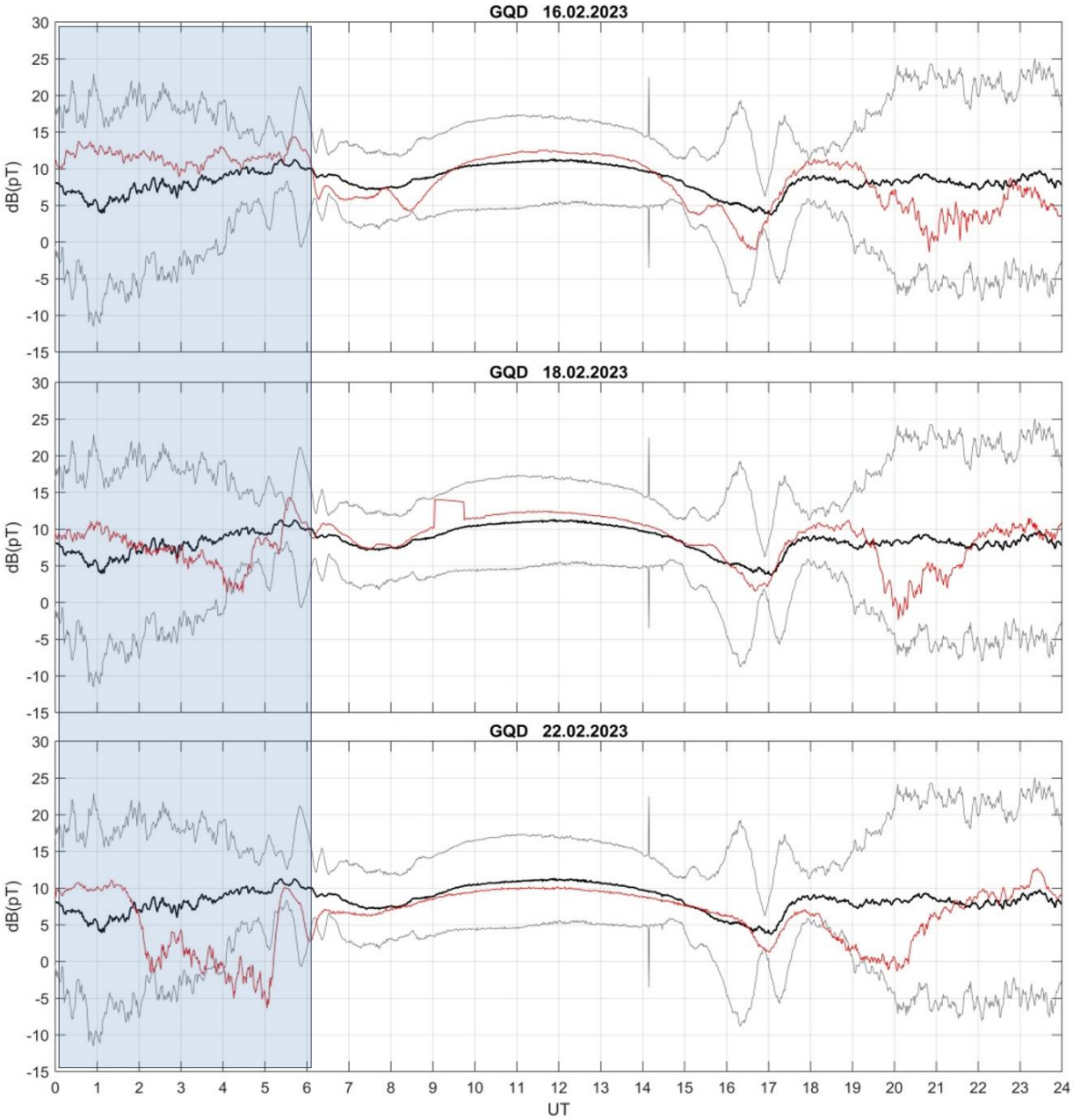


FIGURE 2. Variations in the signal amplitude from the GQD station recorded at the Ulyanovka observatory. The red curves show the daily variations of the signals for 16.02.2022 (upper panel), 18.02.2022 (middle panel) and 22.02.2022 (lower panel). The black curves are the reference signal for the period from 11 to 15 and from 24 to 28 February 2022. The gray curves are the ±3σ curves calculated for the period from 11 to 15 and from 24 to 28 February 2022.

During the period of increased storm activity on 22.02.2022, an anomalous amplitude deviation was observed along the signal propagation path during the night period, reaching the level of 3σ (Figure 2, lower panel). A similar situation was observed for signals from GBZ and NAA stations.

Figure 3 shows the change in the average value of nighttime (from 0 to 6 hours UT) signal amplitudes from NAA, GQD, GBZ stations for the period from February 12 to 27, 2022.

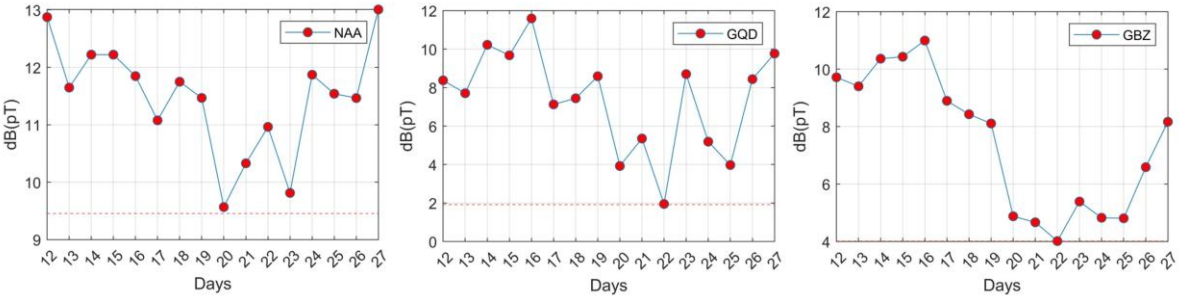


FIGURE 3. Average values of nighttime signal amplitudes from NAA (left panel), GQD (middle panel) and GBZ (right panel) stations for the period from 12 to 27 February 2022. Red horizontal dotted lines mark the minima of the nighttime signal level for the entire observation period in February 2022.

The minimum on the NAA path was observed on 20.02.2022, and on the GQD/GBZ paths - on 22.02.2022. The observed minima in the signal amplitudes at night may be associated with the presence of ionospheric irregularities caused by storm activity [2]. If the signal anomalies are associated with the passage of a storm, then it can be assumed that the disturbance moved from north to south from the NAA - KGD path to the GQD/GBZ - KGD paths.

This study was performed with financial support from the Russian Science Foundation (Project No. 23-77-10004). Experimental data were obtained within the framework of State Assignment No. 122032900175-6.

1. Met Office. (2022). Storms Dudley, Eunice and Franklin, February 2022. Retrieved from [https://www.metoffice.gov.uk/binaries/content/assets/metofficegovuk/pdf/weather/learn-about/uk-past-events/interesting/2022/2022_01_storms_dudley_eunice_franklin_r1.pdf].
2. NaitAmor S., Cohen M. B., Kumar S., Chanrion O., Neubert T. VLF signal anomalies during cyclone activity in the Atlantic Ocean // *Geophysical Research Letters*. 2018. V. 45. Is. 19. P. 10,185–10,192. DOI: 10.1029/2018GL078988.

THE ELECTRICAL ACTIVITY OF CLOUDS CRITERIA BASED ON FIELD OBSERVATIONS DATA

Alena P. Blagina and Maria V. Shatalina

Federal Research Center A.V. Gaponov-Grekhov Institute of Applied Physics of the Russian Academy of Sciences (IAP RAS), Nizhny Novgorod, Russia

Nowadays there are a lot of studies devoted to atmospheric electricity. Changes of the electric field in the atmosphere are connected with different meteorological conditions, that's why studying of the cloud electricity is so relevant. In recent years, the most attention was paid to the thunderstorm clouds which are connected with strong electric fields and dangerous natural events. Howether, clouds that are electrified but not producing lightnings may contribute significantly to the atmospheric electric field as well.

There are some works devoted to the satellite investigation [1], to the aircraft measuring of cloud electricity [2, 3], and to the numerical simulation of cloud electricity in global [4]. On the one hand,

studying of electrified clouds is necessary to investigate its contribution to the global electric circuit. On the other hand, it could help in monitoring the current state of the atmosphere including its parameters of cloudiness, precipitation and electricity, since they are closely related.

In this work we study characteristics of electrified clouds based on nature monitoring of the surface potential gradient (PG) in Nizhny Novgorod. The long-term continuous measurements of the PG using Boltek EFM-100 electric field mill are organized in the Institute of Applied Physics RAS since 2012. According to the concept of a global DC electrical circuit [5], in areas of fair weather, the current density is directed downwards, and in areas of disturbed weather, it is directed upward. In case of presence of charging processes in the cloud [6], it becomes a generator of the upward current density. Therefore, when the sign of the measured PG changes, it means that the cloud over the observation point is electrified.

To exclude an influence of precipitations onto the measured PG and analyze the only cloud-generated electric field we have chosen days without precipitations using meteorological data archive [7]. We have found 23 days during 2023 when there were no precipitation and the PG changed the sign.

We performed a detailed analysis of weather and electrical activity in the atmosphere during the selected days using EFM data, meteorological radar data, numerical simulation of the atmospheric state with WRF model [8] and lightning activity data from WWLLN [9]. An example of the data for one of the selected days is shown at Fig. 1. Three preliminary types of electrified clouds were determined, a nearby thunderstorm, an isolated electrified cloud itself, and a group or front of cumulus clouds without a thunderstorm. All of these types need an accurate and complex investigation.

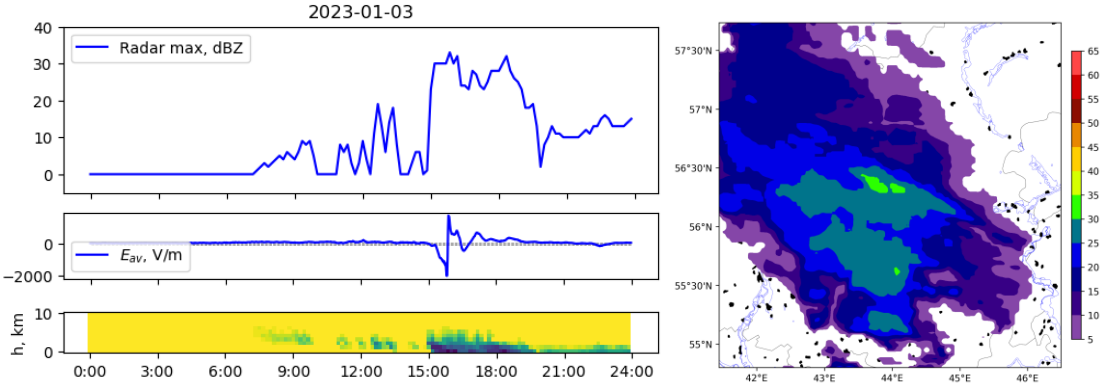


FIGURE 1. Results of complex monitoring of various characteristics of the atmosphere, 3 January, 2023. Left, up to down: maximum of the radar reflectivity of the atmosphere over the observation point; PG variations (1 min averaged); vertical cross section of the radar reflectivity. Right: contours of maximum radar reflectivity over Nizhny Novgorod region 3 January, 2023 at 15:40 (UTC+3).

The work is supported by the state assignment of the IAP RAS No. FFUF-2024-0036.

1. Liu C., Williams E.R., Zipser E.J., Burns G. Diurnal Variations of Global Thunderstorms and Electrified Shower Clouds and Their Contribution to the Global Electrical Circuit. // *Journal of the Atmospheric Sciences.* 2010. V. 67. No 2. P. 309-323. DOI: 10.1175/2009JAS3248.1.
2. Mach D. M., Blakeslee R. J., Bateman M. G., Bailey J. C. Electric fields, conductivity, and estimated currents from aircraft overflights of electrified clouds // *J. Geophys. Res*. 2009. V. 114. Art. no. D10204. DOI:10.1029/2008JD011495.
3. Torgunakov R.E., Mikhailovsky Yu.P., Sinkevich A.A. Airplane studies of electric field strength and aircraft charge in convective clouds at an early stage of development // *Proceedings of the Voyeykov Main Geophysical Observatory named after*. 2017. No 587.

4. Ilin N.V., Slyunyaev N.N., Mareev E.A. Toward a realistic representation of global electric circuit generators in models of atmospheric dynamics. // *Journal of Geophysical Research: Atmospheres.* 2020. V. 125, Art. no. e2019JD032130. DOI: 10.1029/2019JD032130.
5. Williams E., Mareev E. Recent progress on the global electrical circuit // *Atmospheric Research*. 2014. V 135–136, P. 208-227. DOI: 10.1016/j.atmosres.2013.05.015.
6. Saunders C. P. R. Charge separation mechanisms in clouds. // *Space Sci. Rev* 2008. V. 137. P. 335–353. DOI:10.1007/s11214-008-9345-0.
7. URL: https://rp5.ru/Weather_archive_in_Nizhny_Novgorod.
8. WRF model URL: https://www.mmm.ucar.edu/weather-research-and-forecasting-model.
9. World Wide Lightning Location Network. URL: http://wwlln.net/.

STARVISOR: A NIGHT SKY OPTICAL MONITORING PROJECT

Ilya S. Yankovsky, Igor A. Nosikov, Aleksandr V. Timchenko and Maksim V. Klimenko

West Department of Pushkov Institute of Terrestrial Magnetism, Ionosphere and Radio Wave Propagation, Russian Academy of Sciences, Kaliningrad, Russia

Abstract. This paper presents a description of the project “Starvisor - Night Sky Patrol”, which is a system of optical observation of the night sky. The project’s network of cameras distributed throughout Russia allows recording atmospheric and astronomical events. A distinctive feature of the project is free access to observation data in real time, as well as a system of automatic registration and notification of events and phenomena in the night sky.

Introduction. Along with radiophysical instruments of observing the parameters of the upper atmosphere, one of the main types of upper atmosphere monitoring is the optical observation method. Many structures in the distribution of the atmospheric parameters have been identified using optical measurements. For example, the morphology of the dependence of polar lights (precipitating high-energy particles) on local time, latitude and geomagnetic activity has been studied [1]; the coldest region in the entire atmosphere of the Earth, reflected in the formation of noctilucent clouds, has been identified [2].

At present, a small number of scientific organizations in Russia provide continuous (but solar-irradiance-dependent) monitoring of optical phenomena in the upper atmosphere: IKFIA SB RAS, Yakutsk [3]; ISTP SB RAS [4], Irkutsk; PGI, Apatity [5]. Along with professional scientific research of optical phenomena in the upper atmosphere, there has been a trend towards increasing the role of citizen science in identifying new phenomena. Thus, some optical phenomena in the upper atmosphere were discovered by amateur photographers: red sprites [6]; STEVE [7].

The goal of the STARVISOR project is to create a system for monitoring atmospheric phenomena in the night sky, uniting communities of amateur astronomers, volunteers, citizen scientists and researchers in Russia and abroad. STARVISOR is a system for automated monitoring of night sky phenomena using a distributed network of cameras installed throughout Russia. The main focus is on observing auroras (rays, coronas, omega-structure, SAR-arcs, etc.), mesospheric and polar stratospheric clouds, atmospheric glow, meteor activity and thunderstorms of the upper atmosphere (sprites, elves, jets, etc.).

Equipment and methodology of the STARVISOR project. The project uses a network of 32 cameras installed in various regions of Russia. The cameras are equipped with sensitive image sensors, high-aperture wide-angle optics and software for recording and transmitting data to the server. The

cameras have a geographic reference and a fixed direction, as well as time synchronization with the network. Every day, the project automatically operates with more than 100 GB of data, which is sorted, archived and processed without human intervention. Based on the collected data, timelapses and keograms are created every day, reflecting the change in the dynamics of the observed phenomena in a convenient visual form. Some of the cameras are part of the automatic polar lights detection subsystem, which recognizes the phenomenon using machine learning and transmits an alert via an established communication channel.

Camera network. The project's geography covers regions of Russia from the Kaliningrad region to the Chukotka, from the Arctic to the low latitudes of the Caucasus. The highest density of cameras is concentrated in the European part of Russia and the Urals. The current task is to expand the network in Siberia and to the Far East. The possibility of installing cameras abroad is being considered. Current list of cameras: 67°N, 64°E Vorkuta, Komi; 65°N, 111°E Aihal, Yakutia; 64°N, 173°W Provideniya, Chukotka Autonomous Okrug; 61°N, 77°E Strezhevoy, Tomsk region; 60°N, 30°E Pyatirechye, Leningrad region; 60°N, 30°E Vaskelovo, Leningrad region; 59°N, 57°E Berezniki, Perm region; 59°N, 39°E Vologda (western horizon); 59°N, 39°E Vologda; 59°N, 39°E Vologda (eastern horizon); 58°N, 56°E Permian; 57°N, 38°E Popovo, Yaroslavl region; 57°N, 39°E Yaroslavl; 57°N, 40°E Utkino, Yaroslavl region; 57°N, 63°E Irbit, Sverdlovsk region; 57°N, 63°E Irbit (IR>700 nm), Sverdlovsk region; 56°N, 53°E Azevo, Tatarstan; 56°N, 61°E Kamensk-Uralsky, Sverdlovsk region; 55°N, 84°E Yurga, Kemerovo region; 55°N, 37°E Lublin, Moscow; 55°N, 61°E Chelyabinsk; 54°N, 113°E Bagdarin, Republic of Buryatia; 54°N, 52°E Almetyevsk, Tatarstan; 54°N, 20°E Kaliningrad; 54°N, 36°E Kaluga; 54°N, 37°E Tula; 54°N, 40°E Ryazan; 53°N, 59°E Ostrolensky, Chelyabinsk region 47°N, 38°E Russkoe, Rostov region; 45°N, 38°E st. Novotitarovskaya, Krasnodar; 45°N, 40°E Gulkevichi, Krasnodar region; 43°N, 41°E Nizhny Arkhyz, Karachay-Cherkessia.

STARVISOR Observations. Auroras are one of the primary observation targets of the project. The cameras are positioned with sufficiently high spatial resolution in latitude to correlate the actual geographic location of the auroral oval with predictive models and to determine the southern boundary of aurora visibility.

In the adjacent observation area, some subauroral phenomena are also captured, such as the Stable Auroral Red (SAR) arc. To date, the project's observation database contains around five recorded instances of this phenomenon, documented both with stationary cameras at various latitudes and during field expeditions.

During the summer season, the cameras are used to monitor the appearance of mesospheric (noctilucent) clouds. The collected data allows for precise determination of the geographical locations where these clouds form and their spatial characteristics, including area and altitude, as well as comparative analysis of predictive models against the actual observations.

Much more rarely, but still occasionally in winter, the cameras in high-latitude locations capture polar stratospheric (nacreous) clouds. At present, the observation database for this phenomenon is limited, and data collection is ongoing.

Stationary cameras installed in locations with low levels of light pollution, as well as specialized near-infrared cameras, are capable of capturing bright forms of the atmosphere’s natural airglow. The data is primarily suitable for studying the dynamics of atmospheric wave propagation in the mesosphere.

The cameras are georeferenced and time-synchronized, allowing for the detection of bolides and bright meteors, and for calculating the trajectories of celestial objects entering the atmosphere to aid in the search for meteorite material.

During thunderstorm seasons, the project also includes observations of various lightning phenomena, including upper-atmosphere discharges such as sprites and ELVES. The observational database is extensive and continues to grow each year.

Some cameras are located near the launch paths of rockets from the Plesetsk, Baikonur, and

Vostochny cosmodromes, allowing for the observation of anthropogenic phenomena in the atmosphere. These include the so-called “space jellyfish” formed by rocket engine exhaust plumes, as well as burning rocket stages.

Figure 1 shows nighttime atmospheric phenomena recorded by the STARVISOR project cameras: sprites (a), noctilucent clouds (b), auroras (c, d, e), a SAR arc (f), atmosphere airglow (g), and rocket trails (h).

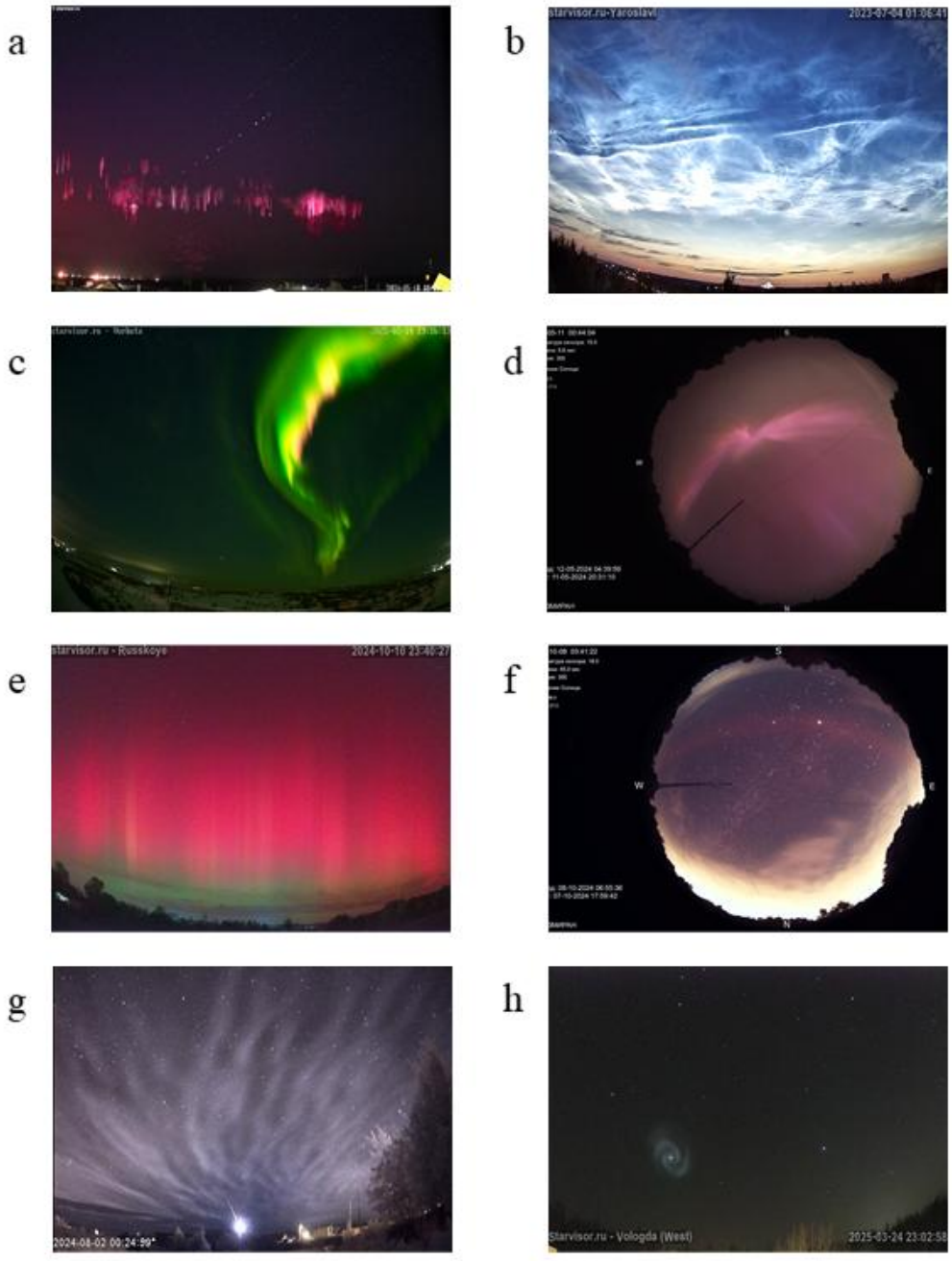


FIGURE 1. Nighttime atmospheric phenomena recorded by the STARVISOR project cameras: sprites (a), noctilucent clouds (b), auroras (c, d, e), a SAR arc (f), airglow (g), and rocket trails (h).

Experimental Observations. The project continuously works to improve the quality of observations and expand the range of observable phenomena. In particular, near-infrared and shortwave infrared imaging technologies are being tested as effective solutions to light pollution. These methods can virtually eliminate interference from LED lighting, providing a clear view of the night sky—even within urban areas—and allowing for the observation of auroras, atmospheric airglow, meteors, and sprites.

Remark. The STARVISOR project is open to collaboration with scientific organizations, educational institutions, observatories, thematic communities, and individual enthusiasts. We invite all those interested in night sky observation and atmospheric studies to take part. Various forms of cooperation are welcome, including joint projects, data sharing, and knowledge exchange.

We offer a modern, technology-driven platform for the study and popularization of atmospheric phenomena, opening up new opportunities for both the scientific community and the general public.

1. Starkov G. V., Feldstein Y. I. Changes in the boundaries of the auroral oval zone // *Geomagnetism and Aeronomy*. 1967. V. 7. No 1. P. 61 – 71 (in Russian).
2. Dalin P. A., Pertsev N. N., Romeyko V. A. Are Noctilucent Clouds 120 Years Old? // *Priroda*. 2005. V. 6. P. 12 – 21 (in Russian).
3. Nikolashkin S. V., Koltovskoy I. I. Optical and satellite studies of the atmosphere in Yakutia // *Science and Technology in Yakutia*. 2022. V. 2. P. 16 – 22.
4. Vasiliev R. V., Artamonov M. F., Beletsky A. B., et al. Scientific objectives of the optical instruments of the National Helio-Geophysical Complex // *Solar-Terrestrial Physics*. 2020. V. 6. No 2. P. 105 – 122. DOI: 10.12737/stp-62202008.
5. Belov A. A., Klimov P. A., Kozelev B. V., Murashov A. S., Roldugin A. V., Trofimov D. A. Modernized optical complex at the "Verkhnetulomsky" testing ground: scientific equipment and first results // *Bulletin of the Russian Academy of Sciences Physics*. 2023. V. 87. No. 2. P. 241–247. DOI:10.3103/S1062873822700940.
6. Rodger C. J. Red sprites, upward lightning, and VLF perturbations // *Reviews of Geophysics*. 1999. V. 37. No 3. P. 317–336. DOI: 10.1029/1999RG900006.
7. Chu X., Wolter L., Malaspina D., Andersson L., Connors M., Chatfield C., Zeller N. Morphological characteristics of Strong Thermal Emission Velocity Enhancement emissions // *Journal of Geophysical Research: Space Physics*. 2020. V. 125. No e2020JA028110. DOI: 10.1029/2020JA028110.

ON THE THREE-DIMENSIONAL MODELING OF THE EVOLUTION OF AN ACOUSTIC ATMOSPHERIC DISTURBANCE CAUSED BY THE GROUND MOVEMENT

Ekaterina S. Smirnova[1,2] and Sergey Yu. Dobrokhotov[1]

[1]Ishlinsky Institute for Problems in Mechanics of the Russian Academy of Sciences, Moscow, Russian Federation
[2]Immanuel Kant Baltic Federal University, Kaliningrad, Russian Federation

A mathematical model of the spatio-temporal evolution of acoustic waves excited by the moving lower boundary of the atmosphere is formed on the basis of an initial-boundary value problem for a hydrodynamic system of linearized differential equations that describe all possible types of atmospheric gas motion [1]. The system is a set of momentum-energy-mass conservation equations which are

formulated in terms of pressure and density variations, $p'(z)$ and $\rho'(z)$ as deviations from background functions $\bar{p}(z), \bar{\rho}(z)$:

$$\frac{\partial \vec{V}}{\partial t} = -\frac{\vec{\nabla} p'}{\bar{\rho}} + \vec{g}\frac{\rho'}{\bar{\rho}},$$
$$\frac{\partial p'}{\partial t} = -\vec{V}\cdot\left(\vec{\nabla}\bar{p}\right) - \gamma\,\bar{p}\left(\vec{\nabla}\cdot\vec{V}\right),$$
$$\frac{\partial \rho'}{\partial t} = -\vec{V}\cdot\left(\vec{\nabla}\bar{\rho}\right) - \bar{\rho}\left(\vec{\nabla}\cdot\vec{V}\right),$$

here $\vec{V}$ is the velocity of the gas flow, $\gamma = C_p/C_v$, C_p , C_v are molar heat capacities at constant pressure and volume correspondingly, $\vec{g} = (0,0,-g)$ is the acceleration field vector.

Moving to new set of variables P, Φ, U:

$$P = p'\cdot\exp\left(\int_0^z \frac{dz'}{2H(z')}\right), \Phi = \varphi'\cdot\exp\left(\int_0^z \frac{dz'}{2H(z')}\right), \vec{U} = \vec{V}\cdot\exp\left(-\int_0^z \frac{dz'}{2H(z')}\right)$$

with introduction of function $\varphi' = p' - \gamma\rho'\,\bar{p}/\bar{\rho}$ (see [1]) following system can be obtained:

$$\frac{\partial U_x}{\partial t} = -\frac{1}{\rho_0}\frac{H(z)}{H(0)}\frac{\partial P}{\partial x},$$
$$\frac{\partial U_y}{\partial t} = -\frac{1}{\rho_0}\frac{H(z)}{H(0)}\frac{\partial P}{\partial y},$$
$$\frac{\partial U_z}{\partial t} = \frac{H(z)}{\rho_0\,H(0)}\left(\frac{\gamma-2}{2\gamma H(z)} - \frac{\partial}{\partial z}\right)P + \frac{\Phi}{\gamma H(0)\rho_0},$$
$$\frac{\partial P}{\partial t} = -\gamma g\rho_0 H(0)\left(\frac{\partial U_x}{\partial x} + \frac{\partial U_y}{\partial y} + \frac{\partial U_z}{\partial z}\right) - g\rho_0\frac{H(z)}{H(0)}\frac{\gamma-2}{2}U_z,$$
$$\frac{\partial \Phi}{\partial t} = \left(1-\gamma-\gamma\frac{dH}{dz}\right)g\rho_0\frac{H(z)}{H(0)}U_z.$$

To simplify the formulation and subsequent solution of the initial boundary value problem, the last system of five differential equations can be reduced to a system of two equations by introducing the following function:

$$W = \frac{\partial U_x}{\partial x} + \frac{\partial U_y}{\partial y},$$

which will bring the system to the following form:

$$\frac{\partial^2 W}{\partial t^2} = g\frac{\gamma-2}{2}\left(\frac{\partial^2}{\partial x^2} + \frac{\partial^2}{\partial y^2}\right)U_z + c^2(z)\left(\frac{\partial^2}{\partial x^2} + \frac{\partial^2}{\partial y^2}\right)\frac{\partial U_z}{\partial z} + c^2(z)\left(\frac{\partial^2}{\partial x^2} + \frac{\partial^2}{\partial y^2}\right)W,$$
$$\frac{\partial^2 U_z}{\partial t^2} = c^2(z)\frac{\partial^2 U_z}{\partial z^2} + a(z)U_z - g\frac{\gamma-2}{2}W + c^2(z)\frac{\partial W}{\partial z},$$
$$\text{where } c(z) = \sqrt{\gamma g H(z)}, \qquad a(z) = \frac{\gamma g}{4H(z)}\left(1 + 2\frac{dH(z)}{dz}\right).$$

A remarkable fact for the last reduced system is that it contains differential equations only for the velocity components. It turns out to be sufficient to set initial and boundary conditions only for the velocity components U_x, U_y, U_z and there is no need to set initial and boundary conditions for the functions P and Φ, which represent pressure and density perturbations.

Let us represent the last system as a problem with a Hamiltonian:

$$\frac{\partial^2 \Psi}{\partial t^2} = \mathcal{H}\Psi,\ \Psi = \begin{pmatrix} W \\ U_z \end{pmatrix},$$

whose eigenvalue can be represented as

$$\lambda_{1,2} = -\frac{1}{2}\left(c^2(z)(p^2 + {p_z}^2) + a(z) \mp \sqrt{\left(c^2(z)(p^2 + {p_z}^2) + a(z)\right)^2 + \alpha}\right).$$

Let us note that the obtained eigenvalue of the hydrodynamic system of equations tends to the eigenvalue of the three-dimensional Klein-Gordon equation when $\alpha \to 0$. Thus, within the framework of the modeling problem, it is relevant to consider the initial boundary value problem for the 3D Klein-Gordon equation:

$$\frac{\partial^2 U}{\partial t^2} - c^2(z)\left(\frac{\partial^2}{\partial x^2} + \frac{\partial^2}{\partial y^2} + \frac{\partial^2}{\partial z^2}\right)U + a(z)\,U = 0,$$

$$U_{t=0} = \frac{\partial U}{\partial t}_{t=0} = 0, \qquad U_{z=0} = F(x, y, t).$$

According to the results [2], the analytical solution of which problem can be presented in the following form:

$$U = \frac{1}{\sqrt{2\pi h}}\, Re \int\limits_{\sqrt{a+c^2p^2}}^{\infty} \int\limits_{\mathbb{R}^2} (U_1 + U_2)\, e^{ipx/h} dp,$$

$$U_1 = \frac{1}{\pi\, h}\, Re \int\limits_0^{\infty} \mathcal{F}(p, \eta, h) e^{\frac{1}{h}\left(i\eta t - \frac{z}{c}\sqrt{a+c^2p^2-\eta^2}\right)} d\eta,$$

$$U_2 = \frac{1}{\pi\, h}\, Re \int\limits_{\sqrt{a+c^2p^2}}^{\infty} \mathcal{F}(p, \eta, h) e^{\frac{i}{h}\left(\eta\tau - \frac{z}{c}\sqrt{\eta^2-a-c^2p^2}\right)} d\eta.$$

Here h is a small parameter that arises with transition to dimensionless variables and functions and $\mathcal{F}(p, \eta, h)$ is the Laplace transform of the Fourier transform for the boundary condition with $s = i\eta$:

$$\mathcal{F}(p, s, h) = \int\limits_0^{\infty} e^{-st}\, dt \int\limits_{\mathbb{R}^2} F(x, y, t)\; e^{-ipx/h} dp.$$

Note that the solution U consists of two parts: a boundary layer function U_1 concentrated in the region $z = 0$ and an oscillating function U_2 that propagates upward.

For the boundary condition of the form

$$F(x, y, t) = \begin{cases} A\, e^{-b(x^2+y^2)/h^2} \mu^2 t\, e^{-\mu t}, & t \geq 0 \\ 0, & t < 0 \end{cases}$$

we present the results of modeling the disturbance, represented by the asymptotic solution [3]:

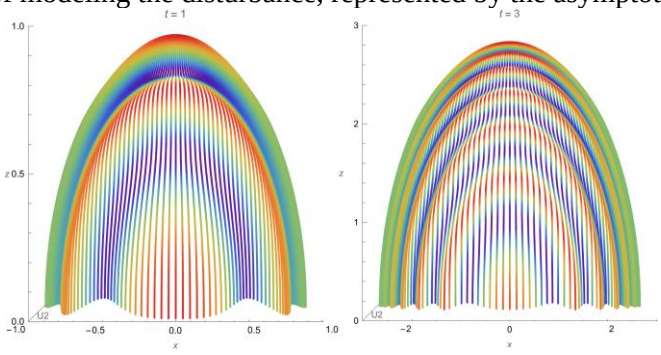


FIGURE 1. The graph shows the results of modeling an acoustic disturbance initiated by a pulse at the lower boundary taking into account the radial symmetry of the problem $x \to (x, y)$, which is implemented on the basis of an asymptotic solution corresponding to the analytical solution of the initial-boundary value problem for the three-dimensional Klein-Gordon equation. The results are formulated for dimensionless variables and functions in which the values $x = z = 1$ and $t = 1$ corresponds approximately 220 km and 11 min.

The proposed modeling procedure is in qualitative agreement with the known results of numerical modeling, presented, for example, in [4].

This investigation was performed with the financial support of state assignment №124012500442-3.

1. Leble S., Perelomova A. Problem of proper decomposition and initialization of acoustic and entropy modes in a gas affected by the mass force // *Appl. Math. Model*. 2013. V. 13. P. 629–635. DOI: 10.1016/j.apm.2012.02.037
2. Smirnova, E. S. Asymptotics of the Solution of an Initial–Boundary Value Problem for the One-Dimensional Klein–Gordon Equation on the Half-Line // *Mathematical Notes*. 2023. V. 114. N. 3-4. P. 608-618. DOI: 10.1134/S0001434623090286.
3. Dobrokhotov S., Smirnova E. Asymptotics of the Solution of the Initial Boundary Value Problem for the One-Dimensional Klein–Gordon Equation with Variable Coefficients // *Russ. J. Math. Phys.* 2024. V. 31. P. 187–198. DOI: 10.1134/S1061920824020043.
4. Kurdyaeva Y.A., Kulichkov S.N., Kshevetskii S.P., Borchevkina O.P., Golikova E.V. Vertical propagation acoustic-gravity waves from atmospheric fronts into the upper atmosphere // *Bulletin of the Russian Academy of Sciences. Physics of the Atmosphere and Ocean*. 2019. V. 55. N. 4. P. 303-311. DOI: 10.1134/S0001433819040078.

SPACE WEATHER VARIATIONS THOSE CAN IMPACT HUMAN HEALTH IN DIVERSE GEOGRAPHIC POINTS

Olga M. Stupishina[1], Elena G. Golovina[1], Sergey N. Noskov[2,3] and Gennady B. Eremin[2]

[1] Russian State Hydrometeorology University, Saint Petersburg, Russia
[2] North–West Public Health Research, Saint–Petersburg, Russia
[3] North–West State Medical University named after I.I. Mechnikov, Saint–Petersburg, Russia

The work presents the results of the investigation that explore Space Weather variations those matching the human health status variation.

The investigation time interval: 1.12.2016 – 29.11.2021. That corresponds to: 24rd Solar Activity (SA) cycle fall branch, the SA minimum, the rise branch of the 25th SA cycle.

Entering data for the human health estimation were received from 8 cities of Russian Federation in the wide geography frame: Arkhangelsk, Lipetsk, Astrakhan, Rostov-on-Don, Mednogorsk, Omsk, Khabarovsk, Petropavlovsk-Kamchatsky. The geographical location of these cities determines the broad scope of the study, the scope of which is 18.2 degrees in latitude and 119.1 degrees in longitude. The exact coordinates of the cities are shown in Table 1. Thus, the study covers a significant part of the Russian Federation, which also determines the significant coverage of Eurasia. The information provided by the medical statistics services of the cities studied includes an indication of the cause of death for 22 categories of diseases (ICD-10).

The treating of the obtained medical statistics data was carried out to identify patterns of behavior of the quantitative characteristics of mortality in each of the studied cities. Figures 1-2 show the time course of mortality (in terms of the absolute number of deaths) in different cities of the Russian Federation. The change in the total number of deaths is shown without dividing into categories of diseases-causes of death, without taking into account the gender and age of the deceased. Figure 1 shows the number of deaths on a logarithmic scale, because the movement of mortality in Mednogorsk is poorly visible in the linear scale due to the small city population. From the Figure 1 one can learn the obvious

common-mode variation of the mortality-number lines in quite different geography points. We have selected 5 season of significant maximums of the value in study in which more than 4 cities have such maximums (they are shown by lines in Figure 1).

TABLE 1. Geographical coordinates of cities in study.

City	Latitude (°N)	Longitude (°E)
Arkhangelsk	64,55	40,58
Omsk	54,99	73,37
Petropavlovsk-Kamchatsky	53,04	158,68
Lipetsk	52,60	39,57
Mednogorsk	51,42	57,60
Khabarovsk	48,52	136,10
Rostov-on-Don	47,24	39,70
Astrakhan	46,34	48,04

The correlation analysis (the nonparametric Spearman analysis) shows the considerable correlation coefficients for this curves especial in the time-interval from autumn 2018 to winter 2021-2022 (Table 2, 3).

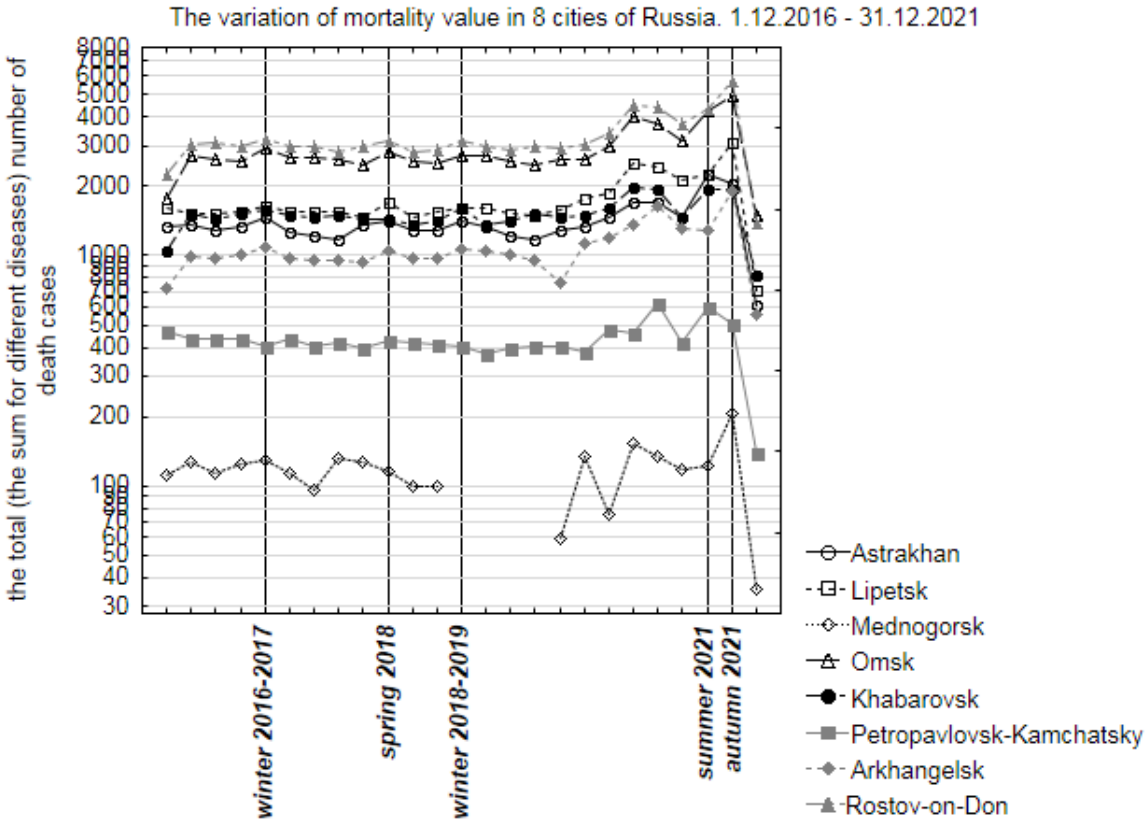


FIGURE 1. The behavior of the total number of deaths-cases in different geographic points. The seasons in which the curves of more than 4 cities have maximums are shown by lines.

TABLE 2. Correlation coefficients of mortality curves of different cities of the Russian Federation. Nonparametric correlation analysis of Spearman and Kendall. The correlation coefficient above 0.60 is highlighted by Italic font, the correlation coefficient above 0.70 is highlighted in bold and Italic font. 01.12.3016-31.12.2021.

	Astrakhan	Lipetsk	Mednogorsk	Omsk	Khabarovsk	Petropavlovsk-Kamchatsky	Archangelsk	Rostov-on-Don
Astrakhan		***0,81***	0,48	***0,80***	*0,64*	0,53	***0,81***	***0,86***
Lipetsk	***0,81***		0,49	***0,81***	***0,64***	0,51	***0,79***	***0,76***
Mednogorsk	0,48	0,49		0,44	0,52	0,35	0,53	0,50
Omsk	**0,80**	***0,81***	0,44		***0,73***	0,55	***0,85***	***0,88***
Khabarovsk	0,64	*0,63*	0,51	***0,72***		0,53	***0,66***	***0,78***
Petropavlovsk-Kamchatsky	0,53	0,51	0,35	0,55	0,53		0,44	0,51
Archangelsk	***0,81***	*0,79*	0,54	***0,84***	***0,66***	0,43		***0,84***
Rostov-on-Don	***0,86***	*0,76*	0,50	***0,88***	***0,78***	0,51	***0,84***	

TABLE 3. Correlation coefficients of mortality curves of different cities of the Russian Federation for the period from autumn 2018 to winter 2021-2022 Nonparametric correlation analysis Spearman, Kendall. The correlation coefficient above 0.60 is highlighted by Italic font, the correlation coefficient above 0.70 is highlighted in bold and Italic font.

	Astrakhan	Lipetsk	Mednogorsk	Omsk	Khabarovsk	Petropavlovsk-Kamchatsky	Archangelsk	Rostov-on-Don
Astrakhan		***0,95***	*0,66*	***0,99***	***0,78***	***0,82***	***0,90***	***0,91***
Lipetsk	***0,95***		***0,83***	***0,96***	***0,75***	***0,77***	***0,96***	***0,93***
Mednogorsk	*0,66*	***0,83***		***0,71***	*0,62*	0,57	***0,82***	***0,76***
Omsk	***0,98***	***0,96***	***0,71***		***0,76***	***0,79***	***0,93***	***0,93***
Khabarovsk	***0,78***	***0,75***	*0,62*	***0,76***		0,53	***0,74***	***0,87***
Petropavlovsk-Kamchatsky	***0,82***	***0,77***	0,57	***0,79***	***0,79***		***0,76***	***0,80***
Archangelsk	***0,90***	***0,95***	***0,82***	***0,93***	***0,74***	***0,76***		***0,93***
Rostov-on-Don	***0,92***	***0,94***	***0,76***	***0,93***	***0,88***	***0,80***	***0,93***	

The conclusion of the information from Figure 1 and Tables 2,3 leads to the assumption that the most probable factors those can impact the human health on the wide territory must be of global character. The first we think about the Space Weather impact.

Space Weather parameters those were included to the investigation:

1. Global variations of Solar Activity (SA) parameters – daily indexes of SA (the full radio-flux on the wavelength of 10.7cm, the sunspot number, the summarized spot area on the solar disk, the number of new Active Regions on the solar disk) [1];

2. Daily characteristics of the SA flare-component in the various bands of the electromagnetic spectrum (the number of optical flares, the same for X-ray flares, the same for radiobursts in different radio-bands and different types of bursts, the number of Coronal Mass Ejection) [1];

3. Variations of Interplanetary Space characteristics in Earth Vicinity – the electron fluxes of different energies, the proton fluxes of different energies, the background X-ray fluxes (0.5-8 Å; 1–8 Å), the speed, density and the temperature of plasma in the solar wind, the galactic ray's fluxes [1, 2, 3]);

4. Variations of Geomagnetic Field (GMF) on the altitude of the geostationary orbit – full GMP vector [2];

5. Variations of GMF in different terrestrial latitudes (high-, middle-latitudes; k-indexes) [1].

Results:

1. The first and the most interesting result is the considerable correlation between the behavior of solar activity global variations and investigated mortality curves. This correlation is most apparent in the time-interval from the summer 2020 to the autumn 2021 (Fig.2).

2. The next stage of the study was to determine the specific dates of the increase in mortality value in each of the cities studied. Only such dates were selected when the peak of mortality was recorded:

a. either in several cities on the same date,

b. or the difference between the registration dates in different cities did not exceed 5 days (5 were selected in accordance with the interval of the folder epoch method used in this study).

The dates of the total number of death-maximums and deaths-minimums were determined. The analysis of the environmental characteristics in the selected days of deaths-maximums vs. death-minimums shows the follow. For people of different sexes, regardless of age (the information was summarized by the results of the study in each age group), the effects of different parameters of space weather are significant.

• For men, only variations of the geomagnetic field were significant, most often (80% of registration cases). These were variations in the value of the minimum geomagnetic field strength per day at middle latitudes.

• For women, variations in the characteristics of space weather on a larger scale turned out to be significant – variations in the number of coronal mass ejections on the Sun, variations in the indices of global changes in solar activity (the integral radio flux from the Sun's disk on the wavelength of 10.7 cm, the Wolf number, and the total area of spots on the Sun's disk). The geomagnetic field turned out to be significant only in terms of the daily variation in intensity. The result obtained corresponds well to the result of our previous work (5).

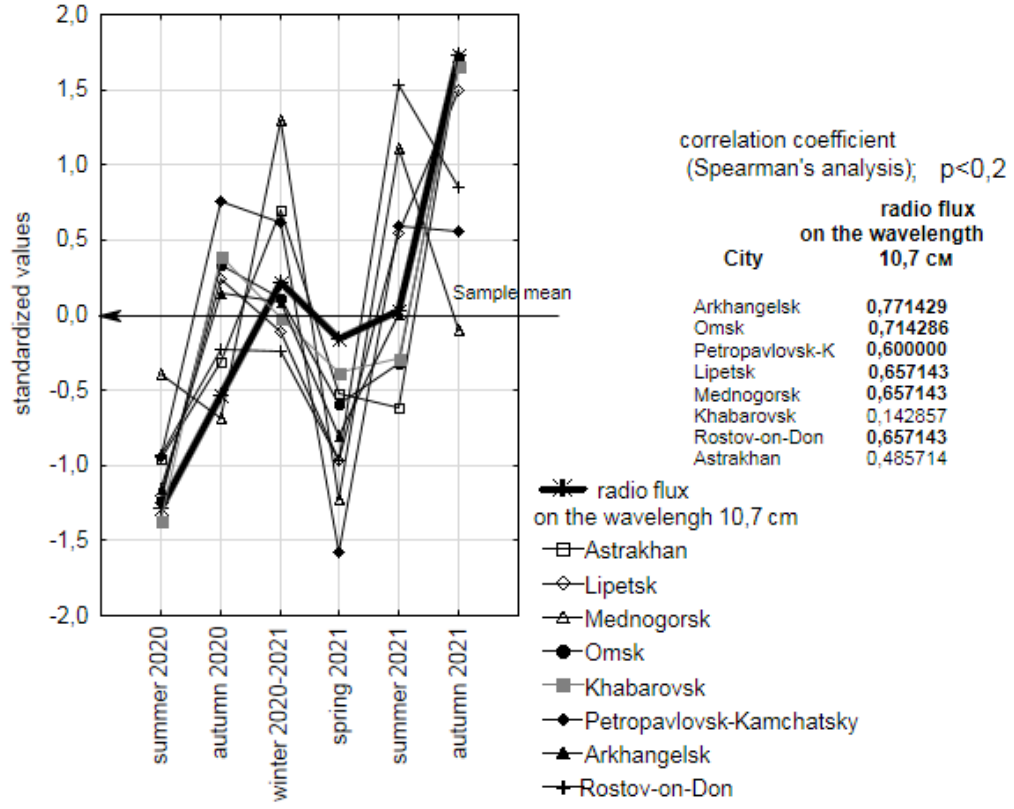


FIGURE 2. The comparison of standardized mortality values with the standardized value of the solar activity index - the integral radio flux on the wavelength of 10.7 cm

1. Solar data source: Space Weather Prediction Center. https://www.swpc.noaa.gov/ (visit 15.03.2025).
2. Satellite GOES data source: Space Weather Prediction Center. https://satdat.ngdc.noaa.gov/sem/goes/data/avg/ (visit 15.03.2025).
3. http://www.srl.caltech.edu/ACE/ASC/level2/lvl2DATA_SIS.html (visit 15.03.2025).
4. https://cdaw.gsfc.nasa.gov/CME_list/UNIVERSAL_ver1/text_ver/univ_all.txt (visit 15.03.2025).
5. Stupishina O.M., Golovina E.G., Noskov S. N., Eremin G.B., Gorbanev S.A. The space and terrestrial weather variations as possible factors for ischemia events in Saint Petersburg // *Atmosphere*. 2022. V. 13. P. 8. DOI: 10.3390/atmos13010008.

POSSIBLE TRIGGERS OF EXPLOSIVE CHANGES IN TROPICAL CYCLONES PARAMETERS AND STRONG EARTHQUAKES DURING THE EARTH'S PASSAGE THROUGH JUNE METEOR SHOWERS

Vladimir M. Kostin, Olga Ya. Ovcharenko, and Elena P. Trushkina

Pushkov Institute of Terrestrial Magnetism, Ionosphere and Radio Wave Propagation, Russian Academy of Sciences, Moscow, Troitsk, Russian Federation

Earthquake forecasting based on meteorological data has been developed at IZMIRAN since 2023.The first results were presented at the "Prognoz-24" conference and are detailed in a presentation on the IZMIRAN website. The earthquake forecast for the days of the conference was accurate in terms of location and timing by 50%. The report also indicated that the catastrophic earthquake in Turkey on February 6, 2023, coincided with a sharp intensification and change in the trajectory of Tropical Cyclone Freddy (slide 5). GENEVA (AP) - "The U.N. weather agency said Tuesday, July 2, 2024 that Tropical Cyclone Freddy, a deadly Indian Ocean storm that lashed eastern Africa last year, was confirmed to be the longest-lasting cyclone ever recorded at 36 days". On February 21, TC Freddy struck Madagascar, crossed the island and reached Mozambique on February 24. In Mozambique, over 1.3 million people were affected; in Madagascar, approximately 200,000 people suffered from the cyclone's first and second landfalls. From February 24 to March 14, eight sharp changes in Freddy's trajectory were observed (slide 11).

The next forecast for October 25-27, 2023, was presented at the RAS ITPS conference. TC Tammy approached the Bermuda Islands and changed its direction on October 25-26. Earthquakes were expected in diametrically opposite areas – an antipodal effect. The forecast was accurate in terms of location and timing. In October 2018, as TC Leslie approached the Bermuda Islands, an earthquake occurred near Waingapu in the antipodal region. The passage of two Category 5 TCs in November 1990 near a system of islands in the Pacific Ocean demonstrated that an entire class of earthquakes can be linked to antipodal passage [1]. Another TC, Otis, unexpectedly intensified from a storm to a Category 5 hurricane within 12 hours on October 25. It passed through Acapulco and devastated the city. Over the next 12 hours, its intensity dropped by 3 times. The unusual development of TCs near the Mexican coast and a magnitude 5.6 earthquake on the Chilean fault on October 26 can be associated with the hypothesis regarding the influence of dark matter asteroid Bose [2-4]. Academician I.I. Tkachev and colleagues from the Institute for Nuclear Research RAS are developing the theory of dark matter

composed of hypothetical Bose particles - axions with a mass of about 10^{-5} eV. Bose particles made from axions may eventually form asteroids (axion stars) with a size ~100 km and a total mass ~10^{14} kg, traveling at a speed ~300 km/s [2-4].

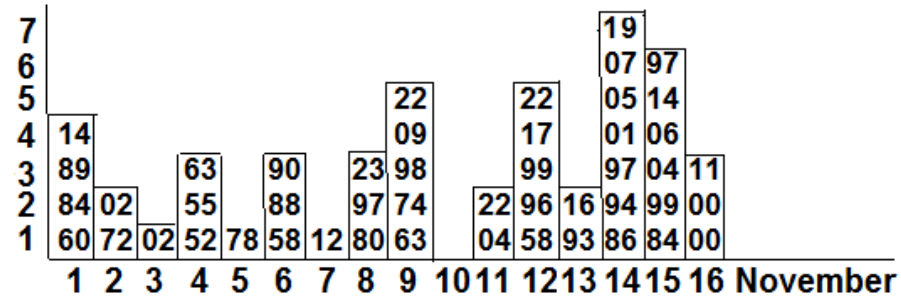


FIGURE 1. Histogram of earthquakes M≥7.0 in November since 1952. The year of each earthquake is indicated in individual boxes.

If such asteroids collide with comets, they can destroy them and move along with meteor showers. The gravitational influence of these dark matter Bose-asteroids on Earth may trigger strong earthquakes and abrupt changes in the trajectories of tropical cyclones (not predicted by meteo forecasts), as well as earthquakes occurring with or without the presence of tropical cyclones. This hypothesis was proposed at the Prognoz-24 conferences at IZMIRAN and Trigger-24 at MIPT. Before the conference at the IKI RAS [5] a histogram of the number of strong earthquakes M≥7.0 since 1952 was constructed (Fig. 1).

It was noted that a strong earthquake could occur during the peak of the Leonids meteor shower on November 14-15, 2024 (slide 420-8 in presentation [5]). A single strong earthquake of magnitude M=6.6 occurred in Papua New Guinea on November 15. TC Usagi passed through the Philippines, and its trajectory sharply turned from northwest to northeast. TC Bheki in the Indian Ocean described a loop prior to the earthquake. In the Atlantic Ocean, TC Sara developed, with an anomalous trajectory (Fig. 2) observed 6.5 hours after the earthquake.

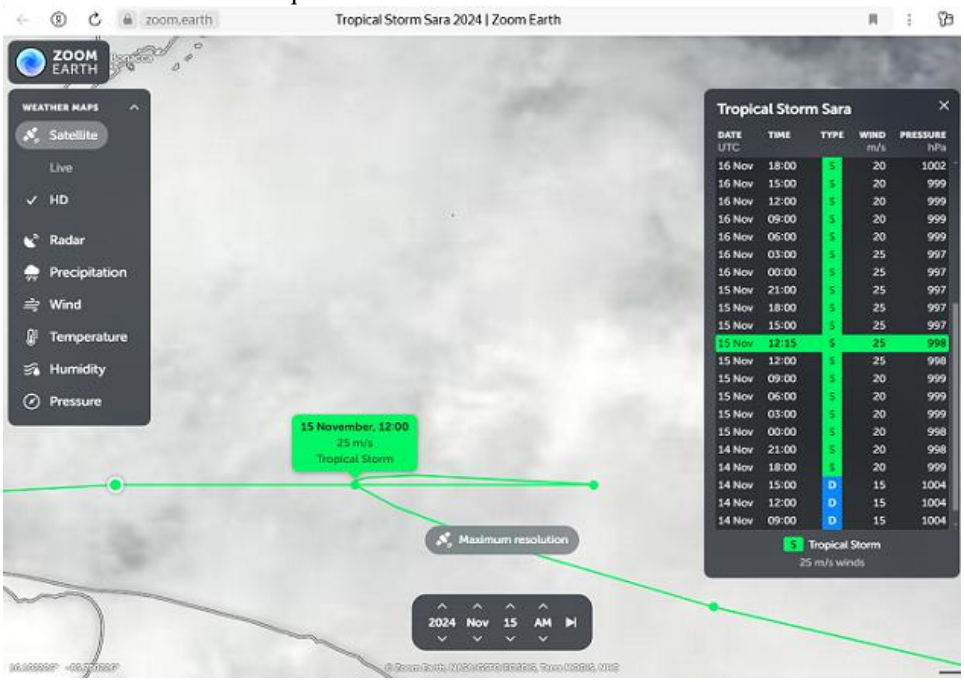


FIGURE 2. Trajectory of TC Sara near the city of Truilo, Honduras.

An analysis of earthquakes M≥5.7 in a square with a side length of approximately 200 km since 2000 showed that there were 83 events in Papua New Guinea. For only one event on October 13, 2005, TC development was observed in three oceans, which also sharply changed characteristics that day. Such events can be interpreted as the influence of dark matter Bose-asteroids. Let's consider the probability of observing effects from the passage of a Bose-asteroid in June 2025.

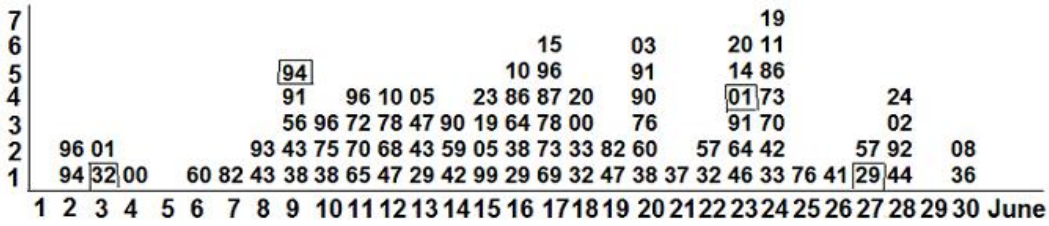


FIGURE 3. Histogram of earthquakes M≥7.0 in June since 1929. The year of each earthquake is indicated in individual boxes. 4 mega earthquakes M≥8.1 are highlighted with squares.

The strongest June earthquake M=8.4 occurred in Peru on June 23, 2001, at 20:33. An earthquake on the Aleutian Arc occurred on June 23, 2014, at 20:53 UT - a difference of 20 minutes. An earthquake on the Aleutian Arc occurred approximately 640 km east on June 24, 2011, at 03:09 UT.

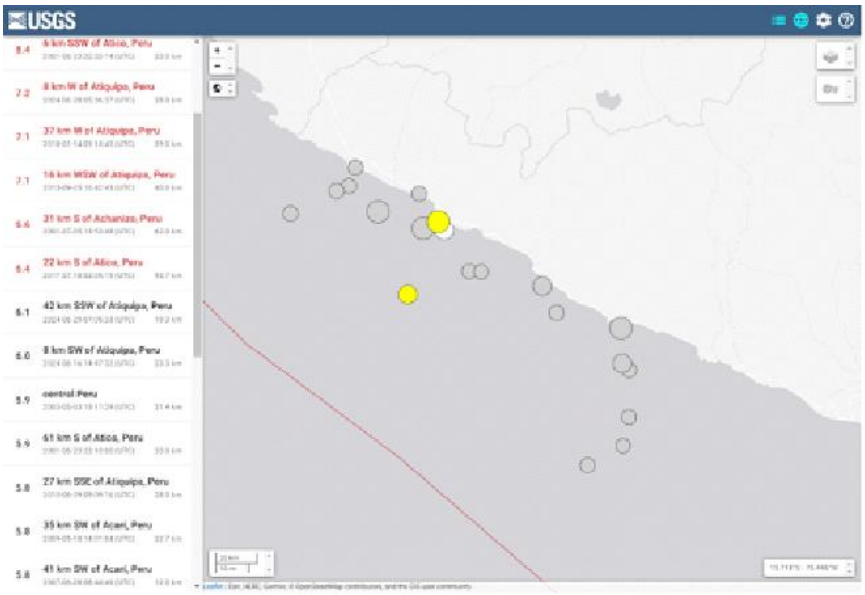


FIGURE 4. Earthquakes M≥5.7 in Peru from 2000 to 2024 in a square with a side of ~200 km and centered over the impacts of M=8.4 on June 23, 2001 (large light circle) and M=7.2 on June 28, 2024 (small).

The maximum number of strong earthquakes in Peru, 7 out of 13 according to the list in Fig. 4, was observed from June 16 to June 29. This interval coincides with the distribution of peaks on the histogram in Fig. 3. The earthquake M=7.2, which occurred on June 28, 2024, coincides with the peak of the June Bootids meteor shower (Table 1).

Table 1. List of June meteor showers – Wikipedia

Name	Dates	Peak	Solar (λ⊙°)	RA (hours)	Dec (degres)	Ventry (km/s)	Parent body
Daytime Arietids	14 May – 24 Jun	7 Jun	76.6	2.9	+24	38	1566 Icarus?
June Bootids	22 Jun – 2 Jul	27 Jun	95.7	14.9	+48	18	7P/Pons-Winnecke

From June 15 to July 2, the Earth passes through the orbit of the disintegrated short-period comet 7P/Pons-Winnecke. Its activity was noted in 1998 (50-100 meteors/hour) and in 2004 (20-50 meteors/hour). The next surge was expected in 2010, repeating every 6 years, but during that time, the activity of the shower did not exceed even 10 meteors/hour. It is known that light dust particles are decelerated more by solar pressure than heavier asteroids. However, they are numerous and completely burn up in the atmosphere, which accounts for the peak of meteor showers. The passage of Bose-asteroids associated with meteor streams is expected to occur before the observed peaks of meteor showers.

If a strong earthquake most likely occurs in the region of Peru or along the Aleutian Arc on June 24, 2025 (19+6, column 24 Fig. 3), and sharp changes in TC dynamics are observed, it would serve as direct evidence for the existence of Bose-asteroids.

This statement is speculative but emphasizes the authors' confidence in the existence of dark matter Bose-asteroids. It should be noted that TC activity and, consequently, the number of earthquakes depend on cosmic rays [6].

This investigation was performed with the financial support of Ministry of Science and Higher Education of the Russian Federation within the framework of the state assignment IZMIRAN.

1. Kostin V., Belyaev B., Ovcharenko O., Trushkina E. American Continent Lithosphere Earthquakes after Nuclear Test of France in November 1990 // *Intern. J. Engineering Research and Science.* 2021. V. 7. No 12. P. 30-34. DOI: 10.5281/zenodo.5809755.
2. Tkachev I., Shtern B. Fun dark matter // *Troitsk variant*. 2021.12.07. No 343. P. 8–9.
3. Levkov D.G., Panin A.G., Tkachev I.I. Gravitational Bose-Einstein condensation in the kinetic regime // *Physical Review Letters*. 2018. V. 121. No 15. P. 151301. DOI: 10.1103/PhysRevLett.121.151301.
4. Dmitriev A.S., Levkov D.G., Panin A.G., Tkachev I.I. Self-similar growth of Bose stars // *Physical Review Letters*. 2024. V. 132. No 9. P. 091001. DOI: 10.1103/physrevlett.132.091001.
5. Kostin V.M., Ovcharenko O.Ya., Trushkina E.P. Strong earthquakes on November 11-15 according to the weather forecast of tropical cyclones // Proceedings of the 22nd International Conference "Modern problems of remote sensing of the Earth from space". Moscow: Space Research Institute RAS. 2024. P. 420. DOI: 10.21046/22DZZconf-2024a.
6. Hegay V.V., Legenka A.D., Abunin A.A. et al. Solar activity, variations of galactic cosmic rays and global seismicity of the Earth // *Geomagnetism and Aeronomy.* 2022. V. 62. No. 1. P. 1–12. DOI: 10.31857/S0016794022010102.

DISTORTIONS OF THE ATMOSPHERIC ELECTRIC FIELD THAT OCCUR DURING ITS MEASUREMENT

Valery V. Denisenko[1] and Sergey E. Smirnov[2]

[1] Institute of Computational Modelling of the Russian Academy of Sciences Siberian Branch, Krasnoyarsk, Academgorodok, Russian Federation

[2] Institute of Cosmophysical Research and Radio Wave Propagation of the Russian Academy of Sciences Far East Branch, Kamchatka region, Elizovskiy district, Paratunka, Russian Federation

When measuring the atmospheric electric field, it is distorted by the measuring system and other objects located near the sensor. Therefore, after calibration in the laboratory, the sensors need additional

calibration to compensate for such distortions. In this paper, using the example of the measuring system of the geophysical observatory in Paratunka [3], the effects of the tower on which the sensor is installed and the forest nearby are considered. We analyze only quasi-stationary measurements. Therefore, the distribution of electric fields and currents in the atmosphere can be found by solving problems for the equation of electrical conductivity. The basic equations for the stationary electric field strength **E** and current density **j** are Faraday's law, the law of conservation of charge, and Ohm's law

$$\mathrm{rot}\,\boldsymbol{E} = 0, \quad \mathrm{div}\,\boldsymbol{j} = 0, \quad \boldsymbol{j} = \sigma\boldsymbol{E}. \tag{1}$$

Since we are considering local phenomena, we consider the conductivity to be constant, and for certainty we set the value $\sigma = 10^{-14}$ S/m characteristic of surface air. By virtue of the first equation (1), an electric potential V can be introduced such that $\mathbf{E} = -\,grad\,V$. Then the system of equations reduces to the current continuity equation:

$$-\mathrm{div}(\sigma\,\mathrm{grad}\,V) = 0, \tag{2}$$

The conductivity of the near surface air is much lower than that of soil and seawater. Therefore, the Earth's surface is usually considered as an ideal conductor. The corresponding boundary condition has the form:

$$V|_G = 0, \tag{3}$$

where G is the boundary of the atmospheric region under consideration. In our models, it consists of the surface of the Earth and the surfaces of bodies which have a sufficiently high conductivity compared to the conductivity of air so that they can be considered as ideal conductors. We suppose that there is a uniform vertical electric field in an undisturbed atmosphere. The corresponding boundary condition has the form:

$$V|_{x^2+y^2+z^2\to\infty} = E_0 z, \tag{4}$$

where x,y,z are Cartesian coordinates with the vertical z axis. For certainty, we assume $E_0 = 260$V/m.

It is not difficult to construct an analytical solution to the problem when an ideally conducting hemisphere rises above the flat surface of the ground. The electric field above the upper point of the hemisphere is vertically directed downward, and its intensity is twice the undisturbed value E_0. It can be said that with such a measurement, the calibration coefficient $K = 0.5$ should be used, by which the sensor readings should be multiplied in order to obtain the vertical component of the electric field strength in the surface air, which is not distorted by such a hemisphere.

A tower is used to measure the strength of the surface electric field in the observatory Paratunka [3]. It is a cylindrical metal platform with a diameter of 4.38 m and a height of 0.56 m. It is raised to a height of 2.8 m on a wooden pole with a diameter of 0.15 m with metal supports from the level of 0.46 m to the lower edge of the platform. The conductivity of wood significantly depends on humidity, from 10^{-11} S/m at 20% humidity to 10^{-6} S/m at 50%. In Kamchatka, the humidity is always high, and the column is dug into the ground, which further increases the humidity of its lower part, which is what interests us. The wooden column with minimum wood conductivity has the same conductance as the conductance of an air column 32 times larger radius. With a really high humidity, the column can be considered an ideal conductor, which we do by extending condition (3) to its surface.

The actual sensor measuring the vertical component of the electric field is located in the center of the upper horizontal platform. In order to limit ourselves to the axisymmetric model, we replace the inclined aluminum beams supporting the upper platform with a circular, ideally conductive cone, for which they form. The possibility of such a coarsening of the model is justified by calculations that have shown that the shape of the surface lying below this platform has little effect on the field of interest above its center. The result is a single conductor with zero potential – the ground and the entire tower. The cross section of the tower is visible in Fig. 1.

We approximately replace the asymptotic condition (4) with a condition on a hemisphere of radius R_∞, large enough not to thereby distort the solution in the area of interest near the tower. The formulated Dirichlet boundary value problem for the Laplace equation (2-4) has a unique solution. We find it

numerically. Our multigrid variational-difference method for a more general case of tensor conduction problems is described in a monograph [1]. The result electric field and current are presented in Fig. 1. Only central part of the calculation domain is shown. The electric field strength above the center of the upper platform of the tower, where the sensor is installed, turned out to be 531 V/m, which is 2.04 times greater than the set field in the free atmosphere. As you can see, the field amplification due to a specific design turned out to be close to the doubling obtained for a spherical tower.

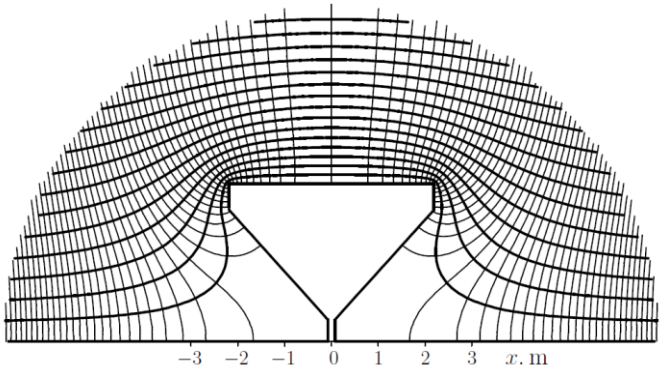


FIGURE 1. The distribution of the electric field and currents in a vertical section drawn through the axis of symmetry of the measuring tower. Equipotentials in increments of 100 V (bold curves), and current lines (thin curves) are sections of current tubes in which the current strength is equal to a current of 10 pA multiplied by 1,2,3,...

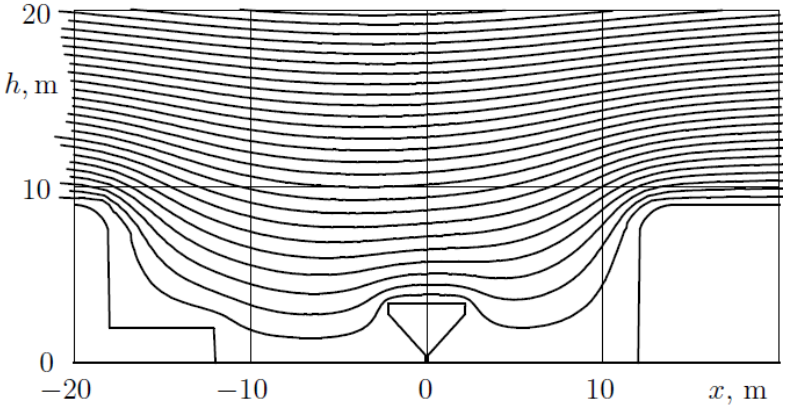


FIGURE 2. Distribution of the electric field in a vertical section drawn through the axis of symmetry of the measuring tower in the absence of snow. Equipotentials in increments of 100 V. The lower equipotential $V = 0$ corresponds to the boundary of the air with the forest, bushes and the tower.

Measurements in the center of a circular clearing in the forest are also simulated. The forest is considered as a solid conductor with a given thickness, since the conductivity of wet wood is many orders of magnitude greater than that of air, and therefore current flows freely through the branches into the ground. That is, a clearing is a pit in the forest. Naturally, the field does not penetrate well into the pit. With a clearing radius of 14 m and a tree height of 13 m, the field is weakened by about 5 times near the ground in the center of the clearing. We can say that the calibration coefficient K=5 should be used for this measurement. One might assume that to eliminate the distortions introduced by both effects, the sensor readings should be multiplied by about K=2.5. However, calculations for a geometrically more complex problem simulating a tower in a clearing give a different result.

In this case, the modeled object no longer has axial symmetry, and it is necessary to solve a three-dimensional version of the problem (2-4). Our finite element multigrid numerical method is described in the article [2]. The field obtained with heights of 9 m trees and 2 m bushes is shown in Fig. 2.

The thickness of the snow cover at the Paratunka Observatory reaches 2.5 m. The characteristic conductivity of snow according to the data [4] is 10^{-3}-10^{-2} S/m. It exceeds the conductivity of air by more than 10 orders of magnitude. So we simulate snow as an ideal conductor with the boundary condition (3). The results of a series of calculations with different snow layers turned out to be close to the quadratic dependence:

$$K = 1.33 + 0.075\,S + 0.015\,S^2, \qquad (5)$$

where S is the thickness of the snow cover S in meters. The calibration coefficient K increases from 1.33 to 1.61 when snow accumulates from 0 to 2.5 m.

Although the calculations were carried out with accuracy better than 1%, the initial data (the upper boundaries of the forest and shrub) are not very accurately determined. For example, if the height of the trees is considered to be 10 m rather than 9 m, in the absence of snow, $K = 1.52$ is obtained instead of $K = 1.33$ from (5).

1. Denisenko V.V. Energy methods for elliptic equations with asymmetric coefficients // *Publ. house of the Russian Academy of Sciences Siberian Branch*, Novosibirsk. 1995. [in Russian].
2. Denisenko V.V., Pomozov E.V. Global electric fields in the Earth's atmosphere calculation // *Journal of Computational Technologies*. 2010. V. 15. No 5. P. 34-50. [in Russian]
3. Smirnov S. Atmospheric electricity measurements in the Pacific Northwest, Russia // *Appl. Sci.* 2023. V. 13. P. 2571-2583. DOI: 10.3390/app13042571.
4. Tentyukov M.P., Ignatiev G.V., Sobolev I.S., Gavrilov R.Y. Physical properties of snow cover and the mechanism of formation of geochemical barriers in snow mass // *Vestnik of Geosciences*. 2022. No. 5. P. 26-37. DOI: 10.19110/geov.2022.5.4.

EARTHQUAKE FORECAST UP TO 5 DAYS BASED ON TROPICAL CYCLONE WEATHER DATA

Vladimir M. Kostin, Olga Ya. Ovcharenko, and Elena P. Truchkina

Pushkov Institute of Terrestrial Magnetism, Ionosphere and Radio Wave Propagation, Russian Academy of Sciences, Moscow, Troitsk, Russian Federation

The authors have been conducting daily monitoring of earthquakes M>5.7 and tropical cyclones (TC) using USGS and ZOOM Earth data since 2023. Joint monthly event maps are compiled and compared with earthquakes since 2000, localized within a distance of up to 100 km.

Good correlation allows, according to the meteorological model NCON of the development of TC with a forecast depth of 5 days, selecting similar developments of TC to give a short-term forecast of strong earthquakes. Fragments of these predictions were presented in conference presentations such as MedGU-23, IZMIRAN “Prognoz-23, 24”, ITPZ RAS, MIPT, IDG RAS and IKI RAS [1]. The reliability of these predictions exceeded 50% in terms of location and time. However, the predictions were disrupted when there were sharp changes in TC trajectories and intensity (not predicted by weather forecasts), or when earthquakes occurred without TCs.

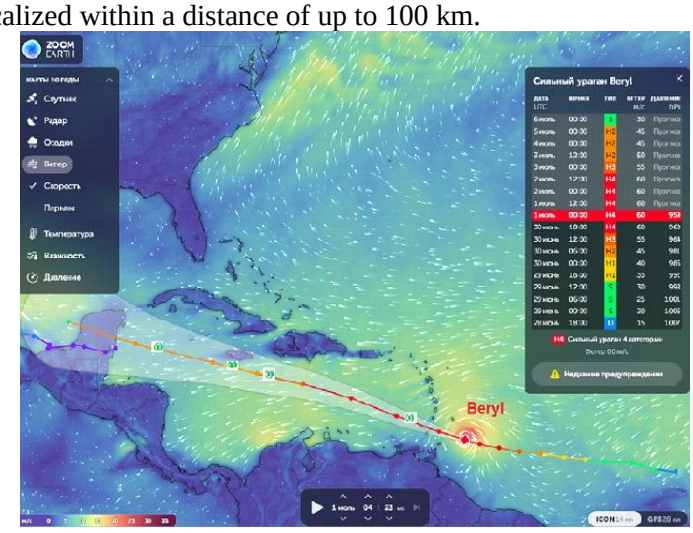


FIGURE 1. Cyclonic activity weather forecast for July 1, 2024. The moments of impact on the Beryl trajectory are indicated by crosses in a square.

Below is the earthquake forecast for July 2-5, 2024 during the "Triggers-24" conference at MIPT.

Since it was not possible to identify an event with solitary analogue TC Beryl, analogues with 4–6 additional TC are provided (Slide 420-3 in presentation [1]). Earthquakes M> 5.7 for 5 days after the TC passed the forecast latitude are shown (Fig.2). Actual earthquakes M ≥ 5.3 on the conference days of July 2-4 are shown in black circles.

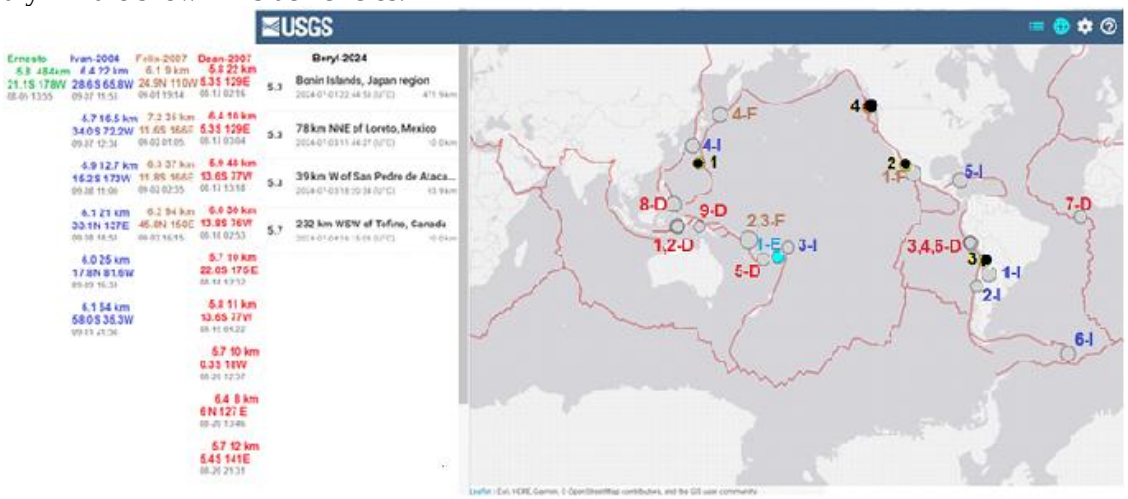


FIGURE 2. Prediction of seismic activity for the period from 2 to 5 July 2024 based on the analysis of TC Beryl analogues. Black circles - earthquakes during the conference days. Analogues are marked with a number and the first letter of TC.

Of the four earthquakes with M>5.3 that occurred, three coincided with the forecast in location with an accuracy of 300 km and in time up to a day (Fig.2). The over-prediction of the number of earthquakes and their magnitude was due to the use of 4 events with similar TC passage. But at the same time more TC were developing, from 4 to 6, and less intensively than the isolated Beryl-24.

The following paper by the authors was intended to be presented at the conference Suzdal2024-GCRAS. Only two earthquakes M>5.7 occurred from September 23 to 27. One was M=6.0 in Corontalo, Indonesia on September 23, and the other was M=6.3 in the Mauritius-Reunion region, depth 10 km, on September 26. The epicenter was located on the southwestern edge of an extended gravitational anomaly centered at (5 N 79 E) [2]. The sea level here is 106 m below the geoid surface. After the impact, a chain of 7 TCs was formed.

Let us highlight, out of 5 similar paired earthquakes since 2000, the events of July 15 and 19, 2017. After the impact of M=6.0 (17.4 S 66.5 E) a chain of 8 TCs was formed the next day (Fig.3). Ionosphere parameters of a chain of 11 TC were recorded by the Cosmos-1809 satellite after two American and one Chinese underground nuclear tests in September 1992 [3]. The formation of the TC chain was interpreted as the generation and nonlinear evolution of planetary magnetized Rossby-Aburjania waves [4]. Aburjania's calculations show that the self-organization of nonlinear large-scale isolated, highly localized vortex structures occurs due to the energy of non-uniform zonal wind in the stratosphere.

Thus, TC can be triggers for earthquakes, and on the other hand, earthquakes can be triggers of TC. Relationship between earthquakes and TC will be presented at the AIS-25 conference in May 2025, as well as a strong earthquake forecast for June 1-4.

Earthquake forecasting based on TC dynamics and their relationships [1,3] can be improved if:

1. Additionally, analyze short-term precursors of earthquakes in the atmosphere and ionosphere [5, 6].
2. Combine with the results of the medium-term earthquake forecast [7, 8].
3. Take into account solar activity data and variations in the cosmic ray fluxes [9].

4. Separately consider the moments of the Earth's passage through meteor showers, which will be presented in another message.

All this can only be realized in a comprehensive program using artificial intelligence.

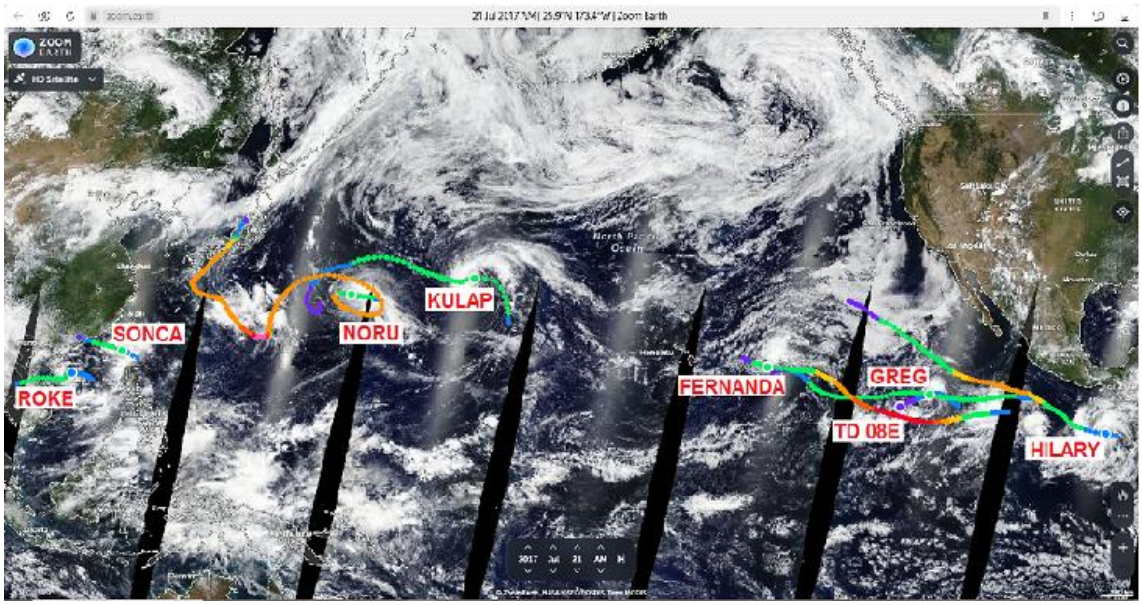


FIGURE 3. The chain of TCs after the earthquake in Mauritius - Reunion region on July 19, 2017. Hurricane Fernanda was in the antipodal region (17.1 N 135.3 W) at the impact time.

This investigation was performed with the financial support of Ministry of Science and Higher Education of the Russian Federation within the framework of the state assignment IZMIRAN.

1. Kostin V.M., Ovcharenko O.Ya., Trushkina E.P. Strong earthquakes on November 11-15 according to the weather forecast of tropical cyclones // *Proceedings of the 22nd International Conference "Modern problems in remote sensing of the Earth from space". Moscow: Space Research Institute RAS*. 2024. P. 420. (in Russian). DOI: 10.21046/22DZZconf-2024a.
2. Padma Rao B., Silpa S. A review of geophysical research: Perspective into the Indian Ocean Geoid Low // *Earth-Science Reviews.* 2023. V. 237. P. 104309. DOI: 10.1016/j.earscirev.2022.104309.
3. Kostin V.M., Belyaev G.G., Ovcharenko O.Ya., Trushkina E.P. Features of the relationship between tropical cyclones and earthquakes // *Current problems in remote sensing of the Earth from space*. 2022. V. 19. No. 1. P. 125-139. (in Russian). DOI: 10.21046/2070-7401-2022-19-1-125-139.
4. Aburjania G.D. Self-Localization of Planetary Wave Structures in the Ionosphere upon Interaction with Nonuniform Geomagnetic Field and Zonal Wind // *Izvestiya, Atmospheric and Oceanic Physics*. 2011. V. 47. No 4. P. 491-502. DOI: 10.11341/S0001433811040025.
5. Pulinets S., Herrera, V.M.V. Earthquake Precursors: The Physics, Identification, and Application // *Geosciences*. 2024. V. 14. P. 209. DOI: 10.3390/geosciences14080209.
6. Pulinets, S., Budnikov P. Atmosphere Critical Processes Sensing with ACP // Atmosphere. 2022. V. 13. P. 1920. DOI: 10.3390/atmos13111920.
7. Zavyalov A.D., Morozov A.N., Aleshin I.M., Ivanov S.D., Holodkov K.I., Pavlenko V.A. Method of medium-term earthquake forecast "Map of Expected Earthquakes" (KOZ): Experience of use and development prospects // *Geophysical processes and biosphere*. 2022. V. 21. No 2. P. 114-131. DOI: 10.21455/GPB2022/2-6.
8. Kosobokov V.G., Schepalina P.D. Times of increased probability of the world's strongest

earthquakes: 30 years of testing the hypothesis in real time // *Physics of the Earth*. 2020. No 1. P. 43-52. DOI: 10.31857/S0002333720010068.
9. Hegay V.V., Legenka A.D., Abunin A.A. et al. Solar activity, variations of galactic cosmic rays and global seismicity of the Earth // *Geomagnetism and Aeronomy*. 2022. V. 62. No 1. P. 1-12. DOI: 10.31857/S0016794022010102.

VARIATIONS OF SCHUMANN RESONANCES CHARACTERISTICS IN THE UPPER VOLGA REGION: OBSERVATIONS AND ANALYSIS

Maria. V. Shatalina[1,2], Fedor G. Sarafanov[1,2], Alexandra V. Volkova[2], Alexey A. Dolinin[1,2] and Yury. V. Shlyugaev[1,2]

[1]Lobachevsky State University of Nizhny Novgorod (UNN), Nizhny Novgorod, Russia
[2]Federal Research Center Institute of Applied Physics of the Russian Academy of Sciences (IAP RAS), Nizhny Novgorod, Russia

Recently, attention to the natural electromagnetic environment of the Earth and, in particular, its possible connections with climate variability and the evolution of biosystems has grown significantly [1, 2]. One of the most important phenomena of the electromagnetic environment are the so-called Schumann resonances [2]: eigenmodes of the Earth-ionosphere resonator excited by natural electrical phenomena - lightning [3, 4]. Understanding the connections between Schumann resonances and large-scale processes occurring in the atmosphere will make it possible to obtain an independent assessment of climate change on Earth[5], which makes it possible to predict climatic conditions both on Earth and on other planets [6]. To solve these problems, in addition to first-principles modeling, it is necessary to create, develop and improve continuous monitoring of various parameters of Schumann resonances.

This paper presents the results of measurements of two horizontal components of the magnetic field in the extremely low frequency (ELF) range in Upper Volga region. The daily and seasonal variations of various characteristics of the first few Schumann resonances are analyzed, and the dynamics of the amplitude of the fundamental harmonic are compared with the results of numerical modeling based on a semi-analytical model [7].To study the variations in magnetic field spectra, it is first necessary to move from magnetic field time series to spectrograms with a high time resolution sufficient to reveal the dynamics of individual resonance characteristics.

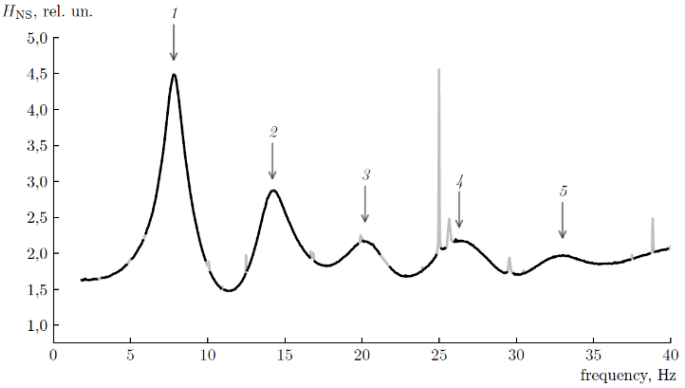


FIGURE 1. Spectrum of Schumann resonances observed in the Upper Volga region from January 1 to January 30, 2024. Interference, in particular, generated by spectrum aliasing during FFT calculations, is highlighted in gray. Arrows and numbers 1–5 mark the first five Schumann resonances at frequencies of 7.8 Hz, 14.3 Hz, 20.2 Hz, 26.3 Hz, and 33 Hz.

This transition was accomplished using the fast Fourier transform (FFT) applied to a 60-s-wide Blackman window with a step of 30 s, sliding over the time series. Half-window overlap is a standard method to avoid information loss when using window functions.

An example of the spectrum of Schumann resonances observed in our measurements is shown in Fig. 1. Note that, despite the fact that the presented picture of resonances is averaged over one-minute spectra of an entire month of observations, the spectrum takes on a characteristic form with significantly smaller time averagings.

The dynamics of the Schumann resonance characteristics is most clearly showed up on a daily scale. This is due to both the change in the intensity of thunderstorm centers during the day and the Earth-ionosphere resonator geometry distortion determined by the terminator motion and the corresponding change in the effective height of the ionospheric reflecting layer [8]. The existence of diurnal variability is well known both in DC GEC [1] and in AC GEC [4].

Fig.2 and Fig.3 present the diurnal variations in the amplitudes and central frequencies of the first three Schumann resonances based on observations of two horizontal components of the magnetic field H_{NS} and H_{EW} for the period from January to December 2024 inclusive. For the second and third harmonics, the figures do not show the value at 14:00 UT, since at this time regular local interference was activated at frequencies close to 15 and 20 Hz.

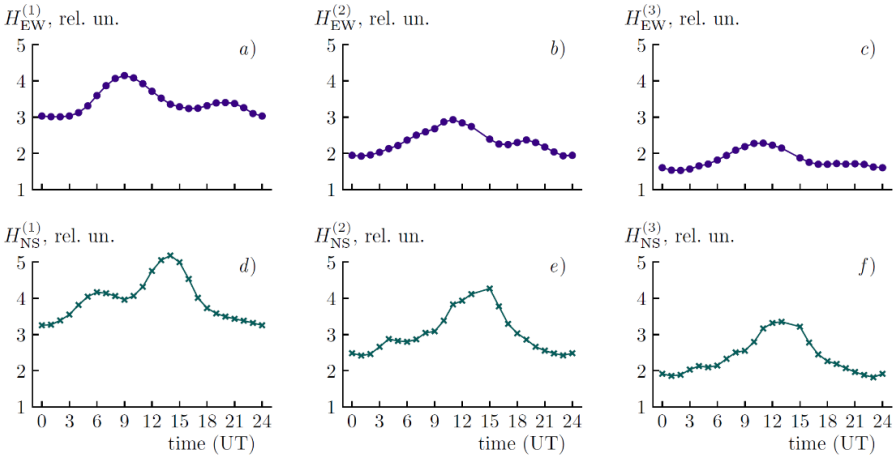


FIGURE 2. Diurnal variation of the amplitude the first three Schumann resonances based on observations for the period from January to December 2024. *a*)–*c*): H_{EW} component; *d*)–*e*): H_{NS} component.

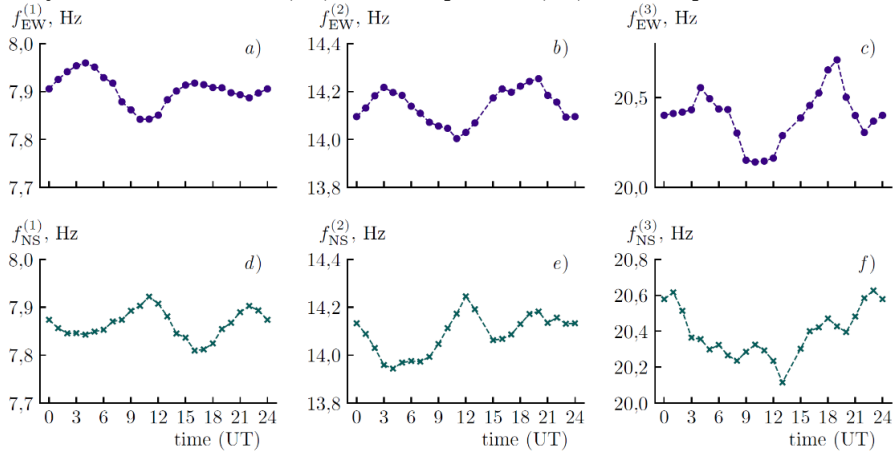


FIGURE 3. Diurnal variation of the central frequency the first three Schumann resonances based on observations for the period from January to December 2024. *a*)–*c*): H_{EW} component; *d*)–*e*): H_{NS} component.

The seasonal variation in amplitude primarily reflects the global variability of the source intensity. The summer maximum is not unexpected; it is known that the number of lightning and thunderstorm clusters also reaches a maximum in June-August, which is also indirectly confirmed by the summer maximum of the DC GEC intensity [9]. This is a consequence of the asymmetry of the distribution of land and ocean, which, in turn, due to the different density of discharges over these types of surfaces, leads to an asymmetry in the distribution of sources with a predominance in the Northern Hemisphere [10].

Fig. 4 shows the seasonal variations in the characteristics of the first Schumann resonance in the observed spectrum.

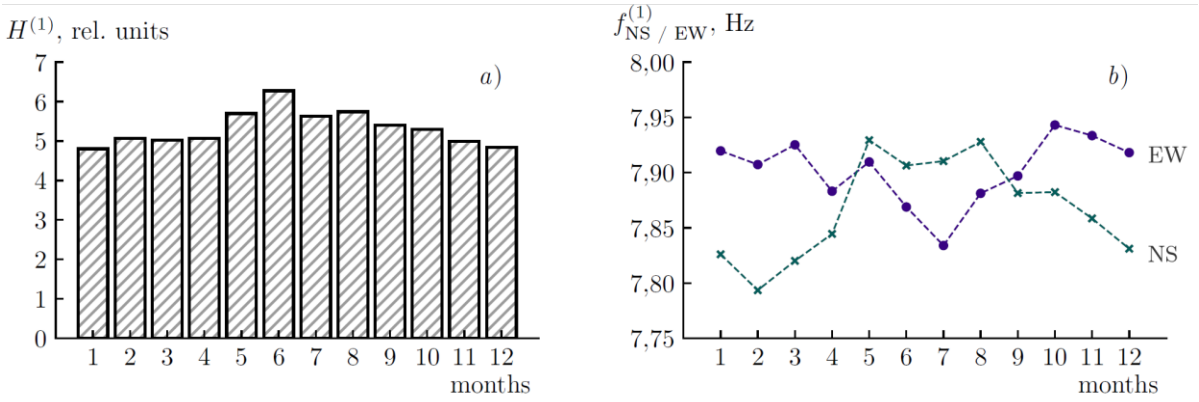


FIGURE 4. Seasonal variations of the first resonance characteristics based on observational data. *a*): variation of the magnetic field amplitude, *b*: variation of the central frequencies for H_{NS} and H_{EW} components

The variation in the central frequency is a more complex characteristic to analyze. The frequency is largely determined not so much by the sources as by the parameters of the Earth-ionosphere resonator, primarily the effective height of the waveguide. The possible mechanisms of the influence of daily variability of the ionosphere due to the movement of the day-night terminator were described above. Indirectly, daily variability of the ionosphere height also manifests itself on a seasonal scale due to changes in the ratio of daylight hours in the Northern and Southern Hemispheres.

The data obtained during observations in the ELF range of perpendicular components of the magnetic field from January to December 2024 in Upper Volga region were used to analyze the characteristics of Schumann resonances. Based on the analysis of the experimental data processing results, it was found that both the central frequencies and amplitudes have pronounced diurnal and seasonal variability. It was demonstrated that the amplitude dynamics reflects the variability in the intensity of the main world thunderstorm centers.

This investigation was performed with the financial support of the Ministry of Science and Higher Education of the Russian Federation within the framework of the state assignment of UNN (No. 0729-2020-0037).

1. Harrison R. The Global Atmospheric Electrical Circuit and Climate // *Surveys Geophys*. 2004. V. 25. P. 441-484. DOI: 10.1007/s10712-004-5439-8.
2. Grinberg M., Mudrilov M., Kozlova E. et al. Effect of extremely low-frequency magnetic fields on light-induced electric reactions in wheat // *Plants Signal Behavior*. 2022. V. 19, № 1. P. 2021664. DOI: 10.1080/15592324.2021.2021664.
3. Schumann W. O. Über die strahlungslosen Eigenschwingungen einer leitenden Kugel, die von einer Luftschicht und einer Ionosphärenhülle umgeben ist // *Z. Für Naturforschung.* 1952. V. 7. No 2. P. 149–154.

4. Bozoki T., Satori G., Williams E. и et al. Day-to-day quantification of changes in global lightning activity based on Schumann resonances// *J. Geophys. Res. Atmos.* 2023. V. 128. No 11. P. e2023JD038557. DOI: 10.1029/2023JD038557.
5. Williams E. R. The Schumann resonance: a global tropical thermometer// *Science.* 1992. V. 256. P. 1184–1187.
6. Evtushenko A. A., Ilin N. V., Kuterin F. A. O sushchestvovanii global'noy elektricheskoy tsepi v atmosfere Marsa *// Vestnik Moskovskogo universiteta. Seriya 3. Fizika. Astronomiya*. 2015. No 1. P. 57–60. [in Russian].
7. Bozoki T., Pracser E., Satori G., et al. Modeling Schumann resonances with schupy // *J. Atmos. Solar-Terr. Phys.* 2019. V. 196. P. 105144. DOI: 10.1016/j.jastp.2019.105144.
8. Nickolaenko A., Galuk Y. P., Hayakawa M. Terminator effect in the model Schumann resonance signals // *J. Atmos. Solar-Terr. Phys.* 2024. V. 256. P. 106195. DOI: 10.1016/j.jastp.2024.106195.
9. Slyunyaev N., Sarafanov F., Ilin N., et al. The seasonal variation of the direct current global electric circuit: 1. A new analysis based on long-term measurements in Antarctica // *J. Geophys. Res.* 2025. V. 130, No. 6. P. e2024JD042633. DOI: 10.1029/2024JD042633.
10. Christian H., Blakeslee R., Boccippio D., et al. Global Frequency and Distribution of Lightning as Observed from Space by the Optical Transient Detector // *J. Geophys. Res.* 2003. V. 108. Is. D1. P. ACL 4-1-ACL 4-15. DOI: 10.1029/2002JD002347.

IONOSPHERIC-MAGNETOSPHERIC RELATIONS

ON THE DIRECT APPROACH FOR MULTI-HOP RAY PATH SEARCH

Igor A. Nosikov and Maxim V. Klimenko

West Department of Pushkov Institute of Terrestrial Magnetism, Ionosphere and Radio Wave Propagation, Russian Academy of Sciences, Kaliningrad, Russia

Ionospheric variability is one of the key factors complicating the operation and forecasting of radio communication, satellite positioning, navigation, and radar systems. In this regard, improving algorithms for real-time ionospheric model corrections, as well as methods and software for radio path calculations, is an important scientific problem in ionospheric and space weather research [1]. This study explores the extension of the direct variational method for calculating multi-hop ray paths. Previously, Coleman [2] noted that computing such rays involves several computational challenges. In the present study, the problem of multi-hop ray calculation is reduced to the search for extremals corresponding to higher-order saddle points. The feasibility of this approach was previously discussed in [3, 4]. Figure 1 presents the results of ray trajectory calculations for two, three, and five hops. The numerical experiment was conducted under the assumption of mirror reflection of the "ionosphere" relative to the Earth's surface. The results demonstrate the fundamental applicability of the method for calculating higher-order saddle-type extremals and highlight the potential for further development of the approach.

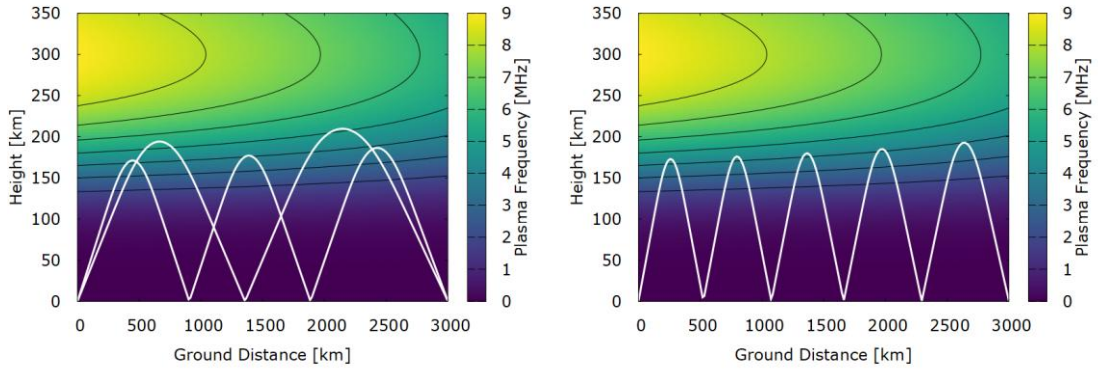


FIGURE 1. Examples of rays with two, three, and five hops using the generalized force method in an analytical ionospheric model [3].

The research was funded by the grant Russian Science Foundation N°– 23–77-10004, https://rscf.ru/project/23–77-10004.

1. Budden K. G. Radio waves in the ionosphere // Radio Waves in the Ionosphere. Cambridge University Press, 2009. 568 p.

2. Coleman C. J. Point-to-point ionospheric ray tracing by a direct variational method // *Radio Science*. 2011. V. 46. No. 5. P. 1-7. DOI: 10.1029/2011RS004748.
3. Nosikov I. A., Klimenko M. V., Zhbankov G. A., Podlesnyi A. V., Ivanova V. A., Bessarab P. F. Generalized force approach to point-to-point ionospheric ray tracing and systematic identification of high and low rays // *IEEE Transactions on Antennas and Propagation*. 2020. V. 68. No. 1. P. 455-467. DOI: 10.1109/TAP.2019.2938817.
4. Nosikov I. A., Klimenko M. V., Padokhin A. M., Nosikova V. V., Bessarab P. F. Generalized force method for point-to-point ray tracing in anisotropic ionosphere: Implementation and applications to NeQuick2 and IGRF13 models // *Radio Science*. 2025. V. 60. No. 3. ID e2024RS008092. P. 1-14. DOI: 10.1029/2024RS008092.

MORPHOLOGY AND DYNAMICS OF MID-LATITUDE AURORAL STRUCTURES OBSERVED IN THE SOUTH OF EASTERN SIBERIA

Aleksander B. Beletsky, Tatyana E. Syrenova, Aleksander V. Mikhalev and Roman V. Vasilyev

Institute of Solar-Terrestrial Physics of Siberian Branch of Russian Academy of Sciences, Irkutsk, Russia

Midlatitude auroras (MLA) are a rare geophysical phenomenon [1]. However, according to [2], subvisual MLAs are observed more frequently. Additionally, the observation of stable red auroral (SAR) arcs at mid-latitudes was previously considered to be extremely rare. According to the study [3], the probability of SAR arcs appears to decrease in Athabasca at subauroral latitudes during higher geomagnetic activity, but at the same time increases at lower latitudes. In addition, in [4], based on the analysis of 27-year observations of the all-sky cameras at Millstone Hill (42.6° N, 288.5° E), it is reported that the SAR arcs frequency was minimal in the years of solar minimum and maximal in the years of solar maximum, in contrast to what is observed in Athabasca (subauroral latitudes). That is, according to the works [3, 4], we can assume a high probability of registering structures of the SAR arc type during observations at the mid-latitude Geophysical Observatory (GphO) of ISTP SB RAS (52N, 103E, Tunka Valley, Republic of Buryatia) in years of high solar activity.

During the monitoring observations at the GphO in the solar cycles 23 and 24, SAR arcs were registered only during four geomagnetic storms. After the commissioning of Optical Instruments (OI) of the National Heliogeophysical Complex (NHC) RAS in April 2021, 62 MLAs have already been registered in the GphO ISTP SB RAS. In 40 cases, structures similar to SAR arcs were observed. NHC optical instruments include all-sky imagers, photometers, spectrometers, and Fabry-Perot interferometers. This work is based on data from the all-sky imagers, which are designed to record the spatiotemporal variations of the night sky glow. The direction of sight is zenith. The angular field of view of the cameras is 180°. The selection of the spectral range is provided by automatically replaceable interference filters. Further, the work presents 630.0 nm spectral channel data (red channel, FWHM 2 nm, the exposure time is 55 s).

Statistical data of MLAs registration by all-sky imagers depending on the geomagnetic situation were obtained (Figure 1a). The Kp and Dst indices were chosen as indicators of geomagnetic disturbance. Figure 1a illustrates the distribution of registered events in relation with the Dst and Kp indices. MLAs without SAR-arcs are marked with solid circles, MLAs with SAR-arcs are marked with

pluses. Based on these data, threshold geomagnetic indices were obtained, at which the operator manually determined MLAs in the frames of all-sky imagers in the red channel: Dst<=25 and Kp>=4.

Figure 1b shows the average number of registered MLAs per month from April 2021 to February 2025. Despite the low statistics, the annual dependence of the expected MLAs number can be traced to an increase in the auroras number in the spring and autumn, in accordance with the seasonal variation effect of the Russell-Mcferrone geomagnetic activity [5].

Figure 1c shows the monthly number of recorded MLAs (red curve) for the entire observation time of OI NHC RAS (as of February 2025) and F10.7 index time course (black curve). There is some correlation between the F10.7 index and the trend in the MLAs registered number.

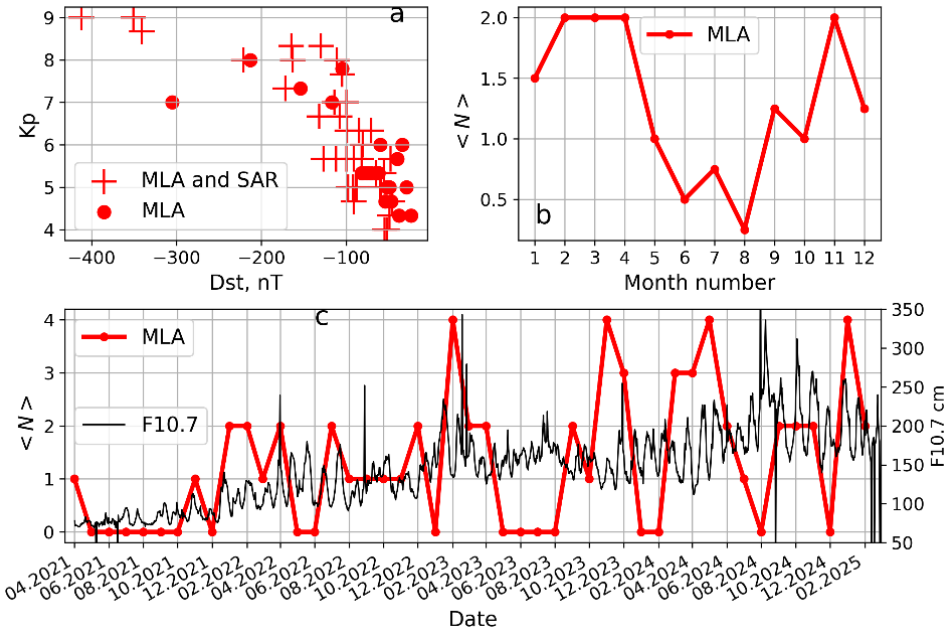


FIGURE 1. The distribution of recorded MLA events as a function of the Dst and Kp indices. MLA with structures similar to SAR arcs are marked with a plus (a). Panel b - the average number of registered MLAs per month from April 2021 to February 2025. Panel c - the monthly number of recorded MLAs from April 2021 to February 2025 (red curve) and F10.7 index time course (black curve, https://kp.gfz-potsdam.de/en/).

During the study the distribution of the geographical latitude of the observed SAR arc as a function of the Dst index was obtained by using NHC all-sky imagers data. The SAR automatic arc position search algorithm tracked the local maximum of the arc intensity, taking into account thresholds such as the maximum latitude shift in consecutive frames and the amplitude of the local maximum. Figure 2 shows the distribution of the geographical latitude of the registered SAR arc as a function of the Dst index (https://wdc.kugi .kyoto-u.ac.jp/wdc/Sec3.html). There is a fairly stable dependence of the arc latitude on the Dst index, except for some cases, for example, 10.05.2024, 11.05.2024, 01.01.2025 (highlighted in dark red, red and blue respectively).

Figure 3 shows the dependence of the geographical latitude of the SAR arc projection position on the Earth's surface (calculated for an altitude of 300 km) on the Dst index on May 10, 2024 (a), May 11, 2024 (b) and on January 01, 2025 (c). The lack of data after 20:00 UT on May 10 to 14:30 UT on May 11 is due to daylight hours. After 16:30 UT on May 11, solid cloud cover prevented further measurements. Based on our observational data, it can be assumed that the arc was present from the beginning of its observation at 17:50 UT on May 10, 2024 to 16:30 UT on May 11, 2024.

SAR arcs are one of the types of auroras observed in subauroral and mid-latitudes during intense geomagnetic storms, and which have a pronounced spatial structure [6]. It should be noted that SAR

arcs are formed and develop against the background of, as a rule, more intense spatially extended diffuse radiation fields of the upper atmosphere in the 630.0 nm emission, which according to some classifications are classified as mid-latitude aurora type “d" [6]. The most intense MLAs of type “d" are observed in the main phases of magnetic storms, SAR arcs are observed both in the recovery phase and in the main phases of geomagnetic storms. The morphology of MLAs type “d” observed in the Far Eastern Federal District of the Siberian Branch of the Russian Academy of Sciences is described quite fully in [7]. Presumably, the high number of registered MLA in the solar cycle 25 can be associated with the high intensity of the solar cycle and is undoubtedly associated with the commissioning of highly sensitive optical instruments of the NHC. The optical instruments of the NHC make it possible to detect and record optical manifestations of geophysical and geomagnetic disturbances in the upper atmosphere in the range of geographic latitudes of ~46-58 degrees north.

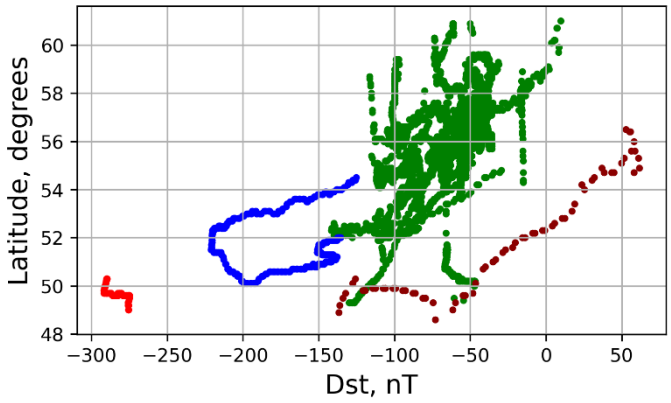


FIGURE 2. Distribution of the geographic latitude of the maximum SAR arc intensity location depending on the Dst index. Calculated for an altitude of 300 km. The distribution for May 10 and 11, 2024 and January 1, 2025 is highlighted in dark red, red and blue respectively.

An analysis of the variations behavior in the dominant 630.0 nm emission intensity in type “d” auroras observed at the Geophysical Observatory (GphO) of the SB of the RAS in the main phases during large geomagnetic storms preliminarily allows us to identify two types of its variations. The first type reflects a high correlation of the I630 with a symmetrical ring current (Dst index) with the superposition of less intense variations in this emission due to sub-storm activations. An example of this behavior can be the events of magnetic storms on March 24, 1991, April 6, 2000, November 20, 2003, etc. [7].

The second type of I630 variation shows a deviation from the predominant dependence of I630 on the Dst index, and extreme values of I630 are observed during substorm activations (substorms), after which there is no increase in I630 with a decrease in the Dst index. A bright example of this variation type is the St. Patrick's Geomagnetic storm event on March 17, 2015 [7]. Behavior of the I630 during the main phase of the geomagnetic storm on May 10, 2024 It allows us to identify the manifestation of both types of this emission behavior - a low-frequency component associated with a symmetrical ring current and more intense in the time range of ~ 18.50-19.50, probably due to sub-storm activations [8].

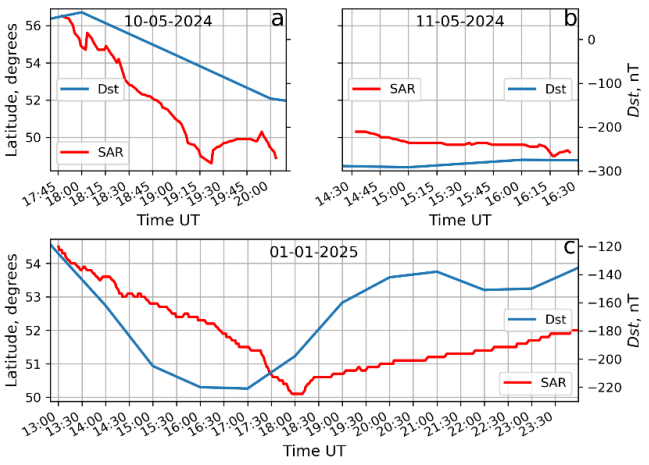


FIGURE 3. Time course of the SAR arc latitudinal position and the Dst index on May 10, 2024 (a) May 11, 2024 (b) and January 01,2025 (c).

Data processing and storage were financially supported by the Ministry of Science and Higher Education of the Russian Federation (Subsidy No. 075-GZ/C3569/278). The experimental data were obtained by using the Large-Scale Research Facilities (LSRF) "Optical instruments" https://ckp-rf.ru/catalog/usu/4138180/.

1. Krakovetsky Yu.K., Loisha V.L., Popov L.R. Chronologiya polyarnyh siyaniy za poslednee tysyacheletie // *Solnechnye dannye*. 1989. N. 2. P. 110–115. (in Russian).
2. Shiokawa K., Ogawa T., Kamide Y. Low-latitude auroras observed in Japan: 1999–2004 // *J. Geophys. Res*. 2005. V. 110. Is. A5. A05202. DOI: 10.1029/2004JA010706.
3. Yadav S., Shiokawa K., Otsuka Y., Connors M. Statistical study of subauroral arc detachment at Athabasca, Canada: New insights on STEVE // *Journal of Geophysical Research: Space Physics*. 2022. V. 127. P. e2021JA029856. DOI: 10.1029/2021JA029856.
4. Mendillo M., Baumgardner J., Wroten J. SAR arcs we have seen: Evidence for variability in stable auroral red arcs // *Journal of Geophysical Research: Space Physics*. 2016. V. 121. No 1. P. 245–262. DOI:10.1002/2015JA021722.
5. Russell C. T., McPherron R. L. Semiannual variation of geomagnetic activity // *J. Geophys. Res*. 1973. V. 78. No 1. P. 92–108. DOI:10.1029/JA078i001p00092.
6. Rassoul H.K., Rohrbaugh R.P., Tinsley B.A., Slater D.W. Spectrometric and photometric observations of low-latitude aurorae // *J. Geophys. Res*. 1993. V. 98. Is. A5. P. 7695–7709. DOI: 10.1029/92JA02269.
7. Mikhalev A. V. Mid-latitude aurora in solar cycles 23–24 from observations in the south of Eastern Siberia // *Solar-Terrestrial Physics*. 2019. V. 5. Iss. 4. P. 66–73. DOI: 10.12737/stp-54201909.
8. Yasyukevich Y., Vasiliev R., Rubtsov A., et. al. The Extreme Magnetic Storm of May 10–19, 2024: Coupling Between Neutral and Charged Components of the Upper Atmosphere and the Effect on Radio Systems. // *Doklady Earth Sciences*. 2025. Vol. 520. Art no. 33. DOI:10.1134/S1028334X24604978.

THE INFLUENCE OF AMPLITUDE AND FREQUENCY VARIATIONS OF THE CHORUS WAVE PACKET ON THE ACCELERATION OF ENERGETIC ELECTRONS

Veronika S. Grach[1], Andrei G. Demekhov[1,2]

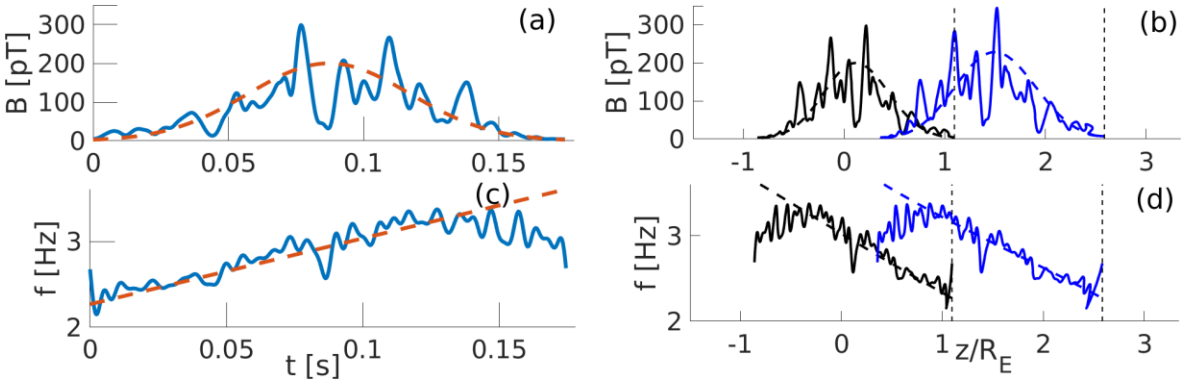
[1]Institute of Applied Physics, Nizhny Novgorod, Russia
[2]Polar Geophysical Institute, Apatity, Russia

The resonant wave-particle interactions play a significant role in the dynamics of Earth's radiation belts [1-3]. For quasi-monochromatic wave packets with high amplitudes (chorus emissions, observed by various satellites [4-6]), nonlinear effects may significantly affect the interaction. Analytical theory on nonlinear interaction was developed for monochromatic wave [7-10]. It was shown that, for whistlers waves, particle trapping can lead to a significant acceleration of the electrons [9-14]. The influence of finite packets length, as well as of frequency and amplitude variations, was studied mostly by numerical simulations [15-17]. The main result of these studies is that amplitude variations (finite packet length) makes acceleration by trapping less effective.

In this paper, we study in detail how amplitude and frequency variations of the wave packet, as well as its location along the geomagnetic field lines, influences the resonant interaction of energetic electrons with a chorus wave packet.

We use test particle method, where the motion equations are solved for an ensemble of electrons in a geomagnetic field and known model wave field. We model the wave packet based on Cluster data for an event of 08:46 UT on 18.04.2002. The instantaneous amplitude and frequency were determined using the Hilbert transform for one electric field component, the resulting temporal profiles are shown in Figs. 1a and 1c. For the 'ideal' packet, we use Gaussian approximation for the amplitude profile and linear frequency profile. We use the following assumptions: dipole geomagnetic field, L=4.4; gyrotropic model of cold plasma density, with N_L=10 cm^{-3} (the subscript L denotes equatorial values); chorus wave packet is generated near the equator and temporal profiles in Figs. 1a and 1c correspond to the equator (z=0, where z is a coordinate along the geomagnetic field line). The spatio-temporal distribution of the wave field is then retrieved under the assumption of field-aligned wave propagation away from the equator with the group velocity determined by cold plasma dispersion relation. Examples of spatial profiles are shown in Figs. 1b and 1d (here R_E is the Earth's radius). We consider 4 wave packets: Gaussian amplitude profile and linear frequency profile ('ideal' packet, no subpackets, hereafter packet I), amplitude variations ("real" profile) and linear frequency (packet II), Gaussian amplitude and frequency variations (packet III) and amplitude&frequency variations (packet IV).

The model wave field is then used to evaluate trajectories of test electrons interacting with chorus waves at the cyclotron resonance. For each packet, we consider 20 locations along the field line, with front packet edge $0.5 \le z_f/R_E \le 3.33$. The upper limit is based on chorus emissions statistics [5]. We use the standard gyro-averaged equations of electron motion, which can be found, e.g., in [11]. The equations of motion are solved numerically by Bogacky-Shampine variant of the Runge-Kutta method. For each location, the ensemble of electrons is placed at the front packet edge z_f and is moving towards the equator (and the wave packet). The single transport of the test particles through the wave packet is studied, wave packet evolution during the interaction is taken into account. The initial parameters of the test electrons are as follows: 300 initial energies W_0 in the range [20, 2000] keV, 145 initial equatorial pitch angles θ_{L0} in the range [5.6°,76°], and 128 initial phases uniformly distributed in [0, 2π). Note that for every z_f the range of W_0, θ_{L0} is further limited by the following factors: the point of mirror reflection for particles should be at $z > z_f$ (i.e., maximum possible θ_{L0} decreases from 76° at $0.5R_E$ and to 22° at $3.33R_E$) and the resonant interaction for a given W_0, θ_{L0} and z_f should be possible (this condition is determined by preliminary analysis).



FUGURE 1. Amplitude (a,b) and frequency (c,d) profiles for the model wave packet. Solid lines correspond to the data, dashed lines to the approximations.

The simulation results for z_f=1.1R_E are shown in Fig. 2. In simulation analysis, we considered the electron trapped if the resonance condition during the interaction was fulfilled at more points than for

unperturbed trajectory (without the wave packet influence). We also assume the interaction nonlinear, if (a) trapped particles are present and (b) phase averaged change in energy is significant.

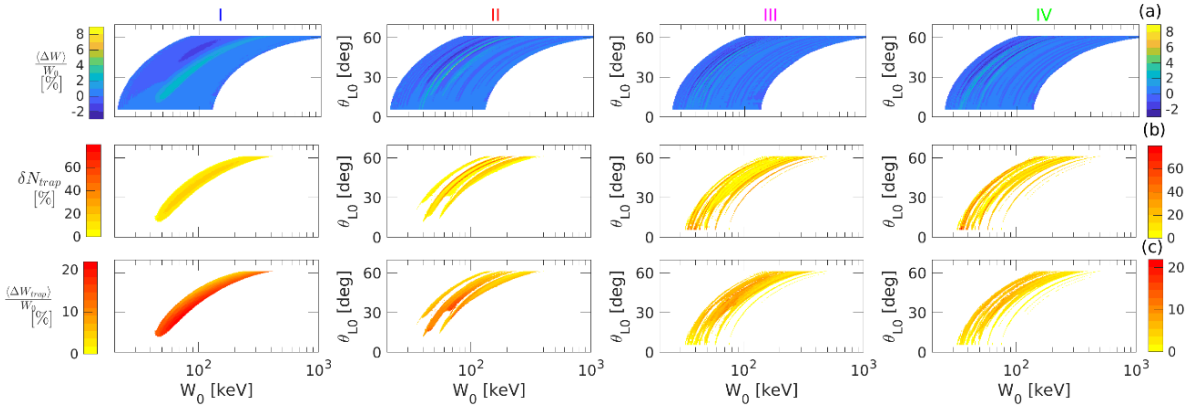


FIGURE 2. Phase averaged relative change in energy (a), fraction of trapped particles (b), phase averaged relative change in energy for trapped particles (c).

As one can see from Fig. 2, for the ideal packet there is a narrow region of W_0, θ_{L0}, where nonlinear interaction prevails. If any subpacket variations are present, the nonlinear region is wider, but has fine structure. Subpacket variations also lead to wider spread in energy gain for trapped particles.

Dynamics of particle acceleration depending on the location of the wave packet is shown in Fig. 3. Top row shows the fraction of W_0, θ_{L0}, for which at the fixed z_f the interaction with specified packet gives the maximum value of phase averaged relative change in energy (a, the value must exceed 2 %), the maximum relative energy gain (b, the value must exceed 10 %) and the maximum fraction of trapped particles (the value must exceed 5 %). Middle and bottom rows show the phase averaged relative energy change (d) and initial energy, corresponding to it (g), maximized over W_0, θ_{L0}, the relative energy gain maximized over all initial electron parameters (e) and the corresponding W_0 (h), the fraction of trapped particles maximized over W_0, θ_{L0} (f), and the corresponding W_0 (i).

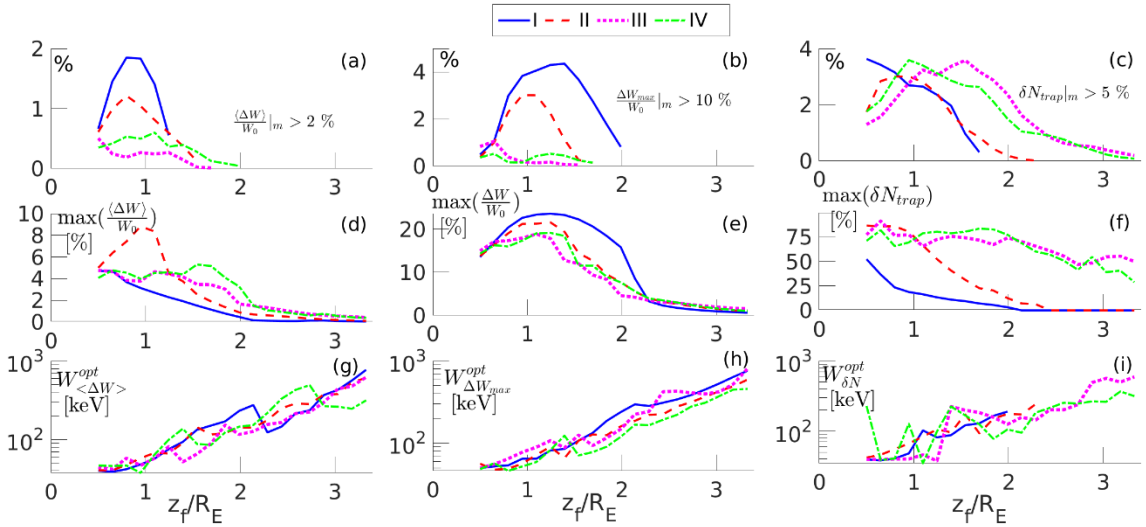


FIGURE 3. Dynamics of electron acceleration in dependence on wave packet location.

As expected, the maximum energy gain takes place for the wave packets which are located near the equator. Initial energies corresponding to the maximum gain increase as the wave packet propagates

from the equator. For $z_f/R_E<2.3$ the maximum relative energy gain had the largest value for the ideal packet, but at the same time the maximum phase averaged change for ideal packet had the smallest value. It is caused by higher trapping probability for the wave packets with variations. But the regions of W_0, θ_{L0}, where the acceleration by the ideal packet (both for maximum and phase averaged energy gain) is the most effective are significantly larger than similar regions for wave packets with variations (for the wave packets not far from the equator). It is important to note that for the wave packets with frequency variations (III and IV) particle trapping by the wave field is possible for all considered z_f, i.e., it is observed for large distances from the equator and high initial energies of hundreds keV. However, the energy gain in the latter cases is rather small.

As a conclusion of this study, we can say the following. In total, over all values of initial parameters, variations (of either/both frequency and amplitude) increase the probability of trapping while decreasing the maximum energy gain. This can be explained as follows. With amplitude variations (see Fig. 1b), there are several regions of high amplitudes, while in the ideal packet there is only a single one; also, with amplitude variations high amplitude regions have higher amplitude gradients. Frequency variations create additional frequency gradients. Thus, variations can create more areas, where condition of the wave trapping is fulfilled, but these conditions would be faster violated, leading to a smaller energy gain. Similar results were obtained for the sequence of subpackets in [17]. However, it is important to note that for some small regions of initial electron parameters, the resonant interaction with wave packets with amplitude and/or frequency variations still causes a significant acceleration (both for maximum and phase averaged energy gain). For more comprehensive analysis, the study of electron distribution function and its evolution is required. This analysis will be performed in future research.

We are grateful to O. Santolik for providing the Cluster data. The work of V. S. Grach (numerical simulations) was carried out as a part of State Assignment of Ministry of Education and Science of the Russian Federation, project No. FFUF-2023-0002.The work of A. G. Demekhov on the problem formulation and interpretation of the results has been supported by the Russian Science Foundation under grant No. 22-62-00048.

1. Kennel C. F., Petschek H. E. Limit on Stably Trapped Particle Fluxes // *J. Geophys. Res.* 1966. V.71, No. 1. P. 1-28. DOI: 10.1029/JZ071i001p00001.
2. Bespalov P. A., Trakhtengerts V. Y. The cyclotron instability in the Earth radiation belts // *Reviews of Plasma Physics*. V. 10 / ed. by M. A. Leontovich. Plenum Publ., N.Y., 1986. P. 155–293.
3. Li W., Hudson, M.K. Earth's Van Allen radiation belts: From discovery to the Van Allen Probes era // *J. Geophys. Res.: Space Physic*s. 2019. V. 124, No. 11. P. 8319–8351. DOI: 10.1029/2018JA025940.
4. Cattell C., Wygant J.R., Goetz K., et al. Discovery of very large amplitude whistler-mode waves in Earth's radiation belts // *Geophys. Res. Lett.* 2008. V. 35. No. Art. no. L01105. DOI: 10.1029/2007GL032009.
5. Santolık O., Kletzing C. A., Kurth W. S., et al. Fine structure of large-amplitude chorus wave packets // *Geophys. Res. Lett.* 2014. V. 41, No. 2. P. 293–299. DOI:10.1002/2013GL058889.
6. Wilder F.D., Ergun R.E., Goodrich K.A., et al. Observations of whistler mode waves with nonlinear parallel electric fields near the dayside magnetic reconnection separatrix by the Magnetospheric Multiscale mission // *Geophys. Res. Lett.* 2016. V. 43. No. 12. P. 5909–5917. DOI: 10.1002/2016GL069473
7. Karpman V. I. Nonlinear Effects in the ELF Waves Propagating along the Magnetic Field in the Magnetosphere // *Space Sci. Rev.* 1974. V.16. No. 3. P. 361-388. DOI: 10.1007/BF00171564.
8. Shklyar D. R., Matsumoto H. Oblique Whistler-Mode Waves in the Inhomogeneous Magnetospheric Plasma: Resonant Interactions with Energetic Charged Particles // *Surveys in Geophysics*. V. 30 P. 55-104. DOI: 10.1007/s10712-009-9061-7.

9. Albert J. M. Gyroresonant interactions of radiation belt particles with a monochromatic electromagnetic wave // *J. Geophys. Res. Space Phys.* 2000. V. 105. No. A9. P. 21191–21209. DOI: 10.1029/2000JA000008.
10. Artemyev A.V., Neishtadt A.I., Albert J.M., et al. Theoretical model of the nonlinear resonant interaction of whistler-mode waves and field-aligned electrons // *Phys. Plasmas.* 2021. V. 28. No. 5. Art. no. 052902. DOI: 10.1063/5.0046635.
11. Demekhov A. G., Trakhtengerts V. Y., Rycroft M. J., Nunn D. Electron acceleration in the magnetosphere by whistler-mode waves of varying frequency // *Geomagnetism and Aeronomy.* 2006. V. 46. P. 711–716. DOI: 10.1134/S0016793206060053.
12. Demekhov A. G., Trakhtengerts V. Y., Rycroft M., Nunn D. Efficiency of electron acceleration in the Earth's magnetosphere by whistler mode waves // *Geomagnetism and Aeronomy.* 2009. V. 49, No. 1. P. 24–29. DOI: 10.1134/S0016793209010034.
13. Omura Y., Furuya N., Summers D. Relativistic turning acceleration of resonant electrons by coherent whistler mode waves in a dipole magnetic field // *J. Geophys. Res. Space Phys.* 2007. V. 112, No. A6. Art. no. A06236. DOI: 10.1029/2006JA012243.
14. Agapitov O. V., Artemyev A. V., Mourenas D., et al. Nonlinear local parallel acceleration of electrons through Landau trapping by oblique whistler mode waves in the outer radiation belt // *Geophys. Res. Lett.* 2015. V. 42. No. 23. P. 10140–10149. DOI: 10.1002/2015GL066887.
15. Tao X., Bortnik J., Thorne R.M., et al. Effects of amplitude modulation on nonlinear interactions between electrons and chorus waves // *Geophys. Res. Lett.* 2012. V. 39, No. 6. Art. no. L06102. 10.1029/2012GL051202.
16. Zhang X. J., Agapitov O., Artemyev A. V. et al. Phase decoherence within intense chorus wave packets constrains the efficiency of nonlinear resonant electron acceleration // *Geophys. Res. Lett*. 2020. V. 47, No. 20. Art. no. e2020GL089807. DOI: 10.1029/2020GL089807.
17. Hiraga R., Omura, Y. Acceleration mechanism of radiation belt electrons through interaction with multi-subpacket chorus waves // *Earth, Planets and Space*. 2020. V. 72. Art. no. 21. 10.1186/s40623-020-1134-3.

MERIDIONAL NET OF INFRARED SPECTRO-GRAPHS AND SOME RESULTS

Igor I. Koltovskoi[1], Petr P. Ammosov[1], Galina A. Gavrilyeva[1] and Vladimir I. Perminov[2]

[1] Yu.G. Shafer Institute of Cosmophysical Research and Aeronomy SB RAS, Yakutsk, Russia
[2.] A.M. Obukhov Institute of Atmospheric Physics RAS, Moscow, Russia

The report presents the idea of creating a meridional network of infrared spectrographs that detect hydroxyl bands in the infrared region (about 1.5 microns), radiating at an altitude of about 87 km. The aim of studying hydroxyl bands in the infrared region is to study variations in mesopause temperature and wave processes. It is generally accepted that the rotational temperature calculated from hydroxyl bands corresponds to the temperature of the mesopause region at a given altitude [1]. The meridian network consists of four identical spectrographs installed at optical stations of different latitude.

Continuous registration of OH(3,1) hydroxyl bands by infrared spectrograph has been carried out at the Maimaga optical station of SHICRA SB RAS since 2014. The Maimaga station (63°N, 129.5°E) is located 120 km north of Yakutsk far from the city lights. The spectrograph consists of a Shamrock monochromator and a highly sensitive infrared photodiode recorder manufactured by ANDOR. The

operating wavelength range is 1490 - 1544 nm. Cooling is -60°C. The angle of view is approximately 3 degrees. The resolution of the spectrograph at an entrance slit width of 0.2 mm is 0.8 nm. The spectra of the hydroxyl molecule OH(3,1), emitted at an altitude of about 87 km, are recorded automatically at an angle of immersion of the Sun greater than 9 degrees every minute and transmitted every day via the Internet to the Institute's server.

From September 2015, a similar infrared spectrograph was installed at Tiksi station (71.6°N, 128.7°E) and from October 2017 at the station in Neryungri (56.7°N, 124.7°E). From 2022, a spectrograph with the same recorder but with the MDR-2 monochromator (66.7°N, 123.3°E) began recording at station Zhigansk. Thus, all four stations have identical light-sensitive infrared spectrographs. According to many recent works, the OH (3,1) band is sufficiently well thermalized and corresponds to the temperature of the surrounding neutral atmosphere at its emission altitude. The choice of the hydroxyl emission band in the infrared region is due to three circumstances. First, the greatest intensity of hydroxyl emissions in this region of the spectrum, second, the smaller contribution of stray light from stars and the Moon, and third, the absence of polar aurora emissions.

Measurements of the infrared spectrograph were carried out at night in cloudless and low-cloud weather. Hydroxyl OH(3,1) emissions with an exposure of 60 seconds were recorded. The coefficients for calculating the synthetic spectra were taken from [2],[3].

The method for determining the temperature from the spectrum of hydroxyl radiation is based on the fact that the intensity distribution in the lines of the rotational bands is related to the “excitation” temperature as

$$S(\lambda,T)=\text{const}\cdot\lambda\ -4I(J)\cdot\exp[-F(J)\cdot c\cdot h/kT],$$

where F(J) is the excitation energy, T is the rotational temperature, J is the rotational quantum number, I(J) is the intensity factor, k is the Boltzmann constant, c is the speed of light, λ is the wavelength, and h is the Planck constant. Comparison of the measured spectrum with the spectrum calculated with allowance for the parameters of the optical system makes it possible to estimate the temperature at which excitation occurs.

The evaluation begins with calculating the line spectrum of the molecular band of the hydroxyl S(λ, T) at a given temperature. Since the actual spectrum is estimated by summation over the columns of the matrix, the output from the device is a discrete series S(i, T) with equal wavelength intervals, where i is the pixel number. The spectral parameters of the rotational lines of the hydroxyl bands were taken from the Night-Sky Radiation Spectrum Atlas.

Then, the synthetic contour S(i) is calculated for a given temperature, for which purpose the molecular band model spectrum S(i, T) is convoluted with the instrument function:

$$S'(i)=\sum S(i,T)\cdot z(i-j),$$

where z(i) is the transfer function of the spectrograph, i is the number of the pixel, and j is the transfer function width in pixels.

In addition to hydroxyl emission lines, the actual spectrum also exhibits a continuous component. This part is composed of night-sky radiation proper, called continuum, and other components, such as twilight, moonlight, stellar component, etc.

These continuous parts enter into the modeled spectrum S"(0) in the form of a linear function:

$$S''(i)=A+B(i)+C\cdot S'(i),$$

where A + B(i) is the continuous component of the spectrum, and C is the fitting coefficient.

It is assumed that the temperature at which the sum of the squares of the deviations of the synthetic spectrum from the real values of F(T) is minimal corresponds to the actual rotational temperature:

$$\text{Min}F(T)=\sum[(E(i)-S''(i,T))]^2,$$

where E(i) is the real spectrum.

Minimizing the functional F(T) yields a system of linear equations with respect to the fitting parameters A, B, and C for a given temperature. The contours are adjusted at temperatures from 100 to

300 K in 2 K steps. As a result, a number of values of F(T) are obtained, the minimum of which corresponds to the temperature at which the synthetic spectrum is best fitted to the spectrum measured with the spectrograph.

As an example, Figure 1 shows the average rotational temperatures of the OH(3,1), measured at different latitudes during one season. It can be seen from the figure that the seasonal change in the rotational temperature of hydroxyl is well traced [4]. So, the temperature heats up from 150K in the middle of August to 210-220 K in the winter months.

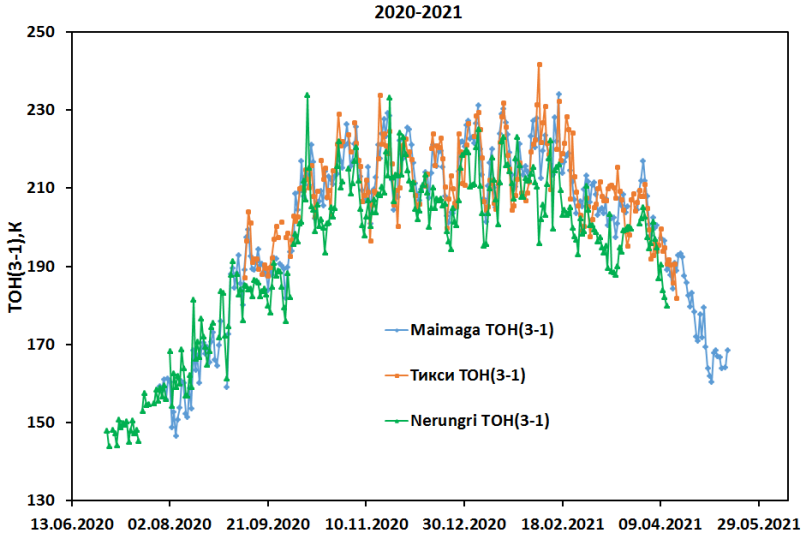


FIGURE 1. Comparison of the mean rotational temperatures of the OH(3,1) band measured at different optical stations.

A comparison was also made between the mean rotational temperatures of the OH(3,1) band measured at Neryungri station and the mean rotational temperatures of the OH(6,2) band obtained at the Zvenigorod research station (56°N, 37°E) of the Obukhov Institute of Atmospheric Physics of the Russian Academy of Sciences for 2 observing seasons (Figure 2).

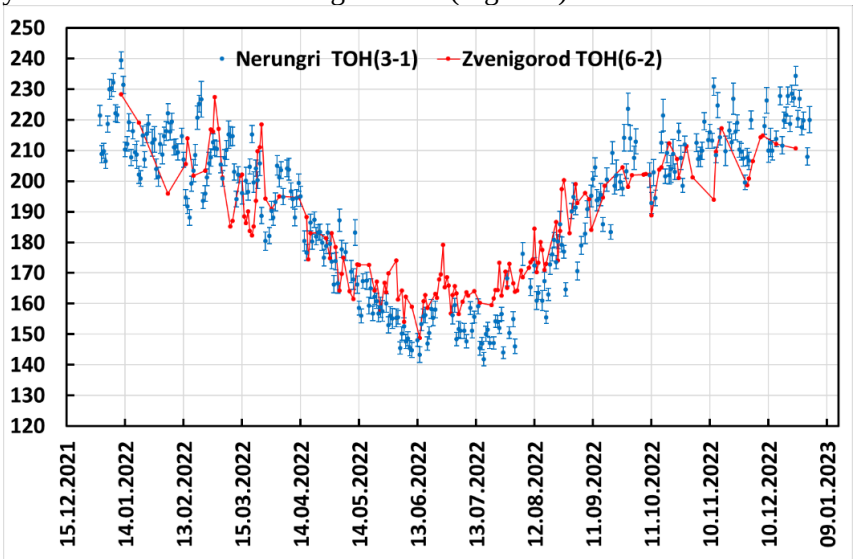


FIGURE 2. Comparison of the mean rotational temperatures of the OH(3,1) and OH(6,2) bands measured at different meridian stations.

Thus, a meridional network of infrared spectrographs was created in order to study variations in mesopause temperature and wave processes. As an example, the seasonal course of the average rotational temperatures of the hydroxyl band is shown. A comparison of these temperatures from two different meridian stations has also been made.

This investigation was performed with the financial support by the Russian Science Foundation grant No 25-27-20119.

1. Shefov N.N., Semenov A.I., Homich V.Yu. Izluchenie verhnej atmosfery – indikator ee struktury i dinamiki [Atmospheric Radiation as an Indicator of Its Structure and Dynamics]. Moscow, GEOS Publ., 2006. 741 p. (In Russian).
2. Mies F.H. Calculated vibrational transition probabilities of OH(X2Π) // *J. Molecular Spectrosc*. 1974. V. 53. № 2. P. 150–188.
3. Krasovskij V. I., Šefov N. N. Airglow // Space Science Reviews. 1964. V. 4. Is. 2. P.176-198.
4. Lubken F.–J., von Zahn U. Thermal structure of the mesopause region at polar latitudes // *J. Geophys. Res*. 1991. V. 96. No D11. P. 20841–20857. DOI: 10.1029/91JD02018.

ENERGETIC PROTONS AND ELECTRONS UNDER THE EARTH RADIATION BELT ON THE MAIN PHASE OF MAGNETIC SUPERSTORM

Alexei V. Dmitriev and Alla V. Suvorova

D.V. Skobeltsyn Institute of Nuclear Physics M.V. Lomonosov Moscow State University, Moscow, Russia

The sudden commencement of superstorm of May 10, 2024 was observed at 17:06 UT, when a strong interplanetary shock hit the Earth such that the solar wind dynamic pressure jumped to about Pd = 50 nPa and Bz component of interplanetary magnetic field (IMF) became strong negative (~-20 nT) as show in Fig. 1. The main phase was developed until 02:20 UT on 11 May and the storm reached maximum with the storm index SYM-H = -512 nT. During the main phase, the IMF Bz was negative most of time with brief reversals. The solar wind pressure stayed strong and exhibited several sharp increases and decreases which were manifested in corresponding variations of SYM-H index.

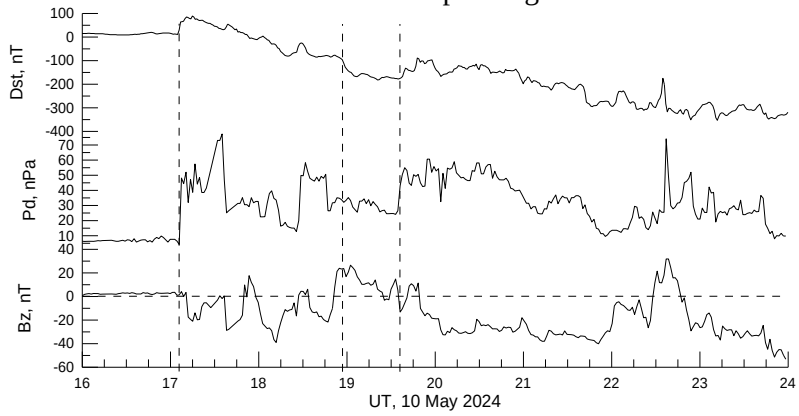
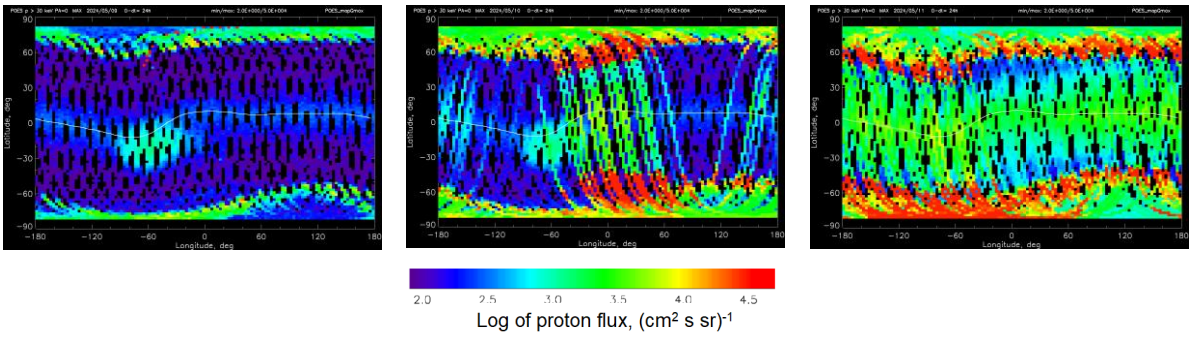


FIGURE 1. Variations of the geomagnetic SYM-H index (upper panel), solar wind dynamic pressure (middle panel), and IMF Bz (lower panel) during the main phase of the superstorm on May 10, 2024. Dashed lines indicate the storm sudden commencement and interplanetary shock at 17:06 UT, the beginning and the end of magnetospheric decompression at 18:57 and 19:36 UT, respectively.

During the main phase, the forbidden zone at low latitudes was temporally populated by energetic electrons and protons. The forbidden zone extends in ~20° vicinity of the dip equator excepting the region of South Atlantic Anomaly (SAA) located in the longitudinal sector from 100W to 0E. In the forbidden zone, energetic charged particles are quasi-trapped, i.e. during their azimuthal drift in the geomagnetic field they inevitable come to the SAA region where the magnetic field lines descend to very low heights such that energetic charged particles loss the energy in ionization of the dense atmosphere. Hence, energetic charged particles can be considered as an additional source of ionization of the ionosphere and upper atmosphere [1].



a b c

FIGURE 2. Geographic maps of >30 keV proton fluxes during a quiet day on May 9 (a) and on the main phase (b) and in the maximum (c) of the superstorm on May 10, 2024. The white curve indicates the dip equator.

In Fig. 2b, one can see that the enhanced fluxes ~50 $(cm^2\ s\ sr)^{-1}$ of >30 keV protons occurred in ~20° vicinity of the dip equator above Pacific in the longitudinal sector from 170E to 127W at drift shells $L < 1.13$ (see Table 1). They were observed by two POES satellites in the prenoon sector. The satellites moved one-by-one such that P8 passed the equator ~12 min earlier than P8 satellite. The earliest enhancement of protons was observed at 19:00 UT on 10 May at longitude 127W by P8 satellite and then at 19:12 UT at longitude 147W by P3 satellite.

TABLE 1. First injection of energetic particles under the inner ERB

SC	LT	Time	Long φ°	*Je*, $(cm^2 s\ sr)^{-1}$ >40 keV	*Je*, $(cm^2 s\ sr)^{-1}$ >130 keV	*Jp*, $(cm^2 s\ sr)^{-1}$ >30 keV	*L*
P8	10.5	19:00	-127	-	-	5E1	1.13
P3	9	19:12	-147	-	-	6E1	1.12
P9	9	19:22	-153	7E4	5E4	5E1	1.11
P5	7	19:37	177	3E6	1E6	5E1	1.10

It is important to note that the fluxes of protons in the forbidden zone are overlapped with very intense fluxes of protons originated from the ring current, which is quickly developed on the main phase of magnetic storms. The ring current protons are characterized by high intensities of $>10^3$ $(cm^2\ s\ sr)^{-1}$ and populate mainly night and evening sectors in the beginning of main phase. At that time, the ring current is asymmetric. In Fig. 2(b), one can see intense proton fluxes at all latitudes in the longitudinal sector from 100W to 100E, which corresponds to evening regions. At low-to-middle latitudes those protons arrive to low altitudes as energetic neutral atoms after charge-exchange interaction in the ring current region, which is located at drift shells above L=2. At low altitudes, the energetic neutral atoms loss their electron and become ionized in interaction with the dense atmosphere. The neutral atoms are not guided by the magnetic field and, thus, they propagate in any direction and populate a wide range of latitudes. At middle-to-high latitudes, very intense ($>10^4$ $(cm^2\ s\ sr)^{-1}$) fluxes are produced by protons

precipitating directly from the ring current region. With developing the main phase, the ring current becomes symmetric and occupies all local times as shown in Fig. 2(c).

Forbidden energetic electron (FEE) enhancements occurred in the Pacific region as one can see in Fig. 3. The increases of electron fluxes were observed in ~20° vicinity of the dip equator in the latitudinal sector from 120E to 140W. The first FEE enhancement occurred at ~19:22 UT near drift shell L=1.11 (see Table 1) in the prenoon sector at longitude 150W. The intensity of electrons was modest and did not exceed 10^5 $(cm^2\,s\,sr)^{-1}$. The next FEE enhancement at 19:37 UT was much stronger ($>10^6$ $(cm^2\,s\,sr)^{-1}$) and observed deeper at L = 1.1 in the morning sector at longitude 177E.

It is important that the enhancements were observed for >30 keV and >100 keV simultaneously. This meant that this longitudinal sector is close to the region of electron injection from the inner radiation belt. Otherwise, one could see only enhancements of >30 keV because the >100 keV electrons escape from the injection region quickly due to short period of the azimuthal drift (Td ~ 4h), while the >30 keV electrons have much longer azimuthal drift (Td ~ 15h). The consequence of the two enhancements with time gap of 15 min in the narrow longitudinal sector can be considered as manifestation of one long-lasting injection above the Pacific region.

As one can see in Table 1, the FEE enhancements were observed simultaneously with the proton enhancements. It should be noted that being injected to low latitudes, electrons and protons drift in geomagnetic field in opposite directions – eastward and westward, respectively. Hence, the injection region should be located somewhere eastward from the proton injection and westward from the electron injection. From comparison of Fig. 2 and 3 we can conclude that the injection region should have a spatial extension and it is located in the longitudinal sector from 120E to 140W. At 19UT this sector corresponds to morning – prenoon local time. Moreover, the injection process should have a duration of the order of 20 min.

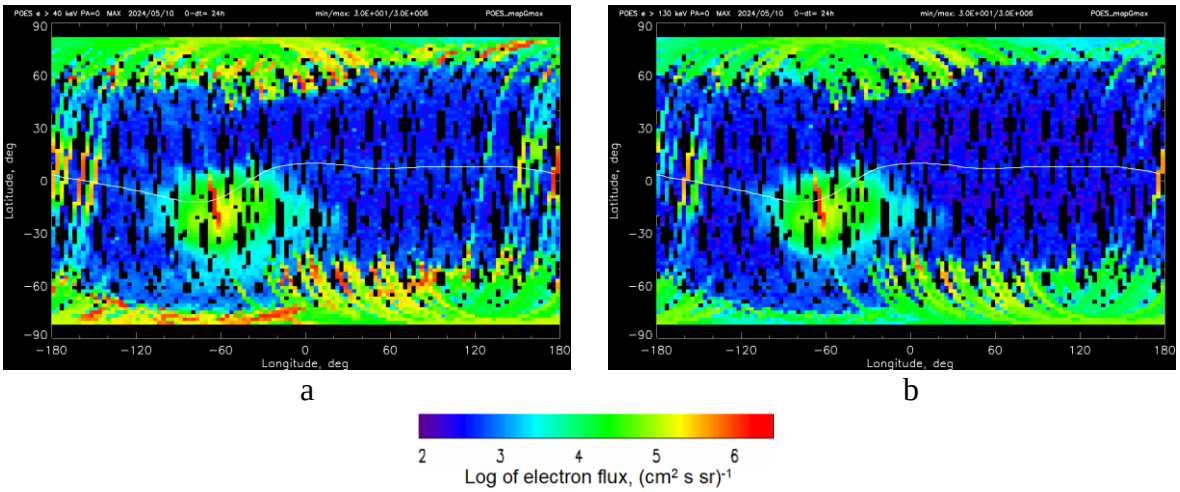


FIGURE 3. Geographic maps of fluxes of electrons with energies >30 keV (a) and >100 keV (b) on the main phase of the superstorm on May 10, 2024. The white curve indicates the dip equator.

During the injection, protons continue drifting westward along the drift shells, which elevate to higher altitudes with decreasing longitude due to the asymmetry of the geomagnetic field. Hence, protons moving to higher altitudes become invisible for the satellite. In contrast, electrons drifting eastward move to lower altitudes and the satellite observes intense electron fluxes coming from higher L-shells with increasing longitude until the SAA region. This complex dynamic results in complicated pattern presented in Fig. 2 and 3. Therefore, we have shown that the injection of protons and electrons in the forbidden zone occurred above Pacific in the morning hours and had the spatial scale of ~100°

and temporal scale of ~20 min. This pattern supports the mechanism of radial transport of energetic particles from the inner radiation belt down to low altitudes due to ExB or electric drift.

The origin of electric field in the inner magnetosphere at very low drift shells of L~1.2 is still unknown. Here we can consider possible external driver of the electric field. As one can see in Fig. 1, the magnetosphere was affected by a sharp negative jump of the solar wind pressure observed by Wind at ~18:45 UT. It should be noted that the time is calculated from the arrival time of the interplanetary shock (that is the time of SSC in the SYM-H) and not necessary correspond to the propagation of the negative jump structure in Pd. The pressure negative jump results in a decrease in SYM-H index at ~18:57 UT. The difference in time is originated from variation of the time delay for solar wind propagation from the location of Wind satellite (near L1 point) to the Earth due to alternation of solar wind structures with various tilts of interplanetary fronts. It is important to note that during that time, the IMF Bz was positive. It meant that we can exclude magneto-plasma effects originated from interaction of IMF with the geomagnetic field.

A solar wind pressure pulse results in generation of global inductive electric field in the Earth magnetosphere [2]. The decrease in SYM-H index for ~100 nT indicates a significant expansion of the magnetosphere that should result in generation of induced electric field, which is pointed westward in according to Faraday's law. At low latitudes, where the geomagnetic field is pointed northward, this electric field causes radial ExB drift of charged particles toward the Earth. The electrons and protons transport in the ExB fields with the same rate. During the transport, they shift in opposite horizontal directions due to azimuthal drift: electrons – eastward and protons – westward. The divergence between electrons and protons depends on the rate of radial transport, which directly depends on the strength of inductive electric field. It was estimated that the electric field of 10 mV/m provides the transport from the lower edge of inner ERB (L=1.15) to L=1.1 within a reasonable time of ~20 min [3]. Hence the mechanism proposed can explain the dynamics of electron and proton enhancements in the forbidden zone.

Acknowledgments. The authors are grateful CDAWeb (Goddard Space Flight Center, NASA, USA) for the providing experimental data from solar wind monitors, NOAA/POES (National Centers for Environmental Information, NOAA, USA) for the providing experimental data from POES satellite and World Data Center for Geomagnetism (Kyoto) for the providing of geomagnetic indices. The study was carried out within the framework of the state assignment of Moscow State University named after M.V. Lomonosov.

1. Golubkov M.G., Suvorova A.V., Dmitriev A.V. et al. Effect of high-intensity electron and proton fluxes on a low-latitude ionosphere // *Russ. J. Phys. Chem. B* 2020. V. 14. No 10. P. 873-882. DOI: 10.1134/S1990793120050206.
2. Ilie R., Daldorff L.K. S., Liemohn M.W., Toth G., Chan A.A. Calculating the inductive electric field in the terrestrial magnetosphere // *J. Geophys. Res.* 2017. V. 122. P. 5391-5403. DOI:10.1002/2017JA023877.
3. Suvorova A.V., Dmitriev A.V. On external drivers of sudden increase of energetic electrons in the forbidden zone during superstorms // *Geomag. Aeron.* 2025. Submitted.

IONOSPHERIC RESPONSE TO MAY 2024 GEOMAGNETIC STORM: IRKUTSK IONOSONDE DATA AND MODELING

Konstantin G. Ratovsky[1], Maxim V. Klimenko[2], Fedor S. Bessarab[2], Vladimir V. Klimenko[2], Kupriyan V. Belyuchenko[2], and Valentin N. Shubin[3]

[1]Institute of Solar-Terrestrial Physics SB RAS, Irkutsk, Russia
[2]West Department of Pushkov Institute of Terrestrial Magnetism, Ionosphere and Radio Wave Propagation RAS, Kaliningrad, Russia
[3]Pushkov Institute of Terrestrial Magnetism, Ionosphere and Radio Wave Propagation, RAS, Moscow

The paper studies the ionospheric response to the 10-12 May 2024 extreme geomagnetic storm based on the Irkutsk ionosonde data and modeling. Model calculations were performed with using the Global Self-consistent Model of the Thermosphere, Ionosphere, and Protonosphere (GSM TIP) [1] and the empirical Global Dynamic Model of the Ionosphere (GDMI) [2] for the geographic coordinates of the Irkutsk ionosonde (52.3° N, 104.3° E).

To compare observations and model calculations, we used the values of the peak electron density (NmF) and the peak height (hmF). The use of the terms NmF and hmF instead of the traditional NmF2 and hmF2 is due to the fact that under daytime conditions on 11 and 12 May, the so-called G-condition [3] was observed: an ionospheric phenomenon when the critical frequency of the F1-layer exceeds the critical frequency of the F2-layer. Accordingly, NmF and hmF are equal to NmF1 and hmF1 when NmF1 > NmF2; and NmF2 and hmF2 when NmF2 > NmF1. The G-condition was observed on 11 May from 07:00 to 16:15 LT (duration 9.25 hours) and on 12 May from 07:30 to 15:00 LT (duration 7.5 hours).

The observed NmF disturbances are relative (percentage) deviations of NmF observations from the 27-day running median of NmF2, and the hmF disturbances are absolute deviations of hmF observations from the 27-day running median of hmF2. The model disturbances are the corresponding deviations of NmF2 and hmF2 from the values obtained on 09 May.

Figure 1 shows the variations in observed NmF and hmF, NmF2 and hmF2 medians, and the dynamics of the Kp index. As seen from Fig. 1, NmF is positively disturbed in the pre-storm period and at the beginning of the storm (late night of DoY 131, 10 May), then NmF sharply decreases and remains negatively disturbed throughout the entire period under consideration. The largest negative NmF disturbance (-90.4%) is seen at night of 11-12 May (DoY 132-133). The largest daytime negative NmF disturbance (-69.5%) is observed around midday on 11 May (DoY 132). In the evening of 11 May (from 16:15 to 17:30 LT), we see a sharp increase in NmF2 (from 2.4 to $7.4 \cdot 10^5$ cm^{-3}). The observed hmF variations in the pre-storm period and at the beginning of the storm are close to the hmF2 medians, then hmF demonstrates an increase (positive disturbance) and a sharp decrease, starting from 07:00 LT on 11 May, which corresponds to the shift in the peak height from F2- to F1-layer (G-condition). The largest positive hmF disturbance (+81.8 km) is seen at night of 11-12 May (DoY 132-133). Just like on May 11, the G-condition is observed during the daytime on 12 May. In the evening and nighttime on 12 May, the hmF variations are close to the hmF2 medians. The sharp increase in NmF in the evening of May 11 practically coincides with the sharp increase in hmF (218-348 km from 16:15 to 17:150 LT). Such a change in NmF2 and hmF2 has all the signs of the dusk effect: a positive evening ionospheric disturbance caused by uplifting the F-region ionosphere due to enhancement in the equatorward wind or the eastward electric field [4].

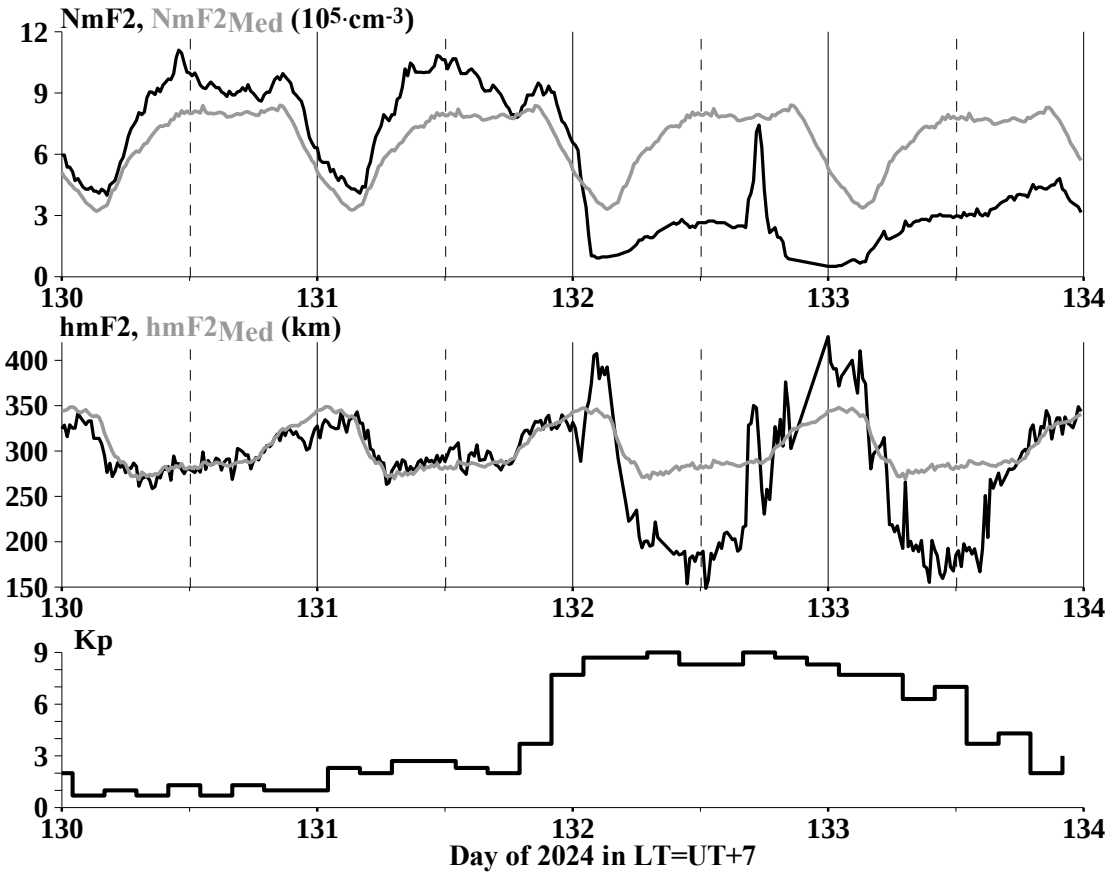


FIGURE 1. Variations in observed NmF (top, black), hmF (middle, black), NmF2 and hmF2 medians (gray), and Kp index dynamics (bottom) from DoY 130 to DoY 133 (09-12 May 2024). DoY boundaries correspond to local time LT (beginning DoY (midnight) is marked by a solid vertical line, noon is marked by dotted vertical line).

Figure 2 shows the variations in observed NmF disturbances (ΔNmF) and NmF2 disturbances (ΔNmF2) calculated by the GSM TIP and GDMI models.

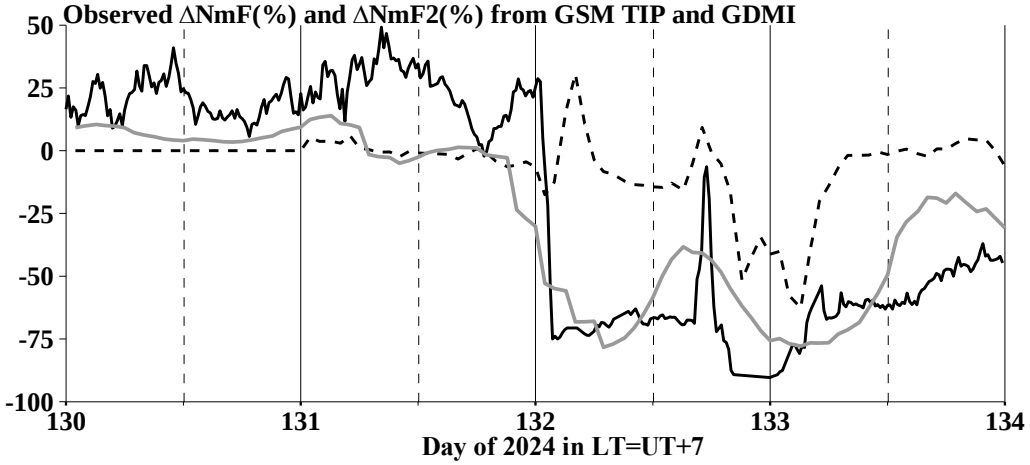


FIGURE 2. Variations in observed NmF disturbances (ΔNmF, solid black) and NmF2 disturbances (ΔNmF2) calculated with using GSM TIP (dotted black) and GDMI (gray) from DoY 130 to DoY 133 (09-12 May 2024). DoY boundaries are the same as in Fig. 1.

As seen from Fig. 2, GSM TIP significantly underestimates the observed negative NmF disturbances, especially in the daytime. At the same time, GSM TIP reproduces the sharp decrease in the ΔNmF amplitude in the evening of May 11 (dusk effect) with a noticeable underestimation of the effect amplitude. GDMI is in good agreement with the observed negative NmF disturbances in the first halves of the day on 11 and 12 May (DoY 132-133) and underestimates the ΔNmF amplitudes in the second halves of these days. GDMI mainly reproduces the dusk effect in ΔNmF, underestimating the effect amplitude and overestimating its duration. Both models do not reproduce positive NmF disturbances at the beginning of the storm.

Figure 3 shows the variations in observed hmF disturbances (ΔhmF) and hmF2 disturbances (ΔhmF2) calculated by the GSM TIP and GDMI models.

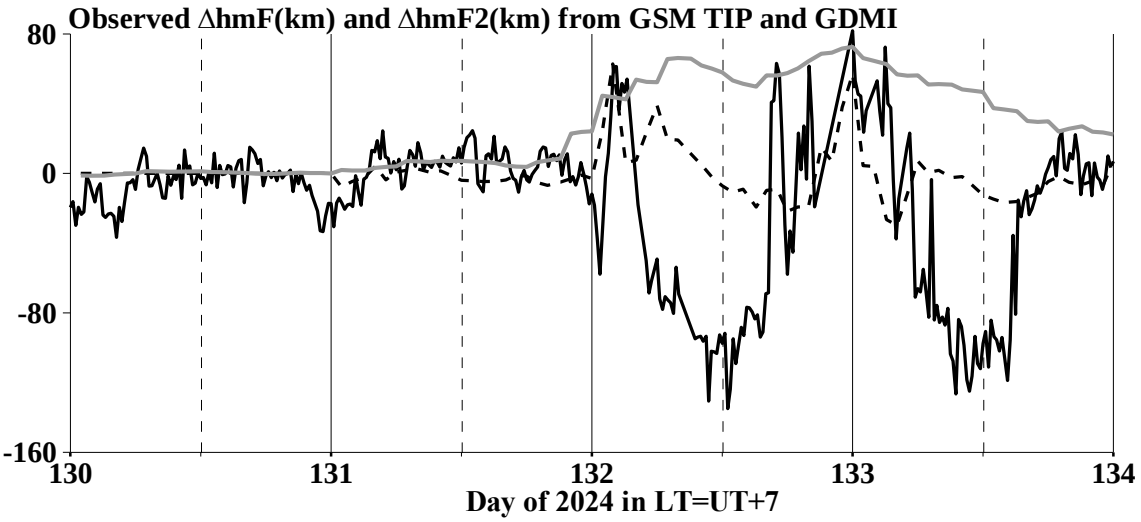


FIGURE 3. Variations in observed hmF disturbances (ΔhmF, solid black) and hmF2 disturbances (ΔhmF2) calculated with using GSM TIP (dotted black) and GDMI (gray). from DoY 130 to DoY 133 (09-12 May 2024). DoY boundaries are the same as in Fig. 1.

As seen from Fig. 3, both models reproduce positive hmF disturbances at night and do not reproduce negative hmF disturbances during the daytime. The latter means that the models do not reproduce the G-conditions observed on 11 and 12 May (days 132-133) under daytime conditions. This discrepancy is not necessarily a disadvantage of the models. The G-condition is recorded in the presence of reflections from the F1 layer and the absence of reflections from the F2 layer on ionosonde ionograms. In the case when foF2 slightly exceeds foF1, the absence of reflections from the F2 layer may be due to the narrowness of the foF1-foF2 range or to large virtual heights of the reflected signal, exceeding the ionosonde height range of the (635 km). To resolve this uncertainty, we plan to use data from the Irkutsk incoherent scatter radar [5-6]. It should be noted that both models do not reproduce the sharp increase in ΔhmF in the evening of 11 May (the dusk effect).

Summarizing the comparison of observations and model calculations for the 10-12 May 2024 extreme geomagnetic storm, we can highlight the following patterns.

(1) GDMI reproduces the observed negative disturbances of the peak electron density better than GSM TIP.

(2) Both models generally reproduce the observed dusk effect in the behavior of the peak electron density and do not reproduce the dusk effect in the behavior of the peak height.

(3) Both models reproduce positive disturbances of the peak height at night.

(4) Both models do not reproduce the G-conditions observed on 11 and 12 May in the daytime conditions.

(5) Both models do not reproduce positive disturbances of the peak electron density at the beginning of the storm.

Acknowledgments: The research was funded by the Russian Science Foundation (project No. 25-27-00217).

1. Korenkov Yu.N., Klimenko V.V., Förster M., Bessarab F.S., Surotkin V.A. Calculated and observed ionospheric parameters for a Magion-2 passage and EISCAT data on July 31, 1990 // *J. Geophys. Res*. 1998. V.103. No A7. P. 14697–14710. DOI: 10.1029/98JA00210.
2. Shubin V.N., Deminov M.G. Global Dynamic Model of Critical Frequency of the Ionospheric F2 Layer // *Geomagn. Aeron*. 2019. V. 59. No 4. P. 429–440. DOI: 10.1134/S0016793219040157.
3. Polekh N.M., Ratovsky K.G., Deminov M.G., Kushnarenko G.P., Kolpakova O.E. Morphology of the G condition occurrence over Irkutsk // *Adv.Space Res*. 2013. V. 52. No 4. P. 575–580. DOI: 10.1016/j.asr.2013.04.013.
4. Buonsanto, M. J. A case study of the ionospheric storm dusk effect // *J. Geophys. Res*. 1995. V. 100. No A12.P. 23857–23869. DOI: 10.1029/95JA02697.
5. Medvedev A.V., Potekhin A.P. Irkutsk Incoherent Scatter Radar: history, present and future // *Hist. Geo Space Sci*. 2019. V. 10. No 2. P. 215–224. DOI: 10.5194/hgss-10-215-2019.
6. Medvedev A.V., Potekhin A.P., Setov A.G., Kushnarev D.S., Lebedev V.P. All-atmosphere IS-MST Radar // *Solar-Terrestrial Physics*. 2020. V. 6.No. 2. P. 41–48. DOI: 10.12737/stp-62202004.

POLARIZATION JET/SAID OCCURRENCES DURING EXTREME GEOMAGNETIC STORMS

Aleksandr A. Sinevich[1,2], Aleksandr A. Chernyshov[1], Dmitrii V. Chugunin[1], Mikhail M. Mogilevsky[1]

[1]Space Research Institute of the Russian Academy of Sciences, Moscow, Russia
[2]Pushkov Institute of Terrestrial Magnetism, Ionosphere and Radio Wave Propagation Russian Academy of Sciences, Troitsk, Moscow, Russia

The polarization jet (PJ), also known as the subauroral ion drift (SAID), was first discovered in 1973 from data from the Soviet Cosmos-184 satellite [1]. The PJ/SAID is a narrow band of fast ion drift in the F-layer of the subauroral ionosphere in the evening and midnight MLT sectors. The band width is 1°-2° latitude wide, and the horizontal ion drift velocity inside the band is more than 1000 m/s. The PJ/SAID is mostly detected during the expansion phase or during the recovery phase of a geomagnetic storm. Inside, the PJ/SAID often consists of strata (PJS) [2,3], which, together with the electron density dip, affect the passage of radio waves through the subauroral ionosphere [4,5]. Numerous studies have revealed that there is a dependence of the PJ/SAID on geomagnetic activity through a number of physical mechanisms of PJ/SAID generation, such as a current generator, a voltage generator, and a short-circuiting.

It should be noted that, according to recent studies, the PJ/SAID is detected also during weak geomagnetic activity, on the so-called “geomagnetically quiet” or “quiet-time” days [6]. The occurrence of higher ion drift velocities during quiet conditions than during geomagnetically disturbed conditions is still not fully understood.

The behavior of the PJ/SAID parameters during extremely high geomagnetic activity is studied even less than the behavior of the PJ/SAID during quiet conditions. In 2024, during the peak of the 25th solar cycle, several large-scale geomagnetic storms occurred, for example, the October Storm on

October 10-12, 2024 and the Victory Day Storm on May 10-12, 2024 [7], which is the strongest geomagnetic event of the 21st century (-412 nT Dst). The state of the magnetosphere and ionosphere during extreme geomagnetic events significantly differs from the state of the magnetosphere and ionosphere during moderate and weak geomagnetic disturbances.

This work examines the behavior of the PJ/SAID parameters during a number of the most powerful geomagnetic disturbances: the Victory Day Storm on May 10-12, 2024, the October Storm on October 10-12, 2024, the St. Patrick's Storm on March 17, 2015, and the Halloween Storm on October 29-30, 2003. The measurements data of plasma parameters inside the PJ/SAID by the DMSP and Swarm satellites are used.

In Fig. 1, the change in the geomagnetic index Dst over time relative to the minimum Dst during each of the considered geomagnetic events is marked in blue. The number of detected PJ/SAID features within one orbit of the DMSP satellite is marked in red. During the October Storm of 2024, there are no detected PJ/SAID features, since there are no DMSP measurement data during the October Storm.

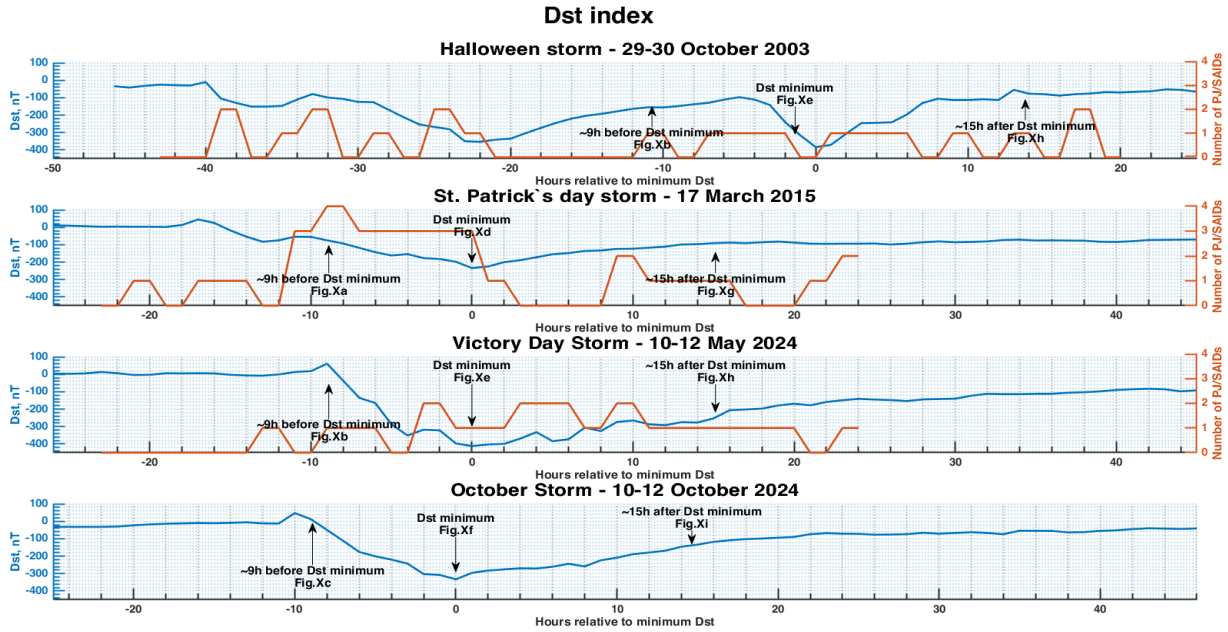


FIGURE 1. Number of detected PJ/SAID features during one circle of DMSP satellite around the Earth (red line) and geomagnetic index Dst (blue line) during various extreme geomagnetic storms

Figure 2 shows the measurement data of horizontal ion drift velocities and electron density based on the DMSP F-16 satellite measurements. The red area marks the time and latitude interval where the PJ/SAID or SAPS (Subauroral Polarization Stream [8], which has probably the same mechanism as PJ/SAID but different dimensions and velocities) is observed. Based on Fig. 2 and 3, it can be concluded that during the Victory Storm, the PJ/SAID is observed much less frequently than during the St. Patrick's Storm. Also, during the St. Patrick's Storm, the PJ/SAID is more pronounced, for example, at the Dst minimum (Fig. 2c), the PJ/SAID is a band of 2°-3° latitude with ion drift velocities of 2 km/s and higher. ~15 hours after the Dst minimum (Fig. 2e), SSAID is observed with two noticeable large PJS in electron density, spatially coinciding with horizontal ion drift peaks.

It is known that the intensity of the PJ/SAID depends on geomagnetic activity. However, during extreme geomagnetic disturbances, the number and intensity of detected PJ/SAIDs are lower than during "classical" disturbances.

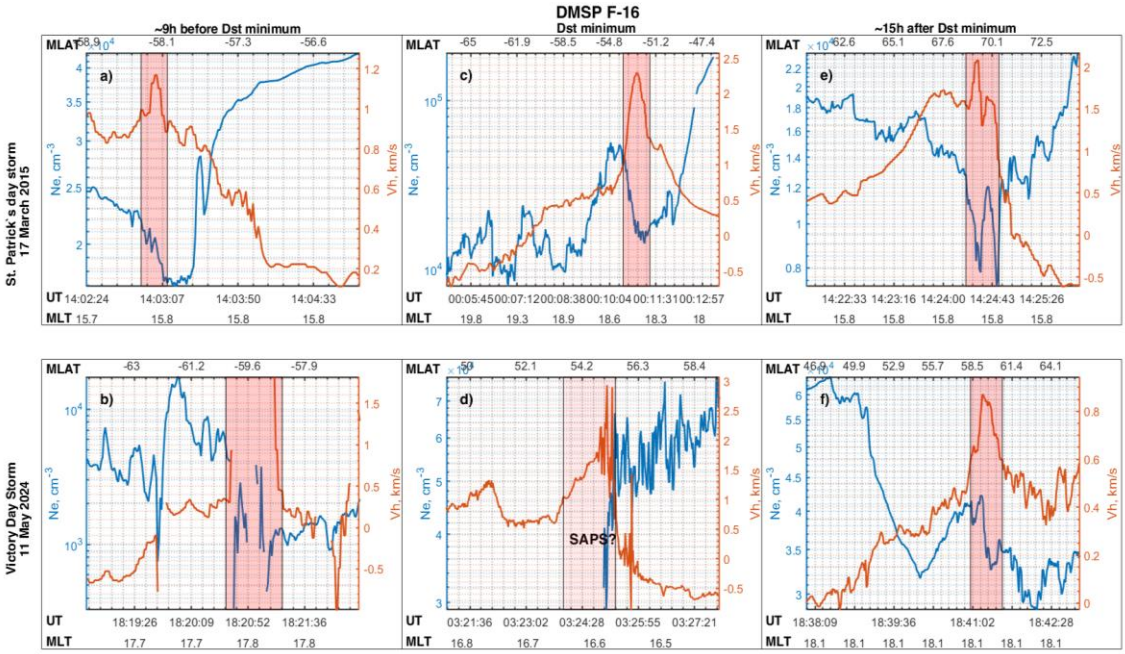


FIGURE 2. Horizontal ion drift velocity (red line) and electron density (blue line) measured by DMSP F-16 satellite during two considered events – St. Patrick's Storm on March 17, 2015 and Victory Day Storm on May 10-12, 2024 (table rows) at three different time intervals (table columns): ~9 hours before the Dst minimum (expansion phase), at the Dst minimum, and ~15 hours after the Dst minimum (recovery phase).

This may be due to the disruption of PJ/SAID generation mechanisms, a drop in the density of the ionospheric plasma, and the mobility of the plasmapause and auroral oval, which does not allow the formation of a stable western plasma flow. In general, according to the DMSP and Swarm satellites, during the maximum of geomagnetic activity during extreme storms, the intensity and number of PJ/SAIDs are minimal, while strong fluctuations in plasma parameters are observed. PJ/SAIDs are more often observed during the expansion and recovery phases of a geomagnetic storm during extreme events.

1. Gal'perin Y. I., Ponomarev V. N., & Zosimova A. G., Plasma convection in the polar ionosphere // *Ann. Geophys.* 1974. V. 30 (1). P. 1-7.
2. Sinevich A. A., Chernyshov A. A., Chugunin D. V., Oinats A. V., Clausen L. B. N., Miloch W. J., Nishitani N., Mogilevsky M. M., Small-scale irregularities within polarization jet/SAID during geomagnetic activity // *Geophysical Research Letters*. 2022. V. 49. P. e2021GL097107. DOI: 10.1029/2021GL097107.
3. Sinevich A. A., Chernyshov A. A., Chugunin D. V., Clausen L. B. N., Miloch W. J., Mogilevsky M.M., Stratified Subauroral Ion Drift (SSAID) // *Journal of Geophysical Research: Space Physics*. 2023. V. 128. P. e2022JA031109. DOI: 10.1029/2022JA031109.
4. Sinevich A. A., Chernyshov A. A., Chugunin D. V., Klimenko M. V., Panchenko V. A., Yakimova G. A., Timchenko A. V., Miloch W. J., Mogilevsky M. M., Multi-instrument approach to study polarization jet/SAID and STEVE // *Journal of Geophysical Research: Space Physics*. 2024. V. 129. P. e2024JA033222. DOI: 10.1029/2024JA033222.
5. Kotova D. S., Sinevich A. A., Chernyshov A. A., Chugunin D. V., Jin Y., Miloch W. J., Strong turbulent flow in the subauroral region in the Antarctic can deteriorate satellite-based navigation signals // *Sci. Rep*. 2025. V. 15. P. 3458. DOI: 10.1038/s41598-025-86960-6.

6. Gallardo-Lacourt B., Nishimura Y., Kepko L., Spanswick E. L., Gillies D. M., Knudsen D. J., et al., Unexpected STEVE observations at high latitude during quiet geomagnetic conditions // *Geophysical Research Letters*. 2024. V. 51. P. e2024GL110568. DOI: 10.1029/2024GL110568.
7. Chernyshov A. A., Klimenko M. V., Nosikov I. A., Borchevkina O. P., Timchenko A. V., Efishov I. I., Sinevich A. A., Ryakhovsky I. A., Yakimova G. A., Bessarab F. S., Yankovsky I. S., Chugunin D. V., Effects in the upper atmosphere and ionosphere in the subauroral region during Victory Day 2024 Geomagnetic Storm (May 10-12, 2024) // *Advances in Space Research*. 2025. DOI: 10.1016/j.asr.2025.02.015.
8. Foster J. C., & Vo H. B., Average characteristics and activity dependence of the subauroral polarization stream // *Journal of Geophysical Research (Space Physics)*. 2002. V. 107(A12). P. 1475. DOI: 10.1029/2002JA009409.

COMPARISON OF TRAPPED AND PRECIPITATING ELECTRON FLUX OF THE EARTH'S OUTER RADIATION BELT ACCORDING TO DATA FROM THE METEOR-M NO. 2 SATELLITE

Irina N. Myagkova

Skobeltsyn Institute of Nuclear Physics, Moscow State University, Moscow, Russia

For the first time electrons of the outer radiation belt of the Earth were registered during the second space flight in human history using scientific equipment from the Moscow State University Institute of Nuclear Physics installed on the Second Sputnik [1]. Despite the fact that many experiments have been carried out since then, both on Russian and foreign spacecraft, the problem of the formation of the outer radiation belt of the Earth (ERB) remains relevant, since despite very long history of experimental observations (e.g, [2-4] and the huge number of theoretical studies [5-7], a theory of electron acceleration has not yet been created that could explain the entire set of available experimental data.

A significant part of the studies were carried out on spacecraft with a circular polar orbit [8, 9]. The advantage of experiments on orbits of this type compared to geostationary ones is, firstly, that these spacecraft successively pass through different L-shells, which allows one to obtain spatial distribution of electrons in the outer ERB, and secondly, identical instruments installed orthogonally allow one to estimate the ratio of trapped and precipitating particles. The magnitude, localization and spectrum of the precipitating electron fluxes are important in terms of their possible impact on the upper atmosphere.

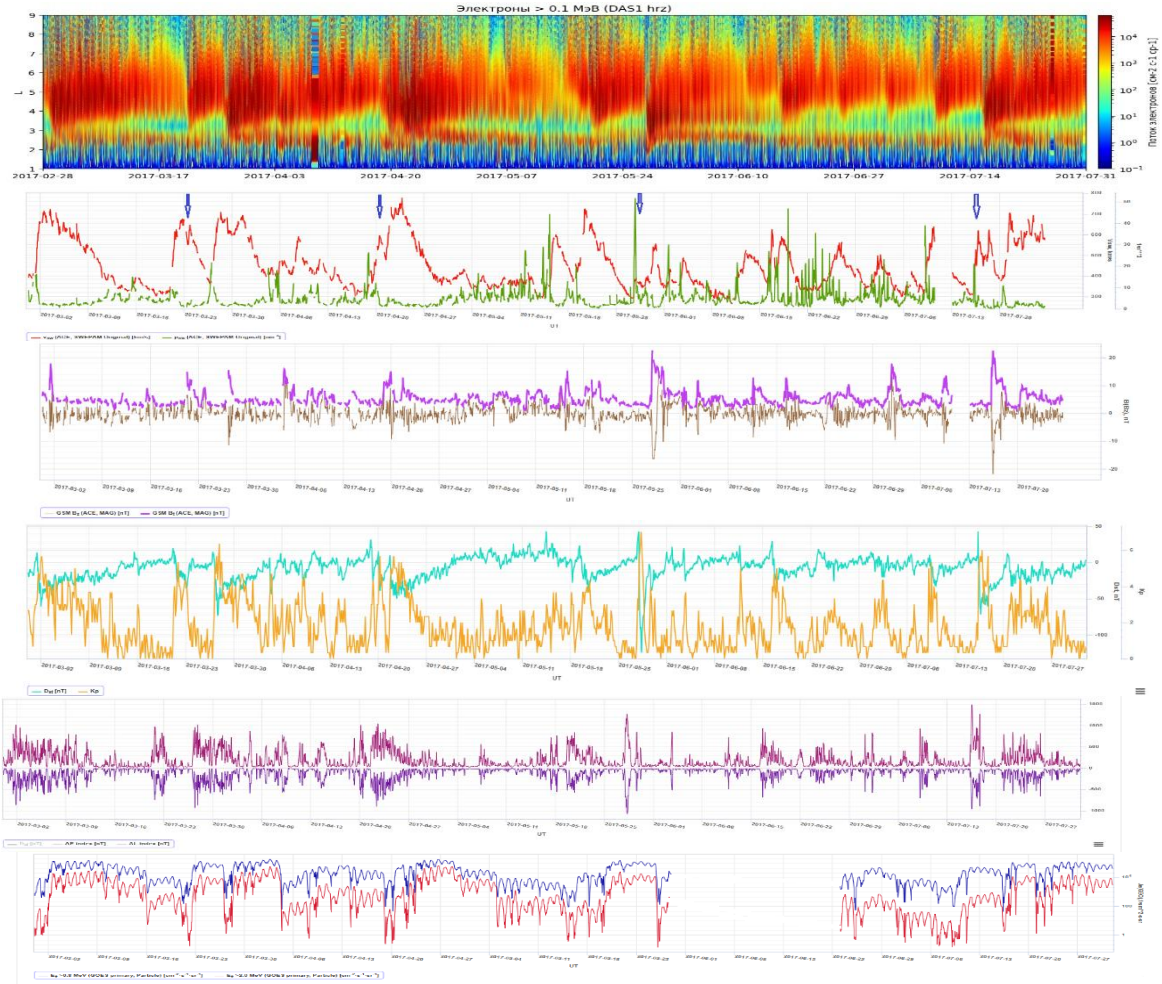
An example of such a spacecraft is the Meteor-M No. 2 satellite (launched on July 8, 2014). The orbit is sun-synchronous, the altitude at the ascending node is h = 832 km, the inclination is i ~ 98.8°, the orbital period is T = 101.3 min. In the experiments on board the Meteor-M No. 2 satellite, electrons of relativistic and sub-relativistic electrons were measured using a telescopic assembly of semiconductor and scintillation detectors. On board the Meteor-M No. 2 satellites, two sets of telescopes with viewing angles of 30° were installed - along the satellite velocity vector and in the perpendicular direction towards outer space.

Five months of 2017, from March to July, were selected for the study. This choice was due to the fact that 2017 belongs to the phase of solar activity decline, when both CMEs and HSS SW from coronal holes were also observed. From numerous experiments it is known that geomagnetic disturbances are caused by coronal mass ejections (CME) and high-speed streams of solar wind (HSS SW) reaching the Earth's orbit, both cause geomagnetic disturbances of different intensity and variations in the outer ERB

[10]. It is know, that usually during the main phase of a geomagnetic disturbance, the electron fluxes of the outer ERB decrease and then increase again, on average about half to a level above the pre-storm level, a quarter return to the pre-storm level, and another quarter do not reach it [11].

This study has two objectives: to study whether there are differences in the behavior of the outer ERB after disturbances, caused by CME and HSS SW and to assess whether there are differences in the behavior of trapped and precipitating particles after these disturbances.

Figure 1 shows 1) the electron flux with energy >100 keV, measured by the Meteor-M No. 2 satellite (SKL instrument, DAS1), the flux intensity is shown in color, 2) SW parameters (velocity - red curve and density - green), 3) interplanetary magnetic field (IMF) parameters - Bt (lilac) and Bz (brown), geomagnetic indices - 4) Dst (cyan) and Kp (orange), 5) AE-AL (crimson and violet), 6) electron fluxes of the outer ERB with energy >800 keV (blue) and >2 MeV (red), measured in geostationary orbit (GOES satellite), 7) and 8) Meteor-M No. 2 data (SKL, DAS1) averaged over 3 hours (two orbit) trapped and precipitating particles (> 100 keV olive and orange, > 2 MeV - dark blue and light blue). Blue arrows in the uppermost panel show four moments of SW increases caused by arrival at the Earth's orbit in accordance with the catalog https://swx.sinp.msu.ru/tools/icme_list.php: Mart 23, April 21, May 27, July 16.



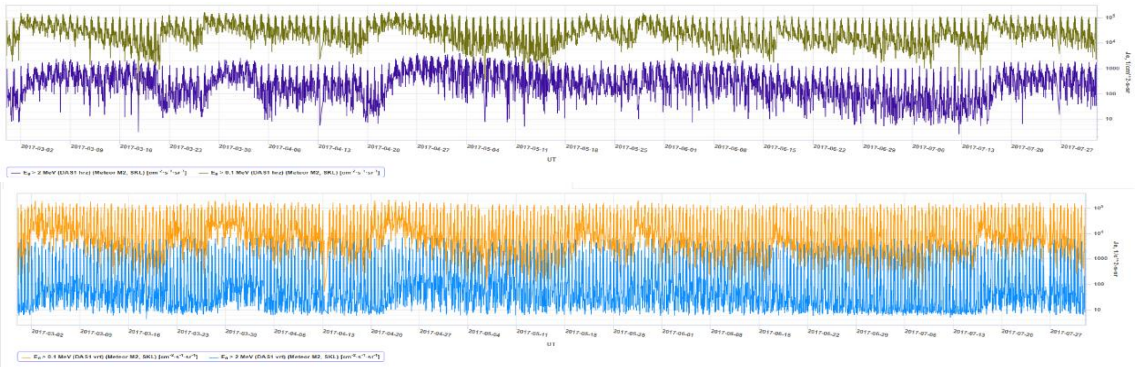


FIGURE 1. Electron fluxes of outer ERB according to Meteor-M No. 2 data (upper and two lower panels), SW and IMF parameters, geomagnetic indices, electron fluxes of the outer ERB in geostationary orbit.

In Figure 1 one can see that: 1) the strongest variations in the outer ERB during the period under consid-eration were caused by the arrival of CME at the Earth;

2) geomagnetic disturbances from CMEs had a shorter duration and as a rule larger amplitude than those from the HSS SW;

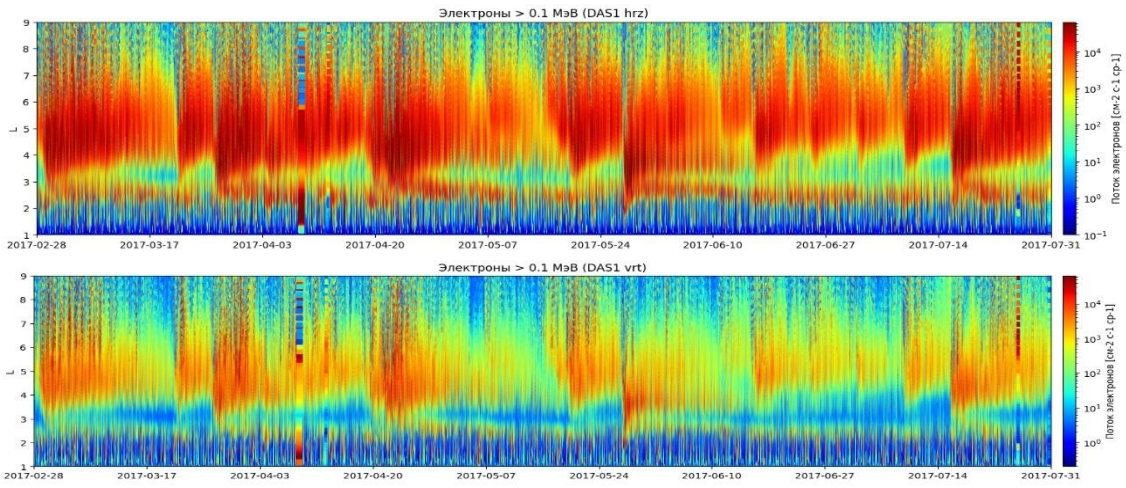
3) decreases in the fluxes of relativistic electrons in the geostationary orbit were not always accompanied by a decrease in the average fluxes of these particles in the circular polar orbit;

4) increase in the average fluxes of relativistic electrons occured more slowly compared to sub-relativistic ones;

5) fluxes of trapped and precipitating electrons averaged over three hours (two orbit) are similar.

For the more detailed analysis of the similarities and differences between the trapped and precipitating electron fluxes, we use Figure 2, which, in addition to the time variations in the fluxes of trapped electrons with energies > 100 keV already shown in Figure 1, simultaneously shows similar data for the electrons > 100 keV measured by the vertical sensor DAS1 (precipitating), as well as variations in the fluxes of trapped and precipitating relativistic electrons (> 2 MeV), also measured by the SKL (DAS1) instrument.

Analyzing Figure 2 we can see that even after relatively small disturbances of the geomagnetic field caused by HSS SW with the velocity of about 500 km/s, such as those observed from mid-June to mid-July, there is an acceleration of sub-relativistic electrons and flows of not only trapped but also precipitating particles are observed, and the maximum of the new, post-storm belt is located, as a rule, closer to the Earth compared to its position before the storm, as in the case of CME storms.



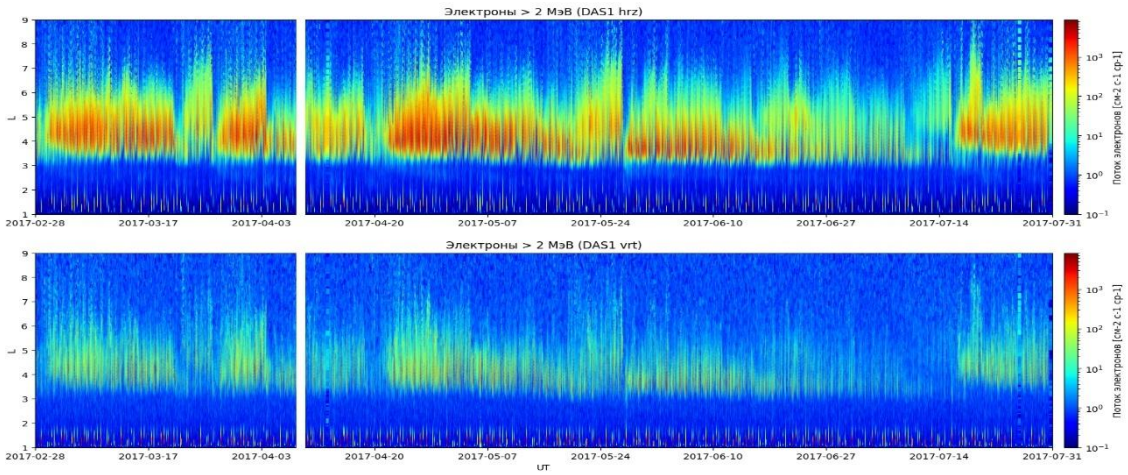


FIGURE 2. Fluxes of trapped (hrz) and precipitated (vrt) electrons with energies > 100 keV and > 2 MeV according to Meteor-M No. 2 data from March 1 to July 31, 2017.

From a joint analysis of Figures 1 and 2, the following conclusions can be done:

- Spatial distributions and fluxes of trapped and precipitating electrons with same energies are similar also but not identical, and what is especially significant is that a decrease in the fluxes of trapped particles is not accompanied by an increase in the fluxes of precipitating ones.
- Both trapped and precipitating relativistic electrons have a spatial distribution that differs significantly from the distribution of sub-relativistic electrons.
- The maximum flux of precipitating relativistic electrons in the period under study was observed after the CME on July 16.

The study was performed with the financial support of the Russian Science Foundation grant No. 22-62-00048, https://rscf.ru/project/22-62-00048/.

1. Vernov S. N., Grigorov N. L., Logachev YU. I., Chudakov A. Ye. Izmereniya kosmicheskogo izlucheniya na iskusstvennom sputnike Zemli // *Doklady Akademii nauk*. 1958. V. 120. No 6. P. 1231–1233. (in russian)
2. Baker D.N., Panasyuk M.I. Discovering Earth's radiation belts // *Phys. Today*. 2017. V. 70. No 12. P. 46–51. DOI: 10.1063/PT.3.3791.
3. Li W., Hudson M. K. Earth's Van Allen radiation belts: From discovery to the Van Allen Probes era // *Journal of Geophysical Research: Space Physics*. 2019. V. 124. P. 8319–8351. DOI: 10.1029/2018JA025940
4. Stepanova M., Pinto V., Antonova E. Regarding the relativistic electron dynamics in the outer radiation belt: a historical view // *Rev. Mod. Plasma Phys*. 2024. V. 8. P. 25. DOI: 10.1007/s41614-024-00165-4.
5. Tverskoy B.A. Ustoychivost' radiatsionnykh poyasov Zemli // *Geomagnetizm i aeronomiya*. 1967. V. 7. No 2. P. 226-242. (in russian).
6. Li X., Temerin M.A. The electron radiation belt // *Space Sci. Rev*. 2001. V.95. P. 569–580. DOI: 10.1023/A:1005221108016.
7. Chu X, Ma D., Bortnik J. et al. Relativistic electron model in the outer radiation belt using a neural network approach // *Space Weather*. 2021. V.19. No 12. P. e2021SW002808. DOI: 10.1029/2021SW002808.

8. Li X., Baker D. N., Kanekal, S. G. et al. Long term measurements of radiation belts by SAMPEX and their variations // *Geophys. Res. Letters*. 2001. V. 28. No 20. P. 3827-3830. DOI: 10.1029/2001gl013586.
9. Myagkova I.N., Panasyuk M.I., Lazutin L.L. et al. December 2006 solar extreme events and their influence on the near-Earth space environment: "Universitetskiy -Tatiana" satellite observation // *Advances in Space Research*. 2009. V. 43. P. 483-494. DOI: 10.1016/j.asr.2008.07.019.
10. Kataoka R., Miyoshi Y. Average profiles of the solar wind and outer radiation belt during the extreme flux enhancement of relativistic electrons at geosynchronous orbit // *Ann. Geophys*. 2008. V. 26. P. 1335–1339. DOI: 10.5194/angeo-26-1335-2008.
11. Reeves G.D., McAdams K.L., Friedel R.H.W. et al., Acceleration and loss of relativistic electrons during geomagnetic storms // *Geophys. Res. Lett*. 2003. V. 30. №10. P.1529. DOI: 10.1029/2002GL016513.

CHANGES OF GEOMAGNETIC ACTIVITY FOR THE PERIOD FROM 1932 TO 2023

Maria A. Abunina, Eugene A. Maurchev, Nataly S. Shlyk, Artem A. Abunin and Anatoly V. Belov

Pushkov Institute of Terrestrial Magnetism, Ionosphere and Radio Wave Propagation Russian Academy of Sciences, Troitsk, Moscow, Russia

The influence of geomagnetic activity on human practical activities was discovered more than 200 years ago, when telegraph lines began to be introduced and failures in their operation were noticed during magnetic storms. Currently, during geomagnetic storms (GMSs), failures in the operation of satellites, power lines and navigation systems are possible, which can lead to communication failures, power outages and navigation errors. GMSs can also cause interference in radio communications and create problems for air travel.

GMSs are caused, in particular, by solar flares and associated coronal mass ejections. When the plasma cloud reaches the Earth, it interacts with the magnetic field of our planet, causing disturbances and, as a result, a magnetic storm. The state of the magnetosphere is described by a number of different indices calculated on the basis of ground-based measurements of the magnetic field [1].

One of the most popular indices of geomagnetic activity is the Kp index [2, 3]. This index is determined by the magnitude of the change in the horizontal component of the Earth's magnetic field, expressed as an integer in the range 0-9, where "0" and "1" mean very small changes, and "5" or more means a GMS. The scale for calculating Kp index has an almost logarithmic scale, therefore, to calculate average values in different time intervals, the Ap index of geomagnetic activity is used, the values of which are integer and are unambiguously related to the values of the Kp index (Table 1). Table 1 also provides a verbal description of the geomagnetic activity depending on the value of the geomagnetic indices.

Many authors study GMSs themselves [4, 5], the mechanism of their formation [6], as well as their interplanetary sources [7, 8]. We will not touch upon these topics; we are interested in studying the general quantitative changes in three-hour intervals of geomagnetic activity both for the entire observation period and separately for solar cycles (SCs).

The purpose of this research is to quantitatively study three-hour Ap indices from 1932 to 2023, estimate the number of different intervals relative to the entire time period and consider their changes over solar activity cycles (for 17–24 SCs).

TABLE 1. Kp and Ap indices values

Geomagnetic activity	Quiet						Unsettled					Active		
Kp	0	0+	1–	1	1+	2–	2	2+	3–	3	3+	4–	4	4+
Ap	0	2	3	4	5	6	7	9	12	15	18	22	27	32

Geomagnetic activity	Minor GMS			Moderate GMS			Strong GMS			Severe GMS				Extreme GMS
Kp	5–	5	5+	6–	6	6+	7–	7	7+	8–	8	8+	9–	9
Ap	39	48	56	67	80	94	111	132	154	179	207	236	300	400

Data. The World Geomagnetism Center in Kyoto (Japan) has been recording the values of the three-hour Ap index. The data are available at https://wdc.kugi.kyoto-u.ac.jp/index.html for the period from January 1, 1932 to December 31, 2023 (a total of 268824 values). The boundaries of the SCs are defined in accordance with the SIDC data (https://www.sidc.be/silso/datafiles).

Analysis of three-hour intervals of geomagnetic activity. First, we considered the general distribution of the values of three-hour indices of geomagnetic activity for the entire period under study. Let us recall that further in the article we will operate only with the Ap index, since it is numerical, unlike the Kp index. Figure 1 shows a histogram of the frequencies of observation of different three-hour Ap index values for 1932-2023. Additionally, the intervals corresponding to different levels of geomagnetic activity according to Table 1 are highlighted in color.

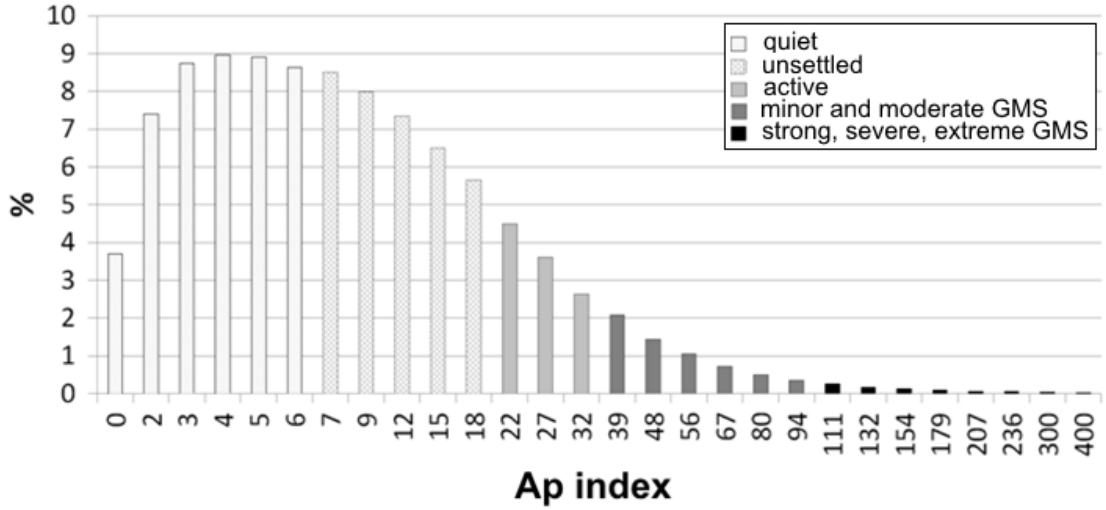


FIGURE 1. Distribution of three-hour values of the Ap index for 1932-2023.

Of all three-hour intervals for 1932–2023, only 6.95% are GMS intervals (i.e., Ap ≥ 39, Kp ≥ 5–), of which only 0.82% are intervals of a strong GMS (Ap ≥ 111, Kp ≥ 7–), 10.74% were observed as disturbed intervals (Ap = 22, 27, 32), and 82.31% were quiet and unsettled (Ap ≤ 18). It should be noted that the average value of the Ap index for the entire study period is 13.3, the median is 7, and the most frequently recorded value is 4 (8.95%), although the value Ap=5 is recorded only slightly less frequently (8.91%). It is clear that these values can vary greatly in different periods, so we reviewed at similar distributions across last 8 solar cycles.

The distribution shape in different SCs is generally similar, but there are some differences. For example, SC 24 had the largest number of quiet intervals (Ap≤6, 64.8%), and SC 18 had the largest number of GMS intervals (Ap≥39, 10.6%). The largest number of GMS intervals with Ap≥111 was recorded in SC 19, 18 and 22 (1.4, 1.2 and 1.1%, respectively), and the smallest – in SC 24 (0.1%, 40 intervals in total). In other cycles the number of GMS intervals varied from 5.3 to 9.1%. For a more visual comparison, we have provided the number (in % of the total number in the cycle) of three-hour Ap index values for different intervals (in %) in the studied SCs in Table 2.

TABLE 2. The fraction (%) of three-hour Ap-index values in different SCs.

Three-hour values of Ap index	SC 17	SC 18	SC 19	SC 20	SC 21	SC 22	SC 23	SC 24
0…6	48.7	37.8	40.1	46.4	36.0	37.1	50.3	64.8
7…18	33.8	38.2	37.9	36.5	42.0	40.6	34.9	27.2
22…32	10.5	13.3	12.9	10.8	13.4	13.1	9.5	5.4
39…94	6.1	9.4	7.7	5.6	7.7	8.0	4.6	2.5
111…400	0.9	1.2	1.4	0.7	0.9	1.1	0.7	0.1

Conclusion. The distribution of three-hour values of the Ap index of geomagnetic activity for 1932-2023 was considered. The average value of the Ap index for the entire study period is 13.3, the median is 7, and the most frequently recorded is 4. Only ~7% of the time, GMS intervals are observed. The largest number of GMS intervals was recorded in SC 18 (10.6%), the smallest – in SC 24 (2.6%).

1. Mayaud P.N. Derivation, meaning and use of geomagnetic indices // *AGU Geophysical Monograph.* 1980. V. 22.
2. Bartels J., Heck N., Johnston H. The Three-Hour-Range Index Measuring Geomagnetic Activity. // *Terrestrial Magnetism and Atmospheric Electricty*. 1939. V. 44. P. 411-454.
3. Bartels J. The stardandization index, Ks, and planetary index Kp // *IAGA Bulletin*. 1955. No. 12. P. 88-101.
4. Hajra R., Tsurutani B. T., Lu Q., et al. The April 2023 SYM-H = −233 nT Geomagnetic Storm: A Classical Event // *Journal of Geophysical Research: Space Physics*. 2024. V. 129. ID. e2024JA032986. DOI 10.1029/2024JA032986.
5. Tsurutani B. T., Sen A. Hajra R., et al. Review of the August 1972 and March 1989 (Allen) Space Weather Events: Can We Learn Anything New From Them? // *Journal of Geophysical Research: Space Physics*. 2024. V. 129. ID. e2024JA032622. DOI: 10.1029/2024JA032622.
6. Kamide Y., Baumjohann W., Daglis I. A., et al. Current understanding of magnetic storms: Storm-substorm relationships// *Journal of Geophysical Research*. 1998. V. 103. P. 17705-17728. DOI: 10.1029/98JA01426.
7. Gonzalez W. D., Tsurutani B. T., Clúa de Gonzalez A. L. Interplanetary origin of geomagnetic storms // *Space Science Reviews*. 1999. V. 88. P. 529-562. DOI: 10.1023/A:1005160129098.
8. Gonzalez W.D, Tsurutani B.T, Lepping R.P, Schwenn R. Interplanetary phenomena associated with very intense geomagnetic storms // *Journal of Atmospheric and Solar-Terrestrial Physics*. 2002. V. 64. P. 173-181. DOI: 10.1016/S1364-6826(01)00082-7.

OBSERVATION AND MODELING OF UPPER ATMOSPHERE RESPONSE TO GEOMAGNETIC STORMS USING WD IZMIRAN TOOLS

Maxim V. Klimenko[1], Fedor S. Bessarab[1], Vladimir V. Klimenko[1], Igor A. Nosikov[1], Olga P. Borchevkina[1], Alexander V. Timchenko[1], Kupriyan V. Belyuchenko[1], Ivan I. Efishov[1], Galina A. Yakimova[1], Konstantin G. Ratovsky[1], Valentin N. Shubin[2]

[1]West Department of Pushkov Institute of Terrestrial Magnetism, Ionosphere and Radio Wave Propagation, RAS, Kaliningrad, Russia

[2]Pushkov Institute of Terrestrial Magnetism, Ionosphere and Radio Wave Propagation, RAS, Moscow, Russia

Since 1964, the Kaliningrad department of IZMIRAN has been conducting regular observations of the parameters of the lower atmosphere, ionosphere and variations in the Earth's magnetic field. The measuring complex located in the Kaliningrad region (54° N, 20° E) consists of: an ionosonde for vertical sounding of the ionosphere; dual-frequency receivers of signals from navigation satellite systems, which are used to determine the ionospheric total electron content; a magneto-variation station; a meteorological weather station; a VLF-range signal receiver; all-sky camera (installed on March 30, 2024). In addition, the West Department of IZMIRAN has developed and actively used (for the interpretation of observational data) models of the upper atmosphere, the whole atmosphere, and magnetosphere-ionosphere coupling processes based on solving a system of hydrodynamic equations for a multicomponent gas mixture and the equation of conservation of the total current density. Simultaneous modeling and observations provides unique opportunities for studying atmosphere-ionosphere coupling during periods of various space weather phenomena, including geomagnetic storms. Klimenko et al., and Ratovsky et al. [1, 2], using data series from the Irkutsk and Kaliningrad ionosondes and modeling results detected, statistically proved the existence of daytime positive ionospheric aftereffects of geomagnetic storms.

The article presents examples of using WD IZMIRAN tools for studies the upper atmosphere response over Kaliningrad to geomagnetic storms of St. Patrick's Day in March 2015 and Victory Day in May 2024. For the recent most intense geomagnetic storm in the 21st century (Victory Day 2024 storm), we will also present the results of comparison with the empirical global dynamic model of the ionosphere GDMI [3], developed at IZMIRAN and, unlike other similar models, taking into account the dependence of the change in the critical frequency on the current level of geomagnetic activity, taking into account the history of its development.

Figure 1 shows the behavior of the foF2 and TEC over Kaliningrad during 17–23 March 2015, as shown by observation (ionosonde Parus-A and GNSS receiver) and GSM TIP simulation. The geomagnetic storm on 17–23 March 2015, which began at 06:00 UT on 17 March did not cause noticeable effects in foF2 and TEC over Kaliningrad at night. The second main phase of the storm, which began at 12:00 UT, was stronger and more long-lasting than the first one. At its initial stage the storm led to formation of the positive ionospheric disturbances over Kaliningrad in the afternoon. Another important feature of the ionosphere dynamics above the Kaliningrad station in the recovery phase of the geomagnetic storm on 21–23 March 2015 is the appearance of the daytime positive disturbances in foF2 and TEC. During the same days at night the negative disturbances in foF2 and TEC were observed and reproduced by model over Kaliningrad. For analysis of spatial extent of after-storm positive disturbances we provide maps of TEC daytime (14 LT) disturbances on 22 and 23 March 2015 according to IGS data. It is evident the formation of daytime positive disturbances with maximal values

more than 10 TECU at mid-latitudes of Northern Hemisphere at longitudinal range from 0 to 120 degree East.

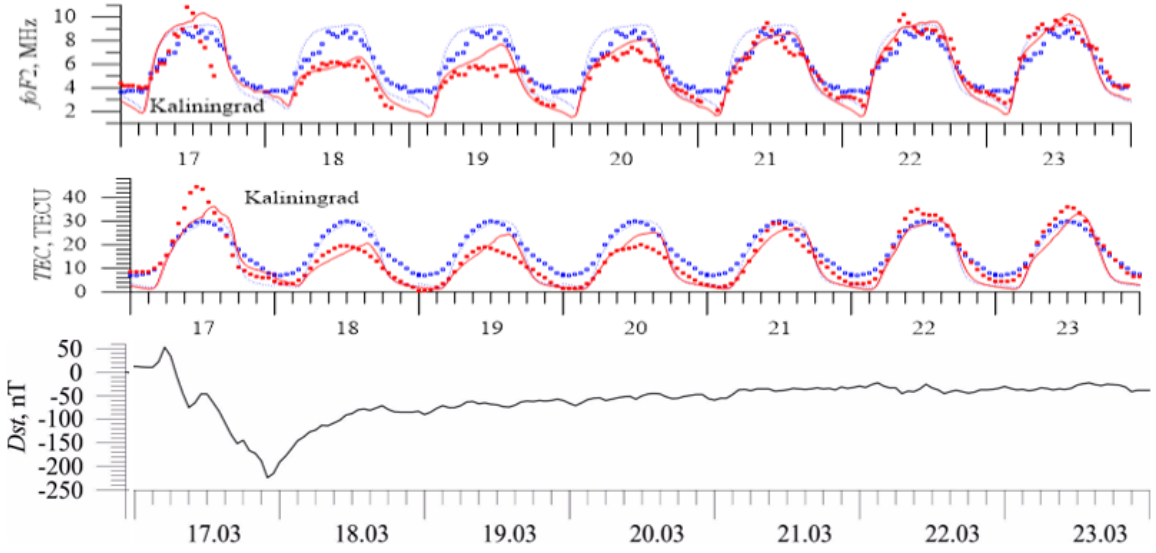


FIGURE 1. Top two panels: Variation of foF2 and TEC as deduced from observations (circles) and GSM TIP model (lines) for the Kaliningrad station during 17–23 March 2015. Quiet values are shown by blue color and disturbed values by red color. The 27-day median is shown as a quiet foF2 and TEC reference. Bottom panel presents Dst index variation for the same time period indicated two onset moments of the main phases of geomagnetic storm on 17 March at 06 and 12 UT.

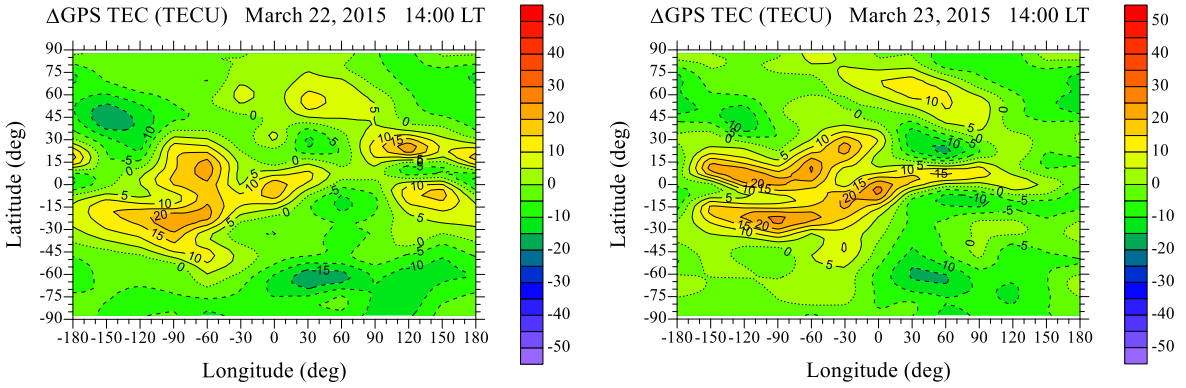


FIGURE 2. Maps of daytime TEC Disturbances as deduced from observations for 22 and 23 March. The 27-day median was selected as a quiet TEC reference.

According to Dst index presented in Figure 3 it is clearly seen the occurrence of most intense in XXI century the Victory Day storm on 10 May and its signature in atmospheric glow over Kaliningrad region for two nights: 10-11 May and 11-12 May. During these nights auroral (rays, omega-structures, corona, etc.) and sub-auroral (STEVE, red-arc) glows were detected over Kaliningrad region. Figure 4 present the ionospheric (TEC, NmF2, NmE) response over Kaliningrad to geomagnetic storm on May 10-12 according to GNSS and ionosond observation, GSM TIP and GDMI model results. GSM TIP qualitatively reproduced dusc effect in TEC and negative disturbances in NmF2 and TEC during 11-12 May. In addition increase in NmE during main storm phase is also well reproduced by GSM TIP simulation. Note that GDMI model had incredible success in reproducing the disturbances in E and F region electron density during such unique geomagnetic storm.

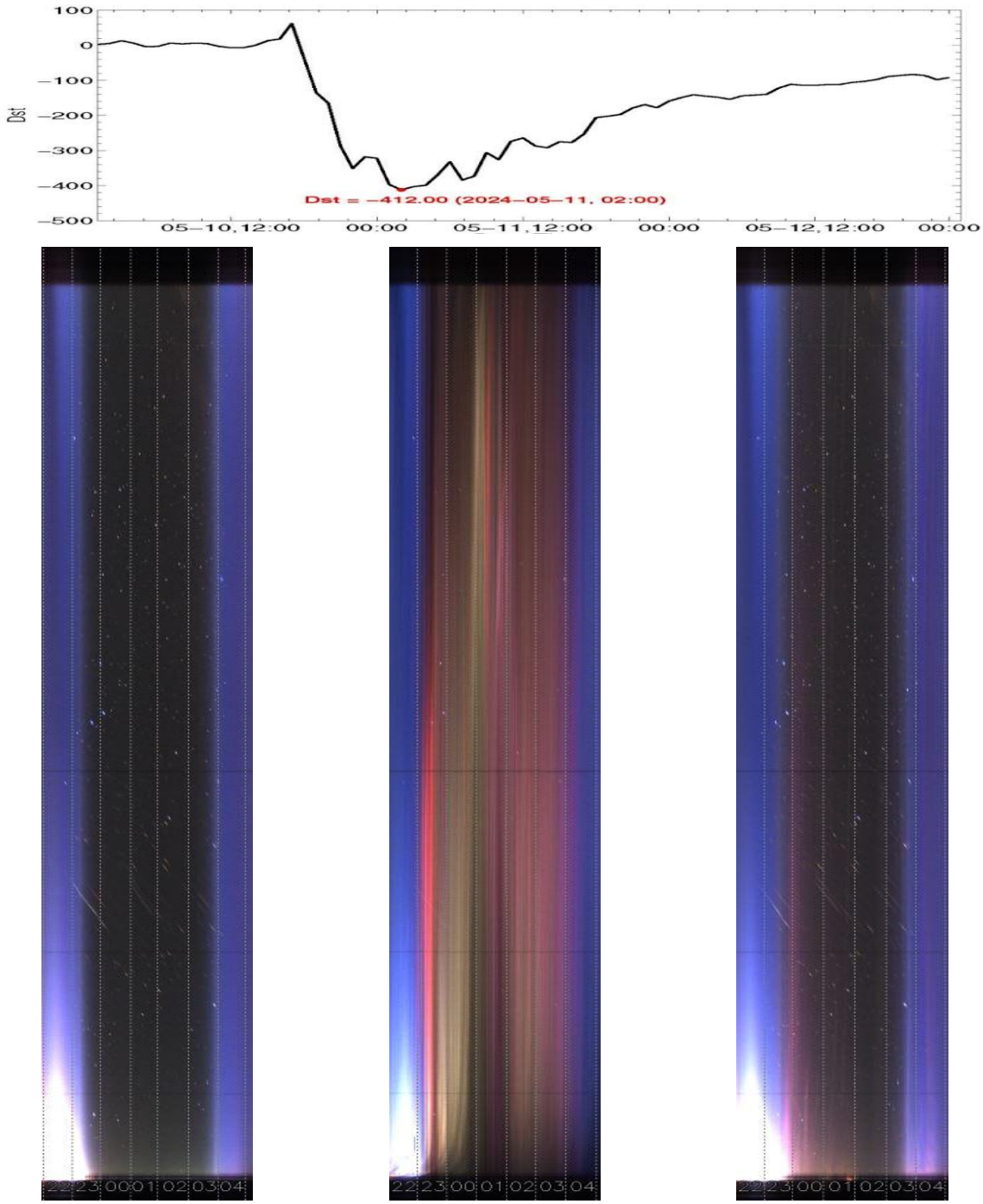


FIGURE 3. Variation of Dst index during 10-12 May 2024 (top panel) and keograms of all-sky camera at night on 7-8 May (left), 10-11 May (center), 11-12 May (right) over WD IZMIAN observatory, Kaliningrad region.

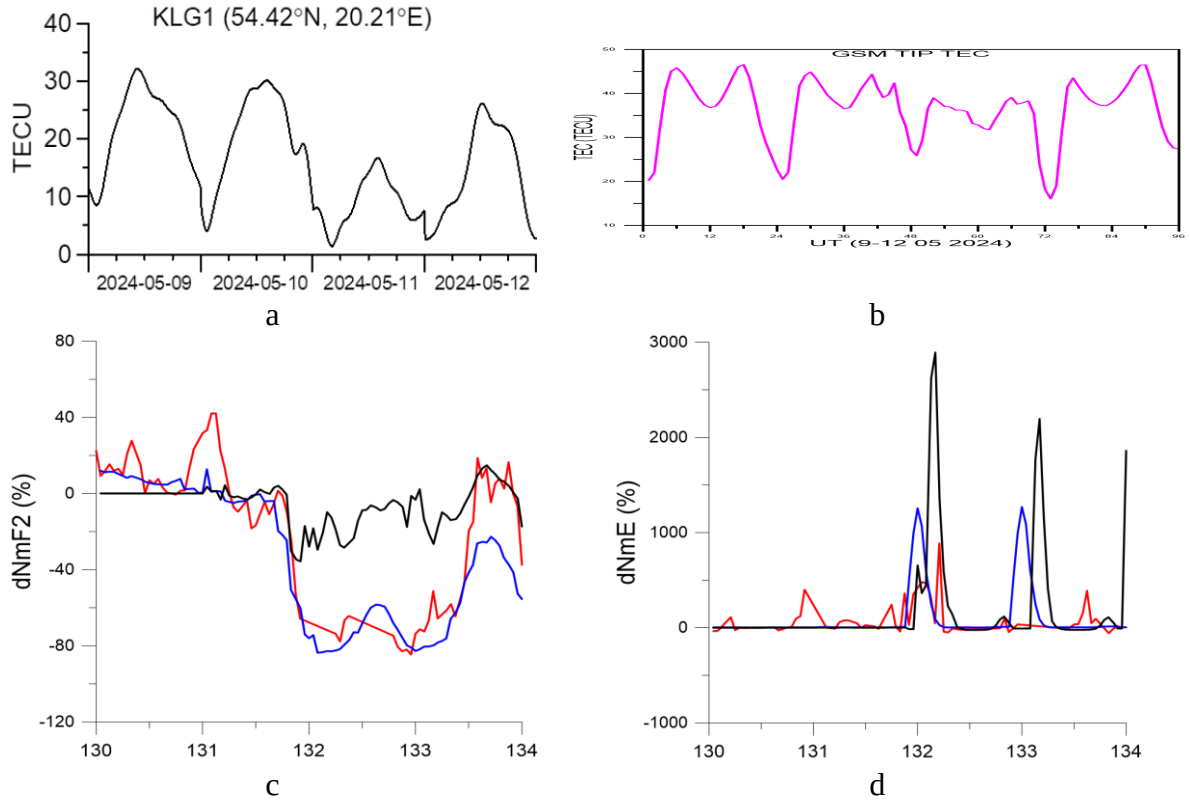


FIGURE 4. Variation during 9-12 May 2024 of TEC over Kaliningrad according to GNSS receiver data (a) and GSM TIP simulation (b), and relative disturbances in NmF2 (c) and NmE (d) according to ionosonde (red line), GSM TIP (black line) and GDMI (blue line) models.

The investigations were performed using financial support of the Russian Science Foundation grant No. 25-27-00217.

1. Klimenko, M.V., Klimenko V.V., Despirak I.V., Zakharenkova I.E., Kozelov B.V., Cherniakov S.M., Andreeva E.S., Tereshchenko E.D., Vesnin A.M., Korenkova N.A., Gomonov A.D., Vasiliev E.B., Ratovsky K.G. Disturbances of the thermosphere-ionosphere-plasmasphere system and auroral electrojet at 30°E longitude during the St. Patrick's Day geomagnetic storm on 17–23 March 2015 // *Journal of Atmospheric and Solar-Terrestrial Physics*. 2018. V.180. P. 78-92. DOI: 10.1016/j.jastp.2017.12.017.
2. Ratovsky K.G., Klimenko M.V., Klimenko V.V., Chirik N.V., Korenkova N.A., Kotova D.S. After-effects of geomagnetic storms: statistical analysis and theoretical explanation // *Solar-Terrestrial Physics*. 2018. V. 4. Iss. 4. P. 26–32. DOI:10.12737/stp-44201804.
3. Shubin V.N., Deminov M.G. Global Dynamic Model of Critical Frequency of the Ionospheric F2 Layer // *Geomagn. Aeron*. 2019. V. 59. P. 429-440. DOI: 10.1134/S0016793219040157.

DOUBLE PLASMA RESONANCE AS A POSSIBLE MECHANISM FOR EXPLAINING NON-THERMAL HECTOMETRIC RADIATION

Alexander A. Chernyshov[1], Mikhail M. Mogilevsky[1], Vladimir E. Shaposhnikov[2], Dmitry V. Chugunin[1], and Daniil A. Dorofeev[1]

[1]Space Research Institute of the Russian Academy of Sciences (IKI RAN), Moscow, Russia
[2]Institute of Applied Physics of the Russian Academy of Science, Nizhny Novgorod, Russia

Non-thermal radiation in the hectometric range of 525–1700 kHz with a narrow band frequency structure and polarization corresponding to the ordinary mode was discovered using ERG (Arase) measurements. Hectometric continuum (HMC) is mainly observed in the nighttime magnetosphere, with its sources likely located near the Earth at distances of (1.1–2)R_E (where R_E is Earth's radius) at low latitudes [1,2]. The mechanism generating this type of emission in the near-Earth environment remained unknown for a long time. This work examines the potential use of electron cyclotron harmonics instability to explain the line structure of hectometric radio emissions for the first time. By analyzing the case of HMC, a proposed mechanism for the creation of a quasi-harmonic frequency structure resulting in quasi-parallel emission bands is discussed. In other words, the double plasma resonance (DPR) effect is suggested as a possible explanation for the observed emission bands in the dynamic spectrum of hectometric radio waves. It was shown [3,4] that under conditions of DPR when the upper hybrid resonance frequency f_{UH} is close to the frequency of one of the electron cyclotron harmonics f_{Be}, that is, $f_{UH} \approx sf_{Be}$ where s is the cyclotron harmonic number, the increment of plasma wave instability increases by one to two orders of magnitude (the effect of DPR on electron cyclotron harmonics). Note this increment is approximately two orders of magnitude greater than the increment of Bernstein wave instability. The DPR effect has been successfully applied to explain the origin of the quasi-harmonic structure (analogous to the line spectrum of Earth's non-thermal continuum) in solar radio radiation and the microwave emission of the pulsar in the Crab Nebula [4] and the literature cited therein).

An example of HMC-type emission measurement recorded by the ERG (Arase) satellite is shown in Fig.1. Here we use ERG (Arase) measurements of the electric field component in the frequency range from 2 kHz to 10 MHz, as well as magnetic field measurements [5,6]. Figure 1 (upper panel) presents a dynamic spectrogram of the measurements of the electric component of the electromagnetic field, taken on August 19, 2019, in the frequency range of 2–2000 kHz. Figure 1 (bottom panel) displays the dynamic spectrogram (in the same frequency range) of the polarization parameter P. This parameter P is the projection of the polarization plane of the electromagnetic wave onto the plane perpendicular to the satellite's rotation axis. When measurements are taken in the nighttime hemisphere in the Northern Hemisphere, $P > 0$ corresponds to right-hand polarization of the wave and $P < 0$ to left-hand polarization. In the daytime hemisphere, it is the opposite: $P < 0$ indicates right-hand polarization, and $P > 0$ indicates left-hand polarization.

In the spectrogram of Fig.1, whistle emissions are observed in the time interval from 21:45 to 22:30 UT. The signal at frequency of ~1800 kHz at 21:40 UT decreases in frequency to 100 kHz by the end of the spectrogram, these are oscillations at the upper hybrid resonance frequency, $f_{UH} = (f^2_{Be} + f^2_{pe})^{1/2}$, where f_{pe} is the electron plasma frequency (or Langmuir frequency). At distances $R > 3RE$ from the Earth, the electron cyclotron frequency becomes much smaller than the plasma frequency, and $f_{UH} \sim f_{pe}$.. The horizontal bands in the spectrogram in the frequency range 1350–1650 kHz represent the non-thermal HMC. These HMC emissions exhibit right-hand polarization $P > 0$ and have constant frequencies throughout the observation period of ~2.5 hours. In this example, the individual frequencies of the HMC are clearly separated, allowing for precise numerical determination: $f_1 = 1367$ kHz, $f_2 =$

1428 kHz, f_3 = 1489 kHz, and f_4 = *1599 kHz*. It is also observed that as the satellite moves away from Earth, the higher frequencies appear first, followed by progressively lower frequencies.

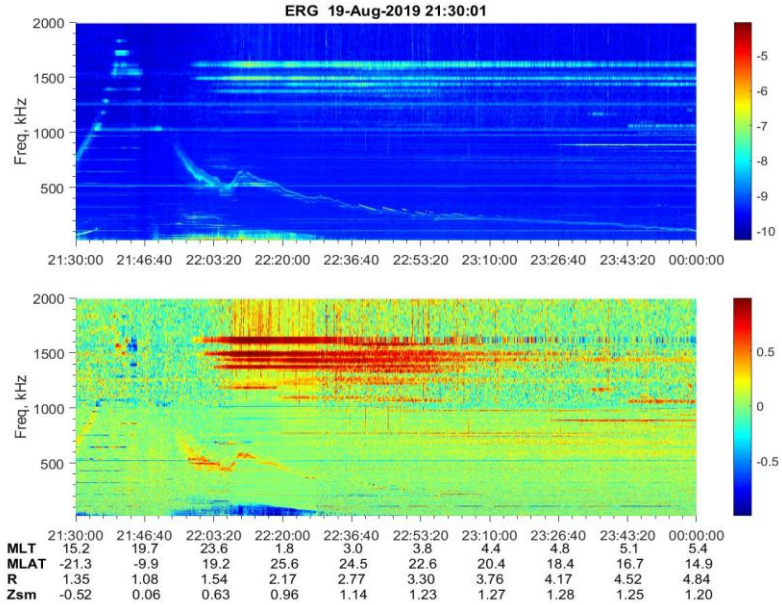


FIGURE 1. Results of the analysis of electric field component measurements on the ERG (Arase) satellite in the frequency range of 2–2000 kHz from August 19, 2019. (upper panel) Dynamic spectrogram of the electric component of the electromagnetic field. (bottom panel) Dynamic spectrogram (in the same frequency range) of the polarization parameter P. Orbital parameters are as follows: MLT - magnetic local time, MLAT - magnetic latitude, R - distance from the center of the Earth to the satellite in Earth radii, Zsm - Z component in the solar-magnetic coordinate system.

The following key properties of HMC can be identified [7]: 1). Frequency range: 600–1700 kHz. 2). Spectrum: Quasi-linear and stationary. 3). Polarization: Ordinary. 4). Frequency drift: No significant frequency drift is observed over long measurement intervals (hours). 5). Local time of registration: Source location in GSM coordinates is in the night-side plasmasphere. 6). Probable source location: Equatorial region at altitudes of approximately 600–1000 km. (spatially limited source of HMC radiation) 7). Geomagnetic dependence: No direct correlation between HMC radiation occurrence and geomagnetic disturbances.

Using the example of a HMC burst recorded on August 19, 2019, we will examine a possible mechanism for the formation of the quasi-harmonic frequency structure observed in its dynamic spectrum, typical for the HMC, which appears as quasi-parallel emission bands. This mechanism is based on the effect of double plasma resonance on electron cyclotron harmonics [2]:

$$f_{UH} = \sqrt{f_{Le}^2 + f_{Be}^2} \approx s f_{Be},$$

Let us consider the application of the DPR effect to interpret the observed quasi-harmonic emission bands in the dynamic spectrum of HMC in the Earth's magnetosphere, as seen in example in Fig.1. Note that the value of plasma environment characteristics in the HMC source was estimated based on measurements taken while the satellite was passing through a region similar to the region of the actual HMC source. Therefore, the measured values were extrapolated to the source location region, assuming more-or-less symmetric distribution of the inner magnetospheric plasma around the Earth at the considered relatively low altitudes. It should be noted that for the development of the DPR theory to explain the HMC radiation in the near-Earth plasma, there is no difference whether the MLAT parameter has a negative or positive value. As a result of the DPR effect, the plasma waves are excited in each of

these regions within a narrow frequency range $\Delta\omega<<\omega$ near the local electron cyclotron frequency harmonic [3]. The particular numbers of the cyclotron harmonics involved in forming the observed emission depend on the local plasma density. It is only necessary to ensure the observed number of quasiharmonic emission bands. Let us assume that the HMC source is an elongated region along the lines of force of the dipole magnetic field, where the magnetic field and plasma density decrease with distance. According to previous studies [1,2], HMC sources are likely located near the Earth, at distances of approximately $(1.1–2)R_E$ in low-latitude regions. It follows from Fig.1 that the number of cyclotron harmonics that the source must contain is 4. The estimates show that near the Earth, the required number of cyclotron harmonics is achieved in a source located on L-shells with $L > 1.5$.

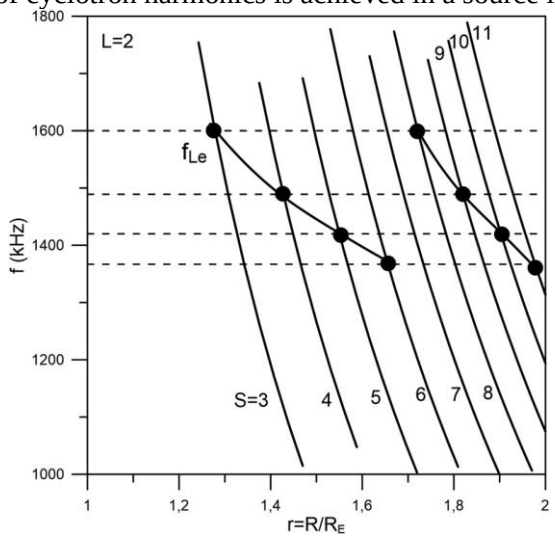


FIGURE 2. Schematic representation of the generation process of the quasi-harmonic HMC emission recorded on August 19, 2019, based on the DPR effect. Black lines indicate the variation of cyclotron harmonics with distance from the Earth's center with the generation region. Lines passing through the solid circles show the plasma frequency variation with height in the source, while the dashed horizontal lines indicate the frequencies of the emission bands at 22:22:00.

Figure 2 demonstrates the scheme for generating hectometric radio emissions in a source located along the magnetic field lines with a McIlwain parameter *L=2*, assuming a dipole magnetic field. It can be seen from the Fig.2 that the possible cyclotron harmonic numbers fall within the range 3-*11*. The concentration of equilibrium plasma in the generation region varies with attitude from $2{,}4*10^4\ cm^{-3}$ to $2{,}1*10^4\ cm^{-3}$. In this case, the generation region of HMC can be situated at magnetic latitudes $-40^o \leq MLAT$. For harmonics involved in the generation with numbers $s = 3\text{-}6$ the generation region occupies the latitude range, $-40^o \leq MLAT \leq -30^o$ while for $s = 8\text{-}11$, the corresponding range is $-20^o \leq MLAT \leq -5^o$. The scheme takes into account that the maximum frequency f_{max} and minimum frequency f_{min} of the HMC burst recorded on August 19, 2019, are approximately $f_{max} \approx 1600$ *kHz* and $f_{min} \approx 1367$ kHz, respectively.

To summarize, we propose a scheme for generation of the non-thermal HMC radiation with a fine frequency structure in the form of quasi-harmonic bands in the near-Earth plasma, based on the DPR effect at electron cyclotron harmonics.

The HMC source occupies an extended area with inhomogeneous magnetic field and plasma density, within which the condition of DPR, $f_{UH} \approx sf_{Be}$, is satisfied in different spatially separated regions [7]. Plasma waves are excited at frequencies close to the electron cyclotron harmonics due to the presence of a small population of non-equilibrium hot electrons, whose velocity distribution function exhibits a deficit of particles with small transverse velocities relative to the magnetic field. The excited plasma waves are converted into electromagnetic radiation, corresponding to the ordinary mode, through scattering on thermal ions of the background magnetospheric plasma. During this conversion, the frequency of the converted electromagnetic wave is approximately equal to the frequency of plasma wave, and there is no broadening of the radiation spectrum. Therefore, the quasi-harmonic structure of the HMC radiation, which is observable in satellite data, is preserved. It should be noted that the observation of HMC on August 19, 2019, is a characteristic case of HMC registration on the ERG (Arase) satellite. Therefore, these results can be generalized to suggest that the DPR mechanism may also lead to the generation of plasma waves responsible for HMC radiation in other cases.

Thus, the mechanism of DPR allows us to explain the existing measurements of HMC radio emissions and may possibly be responsible for the appearance of the HMC in near-Earth space.

We express our thanks to A. Kumamoto, Y. Kasahara, F. Tsuchiya and ERG (Arase) team for providing PWE/HFA-L2 v01.01 data [5,6]. The ERG (Arase) satellite data were obtained from the ERG (Arase) Science Center, operated by ISAS/JAXA and ISEE/Nagoya University, on the website [https://ergsc.isee.nagoya-u.ac.jp/].

1. Mogilevsky M.M., Chugunin D.V., Chernyshov A.A., et al., Localization of sources of two types of continuum radiation // *JETP Lett.* 2021. V.114, P.23-28. DOI: 10.1134/S0021364021130075.
2. Dorofeev D.A., Chernyshov A.A., Chugunin D.V., Mogilevsky M.M., Main statistical properties of hectometric continuum radiation in near-earth space // *Solar-Terrestrial Physics*. 2023. V.9. P.63-71. DOI: 10.12737/stp-94202308
3. Zheleznyakov V.V., Zlotnik E.Y., Cyclotron wave instability in the corona and origin of solar radio emission with fine structure. I. Bernstein modes and plasma wave with a hybrid band. // *Solar Physics*. 1975. V. 43. P. 431–451. DOI: 10.1007/BF00152366
4. Zheleznyakov V.V., Zlotnik E.Y., Zaitsev V.V., Shaposhnikov V.E., Double plasma resonance and its manifestations in radio astronomy // *Phys. Usp.* 2016. V. 59. P. 997-1020. DOI: 10.3367/UFNe.2016.05.037813
5. Kasahara Y., Kasaba Y., Kojima H., S. et al., The Plasma Wave Experiment (PWE) on board the Arase (ERG) satellite // *Earth. Planets Space*. 2018. V. 70. No. 86. DOI:10.1186/s40623-018-0842-4.
6. Kumamoto A., Tsuchiya F., Kasahara Y. et al., High frequency analyzer (HFA) of plasma experiment (PWE) onboard the Arase spacecraft // *Earth. Planets Space*. 2018. V. 70, No. 82. DOI: 10.1186/s40623-018-0854-0
7. Mogilevsky, M. M., Shaposhnikov, V. E., Chernyshov, A. A., Chugunin, D. V., Dorofeev, D. A. On the nature of hectometric continuum-type emissions in the near-Earth plasma // *Physics of Plasmas.* 2025. V. 32. No. 012109. DOI: 10.1063/5.0235182.

DIFFERENTIAL SPECTRA OF NATURAL GAMMA-RADIATION IN 0.1-5 MEV DURING PRECIPITATIONS

Yury V. Balabin, Aleksei V. Germanenko, Evgenia A. Mikhalko, Boris B. Gvozdevsky

Polar Geophysical Institute, Russian Academy of Sciences, Apatity, Russia

Introduction. For many years, X-ray and gamma radiation fluxes coming from the atmosphere have been monitored in Apatity. Increases in radiation are observed during precipitation. Thousands of such events have been accumulated over decades, and a morphological analysis of their profiles has been carried out. However, until recently, all measurements were of an integral nature, so the nature of the observed increases was unclear, although indirect signs indicated that these increases were not associated with the presence of radionuclides in precipitation. In 2023-24, additional continuous measurements of the differential spectrum of gamma radiation coming from the atmosphere were started. Spectrum measurements during increases showed that, although the lines of individual radionuclides are present, their contribution to the spectrum is small.

Integral detectors and results of previous observations. The PGI cosmic ray laboratory has been continuously recording X-ray and gamma radiation fluxes coming from the atmosphere for over 15

years. To date, measurements have been conducted at seven points: Apatity, Barentsburg (Spitsbergen archipelago), Moscow, Neutrino (North Caucasus), Tiksi, Yakutsk, and Mondy (East Sayan Mountains). In Neutrino and Mondy, the detectors are located at an altitude of 1,700 and 3,000 m, respectively. The same type of radiation detectors are used, based on a NaI(Tl) crystal Ø60x20 mm, the effective energy range is 20-600 keV, and the integral output channels are >20, >100, and >200 keV. The detectors are placed in deep lead or steel cups with wall thicknesses of 20-50 mm to cut off radiation coming from the soil and surrounding objects. The field of view of the detectors is a cone of ~90 degrees facing the zenith. The detectors are located in buildings with a light wooden roof and in thermostabilized boxes.

At all points, increases in the X-ray and gamma radiation flux are noted. The amplitude of the increase in individual events reaches 80-100% of the level of clear weather the day before, the increase profiles are almost the same in all channels, which means that the upper energy threshold of this phenomenon is much higher than 600 keV - the upper energy threshold of the detectors. Increases are noted all year round and always occur with precipitation in the form of rain, fog, snow. Examples of increases are shown in Figure1. In Apatity, a precipitation gauge operates in parallel with the radiation detector. Its measurements are not calibrated, they are made in arbitrary units [1]. Precipitation is measured by the amount of backscattering of IR radiation from drops or snowflakes located in the field of view of the precipitation gauge. It can be assumed that during one rainfall the reflectivity of drops remains approximately constant, then the instrument readings are proportional to the precipitation intensity. Figure1A shows that the rain began after 16 UT, until 20 UT it had a low intensity with long pauses, after 20 UT the intense rain continued for more than an hour. It is noteworthy that the local maximum of precipitation intensity corresponds to the growth phase on the radiation intensity profile. The first minor precipitation maximum was around 17 UT, the second one was after 18 UT, a short-term increase in rain was observed after 19 UT, and the main precipitation maximum was around 21 UT.

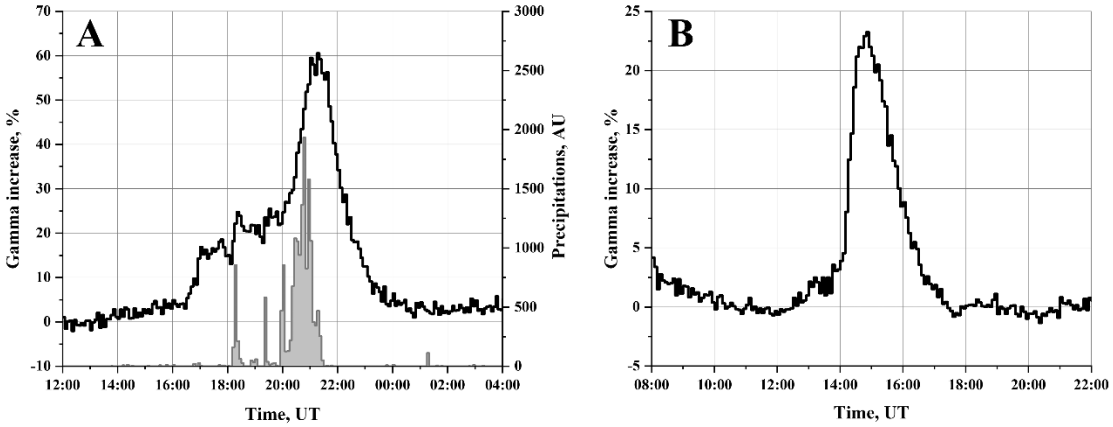


FIGURE 1. An example of increases in background X-ray and gamma radiation during precipitation. **A** – increase on 06.10.2021 in Apatity. Left scale – amplitude of increase relative to the base level before precipitation. Right scale – precipitation gauge readings, arbitrary units. **B** – increase on 20.03.2023 in Neutrino (North Caucasus).

The radiation intensity growth phase corresponds to all these maxima. And the maximum on the radiation profile is reached 20-30 minutes later than the precipitation maximum. During the observation period, more than a thousand increases were recorded in Apatity, hundreds of increases in Barentsburg. The analysis of these events was presented in several works, for example, [2]. In [3] the results of measurements of background radiation coming from the atmosphere during a marine Arctic expedition are presented; a similar detector was used. As a result, it was understood that the increase in the gamma radiation flux from the atmosphere during precipitation is not associated with contamination of the latter with radionuclides of natural or anthropogenic origin, but is caused by some processes of interaction of

secondary cosmic rays and meteorological processes in the lower atmosphere. There are many works [4,5] where such an impact is recorded, in particular, additional acceleration of muons in thunderclouds. However, in our case, increases are observed in the electromagnetic component, at all observation points all year round, regardless of thunderstorm activity.

Spectral measurements in events of gamma radiation increase during precipitation. The observations of radiation fluxes were integral, the spectral composition of both background radiation and additional radiation appearing during precipitation remained unknown. Since 2022, a differential gamma radiation spectrometer has been created in Apatity. The spectrometer is based on a NaI(Tl) scintillation crystal measuring Ø75x75 mm. The device has a thick lead shield and is placed in a thermal box in the attic of the building. The field of view is directed to the zenith and is 1-1.5 sr, the working energy range is 0.1-4 MeV. A high-speed 4096-channel pulse amplitude analyzer is used with the crystal, which ensures measurement of the differential spectrum with a step of ~1 keV per channel for the selected energy range. A longer collection time increases the accuracy of spectrum measurements and reduces fluctuations. However, the duration of increases is often 2-3 hours, it would be desirable to have several spectral measurements during this time in order to be able to select the spectra corresponding to the maximum phase. Based on these two conditions, a compromise value of 30 min was chosen. The spectrometer was calibrated using the lines of several radionuclides: K-40, Na-22, Al-26, Cs-137. The resolution on the Cs-137 line (660 keV) is less than 5%. In addition, experiments were performed to measure incomplete scattering with Na-22, Al-26, Cs-137 sources. For this purpose, the source was placed near the spectrometer so that both the upper and lateral surfaces of the crystal were illuminated approximately equally. The measurements showed that ~40% of the gamma quanta that entered the crystal were subject to incomplete absorption. Above the detector there is a total of 0.8 g/cm2 of iron and ~2 g/cm2 of wood (iron roofing and boards), these values are used to calculate the absorption of radiation in the roof of the building. The efficiency of the detector for different energies is calculated using the RUSCOSMICS software package [6]. These values are used to reconstruct the primary spectrum coming from the atmosphere. The spectrometer is used to monitor the spectra of radiation coming from the atmosphere.

A technique has been developed to obtain the spectrum of the radiation causing the increase. Since the spectra are differential, it is permissible to subtract the spectra in different phases of an increase. The difference represents the spectrum of the added radiation. A single spectrum, despite 30 minutes of collection, has large fluctuations, especially in the high-energy part, where it has a low level. Assuming that in clear weather, before the increase, the radiation flux is constant and its spectrum does not experience large changes, we can take the average spectrum for several hours. Similarly, in the phase of the maximum increase, we assume that the spectra also differ little from each other during this period, therefore, it is possible to obtain an average spectrum during the maximum, usually 2-3 hours, although individual events can have a long maximum. Note that the assumption of constancy of the spectra in the selected periods is easily verified; it is enough to view the spectra separately. As a result, there is an average background (base) spectrum corresponding to the period before the increase in clear weather, and an average spectrum at the maximum of the increase, called the increase spectrum for short. The base spectrum is calculated as the average over 10-15 spectra, which corresponds to a 5-8 hours interval before the increase. The increase spectrum is usually averaged over a shorter interval, since the duration of the increase is 2-4 hours. Subtracting the base spectrum from the increase spectrum, we obtain the differential spectrum of the additional radiation (DSAR), which was added to the background and caused the increase effect. Figure 2 shows an example of the large and long increase with three spectra for it, obtained using the described technique. A similar result was obtained in other events, the spectra are similar, the difference is that in most increases the duration of the maximum phase is shorter, and the difference spectrum of the DSAR has larger fluctuations. Figure2A shows the increase profile. For the interval 18-24 UT, 12 spectra were collected, from which the average spectrum was obtained by

averaging (line 1 in Figure2B). For the period of the maximum increase, the condition >40% is accepted, this corresponds to 07:30-12:30 UT, which gives ten spectra during the increase, from which the average spectrum of the increase was obtained, marked in Figure2B as line 2. Subtracting the first spectrum from the second, we have the spectrum of the radiation that caused the increase event (line 3).

In spectra 1 and 2, the lines of lead-214, bismuth-214, potassium-40, and thallium-208 are clearly defined [7]. The annihilation line is formed by the annihilation of positrons produced in the atmosphere by cosmic rays, and potassium-40 is present in the wood and glass of the photomultiplier bulb. The fact that these two lines disappear in the DSAR means that the intensity of these lines does not change during precipitation. The presence of this pair of lines allows continuous monitoring of the spectrometer operation and the correctness of the energy scale. Several lines can be distinguished in the DSAR spectrum, the clearest of which is the bismuth-214 609 keV line [7]. However, the DSAR contains extended continuum sections without lines. The differential spectrum allows counting the number of quanta in any energy range. The number of quanta of all available lines in the DSAR is ~10% of their total number. As noted above, the crystal check for the effect of incomplete absorption showed a value of 40% of the number of quanta in the line. Thus, radionuclide lines can explain no more than 16% of the total number of quanta in the DSAR. For the base spectrum, this value is even smaller.

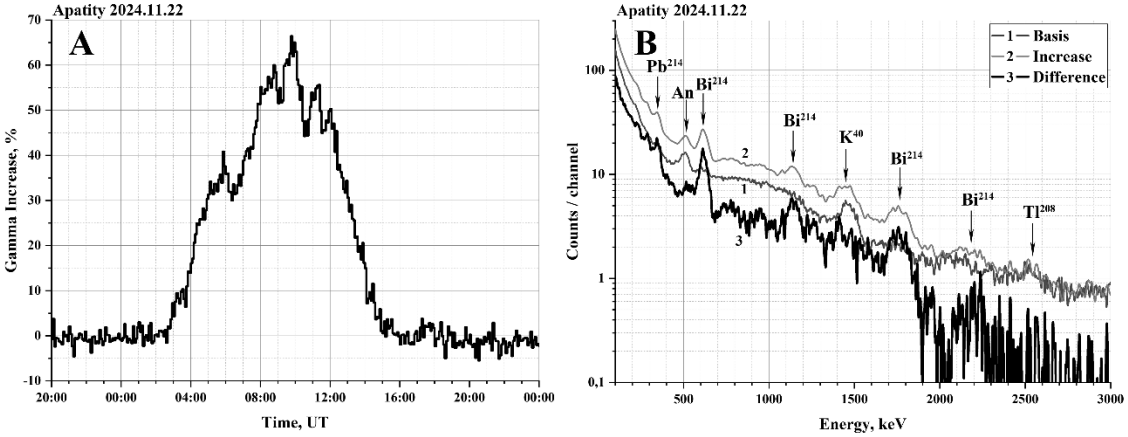


FIGURE 2. An example of registration of an increase and spectra obtained for it. **A** – increase in Apatity. **B** – spectra obtained by the developed method: base (1), with increase (2) and their difference DSAR (3). Arrows indicate radionuclide lines, positron annihilation line (511 keV) is marked as An.

Processing of spectra by the method gave an important result: the upper energy threshold during increase. Previously, indirect measurements gave a result of >>600 keV. Measurements of the differential spectrum of the DSAR provided value: 2-2.5 MeV, as can be seen in Figure2B.

Conclusions. Measurements of differential spectra of gamma radiation coming from the atmosphere in the range of 0.1-5 MeV showed the following results. The spectra have a continuous form with individual lines of radionuclides. During increase, the intensity of the gamma radiation flux increases in the range of 0.1-2.5 MeV. Although there are increases in the lines of radionuclides, their contribution to the whole spectrum is no more than 16%. Therefore, the observed increases in the gamma radiation flux during precipitation are not associated with contamination of the latter with radionuclides. The cause of the observed effect is in the physics of interaction of cosmic rays and meteorological processes in the lower atmosphere.

1. Shishaev V.A., Beloglazov M.I. Automatic recorder of atmospheric precipitation. // *Pribory i tehnika eksperimenta [Instruments and Technique of Experiment]*. 2011. No. 2. P. 156–158. (In Russian).

2. Balabin V.V., Germanenko A.V., Gvozdevsky B.B., Vashenyuk E.V. Variations in the natural X-ray background in the polar atmosphere // *Geomagnetism and Aeronomy*. 2014. V.54. No. 3. P. 347–356. DOI: 10.1134/S0016793214020029.
3. Balabin Y.V., Germanenko A.V., Mikhalko E.A., Maurchev E.A., Larchenko A.V. Observing variations in secondary cosmic ray fluxes during a sea expedition in the Arctic Ocean // *Bulletin of the Russian Academy of Sciences: Physics*. 2022. V.86. No. 3. P. 285–289. DOI: 10.3103/S1062873822030030.
4. Alekseenko V.V., Lidvansky A.S., Petkov V.B., Haerdinov N.S. About different types of increase in space rays before lightning categories // *Izvestiya RAN. Seriya fizicheskaya [Bulletin of the Russian Academy of Sciences: Physics]*. 2002. V.66. No 11. P. 1581–1584. (In Russian).
5. Lidvansky A.S., Petkov V.B., Haerdinov N.S. Cosmic ray muon intensity variations caused by thunderstorm electric fields // *Izvestiya RAN. Seriya fizicheskaya [Bulletin of the Russian Academy of Sciences: Physics]*. 2004. V.68. No 11. P. 1605–1607. (In Russian).
6. Germanenko A.V., Maurchev E.A., Balabin Yu.V. Calculation of registration efficiency functions of NaI(Tl) scintillation detectors and comparison of model operation with real experiment data. // *Trudy Kol'skogo nauchnogo tsentra RAN [Proceedings of the Kola Scientific Center of the Russian Academy of Sciences]*. 2019. V.10. No. 8-5. P. 82–87. (In Russian). DOI: 10.25702/KSC.2307-5252.2019.10.8.82-87.
7. Grigoryev I.S., Melikhov E.Z. *Fizicheskie velichiny. Spravochnik [Physical Quantities. Reference book]*. Energoatomizdat Publ., Moscow, 1991, 1231 p. (In Russian).

MEASUREMENT OF BAROMETRIC COEFFICIENTS FOR NATURAL GAMMA RADIATION COMING FROM THE ATMOSPHERE IN THE RANGE 0.1-5 MEV

Yury V. Balabin, Aleksei V. Germanenko, Evgenia A. Mikhalko, Boris B. Gvozdevsky

Polar Geophysical Institute, Russian Academy of Sciences, Apatity, Russia

Cosmic rays, entering the Earth's atmosphere, interact with air atoms. As a result of such interaction, the nucleus of an atom breaks up, secondary particles are formed, which spread deep into the atmosphere. This flow of particles is called secondary cosmic rays (SeCR), their composition is diverse [1]. Some particles are stable, while others decay. In the process of SeCR propagation deep into the atmosphere, the processes of decay and interaction of particles with the nuclei of air atoms constantly occur. The main condition for interaction with the nuclei of air atoms is sufficient energy of the particles. Let us list the main components of SCR: protons, neutrons, mesons, muons, electrons and positrons, gamma quanta. The latter are generally called the electromagnetic component (EMC). The EMC is more strongly absorbed or scattered in the atmosphere than other components: the mean free path of quanta in the atmosphere is about 40 g/cm^2 [2]. This is due to the fact that for quanta with energies > 1 MeV the mean free path in the atmosphere does not depend on the energy. Quanta with energy > 1.022 MeV begin to produce electron-positron pairs. The efficiency of this process does not depend on the quantum energy [1, 2]. The electrons and positrons can also produce new quanta through the process of bremsstrahlung. Thus, a cascade process occurs in the atmosphere. The analysis of cascade processes is given in detail in [3]. As a result, the electromagnetic component of the SeCR is the most susceptible to the influence of the atmosphere and meteorological processes in it. For this reason, it attracts the least attention, since the EMC flows experience all sorts of variations when passing through the atmosphere,

which are difficult to separate from the variations of the EMC itself, since the state and processes throughout the entire height of the atmosphere are difficult to record. The thickness of the atmosphere that the SeCRs pass through depends on the pressure. This causes the barometric effect: the variations in the SeCR flows become dependent on the pressure. In order to eliminate the variations associated with atmospheric pressure, barometric corrections are introduced. The main parameter here is the barometric coefficient (BC) β, which has a specific value for each type of SeCR. For the neutron component, the BC has a value of $\beta \sim 0.007$ mb^{-1}. For the muon component $\beta \sim 0.002$ mb^{-1}. Since 2022 we monitor the differential spectrum of gamma radiation in the range of 0.1-5 MeV. A NaI(Tl) Ø75x75 mm spectrometric crystal is used. The spectrometer is located in the attic of a building with a roof made of lightweight materials. To obtain the primary spectrum, the measured spectrum is corrected for the absorption in the roof material. It is taken into account that the absorption coefficient in the roof material depends on the energy of the quanta [4]. A significant array of spectra has been accumulated. Atmospheric pressure is also recorded. The EMC reaching the ground level has a complex origin. The flux of the SeCR, the decay or interaction of which with the atmosphere generates gamma radiation deep in the atmosphere, is affected by the atmospheric pressure, which should create a barometric effect for the EMC as well. The working energy range of 0.1-5 MeV is quite large, and radiation from different types of particles falls into it. It would be useful to see what the BC is for the EMC, whether it is constant over the entire energy range. Determining the BC for different energies can clarify which components of the SeCR mainly produce the EMC in a given energy range. For this purpose, the differential spectrum was transformed into profiles of radiation fluxes in successive energy bands, for example: 100-200 keV, 200-300 keV, etc. The width was chosen based on the acceptable count rate in each band. Figure 1 shows the primary spectrum of the EMC and its division into bands. In Figure 1 the arrows mark the 511 keV annihilation line and the 1460 keV potassium-40 line. These lines are always present in any spectrum and are used to control the energy scale. Qualitative analysis of the spectrum shows that at energies of ~500 keV, a "break" in the spectrum occurs. At E < 500 keV, the spectral function drops steeply (soft spectrum), and at E > 500 keV, the spectrum slope becomes noticeably smaller (hard spectrum).

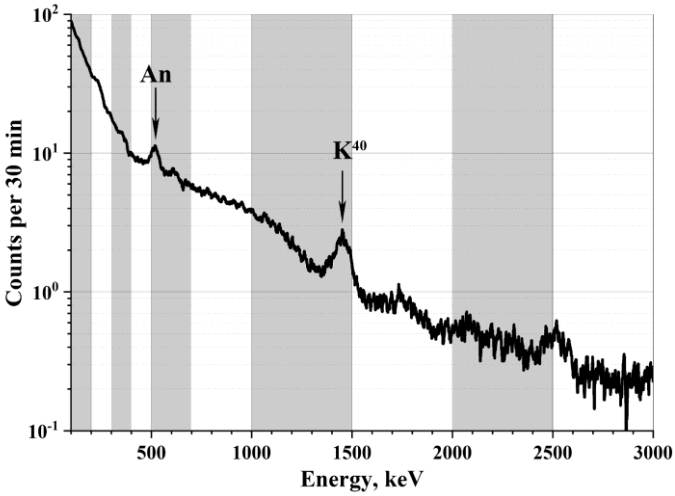


FIGURE 1. Example of a primary spectrum and division of the energy range into bands. Arrows indicate two lines that are invariably present in all spectra. They are used to control the spectrometer scale.

The method for determining the BC is well developed for the nucleon and muon components [5], since they experience significant variations caused by changes in atmospheric pressure. A similar method is used to determine the BC for a set of EMC bands. The spectra from June 2022 to March 2023 were used to calculate the BC. The periods of EMC increase during precipitation were excluded, since such a change in the EMC flux is caused not by a change in pressure, but by other reasons. To construct the barometric dependence, the natural logarithm of the counting rate is used instead of the counting rate. For the obtained point clouds in the coordinates "ln(N) - pressure", the best approximation by a linear function is

determined by standard methods. The linear coefficient of the dependence "ln(N) - pressure" is the barometric coefficient for this set of points. Figure 2 shows the point clouds and linear regression lines for the counting rate in some bands. The table 1 contains the results of BC determination for the energy intervals into which the entire spectral working range was divided.

TABLE 1. Barometric coefficient values depending on radiation energy.

bar, keV	coeff. β, mb^{-1}	bar, keV	coeff. β, mb^{-1}
100-200	0.0006	700-1000	0.0036
200-300	0.0008	1000-1500	0.0034
300-400	0.0010	1500-2000	0.0036
400-500	0.0022	2000-2500	0.0030
500-700	0.0026	2500-3000	0.0020

The obtained results show the following. For energies up to 400 keV, the BC is very small, then it increases with increasing energy, and above 2 MeV it decreases again to the BC value for muons. The latter is quite consistent with the fact that gamma radiation deep in the atmosphere arises from particles of secondary cosmic rays, which, due to their high energy, are able to penetrate deep into the atmosphere.

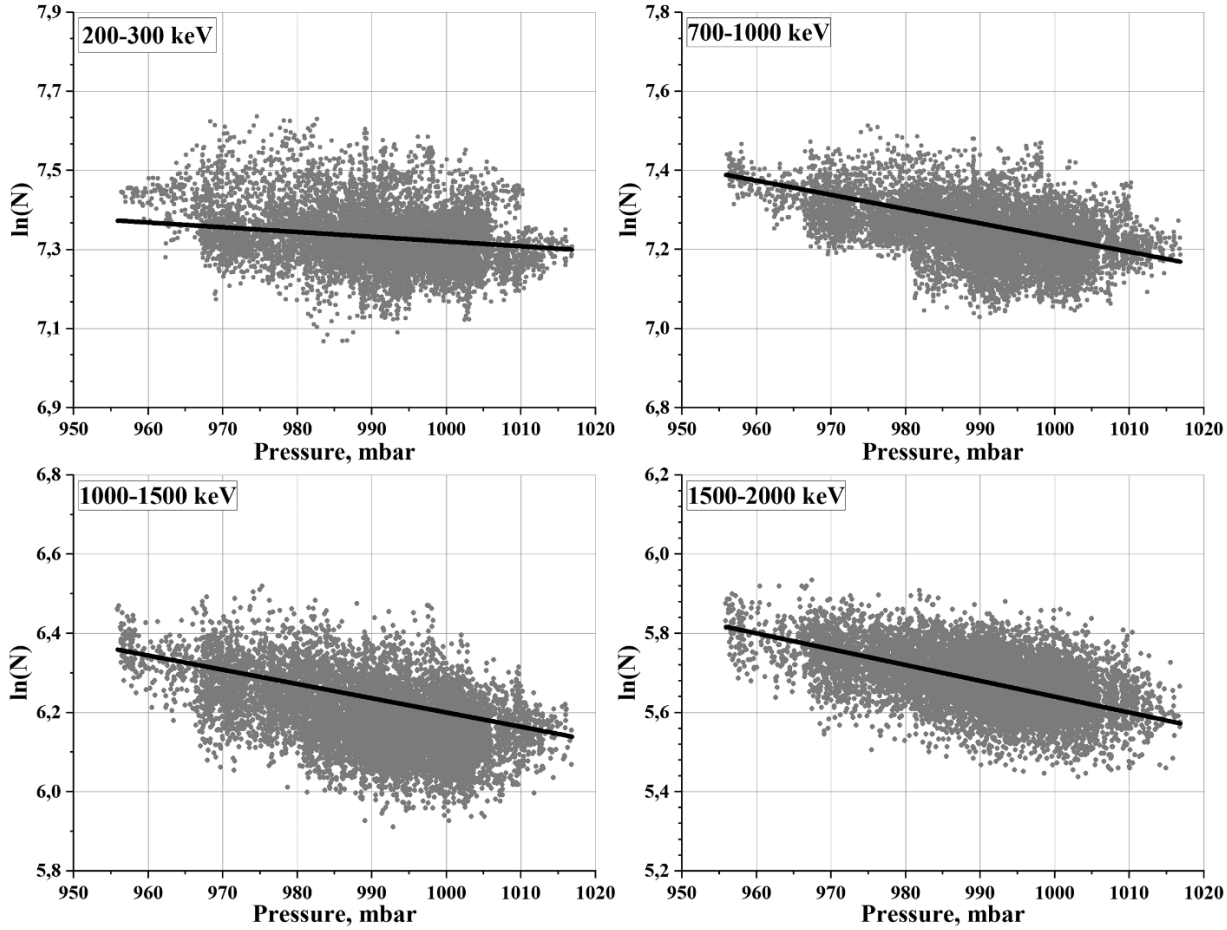


FIGURE 2. Examples of determining the barometric coefficient for the corresponding energy bands of the EMC. Point clouds and linear regression lines.

The greatest contribution to gamma radiation is made by muons, the decay of which produces light charged particles (electrons and positrons) of high energy. The BC of muons is 0.0016-0.0018 [5]. Bremsstrahlung of light particles, as well as Compton scattering of gamma radiation quanta, create a continuous spectrum of gamma radiation in the surface layer of the atmosphere. The small BC at energies < 400 keV is also quite explainable. Quanta of these energies are formed as a result of multiple scattering of high-energy quanta. The scattering efficiency increases with increasing pressure, and the two effects compensate each other. The increase in the BC at energies of 0.5-2 MeV may be due to the following. The BC of the nucleon component (neutrons, protons, pi-mesons) is about 0.007 mb^{-1} [5]. The growth of the BC in this energy range may mean that this component of the SeCR is largely involved in the generation of quanta of these energies. The nucleon component has a relatively large cross section of inelastic interaction with the nuclei of the surrounding atoms, leading to the excitation of nuclei with subsequent emission of quanta. Then, with increasing energy, the contribution of this component decreases, and the muon component becomes the main source of generation. A twofold increase in the BC compared to the BC for muons indicates that the contribution of the nucleon component is significant.

The availability of a large array of differential spectra of gamma radiation coming from the atmosphere made it possible to measure the barometric coefficient for EMC in the range of 0.1-5 MeV. The range was divided into 10 bands. The barometric coefficient for each band was determined. It was found that for energies < 400 keV the barometric coefficient is very small, then it increases to values of 0.0036 mb^{-1}, which is twice as large as the barometric coefficient for muons. This indicates that the nucleon component makes a significant contribution to the generation of EMC in the ground layer of atmosphere.

1. Hayakawa S. *Cosmic Ray Physics: Nuclear and Astrophysical Aspects*. Wiley Interscience Publ., New York, 1969, 774 p.
2. Murzin V.S. *Vvedenie v fiziku kosmicheskikh luchei [Introduction to the Physics of Cosmic Rays]*. MSU Publ., Moscow, 1988, 320 p. (In Russian).
3. Belenkiy S.Z., Ivanenko I.P. Cascade theory of showers // *Uspekhi Fizicheskikh Nauk [Advances in Physical Sciences]*. 1959. V.69. P. 591–656. (In Russian).
4. Grigoryev I.S., Melikhov E.Z. *Fizicheskie velichiny. Spravochnik [Physical Quantities. Reference book]*. Energoatomizdat Publ., Moscow, 1991, 1231 p. (In Russian).
5. Dorman, L.I., *Meteorologicheskie effekty kosmicheskikh luchei [Meteorological Effects of Cosmic Rays]*. Nauka Publ., Moscow, 1972, 211 p. (In Russian).

COMPARISON OF IONOSPHERIC DISTURBANCES FOR STORMS IN MARCH 2015 AND MAY 2024 AT MID-LATITUDES

Kuprian V. Belyuchenko[1], Maksim V. Klimenko[1], Vladimir V. Klimenko[1], Konstantin G. Ratovsky[2]

[1]West Department of Pushkov Institute of Terrestrial Magnetism, Ionosphere and Radio Wave Propagation, RAS, Kaliningrad

[2]Institute of Solar-Terrestrial Physics SB RAS, Irkutsk, Russia

The Earth's ionosphere is a dynamic system that reacts sensitively to changes in solar activity and geomagnetic conditions. Geomagnetic storms cause significant disturbances in the ionosphere [1, 2],

which affects radio communications, navigation systems, and the operation of radiophysical instruments on satellites. Of particular interest are comparative studies of ionospheric disturbances for different geomagnetic storms. Studies of the ionospheric response to geomagnetic storms based on statistical analysis have shown that, despite the fact that general patterns in the behavior of ionospheric parameters during geomagnetic disturbances are known, ionospheric disturbances can differ significantly from event to event [3]. This paper considers two specific cases: the geomagnetic storm of March 2015 and the storm of May 2024. The study is conducted for the mid-latitudes of the Northern Hemisphere, for the main phase of the geomagnetic storm. The aim of the work is a comparative analysis of disturbances of ionospheric parameters, such as the total electron content (TEC), the height of the maximum electron concentration in the F2 layer (HmF2), disturbances in the concentration of atomic oxygen (n(O)), the temperature of neutral particles (Tn) and the meridional component of the thermospheric wind (VnΘ).

The studies were performed using the results of calculations of the Global Self-Consistent Model of the Thermosphere, Ionosphere and Protonosphere (GSM TIP). In previous works, model studies were conducted for the geomagnetic storm of March 17–23, 2015 with different onset times in UT [4-6]. Historically, the geomagnetic storm began on March 17, 2015 at 12 UT. Four scenarios of absolutely identical geomagnetic storms with onset times of 00, 06, 12 and 18 UT were considered. For this work, we calculated the ionospheric response to the geomagnetic storm of May 10–14, 2024. We considered the calculation results for two points with coordinates corresponding to two ionospheric stations, Kaliningrad (55°N, 20°E) and Irkutsk (52°N, 104°E). In this paper, we will consider the following time periods: 1) for the 2024 storm, this is May 9–12; 2) for the 2015 storm, this is March 16–19.

Figure 1 shows the dTEC and dHmF2 disturbances for the calculations with the shift in the onset time of the March 2015 storm for two stations: Kaliningrad (KAL) and Irkutsk (IRK).

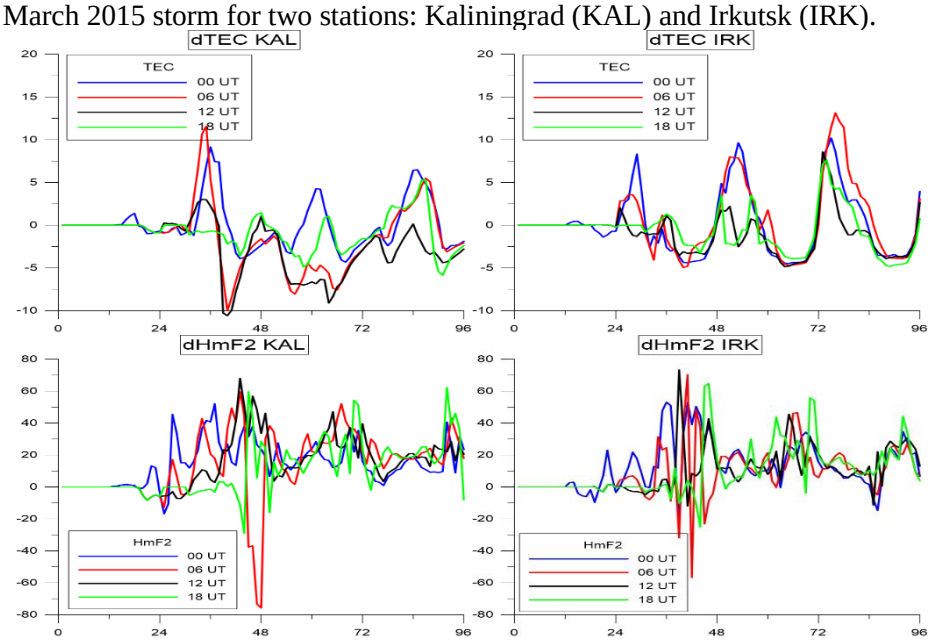


FIGURE 1. Perturbations of the total electron content (dTEC) and the height of maximum electron density (dHmF2) for calculations with a time shift in the storm onset.

Considering the results obtained with the shift in the onset time of the storm, several features can be noted: 1) for Kaliningrad, stronger negative disturbances in dTEC are observed, and they occur in the cases with the onset time of the storm at 06 and 12 UT; 2) the strongest positive effect in dTEC can be observed for the case with the onset time of the storm at 06 UT; 3) the weakest positive effect in dTEC is observed for the case with the onset time at 12 UT at both stations; 4) for disturbances in dHmF2, it can be noted that the strongest negative disturbances are observed for the case of the

geomagnetic storm with the onset at 06 UT at both stations, and the strongest positive effect is for the case with the onset at 12 UT at both stations. It is important to note that a drop in the maximum height by more than 40 km means the formation of the G-condition, when the electron concentration in the F1 layer maximum exceeds the concentration in the F2 layer. The rise in the height of the F2 layer maximum is associated with the action of the storm wind to the equator and the intensification of recombination due to an increase in n(N2).

Next, we propose to consider the results of the GSM TIP calculations for March 2015, but only for the version with the storm start time at 12 UT. Figure 2 shows the disturbances dTEC and dHmF2, dn(O), dTn and dVnΘ for the Kaliningrad and Irkutsk stations.

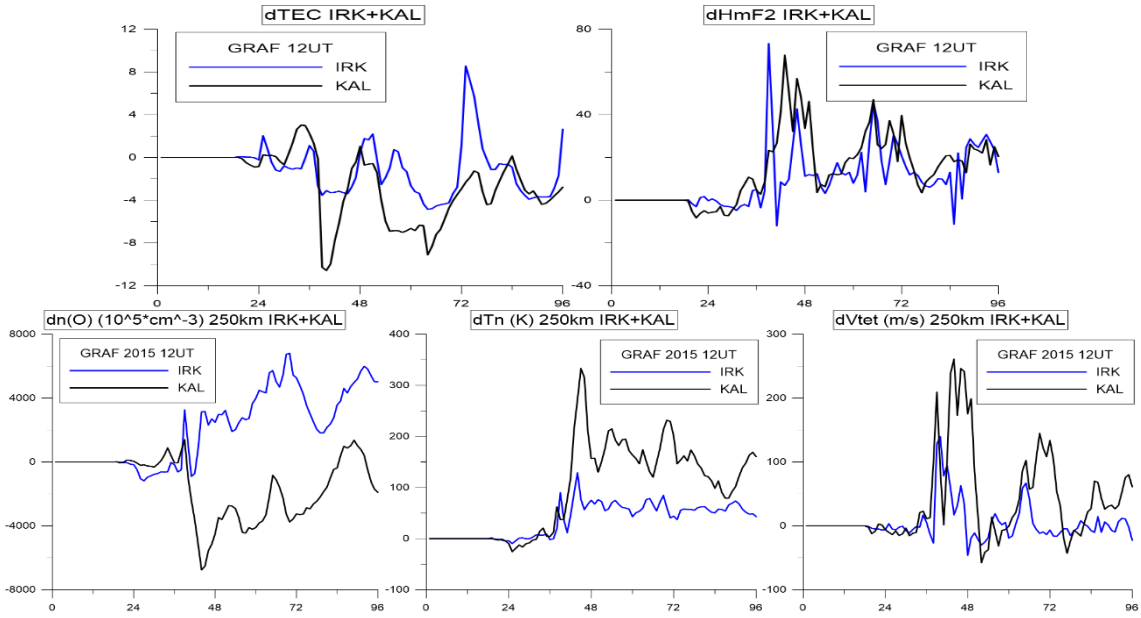


FIGURE 2. Perturbations dTEC and dHmF2 on the upper panel, dn(O), dTn, dVnΘ on the lower panel for two stations, Kaliningrad (black line) and Irkutsk (blue line). Calculations for March 2015 with the storm onset time at 12 UT.

The effects of geomagnetic storms in the upper atmosphere are a consequence of heating of the thermosphere, causing the appearance of additional thermospheric wind to the equator and the restructuring of the neutral composition of the thermosphere. As is known, an increase/decrease in n(O) leads to an increase/decrease in TEC, a storm-induced increase in the wind to the equator leads to the emergence of positive disturbances in dHmF2 at middle and low latitudes, and negative disturbances in n(O) lead to the emergence of negative disturbances in dHmF2 at high and middle latitudes [7][8]. Looking at Figure 2, we can note the following: 1) the dHmF2 disturbances behave very similarly for both stations; 2) the dTEC disturbances have differences for these stations, in Kaliningrad a stronger decrease in TEC is observed on the day of the storm, and in Irkutsk a strong positive effect is observed on the 3rd day after the storm; 3) the difference in TEC disturbance is reflected in dn(O), for Kaliningrad we observe a general drop in concentration and a slow recovery, while for Irkutsk we observe an increase in atomic oxygen concentration after a short initial drop in concentration; 4) the differences in dn(O), in turn, are related to dTn and dVnΘ, stronger heating and equatorial wind lead to a decrease in atomic oxygen concentration for Kaliningrad compared to Irkutsk;

Also, within the framework of this work, a comparison was made between the March 2015 storm and the May 2024 storm. Figure 3 shows the dTEC and dHmF2 response for the two stations under consideration to these two strong geomagnetic storms. In conclusion, it should be noted that the May

2024 storm was more than 2 times stronger than the March 2015 storm, but at the longitude of Kaliningrad, the differences in dTEC disturbances are not very noticeable, although disturbances in the height of the F2 layer maximum increased by about 2 times. For Irkutsk, there is already a noticeable increase in positive and negative responses in both dTEC and dHmF2.

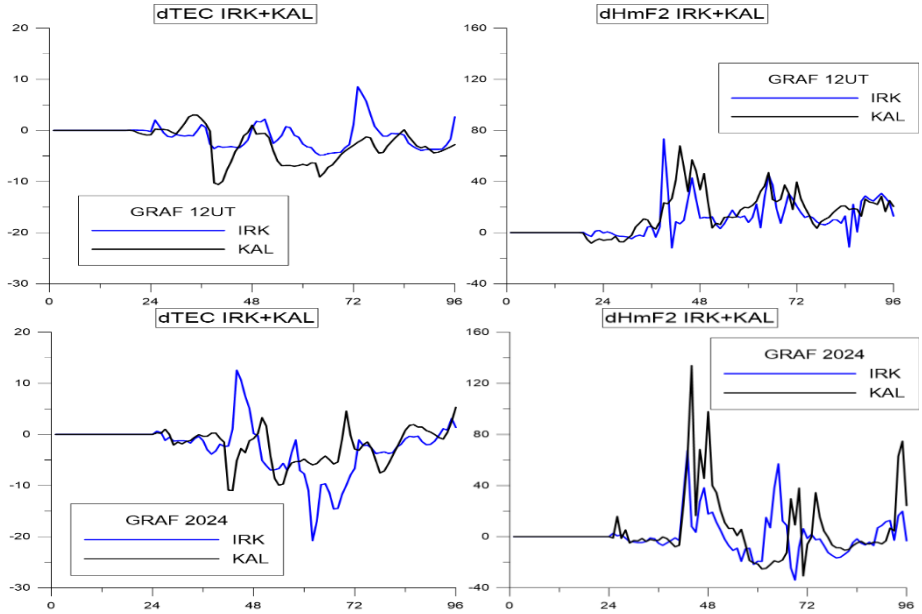


FIGURE 3. dTEC and dHmF2 disturbances, on the top panel for the March 2015 storm, on the bottom panel for the May 2024 storm. At 2 stations, Kaliningrad (black line) and Irkutsk (blue line).

The work was supported by a grant from the Russian Science Foundation № 25-27-00217.

1. Buonsanto M.J. Ionospheric storms: A review // *Space Sci. Rev*. 1999. V. 88. No. 3. P. 563-601. DOI:10.1023/A:1005107532631.
2. Prolss G.W. Ionospheric Storms at Mid-Latitude: A Short Review // *Geophysical Monograph Series*. 2013. V. 181. P. 9-24. DOI: 10.1029/181GM03.
3. Ratovsky K.G., Klimenko M.V., Klimenko V.V., Chirik N.V., Korenkova N.A., Kotova D.S. After-effects of geomagnetic storms: statistical analysis and theoretical explanation // *Solar-Terrestrial Physics*. 2018. V. 4. No. 4. P. 26-32. DOI: 10.12737/stp-44201804.
4. Klimenko M.V., Klimenko V.V., Ratovsky K.G., Goncharenko L.P., Sahai Y., Fagundes P.R., de Jesus R., de Abreu A.J., Vesnin A.M. Numerical modeling of ionospheric effects in the middle- and low-latitude F region during geomagnetic storm sequence of 9–14 September 2005 // *Radio Science*. 2011. V. 46. No. 03. P. 1-18. DOI: 10.1029/2010RS004590.
5. Belyuchenko K.V., Klimenko M.V., Klimenko V.V., Ratovsky K.G. Modeling of zonal mean ionospheric disturbances on the example of the march 2015 geomagnetic storm with different onset moments // *Atmosphere, Ionosphere, Safety*. 2023. P. 55-58. DOI: 10.59043/9785604204474_55.
6. Belyuchenko K.V., Klimenko M.V., Klimenko V.V., Ratovsky K.G. Modeling the UT effect of zonal-averaged perturbations in the parameters of the upper atmosphere for the example of a geomagnetic storm in march 2015 // *Proceedings of the USSR Academy of Sciences. The series is physical*. 2024. V. 88. No. 3. P. 356-362. DOI: 10.31857/S0367676524030032.
7. Mayr H.G., Harris I., Spencer N.W. Some properties of upper atmosphere dynamics // *Reviews of Geophysics*. 1978. V. 16. No. 4. P. 539-565. DOI: 10.1029/RG016i004p00539.

8. Prölss G.W. Magnetic storm associated perturbations of the upper atmosphere: Recent results obtained by satellite-borne gas analyzers // *Reviews of Geophysics*. 1980. V. 18. No. 1. P. 183-202. DOI: 10.1029/RG018i001p00183.

MODELING OF IONOSPHERIC DISTURBANCES VARIATIONS CAUSED BY THE PASSAGE OF ATMOSPHERIC WAVES FROM THE TROPOSPHERE

Yuliya A. Kurdyaeva[1], Olga P. Borchevkina[1] and Artem M. Padokhin[2,3]

[1]West department of Pushkov Institute of Terrestrial Magnetism, Ionosphere and Radio Wave Propagation, Russian Academy of Sciences, Kaliningrad, Russia
[2]Pushkov Institute of Terrestrial Magnetism, Ionosphere and Radio Wave Propagation, Russian Academy of Sciences, 142191, Troitsk, Moscow, Russia
[3]M. V. Lomonosov Moscow State University, 119991, Moscow, Russia

Various events in the lower atmosphere such as hurricanes, earthquakes, and volcanic eruptions can be the source of atmospheric waves of a wide spectral range. Acoustic (AGWs) and internal gravity waves (GWs) propagating from the troposphere can reach the heights of the thermosphere and ionosphere and have a significant influence on their parameters. One of the effective methods to study the effect of these waves on the upper atmosphere is numerical modeling. Some modern numerical models can qualitatively consider the influence of AGWs, however, such calculations are implemented mainly for the neutral atmosphere, which makes us search for others approaches to modeling changes in the ionosphere. Processes in the real atmosphere are complex and include photoionization, recombination, a variety of chemical reactions, and movements of neutrals determined by atmospheric waves, electric fields, plasma diffusion, and the action of the geomagnetic field [1].

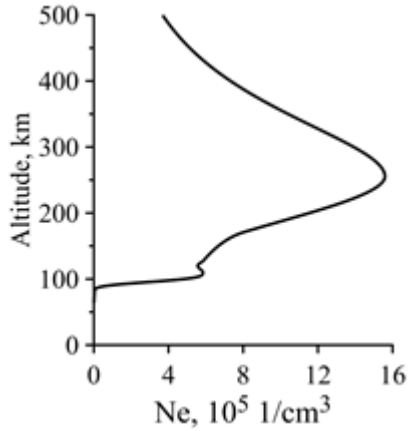


FIGURE 1. The high-altitude electron concentration profile constructed using the IRI model, for May 29, 2017.

AGWs influence the intensity of all these processes by affecting atmospheric pressure, density, temperature, and velocity. According to the works [2, 3], motion of particles in the neutral atmosphere by means of collisions sets ionospheric plasma in motion. Therefore, it is possible from the continuity equation for the ionospheric plasma density, neglecting the emergence and annihilation of charged particles, to obtain an expression for calculating the change of the electron concentration in the ionosphere at the passage of AGWs in a point of space at a certain moment of time. To calculate variations in the electron content using this approach, it is necessary to have information on the variation of hydrodynamic functions with high resolution in time and space.

In this study, the approach of calculating the change in electron concentration using the formula proposed in [2, 4] is implemented. Model AtmoSym, described in [5], provides such values for the

velocity, temperature, density, and pressure components. A three-dimensional version of the high-resolution AtmoSym model was used to simulate the effects in the neutral atmosphere. A tropospheric meteorological source was assumed as the AGWs source in the calculations.

A strong meteorological event [6], which was observed on May 29, 2017, over the territory of the Moscow region (55°N, 37°E), was considered as the source of waves in the modeling. A detailed analysis of the effect of this meteorological event on the state of the thermosphere-ionosphere system using a multimodel approach is presented in [7].

The velocity fields obtained in the course of AtmoSym model calculations allowed us to calculate variations of the electron concentration. The high-altitude background profile (Fig. 1) of electron concentration, necessary for calculation of Ne variations, was obtained using the IRI ionospheric model in 01:00 UTC May 29, 2017 [8].

The modeling allowed us to calculate the spatial distributions of electron density perturbations in the ionosphere caused by the AGWs propagation from the meteorological one in the troposphere for different moments of time (Fig. 2). The maximum change of variations of electron concentration variations from the background ionosphere is about 10%, which corresponds to modern ideas about the AGWs influence on the ionosphere. The results of studies of recent years show that the contribution of wave processes of the lower and middle atmosphere to the variability of parameters of the ionosphere can reach 20%.

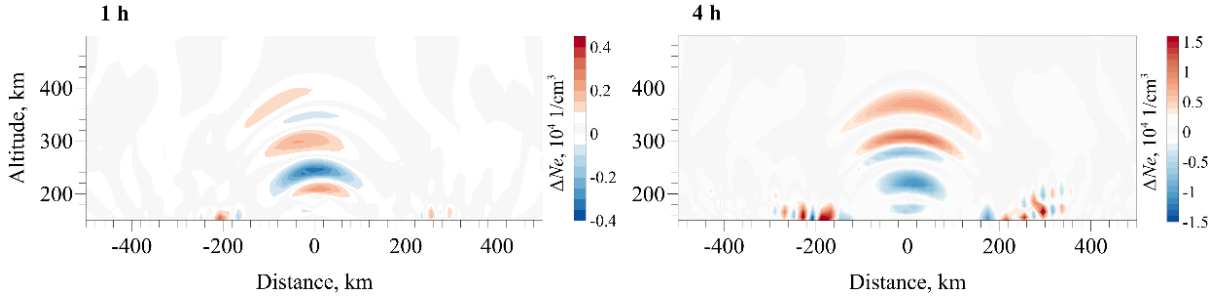


FIGURE 2. Electron density variations caused by AGWs propagation from the troposphere for the time moments 1 hour after the beginning of calculations (left), 4 hours after the beginning of calculations (right).

The obtained spatial and temporal distributions of electron density variations allow us to clarify the parameters of the medium during extreme events in the lower atmosphere. This is necessary for further qualitative modeling and forecasting of the thermosphere-ionosphere system and for improving the methods of mathematical modeling when taking into account the processes occurring in the lower atmosphere.

The research was funded by the grant Russian Science Foundation N°– 23–77-10004, https://rscf.ru/project/23–77-10004.

1. Yiğit E., Knížová P. K., Georgieva K., Ward W. A review of vertical coupling in the Atmosphere–Ionosphere system: Effects of waves, sudden stratospheric warmings, space weather, and of solar activity // *J. Atmos. Sol.-Terr. Phys.* 2016. V. 141. P. 1-12. DOI: 10.1016/j.jastp.2016.02.011.
2. Andreeva E.S., Kunitsyn V.E., Gokhberg M.B. et al. Radiotomographical detection of ionosphere disturbances caused by ground explosions // *Cosmic Research*. 2001. V. 39. No 1. P. 10-14. DOI: 10.1023/A:1002827609677.
3. Macleod M. A Sporadic E Theory. I. Collision-Geomagnetic Equilibrium // *J. Atmos. Sci*. 1966. V. 23. P. 96–109. DOI: 10.1175/1520-0469(1966)023<0096:SETICG>2.0.CO;2.
4. Akhmedov R.R., Kunitsyn V.E Simulation of the ionospheric disturbances caused by earthquakes and explosions // *Geomagn. Aeron.* 2004. V. 44. No 1. P. 95-101.

5. Gavrilov N.M., Kshevetskii S.P. Numerical modeling of propagation of breaking nonlinear acoustic-gravity waves from the lower to the upper atmosphere // *Adv. Space Res.* 2013. V. 51. No 7. P. 1168-1174. DOI: 10.1016/j.asr.2012.10.023.
6. Kulichkov S.N., Chunchuzov I.P., Popov O.E. et al. Internal gravity and infrasound waves during the hurricane of May 29, 2017, in Moscow // *Izv. - Atmos. Ocean. Phys*. 2019. V. 55. No 2. P. 167-177. DOI: 10.1134/S0001433819020105.
7. Kurdyaeva Y., Bessarab F., Borchevkina O., Klimenko M. Model study of the influence of atmospheric waves on variations of upper atmosphere and ionosphere parameters during a meteorological storm on May 29, 2017 // *Adv. Space Res.* 2024. V. 74 No 5. P. 2463-2474. DOI: 10.1016/j.asr.2024.05.062.
8. Bilitza D. IRI the International Standard for the Ionosphere // *Adv. Radio Sci.* 2018. V. 16. P. 1-11. DOI: 10.5194/ars-16-1-2018.

STATISTICS OF TOTAL ELECTRON CONTENT VARIATIONS IN THE KALININGRAD STATION IN 2023

Olga P. Borchevkina, Ivan I. Efishov, Alexander V. Radievsky, Nadezhda Y. Tepenitsyna, Irk I. Shagimuratov, Galina A. Yakimova

West Department of Pushkov Institute of Terrestrial Magnetism, Ionosphere and Radio Wave Propagation RAS, Kaliningrad, Russia

Introduction. Regular ionospheric observations at the ionospheric station Kaliningrad have been carried out since the mid-sixties of the last century. Complex diagnostics of ionospheric parameters is carried out using ionosondes, a magnetovariation station, an ionosonde sensing, a meteorological station, lidars, GPS and GLONASS receivers and others. Since 2009, continuous observations and recording of signals of GPS and GLONASS navigation systems have been carried out. In the course of these studies, our own advanced methods of satellite signal processing have been developed and tested. These techniques are successfully applied to obtain local variations of the total electron content (TEC) and to construct regional and global TEC maps [1]. Over the past decades, a unique database of global and local TEC variations has been formed, which together with ionosonde, meteorological, and magnetic bases can serve as a source material for establishing statistical regularities of TEC distribution directly and for revealing correlation geophysical factors determining TEC properties over Kaliningrad.

Experimental data processing technique. For the statistical study, we used the TECU(t) observations for the year 2023, with 10 min post-processing. Recall that the vertical TEC is directly related to the electronic concentration *Ne(h)* along the signal propagation path from the satellite to the receiver [1]:

$$TEC(t) = \int Ne(t,h)(1/\cos\chi)dh\,.$$

Figure 1 shows a typical time dependence of TEC variations in March 2023. It is known that *TEC(t)* contains a daily and annual component associated with the change in the duration of day and night hours.

For correct trend removal, we will apply the standard 15-day moving window for ionospheric time series [2] and use the average for the observation interval (144 samples over 24 hours every 10 minutes) value:

$$< TEC >_{15} = \frac{1}{144}\sum_{i=0}^{143} < TEC >_{15}^{i} \qquad (1)$$

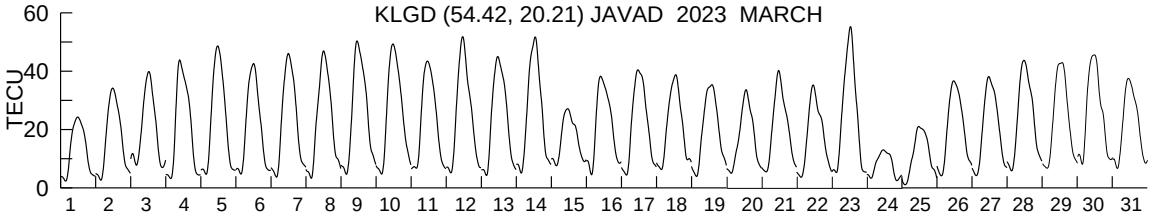


FIGURE 1. TEC variations in March 2023.

Where *i* is the number of 10 minute count in the current hour. A universal statistical characteristic suitable for describing both discrete and continuous random variables is the distribution function $F(x) = P\{X < x\}$ [3]. Based on the results of observations, we calculate the sample distribution function *F*(x)*, which tends to *F(x)*. In our case, the sample sizes contain about 1000 samples and, therefore, the condition *F*(x)=F(x)* is satisfied with a high degree of accuracy. For discrete experimental data, *F(x)* is stepwise and can be easily calculated for any reference *i*= 0-143 or any given time interval:

$$F_i(x) = P_i\{X < x\} = n(TEC_i < x) / N_i \quad (2)$$

where N_i is the total number of samples (days), and $n(TEC_i < x)$ the number of samples for which $TEC_i < x$. To construct the distribution density *f(x)* [2], as an alternative to the histogram method, we use the numerical differentiation (2) of the smoothed experimental distribution function as an alternative to the histogram method:

$$f(x) = dF(x) / dx \quad (3)$$

Calculation results and conclusions. The distribution function and probability density function $f(x) = dF(x) / dx$ of the random variable TEC_i calculated from the experimental data are presented in fig. 2a,b.

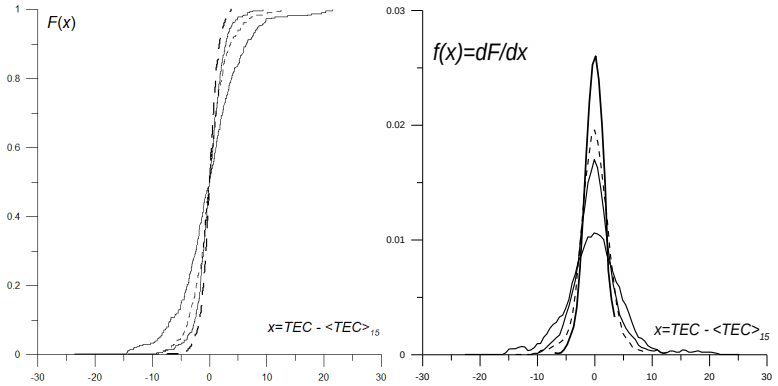


FIGURE 2. The distribution function (left) and probability density function (right).

$f(x) = dF(x) / dx$ experiences insignificant diurnal changes. In addition, almost all central moments and, accordingly, the characteristics of the distribution position depend on the time of day: mean value, dispersion, asymmetry.

In our case, during 2023, the asymmetry of the distribution density $A = M(X - MX)/(DX)^{3/2}$ changed slightly in magnitude, with A changing sign (see Fig. 3). For the density excess E, (see Figure 4). For Gaussian distributions *A=0, E=1*. The difference from these values, even a weak one, can serve as one of the criteria rejecting the applicability as an analytical approximation of the normal distribution.

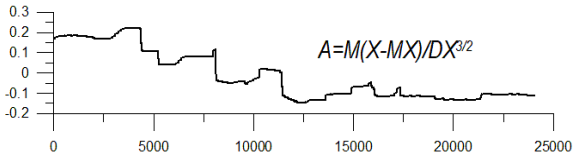


FIGURE 3. The asymmetry of the distribution density during 2023.

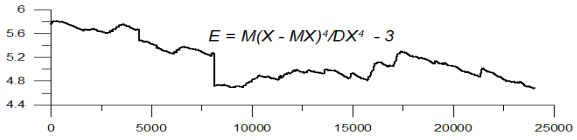


FIGURE 4. Density excess *E* during 2023.

Note [4] that in different years both positive and negative values of asymmetry were recorded at a number of other observation stations, including midlatitudinal stations.

To construct the autocorrelation function $K_X(\tau)$, we use the ergodicity of the detrended series of observations. For this purpose, we replace our "ensemble" from the system of daily observations with a single annual sequence of samples. The use of current mean values $< TEC(t) >_{15}$ allows us to partially exclude the constant shift and long-period (τ_k >24 h) components from the autocorrelation function $K_X(\tau)$:

$$K_{\Delta(TEC)}(mT/n) = (n-m)^{-1}\sum_{i=1}^{n-m}[(TEC(t_i) - < TEC(t_i) >_{15}) \cdot (TEC(t_{i+m}) - < TEC(t_{i+m}) >_{15})] \quad (4)$$

where *T* is the time interval under study, *n* is the number of complete samples in this interval, $\tau = m\Delta t = mT/n$.

Fig. 5 presents the unit-normalized autocorrelation function (4) calculated for 2023. The study of the behavior of this function is of applied importance and is of independent interest for further scientific work.

The research was carried out under the grant Russian Science Foundation № 25-27-00213, https://rscf.ru/project/25-27-00213/

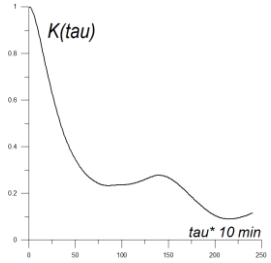


FIGURE 5. Unit normalized autocorrelation function calculated for 2023.

1. Shagimuratov I.I., Chernyak Y.V., Zakharenkova I.E., Yakimova G.A. Use of total electron content maps for analysis of spatial-temporal structures of the ionosphere // *Russian Journal of Physical Chemistry B*. 2013. V. 7. No 5. P. 656-662. DOI: 10.1134/S1990793113050230.
2. Deminov M.G., Deminova G.F., Zherebtsov G.A., Pirog O.M., Polekh N.M. Variability of parameters of the f2-layer maximum in the quiet midlatitude ionosphere under low solar activity: 1. statistical properties // *Geomagnetism and Aeronomy*. 2011. V. 51. No 3. P. 348-355. DOI: 10.1134/S0016793211020058.
3. Ventzel E.S. Probability theory, M.: Nauka. 1964. - 576 p. (in russian).
4. Kalinin Y.K., Kuznetsov V.A., Platonov T.D., Velichko V.V., Sergeenko N.P., Dzvonkovskaya A.L. Statistical modeling of relative variations in the critical frequencies of the ionospheric F region // *Geomagnetism and Aeronomy*. 2010. V. 50. No 1. P. 64-68. DOI: 10.1134/S0016793210010081.

A NEW APPROACH TO MODELING OF VERTICAL SOUNDING IONOGRAMS. COMPARISON WITH OBSERVATIONAL DATA

Nikolay V. Buryak[1], Aleksandr R. Vilutis[1], and Igor A. Nosikov[2]

[1]Immanuel Kant Baltic Federal University, Kaliningrad, Russia
[2]West Department of Pushkov Institute of Terrestrial Magnetism, Ionosphere and Radio Wave Propagation RAS, Kaliningrad, Russia

Abstract. The paper presents preliminary results of ionogram modeling for vertical sounding using the direct variational method. Within the proposed approach, the calculation of radio wave ray trajectories is carried out with modified boundary conditions – the reflection point of the ray from the ionosphere is not fixed. The distance-frequency characteristic obtained from the calculations for various operating frequencies is compared with vertical sounding data.

Introduction. Currently, providing radio communication systems with modern radio path calculation software, along with up-to-date data on current and forecasted ionospheric parameters, is an important scientific task. Long-term observations of ionospheric parameters, conducted using ground-based and satellite methods, have formed the basis for several international models [1, 2] used for ionospheric weather forecasting and ensuring the operation of radio communication systems. As a rule, such models perform well under calm geomagnetic conditions at mid-latitudes. However, under disturbed geomagnetic and atmospheric conditions, the accuracy of ionospheric weather forecasts based on empirical models decreases. As a result, reliable information on ionospheric parameters can only be obtained through continuous observations. Thus, the forefront of ionospheric research is focused on assimilating observational data into ionospheric models (see, for example, [3, 4]). This study aims to develop a numerical approach to modeling ionospheric radio wave propagation based on Fermat's principle, which, in the long term, will enable the creation of an effective tool for ionogram modeling.

Observational data and simulation. The solution of the direct problem of vertical sounding (calculation of rays reflected from the ionosphere) was carried out using a modified variational method. The main difference from the ray calculation using the generalized force method, previously applied for oblique sounding modeling [5], lies in the changes to the boundary conditions. The initial point of the ray is fixed, while the final point (the reflection point from the ionosphere) is constrained to a curve corresponding to the reflection height for a given operating frequency. The desired ray trajectory represents an extremal path connecting the initial point to the optimal reflection point.Figure 1 shows an example of a vertical sounding ionogram for 08:00 UT on January 1, 2025, obtained using the "Parus-A" ionosonde at the observatory of WD IZMIRAN.

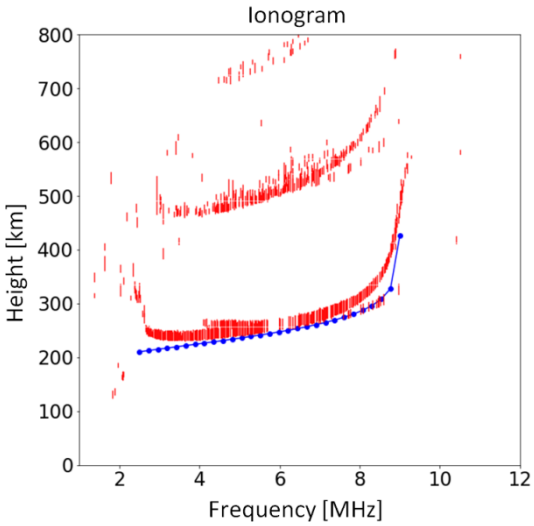


FIGURE 1. Comparison of observational data obtained using the Parus-A ionosonde, located at the observatory of WD IZMIRAN, with simulation results performed using the variational method.

The observational data are supplemented with model calculations of the distance-frequency characteristic based on Fermat's principle. The presented calculation results were obtained using an

analytical ionospheric model [5]. The parameters of the F-layer maximum and its half-thickness were adjusted to achieve the required agreement with the observational data.

Summary. The paper presents preliminary results of modeling the distance-frequency characteristic of vertical sounding. It is shown that modifying the boundary conditions within the variational approach enables the consideration of vertical sounding modeling problems for the ionosphere. In the future, the development of a numerical model for radio wave propagation based on Fermat's principle is expected to yield important results in terms of interpreting observational data and developing new approaches to solving inverse problems and correction tasks.

This study was financially supported by the Russian Science Foundation (Grant 23-77-10004).

1. Bilitza D., Pezzopane M., Truhlik V., Altadill D., Reinisch B.W., Pignalberi A. The International Reference Ionosphere model: A review and description of an ionospheric benchmark // *Reviews of Geophysics*. 2022. V. 60. No. 4. P. e2022RG000792. DOI:10.1029/2022RG000792.
2. Nava B., Coisson P., Radicella S. M. A new version of the NeQuick ionosphere electron density model //*Journal of Atmospheric and Solar-Terrestrial Physics*. 2008. V. 70. No. 15. P. 1856-1862. DOI:10.1016/j.jastp.2008.01.015.
3. Schunk R. W., Scherliess L., Sojka J.J., Thompson D.C. et al. Global assimilation of ionospheric measurements (GAIM) // *Radio Science*. 2004. V. 39. No. 1. P. 1-11. DOI: 10.1029/2002RS002794.
4. Bilitza D., Altadill D., Truhlik V., Shubin V., Galkin I., Reinisch B., Huang X. International Reference Ionosphere 2016: From ionospheric climate to real-time weather predictions // *Space Weather*. 2017. V. 15. No. 2. P. 418-429. DOI: 10.1002/2016SW001593.
5. Nosikov I. A., Klimenko M. V., Zhbankov G. A., Podlesnyi A. V., Ivanova V. A., Bessarab P. F. Generalized force approach to point-to-point ionospheric ray tracing and systematic identification of high and low rays // *IEEE Transactions on Antennas and Propagation*. 2020. V. 68. No. 1. P. 455-467. DOI: 10.1109/TAP.2019.2938817.

A NEW APPROACH TO MODELING VERTICAL SOUNDING IONOGRAMS. CALCULATION TECHNIQUE

Aleksandr R. Vilutis[1], Nikolay V. Buryak[1], and Igor A. Nosikov[2]

[1]Immanuel Kant Baltic Federal University, Kaliningrad, Russia
[2]West Department of Pushkov Institute of Terrestrial Magnetism, Ionosphere and Radio Wave Propagation RAS, Kaliningrad, Russia

Abstract. The paper presents the problem statement and preliminary results of simulating vertical sounding of the ionosphere using the direct variational method. The development of this computational method for ray path calculation has broad prospects for advancing the modeling of multipath effects in the interpretation of radio sounding ionograms.

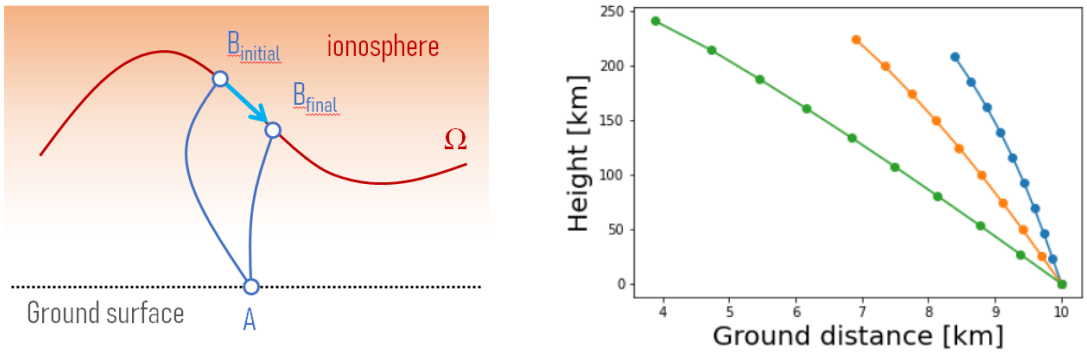
Introduction. One of the most relevant challenges in processing ionospheric radio sounding data is the interpretation of ionograms, which often exhibit a complex modal structure. Atypical traces on ionograms frequently indicate dynamic processes in the ionosphere associated with ionization effects and plasma transport, especially during geomagnetic storms. As a result, multipath propagation effects are observed when radio waves travel through inhomogeneous plasma. This paper presents the problem

statement and preliminary results of ray path modeling based on the variational method for vertical sounding applications.

Method. The solution to the direct problem of vertical sounding (calculating rays reflected from the ionosphere) will be carried out based on Fermat's principle [1].

$$\delta S[\gamma] = \delta \int_A^B n(\vec{r})\, dl = 0. \qquad (1)$$

Here, integration is performed along the curve γ, which defines the ray trajectory connecting points A and B. The function $n(\vec{r})$ represents the refractive index at point $\vec{r} = (x, y, z)$ lying on the curve γ, and dl is the length element along γ. The key difference from the ray calculation using the generalized force method, previously applied for oblique sounding modeling, lies in the boundary conditions. The initial point (the transmitter's position) is fixed. The final point (the reflection point in the ionosphere) is constrained to lie on the curve (or a surface in the three-dimensional case), which corresponds to the reflection height for a given operating frequency f. Thus, the solution is sought within the class of extremal curves that connect the initial point with possible locations of the final point (see Fig. 1a). Similar problem formulations have been previously proposed for calculating optimal libration trajectories in quantum mechanics to describe tunneling effects [2]. A comparable approach is used for solving the problem of ray reflection at medium interfaces in the context of tsunami wave propagation near the coastline [3].



a) b)

Preliminary results. Fig. 1b presents the results of ray calculations for different operating frequencies using an analytical ionosphere model that accounts for the horizontal gradient of ionospheric plasma. It is shown that modifying the boundary conditions enables the adaptation of the method for determining ray trajectories in vertical sounding problems. The advantages of this approach include the following:

1. The algorithm is based on direct minimization, which ensures the guaranteed determination of the desired extremals (minima or maxima).
2. Considering only half of the path (since the trajectory from the initial point to the reflection and back follows the same path) avoids the consideration of extremals corresponding to saddle-type solutions.

It should be noted that we do not consider here the class of special rays (e.g., looped rays), which are also possible within vertical sounding modeling. Their analysis in the future will be associated with the optimization of higher-order saddle points, which is a subject for further research.

This study was financially supported by the Russian Science Foundation (Grant 23-77-10004).

1. Nosikov I. A., Klimenko M. V., Zhbankov G. A., Podlesnyi A. V., Ivanova V. A., Bessarab P. F. Generalized force approach to point-to-point ionospheric ray tracing and systematic identification of high and low rays // IEEE Transactions on Antennas and Propagation. 2020. V. 68. No. 1. P. 455-467. DOI: 10.1109/TAP.2019.2938817.
2. Anikin A.Y., Dobrokhotov S.Y., Nosikov I.A. Librations with large periods in tunneling: Efficient calculation and applications to trigonal dimers // *Theoretical and Mathematical Physics.* 2022. V. 213. No. 1. P. 1453-1476. DOI: 10.1134/S0040577922100117.
3. Nosikov I.A., Tolchennikov A.A., Klimenko M.V. Boundary Value Problem of Calculating Ray Characteristics of Ocean Waves Reflected from Coastline // *Computational Mathematics and Mathematical Physics.* 2024. Vol. 64, No. 3. P. 497-508. DOI: 10.1134/S0965542524030126.

CONDUCTING SPECTRAL OBSERVATIONS OF NATURAL GAMMA RADIATION IN THE RANGE OF 0.1-5 MEV IN VARIOUS GEOGRAPHICAL LOCATIONS AND COMPARING THE SPECTRA

Yury V. Balabin, Aleksei V. Germanenko, Evgenia A. Mikhalko, Boris B. Gvozdevsky

Polar Geophysical Institute, Russian Academy of Sciences, Apatity, Russia

We have installed differential gamma-ray spectrometers at various geographical points to monitor gamma radiation in the energy range of 0.1-5 MeV coming from the atmosphere. The locations are: Apatity (Murmansk region), Tatsinskaya (Rostov region) and Barentsburg (Spitsbergen archipelago). The spectrometers are based on a NaI(Tl) Ø75x75 mm spectrometric crystal. After assembling the instruments were checked and tested. The resolution on the 660 keV line (cesium-137) is less than 5%. The following radiation sources were used to calibrate the energy scale: potassium-40, aluminum-26 and sodium-22. The collection time of one differential spectrum was set to 30 min. The presence of constant lines of 511 keV (annihilation of positrons produced in the atmosphere by cosmic rays) and 1460 keV (potassium-40) in the spectra allows continuous monitoring of the spectrometer energy scale. The detector efficiency for different energies was calculated using the RUSCOSMICS software package [1]. The spectrometers have a lead shield with a wall thickness of 20-50 mm to exclude radiation from surrounding objects and soil. The field of view of the detectors is a cone of ~90 degrees directed to the zenith. The devices are placed in thermostabilized boxes in buildings with light roofs. The similarity of the spectrometers and the conditions of their placement allows to compare the parameters of the obtained spectra, and to identify common characteristics for such geographically distant points.

The purpose of these observations is to compare the gamma radiation spectra during precipitation, when the radiation flux increases by tens of percent compared to the background level in clear weather the day before. It should be noted that Apatity is located beyond the Arctic Circle, Tatsinskaya is in a steppe region with hot and dry summers, and Barentsburg is in the permafrost zone and on the seashore, thousands of kilometers from populated or industrial areas. At the same time, at all observation points throughout the year, during precipitation, increases in gamma radiation coming from the atmosphere are observed; more details about this phenomenon and previously conducted measurements can be found in [2-3]. As a result, it was understood that an increase in the gamma radiation flux from the atmosphere during precipitation is not associated with contamination of the latter with radionuclides of natural or anthropogenic origin, but is caused by some kind of interaction of secondary cosmic rays with meteorological processes in the lower atmosphere.

Figure 1 shows typical gamma radiation spectra in Tatsinskaya and Barentsburg. In Barentsburg, increases in gamma radiation during precipitation occur less frequently than in other observation points, the amplitude of such events is lower. For Apatity the typical amplitude is 25-40%, in summer periods it reaches 80%, while for Barentsburg 25% is a rare event. Figure 1A shows spectra of an increase with an amplitude of 14%, which is the largest increase in Barentsburg since we started the spectrum registration. The amplitude of the increase in Tatsinskaya, the spectra of which are shown in Figure 1B, was 49%.

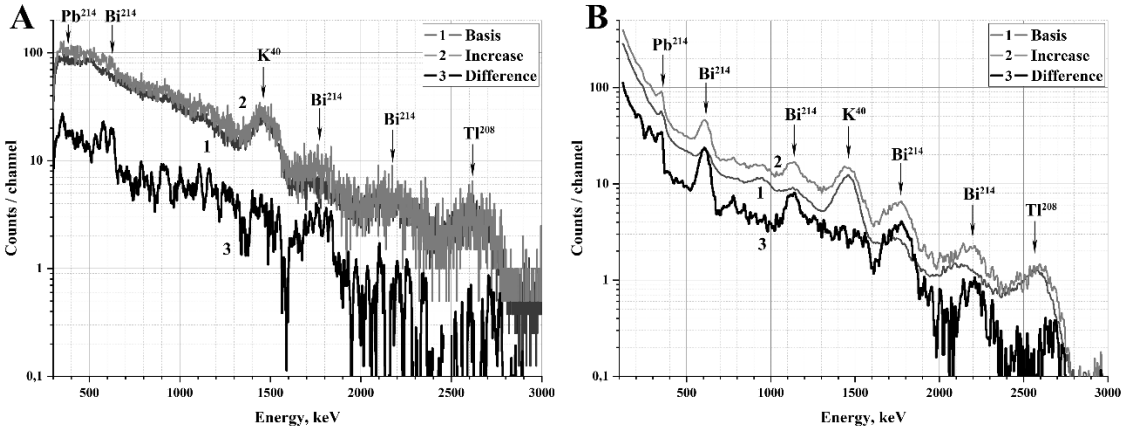


FIGURE 1. Examples of gamma radiation spectra in Barentsburg on 12.09.2024 (A) and Tatsinskaya on 26.06.2023 (B).

A single spectrum has large fluctuations, especially in the high-energy part, where the flux decreases. A special technique has been developed to obtain spectra of acceptable accuracy. Viewing single spectra shows that there is no significant difference in successive spectra. Assuming that in clear weather before the increase with a constant radiation flux its spectrum does not change, we can take the average spectrum for a significant period of 5-10 hours. Similarly, in the region of the maximum increase, we assume that the spectra in this period also differ little from each other, therefore, we can obtain the average spectrum during the maximum, usually 2-3 hours. As a result, we have an average base spectrum corresponding to the period before the increase in clear weather, when the radiation flux was constant, and an average spectrum at the maximum of the increase, called the increase spectrum for short. Subtracting the base spectrum from the increase spectrum (and this is quite acceptable, since the spectra are differential), we obtain the differential spectrum of the additional radiation (DSAR), which was added to the background and caused the increase effect. The result of processing any event is a set of these three spectra. The spectra shown in Figure 1 were obtained in this way.

In spectra 1 and 2 in Tatsinskaya, the lines of lead-214, bismuth-214, potassium-40 and thallium-208 are clearly seen. The potassium-40 radionuclide is present in the wood and the photomultiplier bulb; this line is present in all spectra. Of the uranium family radionuclides, the most noticeable and constant was the 609 keV line from bismuth-214 [4]. These two lines (potassium-40 and bismuth-214) are used to control the energy scale of the spectrometer. The potassium-40 and thallium-208 lines disappear on the DSAR (line 3 in Figure 1B), which means that the intensity of these lines does not change during precipitation, therefore, their sources are outside the atmosphere and precipitation. The DSAR clearly shows several bismuth-214 lines and one lead-214 line brought with precipitation. However, the number and intensity of the lines are insufficient to form the DSAR as a whole. There are large sections of the continuum spectrum that correspond to the spectrum of bremsstrahlung of light charged particles.

The emission spectrum during the increase in Barentsburg is similar to the corresponding spectrum in Tatsinskaya, although some of the radionuclide lines are only guessed. This is due to the significantly lower amplitude of the increase event in Barentsburg (14 versus 49 percent). The main fact is the same:

the DSAR (line 3 in Figure 1A) during the increase has a continuous character and is not associated with any radionuclides.

Figure 2 shows the spectra in Apatity, obtained as an average for ten large increases in the 2023 with an amplitude > 30%. Analyzing the spectra at all three stations, we can confidently draw the following important conclusions.

1. At all three points of spectrum measurement for all increase events, the upper limit of the DSAR is constant and is about 2.5 MeV. In Apatity, this threshold is determined by a hundred registered increases, including two increases with amplitude > 60%, in Tatsinskaya – by ten increases, in Barentsburg – by three increases with an amplitude < 15%.

2. The spectra contain lines of natural radionuclides, however, their fraction both in the increase spectrum and especially in the DSAR is small. The shape of the spectra at all stations is similar, the slope of the spectra at energies > 500 keV corresponds to bremsstrahlung.

3. Comparison of the DSAR at three stations shows that the increase in the amplitude is provided by a proportional increase in the flux at all energies up to 2.5 MeV with the preservation of the general shape of the spectrum. In other words, it is possible to normalize the DSAR to the amplitude of the increase, and in this case the DSAR at all three stations will be very close. For now, this is a qualitative conclusion, since there is little data for Barentsburg, but it will be confirmed with the accumulation of data.

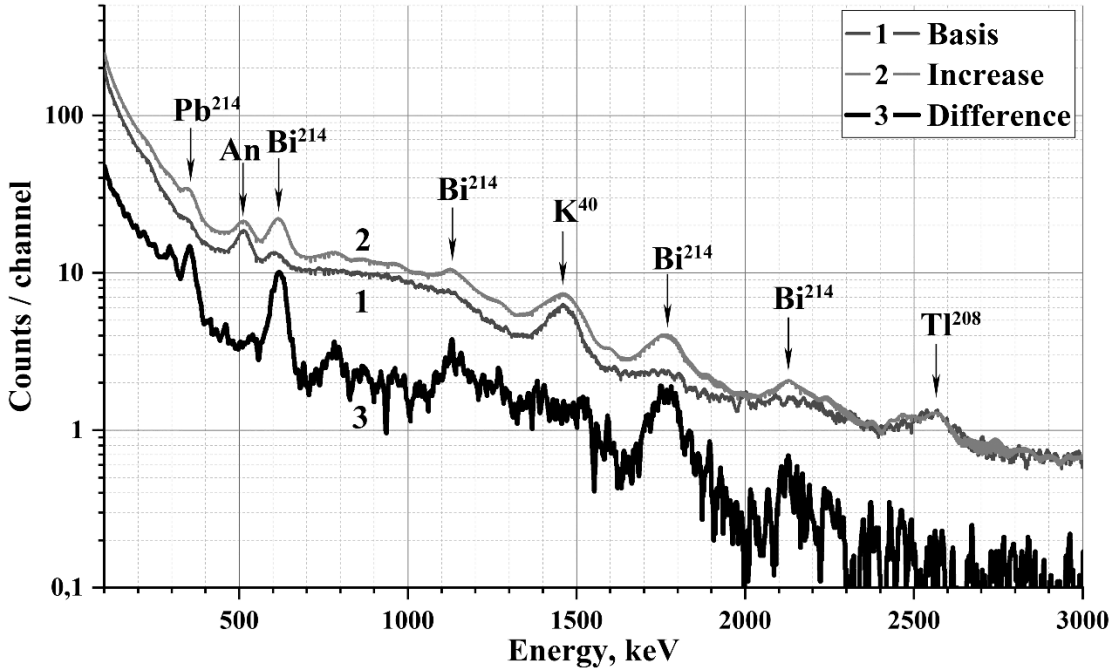


FIGURE 2. Average spectra for ten major increases in Apatity in the 2023 year.

The results of spectra measurements during precipitation in Korea are presented in [5]. A spectrometer of similar design was used. The measured spectra are similar to those presented here, except for the DSAR spectrum, which the authors do not calculate. The authors have the task of determining the degree of contamination of precipitation with radionuclides. However, from the presented results and spectra, it is easy to determine the upper energy of the flux that caused the increase: it is also equal to ~2.5 MeV. And the same radionuclide lines are present in the spectra.

Measurements of differential spectra of gamma radiation coming from the atmosphere at three different points (Spitsbergen, Apatity, Tatsinskaya) showed the following: increases of the radiation flux

during precipitation are not due to separate radionuclide spectral lines only. The additional gamma radiation flux has a continuous spectrum with rare lines of natural radionuclides. The upper energy limit of this flux is 2.5 MeV at all three observation points. The shape of the spectrum does not depend on either the amplitude of the increase or the observation point.

1. Germanenko A.V., Maurchev E.A., Balabin Yu.V. Calculation of registration efficiency functions of NaI(Tl) scintillation detectors and comparison of model operation with real experiment data. // *Trudy Kol'skogo nauchnogo tsentra RAN [Proceedings of the Kola Scientific Center of the Russian Academy of Sciences]*. 2019. V.10. No. 8-5. P. 82–87. (In Russian). DOI: 10.25702/KSC.2307-5252.2019.10.8.82-87.
2. Balabin V.V., Germanenko A.V., Gvozdevsky B.B., Vashenyuk E.V. Variations in the natural X-ray background in the polar atmosphere // *Geomagnetism and Aeronomy*. 2014. V.54. No. 3. P. 347–356. DOI: 10.1134/S0016793214020029.
3. Germanenko A.V., Balabin Yu.V., Vashenyuk E.V., Gvozdevsky B.B., Schur L.I. High-energy photons connected to atmospheric precipitations // *Astrophys. Space Sci. Trans.* 2011. V.7. P. 471–475. DOI:10.5194/astra-7-471-2011.
4. Grigoryev I.S., Melikhov E.Z. *Fizicheskie velichiny. Spravochnik [Physical Quantities. Reference book]*. Energoatomizdat Publ., Moscow, 1991, 1231 p. (In Russian).
5. Lee M.S. Gamma-ray exposure rate monitoring by energy spectra of NaI(Tl) scintillation detectors //*Journal of Radiation Protection and Research*. 2017. V.42, iss. 3. P. 158–165. DOI: 10.14407/jrpr.2017.42.3.158.

LONGITUDINAL FEATURES OF GPS SIGNAL SCINTILLATIONS DEVELOPMENT DURING THE NOVEMBER 2021 STORM

Ivan I. Efishov, Irk I. Shagimuratov

West Department of Pushkov Institute of Terrestrial Magnetism, Ionosphere and Radio Wave Propagation RAS, Kaliningrad, Russia

Introduction. Ionospheric irregularities of different scales at high latitudes cause fluctuations/scintillations of navigation signals [1]. At high latitudes phase fluctuations/scintillations are dominant. Fluctuations can complicate phase ambiguity resolution, increase the number of undetected and uncorrected cycle slips and losses of signal lock in GNSS as a consequence it led to increase of navigation errors [2-4]. The irregularities are structured by latitude in accordance with the division of the high-latitude ionosphere into the subauroral, auroral, cusp, and polar cap. In the polar region (78°-82° magnetic latitude) intense fluctuations are associated with polar patches, in the auroral oval and cusp particle precipitation [5, 6]. In the auroral region phase fluctuations are usually observed during periods of auroral disturbances near local magnetic midnight and are closely related to the dynamics of the auroral oval [7]. High-frequency (fast) fluctuations, called scintillations, are caused by signal diffraction on small-scale irregularities, low-frequency (slow) fluctuations are caused by signal refraction on large-scale irregularities with sizes greater than 300 m [1]. The low-frequency phase fluctuations can be directly estimated by the TEC changes along the ray path for a dual-frequency receiver.

Currently, there are a large number of stations in the world providing regular standard GPS observations. Standard measurements allow obtaining TEC data with a 30 sec interval. The most widely used indicator of fluctuation activity is the ROT (Rate of TEC change) parameter and the fluctuation intensity index ROTI. The index allows detecting the presence of ionospheric irregularities [8]. In this work an analysis of the features of phase fluctuations occurence in the auroral and polar ionosphere at the longitudes of Europe and Alaska during the geomagnetic storm of November 4, 2021 is presented.

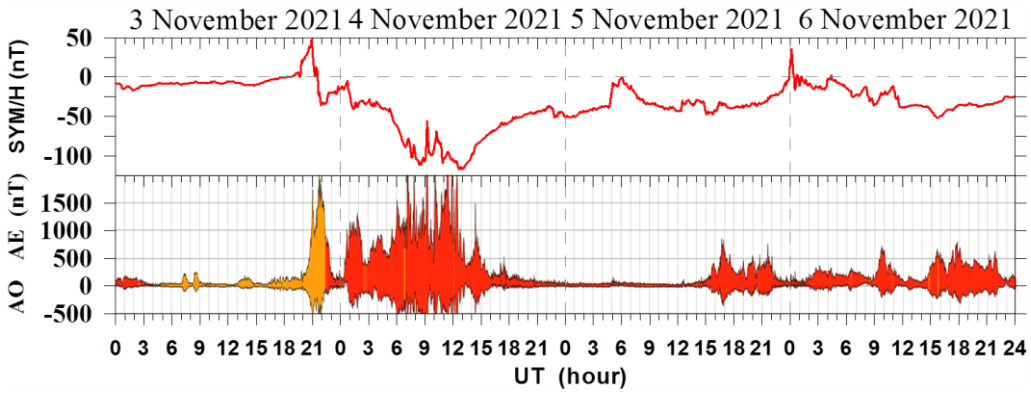


FIGURE 1. Geomagnetic conditions November 3-6, 2021.

Latitudinal development of TEC fluctuations. Fig. 2 shows the variations ROT for all satellites observed over station and the intensity of the fluctuations (ROTI). The intensity fluctuations (circles) is presented in corrected geomagnetic latitude and local magnetic time coordinates. Fluctuations are shown at polar, auroral and subauroral stations located at the longitudes of Europe and Alaska. In general, the behavior of the fluctuations at different longitudes is similar and corresponds to their geomagnetic location. The difference is occurred at the polar stations NYA1 and SG27. Station NYA1 (75°N MLAT), apparently, for the given geophysical conditions, was in the cusp region, while SG27 (70°N MLAT) was closer to the polar boundary of the auroral oval. Fluctuations at polar latitudes reflect the appearance of daytime precipitation [6]. The occurrence of fluctuations at SG27 is similar to the behavior of fluctuations at the AB27 auroral station. The intensity of fluctuations decreases with decreasing latitude. The equatorial boundary of the appearance of fluctuations falls at 57°-59° magnetic latitude.

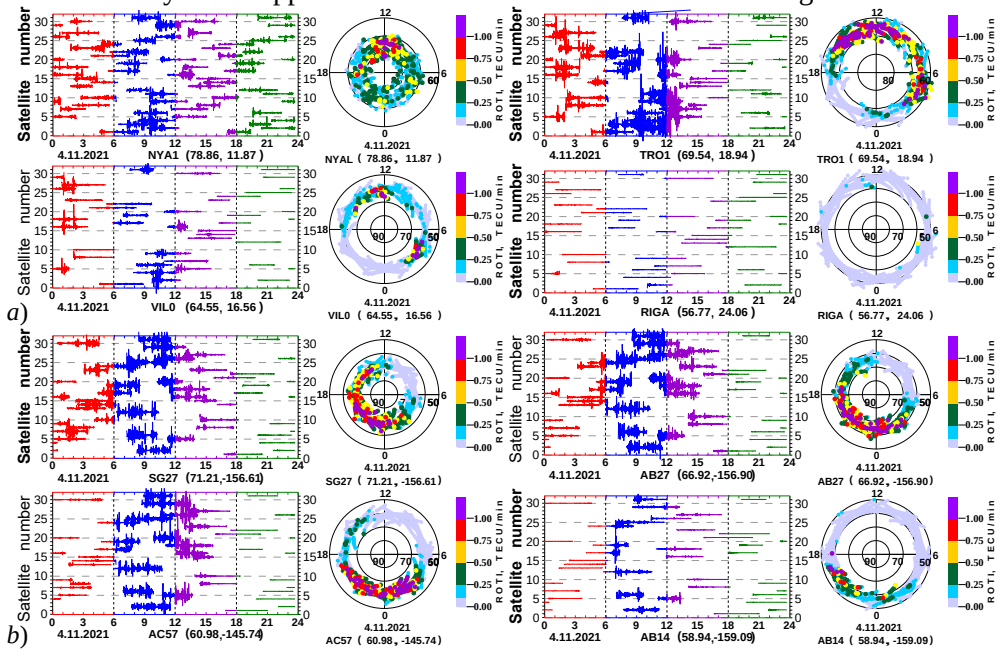


FIGURE 2. Latitudinal development of TEC fluctuations over Europe and Alaska.

TEC fluctuations and auroral oval dynamics. Analysis of the latitudinal occurrence of fluctuations showed that fluctuations are most clearly observed at stations located at auroral latitudes. Fig. 3 shows ROT variations at all satellite passes by VARS and AB27 stations and the fluctuation intensity, as well as their comparison with auroral ovals. The stations are located at the same magnetic

latitudes (MLAT ~66°N) at the longitudes of Europe and Alaska. The figure below shows the structure of the auroral oval during a storm for different UT (Ovation model). The intensity and structure of the oval are presented in magnetic latitude-local magnetic time (MLAT-MLT) coordinates.

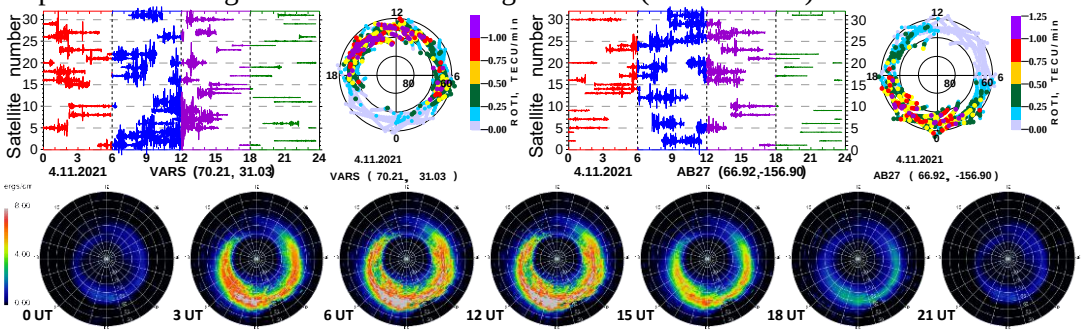


FIGURE 3. Comparison ROT and ROTI (circles) on VARS and AB27 stations with auroral oval.

Fluctuations are observed at both stations during the daytime. There is a good correspondence between the fluctuation development and the auroral activity (AE index, Fig. 1). At different sectors, the fluctuations are registered approximately at the same universal time (UT effect). The maximum intensity of fluctuations corresponds to the greatest intensity of the oval, precipitation intensification. In general, the intensity of fluctuations at the AB27 station is slightly lower than at VARS. At the longitudes of Europe the fluctuations intensification occurred around magnetic noon, a time when one at the longitudes of Alaska du around midnight. This reflects the peculiarity of the development of the geomagnetic storm under consideration.

Fig. 4 illustrate the development of fluctuations (in magnetic coordinates) over TIXI station. The intensification of fluctuations occurs after 18 MLT, intermediate position between TRO1 and AB27. An increase fluctuations at AB27 during nighttime and evening correlates with dynamics of auroral oval. This confirms the contribution of particle precipitation in E layer to increase the TEC fluctuation. In contrast it at VARS the strong intensive fluctuations are registered in day time (MLT). Such development of fluctuations was observed by Belakhovsky at Apatity station (63.86° MLAT) during this storm [9]. Daytime positive effect in TEC variations is registered during November 4, 2021 (Fig. 4). It is known GPS TEC is attributed to F region of the ionosphere. We believe that strong fluctuations observed in daytime over VARS are associated with positive effect of TEC in range 06-14 UT (09-17 MLT).

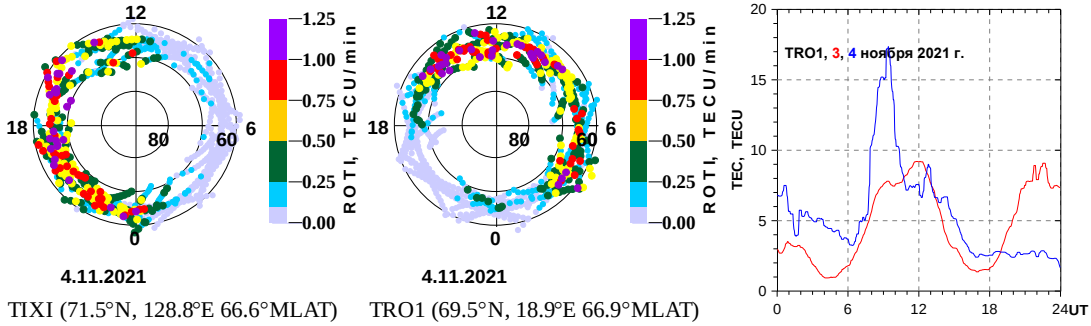


FIGURE 4. ROTI for TIXI and TRO1 stations and TEC variations during 3 and 4 November over TRO1.

Summary. Observations from the European (60°-76° MLAT), American (Alaska, 60°-70° MLAT) GPS network were used to analyze the spatiotemporal effects of TEC fluctuations during the storm on November 4, 2021. It was found that the development of fluctuations at different longitudes is very similar and develops in accordance with geomagnetic activity. The temporal development of fluctuations at the longitudes of Europe and America occurs almost simultaneously in range 06-13 UT

during the greatest auroral disturbance. The equatorial boundary of the appearance of fluctuations at different longitudes reached latitudes of 57°-59° MLAT.

1. Kintner P.M., Ledvina B.M., de Paula E.R. GPS and ionospheric scintillations // *Space Weather*. 2007. V. 5. No 9. DOI: 10.1029/2006SW000260.
2. Fabbro V., Jacobsen K.S., Andalsvik Y.L. GNSS positioning error forecasting in the Arctic: ROTI and Precise Point Positioning error forecasting from solar wind measurements // *J. Space Weather an Space Clim*. 2021. V. 11. No 43. DOI:10.1051/swsc/2021024.
3. Shagimuratov I.I., Filatov M.V., Efishov I. I. et al. Seasonal Features of the Phase Fluctuations of Navigation Signals and Positioning Errors in the Auroral and Polar Ionosphere// *Bull. Rus. Ac. Sci: Phys*. 2022. V. 86. No. 12. P. 1526–1531. DOI: 10.3103/S1062873822120231
4. Shagimuratiov I.I., Filatov M.V., Efishov I.I. et al. Fluctuations of Navigation Signals and Positioning Errors over Europe in March 2015 // *Bull. Rus. Ac. Sci: Phys*. 2022. V. 86. No. 3. P. 237-242. DOI: 10.3103/S1062873822030224.
5. Belakhovsky V.B., Jin Y., Miloch W.J. Influence of different types of ionospheric disturbances on GPS signals at polar latitudes // *Ann. Geophys*. 2021. V. 39. No 4. P. 687-700. DOI: 10.5194/angeo-39-687-2021.
6. Belakhovsky V.B., Jin Y. and Miloch W. Dayside Scintillations of GPS Signals According to the Observations on the Svalbard Archipelago // *Bull. Rus. Ac. Sci: Phys*. 2022. V. 86. No 3. P: 3-6. DOI: 10.3103/S1062873822030066.
7. Chernous, S.A., Shagimuratov, I.I., Ievenko, I.B. et al. Auroral Perturbations as an Indicator of Ionosphere Impact on Navigation Signals // *Russ. J. Phys. Chem. B*. 2018. V. 12. P. 562–567. DOI: 10.1134/S1990793118030065.
8. Zakharenkova I.E., Cherniak I.V., Shagimuratov I.I. et al. Features of high-latitude ionospheric irregularities development as revealed by ground-based GPS observations, satellite-borne GPS observations and satellite in situ measurements over the territory of Russia during the geomagnetic storm on March 17-18, 2015 // Geomag. and Aeronomy. 2018. V.58. No 1. P.70-82. DOI: 10.1134/S0016793217050176.
9. Belakhovsky V.B, Budnikov P.A., Kalishin A.S. et al. Influence of geomagnetic disturbances on scintillations of GLONASS and GPS signals as observed on the Kola peninsula // Solar-Terrestrial Physics. 2023. V. 9. No 3. P. 54-67. DOI: 10.12737/stp-93202307.

SIGNATURE OF A POLARIZATION JET IN TEC OBSERVATIONS: CASE STUDY

Irk I. Shagimuratov, Maksim V. Klimenko, Galina A. Yakimova and Ivan I. Efishov

West Department of Pushkov Institute of Terrestrial Magnetism, Ionosphere and Radio Wave Propagation of the Russian Academy of Sciences, Kaliningrad, Russia

Introduction. Polarizing Jet (PJ) or Subauroral ion drifts (SAID) is known as a narrow latitude region of rapid westward ion drift [1]. SAID and PJ are always observed equatorward of the auroral electron precipitation boundary and are closely associated with the midlatitude trough move to lower latitudes with increasing magnetic activity (Kp). With the phenomenon was associated formation of very deep density troughs in the F region [2]. At altitudes of the F region the latitudinal extent of PJ is 1°-2°, and the drift velocity is exceeded more 1 km/s. The statistics on solar cycle, seasonal and diurnal

variations according to DMSP (Defense Meteorological Satellite Program) satellite data for the period 1987-2012 is presented by He et al., 2014 [3]. Statistical results showed that the PJ is more often located at latitude of about 60° MLAT, in the range 56-65° MLAT over a large magnetic local time (MLT) range, from at least 16:00 to 24:00 MLT. The width of PJ increases to the south and have a greater extent at the maximum of solar activity. The seasonal variation of SAID latitude has two valleys in spring and fall, and SAID width has a valley distribution with a minimum in summer. SAIDs exhibit a clear MLT variation in latitude The PJ phenomena have been observed and investigated using both satellite data and ground-based measurements [4-6]. Recent studies of PJ based on NorSat-1 satellite data have been conducted on fine spatial structure of PJ [7, 8]. In this study the occurrence of PJ and detailed spatial-temporal PJ structure in GPS TEC observations for two events are presented.

Event of 18 March 2018. The event of March 18, 2018 attributed our interest; firstly, it is known that PJ is more often registered at the equinox. In addition, this event was discussed in detail by Sinevich et al., 2024. In this work the appearance of PJ in different instruments was demonstrated [9]. It is also interesting that this magnetic storm was characterized as low in intensity. Recently, there has been renewed interest in this phenomenon, with most of the research focused on jet analysis in the Siberian region [6]. According to Sinevich [9] the jet appeared in the European region at latitude of about 53° MLAT at ~ 00 MLT A dense network of GPS stations, which makes it possible to identify the PJ signature in TEC observations.

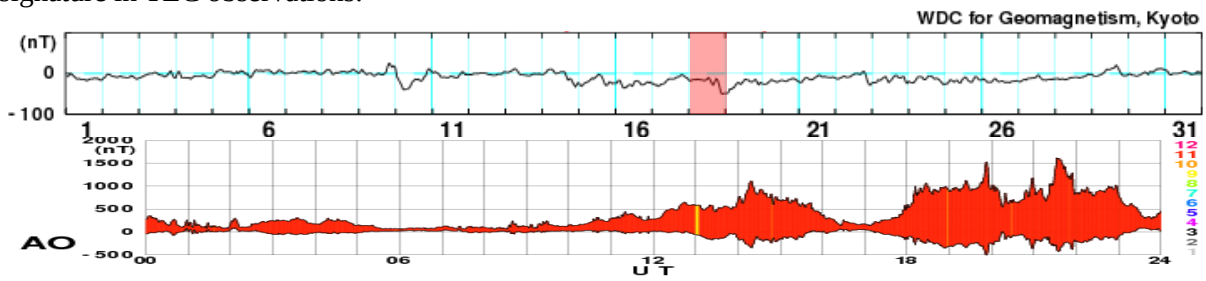


FIGURE 1. Dst index March 2018 and AE index during 18 March 2018.

The geomagnetic disturbance on 18 March 2018 is characterized as low, maximal Dst was 38 nT in evening time (21-22 UT) on 18 March. Auroral index AE on 18 March is reached 1000 nT (Fig. 1). Fig. 2 illustrates the latitude-longitude distribution of TEC over Europe (TEC maps) in evening time. TEC maps were formed using Madrigal data base for latitudes above 30°N. The TEC measurements in the Madrigal database are presented with a maximum spatial resolution of 1°×1° in latitude and longitude, with a time interval of 5 min.

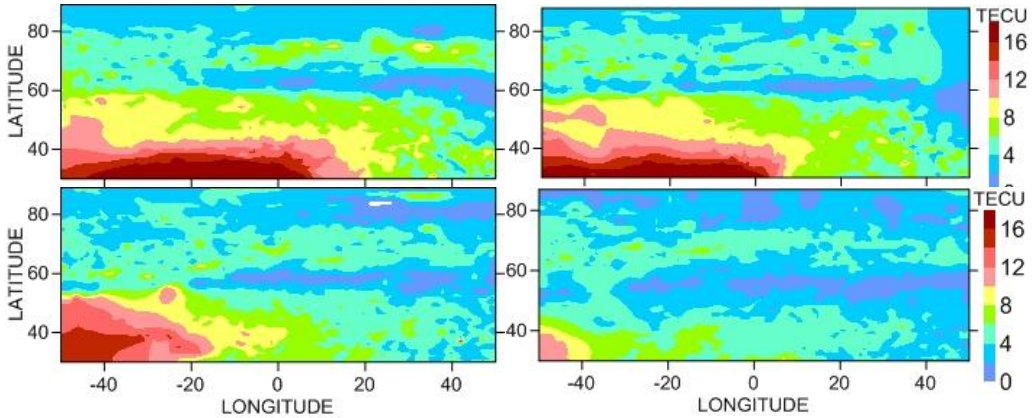


FIGURE 2. TEC maps over Europe at 18, 19, 20, 23 UT on 18 March 2018.

On the maps it can see the latitudinal narrow and longitudinally extended trough located low than 65-60° N. The spatial and temporal development of the trough is matched to descriptions of Jet occurrence which was revealed by NorSat-1 satellite measurements. Jet structure was observed at ~22:25 UT (00 MLT) – 54° MLAT [9]. Taking into account of this point we associated the narrow trough as JET signature in TEC. The longitudinally extent of trough is 40° E -20° W.

Fig. 3 presents the latitudinal profiles related with trough in TEC at longitudes around 15° E. The trough dynamics is clearly recognized at pictures. The values of TEC in trough were less than 1.5 TECU. The trough shifted to equatorward with time. At 18 UT (MLT = UT + 2 hour) trough locate near 64° N, to 23 UT that locate near 55° N (MLAT ~51°N). According to Sinevich, the Jet occurred on 00 MLT at 53 MLAT. Statistical results show that SAIDs occur mostly at 60° MLAT and 22:30 MLT with majority between 56° and 65° and between 20:00 and 23:00 MLT, respectively, which is in consistent with previous statistical studies [He, 2014].

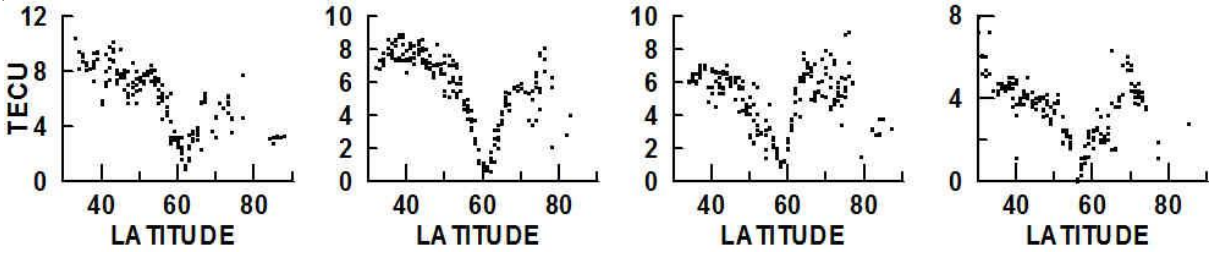


FIGURE 3. Latitudinal profiles TEC (geographic coordinates) during 18-23 UT (from left to right: 18, 19, 21, 23UT).

Ionospheric irregularities associated with Jet structures (GPS fluctuations).

Pi et al. [9] introduced into usage two GPS-based indices: ROT and ROTI. The ROT (rate of TEC change) is the time derivative of TEC and is considered as a measure of the phase fluctuation activity. ROTI (rate of TEC index) represents a standard deviation of the ROT over a selected time interval. The ROTI characterizes the severity of the GPS phase fluctuations and detects the presence of the ionospheric irregularities, as well as it measures the irregular structure of the TEC spatial gradient. ROTI index can be effectively used to detect the presence of the ionospheric irregularities and even indicate the intensity of these irregularities.

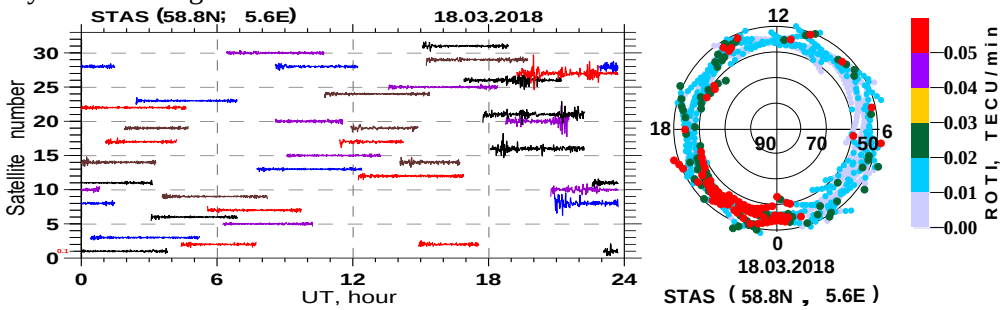


FIGURE 4. TEC fluctuations (ROT) and ROTI for GPS station STAS for 18 March 2018. Intensity TEC fluctuations (ROTI) index is presented in magnetic local time (MLT) and corrected magnetic latitude (MLAT).

Intensification of TEC fluctuations occur after 20 MLT at low than 60°MLAT inside Jet. Spatial-temporal evaluation of TEC irregularities demonstrated high correlation with dynamics of JET according to Sinevich et al., 2024 [9] results.

Event of 17 September 2021.

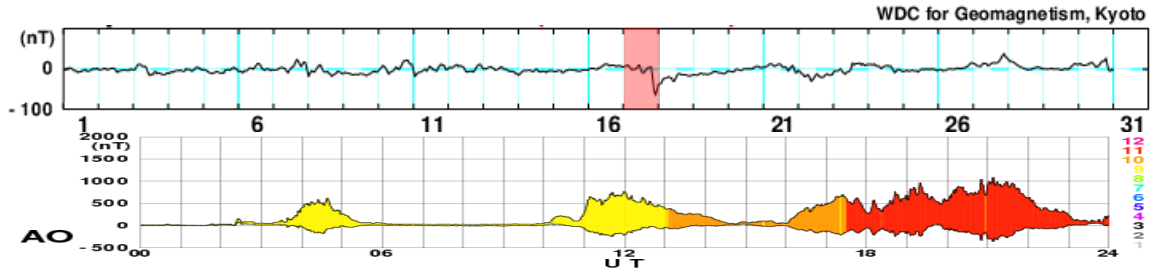


FIGURE 5. Dst index in September 2021 and AE index during 17 September 2021.

Geomagnetic conditions for this event is very similar to that March 2018. The disturbance is characterized also as low, maximal Dst was 64 nT in evening time (21-23 UT) 17 September. Index AE is reached 1000 nT during September 17 (Fig. 5).

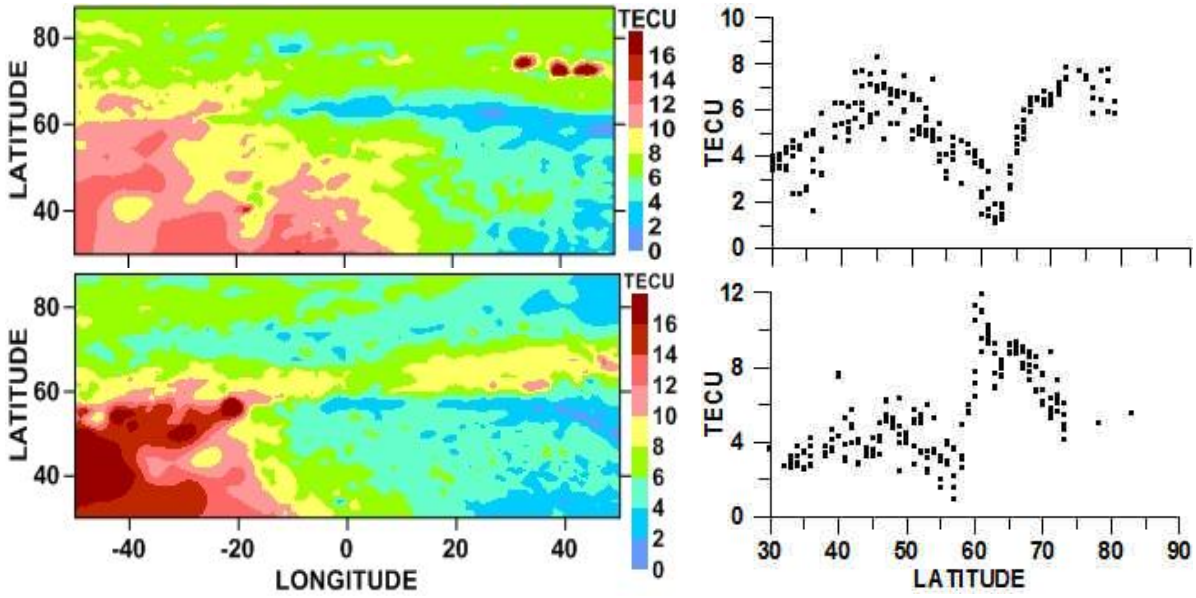


FIGURE 6. TEC maps and latitudinal profiles for 18, 21 UT during 17 September 2021 (19 and 21 UT).

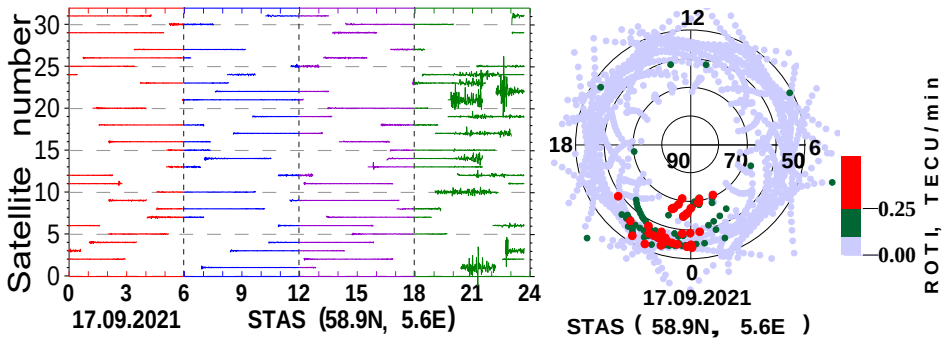


FIGURE 7. Occurrence of TEC fluctuations (ROT) and intensity its (ROTI) over GPS station STAS during 17 September 2021

Figs. 6 and 7 illustrated the structures of TEC, ROT and ROTI during 17 September 2021 that is similar to the same one for 18 March 2018 during PJ occurrence. More comprehensive analyses are needed for estimation of PJ signature in TEC maps, ROT and ROTI structures.

1. Galperin Y.I., Ponomarev V.N., Zosimova A.G. Plasma convection in the polar iono-sphere // *Annals of Geophysics*. 1974. V. 30. No 1. P. 1-7.
2. Spiro R.W., Heelis R.A., Hanson W.B. Rapid subauroral ion drifts observed by Atmosphere Ex-plorer C // *Geophys. Res. Letters*. 1979. V. 6. No 8. P. 657-660.
3. He F., Zhang X.-X., Chen B. Solar cycle, seasonal, and diurnal variations of subauroral ion drifts: statistical results // J. *Geophys. Res*. 2014. V. 11. No 6. P. 5076-5086.
4. Anderson P. C., Carpenter D. L., Tsuruda K. et al. Multisatellite observations of rapid subauroral ion drifts (SAID) // *J. Geophys. Res*. 2001. V. 106. No A12. P. 29585-29599.
5. Makarevich R.A., Bristow W.A. Fine structure of subauroral electric field and electron content // *J. Geophys. Res.: Space Physics*. 2014. V. 119. No 5. P. 3789–3802.
6. Stepanov A.E., Khalipov V.L., Golikov I. A., Bondar E.D. *Polyarizatsionnyi dzhet: uzkie i bystrye dreify subavroral'noi ionosfernoi plazmy* [Polarizing jet: narrow and fast drifts of subauroral ionospheric plasma], Yakutsk: Izdatelskii dom SVFU Publ., 2017, 176 p.
7. Sinevich A.A., Chernyshov A.A., Chugunin D.V. et al. Studying the small-scale structure of a polarization jet during the April 20, 2018 geomagnetic storm // *Solar-Terrestrial Physics*. 2021. V. 7. No 1. P. 17–26.
8. Sinevich A.A., Chernyshov A.A., Chugunin D.V. et al. Small-scale irregularities within polari-zation Jet/SAID during geomagnetic activity // *Geophys. Res. Let*. 2022. V. 49. No 8. e2021GL097107.
9. Sinevich A.A., Chernyshov A.A., Chugunin D.V. et al. Multi-instrument approach to study polarization jet/SAID and STEVE // *Journal of Geophysical Research: Space Physics*. 2024. V. 129. e2024JA033222. DOI:10.1029/2024JA033222.
10. Pi X., Mannucci A.J., Lindqwister U.J., Ho C.M. Monitoring of global ionospheric irregularities using the Worldwide GPS Network // *Geophys. Res. Lett*. 1997. V. 24. P. 2283–2286.

OCCURRENCE OF THE POLAR TONGUE OF IONIZATION IN THE TOTAL ELECTRON CONTENT MEASUREMENTS DURING 14 JANUARY 2022 MAGNETIC STORM

Irk I. Shagimuratov, Galina A. Yakimova, Nadezda Yu. Tepenitsyna and Ivan I. Efishov

Kaliningrad Branch of Pushkov Institute of Terrestrial Magnetism, Ionosphere and Radio Wave Propagation, Russian Academy of Sciences, Kaliningrad, Russia

The TOI – tongue of ionization is often observed in the polar ionosphere during geomagnetic storms. The TOI is characterized as an area of increased ionization, which is a result of convection moves from the daytime mid-latitude ionosphere through the cape to the night ionosphere [1-3]. The TOI source is associated with the formation of a mid-latitude increase in SED (Storm Enhanced Density) ionization during geomagnetic storms. SED is observed as an increase in electron density in the afternoon hours [4]. The favorable conditions for the formation of SED/TOI are the North American sector. The TOI structure was practically not observed at the time of 06-12 UT and the prevailing conditions for the occurrence of TOI were in winter [5]. At some time the SED/TOI structure was observed in equinox [6, 7]. The occurrence of TOI structures and their intensity depend on various geophysical factors: UT, season, longitude, and geomagnetic conditions. Most of the research related to TOI analysis focuses on the occurrence of these structures during strong geomagnetic disturbances. This paper presents an analysis of effects which were observed at high latitudes during a moderate storm on

January 14, 2022 (Fig. 1). Special attention is paid to the analysis of the spatial structure and dynamics of TOI.

Measurements of the total electronic content (TEC) of the Madrigal database were used to analyze the occurrence of the TOI (http://cedar.openmadrigal.org). Based on them, TEC maps of the northern hemisphere were formed for latitudes above 40°N. The TEC measurements in the Madrigal database are presented with a maximum spatial resolution of 1°×1° in latitude and longitude, with a time interval of 5 minutes [8]. The high spatial and temporal resolution of the maps made it possible to reveal in detail the structure of the TOI and its evolution.

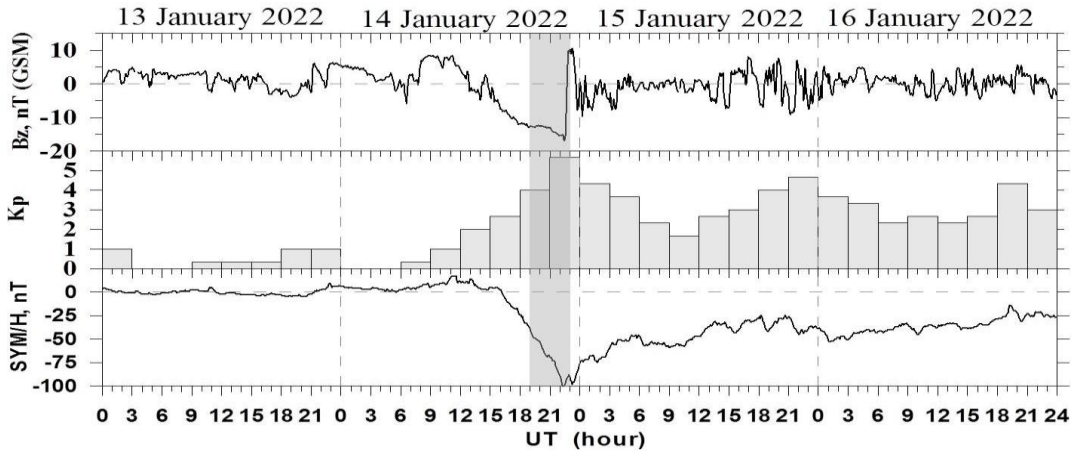


FIGURE 1. Variations of interplanetary magnetic field Bz, Kp and SYM-H indices during the 14-16 January 2022 geomagnetic storm. The shaded areas denote the interval of SED/TOIs.

Results. Fig. 2 shows the spatiotemporal distribution of TEC during storm. TEC maps are presented in geographic coordinates. The area in which the plume starts (the base) occurs at mid-latitudes and remains fixed at local noon as the Earth rotates [8].

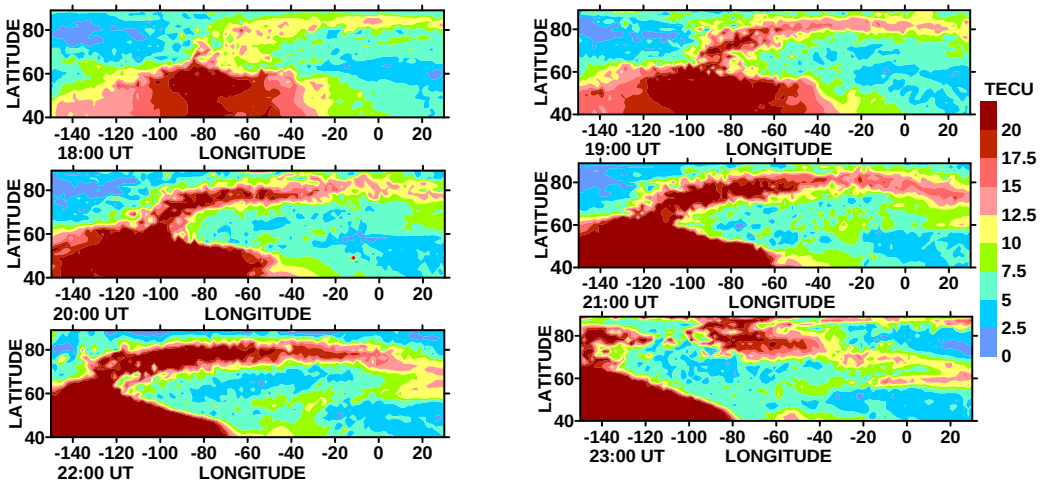


FIGURE 2. The formation and evolution of TOI during the storm (1 TECU = 10^{16} el/m2).

The figure shows the evolution of the SED structure and its further development in TOI. The TOI was formed on the basis of the SED structure at longitudes of around 80°W and latitudes of about 55-60°N. The start of the TOI was 18 UT, around local noon. As shown in [9], the SED/TOI structure was most often observed in the range of 15-21 UT [4]. After 19 UT the toque is clearly recognized at

longitudes of ~40°W, reaching latitudes of about 80°N. At longitudes of 80-60°W, high TEC values (more than 20 TECU) are observed at latitudes of 50-60°N in the SED region, which is the source for TOI formation.

It is interesting to note that high values of the electron content (~12 TECU) persist at longitudes less than 30°E (in the European sector). The TOI structure continues to be preserved, but with less intensity. It should also be noted that the maximum of the electronic content shifted to lower latitude toward night ionosphere until about 70°N.

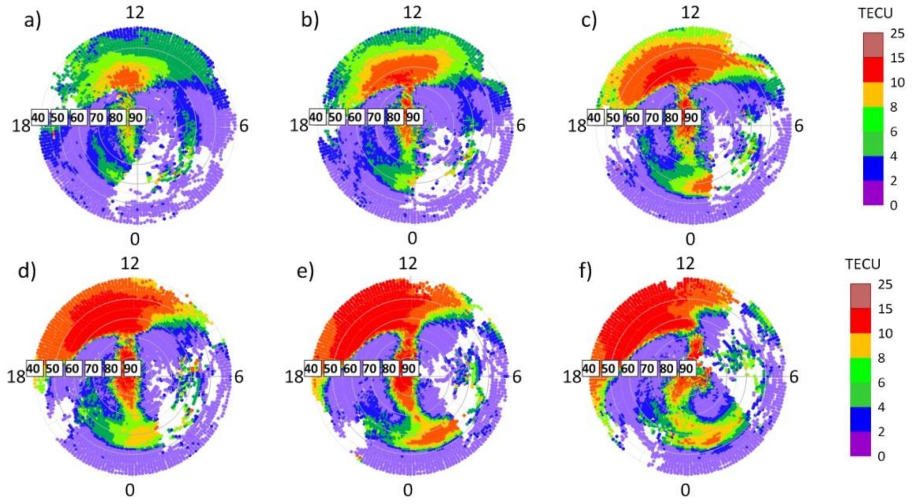


FIGURE 3. Differential TEC maps s between 14 and 13 January 2022 during 19–23 UT with one-hour interval. The coordinate system is magnetic local time (MLT) and corrected magnetic latitude (MLAT). Polar view map covers 00–24 MLT and 40°–90° MLAT. In each map, magnetic noon/midnight is at the top/bottom. a), b), c), d), e), f) correspond to 18, 19, 20, 21, 22, 23 UT.

Fig. 3 shows polar TEC maps in contrast to the above maps of the spatiotemporal distribution of the TEC in magnetic local time (MLT) and magnetic latitude (MLAT). Polar maps allow us to trace the motion of plasma through the polar cap and highlight the occurrence and evolution of SED/TOIs during a storm. The picture is visualized the dynamic evolution spatial structure of the TOI in greater detail.

The formation TOI structure started around 18 UT at north American sector, after noon (near 13 MLT). Fig. 3 demonstrates the signature of the TOI structures as well as the formation of a storm enhanced density (SED) and the evolution of a SED into a polar tongue of ionization (TOI). The dayside source of the TOI is the SED The base of TOI was SED structure which occurred near 65°MLAT. The extension of SED increased with time and exeeded more than 6 hours, TEC value amounted about 25-28 TECU.

The TOI structure is transported by antisunward convection across the polar cap to the nightside ionosphere in low latitude direction. At 23 UT the TOI reached 55° magnetic latitudes. It is interested that at low latitudes (60°MLAT) the TOI structure is extended night and morning sectors. After 23 UT TOI structure almost disappeared. Such pictures of spatialtemporal development of TOI were observed during a moderate magnetic storm on 14 October 2012 [9].

Fig. 4 presents the latitude structure of the TOI at different longitudes along trace in the form of latitude profiles. Very high values (25-30 TECU) are recorded at latitudes of about 80-85°N in the area of TOI occurrence. Note here that during November 7, 2022 TEC inside TOI reached 40 TECU [5]. It is interesting to note that high values of the electron content (~25 TECU) persist to longitudes less than 30°E. This confirms that the structure of the TOI continues to be preserved, but with less intensity. It should also be noted that the maximum of the electronic content shifted to lower latitudes. This indicates

that plasma convection proceeded to latitudes of about 70°N. The figure shows that significant TEC gradients are observed in vicinity of the TOI. Note that the gradients show a wide variation: the maximum values reached 10-20 TECU/degree. Such gradients are typical on the polar wall of the SED structure [11]. Low TEC values are observed at latitudes of 65-75°N. The gradients in this region are an order of magnitude smaller than at latitudes of 80°N in the TOI region. In the region of large gradients, irregularities of various scales are generated [10]. The significant irregularities were detected at front of the ionization tongue [11]. The irregularities associated with TOI were revealed during 7 November 2022 storm on the base of GPS observations [12].

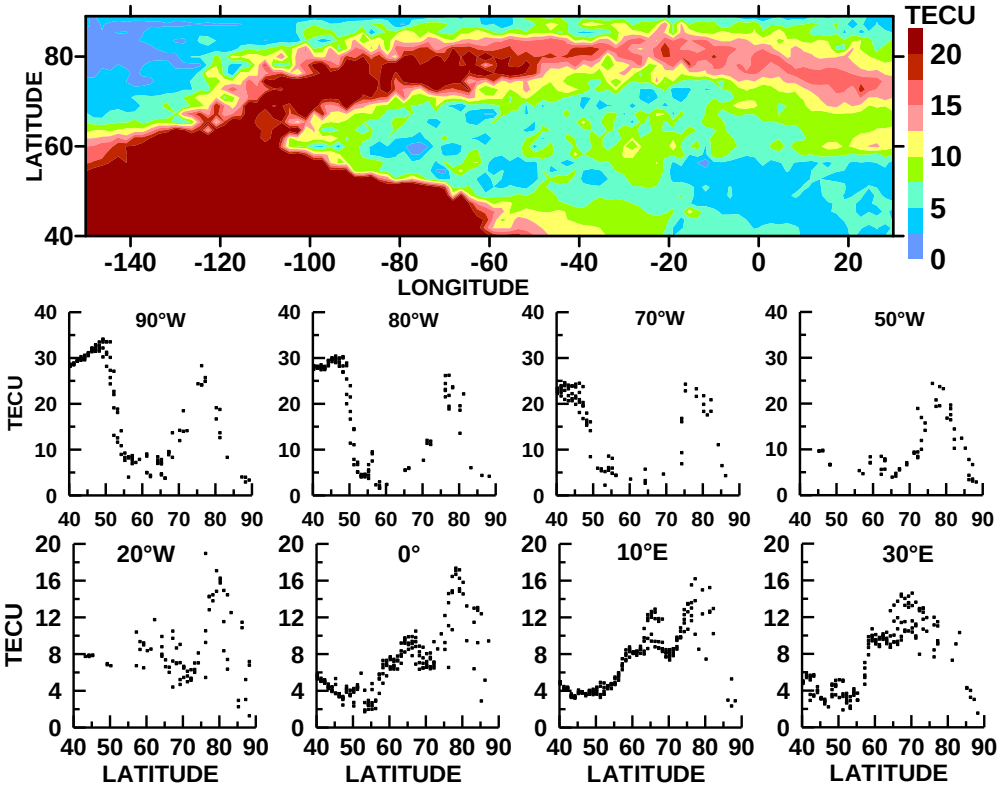


FIGURE 4. Latitudinal profiles of TEC at different longitudes correspond to TOI trace.

Summary. During the 14 January 2022 geomagnetic storm a very appreciable increase in the TEC associated with the ionization language (TOI) was observed in the afternoon in the polar cap region. The TEC inside the TOI is 2–2.5 times higher than the background.

It is shown that the formation of the TOI occurs as an evolution of the SED/Plume structure during plasma convection from the middle latitudes through the cape to the night ionosphere. The base of the TOI is SED locate at longitudes of about 60°W and at latitudes of about ~60°N. The TOI was pronounced at latitudes of ~85°N and extended to longitudes of more than 20 °E.

1. Foster J.C. Plasma Transport at Middle and High Latitudes // *J. Geophys. Res.* 1993. V. 98. No. A2. P. 1675. DOI: 10.1029/92JA02032.
2. Foster J.C., Rideout W. Midlatitude TEC enhancements during the October 2003 superstorm // *J. Geophys. Res. Lett.* 2005. V. 32. No. 12. Art. No. L12S04. DOI: 10.1029/2004GL021719.
3. Heelis R.A., Sojka J.J., David M. and Schunk R. W. Storm time density enhancements in the middle-latitude dayside ionosphere // *J. Geophys. Res.* 2009. V. 114, DOI:10.1029/2008JA013690.

4. David M., Sojka J.J., Schunk R.W. and. Coster A.J. Polar cap patches and the tongue of ionization: A survey of GPS TEC maps from 2009 to 2015 // *Geophys. Res. Lett.* 2016. V. 43. P. 2422–2428 doi:10.1002/2016GL068136.
5. Shagimuratov I.I., Klimenko M.V., Efishov I.I. et al. Features of the November 7, 2022 Geomagnetic Storm Development in the Ionospheric Total Electron Content Observations // *Bull. Russ. Acad. Sci. Phys*. 2024. V. 88. No. 3. P. 310–317. DOI: 10.1134/S1062873823705457.
6. Klimenko M.V., Zakharenkova I.E., Klimenko V.V. et al. Simulation and observations of the polar tongue of ionization at different heights during the 2015 St. Patrick's Day storm // *Space Weather*. 2019. V. 17. No. 7. P. 1073. DOI: 10.1029/2018SW002143.
7. Zhang K., Wang H., Liu J. et al. Dynamics of the tongue of ionizations during the geomagnetic storm on September 7, 2015 // *J.Geophys. Res.: Space Physics.* 2021. V. 126. e2020JA029038, DOI:10.1029/2020JA029038.
8. Coster A.J., Colerico M.J., Foster J.C. et al. Longitude sector comparisons of storm enhanced density // *Geophys. Res. Lett.* 2007. V. 34. No. 18. Art. No. L18105. DOI:2007GL030682.
9. Liu J., Nakamura T., Liu L. et al. Formation of polar ionospheric tongue of ionization during minor geomagnetic disturbed conditions // *J. Geophys. Res.* 2015. V. 120. No. 8. P. 6860. DOI: 10.1002/2015JA021393.
10. Vo H.B., Foster J.C. A quantitative study of ionospheric density gradients at midlatitudes *// J. Geophys. Res.* 2001. V. 106. No A10. P.555–21563. DOI:10.1029/2000JA000397.
11. van der Meeren C., Oksavik C.K., Lorentzen D. et al. GPS scintillation and irregularities at the front of an ionization tongue in the nightside polar ionosphere // *J. Geophys.Res.: Space Physic*. 2014. V. 119. P. 8624–8636. DOI:10.1002/2014JA020114.
12. Shagimuratov I.I , Efishov I.I., Yakimova G.A. et al. Occurence of the polar tongue of ionization and ionospheric irregularities in the total electron content meaurements during November 2022 magnetic storm // *Bull. Russ. Acad. Sci. Phys*. (In print).

MULTI-INSTRUMENTAL STUDY OF NIGHT MID-LATITUDE TRAVELING DISTURBANCES IN THE EARTH'S ATMOSPHERE

Alexey V. Oinats[1], Yuliya A. Kurdyaeva[2], Maxim V. Tolstikov[1], Tatiana E. Syrenova[1] and Maxim F. Artamonov[1]

[1]Institute of Solar-Terrestrial Physics, Siberian Branch of the Russian Academy of Sciences, Irkutsk, Russia
[2]Kaliningrad Branch of Pushkov Institute of Terrestrial Magnetism, Ionosphere and Radio Wave Propagation, Russian Academy of Sciences, Kaliningrad, Russia

The propagation of internal gravity waves (IGWs) affects the dynamic processes in the ionosphere, which can lead to the traveling ionospheric disturbances (TIDs) occurrence. However, various ionospheric plasma instabilities can also be a source of TIDs, which complicates the IGWs analysis from ionospheric data. Multi-instrumental approach for the analysis and comparison of disturbances in the neutral atmosphere and ionosphere in order to determine TIDs origin will allow their physical nature to be better studied. One of the ways to determine TIDs origin is to check the measured parameters for correspondence with the dispersion relations, which relates the wave vector and frequency of the TIDs to the known parameters of the propagation medium. This method requires measurements of the full

three-dimensional wave vector of the TIDs and, consequently, measurements of the electron density height profiles at at least three spatially spaced points [1].

However, a qualitative TIDs study requires multi-instrumental observation of the neutral atmosphere and ionosphere parameters. The Large-Scale Research Facilities (LSRF) “Optical Instruments” is located on the Geophysical Observatory of the Siberian Branch of the Russian Academy of Sciences in the Tory village (52° N, 103° E) Tunkinsky district of the Republic of Buryatia. This equipment allows monitoring the structure and dynamics of the upper and middle atmosphere using optical methods, including Fabry-Perot interferometers (FPI) and all-sky imagers (ASI) [2]. Continuous monitoring is organized on the basis of the multi-position chirp ionosonde [3] utilising vertical and quasi-vertical sounding of the ionosphere.

In this paper, a multi-instrumental approach is proposed for the study of TIDs, including the use of FPI, ASI and a multi-position chirp ionosonde. For the analysis, we use the observational data obtained on January 2, 2022 from 10:00-19:00 UT. The time interval corresponds to the local night. The night is characterized as magnetically quiet (Kp=2+, Dst=-10 nT). The optical data are complete, free from the clouds and the storm and sub-storm phenomena effects.

A multi-position chirp ionosonde is a spaced network of transmitters (Usolye and Tory) and receivers (Tory and Patrony) located at the vertices of a triangle with sides of 105-120 km. Quasi-vertical paths between vertices have reflection points in the center of the triangle sides. The reflection points are spaced 50-60 km apart from each other, forming a triangle. Sounding is conducted in the range of 1-12 MHz with a cadence of 15 seconds simultaneously on three quasi-vertical sounding paths and one vertical sounding path providing four ionograms. Further processing of the ionosonde data consists of several stages. First, echoes with significant amplitudes are selected on the ionograms, corresponding to regular HF reflection traces from the F2 ionospheric layer. Time series of virtual heights are formed for each sounding frequency. In order to determine TID’s parameters, cross-correlation is calculated allowing to estimate the delays between variations in virtual heights on different paths and at different true heights.

The true reflection heights are calculated using simulated virtual height traces for electron density profiles obtained from IRI-2020 model adapted to critical frequency and height of maximum of F2 ionospheric layer. At the last stage, the disturbance model in the form of a flat spatial wave is adjusted to the delays obtained by the least squares method. As a result of the processing, the full wave vector of the disturbance, its period and relative amplitude are determined.The FPI KEO Scientific "Arinae" is a type of high-resolution spectrometer adapted for atmospheric observations.

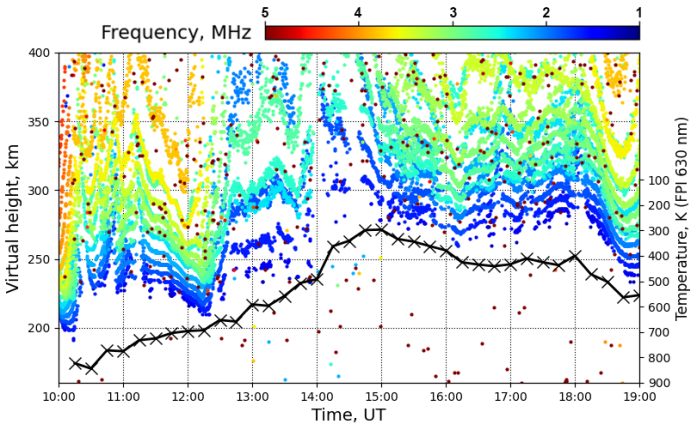


FIGURE 1. The effective height of the radio waves reflection from the F2 layer of the ionosphere during vertical LFM sounding in the Tory. The black line is the neutral atmosphere temperature according to FPI data.

The instrument allows us to measure linear spectra properties of atmosphere's airglow. There are three parameters such as intensity, Doppler shift, and spectral line broadening that can be obtained by interferogram processing. It is possible to calculate winds and temperatures of the atomic oxygen [OI] (neutral) with 630 nm emission line and expected maximum intensity height at ~250 km., During the

time period under study temperatures, meridional and zonal wind velocities were averaged within fifteen-minute intervals to be linked to an uniform time grid.

The temperature change is shown by a black line with crosses in Fig. 1. This correlation indicates the relationship between the neutral and charged components of the atmosphere, on the one hand. And the effect of the high-altitude profile of the electron concentration on measurements of the emission intensity by ASI and FPI, on the other hand.

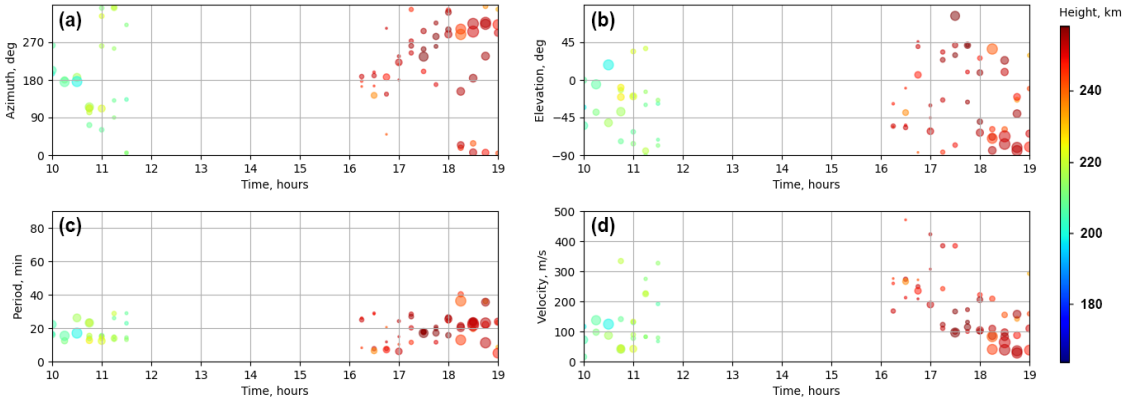


FIGURE 2. The TIDs parameters according to the LFM ionosonde are: (a) azimuth, (b) angle of inclination, (c) period and (d) phase velocity. The size of the circles corresponds to the disturbance amplitude. The color corresponds to the true height where the TIDs was registered, according to the color scale on the right.

Figure 2 shows that in the intervals 10-12, 12:30-13:30 and 16-18 UT, variations with periods from ~5 to 45 minutes are clearly visible. The absolute value of the standard deviation of the variations in the effective reflection height is used as a measure of the amplitude. In the range of 10-12 UT, TIDs prevail with periods of 15-30 minutes, propagating southward and southeastward at speeds of 50-150 m/s at altitudes of 200-220 km. The front inclination angle varies from 20° to -45°. In the range of 16-17 UT, TIDs prevail with periods of 5-10 minutes, propagating southward at speeds of 200-300 m/s at altitudes of 230-240 km. The front inclination angle varies from 0° to -60°. In the range of 17-19 UT, TIDs with periods of 15-40 minutes propagate northward and northwestward at speeds of 20-200 m/s. According to the inclination angle of the front, two groups are distinguished: from 0° to 45° and from -60° to -90°. The altitude range varies from 240-260 km.

The ASI used for the analysis, which are part of the LSRF “Optical Instruments", have a field of view of 180°. The choice of the spectral range is provided by automatically replaceable interference filters. The following filters are installed on two ASI: 557.7 nm, 630.0 nm, 865.0 nm, 427.8 nm, 589.3 nm, 840.0 nm, 846.5 nm, 857.0 nm and a broadband filter of 715-930 nm. To determine the spatial and temporal parameters of the observed objects, the method of geographic reference of frames to the Earth's surface is used [4]. To determine the time periods of disturbances that may be associated with TIDs, an analysis of changes in the emission intensity in various areas of the images (630.0 nm line) was performed. For this, 4 quadrants of 50x50 pixels were selected. The center of each quadrant corresponds to: the location of the LFM ionosonde in Tory (tt), the middle of the Usolye-Tory (ut) track, the middle of the Usolye-Patrony (up) track, and the middle of the Tory-Patrony (tp) track. The median average was found for each of the quadrants. Since the data series is uneven due to unhindered sampling, the Lomb-Scargle algorithm was used to obtain periodograms.

We can identify some areas in Fig. 3, that have clearly similar periods in shape, but are observed in the quadrants at different points in time. Thus, in Fig. 3, some areas are marked for which it is possible to estimate the disturbance traveling velocity. The disturbance marked in Fig. 3 with the letter (a) is moving mainly in a northward direction at a speed of about 65 m/s and has a period of about 40 minutes.

Variations with a period of about 35 minutes, marked with the letter (b), move mainly in a southward direction at a speed of about 40 m/s. Variations (c) have a period of 20 minutes and move mainly in a northward direction at a speed of about 20 m/s. The results obtained do not contradict the TIDs parameters described above.

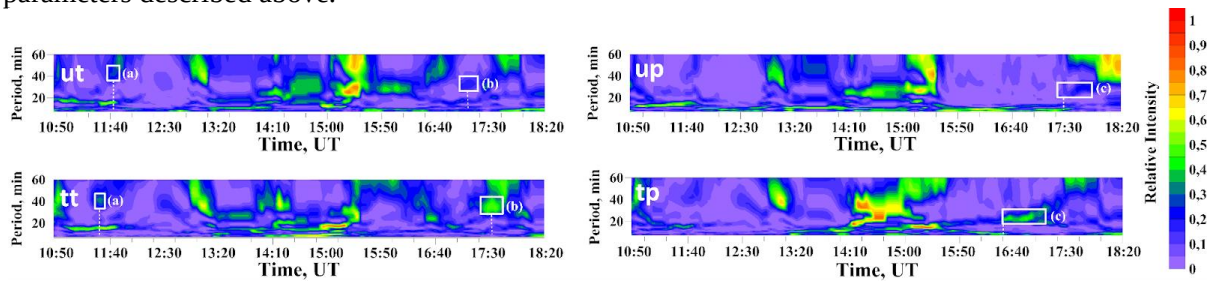


FIGURE 3. The Lomb-Scargle periodogram for variations in emission intensity in each of the studied squares of the ASI images.

The images from ASI should have foreshortening sensitivity. For example, from Fig. 2b it can be seen that a significant part of the TIDs has an inclination angle of the front close to -90°. Such disturbances obviously cannot have a noticeable effect on the horizontal distribution of the integral emission intensity. The crests of disturbances will be almost perpendicular to the rays of vision in a significant area of the ASI's field of view. On the contrary, disturbances with tilt angles close to 0° should appear noticeably better in the images.

Verification of the measured parameters for compliance with the dispersion relations during the time period under review diagnosed 76 TIDs observation events according to the LFM ionosonde data. About 54% (74%) of the disturbances lie under the curve of the dispersion relation, assuming that the Brent-Weiss frequency is 11.5 minutes (8 minutes) respectively. Such disturbances can be considered as belonging to the IGWs. The remaining 46% (26%) lying above the dispersion relation curve presumably relate to disturbances generated by plasma instabilities. The percentage of disturbances propagating against the wind in each group was calculated using the HWM14 neutral wind model. In the first group (IGWs), 70% (71%) of the disturbances propagate against the wind, in the second group, 60% (56%). If a similar percentage of disturbances is calculated using FPI data, we get that in the first group (IGWs) 59% (59%) of the disturbances propagate against the wind, in the second group 49% (38%).

The paper illustrates the main stages of a joint approach to the problem of studying traveling disturbances in the neutral atmosphere and ionosphere of the Earth. The results showed that in the time periods from 11-12 UT and 16-18 UT, similar variations were found, which can be defined as a wave-type TIDs. The proposed approach can be improved and implemented for other time periods as well.

This study was supported by the Ministry of Science and Higher Education of the Russian Federation. The results were obtained using the equipment of Institute of Solar–Terrestrial Physics, Siberian Branch, RAS, which is a part of the Angara Shared Research Facility (http://ckp-rf.ru/ckp/3056/). The experimental data were obtained by using the Large-Scale Research Facilities (LSRF) "Optical instruments" (https://ckp-rf.ru/catalog/usu/4138180/).

1. Medvedev A.V., Ratovsky K.G., Tolstikov M.V et al., Method for Determining Neutral Wind Velocity Vectors Using Measurements of Internal Gravity Wave Group and Phase Velocities // *Atmosphere*. 2019. V. 10. No 9. P. 546. DOI: 10.3390/atmos10090546.
2. Vasilyev R.V., Artamonov M.F., Beletsky A.B. et al., // Scientific goals of optical instruments of the national heliogeophysical complex // *Solar-Terrestrial Physics*. 2020. V. 6. No 2. P. 84-97.
3. Cedrik M.V., Podlesnyi A.V., Kurkin V.I. Three-position reception of LFM signals with quasi-vertically incident sounding of the ionosphere // *Vseross. Otkr. Armandovskie chten. Sovremennye*

problemy distancionnogo zondirovaniya, radiolokacii, rasprostraneniya i difrakcii voln. 2022. P. 223-229. DOI: 10.24412/2304-0297-2022-1-223-229.
4. Syrenova T.E., Beletsky A.B., Vasilyev R.V. Geo-referencing images of wide-angle optical systems // *Technical Physics*. 2021. V 91. P.1990-1996. DOI: 10.21883/JTF.2021.12.51765.172-21.

IONOSPHERIC EFFECTS OF THE VICTORY DAY GEOMAGNETIC STORM BASED ON IONOSONDE DATA AT THE WD IZMIRAN OBSERVATORY

Vera V. Nosikova[1], Aleksandr V. Timchenko[1], and Igor A. Nosikov[1]

[1]West Department of Pushkov Institute of Terrestrial Magnetism, Ionosphere and Radio Wave Propagation, Russian Academy of Sciences, 236016, Kaliningrad, Russian Federation

Abstract. Major solar flares on May 8–9, 2025, caused the strongest geomagnetic storm of the past two decades. Based on data from a network of geophysical stations, the planetary K-index reached the maximum value of 9 on May 10 and 11, while the minimum Dst index fell below –400 nT. During the active phase of the geomagnetic storm, auroras were observed at middle and low latitudes. In the Kaliningrad mid-latitude region, the storm's effects were recorded by a suite of geophysical instruments at the Western Department of the IZMIRAN observatory, notably including the 'Parus-A' vertical ionosonde. This study presents a comprehensive analysis of vertical sounding data during the onset, progression, and aftereffects of the geomagnetic storm. The analysis and interpretation of amplitude and height maps enabled the identification of the storm's main effects on shortwave radio propagation, as well as anomalies in the diurnal variations of ionospheric layers.

Introduction. One of the methods for representing radio sounding data is constructing amplitude, height, and frequency characteristics of the signal as functions of observation time, namely A-, H-, and F-maps. This representation allows for analyzing ionospheric dynamics, including the effects of traveling ionospheric disturbances [1]. This paper examines the ionospheric effects of the extremely strong Victory Day geomagnetic storm (May 10–12, 2024) based on vertical sounding data obtained by the "Parus-A" ionosonde at the observatory of the West Department of IZMIRAN [2]. The analysis of storm effects is conducted for three time intervals: the pre-storm period (May 8–9), the storm days (May 10–12), and the post-storm period (May 13–21).

Pre-storm period (May 8–9). Figure 1 presents the A- and H-maps of the ionospheric E and F layers for the period from May 8 to 12. The pre-storm days were characterized by typical diurnal variations in the E and F layers: daytime values of foE and foF2 were 5 MHz and 9 MHz, respectively, while the nighttime foF2 value was 6 MHz. The maximum development of the Es layer was observed on May 9 at 19:00 UT.

Geomagnetic storm (May 10–12). The onset of the storm, according to observational data, was recorded on May 10 at 18:30 UT. During the first hour of the storm, a sharp decrease in foF2 in the F-region was observed, dropping from 8 to 4 MHz. Additionally, starting at 19:00 UT, a rapid increase in electron concentration in the E-region was noted: the auroral foEs parameter exceeded 8 MHz, and the virtual reflection height rose to 170 km. By 21:00 UT, the auroral Es layer had completely shielded the F-region. During the following storm days (May 11–12), reflections from the F-region were practically absent in the ionosphere. In rare instances, foF2 did not exceed 4 MHz at altitudes above 400 km. The

recovery of the ionosphere and the return to typical diurnal variations in the E and F layers began on May 12 at 10:00 UT.

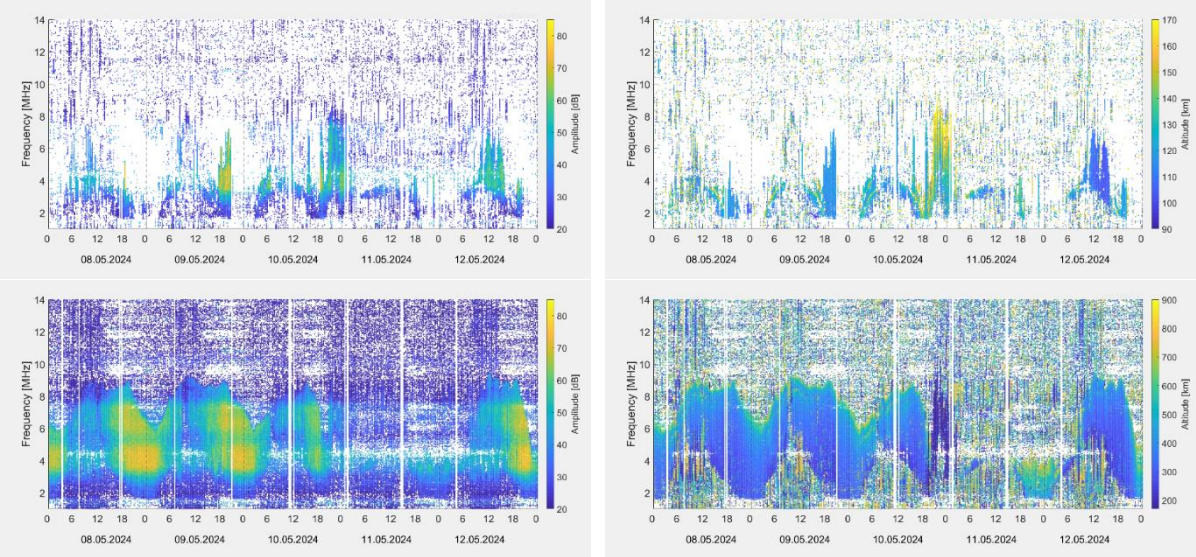


FIGURE 1. Amplitude (A-) and height (H-) maps for the period from May 8 to 12, 2025, based on vertical sounding data from the WD IZMIRAN observatory.

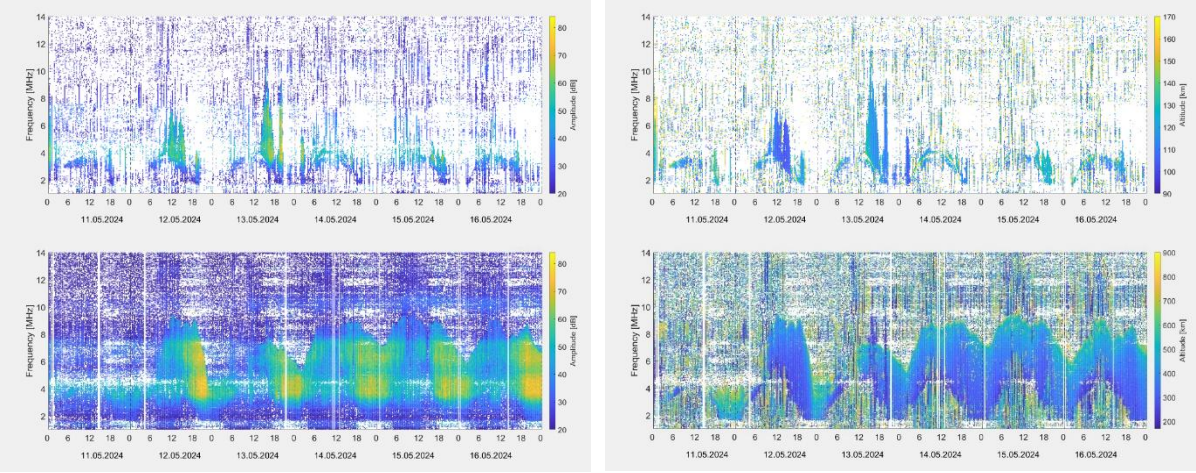


FIGURE 2. Amplitude (A-) and height (H-) maps for the period from May 11 to 16, 2025, based on vertical sounding data from the WD IZMIRAN observatory.

Post-storm period (May 13–21). The storm aftereffects were characterized by a series of Es layers, with maximum foEs values exceeding 8 MHz on May 13 and 10 MHz on May 21. A significant reduction in the diurnal variation of the F-region was recorded on May 13 and 18. An atypical stratification of the F-region was observed on May 18 from 04:00 UT.

Discussion. The analysis of observational data revealed a series of ionospheric effects. The occurrence of sporadic and auroral Es layers was observed throughout the period under consideration.

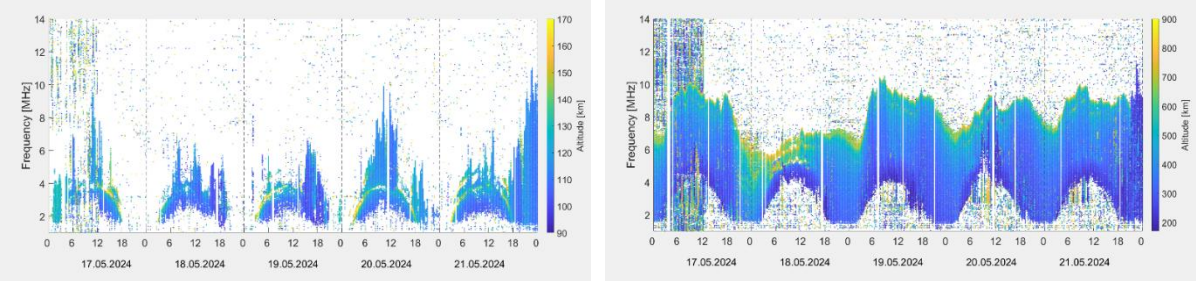


FIGURE 3. Height (H-) map for the period from May 17 to 21, 2025, based on vertical sounding data from the WD IZMIRAN observatory.

The most significant effects were recorded in the F-region of the ionosphere. From May 10 to 12, the foF2 value decreased to 4 MHz, while the maximum hmF2 height exceeded 500 km. These dynamics are consistent with the general understanding of ionospheric plasma behavior mechanisms during disturbed periods. The decrease in electron concentration in the F-region of the ionosphere is attributed to vertical drift, thermospheric expansion, changes in chemical composition due to the influence of particles from the magnetosphere, and plasma redistribution by wind flows. A "negative ionospheric storm" was observed during this period, characterized by reduced electron concentration and deteriorated radio communications.

This study was part of the state project "Investigation of the Ionosphere and Radio Wave Propagation" (Reg. No. 01201356396).

1. Yusupov K. M., Mathews J., Maruyama T., Akchurin A.M., Tolstikov M., Sherstyukov O., Filippova E., Safiullin A. Amplitude variations of the reflected signal during vertical sounding of the ionosphere at middle latitudes // *Solar-Terrestrial Physics*. 2020. V. 6. No 3. P. 72-80. DOI: 10.12737/stp-63202010.
2. Chernyshov A. A., Klimenko M.V., Nosikov I.A., Borchevkina O.P. et al. Effects in the upper atmosphere and ionosphere in the subauroral region during Victory Day 2024 Geomagnetic Storm (May 10-12, 2024) // *Advances in Space Research*. 2025. DOI: 10.1016/j.asr.2025.02.015. In press.

SEARCH FOR ANOMALIES IN LONG SERIES OF MEASUREMENTS OF THE CRITICAL FREQUENCY OF THE IONOSPHERIC F2-LAYER AT THE WD IZMIRAN OBSERVATORY

Ilya V. Hamov[1], Kirill R. Safianov[1], Olga P. Borchevkina[2] and Fedor S. Bessarab[2]

[1]Immanuel Kant Baltic Federal University, Kaliningrad, Russia
[2]West department of Pushkov Institute of Terrestrial Magnetism, Ionosphere and Radio Wave Propagation, Russian Academy of Sciences, Kaliningrad, Russia

Regular studies of the ionosphere using the vertical sounding method have been conducted at the Kaliningrad branch of IZMIRAN since 1964. Over six decades of continuous measurements, a comprehensive dataset of ionospheric parameters—particularly the critical frequency of the F2-layer (foF2)—has been amassed. The methods well developed for the analysis of time series can be applied to the obtained data: identification of trends, search for statistical regularities, construction of regression

models. Currently, research interest in foF2 trends remains significant, as evidenced by recent studies [1-3].

Anomalous features in foF2 regular variations are frequently observed, lasting from several hours to several days. Typically, these anomalies arise during strong geomagnetic disturbances and are clearly distinguishable over short time scales (up to several days). However, identifying such anomalies in multi-decadal time series presents a nontrivial challenge. Moreover, among the cases of significant foF2 deviations from regular variations, instances unrelated to high geomagnetic activity are of particular interest.

In the presented paper we consider the search for anomalous - i.e., significantly different from regular - values of foF2 on the example of analysis of a long series of measurements performed in the WD IZMIRAN.

As raw data, we use the values of the critical frequency of the F2 layer obtained with the PARUS-A vertical sounding ionosonde at the Kaliningrad Observatory of IZMIRAN since 1964. The ionosonde operates with a 15-minute resolution, but only hourly data is processed in the manual mode. Due to the limitations of the automatic ionogram processing algorithm, which sometimes introduces errors, only hourly data were used in this study.

For preliminary anomaly detection in the time series, classical statistical methods can be employed. Figure 1 presents the foF2 critical frequency variations for 2024, highlighting anomalies identified using the two-sigma rule (top panel) and Interquartile range (IQR) analysis (bottom panel). The results demonstrate that pronounced foF2 deviations are clearly detected during periods of intense geomagnetic activity in May, August, and October. However, the two methods yield slightly differing outcomes: notably, the IQR method classifies several events in January and February as anomalous, whereas these are not flagged by the two-sigma criterion.

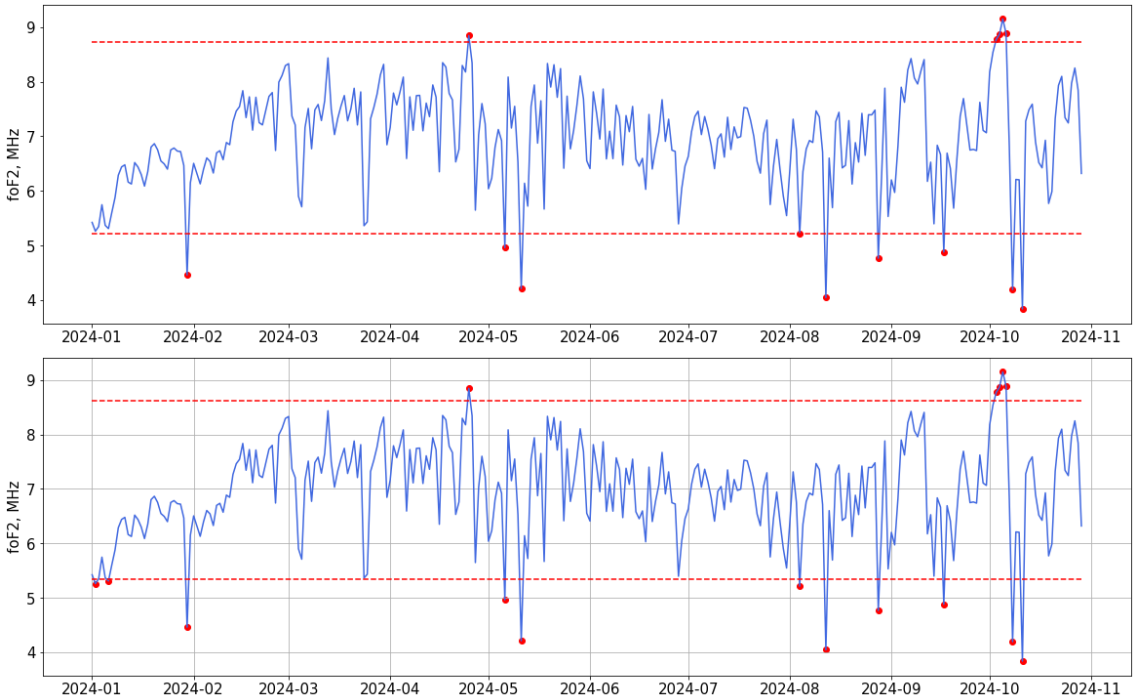


FIGURE 1. Variations in foF2 critical frequency for 2024 yr and anomalies highlighted using the two sigma rule (top panel) and IRQ analysis (bottom panel).

The presence of trends also poses significant challenges for reliable anomaly detection, highlighting the importance of methods that extract regular components when analyzing non-stationary time series. Note that classical methods refer to anomalous cases that fall outside the boundaries of some specified interval. No less interesting can be the results of measurements that violate the regularity of the signal behaviour. In this case other approaches should be used, as, for example, in [4].

The research was funded by the grant Russian Science Foundation N°– 23–77-10004, https://rscf.ru/project/23–77-10004.

1. Laštovička J., Burešová D. Relationships between foF2 and various solar activity proxies // *Space Weather*. 2023. V. 21. Is. 4. ID e2022SW003359. DOI: 10.1029/2022SW003359.
2. Danilov A. D, Konstantinova A.V. Long-term changes in the relation between foF2 and hmF2 // *Geomagnetism and Aeronomy*. 2016. V. 56. N 5. P. 577–584. DOI: 10.1134/S0016793216050042
3. Danilov A.D., Berbeneva N.A. Trends in the critical frequency of the F2 layer during the recent decade // *Geomagnetism and Aeronomy*. 2023. V. 63. No 2. P. 113-120. DOI: 10.1134/s0016793222600886.
4. Mandrikova O.V., Glushkova N.V., Zhivet'ev I.V. Modeling and analysis of ionospheric parameters by a combination of wavelet transform and autoregression models // *Geomagnetism and Aeronomy*. 2014. V. 54. No 5. P. 593-600. DOI: 10.1134/S0016793214050107.

SEASONAL FEATURES OF THE ES-LAYER CHARACTERISTICS OVER THE KALININGRAD REGION DURING SOLAR 24 AND 25 CYCLES

Egor D. Senyagin[1], Aleksandr V. Timchenko[2], Fedor S. Bessarab[2]

[1]Immanuel Kant Baltic Federal University, Kaliningrad, Russia
[2]West Department of Pushkov Institute of Terrestrial Magnetism, Ionosphere and Radio Wave Propagation, Russian Academy of Sciences, Kaliningrad, Russia

Introduction. The ionosphere, a crucial component of the Earth's atmosphere, plays a main role in the transmission of radio waves and the operation of satellite communication and navigation systems. One of the most significant aspects of the ionosphere is the Es-layer, also known as the sporadic E-layer, which represents thin, highly ionized regions located within the E-region at altitudes ranging from 95 to 180 kilometers above the surface of the Earth.

Over the Kaliningrad region, the Es-layer exerts a profound influence on radio communication, both facilitating and obstructing the propagation of radio signals. The impact of this layer on radio communication has been extensively studied by researchers, such as [1], who have explored its intricate dynamics and effects. The formation of the Es-layer can be explained using the theory of windshear, first proposed by [2]. Windshear is characterized by an increase in the gradient of horizontal wind velocities (zonal and meridional) with increasing altitude.

According to this theory, horizontal windshear causes the redistribution of ions and electrons, resulting in the creation of thin layers of ionisation. Long-lived metallic ions also play a significant role in the formation of these sporadic layers, as described by [3,4]. These ions come from burnt meteorites in the upper atmosphere.

During solar cycles 24 and 25, there have been significant changes in solar activity, which directly affect the ionosphere. Both regular and irregular variations in solar activity influence chemical reactions and physical processes within the ionosphere, as discussed by [5]. Specifically, changes in ultraviolet and X-ray solar radiation affect the density and distribution of ionisation in the Es-region. The objective of this research is to delve into the seasonal patterns of the Es-layer characteristics in the Kaliningrad region during the time frame encompassing the peaks of solar cycles 24 and 25. The analysis encompasses parameters such as the critical frequency (foEs) and the layer altitude (hvEs), as well as their temporal fluctuations.

Data and method. The data used in this study consist of variations in the critical frequency and altitude of the sporadic E-layer, measured by the vertical sounding ionosonde 'PARUS-A' at the Kaliningrad Magnetic-Ionospheric Observatory (54.36° N, 20.12° E) from December 2014 to December 2024.". The ionosonde operates in a 15-minute mode, the frequency range is 1 – 20 MHz Ionograms were obtained with a period at the time when laboratory assistants process data. Since automatic ionogramm processing allows for many errors, especially at the considered altitudes, only hourly data were used in the work.

For further study of the Es layer, the frequency of Es observation per day was calculated:

$$N_f = \frac{N_{spor}}{N_{tot}}, \quad (1)$$

where N_f is the frequency of Es-layer observation per day, N_{spor} represents the number of sporadic E observations, and N_{tot} denotes the total number of observations. Under ideal conditions, the total number of observations N_{tot} would be 24. However, due to various factors such as power outages, the actual number of observations may vary. If the number of observations taken per day is less than 10, that day is considered a non-observation day and is excluded from the overall data set.

To determine the trend, we used the empirical mode decomposition (EMD) method proposed by Huang et al. [6], which is a component of the Hilbert-Huang transformation. This method involves finding the so-called intrinsic mode functions (IMFs) which satisfy two conditions: In the entire dataset, the number of extrema and the number of zeros must either be equal or differ by at most one. At each data point, the mean of the envelope calculated using local maxima should be zero, and the same for the envelope calculated using local minima. The IMFs are obtained by constructing an envelope using local maxima and minima, and then calculating the mean of this envelope. The mean is then subtracted from the original dataset to obtain the IMF. The last IMF can be interpreted as either a trend or a constant value.

Results and Discussion. The fig. 1 illustrates the variations in the critical frequency (foEs) (upper plot) and altitudes (hvEs) (bottom plot) of the Es-layer obtained over the Kaliningrad region from December 2014 to December 2024. The foEs range from ~ 1.5 MHz to 14 MHz, with a maximum value of 14 MHz owing to the limitation imposed in the "Parus operator" ionogramm processing software. This limitation is set for the convenience of processing regular E and F layers. The hvEs varies from approximately 95 km to 180 km, contingent on the type of sporadic E-layer. The values presented in this paper represent the virtual altitudes and not the altitude of maximum electron density for the layer.

The plot of long-term foEs measurements (Fig. 1, upper plot) clearly shows seasonal variability: the maximum values of the critical frequency occur in the summer period, which has been noted by many authors, see, for example, Whitehead [7]. In winter, most of the observed foEs values correspond to the annual minimum, but a small number of foEs measurements form a second maximum in the seasonal variation. The period from the summer of 2023 to the end of 2024 stands out from the rest of the data; an increase in the spread of the Es-layer critical frequency values is observed in this period of time. In the spring months, foEs increase toward the summer maximum, and in the fall, it decreases toward the winter minimum.

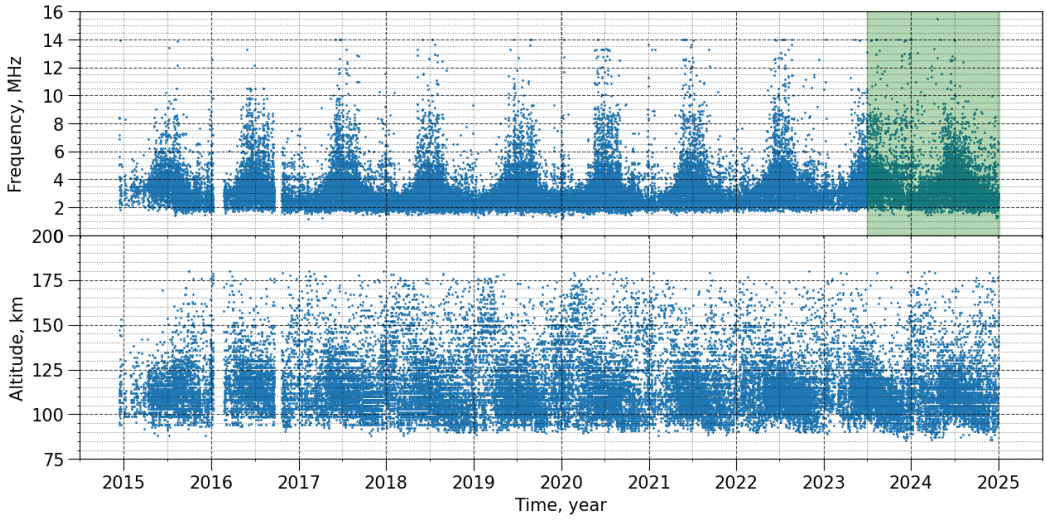


FIGURE 1. Shows variations in the critical frequency (upper plot) and altitude (bottom plot) of the Es-layer.

Seasonal dependence is also observed in Es altitude variations (Fig. 1, bottom plot). The graph shows that most of all hvEs are located at altitudes from 100 to 140 km, but in winter there is an increase in cases in which hvEs is recorded at higher altitudes — up to 180 km. In summer, an increase in the number of Es observed at altitudes of 90–130 km is noted. In the summer periods of 2017, 2018, 2021–2024, a slight increase in the minimum altitude can be seen. The same increase is observed in January 2023 and 2024.

The Figure 2 shows a graph of the Es layer observation frequency for the period under consideration, calculated using Eq. (1).

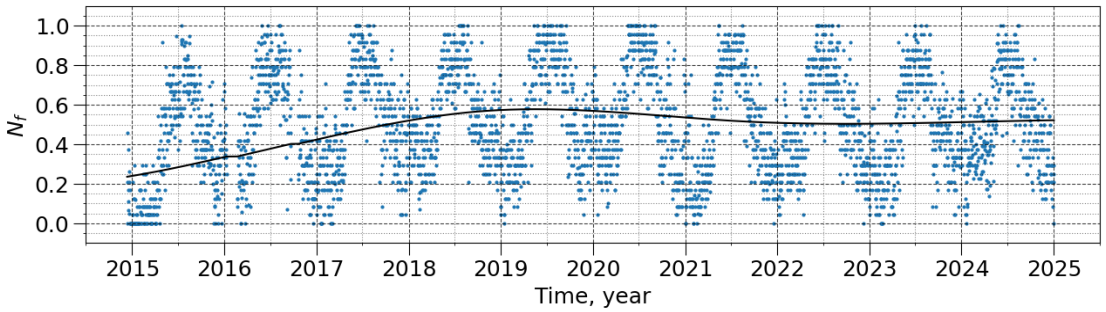


FIGURE 2. Shows the frequency of observation of sporadic Es-layer events per day for the period December 2014 through December 2024. The black line indicates a trend.

This graph also shows pronounced seasonality: the highest frequency of occurrence is in summer, the lowest is in winter, spring and autumn are transitional periods. Winter 2024 stands out from other years the most; it is clear that the total number of recorded sporadic E increased during this period. Using the EMD method, a trend was constructed for the Es observation frequency (Fig. 2, black line). An upward trend was observed from 2015 to 2019, after which it became almost constant. This behavior may be due to the fact that the available data series is insufficient to find a trend. An upward trend is also observed before the minimum solar activity, which may indicate that the Es occurrence frequency may increase with lower solar activity.

As previously mentioned, metal ions and atmospheric winds at the altitudes of the upper mesosphere – lower thermosphere are significant for the formation of the Es-layer in the ionosphere. Considering the processes associated with seasonal changes in the neutral wind circulation at these

altitudes, the dominant annual pattern in the behavior of Es-layer parameters is linked to this factor. One of the factors determining deviations from the annual periodicity in the variations of the Es layer parameter may be geomagnetic activity. To investigate this hypothesis, the Dst index values were selected for the period from 2014 to 2024 when they were less than -50 nT (Fig. 3). The time periods when the index values are below -50 nT correspond to geomagnetic storm conditions.

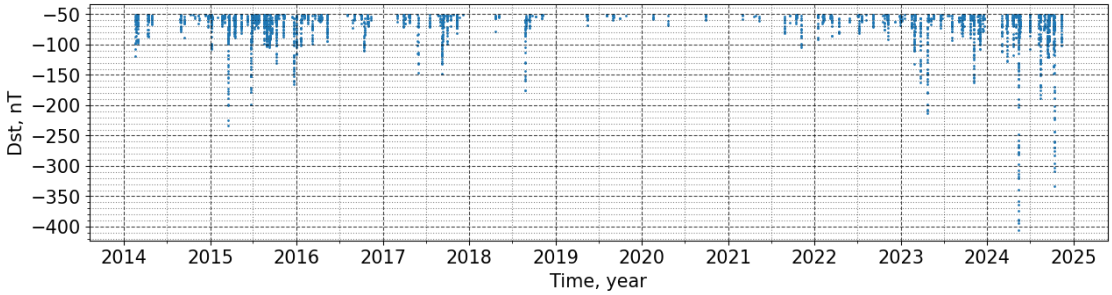


FIGURE 3. Variations in the Dst index after excluding background values.

The Figure 3 clearly shows the increase in geomagnetic activity in the period from 2015 to 2016, as well as from 2023 to the end of 2024, which correspond to the maxima of solar activity.

Comparing Fig. 2 and Fig. 3, it can seen that the number of sporadic Es-layers recorded per day is greatest during periods of calm or weakly disturbed geomagnetic activity. Such conditions correspond to the winters of 2017 – 2018, 2019 – 2020 and 2021 – 2022. In the winter of 2023 – 2024, when a general increase in the frequency of Es observations is also observed. During this period, there was only a geomagnetic storm, during which the Dst index dropped below -160 nT. Based on this behavior, it can be assumed that the increase in the frequency of Es observations occurs with a period of 2 years, and occurs during weak geomagnetic activity.

Also, when comparing Fig. 2 and 3 show that during strong geomagnetic storms (Dst ≤ -170 nT) the number of observed sporadic layers also increases, with the exception of the St. Patrick's storm on March 17, 2015. This increase may be due to the expansion of the auroral oval and increased ionization caused by precipitating particles. Such particles cause the appearance of aurora and sporadic layers of the auroral type.

Conclusion. In this paper, we studied the seasonal features of the Es layer characteristics over the Kaliningrad region in the period between the maxima of the 24th – 25th solar cycles. It was shown that:

1. Variations in the critical frequency of the Es layer have maxima in summer periods and minima in winter, with an additional maximum. Spring and autumn are transitional periods. An exception is the period from summer 2023 to winter 2024, during which time a strong increase in the spread of the Es-layer critical frequency values is observed.
2. In the variations in altitudes of the Es-layer in winter periods, an increase in the altitude of most of the observed layers is noticed, in summer periods, most of the recorded layers are located at altitudes of 100 – 130 km. The formation and behavior of maxima in the variations in the critical frequency of the Es-layer require further study.
3. The frequency of Es observation has a clear seasonality: in summer, the greatest number of Es per day is recorded, in winter - the smallest. Spring and autumn are transitional periods.
4. During strong geomagnetic storms, the frequency of Es observations increases. The exception is the St. Patrick's storm.
5. The trend in the frequency of Es observations shows that there is an increase in the number of sporadic layers as the solar activity minimum approaches. However, due to the insufficiently long-time interval of the data, it is too early to draw final conclusions.

6. Every 2 years, there is an increase in the number of Es recorded in the winter period, in the solar cycle under consideration.

The research was funded by the grant Russian Science Foundation N°– 23–77-10004, https://rscf.ru/project/23–77-10004.

1. Sakai J., Hosokawa K., Tomizawa I., Saito S. A statistical study of anomalous VHF propagation due to the sporadic-E layer in the air-navigation band // *Radio Science*. 2019. V. 54. No 5. P. 426 – 439. DOI: 10.1029/2018RS006781.
2. Whitehead J. D. The formation of the sporadic-E layer in the temperate zones. // *Journal of Atmospheric and Terrestrial Physics*. 1961. V. 20 Is. 1. P. 49 – 58. DOI:10.1016/0021-9169(61)90097-6.
3. Istomin V. G., Magnesium and calcium ions in the earth's upper atmosphere // *Dokl. Akad. Nauk SSSR*. 1961. V. 136. P. 1066-1068 (in Russian).
4. Bakhmet'eva N.V., Belikovich V.V., Ignat'ev Y.A., Ponyatov A.A. Vertical motions in the lower ionosphere and a sporadic E-layer // Radiophysics and Quantum Electronics. 1999. V. 42. No 1. P. 26-35. DOI: 10.1007/BF02677637.
5. Liu L., Wan W., Chen Y. et al. et al. Solar activity effects of the ionosphere: A brief review // *Chinese Science Bulletin*. 2011. V. 56. P. 1202–1211. DOI: 10.1007/s11434-010-4226-9.
6. Huang N. E., Shen Z., Long S.R., Wu M.C. et al. The empirical mode decomposition and the Hilbert spectrum for nonlinear and non-stationary time series analysis. // *Proceedings of the Royal Society of London. Series A: mathematical, physical and engineering sciences.* 1998. V. 454. I. 1971 P. 903 – 995. https://doi.org/10.1098/rspa.1998.0193.
7. Whitehead J. D. Recent work on mid-latitude and equatorial sporadic-E // *Journal of Atmospheric and Terrestrial Physics.* 1989 V. 51. Is. 5. P. 401 – 424. doi:10.1016/0021-9169(89)90122-0.

DEPENDENCE OF THE OBSERVATION PROBABILITY OF RELATIVISTIC ELECTRON PRECIPITATION WITH DIFFERENT FORMATION MECHANISMS ON THE PARAMETERS OF THE SOLAR WIND AND GEOMAGNETIC ACTIVITY

Tatyana A. Yahnina, Andrey G. Demekhov, Tatyana A. Popova

Polar Geophysical Institute, Apatity, Russia

Introduction. The paper considers relativistic (800 keV) electron precipitation (REP) caused by four different mechanisms based on NOAA/POES satellite data. According to the criterion presented in [1, 2], REP of the 1st group are associated with the geometry of geomagnetic field lines in the night sector. These precipitationsare observed near the isotropy boundary of electron fluxes [3, 4]. REP of the 2nd group are always observed simultaneously with intense precipitation of energetic (> 40 keV) electrons. Apparently, they are caused by the interaction with VLF waves. REP of the 3rd group, accompanied by energetic (> 39 keV) proton precipitation, are associated with EMIC waves. The mechanism of REP of the 4th group is associated with the entry of energetic particles into the drift loss cone in the distorted magnetic field [5] in the vicinity of the South Atlantic Magnetic Anomaly. Of interest is the analysis of the relationship between the REP of each group and the solar wind parameters,

such as pressure, density, speed and geomagnetic activity indices: the substorm activity index AE and the storm activity indexes SYM-H and Dst.

Data sources. We used low-orbiting (~850 km) spacecraft NOAA/POES data from MEPED instruments [6] detecting energetic charged particles in two orthogonal directions (horizontal and vertical). Energetic proton fluxes are measured in channels P1 to P6 (30–80 keV, 80–250 keV, 250–800 keV, 800–2500 keV, 2500–6900, and >6900 keV, respectively). The latter channel (P6) is also sensitive to relativistic electrons (> 800 keV), so it measures these electrons if there are no protons in P5. Also we used OMNI database obtained from https://cdaweb.gsfc.nasa.gov/

Results. Based on the NOAA/POES satellite data the probability of observing relativistic (~800 keV) electron precipitation is analyzed for two intervals: October 8-18, 2017 and the entire year 2017. The first interval includes a moderate geomagnetic storm ($SYM\text{-}H_{min}$ = -67 nT) with intense auroral activity, which is confirmed by an increase in the AE index to AE=1916 nT and an average AE index of 256 nT. The second interval contains REP events conjugated with the Lovozero observatory (up to 2.5 MLT in distance) for the entire year 2017. This year is close to the minimum of solar activity between the cycles 24 and 25 and falls on the decline of the weakest cycle in a century. The average AE index for the second interval is 189 nT.

Table 1 shows the number of REP events for each of the four groups in the two intervals. The average values of solar wind and geomagnetic activity parameters are shown, both in the interval and for the observed REP events.

TABLE 1.

	1 group		2 group		3 group		4 group	
	1st interval	2nd interval	**1st interval**	2nd interval	**1st interval**	2nd interval	**1st interval**	2nd interval
Number of the REP events	**111**	105	**141**	462	**58**	240	**790**	2074
Northern Hemisphere	**31**	48	**66**	122	**26**	122	**136**	33
Southern Hemisphere	**80**	57	**75**	340	**32**	118	**654**	2041
AE index, nT interval/events	**256/519**	189/487	**256/458**	189/391	**256/409**	189/413	**256/206**	189/161
Dst index, nT interval/events		-12,66/ -26		-12,66/ -19		-12,66/ -10		-12,66/ -7
SYM-H index, nT;for interval/events	**-20,4/ -37,8**		**-20,4/ -33,2**		**-20,4/ -22,8**		**-20,4/ -17,8**	
P_{sw}, nPa for interval/events	**2,64/3,28**	2,19/2,30	**2,64/3,02**	2,19/2,50	**2,64/3,67**	2,19/3,50	**2,64/2,30**	2,19/2,00
V_{sw}, km/s for interval/events	**476/575**	451/558	**476/557**	451/521	**476/466**	451/447	**476/464**	451/441
N_{sw}, $cm^{-3}$for interval/events	**6,30/5,15**	6,35/5,29	**6,30/5,43**	6,35/5,77	**6,30/9,67**	6,35/10,21	**6,30/5,97**	6,35/6,56

Comparative histograms of all precipitation groups depending on the, solar wind dynamic pressure (P) and speed (V), AE, SYM-H and Dst indexes are shown in Figure 1 and Figure 2.

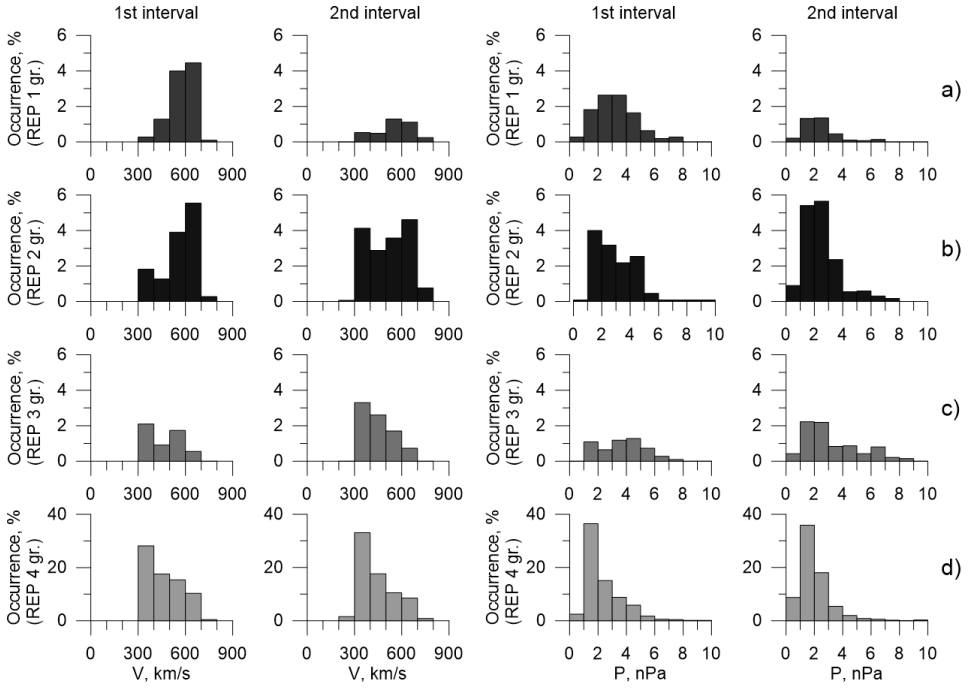


FIGURE 1. Dependences of the probability of REP observation for: 1 group (a), 2 group (b), 3 group (c), 4 group (d) on the solar wind pressure and speed for two intervals.

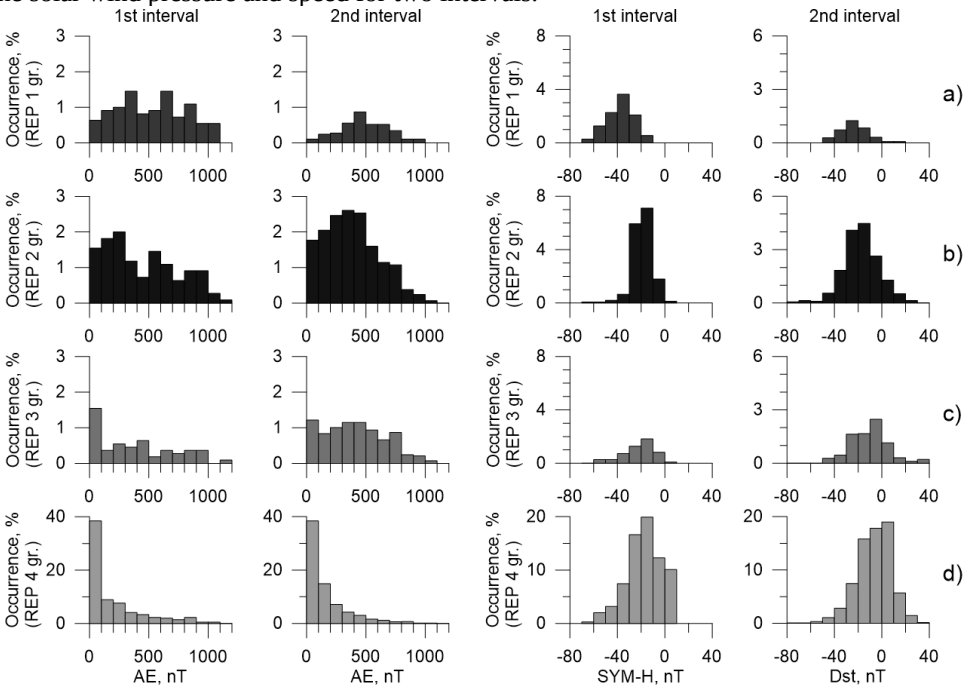


FIGURE 2. Dependences of the probability of REP observation for: 1 group (a), 2 group (b), 3 group (c), 4 group (d) on the auroral index AE, SYM-H and Dst storm indexes for two intervals.

These distributions are not normalized to the duration of intervals with the corresponding activity, but are normalized to the total number of events in all groups observed during the interval. Nevertheless, even from these histograms, one can make a number of important, well-justified conclusions about the dependence of the REP properties on the parameters of geomagnetic activity and the solar wind. Thus, REP of the 4th group are more often observed at the lowest solar wind pressures and speeds and at low substorm activity, compared to precipitation of the other groups. One can also note a clear increase in the events of the 1st and 2nd groups in intervals with high-speed solar wind. As for precipitation of the 3rd and 4th groups, their number gradually decreases with an increase in the solar wind speed.

Summary and conclusions. Comparison of relativistic electron precipitation in more disturbed first interval (average value AE=256 nT) and less disturbed second interval (AE=189 nT) showed the following.

Relativistic electron precipitations of the 1st, 2nd and 4th groups are more often recorded in the southern hemisphere. In more disturbed conditions (the first interval), the difference is especially noticeable for the events of the 1st group. The calmer the conditions, the more events of the 2nd and 4th groups are observed in the southern hemisphere. Precipitation of the 3rd group are found approximately equally in both hemispheres (see Table 1).

Comparison with solar wind density showed that the events of the 3rd group are observed at a higher average density than the average density in the interval under consideration. For the remaining groups, this difference is insignificant (see Table 1).

The number of events of the 1st and 2nd groups increases with increasing solar wind velocity in both intervals.The number of precipitations of the 3rd and 4th groups smoothly decreases with an increase in solar wind speed in both intervals (Figure 1).

The REP events of the 4th group are more often observed at the lowest pressures and solar wind speeds and at low substorm (AE index) and storm (SYM-H index) activity, compared to precipitation of other groups. In the more disturbed (the first) interval, the 1st and 3rd groups were observed at P=1-6 nPa with maxima at 2-4 nPa and 3-5 nPa, respectively. In the less disturbed (the second) interval, the number of REP events in all groups was maximum at solar wind pressures P=1-3 nPa.

The obtained results are in agreement with the known formation mechanisms of relativistic electron precipitation and contribute to the understanding of still unknown mechanisms.

For the 1st group: The probability of observation increases during high-speed solar wind flows and increased geomagnetic activity. It is known, for example, that with increasing disturbance, the electron isotropy boundary, near which the REP of the 1st group are formed, is shifted from the midnight (00 MLT) to the pre-midnight (22 MLT) sector. Apparently, the curvature of the geomagnetic field in the night sector provides conditions that are more favorable for the generation of REP of this group. *For the 2nd group*: It is generated in a wide range of geomagnetic activity values and at high-speed solar wind flows. These precipitations make up ~50% of the precipitation for the first three groups. The mechanism of their formation has not been fully established, but it is assumed that it is due to interaction with VLF waves. *For the 3rd group*: The decrease in the probability of observation with increasing solar wind speed is consistent with the conditions for generating EMIC waves (Pc1 pulsations). *For the 4th group*: The calmer the geomagnetic conditions and solar wind parameters, the more particles can enter the drift loss cone. This is what we observe.

Acknowledgments. *This investigation was performed with the financial support from the Russian Science Foundation grant No. 22-62-00048. The authors thank NOAA for the access to the POES/MetOp and OMNI databases https://cdaweb.gsfc.nasa.gov/.*

1. Yahnin A.G., Yahnina T.A., Semenova N.V., Gvozdevsky B.B., Pashin A.B. Relativistic electron precipitation as seen by NOAA POES // *J. Geophys. Res. Space Physics*. 2016. V.121, No.9. P.8286-8299. DOI:10.1002/2016JA022765.

2. Yahnin A.G., Yahnina T.A., Raita T., Manninen J. Ground pulsation magnetometer observations conjugated with relativistic electron precipitation // *J. Geophys. Res. Space Physics*. 2017. V.122, No.9. P.9169-9182. DOI: 10.1002/2017JA024249.
3. Sergeev V.A., Tsyganenko N.A. Energetic particle losses and trapping boundaries as deduced from calculations with a realistic magnetic field model // *Planet. Space Sci*. 1982. V.30. No.10. P.999–1006. DOI: 10.1016/0032 0633(82)90149-0.
4. Imhof W.L., Voss H.D., Mobilia J., Datlowe D.W., Gaines E.E. The precipitation of relativistic electrons near the trapping boundary // *J. Geophys. Res*. 1991. V.96. No. A4. P.5619–5629. DOI: 10.1029/90JA02343.
5. Blake J.B., Inan U.S., Walt M., Bell T.F., Bortnik J., Chenette D.L., Christian H.J. Lightning-induced energetic electron flux enhancements in the drift loss cone // *J. Geophys. Res*. 2001. V.106. No. A12. P.29733-29744. DOI: 10.1029/2001JA000067.
6. Evans D.S., Greer M.S. Polar orbiting environmental satellite space experiment monitor-2: Instrument descriptions and archive data documentation // NOAA Tech. Memo 1.4, Boulder, Colorado: NOAA OARL Space Environment Center, 2004.

AKR SPECTRUM MODIFICATION AS A RESULT OF PROPAGETION IN INHOMOGENEOUS PLASMA

Valeriia I. Kolpak[1,2], Mikhail M. Mogilevsky[1], Dmitry V. Chugunin[1], Aleksandr A. Chernyshov[1], Irina L. Moiseenko[1]

[1]Space Research Institute, Russian Academy of Sciences, Moscow, Russia
[2]Pushkov Institute of Terrestrial Magnetism, Ionosphere, and Radio Wave Propagation, Russian Academy of Sciences, Troitsk, Moscow, Russia

Based on data obtained from the ERG (Arase) satellite [1], the study proposes new models describing the spatial distribution of plasma irregularities and their impact on the characteristics of the AKR spectrum. It has been established that plasma irregularities elongated along the magnetic field lines play a key role in transforming the radiation spectrum.

Auroral kilometric radiation (AKR) arises as a result of the development of cyclotron maser instability in auroral regions of the magnetosphere, within low-density plasma cavities [2], under the condition $f_{pe} < f_{Be}$, where f_{pe} is the plasma frequency, and f_{Be} is the gyrofrequency.

Previous studies have shown that auroral radiation can be efficiently transported from the generation region to near-equatorial areas via plasma channels, which are low-density irregularities elongated along magnetic field lines [3-5]. However, several questions remain regarding the stability of such channels, their spatial configuration, and the impact of dynamic changes in the magnetosphere on AKR parameters.

We propose an alternative mechanism for transferring radiation between hemispheres, involving the trapping of AKR within low-density channels. The modeling of radiation propagation was performed using the geometric optics approximation, under the following assumptions: a sharp density boundary between the channel and the surrounding plasma, the invariance of channel geometry over the measurement period, and the neglect of magnetic field line curvature. The calculations include determining the reflection and transmission coefficients of the radiation, as well as estimating energy losses at the channel boundaries.

Figure 1 shows an example of processed measurements from the HFA instrument [6] onboard the ERG satellite for January 31, 2019, during the time interval from 13:20 UT to 14:15 UT. In the low-frequency part of the spectrogram, a narrowband signal is observed at frequencies up to 100 kHz, corresponding to the upper hybrid resonance frequency: $f_{UHR} = \left(f_{pe}^2 + f_{Be}^2\right)^{1/2}$, where f_{pe} is the local electron plasma frequency, defined as $f_{pe} = \left(4\pi e^2 N/m_e\right)^{1/2}$ (in CGS units), $f_{Be} = eB/m_e c$ is the local electron gyrofrequency. Here e is the electron charge, N is the electron density, m_e is the electron mass, and B is the magnetic induction.

In the first approximation, it can be assumed that the upper hybrid resonance frequency (f_{UHR}) depends primarily on the plasma density.

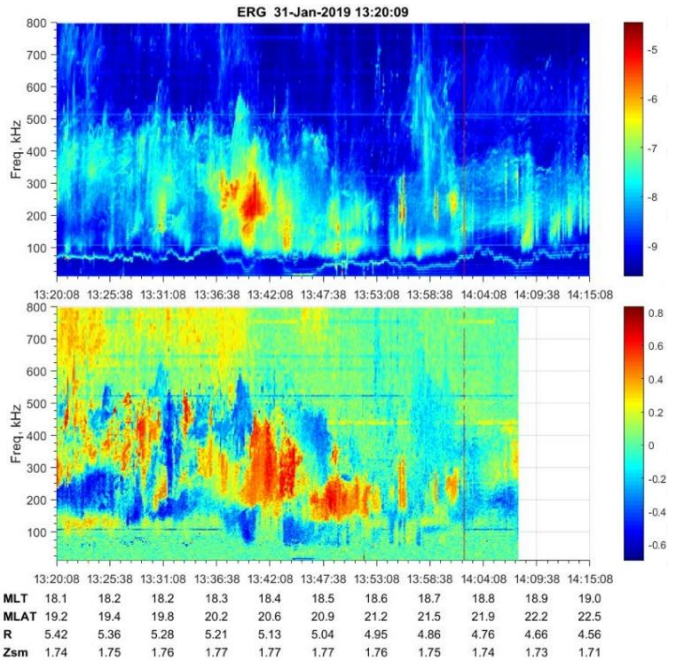


FIGURE 1. AKR measurements in a region with low-density channels on January 31, 2019. The top panel shows a dynamic spectrogram of the power spectrum in the frequency range of 10–800 kHz, while the bottom panel presents a spectrogram of the polarization parameter.

In quiet conditions, when there are no plasma channels in the plasma, an "rectangular" AKR spectrum is observed, as shown in Fig. 2.

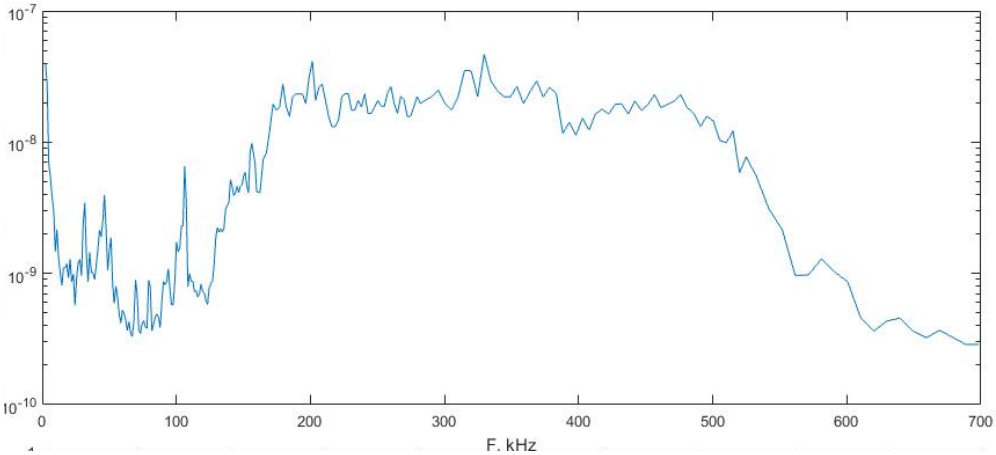


FIGURE 2. AKR spectrum when there are no irregularities in the plasma. June 21, 2017, 19:32:38 UT.

An interesting interval is observed in the frequency range from 100 kHz to 500 kHz, which includes the active phase of the AKR. At a frequency of ~110 kHz, a narrowband signal is observed, corresponding to the upper hybrid resonance frequency f_{UHR}. The sharp increase in intensity following this burst, reaching two orders of magnitude in the frequency range from 180 kHz to 500 kHz, is characteristic of cases when the radiation propagates in a medium without interaction with plasma irregularities.

However, in some cases, the spectrum undergoes a transformation (Fig. 3): after a sharp intensity jump, a gradual decrease is observed. The upper boundary of the spectrum takes on a slope, forming a "triangular" shape, which indicates the influence of plasma irregularities during the propagation of the radiation.

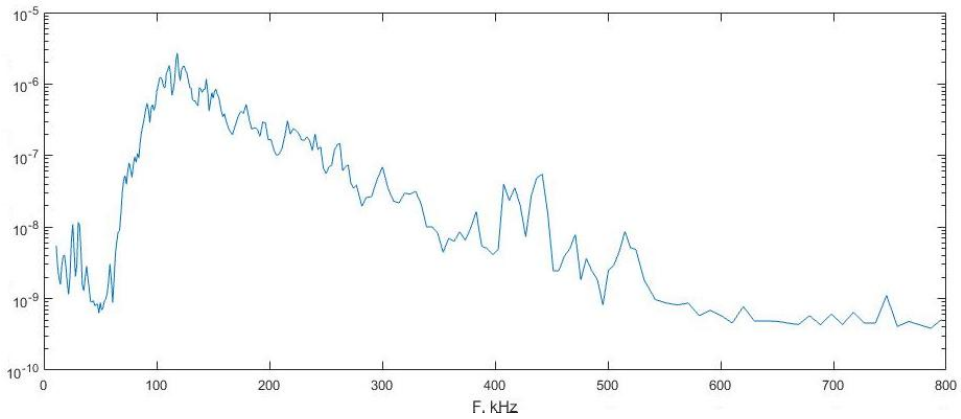


FIGURE 3. Triangular AKR spectrum on the ERG satellite. January 31, 2019, at 13:43:37 UT.

As the radiation passes through regions of lower density, it is reflected from the inner walls of the channel, leading to a significant attenuation of intensity. This occurs due to energy losses caused by both scattering and partial absorption of the radiation in these inhomogeneous environments.

One consequence of such interactions is the truncation of the radiation spectrum. This is observed in the frequency range from 120 kHz to 500 kHz at the upper boundary of the spectrum, where the intensity sharply decreases with a steep slope. This phenomenon indicates that, despite the main direction of propagation being maintained, the radiation loses its energy during reflections and interactions with inhomogeneous structures, which limits the transmission of higher frequencies. As a result, the radiation spectrum undergoes significant distortion in areas where the channel is the primary propagation path for the wave.

The characteristic width of such channels ranges from several tens to hundreds of kilometers, and the depth of the density dips varies from 0.36 to 0.64 relative to the background values.

Figure 4 shows the results of the reflection coefficient calculations [7]:

$$K = \left(\frac{n_2 \cos\theta_2 - n_1 \cos\theta_1}{n_2 \cos\theta_2 + n_1 \cos\theta_1}\right)^2,$$

where n_1 and n_2 are the refractive indices for the extraordinary electromagnetic wave in the plasma outside and inside the channel, respectively; θ_1 and θ_2 are the angles of incidence and refraction.

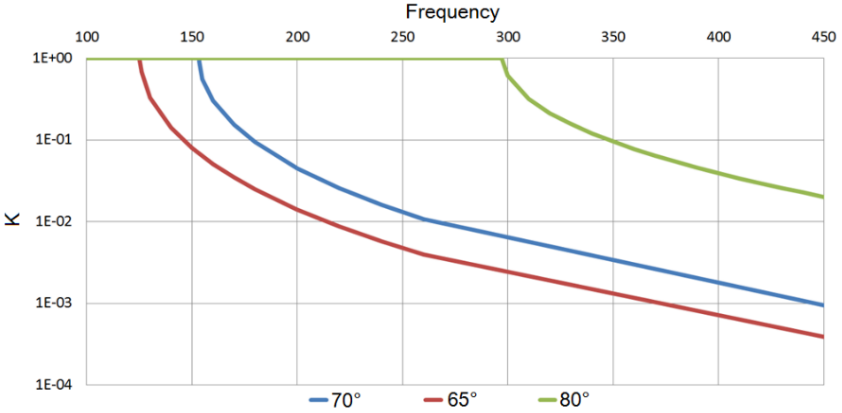


FIGURE 4. Results of reflection coefficient calculations from the channel wall for three angles of incidence: 80° (green line), 70° (blue line), 65° (red line).

All three graphs, plotted for three angles of incidence of the radiation, show that as the frequency increases by 150-200 kHz, the value of K decreases by two orders of magnitude, which corresponds to the results obtained from the measurements.

Spectral analysis of the AKR revealed patterns associated with the transformation of the spectrum: an increase in intensity at low frequencies and a decrease at high frequencies, which is consistent with the modeling results. The level of high-quality components of the spectrum decreases, as some of the energy escapes into the channel, seeping through the walls. This suggests that the interaction of AKR with plasma irregularities plays a key role in shaping the spectral characteristics of the radiation, limiting its amplitude and width, and also altering the shape of the spectrum depending on the physical properties of the medium.

1. Miyoshi Y., Shinohara I., Takashima T., Asamura K., Higashio N., Mitani T., Kasahara S., Yokota S., Kazama Y., Wang S.-Yu, Tam S.W.Y., Ho P.T.P., Kasahara Y., Kasaba Y., Yagitani S., Matsuoka A., Kojima H., Katoh Y., Shiokawa K., Seki K. Geospace Exploration Project ERG // *Earth, Planets and Space*. 2018. V. 70. No 155. DOI:10.1186/s40623-018-0862-0.
2. Wu C.S., Lee L.C. A theory of the terrestrial kilometric radiation // *Astrophysical Journal.* 1979. V. 230. P. 621–626.
3. Chernyshov A.A., Mogilevsky M.M., Chugunin D.V., Kolpak V.I. Simultaneous observation of auroral kilometric radiation from northern and southern sources // *Bulletin of the Russian Academy of Sciences: Physics.* 2022. V. 86. No 3. P. 295–299. DOI: 10.3103/S1062873822030078.
4. Kolpak V.I., Mogilevsky M.M., Chugunin D.V., Chernyshov A.A., Moiseenko I.L., Kumamoto A., Tsuchiya F., Kasahara Y., Shoji M., Miyo-shi Y., Shinohara I. Statistical properties of auroral kilometer radiation: based on ERG (Arase) satellite data) *// Solar-Terrestrial Physics.* 2021. V. 7. No 1. P. 11–16. DOI: 10.12737/stp-71202102.
5. Kolpak V.I., Mogilevsky M.M., Chugunin D.V., Chernyshov A.A., Moiseenko I.L. Transfer of auroral kilometric radiation through low-density channels at the boundary of plasmasphere // *Solar-Terrestrial Physics*. 2024. V. 10. No 1. P. 19–28. DOI: 10.12737/stp-101202403.
6. Kumamoto A., Tsuchiya F., Kasahara Y., et al. High Frequency Analyzer (HFA) of Plasma Wave Experiment (PWE) onboard the Arase spacecraft // *Earth, Planets and Space*. 2018. V. 70. P. 82. DOI: 10.1186/ s40623-018-0854-0.
7. Landsberg G.S. *Optica: ucheb. posobie dlya vuzov*, Fizmatlit Publ., Moscow, 2003, 848 p.

RELATIONSHIP BETWEEN WAVE INTENSITY IN THE MAGNETOSPHERE AND PRECIPITATING ENERGETIC PARTICLE FLUXES

Andrei G. Demekhov[1], Tatyana A. Yahnina[1], and Tatyana A. Popova[1]

Polar Geophysical Institute, Apatity, Russia

Introduction. Precipitation of energetic charged particles from the ring current and radiation belts into the ionosphere forms an important loss channel for these particle populations [1-6]. Precipitating relativistic electrons may affect the upper atmosphere chemistry [7]. These factors explain extensive studies of properties and mechanisms of the precipitation. Resonant interactions with wave turbulence in the magnetosphere serve as one of the main precipitation mechansims. Quantitative assessment of these effects is a subject of ongoing active research.

In this paper, we present the results of a study of wave activity and related precipitation of relativistic (> 800 keV) electrons during a moderate magnetic storm of 10 to 17 October 2017. A characteristic feature of this storm is an intense substorm activity during both main and recovery phases. We focus our attention on the wave activity in the very-low frequency range (VLF, ~1 to ~10 kHz) and try to reveal a qualitative and quantitative relationship between the wave parameters in the magnetosphere and precipitating electron flux.

Some general results about relativistic electron precipitation (REP) during the considered time interval can be found in [8]. Similar to that paper, we use NOAA/POES and MetOp low-orbit spacecraft data on particle fluxes (from MEPED instruments). For VLF waves and energetic particle fluxes in the magnetosphere, we use the data from Van Allen Probes (former RBSP) and ERG/Arase spacecraft.

Event characteristics. Figure 1 shows the solar wind parameters and geomagnetic activity indices during the event, and also presents statistical results on relativistic electron precipitation. These results are summarized from [8]. Three curves of different color on panels 1e and 1f show the results for three groups of precipitation events detected by low-orbiting spacecraft, according to the classification introduced in [1, 2].

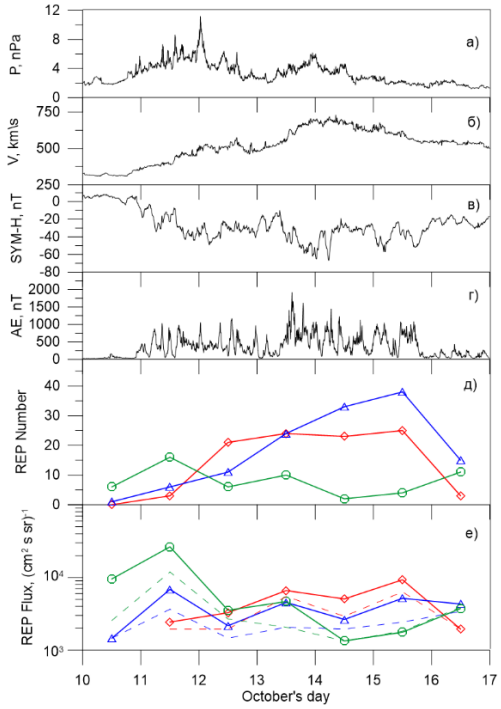


FIGURE 1. Solar-wind dynamic pressure (a) and speed (b), geomagnetic activity indices SYM-H (c) and AE (d), number of (e) and flux in (f) REP events belonging to groups 1 (red), 2 (blue), and 3 (green) during the event of 10-17 October 2017. Solid and dashed lines on panel (e) show mean and median values.

Group 1 is related to particle loss of adiabaticity because of strongly curved geomagnetic field lines [9]. Group 2 is accompanied by lower-energy electron precipitation (~40-100 keV) and is most probably related to the interactions with whistler mode waves [10]. Group 3 is characterized by the coincidence with localized precipitation of energetic protons (LPEP) [11] and often is accompanied by Pc1 pulsations detected on the ground. This latter group is related to the resonant interactions with electromagnetic ion-cyclotron (EMIC) waves generated by ring current protons.

Figure 2 shows the VLF wave spectral density onboard Van Allen Probes and ERG as well as the plasma number density measured by those spacecraft during the entire event interval. These waves belong to whistler mode (polarization is not shown for brevity). ERG data shows fairly low wave activity, which may be related to spacecraft location in the evening sector. Emissions detected by RBSP are of two main kinds. The waves with frequencies near and below 0.5 f_{ce} (white line on the plots, f_{ce} is the electron gyrofrequency) that are mainly observed at low plasma density are chorus emissions, while the signals with frequencies near and above the lower hybrid frequency observed in the plasmasphere are plasmaspheric hiss.

Calculations. Using RBSP wave data, we calculated the pitch-angle diffusion coefficient for low pitch angles. Only waves with low wave normal angles to the geomagnetic field (< 40°) were used for the calculations, and we assume them to propagate strictly along the geomagnetic field. Note that the data in Fig. 1 are related to relativistic electrons only (> 800 keV), and it is known [12, 13] that such

electrons are in cyclotron resonance with VLF waves only at sufficiently high magnetic latitudes (MLAT above 30°). So we present here the results of calculations assuming that the VLF waves with the same intensity as measured by RBSP are also present at MLAT = 40°. By using the pitch-angle diffusion coefficient $D_{\alpha\alpha}$, we calculate the parameter $Z = (8\, D_{\alpha\alpha}\, T_b / \mu_c)^{1/2}$, where $\mu_c = \sigma^{-1}$ is the loss-cone size (σ is the mirror ratio of the geomagnetic trap), and T_b is the electron bounce-oscillation period. The Z parameter determines the degree of loss cone filling: the ranges $Z < 1$ and $Z > 1$ correspond to the weak and strong pitch-angle diffusion, respectively [10]. As is shown in [14] by using the well-known solutions of the theory of the cyclotron instability in the magnetosphere [10], the ratio of precipitating and trapped particle fluxes measured by a low-orbit spacecraft is an almost universal function of the Z parameter.

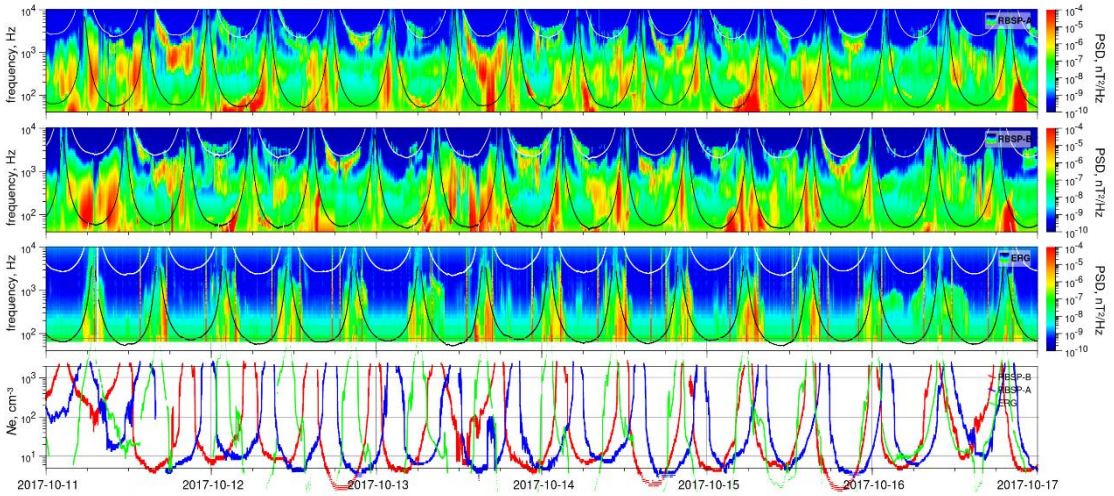


FIGURE 2. Very-low frequency wave intensities (magnetic component) measured by RBSP-A, RBSP-B, and ERG spacecraft during the interval 11-17 October 2017. White and black lines show, respectively, one half of electron gyrofrequency and lower hybrid frequency. Lower panel shows electron number densities along the spacecraft trajectories.

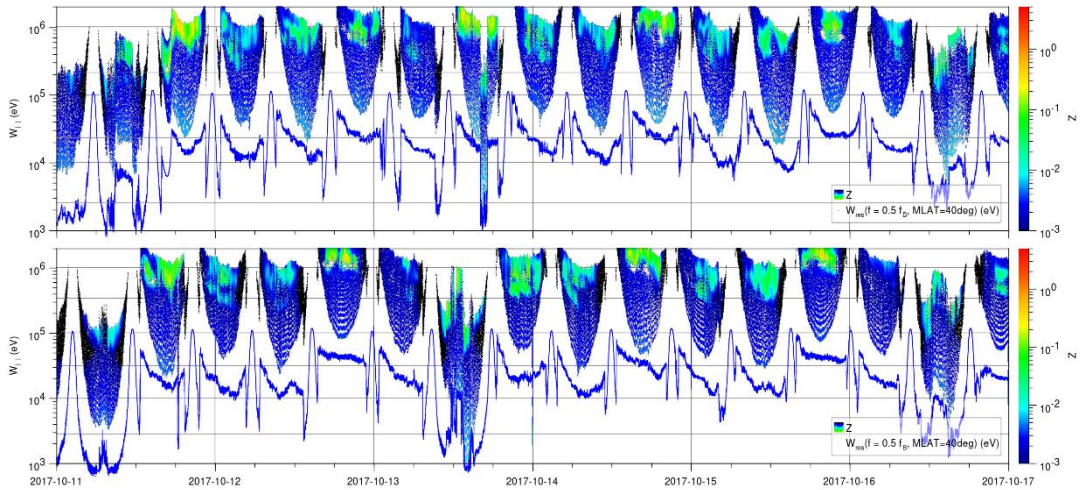


FIGURE 3. The parameter Z quantifying the strength of pitch-angle diffusion calculated by using RBSP-A (top) and RBSP-B (bottom) data obtained during the interval 11-17 October 2017. The measured wave intensities were assumed to be the same at a magnetic latitude MLAT = 40°. Blue lines show the cyclotron resonance energy for one half of electron gyrofrequency at MLAT = 40°.

Results. The results of Z calculation are shown in Fig. 3. Comparing these results with wave data in Fig. 2, we see that the highest Z values that are reached at ~1 MeV are provided by chorus emissions observed below 0.5 f_{ce}. These values in some cases reach Z ~ 1, i.e., a strong pitch-angle diffusion regime can be operating in the corresponding time-energy intervals. Most of the time and in the main energy range, however, $Z \sim 10^{-1}$ or lower. According to [14], the ratio of precipitating to trapped flux falls from ~1 at $Z \sim 1$ to $\sim 10^{-4}$ at $Z \sim 10^{-1}$. Trapped fluxes at ~1 MeV (not shown) are $\sim 10^6$ cm^{-2} s^{-1} sr^{-1}, i.e., they agree with precipitated fluxes of $\sim 10^3$ to 10^4 with $0.1 < Z < 1$.

Acknowledgments. *This work was supported by the Russian Science Foundation (grant No. 22-62-00048). We thank NOAA for the access to the POES/MetOp and OMNI databases https://cdaweb.gsfc.nasa.gov/, the RBSP and ERG teams for the access to the project data, in particular, EMFISIS (PI C. Kletzing), ECT HOPE (PI H. Funsten) and MAGEIS (PI J. Blake) instruments of RBSP, and PWE (PI Y. Kasahara) and MGF (PI A. Matsuoka) instruments of ERG project (PI Y. Miyoshi).*

1. Yahnin A.G., Yahnina T.A., Semenova N.V., Pashin A.B. Relativistic electron precipitation as seen by NOAA POES // *J. Geophys. Res. Space Phys.* 2016. V. 121, No.9. P. 8286-8299. DOI: 10.1002/2016JA022765.
2. Yahnin A.G., Yahnina T.A., Raita T., Manninen J. Ground pulsation magnetometer observations conjugated with relativistic electron precipitation // *J. Geophys. Res. Space Phys.* 2017. V. 122, No. 9. P. 9169-9182. DOI: 10.1002/2017JA024249.
3. Semenova N.V., Yahnin A.G., Yahnina T.A., Demekhov A.G. Properties of localized precipitation of energetic protons equatorward of the isotropic boundary // Geophys. Res. Lett. 2019. V.46, No.20. P.10932-10940. DOI: 10.1029/2019GL085373.
4. Grach V.S., Demekhov A.G. Precipitation of relativistic electrons under resonant interaction with electromagnetic ion cyclotron wave packets // J. Geophys. Res. Space Phys. 2020. V.125, No. 2. e2019JA027358. DOI:10.1029/2019JA027358.
5. Artemyev A.V., Demekhov A.G., Zhang X.-J., Angelopoulos V., et al. Role of ducting in relativistic electron loss by whistler-mode wave scattering. J. Geophys. Res. Space Phys. 2021. V.126, No. 11. e2021JA029851. DOI: 10.1029/2021JA029851.
6. Angelopoulos V., Zhang X.-J., Artemyev A.V., Mourenas D., et al. Energetic Electron Precipitation Driven by Electromagnetic Ion Cyclotron Waves from ELFIN's Low Altitude Perspective // Space Sci. Rev. 2023. V. 219. Art. no. 37. DOI: 10.1007/s11214-023-00984-w.
7. Thorne R.M. The importance of energetic particle precipitation on the chemical composition of the middle atmosphere // Pure Appl. Geophys. 1980. V.118, No.1. P.128-151. DOI: 10.1007/BF01586448.
8. Yahnina T.A., Demekhov A.G., Popova T.A., Lyubchich A.A. Relativistic electron precipitation related to the decreased magnetic field near the South-Atlantic Anomaly during the geomagnetic storm of 10 – 17 October 2017 // *Physics of Auroral Phenomena*, Proc. XLVII Annual Seminar. 2024. P.64-67. DOI: 10.51981/2588-0039.2024.47.014.
9. Sergeev V.A., Tsyganenko N.A. Energetic particle losses and trapping boundaries as deduced from calculations with a realistic magnetic field model // *Planet. Space Sci*. 1982. V. 30, No. 10, P. 999–1006. DOI: 10.1016/0032-0633(82)90149-0.
10. Trakhtengerts V.Yu., Rycroft M.J. Whistler and Alfven Ion Cyclotron Masers in Space // Cambridge Univ. Press. 2008. Russian Translation: Fizmatlit, Moscow. 2011. DOI: 10.1017/CBO9780511536519.
11. Yahnin A.G., Yahnina T.A., Frey H., Pierrard V. Sub-oval proton aurora spots: Mapping relatively to the plasmapause // *J. Atmos. Sol.-Terr. Phys.* 2013. V.99. P.61-66. DOI: 10.1016/j.jastp.2012.09.018.

12. Thorne R.M., O'Brien T.P., Shprits Y.Y., Summers D., Horne R.B. Timescale for MeV electron microburst loss during geomagnetic storms // *J. Geophys. Res.* 2005. V.110, No.A9. A09202. DOI: 10.1029/2004JA010882.
13. Miyoshi Y., Saito S., Kurita S., Asamura K., Hosokawa K., Sakanoi T., et al. Relativistic electron microbursts as high-energy tail of pulsating aurora electrons // *Geophys. Res. Lett.* 2020. V. 47, No.21. e2020GL090360. DOI: 10.1029/2020GL090360.
14. Demekhov A.G. Pitch-Angle Diffusion of Radiation Belt Electrons and Precipitating Particle Fluxes: Dependence on VLF Wavefield Parameters // Geomagn. Aeron. 2024. V. 64, No. 2. P. 264–271. DOI: 10.1134/S0016793223601114.

PROPERTIES OF RELATIVISTIC ELECTRON PRECIPITATION IN YEARS OF QUIET (2017) AND DISTURBED (2023) GEOMAGNETIC CONDITIONS

Tatyana A. Popova, Tatyana A. Yahnina and Andrei G. Demekhov

Polar Geophysical Institute, Apatity, Russia

Introduction. This work investigates the impact of geomagnetic and solar activity on relativistic (with energies >700 keV) electron precipitation (REP) events, observed in the auroral and subauroral regions at altitudes of ~850 km (based on NOAA/POES and MetOP satellite data). Two years were selected for analysis, one (2017) with low and the other (2023) with high solar activity. Catalogues of events were compiled for these two periods when relativistic electron precipitation (REP) was observed near the Lovozero observatory and its magnetically conjugate region in the Southern Hemisphere. The vicinity of the observatory was defined as a longitudinal sector extending 75° in magnetic longitude; this area was chosen to correlate precipitation with ground-based observations of VLF waves and Pc1 geomagnetic pulsations. In the obtained catalogues, the events were classified into three groups according to the criterion presented in the works [1, 2]. Each group in this classification has distinct formation mechanisms. We analyze the occurrence rates of REP events and the fluxes of both trapped and precipitating energetic electrons within each group, examining their dependence on solar wind parameters (e.g., velocity, IMF Bz) and geomagnetic conditions (Kp, Dst, and AE indices) during high and low solar activity phases.

Data sources. The work used data from low-altitude polar-orbiting satellites MetOp and NOAA/POES (orbit altitude ~850 km, orbit period ~102 minutes). Each satellite carries identical Medium Energy Proton and Electron Detectors (MEPED), featuring two pairs of directional telescopes: electron and proton. In each pair, one telescope is directed toward the zenith and measures the fluxes of precipitating particles at auroral and subauroral latitudes, while the other is directed against the direction of motion and measures the fluxes of trapped particles. Data from the induction magnetometer of the Lovozero ground observatory (LOZ; 68°N, 35°E) of the Polar Geophysical Institute was also used. Solar activity levels were quantified using sunspot numbers and flare indices from the Solar Influences Data Analysis Center (SIDC, Belgium).

Results. To determine the influence of solar activity on REP, two one-year periods were selected for analysis. Quiet conditions were examined using 2017 data, which coincided with the declining phase of solar cycle 24 — the weakest cycle of the past century. At the time of this study, the most active year over the last two solar cycles with a complete database was 2023. It did not turn out to be the year of

the maximum of cycle 25, which continued to grow, but in terms of the number of sunspots it exceeded the expected value of 115, which indicates fairly high solar activity during this period. According to SIDC records, the mean annual sunspot numbers — calculated as the arithmetic average of daily total sunspot counts — were 21.7 for 2017 and 125.5 for 2023. In total, there were 4,575,885 NOAA/POES satellite passes near LOZ and the conjugate region in the Southern Hemisphere in 2017 (including 2,869 REP events), and 4,342,911 passes in 2023 (including 1,676 REP events). The magnetic conjunction enabled comprehensive monitoring of geomagnetic pulsations correlated with magnetospheric dynamics and take them into account when classifying REP events into four groups. Precipitation events of the 1st group are associated with violation of the first adiabatic invariant due to the small curvature radius of the field lines in the nightside magnetosphere [3]. These precipitations are observed near the boundary of isotropy of energetic electron fluxes. The second group is characterized by the observation of REP simultaneously with intense precipitation of energetic (>40 keV) electrons, which suggests their probable association with the excitation of VLF waves, which can be responsible for the precipitation of energetic electrons. Events of the 1st and 2nd groups are observed during PiB pulsations and intense PiC. REP of the third group, accompanied by localized precipitation of energetic (>39 keV) protons, are associated with EMIC waves. In this case, the ground station almost always records pulsations in the range of 0.2-5 Hz (Pc1, IPDP). A fourth group was also identified, which included all extended-duration events that occupied a wide region equatorward of the electron and proton isotropy boundaries. In this case, there are no intense precipitations of protons and energetic electrons, and at the ground station there may be no disturbances or very weak pulsations in the range of 0.2-5 Hz are observed.

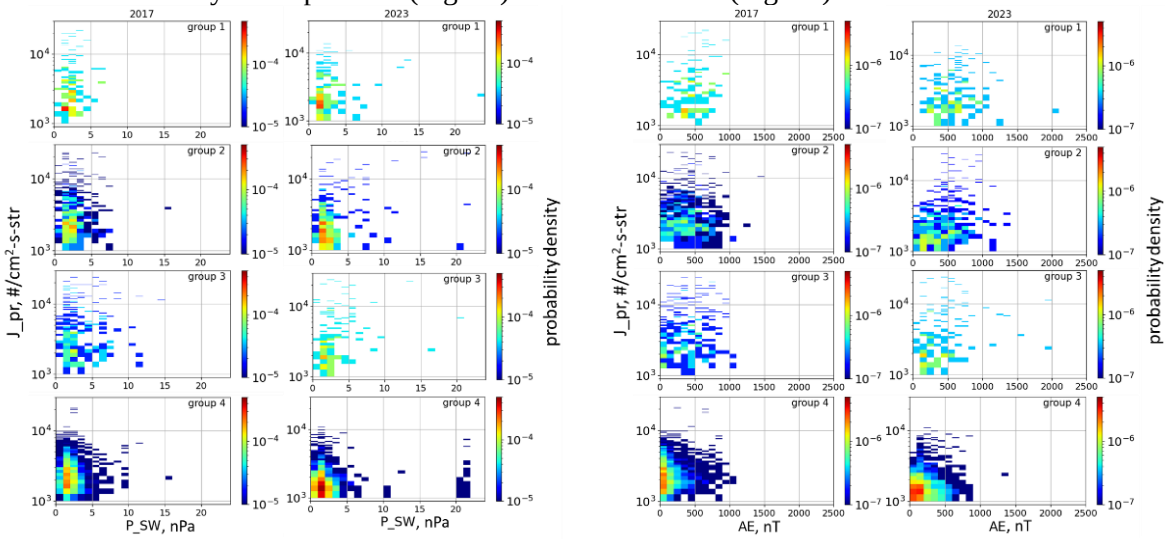
TABLE 1. Event classification over two years and mean (median) values of selected geophysical parameters.

	1 group		2 group		3 group		4 group	
	2017	**2023**	**2017**	**2023**	**2017**	**2023**	**2017**	**2023**
Number of the REP events	104 3,6%	118 7%	463 16%	265 16%	242 8%	121 7%	2087 72%	1172 70%
Northern Hemisphere	47	43	123	80	124	52	32	13
Southern Hemisphere	57	75	340	185	118	69	2055	1159
AE index, nT	487 (482)	588 (580)	391 (366)	448 (444)	413 (390)	439 (396)	161 (89)	205 (147)
Dst index, nT	-26 (-23)	-32 (-29)	-19 (-18)	-24 (-24)	-10 (-10)	-10 (-9)	-7 (-6)	-13 (-11)
Kp	3.4 (3.3)	3.4 (3.3)	3 (3)	3.2 (3)	2.9 (3)	2.8 (2.7)	1.7 (1.3)	1.9 (1.7)
P_{sw}, nPa	2.3 (2.2)	5.7 (2.0)	2.5 (2.2)	5.3 (2.0)	3.5 (2.6)	5.9 (2.7)	2.0 (1.8)	4.6 (1.5)
$V_{sw,}$ km/s	558 (557)	3536 (480)	521 (533)	2986 (479)	447 (420)	2925 (392)	441 (405)	3400 (423)

It can be noted that the number of events when REPs were observed in the studied regions was greater in 2017 than in 2023 (Tab. 1). At the same time, the number of events of the 1st group is almost the same in both periods, while for the remaining groups in 2023 the number of events decreased by 1.7 times compared to 2017 (while their share in the number of events remains nearly the same). Thus, precipitation of the 1st group is less dependent on solar activity, which is consistent with their formation mechanism. The substorm (AE) and storm (Dst) activity indices, as expected, reflect greater disturbance in 2023, with the exception of group 3, where their values are comparable in both years. This situation can be explained by the fact that EMIC waves, which are associated with precipitation of relativistic electrons of group 3, are generated due to the development of ion-cyclotron instability under conditions of geomagnetic disturbance [4]. At the same time, the average values of the planetary index Kp for the

analyzed events have almost no difference between 2017 and 2023 and their values correspond toquiet enough geomagnetic conditions. The average values of pressure (P_{sw}) and solar wind speed (V_{sw}) in 2023 are noticeably higher, which confirms greater solar activity during this period.

To identify the properties of each REP group in quiet and disturbed conditions, the probability density distributions for all parameters were analyzed. In this paper, such distributions will be presented for the solar wind dynamic pressure (Fig. 1a) and the AE index (Fig. 1b).



(a) (b)

FIGURE 1. Probability density of REP events (J_pr) for each group depending on (a) solar wind pressure and (b) AE index

The probability density of precipitation of groups 1 and 4 at low values of solar wind pressure P_{sw} are similar for both periods, and for groups 2 and 3 the probability density in 2023 is noticeably higher. The latter fact, in spite of lower total number of events, is explained by concentration of events in the interval 1-3 nPa. For group 1 in 2017, the presence of higher fluxes of precipitating electrons can be noted. For all groups in 2023, with an increase in the parameter, the probability of observing precipitation appears (and for groups 1-3 it is significant), unlike 2017, in which only rare events of about 15 nPa are possible for groups 2-4.

The probability density of events in groups 1-3 remains high with increasing AE index values. However, in 2023, no events from groups 2 and 4 were observed when AE exceeded 1500 nT, while groups 1 and 3 maintained significant probability densities even at AE values around 2000 nT. During the period of high solar activity (2023), the electron flux in group 2 showed a clear increase with rising AE index values.

Summary and conclusions. We analyzed relativistic electron precipitation (REP) events observed at ~850 km altitudes near the LOZ, comparing event properties across four classification groups during two distinct solar activity periods: near solar minimum (2017) and near maximum (2023). The total number of detected events in 2023 was 1.7 times lower than in 2017. This reduction may result from an inward shift of the precipitation region toward stronger magnetic fields during high solar activity, where cyclotron instability is weaker. Consequently, wave-associated precipitation (groups 2 and 3) likely occurs less frequently. This interpretation is supported by the consistent count of group 1 events (not wave-related) between both years, while the relative proportions of groups 2-4 remained stable, which excludes the technical insufficiency of the database for 2023.

Event analysis revealed that despite fewer occurrences in 2023, groups 2-4 exhibited higher probability densities due to more clustered parameter distributions, contrasting with the broader dispersion seen in 2017. Key characteristics of the probability distributions include: (1) group 1 precipitation shows weak correlation with solar activity across all parameters, and (2) groups 2-4 demonstrate higher occurrence probabilities during periods of enhanced solar activity.

The geomagnetic disturbance indices (AE and Dst) during the REP events varied by less than 20% between solar minimum and maximum years, while the planetary Kp index remained essentially unchanged. This modest variation in geomagnetic activity parameters may explain why the 2023 REP distributions showed less pronounced differences than anticipated, despite increased geomagnetic activity levels.

This work was supported by the Russian Science Foundation grant No. 22-62-00048. The authors thank NOAA for the access to the POES/MetOp and OMNI databases https://cdaweb.gsfc.nasa.gov/ and Solar Influences Data Analysis Center (SIDC) https://www.sidc.be.

1. Yahnin A.G., Yahnina T.A., Semenova N.V., Pashin A.B. Relativistic electron precipitation as seen by NOAA POES // *J. Geophys. Res. Space Physics*. 2016. V. 121, No.9. P. 8286-8299. DOI: 10.1002/2016JA022765.
2. Yahnin A.G., Yahnina T.A., Raita T., Manninen J. Ground pulsation magnetometer observations conjugated with relativistic electron precipitation // *J. Geophys. Res. Space Physics*. 2017. V. 122, No.9. P. 9169-9182. DOI: 10.1002/2017JA024249.
3. Sergeev V. A., Tsyganenko N. A. Energetic particle losses and trapping boundaries as deduced from calculations with a realistic magnetic field model // *Planet. Space Sci*. 1982. V. 30, No. 10 P. 999–1006. DOI: 10.1016/0032-0633(82)90149-0.
4. Semenova N. V., Yahnin A. G., Yahnina T. A., Demekhov A. G. Properties of Localized Precipitation of Energetic Protons Equatorward of the Isotropic Boundary // *Geophysical Research Letters*. V. 46. Is. 20. P. 10932-10940. DOI: 10.1029/2019GL085373.

GLOBAL MEDIAN MODEL OF THE IONOSPHERIC E-LAYER BASED ON RADIO OCCULTATION DATA

Valentin N. Shubin

Pushkov Institute of Terrestrial Magnetism, Ionosphere and Radio Wave Propagation of Russian Academy of Sciences (IZMIRAN), Troitsk, Moscow, Russia

In recent years, the radio occultation measurements of the Earth's atmosphere and ionosphere onboard low-orbit satellites using the global positioning system signals have become one of the main sources of ionospheric data. The satellite data provide information on the vertical distribution of electrons at various points on the Earth's surface, so their use makes it possible to construct the global ionospheric models. In this paper, an attempt was made to construct a global median model of the ionospheric E-layer (GMME) based on satellite radio occultation measurements using the expansion of the critical frequency *foE* and the height *hmE* in a series of harmonic functions. The expansion coefficients were determined using the least squares method [1].

To build the models, we used the radio occultation profiles of the electron density of the low-orbit satellites CHAMP (2001–2008), COSMIC (2006–2020), COSMIC-2 (2019–2023), FY-3C (2014–

2020), FY-3D (2019–2023), and FY-3E (2022–2023). From the obtained radio occultation profiles, the electron density maxima were identified in the altitude range of 90–135 km. In this case, “questionable” radio occultation profiles were removed using the special filters and median values. In addition, we constructed the filters to remove electron density profiles associated with large altitude gradients (sporadic E layers).

The constructed GMME model is compared with the International Model of the Ionosphere IRI (*foE*) [2], with the reference model of the ionosphere SMI (*hmE*) [3] and the data from ground-based ionospheric stations. **Figure 1** shows an example of the global distribution of *foE* at 00UT on 15-01-2024, calculated using the GMME and IRI models.

As can be seen from Fig. 1, the main difference in the *foE* distributions constructed using the GMME and IRI models is observed in the high-latitude region, where the *foE* value in nighttime conditions of the GMME model significantly exceeds the *foE* constructed using the IRI model. This is due to the fact that GMME reproduces the electron density of the ionosphere caused by particle precipitation in the auroral oval.

Figure 2 shows the latitude dependences of *foE* and *hmE* for 06 and 07 LT. It should be noted that the medians of ground-based and satellite data do not differ much from each other, which may indicate the possibility of constructing models of the ionospheric E-layer based on the radio occultation measurements.

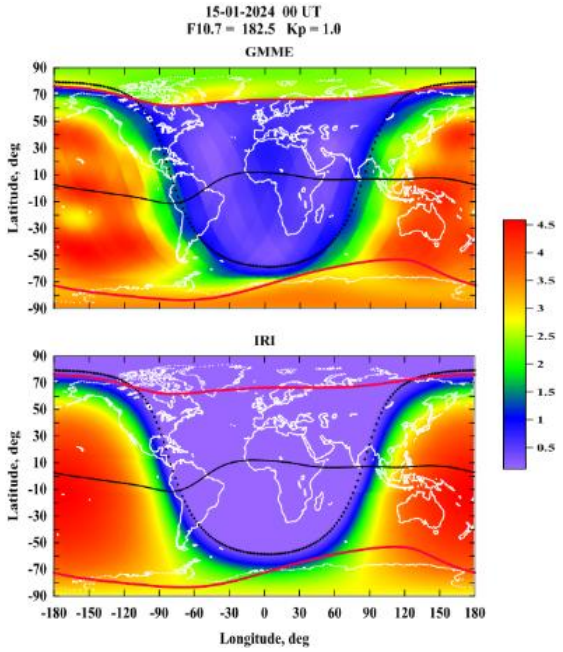


FIGURE 1. The global distribution of the critical frequency *foE* calculated by the GMME and IRI models. The red lines are the equatorial boundaries of the auroral oval, the black lines are the geomagnetic equator, and the dots are the terminator lines.

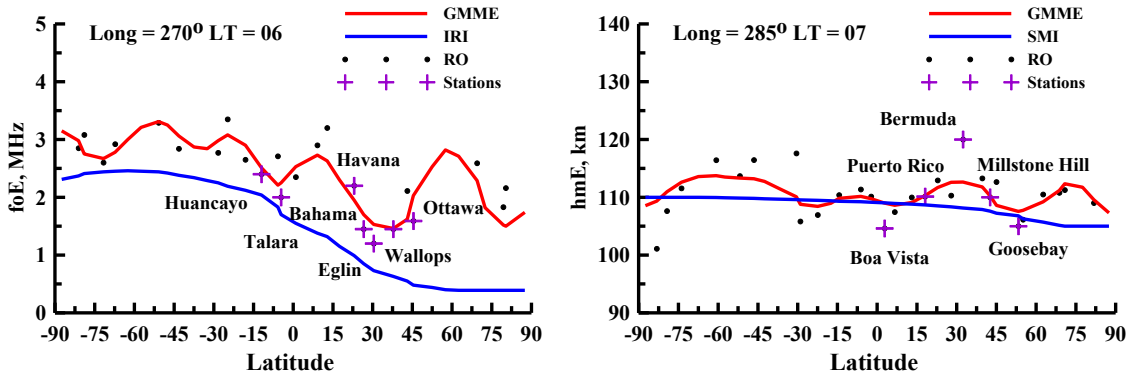


FIGURE 2. The dependences of *foE* and *hmE* on latitude are shown. The red lines – GMME, blue – IRI and SMI, dots – medians of radio occultation data, crosses – medians of ground-based ionospheric stations.

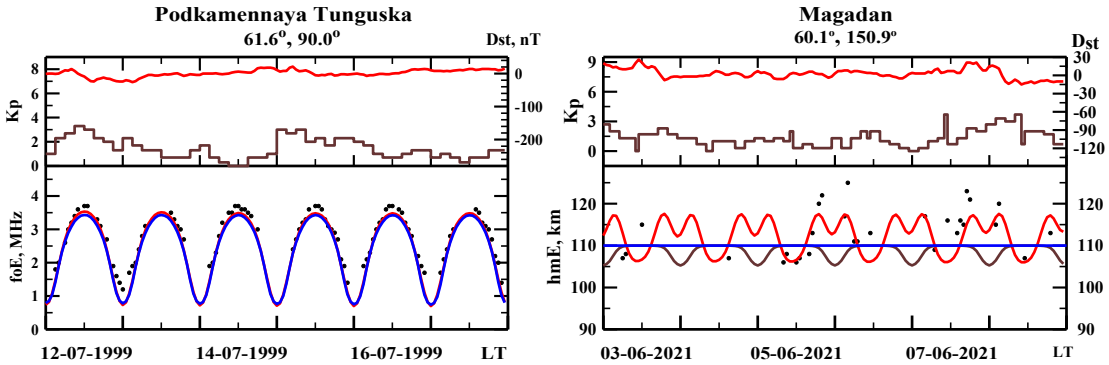


FIGURE 3. The dependences of *foE* and *hmE* at Podkamennaya Tunguska and Magadan station is presented on local time. On the top panel are geomagnetic indices: red lines – Dst, brown – Kp. On the bottom left panel: dots – hourly data of *foE*, red line – GMME, blue – IRI. On the bottom right panel: dots – hourly data of *hmE*, red line – GMME, blue – IRI, brown – SMI.

Figure 3 shows the dependences of *foE* and *hmE* on local time at Podkamennaya Tunguska (12–18.07.1999) and Magadan (03–08.06.2021) stations. As can be seen from Fig. 3, the critical frequencies of the E layer of the GMME and IRI models are practically the same with root-mean-square errors of 0.25 and 0.29 MHz, respectively. The height of the E layer maximum in IRI is 110 km for all LT hours. In the SMI model, the root-mean-square error is 7.1 km and the correlation coefficient is 0.45. In GMME, the root-mean-square error is 4.4 km and the correlation coefficient is 0.65.

Thus, based on the radio occultation data, a global median model for the critical frequency and the height of the maximum of the ionospheric E layer has been developed. The input parameters of the model are the integral indices of solar (with a 27-day history) and geomagnetic activity Kp (with a 6-hour history), as well as geographic latitude, longitude and time (LT or UT). The model's performance is confirmed by data from the ground-based ionosondes.

1. Shubin V.N. Global median model of the *F*2-layer peak height based on ionospheric radio-occultation and ground-based digisonde observations // *Adv. Space Res.* 2015. V. 56. P. 916–928. DOI: 10.1016/j.asr.2015.05.029.
2. Bilitza D., Altadill D., Truhlik V., Shubin V., Galkin I., Reinisch B., Huang X. International Reference Ionosphere 2016: from ionospheric climate to real-time weather predictions // *Space Weather*. 2017. V. 15. P. 418–429. DOI:10.1002/2016SW001593.
3. Chasovitin Yu.K., Shirochkov A.V., Besprozvannaya A.S. et. al. An empirical model for the global distribution of density, temperature and effective collision frequency of electrons in the ionosphere // *Adv. Space Res*. 1987. V. 7. No.6. P. 49–52. DOI: 10.1016/0273-1177(87)90270-5.

ELECTROMAGNETIC AND OPTICAL PHENOMENA IN THE ATMOSPHERE INCLUDING LONG-LIVED AND PLASMA OBJECTS

PHYSICS OF EXPANDING PLASMA CLOUDS AT ION GYRORADIUS SCALE

Ildar F. Shaikhislamov, Alexey A. Chibranov, Artem B. Berezutskii, Vitaly G. Posukh, and Marina S. Rumenskikh

Institute of Laser Physics SB RAS, Novosibirsk, Russia

Among the problems of plasma physics, the expansion of a hot plasma cloud into background magnetic field is one of the fundamental and long-standing. It is accompanied with several processes that are characteristic of a wide range of phenomena in astrophysical, near-Earth and laboratory plasmas. Despite the simple formulation, a large number of new effects have been discovered in the problem, one of which is the subject of this paper. We consider a sub-Alfvenic expansion in a rarified background ($V_o << V_A$), so as the plasma, being highly conductive, expels the external magnetic field, and is decelerated by it at a radius R_b determined by conservation of energy [1]: $E_o = 0.3 N_i m_i V_o^2 \approx R_b^3 B_o^2 / 3$.

Starting from the first active magnetospheric plasma releases AMPTE [2], and many laboratory experiments, it became apparent that at a low ion magnetization $R_L \sim R_b$ plasma cloud behaves rather differently in comparison to the MHD case $R_L << R_b$. The fragmentation of decelerating cloud boundary, so called flutes, grows much faster due to the Hall effects [3], in comparison to the classic Kelvin-Helmholtz instability. The other novel behavior consists in an anomalously fast magnetic cavity collapse, which can't be explained by Coulomb or turbulent resistivity [4].

Laboratory plasma provides opportunities for detailed study in a wide range of parameters. For modeling space processes of an explosive nature, a laser-produced plasma is the most suitable tool. We report on experiments conducted at the large-scale laser-plasma facility KI-1 of ILP SB RAS. Spherical clouds were generated by a novel 4-beam regular tetrahedron irradiation scheme of a spherical pellet [5]. A CO_2 laser was used delivering ~200 J of energy in ~70 ns pulse with a microsecond tail. The pellet was put at a center of 5× Ø1.2 m cylinder chamber evacuated to a residual pressure of $\sim 10^{-6}$ Torr. A uniform magnetic field was applied inside the chamber by external coil. The measurements were carried out by movable probes consisting of combined three-component magnetic and double asymmetric Langmuir probes with a spatial resolution of 0.5 cm and a time resolution of 20 ns.

Figure 1 shows the LPC structure in free expansion and in a vacuum magnetic field. One can see the spherically symmetric plasma cloud, which develops pronounced flutes under the deceleration by magnetic field. Measurements at $B_o=0$ at various directions from the pellet allowed to deduce that the expansion velocity of the LPC front is about $V_o=100$ km/s, total number of ions in the LPC is about

10^{18}, while the average total energy is E_o=25 J. These corresponds to gyroradius of carbon ions C^{3+} R_L=10 cm, and deceleration radius R_b=17 cm.

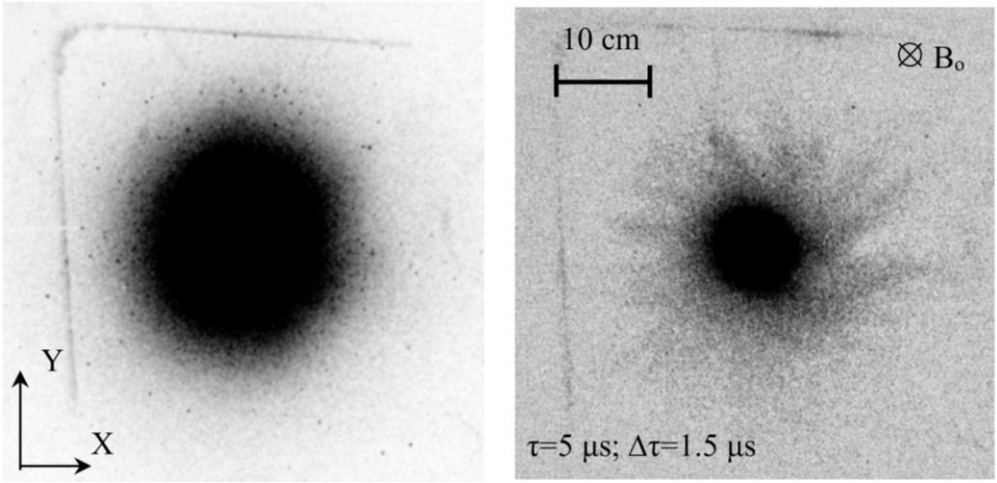


FIGURE 1. LPC images obtained without and in a magnetic field of B_o=400 G.

The main experimental finding is the anomalous cavity collapse. Figure 2 shows how the cavity is formed at the initial phase of LPC expansion, and reaches at about 2.5 μs the maximum radius of about R=14 cm, which is slightly less than theoretical radius R_b. Immediately after that the backward motion of the cavity front starts proceeding as a translation back into plasma. At the same time as cavity collapses, the plasma shows almost stagnant behavior without backward motion. Thus, magnetic field evolves independently of plasma density and on a time scale which is about two orders of magnitude shorter than the diffusion due to Coulomb collisions for the typical electron temperature of 10 eV.

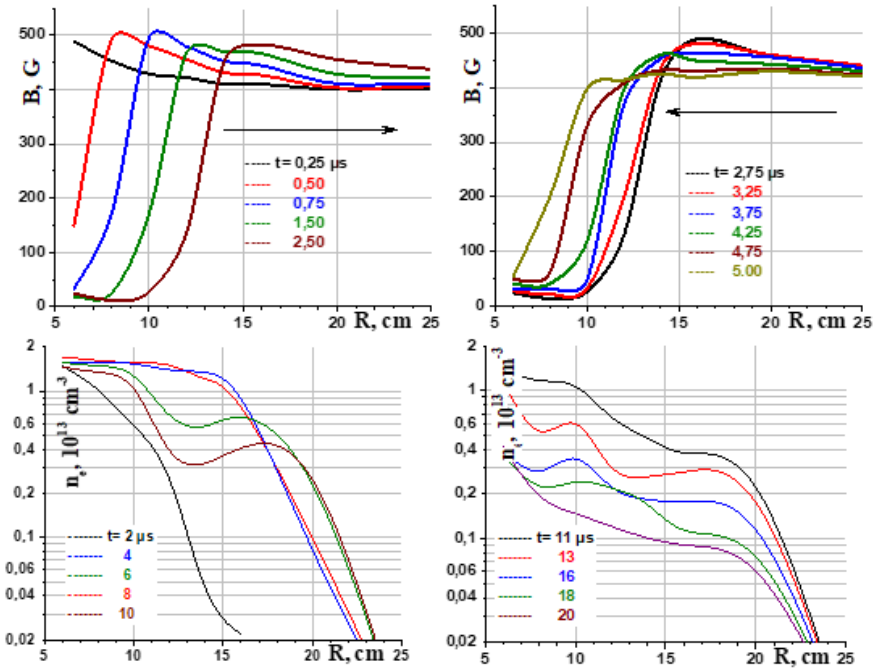


FIGURE 2. Spatial profiles at sequential times (marked by different colors) of the main component of magnetic field B_Z (upper panels) and plasma density (bottom panels). For magnetic field the curves are divided in two groups – cavity expansion (left) and collapse (right). Profiles have been obtained by multiple measurements at a number of spatial points.

For the study how the ion magnetization affects the cavity collapse we performed experiments with pellets of two diameters – 10 and 3 mm with other parameters exactly the same. The size of the laser target determines the number of ions in LPS and its total energy, while its velocity doesn't change. Table 1 lists the corresponding parameters of conducted experiments.

TABLE 1. Parameters of experiments. Gyroradius R_L is an average for H^+ and C^{3+} ions.

Pellet Ø, mm	$\mathbf{E_o}$, J	$\mathbf{V_o}$, km/s	$\mathbf{B_o}$, G	$\mathbf{R_L}$, cm	$\mathbf{R_b}$, cm	$\mathbf{R_L / Rb}$
3	4	106	200	13.3	13	1.1
10	25	121	200	15.1	22	0.69

For a 3 mm pellet, the plasma density is in average 2.5 times less than for 10 mm, while energy about 5 times less. Figure 3 shows the R-T diagrams of phase motion of plasma and magnetic field fronts. At first stage one can see the plasma expansion which drives the formation of magnetic cavity. For each pellet the diamagnetic cavity reaches its maximum which is slightly less than the theoretical value. After reaching the maximum size, the diamagnetic cavity reverses its motion. Plasma also exhibits backward flow after total deceleration. For a 10 mm pellet, the trailing edge of the magnetic cavern coincides well with the reverse plasma flow. For a 3 mm pellet the cavity collapse takes place significantly earlier, while reverse plasma flow is observed much later after that.

It was found that behind such dynamics of magnetic field is the Hal processes described by the Hall term in the Ohm law, $\partial \mathbf{B}/\partial t = rot\left(\mathbf{V}\times\mathbf{B} - \mathbf{J}\times\mathbf{B}/ne\right)$. Diamagnetic azimuthal current generates the azimuthal magnetic field (or Hall field). When the plasma density is low enough, the Hall currents, instead of ions, drive the main magnetic field via the term $\mathbf{J}\times\mathbf{B}/ne$. Hall magnetic field has a distinctive quadrupole (bipolar) structure, changing sign at crossings between quadrants in plane which includes the main magnetic field. Physically similar picture takes place at an ion-inertia region around X-point in a well-known reconnection problem.

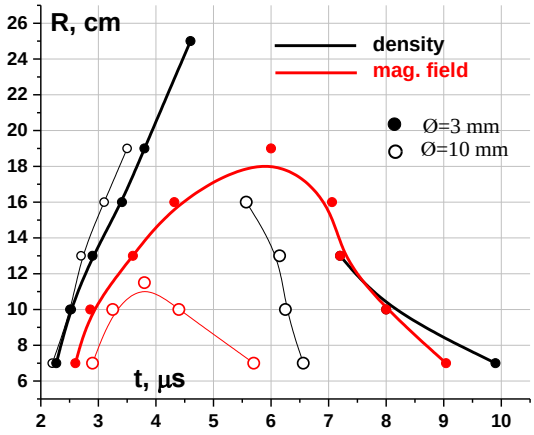


Figure 3. Time-of-flight diagrams of the plasma front motion and the plasma reverse flow (black lines), front of expansion and collapse of the magnetic cavity (red lines) for a 10 mm pellet (solid circles) and a 3 mm pellet (empty circles).

Experimental measurements fully confirmed the role of Hall fields. It was found that at the front of the collapsing cavity double Hall field is generated – one from the inner side of the current layer, and the second – outside. Both have quadrupole spatial structure, which was deduced from systematic multi-point measurements. Also, as the Hall field depends quadratically on B_o, it was confirmed that the sign of azimuthal field doesn't change with reversal of the main field. All these features are demonstrated in Figure 4.

Thus, in a series of experiments with expanding laser-produced plasmas we described a new process – fast penetration of magnetic field back into plasma which proceeds as a translation with a sharp gradient, rather than a diffusion. We have demonstrated that the diamagnetic cavity collapse is related with generation of the Hall fields. At late stage of LPC expansion when the plasma density becomes low, the Hall currents becomes much faster than ion motion and govern the dynamics of the main field.

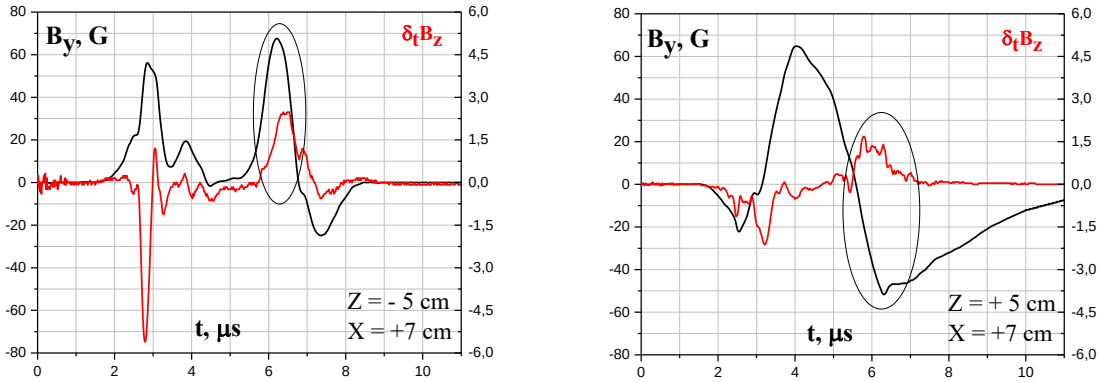


FIGURE 4. Dynamic signals of the main magnetic field B_z (time derivative showing the formation and collapse of the cavity, red lines) and Hall component (black) for two spatial points relative to the target (coordinates are indicated in the figure legend). Circles indicate the time of cavity collapse.

The study was performed under the ELAG program of National Center for Physics and Mathematics.

1. Rajzer Y.P., Surzhikov S.T. Magnetohydrodynamic description of collisionless plasma expansion in the upper atmosphere // AIAA journal. 1995. V. 33. No. 3. P. 486-490. DOI: 10.2514/3.12602.
2. Bernhardt P.A., Roussel-Dupre R.A., Pongratz M.B. et al. Observations and theory of the AMPTE magnetotail barium releases // *Journal of Geophysical Research: Space Physics*. 1987. V. 92. no. A6. P. 5777-5794. DOI: 10.1029/JA092iA06p05777.
3. Zakharov Y.P., Orishich O.M., Ponomarenko A.G. et al. Experimental study on the efficiency of slowing-down of exploding diamagnetic plasma clouds by a magnetic field // *Fiz. Plazmy* (Moscow). 1986. V. 12. No. 10.
4. Winske D., Huba J.D., Niemann C. et al. Recalling and updating research on diamagnetic cavities: Experiments, theory, simulations // *Frontiers in Astronomy and Space Sciences*. 2019. V. 5. P. 51. DOI: 10.3389/fspas.2018.00051.
5. Berezutsky A.G., Chibranov A.A., Efimov M.A. et al. Sub-Alfvenic Expansion of Spherical Laser-Produced Plasma: Flutes, Cavity Collapse and Field-Aligned Jets // *Plasma Physics Reports*. 2023. V. 49. no. 3. P. 351-361. DOI: 10.1134/S1063780X22601195.

SPECIAL PROPERTIES OF BALL LIGHTNING

Vladimir L. Bychkov, Aleksandr A. Logunov, Dmitry V. Bychkov and Dmitry N. Vaulin

Faculty of Physics, Lomonosov Moscow State University, Moscow, Russia

The problem of ball lightning (BL) attracts attention due to the lack of an unambiguous point of view regarding this phenomenon. When analyzing, it is necessary to take into account many properties that often contradict the known properties of plasma. For example, the lifetime of the BL, known observational data indicate lifetimes in seconds and minutes. They significantly exceed the decay times of plasma in air, which is used in many BL models. Not only plasma glows, but also a hot [1] non-ionized gas, whose temperature is much lower than the plasma temperature of about 6,000 K [2]. At the same time, the glow time of a hot gas is significantly longer than the glow time of a plasma. Often, based on unreliable data, observers believe that the temperature of the BL is low, on the order of room

temperature [3], without taking into account that there is reliable data on the high temperature of the BL [4,5]. It would be difficult to explain the causes of ignition of various objects when exposed to BL if its temperature was lower than their ignition temperature, which is usually higher than room temperature. Therefore, when constructing a BL model, it is necessary to consider an object with a high surface temperature, but not equal to typical plasma temperatures.

Another important issue in constructing the BL model is the question of its shape. Why does the BL often have a ball shape? If it were purely plasma, its shape would not be stable. How can we explain the shape of the BL in the form of a ribbon, spiral [4] and folding from a ribbon into a ball without considering the possibility of the existence of a shell over the BL? Observers describe the BL as an object with a shell through which the inner regions of the BL or luminous components are visible [4]. It is known that when a BL is destroyed (when a gun is fired at it [5]), its surface disintegrates into luminous thin films that slowly fade over time. These observations show that the shell cannot be ionic or clustered, as it would disintegrate in microsecond times. The presence of a thin shell and a gas core may explain the passage of BL through small holes. A BL with an elastic shell with a gas core can explain the cause of loud explosions when the BL is destroyed [6,7]. Hollow and gas-filled spheres are obtained in practice and technology in "hot" conditions, for example, glass spheres are produced as waste in coal-fired power plants. So the formation of the shell is analogous to the known process of thermal rapid oxidation [8] of Si.

It is the presence of a solid elastic non-plasma shell that was not previously taken into account in BL models. Numerous observations and analysis of the interaction of BL with various objects [4,5] show that BL has an excessive electric charge of one sign. The presence of excessive surface charge during rotation of the BL will manifest itself in the form of a current, which will implement the magnetic field of the BL. In addition, an excessive charge can lead to an electric shock to the observer. Such a BL can be formed when a linear lightning strikes various, for example, metallic or some dielectric objects, BL with a metallic composition has been observed.

According to a simple BL model, this object has a shell and a core, and can be charged. It is formed when a discharge (electric or lightning) is struck, which transfers a lot of energy. Part of it is spent on evaporation of the substance with which it interacts: a vapor core and a shell of oxidized material are formed. When a linear lightning bolt charged unipolarly is struck, charges of the same sign can be transferred to the formed ball, i.e. a charged object is formed. The energy of such an object consists of the thermal and electrostatic energies transferred from the discharge. Energy of the object Part of the BL energy generated by heating the material during a lightning discharge is related to its parameters by the expression following from the Clapeyron -Mendeleev equation [1]

$$E_{term} = \frac{m}{\mu}\frac{\bar{R}T}{}, \tag{1}$$

where $\bar{R} = 8.3 \cdot 10^3$ J/(Kmol · K) is the gas constant. The other part of the BL energy is electrical, described by the relation [9]

$$E_{el} = \frac{1}{8\pi\varepsilon_0}\frac{Q^2}{R}\ , \tag{2}$$

where Q is the charge of BL, R is the radius of the ball excluding the shell, and $\varepsilon_0 = 8.85 \cdot 10^{-12}$ F/m is the electric constant. In this case, the internal energy of BL due to both excitation mechanisms is equal to

$$E_{\Sigma} = E_{el} + E_{term} = \frac{1}{4\pi\varepsilon_0}\frac{Q^2}{R} + \frac{m}{\mu}\bar{R}T\ , \tag{3}$$

and the energy density

$$W_{\Sigma} = W_{el} + W_{term} \approx \frac{3}{(4\pi)^2 \varepsilon_0} \frac{Q^2}{R^4} + \frac{m}{\mu} \frac{\bar{R}T \cdot 3}{4\pi R^3} \quad , \tag{4}$$

where m is the mass of the BL material (the substance of atoms), $\bar{R}$ is the universal gas constant, T is the temperature of the BL material, and μ is the molecular weight of the dissociated molecules. In (4), the shell thickness δ is neglected compared to R. For estimates in this case, silicon is considered, the content of which in the earth's crust reaches 50%. At the same time, in the model, we believe that SiO_2 dissociation occurs (μ_{Si+O2}=28.09+32), and the molecular weight of the resulting particles is μ_p = 30. The issue of a hot shell has not been yet investigated in the literature. The vapor consists of Si and O_2 particles, and the shell consists of a modified SiO_2 melt and its alloy with material components, and in the case of lightning interaction with metals such as steel, tin, aluminum, and solder, the vapor consists of atomic particles of the corresponding metal. For estimates, we assume that the temperature of the gas inside the shell is close to 2000 K and is equal to the typical boiling point of SiO_2. Studies on flexible shells [6] show that up to the moment of loss of stability, compressive stresses σ occur in all normal sections of the shell, the magnitude of which is equal to:

$$\sigma = \frac{q \cdot R}{2\delta}, \text{ or } \sigma = \frac{P_a \cdot R}{2\delta}, \tag{5}$$

where q is the uniformly distributed transverse load from the bulge, h is the thickness of the shell, R is the radius of the sphere, $P_a = 1,03 \cdot 10^5$ Pa is atmospheric pressure. The value

$$F_{el} = \frac{1}{4\pi\varepsilon_0} \frac{Q^2}{R^2} \tag{6}$$

is the expression known [9] for the Coulomb effect of charges of the same sign on the surface of a ball, Q is the charge of the ball. It follows from the expression for the Coulomb pressure of charges of the same sign acting on the shell,

$$P_{el} = \frac{Q^2}{4\pi^2 \varepsilon_0 R^4} \cdot \tag{7}$$

We believe that it is the processes of atomization of matter, Coulomb repulsion and mechanical compression of the shell that lead to the establishment of pressure inside the ball. The pressure force of SiO_2 type particles inside the ball is equal to

$$P_w = \frac{m}{\mu} \bar{R}T (\frac{4}{3}\pi R^3)^{-1} \approx \frac{m}{\mu} \bar{R}T \cdot \frac{3}{4\pi R^3}, \tag{8}$$

and the stress on the shell

$$\sigma = P_a \cdot R/(2\delta) = \frac{m}{\mu} \bar{R}T \frac{3}{4\pi R^3} R/(2\delta) = \frac{m}{\mu} \bar{R}T \frac{3}{8\delta\pi(R)^2} \cdot \tag{9}$$

From these expressions the equation follows for determining the balance of the forces acting on the surface of the BL, T is the temperature of the gas particles inside the BL. Table 1 shows the parameters of a charged ball depending on the magnitude of the charge and its radius for R=0.1 m and R=0.2 m.

TABLE 1. Parameters of a charged ball

R, м	Q, C	10^{-6}	10^{-5}	10^{-4}	10^{-3}	10^{-2}	10^{-1}
0.1	P_{el}, Pa	28.6	$2.86 \cdot 10^3$	$2.86 \cdot 10^5$	$2.86 \cdot 10^7$	$2.86 \cdot 10^9$	$2.86 \cdot 10^{11}$
0.1	W_{el}, J/m^3	21.5	$2.15 \cdot 10^3$	$2.15 \cdot 10^5$	$2.15 \cdot 10^7$	$2.15 \cdot 10^9$	$2.15 \cdot 10^{11}$
0.2	P_{el}, Pa	1.79	$1.79 \cdot 10^2$	$1.79 \cdot 10^4$	$1.79 \cdot 10^6$	$1.79 \cdot 10^8$	$1.79 \cdot 10^{10}$
0.2	W_{el}, J/m^3	1.34	$1.34 \cdot 10^2$	$1.34 \cdot 10^4$	$1.34 \cdot 10^6$	$1.34 \cdot 10^8$	$1.34 \cdot 10^{10}$

The table shows that the energy density of a charged BL increases with the amount of charge it possesses, while the charge pressure on the shell increases. Already at $Q > 10^{-4}$ C, the charge pressure on the shell is compared with the atmospheric pressure. In this case, an explosion is possible if the shell is accidentally broken.

Table 2 shows the internal energy of a BL as a function of its weight at a vapor temperature of T = 2000K, with a shell thickness of δ=100 microns, and with an average atomic weight of μ=30 (as for dissociated SiO_2), with a shell size of R = 0.1 m and R = 0.2 m. We present the stress across the shell (9).

TABLE 2. The internal energy of the BL as a function of weight at δ=100 microns, T=2000 K, μ=30.

R, m	M, kg	10^{-3}	10^{-2}	10^{-1}	1	10
0.1	W_{term}, J/m^3	$1.32\cdot10^5$	$1.32\cdot10^6$	$1.32\cdot10^7$	$1.32\cdot10^8$	$1.32\cdot10^9$
0.1	P_w, Pa	$1.32\cdot10^5$	$1.32\cdot10^6$	$1.32\cdot10^7$	$1.32\cdot10^8$	$1.32\cdot10^9$
0.1	σ, Pa	$6.6\cdot10^7$	$6.6\cdot10^8$	$6.6\cdot10^9$	$6.6\cdot10^{10}$	$6.6\cdot10^{11}$
0.2	W_{term}, J/m^3	$1.65\cdot10^4$	$1.65\cdot10^5$	$1.65\cdot10^6$	$1.65\cdot10^7$	$1.65\cdot10^8$
0.2	P_w, Pa	$1.65\cdot10^4$	$1.65\cdot10^5$	$1.65\cdot10^6$	$1.65\cdot10^7$	$1.65\cdot10^8$
0.2	σ, Pa	$1.65\cdot10^7$	$1.65\cdot10^8$	$1.65\cdot10^9$	$1.65\cdot10^{10}$	$1.65\cdot10^{11}$

At m = $5.15\cdot10^{-3}$ kg, the weight of the BL is compared with the weight of the ambient air. From the Table 2 it can be seen that the thermal energy increases with increasing weight of the BL, while the mechanical stress on the surface of the BL increases. With a BL mass of the order of 10^{-5} kg, the stress on the shell exceeds the atmospheric pressure and the BL can collapse at a random fluctuation of the BL parameters. Since BL has both the charge value and the mass value of matter, they can affect the conditions of existence, the effect of these factors will add up. In this case, the total energy density can vary widely and reach a value of 10^9-10^{10} J/m^3, which is in agreement with some observations [4,10]. At $Q > 10^{-3}$ C, the charge pressure on the shell and at m>10^{-5}kg, the pressure and voltage are compared with atmospheric pressure and the BL state becomes unstable. The high values of charges and masses at which anomalous BLs are observed raises the question of the reality of such BLs. BL with a mass of up to 10 kg fall into the energy density region of 10^8-10^9 J/m^3, which is not abnormal. There are observations when a moving BL broke several trunks of thick trees [8]. BL with a charge of 10^{-2} - 10^{-1} C fall into the observation area of an energy density of 10^{10}-10^{11} J/m^3.

The electric field of a highly charged BL. Estimates of the electric field strength near charged spheres having the parameters of the observed high-energy BL raise the question of why a discharge to the ground is not realized. This issue is investigated in detail in [4,5]. A charged sphere is considered in an electric field created by a large intrinsic charge of the ball. This electric field on the surface of the ball is large and capable of ionizing the air. A plasma with a high concentration of electrons appears, which in turn shields the electric field of the sphere, as if a metal screen appears. The resulting field decreases, ionization stops, and the plasma decays, but when the field is strong, $E = Q/4\pi\cdot\varepsilon_0\cdot R^2$, high-concentration electrons reappear and the plasma decay process repeats. Thus, plasma processes turn off the electric field. Plasma [4,5] in strong fields appears at $t \sim 10^{-9}$ and less, so that the electric field turns off. Therefore, no breakdown phenomena occur in this spatial region. There is a pulsating formation and death of plasma. This may explain the appearance of the oscillating electric field observed in BL. The presence of a super-strong electric field in a highly charged BL is not a limitation for the existence of BL in air, this conclusion is confirmed by the results of the implementation of corona discharges in fields on the surface of a high-voltage electrode 2 orders of magnitude larger than the breakdown [11].

Properties such as BL lifetime and equilibrium radiation of Bl are in detail discussed in [5].

A model of a BL is presented, which is a luminous charged sphere with a solid shell and a core filled with hot gas. The solid shell compresses the hot gas, and the electric charge on the surface causes the surface to stretch. The equations of the internal energy of this object due to the pressure of charges and the thermal expansion of a hot gas are presented. Calculations of the internal energy of this object, the pressure of charges on the shell and the shell stress caused by the pressure of hot gas inside the shell are carried out. Calculations show that the internal energy of this object can reach a value of 10^9-10^{11} J/m^3, which is in agreement with observations.

1. B.M. Smirnov, *Introduction to plasma physics*, Nauka, Moscow, 1987.
2. Y.S. Protasov, S.N. Chuvashev, *Physical electronics of gas discharge devices. Plasma electronics*, Higher School, Moscow, 1993, 249 p.
3. I.P. Stakhanov, *On the physical nature of ball lightning*, Energoatomizdat, Moscow, 1985.
4. A.I. Grigoriev, *Ball lightning*, Yaroslavl State University, Yaroslavl, 2006.
5. V.L. Bychkov, *Natural and Artificial Ball Lightning in the Earth's Atmosphere*, Springer Atmospheric Sciences, Switzerland, 2022. DOI: 10.1007/978-3-031-07861-3.
6. Y.E. Geguzin, *Bubble*, Nauka, Moscow, 1985.
7. Bychkov V.L., Sorokovykh D.E., Bychkov D.V. Luminous formation with a solid shell and a gaseous core // *Advances in Applied Physics*. 2024. No 3. P. 223-232. DOI: 10.51368/2307-4469-2024-12-3-223-232.
8. Zhang J.X.J., Hoshino K. Fundamentals of nano/microfabrication and scale effect // *Molecular Sensors and Nanodevices*. 2019. P. 43–111. DOI: 10.1016/b978-0-12-814862-4.00002-8.
9. Nikitin A.I, Bychkov V.L., Nikitina T.F., Velichko A.M., Abakumov V.I. // *IOP Conf. Series: Journal of Physics: Conf. Series.* 2018. V. 996. 012011 DOI:10.1088/1742-6596/996/1/012011.
10. A. Olkhovatov, *The Tunguska phenomenon of 1908*, BKL Publishers BINOM Knowledge Laboratory, Moscow, 2008.
11. Akishev Y.S., Grushin M.E., Kochetov I.V., et al. Transition of a multipin negative corona in atmospheric air to a glow discharge // *Plasma Physics Reports*. 2000. V. 26. P. 157–163. DOI: 10.1134/1.952826.

STUDY OF ELECTROPHYSICAL PROCESSES IN AN LONGITUDINAL HETEROGENEOUS PLASMA SWIRL FLOW

Anatoly I. Klimov

Joint Institute for High Temperatures Russian Academy of Sciences, Moscow, Russia

It is well known that inside large atmospheric vortices, such as tornadoes or whirlwinds, complex electrical, optical and acoustic phenomena associated with the process of electrical charging of the heterophase in the vortex flow can be observed [1]. It is noted that linear and ball lightning are observed inside the core of the atmospheric vortexes. Electrophysical and optical precursors were often observed before the formation of a tornado.

The purpose of this work is to study the electrophysical processes in an longitudinal heterogeneous plasma vortex formed in the working gas flow: air flow + water vapor (aerosol). We hope that the results of this work can be used for explanation the physical mechanism of the creation of the above-mentioned plasma formations inside a tornado, as well as in studying the energy flows inside natural tornadoes and whirlwinds.

To study the tasks, a laboratory plasma reactor PVR was created. This reactor was described in detail in our previous works [2, 3]. In this work, we used a PVR in which the longitudinal size of the plasma zone varied from 40 mm to 600 mm, Fig. 1. The swirl heterogeneous gas flow was created using a vortex generator with four tangential nozzles. The diameter of the working section was 60 mm, its length was 500 mm. An longitudinal electric discharge in the working chamber was created using axial nickel electrodes with a diameter 6 mm and a powerful modulated RF generator.

Typical experimental conditions were the followings:

Distance between electrodes	180 mm
Type of discharge	modulated RF discharge
RF frequency	450 kHz
Frequency of discharge modulation	10 Hz - 100 kHz
Working gasflow	air + water vapor
Air flow rate	M_{Air} = 10 G/s
Water vapor flow rate	M_{H2O} ~ 1 G/s
Experiment time 600 s	

Main goals of this work. Study of scaling laws (similarity) of thermophysical processes at the PVR reactor. Study of features of plasmoid formation in longitudinal heterogeneous plasma created by a powerful RF discharge.

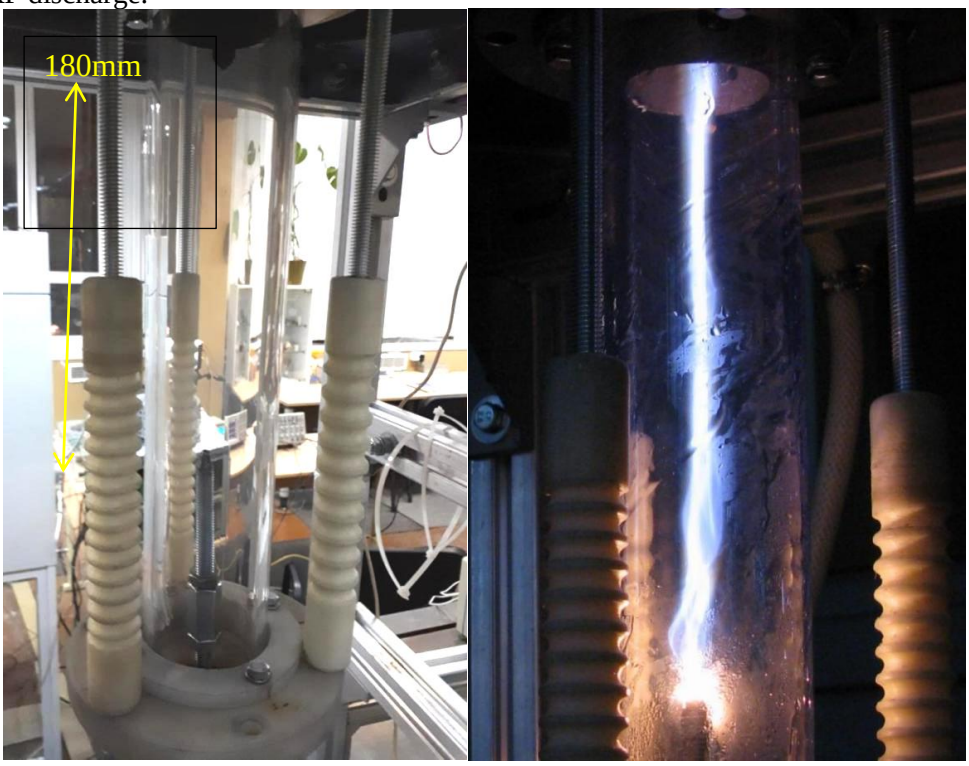


FIGURE 1. Modified PVR. The distance between the electrodes - 180 mm. High-frequency plasmoid in a heterogeneous mixture: H_2O steam + air = 1:10 (right).

1. *Heat release in an extended heterogeneous plasma.*

In calorimetric experiments on the PVR, air and water vapor flow rates were measured by using mass flow meters Tektronix. The spatial temperature distribution in the cross-section of the outlet nozzle was measured using a comb of calibrated thermocouples. Typical experimental results for measuring the output thermal power from the PVR are shown in this Table:

Output average temperature from the PVR	T_2 = 318C
Input average temperature of the mixture	T_1 = 64C
Output thermal power of the air flow	Q_{Air} = 2560 W
Output thermal power of steam	Q_{H2O} = 710 W
Total thermal power of the gas flow	Q = 3270 W
Consumed electric power	N_e = 1070 W
Calibration of the PVR with argon flow (heat losses)	$K_p = Q_{Ar}/N_{e,Ar}$ = 0.5
Extra energy release K_{in}	$K_{in}=Q/N_e$= 3.1
Total value K_{in*}	$K_{in*} = K_{in}/K_p$ = 6.2 at K_p = 0.5

The output thermal powers of heated airflow Q_{Air} and water vapor flow Q_{H2O} were calculated using the following formulas:

$Q_{Air} = C_{p,Air}M_{Air}(T_2 - T_1)$; $Q_{H2O} = C_{p,H2O}M_{H2O}(T_2 - T_1)$

Conclusions to the section.

The obtained value $K_{in*} \sim 6$, achieved in this experiment with an longitudinal heterogeneous plasma (L=180 mm) significantly exceeds the value K_{in} = 2.4, obtained in an additional experiment with a short plasma (L= 40-50 mm), under other similar experimental conditions. This result is expected, since heat losses in a heterogeneous plasmoid (as in any heat source) are determined by the ratio of its volume to its surface, under the condition of a constant specific energy release of a specific plasma-chemical reaction. Possible physical mechanism explaining the extra thermal energy release in the PVR due to change of the internal bind energy of the transmuted element nuclears is considered below.

2. *Formation of local long-lived energy-intensive plasmoids (LEP) in the PVR.*

It was obtained that local spherical LEPs can form in a swirl heterogeneous flow (air + water vapor) in the PVR when creating a pulse-periodic discharge in it. A typical form of such a plasmoid is shown in Fig. 2. The diameter of such a LEP can reach 1-2 cm. Analysis of individual frames of a high-speed video film allows us to study the dynamics of the creation and death of such LEPs. It was found that LEPs are formed from the products of erosion or destruction of the cathode electrode material (nickel). At the moment switch on of a current pulse (pulse current above 10 A, pulse duration - 10 μs, pulse repetition frequency - 10 kHz), many microdroplets of molten cathode material (nickel) are observed near the cathode electrode region. The characteristic diameter of these droplets does not exceed 0.3 mm. When a microdroplet of molten metal enters the discharge channel, it undergoes a process of rapid evaporation. In this case, a spherical plasmoid consisting of nickel nanoclusters is formed around the microdroplet (see below). It was measured that the charge of these microdroplets is negative. Their potential is close to the cathode potential. They moved against the gas heterogeneous flow along the electric field. Many of them reached the anode and stuck to it. When the microdroplet evaporated with an electric anode streamer starting from the anode, the plasma shell was charged with a positive charge. Direct measurements of the electric potential of this plasma shell using electric microprobes confirmed this conclusion. Thus, a spherical plasma capacitor with a positively charged shell and a negatively charged core was formed. It is important to note that such a LEP was practically not drifted away by the incoming gas flow and did not move along the electric field (unlike charged microdrops). When the LEP approached the cathode, the positively charged shell was attracted to it (was blown away by the electric field), exposing the core-microdroplet, Fig. 2 (left). Thus, the process of LEP destruction near the cathode electrode is observed. This result also proves that the charges of the core and shell of the LEP are different. The final products of LEP decay were collected behind the cathode electrode using a water seal [2]. Then the water sediment was analyzed using an electron microscope and the EDS spectroscopy method. The analysis showed that the shell consists of nanoparticles. The characteristic size of nanoclusters was 10-30 nm. The results of the chemical analysis of the nano-clusters are given in our previous work [2]. These particles contain many new elements, such as Al, Si, Cu, Zn, etc., which were

absent in the initial material of the electrodes and reactor units. The author supposes that these chemical elements are obtained as a result of cold transmutation of the cathode material as a result of the low-threshold nuclear reaction LENR [3], during the interaction of nickel microdroplets with hydrogen ions (a product of the dissociation of water molecules). However, for the final confirmation of this hypothesis, it is necessary to conduct an isotopic analysis of the final products of the PVR using an ion mass spectrometer. Taking into account the change in the internal binding nuclear energy of the transmuted chemical elements can explain the significant extra energy release in the PVR reactor.

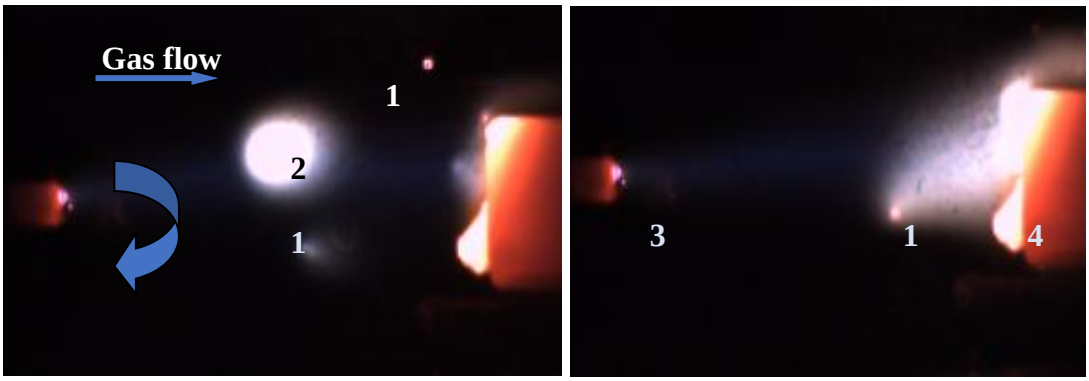


FIGURE 2. Formation and destruction of a spherical DEP. 1- microdroplets of molten cathode, 2- DEP (core + shell), 3- anode, 4- DEP shell, 5- cathode with melt

This investigation was performed with the financial support of the Ministry of Science and Higher Education of the Russian Federation (State assignment No. 075-01129-23-00).

1. D.V. Nalivkin, *Hurricanes, storms and tornadoes*, Nauka, Leningrad, 1970, p. 487.
2. Klimov A.I., Kazanskii P.N., Belov N.K., et al. Thermal Energy Release and Hydrogen Production in Swirl Heterogeneous Plasma-Chemical Reactor // *IOP Conf. Series: Journal of Physics: Conf. Series.* 2018. V. 1112. 012024. DOI: 10.1088/1742-6596/1112/1/012024.
3. Klimov A.I., Altunin S.E., Kulakovsky O.M., Zakharov A.V. Method for Obtaining Thermal Energy, Extracting Hydrogen and a Device for its Implementation // *Patent* No. RU 2 788 267 C1, 17.01.2023.
4. Klimov A.I. Decay-Instability of Transmuted Chemical Elements Obtained in LENR Experiment // *J. Condensed Matter Nucl. Sci.* 2022. V. 23. P.1-7. DOI:10.70923/001c.72605.

EVALUATION OF THE EFFECTIVENESS OF USING MEDIUM-ENERGY HEAVY IONS TO GENERATE LINEAR LIGHTNING

Vladimir V. Gorev[1,2 3] and Denis Yu. Smyslov[1,2]

[1]Bauman Moscow State Technical University, Moscow, Russia
[2]Mendeleev University of Chemical Technology of Russia, Moscow, Russia
[3]National Research Centre "Kurchatov Institute", Moscow, Russia

To date, lightning remains a phenomenon that has not been fully studied. The main difficulties in constructing a full-fledged theory are caused by the chaotic spread of affected areas, technical limitations in studying processes occurring inside a cloud environment, and the lack of similarity in the phenomena

of electrical breakdown of the atmosphere at different scales [1, 2]. A new approach to solving these problems was proposed in [3] using an experiment that allows simulating linear lightning in real conditions.

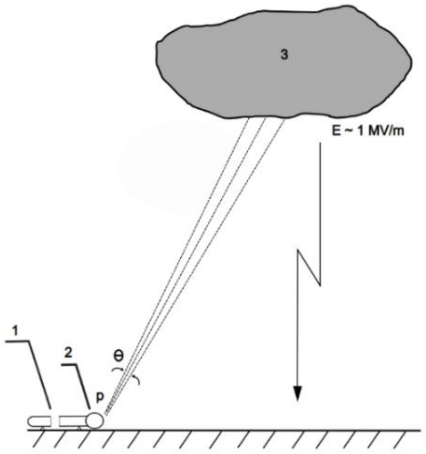


FIGURE 1. Diagram of generation of atmospheric electrical discharges: 1 - linear accelerator of medium-energy protons; 2 - deflecting magnets at the accelerator output; 3 - rain cloud; p - proton beam; and θ - angle of multiple scattering and deflection of protons in the cloud field. [3]

Fig. 1 shows the scheme of this experiment, the idea of which is to charge a rain cloud (natural or artificial) with a beam of high-energy protons using a medium-energy linear accelerator to an electric field strength of about 1 MV/m, at which a breakdown occurs in real atmospheric conditions.

The present work is a continuation of this topic and consists of evaluating the effectiveness of using ions of a wide range of masses (1 - 240 a.m.u) and energies (100 - 5000 MeV) in the proposed experiment.

Path length and angle of multiple scattering as a function of particle energy and mass. The main processes occurring during the passage of heavy charged particles in the atmosphere are associated with energy losses due to ionization and multiple scattering on the atoms of the medium. To study the nature of the dependence of these processes on the mass and energy of the particles used, the Bethe-Bloch formula and the formula for the mean square angle of multiple scattering were used [4, 5].

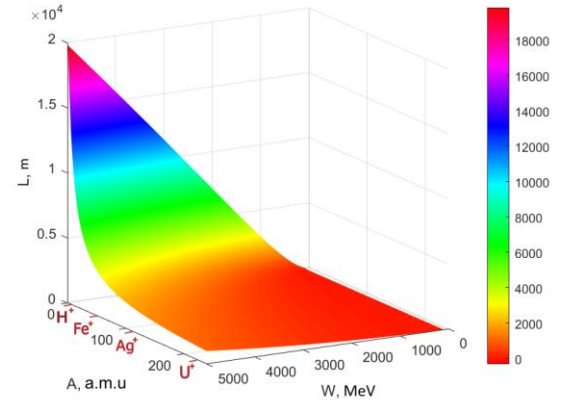


FIGURE 2. The mean free path in air depending on the energy and atomic mass of the particles.

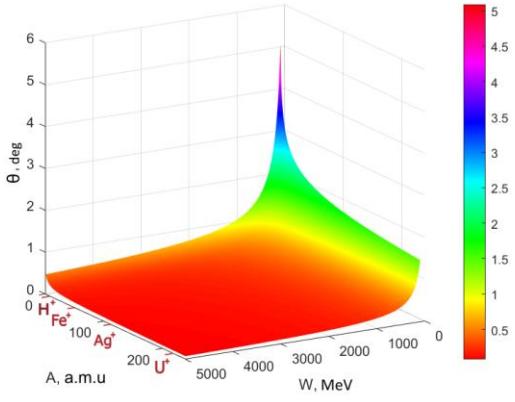


FIGURE 3. The angle of multiple scattering in air depending on the energy and atomic mass of the particles.

As a result of the calculations, it was established that the ion path length increases with increasing energy and decreases with increasing mass. In turn, the multiple scattering angle decreases both with increasing mass and with increasing energy (Figs. 2, 3).

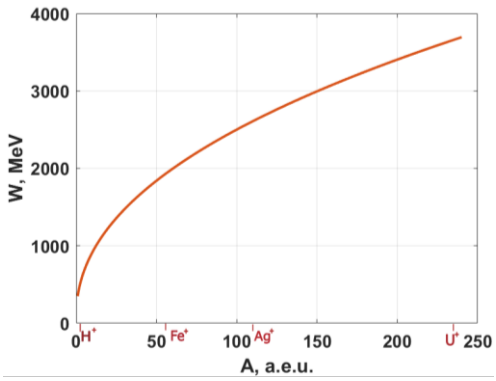
It follows from the obtained results that in order to reach a cloud at a given altitude, particles with a larger mass must be given a larger initial energy, but this will significantly reduce the angle of their multiple scattering. To clarify the effectiveness of using heavy ions, let us consider this situation in more detail using the example of a cloud located at an altitude of h = 500 m.

In the calculations, the following parameters were assumed to be fixed: the angle of departure from the accelerator relative to the horizon $\alpha = \pi/3$; the height of the cloud h=500 m; the density of the cloud ρ_{cloud} = 1,31 kg/m^3; the water content of the cloud ω= 0.017 kg/m^3; the accelerator beam current I_b = 0.1 A; the radius of the beam at the exit from the accelerator r_b = 0.01 m (the influence of the electric field of the cloud on the trajectory of the particles and the parasitic current discharging the cloud were not taken into account in this work) [3].

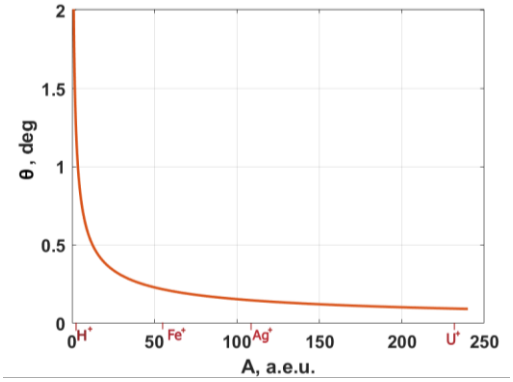
As expected, with increasing particle mass, the initial energy W required to reach the cloud at a height of 500 m increases, and the multiple scattering angle Θ decreases (Fig. 4(a), 4(b)). This leads to a significant decrease in the minimum cloud radius R required for all particles to enter and the cloud irradiation time t, sufficient to achieve an electric field strength of about 1 MV/m near it, at which breakdown occurs under real atmospheric conditions (Fig. 4(c), 4(d)).

Figure 4(e) shows the dependence of the maximum permissible beam current density j_s on the atomic mass of the element. As follows from [3, 6, 7], consideration of the Boguslavsky-Langmuir law in the case of spherical geometry is sufficient for a guaranteed estimate of the maximum permissible beam current density in the form of a cone. From a comparison of Fig. 4(e) with Fig. 4(f) it is evident that although the beam current density near the cloud j_p increases faster than the maximum permissible current density j_s with an increase in the particle mass, the extreme value $j_p \approx 0.035$ A/m^2 at the point A=238 a.m.u. still turns out to be an order of magnitude less than the maximum permissible current density $j_s \approx 0.28$ A/m^2 at the same point. Thus, the condition $j_p << j_s$, necessary for all particles to reach the cloud, is satisfied with a large margin over a wide range of their energies and masses.

(a)



(b)



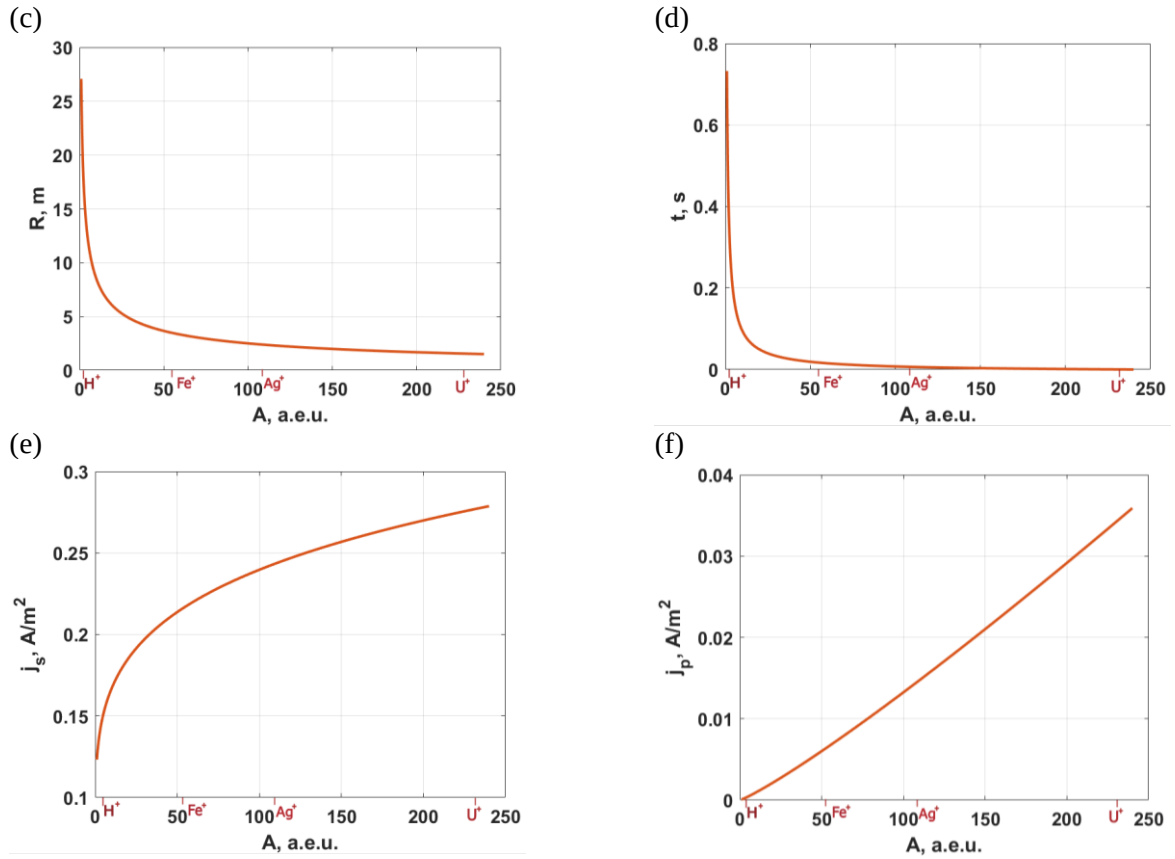


FIGURE 4. Dependence of various parameters of the problem on the atomic mass of particles at a fixed cloud height h=500 m. (a) Minimum ion energy required to reach the cloud. (b) Multiple scattering angle. (c) Minimum cloud radius required for all particles to enter. (d) Cloud charging time. (e) Maximum permissible beam current density of spherical geometry. (f) Actual beam current density near the cloud.

TABLE 1. Obtained values of experimental parameters for some elements.

Particle	Energy W, MeV	Scattering angle Θ, deg	Cloud radius R, m	Mass of water in a cloud, kg	Cloud charging time t, s
$^{+}_{1}$H	360	1.9975	25	1113	0.6777
$^{+}_{55}$Fe	1920	0.2159	4	4.56	0.0140
$^{+}_{108}$Ag	2590	0.1471	3	1.92	0.0058
$^{+}_{238}$U	3680	0.0938	2	0.57	0.0035

For greater clarity, we will show how the parameters required to reach a cloud at an altitude of 500 m will change when switching from using hydrogen ions $^{+}_{1}$H to iron ions $^{+}_{55}$Fe. As follows from Tab.1, the minimum initial energy must be increased by 6 times, then the scattering angle will decrease by 9 times, the minimum required radius of the cloud will decrease by 6 times, the required mass of water in the cloud will decrease by 244 times, and the cloud charging time will drop by 48 times.

Based on the results of the calculations, the following conclusions can be made regarding the use of heavy ions in the proposed experiment on the generation of linear lightning:
1. When using heavy ions, there is a significant gain in the required cloud size, the mass of water contained in it, and the charging time sufficient to form atmospheric electrical discharges.
2. The effect of space charge on the transport of heavy ions in the atmosphere is insignificant over the entire range of masses and energies.
3. The disadvantages of using heavy ions include technical difficulties in obtaining them and power limitations of existing linear ion accelerators.

1. E.M. Bazelyan, Y.P. Raiser, *Physics of lightning and lightning protection*, Fizmatlit, Moscow, 2001.
2. Dwyer J. R., Uman M. A. The physics of lightning // *Phys. Rep*. 2014. V. 534. No 4. P. 147. DOI: 10.1016/J.PHYSREP.2013.09.004.
3. Gorev V.V., Smyslov D.Y. Simulation of high power electrical atmospheric discharges using medium energy proton accelerators // *Journal of Technical Physics*. 2024. V. 94. No 10. P. 1720–1728. DOI: 10.61011/JTF.2024.10.58867.253-23.
4. B.S. Ishkhanov, I.M. Kapitonov, N. P. Yudin, *Particles and atomic nuclei*, Lenand, Moscow, 2019.
5. I.K. Kikoin, *Tables of physical quantities. Handbook*, Atomizdat, Moscow, 1976.
6. A.V. Ivanov, *Dynamics of charged particles and intense beams in stationary fields*, NSTU Publishing House, Novosibirsk, 2020.
7. V.L. Granovsky, *Electric Current in gas. Steady current*, Nauka, Moscow, 1971.

LASER PLASMA SPECTROSCOPY AND COLLISIONLESS INTERACTION IN MAGNETIZED MEDIA

Marina S. Rumenskikh, Alexey A. Chibranov, Artem G. Berezutsky, Vitaly G. Posukh, Pavel A. Trushin, Yuriy P. Zakharov, Ilya B. Miroshnichenko, and Ildar F. Shaikhislamov

Institute of Laser Physics SB RAS, Novosibirsk, Russia

The impulsive expansion of a localized plasma cloud into a relatively rarefied, magnetized surrounding plasma characterizes many astrophysical and space phenomena. In such rarefied environments, collisionless electromagnetic processes, rather than Coulomb collisions, determine the transfer of momentum and energy from the cloud to the background plasma [1,2].

Interacting plasmas in the space environment are often represented by ions of different types. Separate diagnostics of a wide range of ions is possible due to the development of spectral methods. In addition, the use of optical methods in laboratory modeling of space processes allows for the most accurate reproduction of experimental conditions using space telescopes, without introducing disturbances into the area under study.

This paper contains the results of laboratory modeling of the expansion of a quasi-spherical cloud of laser plasma into a magnetized background hydrogen plasma [3], in particular, measuring the rotation of ions of different types at the interaction boundary. The experiment was conducted on the vacuum stand "KI-1" of the Laboratory of Power Engineering of Superpower Lasers of the Institute of Physics of the Siberian Branch of the Russian Academy of Sciences. To demonstrate the effect of rotation of ions of laser and background plasmas, the emission spectra of ions of laser and background plasmas, as well as the data of ion flux measurements are presented.

The main goal of spectral diagnostics in the present series of experiments was to study the interaction of laser and background plasma ions with each other and with the magnetic field. It was

assumed that the features of this interaction would be expressed in the effect of rotation of background, predominantly hydrogen, plasma ions during its interaction with the laser plasma cloud and the external magnetic field due to the magnetic-laminar mechanism and the Lorentz force.

The ion rotation was observed in the equatorial (XY) plane. For this purpose, the optical axis was directed across the chamber, as shown in Fig. 1 (green line). Return ion flows were recorded with a longitudinal configuration of the optical axis (Fig. 1, orange line). To verify the ion rotation effect studied by spectral diagnostics, measurements of azimuthal plasma flows were performed using ion collectors installed at the boundary of the magnetic cavity (8 in Fig. 1 on the left).

Spectral measurements on the KI-1 stand were performed by a system consisting of an MDR-12 monochromator with CCD matrix registration and a photomultiplier tube, combined in one device [4]. The instrumental line broadening by the monochromator does not exceed 0.2 nm. The CCD array was used to record the shape of spectral lines in one operation. The matrix is a linear assembly of photodiode cells (2048 cells by 29 mm), and in combination with the monochromator, provides a spectral resolution of 0.033 nm / pixel. The CCD shutter pulse allows varying the signal recording duration, which in the present experiments varied from 3 to 20 μs depending on the measurement mode. The FEU-84 photomultiplier tube was used to record the radiation dynamics in the selected line at the monochromator output with a time resolution of at least 1 ns . To detect the dynamic signal of plasma glow and the spectral shape of the selected line in one operation, the division of the light flux at the output slit of the monochromator was used.

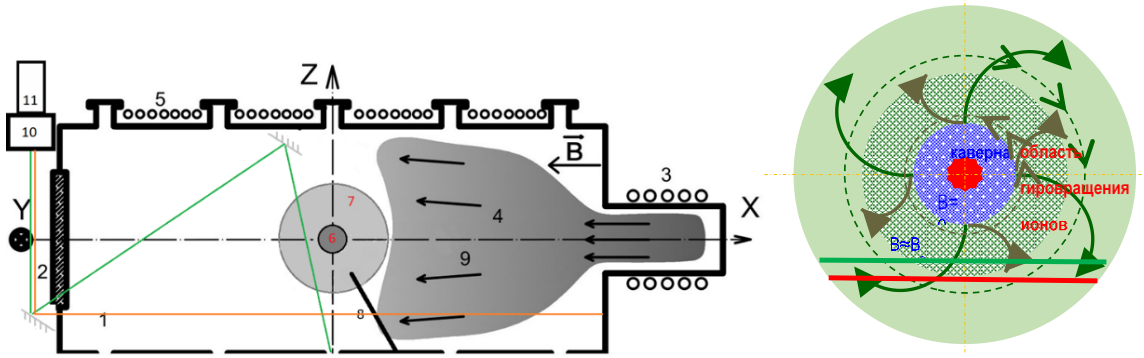


FIGURE 1. Measurement setup: 1 – 5×1.2 m vacuum chamber, 2 – viewing window, 3 – theta pinch, 4 – background plasma flow, 5 – solenoid, 6 – polyethylene target, 7 – laser plasma, 8 – ion collector, 9 – rotating mirrors, 10 – monochromator, 11 – combined device. Colored lines indicate the optical axis path (left panel). Schematic representation of the experiment for recording the effect of laser plasma ion rotation. The image is in the equatorial plane, the target is in the center, the optical axis location is marked by red and green lines (right panel).

To measure the rotation of the background plasma ions during interaction with the laser plasma cloud due to expansion into the magnetic field, a transverse configuration of the optical axis was used, at a distance of R ~ 20 cm from the target, corresponding to the boundary of the magnetic cavity, as shown by the red arrow in Fig. 1 on the right. The displacement of the optical axis to short distances (R ~ 17, inside the cavity, green line in Fig. 1 on the right) was performed using a Hartmann diaphragm. To record the spectral profiles in Fig. 2 on the left, an exposure of 15 μs was used, corresponding to the full expansion time of the laser plasma.

Hα line measurements showed significant Doppler shifts at a distance of 20 cm from the target at a field strength of 50 G (Fig. 2 on the left, red solid line), indicating the occurrence of azimuthal flows in the background plasma during the interaction with the spherical cloud of the laser plasma. This acceleration occurred due to the azimuthal electric field, which arose due to the motion of laser plasma ions in a uniform longitudinal magnetic field. As a result, the background plasma ions were first

accelerated transversely and then began to rotate around the magnetic field lines. Increasing the magnetic field to 100 G led to the compression of the cavity, and at a distance of 20 cm, the motion of laser plasma carbon ions was observed, as evidenced by the increase in the intensity of carbon lines (Fig. 2 on the left, blue solid lines). These results are in qualitative agreement with the conclusions of [5], where the expansion of laser plasma carbon ions into the background helium plasma was considered.

The effect of rotation of ions of different types was also monitored by collector diagnostics implemented by Faraday cup. Fig. 2 on the right shows typical collector oscillograms displaying the dynamics of the ion flows at different distances from the target in the mode of expansion of laser plasma into the background plasma with an external magnetic field. The collectors were installed in such a way as to obtain azimuthal ion flows directed clockwise ("slit up") and counter-clockwise ("slit down") under the condition of observing the rotation from the end of the chamber. At the boundary of the cavity, a counter-clockwise ion flow is observed, corresponding to the formation of azimuthal ion flows of the background plasma.

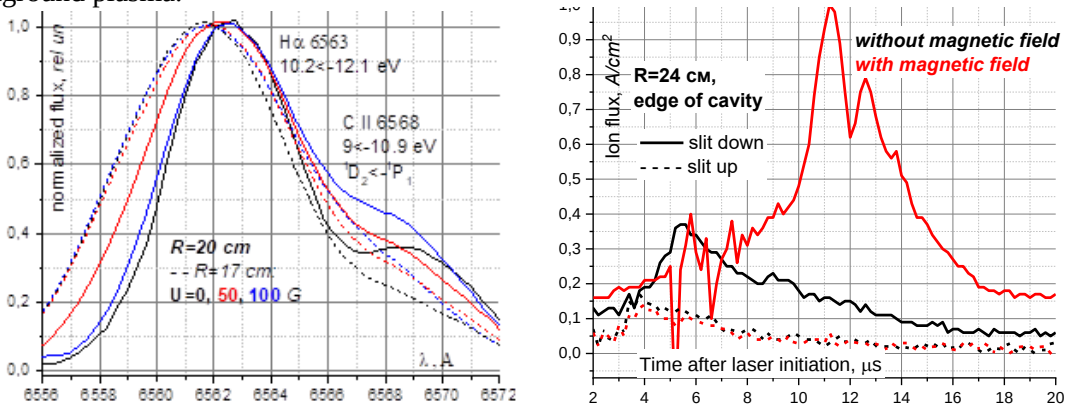


FIGURE 2. Emission lines obtained in different configurations of the optical axis – closer (R ~17 cm) and further (R ~20 cm) from the target, during the expansion of the laser plasma into the background and into the MF of different sizes (left panel). Oscillograms of collectors obtained during the registration of azimuthal ion flows clockwise (“up”, red and purple lines) and counterclockwise (“down”, black and gray lines), obtained at different radial distances from the target (right panel).

The experiments demonstrate that the interaction of laser plasma with magnetized background plasma leads to complex ion dynamics, including their rotation and formation of azimuthal flows. The observed phenomena, such as return proton flows and counterclockwise ion rotation, are important for understanding the physics of plasma interactions in astrophysical and space conditions.

The obtained results confirm that laboratory experiments can successfully model key aspects of astrophysical processes, which opens up new possibilities for studying plasma interactions under controlled conditions.

The work was supported by the Experimental Laboratory Astrophysics and Geophysics program of the National Center for Physics and Mathematics.

1. Bashurin V.P., Golubev A.I., Terekhin V.A. The collisionless deceleration of an ionized cloud dispersing in a uniform plasma in a magnetic field // J. *Appl. Mech. Tech. Phys*. 1984. V. 24. No 5. P. 614-620. DOI: 10.1007/BF00905870.
2. Golubev A.I., Terekhin V.A. Collisionless dispersion of an ionized cloud into a homogeneous magnetized plasma // J. *Appl. Mech. Tech. Phys*. 1978. V. 19. No 5. P. 602-609. DOI: 10.1007/BF00850600.
3. Berezutsky A.G., et al. Sub-Alfvenic Expansion of Spherical Laser-Produced Plasma: Flutes, Cavity Collapse and Field-Aligned Jets // *Plasma Physics Reports*. 2023. V. 49. No 3. P. 351-361. DOI: 10.1134/S1063780X22601195.

4. Efimov M.A., et al. Study of interaction of plasma flows by the method of spectral diagnostics of ion glow // *Bulletin of the Russian Academy of Sciences. Series physical*. 2020. V. 84. No 7. P. 977-981. DOI: 10.31857/S0367676520070091.
5. Bondarenko A.S., Schaeffer D. B., Everson E. T., et al. Laboratory study of collisionless coupling between explosive debris plasma and magnetized ambient plasma // *Physics of plasmas*. 2017. V. 24. No 8. 082110. DOI: 10.1063/1.4995480.

LONG-LIVED LUMINOUS FORMATIONS BY THE EROSIVE PLASMA GENERATOR

Vladimir L. Bychkov, Dmitry E. Sorokovykh, Dmitry V. Bychkov and Aleksandr A. Logunov

Faculty of Physics, Lomonosov Moscow State University, Moscow, Russia

Studies of long-lived luminous formations (LF) have been carried out for a long time [1-5], which is associated with the search for an explanation of the physical nature of natural ball lightning in connection with the possibility of applying this phenomenon in practice. In the second half of the 20th century, in studies of plasma discharges of various types, long-lived luminous formations were obtained, so in [2] it was reported that large luminous balls appeared when battery electrodes were closed in submarines, and in [3] luminous balls appeared when metal electrodes were closed in liquid. In [4] a specially designed powerful plasma generator was applied in which at destruction of one electrode appeared a sphere of about 10 cm size with a lifetime about of 1 second. In experiments [5] was realized and explosion of a wire-coil under action of strong current and a sphere of about 5 cm in size and a lifetime of about 0.5 seconds was realized.

There are known works on the physical and chemical production of ash microspheres using low-temperature plasma [6]. It has been established that the heating process in plasma conditions is much more efficient than in natural conditions [7]. They are realized in practice in hot conditions. One type of them, glass spheres, is found in waste at coal-fired power plants. In this case, a matter in seconds is converted from a gaseous state to a solid state with the release of a large amount of heat and an increase of pressure. The realization of spheres with solid cover was reported in [8].

A large number of experiments were conducted with the effect of different plasma natures on electrodes and materials, when luminous formations appeared in the discharge volume during the experiments, see, for example, [9, 10]. In this case, electrode materials and substances with which the plasma interacted played an important role.

In experiments [11] a silicon wool was placed inside the discharge tube, and when discharged, luminous balls with a thin shell flew out of a specially made hole in the tube. Some of them exploded. In the experiment was shown that luminescent formation had a shell.

In studies with capillary discharges [12, 13] based on standard schemes of [1], luminous balls also appeared when plasma jet was exposed to a surface of metal samples from solder. Mass spectrometric analysis of the small balls and cover material was held also. The composition of the sphere (a small ball) was O: Sn: Pb = 14.95: 67.59: 17.34%. The composition of the cover was O: Sn: Pb = 18.95: 54.71: 26.64%. From these numbers can be concluded that the cover and the ball (core) consist of the same substances. However, an amount of oxygen is higher in the cover. Its thickness was 10 μm and higher, it was detected by electronic microscope [12,13]. An appearance of the metallic ball in the “hollow” sphere when it falls into the water indicated the condensation of a vapor inside the metallic sphere at its

cooling in water. This confirmed the conclusion of [12,13] on the possibility of the objects formation filled with a metallic steam at interaction of the plasma with metallic objects.

The main unit of applied experimental set up is the capillary plasma generator. A principle scheme of which is presented in Fig.1. [1,5,12,13]. Usually, this capillary plasma generator has the following characteristics: pulse duration of 7 ms, pulse energy of 200-220 J, discharge voltage of 300-310 V, maximum pulse current of 100-120 A. Temperature measurements and the distribution of the electron concentration in the plasma jet created using this plasma generator with a plexiglass capillary were carried out earlier [14].

It followed from the experiments that the concentration of electrons (ions) varies along the discharge axis in the range 10^{16}-10^{18} cm^{-3}, and in the radial direction in the range 10^{15}-10^{17} cm^{-3}.

In this case, the axial temperature distribution in the plasma jet was 5000-6000 K in height about 8-9 cm and the radial temperature distribution of 4000-6000 K in radius is about 6 mm.

Table 1 shows typical parameters of a capillary plasma generator: the capacity of a capacitor bank, the energy inputted in the discharge, the maximum value of the current and the voltage; the duration of the pulse.

The material of the plates and wire was varied over the experiments, and for a given experiment, the material was either steel, aluminum, tin, solder (in case of wire its diameter was 1.5 mm, the composition: Sn – 59-61%, Pb – 39-41%), or copper.

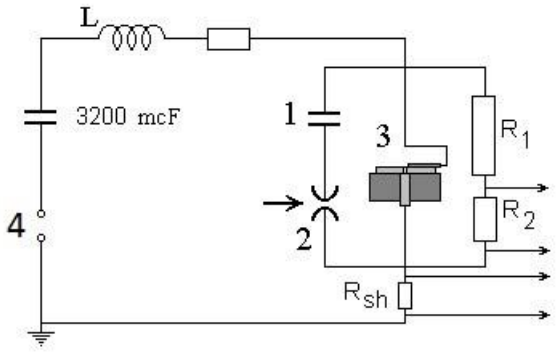


FIGURE 1. The general scheme of the capillary plasma generator. 1 is the initiating capacitance, 2 is the switch, 3 is the capillary, R1, R2 are the resistances of the voltage divider, Rsh is the resistance of the shunt to determine the discharge current. It is a circuit comprising a switchboard, a capacitance and a discharge device, which consists of flat electrodes separated by a dielectric with a capillary with a diameter usually of 2 mm and a length of 4.5 mm.

TABLE 1. Parameters of the plasma generator.

Capacitance, μF	The energy inputted in the discharge, J	I_{max}, A	U_{max}, V	t, ms
13070	1176	72.3	172	15.4
16360	1472	72.3	192	25.3

With an increase of the energy inputted in the discharge, the current and voltage on the discharge increase, as well as its duration. At the same time, about 5-7% of the initially inputted energy is consumed in the discharge The rest energy goes to radiation.

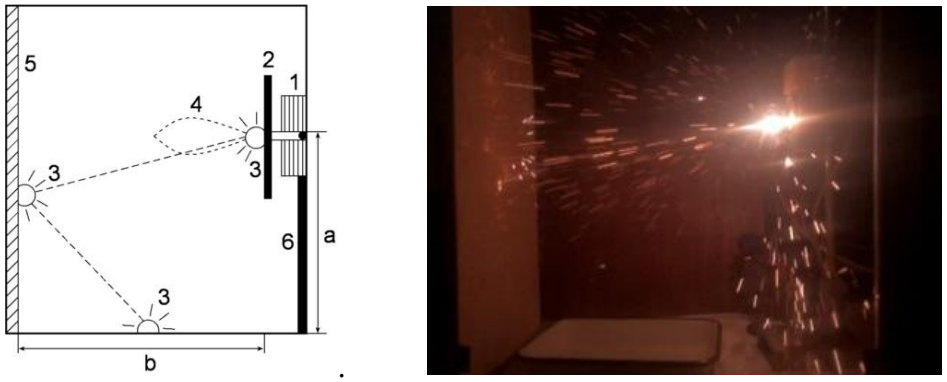
The potential value did not allow the plates to be charged above 10^{-9} C (estimates were made based on the charged disk model [15]). It was assumed that the applied voltage would affect the scattering of plasma-charged particles formed from the sample material. Initially we wanted to rise the charge of the metal plate, in order to realize charged spheres, however we did not detect change of behavior of glowing particles.

Steel, lead, aluminum, copper and solder (with a diameter of 1.5 mm, the composition of which is: Sn – 59-61%, Pb – 39-41%) were used as the object under study.

For realization of LF we applied the following experimental scheme represented in Fig.3a. Plasma jet from the plasma generator 1 interacts with metallic sample 2. A hole in it appears from which moves

plasma and the luminescent particles 4 including the big ones 3. One can see the trajectory of such particles. Sometimes they reach the wall of experimental setup and explode hitting the wall, or they are reflected off the wall and continue to move to the bottom of the installation, where they explode or go out. The photo of such particles motion is presented in Fig.2b.

The length **b** of the installation was about 30 cm and the height **a** of the plasma generator's location was about 25 cm. In all the experiments, the highest available energy inputted in the discharge was approximately 1.5 kJ.



a b

FIGURE 2. a) 1 – plasma generator; 2 – metallic target; 3 – luminous formation; 4 – area of plasma and luminescent particles; 5 – installation's wall; 6 – a rack; a – height of the plasma generator's location, b –length of the installation. b) The frame of luminous formation departure from the lead plate.

Some of the glowing objects exploded in the air. The diameter of the object at the 0.2 s is about 0.7 cm. By the video (frames are captured every 4.2 ms), it was possible to determine the lifetime from the moment of birth to the destruction of LF. The longest-lived LF in the experiments had a lifetime of about 7 s.

In all the conducted experiments the motion of LF one can describe as follows. When it comes into contact with some surface, it jumps to a certain height of about several centimeters. Then fell again and jumps up again. This movement was observed throughout its entire life, while the amplitude of each subsequent jumps decreased and the length increased.

Some of these LF's exploded when they fell on the surface of a table or paper, splitting into smaller LF's. They left burnt traces on the paper.

In experiments with lead, aluminum and solder target samples (not electrodes) we studied LF interaction with water. In all the cases similar to [12,13] when LF fell into a cuvette with water, a small metallic ball fell out of it, and a translucent shell with a thickness higher than 100 microns (which was determined by the electronic microscope) was observed on the surface of the liquid. In experiments with a copper plate, the shells were not observed, this indicated poor oxidation of copper samples. According to [12] the thickness of the shell is about 20 mcm. So the formation of the shell is analogous to the process of thermal rapid oxidation of Si [15].

In another series of experiments with lead, the fallen LF first decreased from the starting value (which was about 1.5 cm) to 1 cm, and then it began to grow. This lasted for 0.02 s, when it grew to 2 cm, and then began to slowly decrease. From the size of 1 cm it decreased to 0.5 cm in 3 seconds.

We carried out studies on the interaction of plasma of the capillary discharge with metal samples of aluminum, iron, copper, solder, etc. Main purpose was production of luminous formations by the capillary erosive plasma generator in different conditions. At the inputted energies in the plasma generator (1200-1500 J), the plasma of the jet interacted with a metal and formed a luminous formation with an internal vapor region and an oxide shell. The best results were obtained using aluminum, lead

and solder samples in which there was a noticeable formation of the shell. As the energy inputted increased, the size of the object increased.

At an energy input of about 1500 J, a formation with a diameter of up to 1.0-1.5 cm, with a shell thickness of up to 100 microns (which was determined by the electron microscope) and a lifetime of up to 7 s was observed.

These luminous formations sometimes exploded. They left traces in the form of dots of soot when they interacted with paper and traces of an explosion in the form of a star on the paper.

These formations are similar to those, which appear during thunderstorms in electric circuits and power sockets, because they have low electric charge they differ from natural ball lightning. However according to the parameters: long glow (long lifetime), the ability to jump, disintegration into several objects, high density of internal energy, they are analogs of real ball lightning.

1. Avramenko R.F., Bakhtin B.I., Nikolaeva V.I., Poskacheeva L.P., Shirokov N.N. Experimental study of plasma formations initiated by an erosive discharge // *J. Tekh. Fiz*. 1990. V. 60. No 12. P. 73-78.
2. Silberg P.A. Ball lightning and plasmoids // *J. Geophys. Res.* 1962. V. 67. P. 4941-4942. DOI: 10.1029/JZ067i012p04941.
3. Golka Jr. R.K. Laboratory-produced ball lightning // *J. Geophys. Res. Atmos*. 1994. V. 99. No D5. P. 10679-10681. DOI: 10.1029/93JD03579.
4. Kunin V.N., Pleshivtsev V.S., Furov L.V. Experiments on the study of the nature of ball lightning // *Teplofiz .Vysok. Temper*. 1997. V. 35. No 63. P. 866-870.
5. Vlasov A.N., Dubkov M., Byrobin M.A., Manoshkin A.B. Formation of dense plasma by electric explosion of toroidal spirals and creation of submillisecond generator with peak current up to 400 kA // *Int. XLII Conf. Plasma Phys. and TCB*, Zvenigorod, 2015, P. 260.
6. Volokitin G.G., Shekhovtsov V.V., Skripnikova N.K., et al. Physico-Chemical Processes of Spherical particle Production Using Low-Temperature Plasma // *Vestnik TGASU*. 2016. No 3. P. 139.
7. Bulina N.V., Gromyko A.I., Bondarenko G.V., et al. About globules formed at cooling of iron contained plasma // *The physics of metals and metallography*. 2006. V. 102, Suppl. 1. P. S.94-S.95.
8. Dorovskoj V.M., Elesin L.A., Stoliarov V.L., et al. Research of yields of an electric explosion of titanium foils by an electron microscope // *Priklad. Fiz.* 2006. No 4. P. 28-34.
9. Piva G.S., Pavão A.C., de Vasconcelos E.A., Jr. Mendes O., da Silva E.F. Production of ball-lightning-like luminous balls by electrical discharge in silicon // *Phys Rev Lett.* 2007. V. 98. 048501. DOI: 10.1103/PhysRevLett.98.048501.
10. V.L. Bychkov, *Natural and Artificial Ball Lightning in the Earth's Atmosphere*, Springer Atmospheric Sciences, Switzerland, 2022. DOI: 10.1007/978-3-031-07861-3.
11. Emelin S.E., Semenov V.S., Bychkov V.L., Belisheva N.K., Kovshik A. Some objects formed in the interaction of electrical discharges with metals and polymers // *Tech. Phys.* 1997. V. 42. No 3. P. 269-277. DOI: 10.1134/1.1258677.
12. Bychkov V.L., Chernikov V.A., Osokin A.A., Stepanov A.I., Stepanov I.G. Modeling of Artificial Ball Lightning with a Help of Capillary Discharge // *IEEE Trans. Plasma Sci.* 2015. V. 43. No 12, P. 4043-4047. DOI: 10.1109/TPS.2015.2478441.
13. Abakumov V.I., Bychkov V.L., Bikmukhametova A.R., et.al. Production of long-lived heterogeneous structures using plasma // *J. Phys.: Conf. Ser*. 2018. V. 1112. 012022. DOI: 10.1088/1742-6596/1112/1/012022.
14. Ershov A.P., Rozanov V.V., Sysoev N.N., et.al. Experimental studies of subsonic plasma jets // *Physical hydrodynamics. #4. Preprint of physical faculty of MSU*. 1994. No 8.
15. Zhang J.X.J., Hoshino K. Fundamentals of nano/microfabrication and scale effect // *Molecular Sensors and Nanodevices*. 2019. P. 43–111. DOI: 10.1016/b978-0-12-814862-4.00002-8.

KEY OBSERVATIONS OF BALL LIGHTNING AS A BASIS FOR CREATING ITS MODEL

Anatoly I. Nikitin

Semenov Federal Research Center for Chemical Physics, Russian Academy of Sciences, Moscow, Russia

Ball lightning properties. Most information about the properties of ball lightning is obtained by observing it through the eyes of witnesses. The imperfection of the human senses and the ways of remembering information gives some skeptics a reason not to recognize the results of these observations and even doubt the existence of ball lightning. In recent years, thanks to the widespread use of video cameras and smartphones, films have appeared. Analysis of these films allows us to obtain reliable information about the behavior of ball lightning, which usually escapes our attention during its visual observation. The data from this analysis can form the basis for constructing a model of ball lightning. In cases of observing ball lightning from a close distance, witnesses talk about a sphere with sharp boundaries, inside which luminous sparks move randomly. In the frames of a video filmed in Blagoveshchensk, the structure of ball lightning is clearly visible – a luminous spherical core surrounded by a luminous shell [1]. Information about the discrete structure of the core of ball lightning is confirmed by a case of filming a collision of ball lightning with a car [2]. A cloud of luminous sparks flies out of the torn shell of ball lightning. This suggests that the elements of the ball lightning core have an electric charge of the same sign and are held inside the shell by some force. If this is so, then ball lightning must have an electric charge. This is confirmed by the case when ball lightning split into two fragments, which flew apart to a distance of x during the observation period [3]. Analysis of the scattering process showed that this distance changed as $x = C \cdot t^{1/2}$, which is typical for the movement of charged balls in the air. Ball lightning can move, carried by the wind, but sometimes it can fly against the wind. In July 2015, ball lightning was filmed in Mitino by three operators simultaneously [4]. Analysis of its trajectory showed that for 80 seconds it moved in a 12 m wide zone perpendicular to the wind speed. This happened due to the attraction of its charge to the negative charge located at the bottom of the approaching thundercloud. Thus, the described observations indicate that ball lightning is actually one of the electrodes of a large capacitor, the second electrode of which is the surface of the earth. It actively interacts with the environment, changing its properties. If ball lightning approaches a grounded object, the charge flowing from it will end up in the area between it and the object. Its repulsion from this charge can create conditions in which ball lightning will hover above the conducting surface. The presence of a charge in ball lightning causes it to move along the lines of force of the atmospheric electric field and penetrate into buildings through small openings and window panes. Analysis of the glass through which ball lightning passed showed that traces of intense heating remained on it [5]. This means that ball lightning has energy that can be transferred to material objects. The ability to possess great energy is the most mysterious property of ball lightning. In 1936, ball lightning, having fallen into a barrel with 18 liters of water, heated it to boiling. Based on this, it was found that the energy density contained in ball lightning was higher than $\rho_E = 10^{10}$ J/m^3 [6]. According to the virial theorem, in order to hold particles with such an energy density inside a container, it must withstand a pressure of $P = \rho_E/3 = 3.3 \cdot 10^9$ Pa = $3.3 \cdot 10^4$ atm. The first thought about the source of this energy is the presence of high temperature of the substance of ball lightning. However, witnesses say that there is no heat coming from ball lightning. Moreover, there is a known case when ball lightning lying on snow did not melt it [3]. On the other hand, ball lightning that hit a barrel of water somehow transferred energy to it. A possible explanation for this may be that the water was heated by radio frequency electromagnetic radiation (like in household microwave ovens). Experience has shown that snow placed in a microwave oven does not melt [3]. There are cases of evaporation of ring-shaped metal objects (rings, chains, bracelets) when a ball

lightning explosion occurred near them [3]. This can be explained by the action of electromagnetic radiation. Analysis of the observation results indicates that there are two types of ball lightning – low-energy and high-energy ball lightning [3]. The former usually slowly flow out of the sockets in the form of luminous streams, which then swell into a luminous ball. Ball lightning of the second type is formed by linear lightning discharges in clouds [7]. Such ball lightning, exploding inside wooden houses, pushes out their walls [2]. The formation time of such ball lightning does not exceed 1/30 of a second.

Ball lightning model. Let's discuss whether it is possible to create a container that can withstand the pressure of the energy core of ball lightning ($3.3 \cdot 10^3$ MPa) and, in addition, the force of Coulomb repulsion of charges. Only “at hand” material, such as water, is allowed to be used to create the container. We will begin the discussion with the problem of holding motionless charge carriers $Q = 5 \cdot 10^{-3}$ C inside a spherical shell with an internal radius $R_{in} = 5 \cdot 10^{-2}$ m. The charge carriers stretch the sphere with a force

$$F_Q = Q^2/8\pi\varepsilon_0 R_{in}^2 = 4.496 \cdot 10^7 \text{ N}. \quad (1)$$

Here $\varepsilon_0 = 8.854 \cdot 10^{-12}$ F·m is the dielectric constant. The electric field strength created by a charge $Q = 5 \cdot 10^{-3}$ C at a distance of $R_{in} = 5 \cdot 10^{-2}$ m is:

$$E = Q/4\pi\varepsilon_0 R_{in}^2 = 1.798 \cdot 10^{10} \text{ V/m}. \quad (2)$$

Let's place a water molecule (an electric dipole with a moment $p_w = 6.327 \cdot 10^{-30}$ C·m) on the surface of the sphere of radius R_{in}. The condition for complete polarization of the dipole is the requirement [3]:

$$E > E_{min} = 3k_B T. \quad (3)$$

Substituting into formula (3) $k_B = 1.38 \cdot 10^{-23}$ J/K, and $T = 300$ K, we find $E_{min} = 2 \cdot 10^9$ V/m. Condition (3) is satisfied, and the water molecules on the surface of the sphere will be oriented along the electric field strength vector. In a non-uniform electric field E, a water molecule will be attracted to the center of the sphere with a force of:

$$f_q = p_w \text{ grad } E = -2p_w Q/4\pi\varepsilon_0 R_{in}^3. \quad (4)$$

Let’s imagine a water molecule as a ball with a diameter of $d_w = 4 \cdot 10^{-10}$ m. On the surface of a sphere with a radius of R_{in}, $n_w = 4\pi R_{in}^2/d_w^2$ water molecules can fit. A shell consisting of one layer of water molecules will be attracted to the center of the sphere with a force

$$f_w = f_q \cdot n_w = 2p_w Q/\varepsilon_0 d_w^2 R_{in} = 8.93 \cdot 10^{-1} \text{ N}. \quad (5)$$

The force f_w is less than the force F_Q by $F_Q / f_w = 5 \cdot 10^7$ times. The force F_Q can be compensated by a shell of $5 \cdot 10^7$ layers of water molecules. Its thickness is $a = 5 \cdot 10^7 \cdot d_w = 2 \cdot 10^{-2}$ m.

Now let’s consider ball lightning with an “active” core consisting of particles with a kinetic energy density of $\rho_E = 10^{10}$ J/m^3. Let the inner radius of the shell be $R_{in} = 5 \cdot 10^{-2}$ m, and the charge of the core be $Q = 5 \cdot 10^{-3}$ C. The pressure of the core on the surface of the shell is $P = 3.3 \cdot 10^9$ N/m^2, and the force acting on the shell is $F_E = P \cdot 4\pi R_{in}^2 = 10^8$ N. To compensate for this force, $n_E = F_E/f_w = 1.12 \cdot 10^8$ layers of water molecules must be added to the shell. Its thickness will increase by $b = n_E \cdot d_w = 4.48 \cdot 10^{-2}$ m. The total thickness of the shell will increase to $a + b = 6.48$ cm, and the radius of the ball lightning will become equal to $R_{bl} = R_{in} + a + b = 11.48$ cm.

Let’s assume that the shell is filled with a gas whose density is equal to the density of air at normal pressure. One gram-molecule ($6.023 \cdot 10^{23}$ molecules) occupies a volume of $22.41 \cdot 10^{-3}$ m^3. In 1 m^3 there are $N_m = 2.688 \cdot 10^{25}$ molecules, each of which has the energy $E_m = \rho_E/N_m = 3.72 \cdot 10^{-16}$ J $= 2.325 \cdot 10^3$ eV. Molecules with such energy will be ionized, and the shell will be filled with plasma with a temperature $T_p = E_m/k_B = 2.69 \cdot 10^7$ K. No shell can withstand such a temperature. It is more realistic to assume that systems with rotating particles serve as energy accumulators. An element capable of containing a large amount of energy can be a dynamic electric capacitor, the basic diagram of which is shown in Fig. 1 [3, 7].

In the center of the system are electrons moving in a ring orbit of radius r. Protons move around the electrons in an orbit of radius R. The combination of the magnetic field H created by the movement of the protons and the electric field E causes the electrons to drift in the direction perpendicular to the vectors $\boldsymbol{E}$ and $\boldsymbol{H}$. To create the magnetic field needed to hold electrons in orbit, the number of protons

must be greater than the number of electrons, so this system has a positive electric charge. The movement of electrons in a dynamic capacitor is similar to the movement of electrons in a magnetron. The speed of the electrons is close to the speed of light. Moving along the orbit, they oscillate in the direction perpendicular to their velocity vector. The movement of electrons in a closed orbit is the cause of generation of synchrotron, undulator and radio frequency radiation [1].

The radiation power depends on the degree of uniformity of the electron distribution along the orbit. When uniformly distributed, the radiation power is low, and when the uniformity is violated, it increases. Because of this, the intensity of the glow of ball lightning oscillates chaotically [1]. A large number of dynamic electric capacitors are located inside a spherical shell of polarized water molecules [3]. In reality, the dynamic capacitor has a more complex structure.

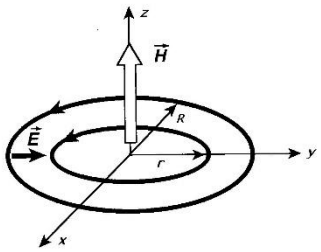


FIGURE 1. Dynamic electric capacitor.

Protons rotate in orbits whose planes are inclined to the plane of the electron orbit. Their movement creates a barrel-shaped magnetic field. Due to this, a force arises that stabilizes the position of the electron orbit. A similar scheme for holding electrons in orbit is implemented in betatrons.

A dynamic electric capacitor, like any system of electrons and positive ions, held by their own fields, tends to expand. It can exist only in a device that creates a force that prevents its expansion. The action of the expanding dynamic capacitor on the shell wall turns out to be "softer" than the action of randomly moving particles can be. This is due to the fact that the protons during contact with the shell move parallel to the shell plane and transfer to it not all the kinetic energy they possess, but only part of the energy associated with the radial expansion of the capacitor. Another source of the glow of ball lightning is a corona discharge on its surface. The result of this discharge is the formation of nitrogen dioxide NO_2 and ozone O_3. Ball lightning, possessing high energy, may be formed near the turn of the linear lightning channel through which the current pulse passes [7]. The current causes the appearance of a magnetic field and a vortex electric field. Ultraviolet radiation of the channel ionizes the air. Due to the combined action of the electric and magnetic fields, a spatial separation of charges and their acceleration occurs. In this case, some of the electrons leave the place where the core of the ball lightning is formed, and it becomes positively charged. In the presence of a sufficiently large number of water drops, a shell is formed around the core [7].

Conclusion. Based on the above, we can assume that the described model is capable of explaining almost all the details of the properties of ball lightning. A main property of ball lightning is its ability to hold an electric charge of 10^{-3}-10^{-1} C inside itself. The container for holding electric charges in ball lightning is a shell of water molecules. For some time, this system is in a state of stable equilibrium [3]. Due to the shell conductivity ball lightning charge gradually flows into the atmosphere. The lifespan of ball lightning, which can be from 1 second to 10 minutes, depends on the rate of charge flow. The hypothesis of the existence of structures in the core of ball lightning that have a mechanical torque (dynamic electric capacitors) allows us to find an explanation for cases of ball lightning rotation. The occurrence of rotation and its stop can occur due to a change in the orientation of the moments of rotation of the elements of its energy core.

1. Nikitin A.I., Nikitin V.A., Velichko A.M., Nikitina T.F. Features of the mechanism of ball lightning electromagnetic radiation // *J. Atmos. Sol.-Terr. Phys*. 2021. V. 222. 105711. DOI: 10.1016/j.jastp.2021.105711.
2. Nikitin A.I., Nikitin V.A., Velichko A.M., Nikitina T.F. Explosions of ball lightning inside enclosed spaces // *Atmosphere*. 2024. V. 15. P. 2. DOI: 10.3390/atmos15010002.

3. A.I. Nikitin, *My Ball Lightning*, Nauka, Moscow, 2022 (in Russian).
4. Nikitin A.I., Velichko A.M., Nikitina T.F. Stepanov I.G. Analysis of the unique case of ball lightning observation in Mitino, the northwest district of Moscow // *J. Atmos. Sol.-Terr. Phys.* 2018. V. 179. P. 97–104. DOI: 10.1016/j.jastp.2018.07.001.
5. Bychkov V.L., Nikitin A.I., Ivanenko I.P., et al. Ball lightning passage through a glass without breaking it // *J. Atmos. Sol.-Terr. Phys.* 2016. V. 150. P. 69-76. DOI: 10.1016/j.jastp.2016.10.018.
6. Goodlet B.L. Lightning // *Journal of the Institution of Electrical Engineers*.1937. V. 81. No 487. P. 1–26. DOI: 10.1049/jiee-1.1937.0104.
7. Nikitin A.I. Possible process of ball lightning training in nature // *J. Atmos. Sol.-Terr. Phys.* 2019. V. 190. P. 54–61. DOI: 10.1016/j.jastp.2019.05.001.

MULTIPLE-CHARGED CLUSTERS AS AN AGENT REDUCING AIR HUMIDITY BEFORE AN EARTHQUAKE

Anatoly I. Nikitin, Vadim A. Nikitin, Alexander M. Velichko, Tamara F. Nikitina

Semenov Federal Research Center for Chemical Physics, Russian Academy of Sciences, Moscow, Russia

Earthquake precursors. The creating a reliable way to predict earthquakes could save many lives. It has long been known, that thermal anomalies are recorded in the atmosphere before an earthquake. These anomalies can be represented using the parameter (ACP) – Atmospheric Chemical Potential, described in detail in the monograph [1]. The ACP potential, measured in electron-volts, relates the air temperature near the earth's surface T_g with relative humidity H:

$$\mathrm{ACP} = 5.8\cdot10^{-10}\,(20T_g + 5763)^2\cdot\ln\,(100/H). \qquad (1)$$

Temperature T_g is measured in degrees Celsius and relative humidity H is measured in percent.

Figure 1 shows how the ACP value changed before a strong earthquake of magnitude M 7.3 that occurred near the western coast of Honshu Island in Japan on March 17, 2022 [2]. On March 12, 2022, 5 days before the main shock, a sharp increase in the ACP parameter was observed, the cause of which was a sharp decrease in air humidity, possibly down to several percent. A similar picture of a sharp increase in the ACP parameter before an earthquake was observed in other cases of monitoring the state of the atmosphere [2].

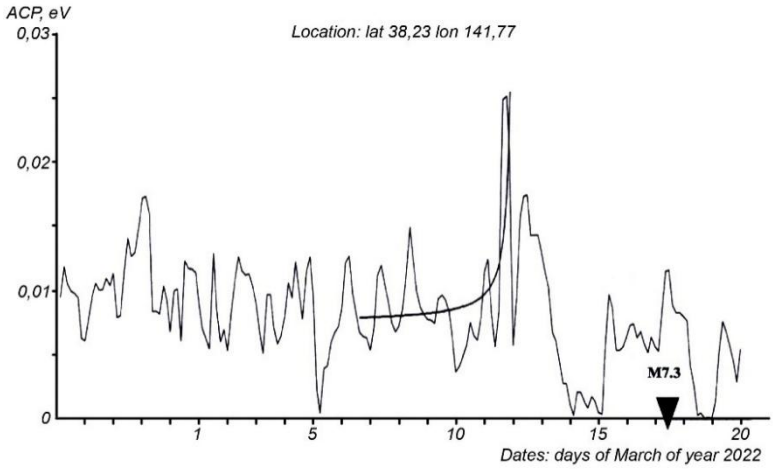


FIGURE 1. Change in the ACP value on the western coast of Honshu Island before the earthquake of magnitude M 7.3 that occurred on March 17, 2022. The curved line is a hyperbolic approximation of the ACP growth process.

A likely reason for the decrease in air humidity may be the formation of condensation centers for water molecules. These centers can appear during the decay of radon nuclei (^{222}Rn). Before an

earthquake, cracks appear in the earth's crust through which radon escapes into the atmosphere. The radon nucleus decays to form a polonium (^{218}Po) nucleus and alpha particle ($T_{1/2}$ = 3.825 days). The polonium nucleus is transformed into a lead nucleus (^{214}Pb) by alpha decay ($T_{1/2}$ = 3.05 minutes). As a result of the cascade of two decay reactions, energy 11.48 MeV is released. An alpha particle collides with air molecules, ionizing them. Energy of 40 eV is required to form a pair of ions. Consequently, when one radon nucleus decays, $5.74 \cdot 10^5$ ions of different signs are formed. In a humid atmosphere, the ions join water molecules. Due to the action of the ion's electric field, a cluster of 10 water molecules may be formed, and further growth of the cluster is a statistical process of joining water molecules due to dipole-dipole interaction [3]. At 100% humidity, one cubic meter of air contains 17.27 g of water or $6 \cdot 10^{23}$ molecules. The half-life of ^{222}Rn atoms is $T_{1/2} = 4.8 \cdot 10^6$ s. Decay constant $\lambda = 0.693/T_{1/2} = 1.4426 \cdot 10^{-7}$ s^{-1}. In order for one nucleus to decay per second in a volume of 1 m^3, the number of radon atoms in it must be no less than $N_1 = 1/\lambda = 6.94 \cdot 10^5$ m^{-3}. The background activity of radon in the atmosphere is $A_{ph} = 2 \cdot 10^3$ Bk/m^3, which corresponds to 2000 decays per second in a volume of 1 m^3 [2]. The background number of radon atoms in 1 m^3 of air is $N_{Rph} = N_1 \cdot A_{ph} = 6.926 \cdot 10^6 \times 2 \cdot 10^3 = 1.385 \cdot 10^{10}$. Before an earthquake, radon activity increases to $A_{gq} = 4.5 \cdot 10^6$ Bk/m^3, which corresponds to the formation of $N_m = N_1 \cdot A_{gq} = 3.157 \cdot 10^{12}$ water condensation centers. These centers must gather $6 \cdot 10^{23}$ water molecules around themselves, or $N_{wi} = 6 \cdot 10^{23}/3.157 \cdot 10^{12} = 1.9 \cdot 10^{11}$ water molecules around each ion. The mass of a water molecule is $m_w = 3 \cdot 10^{-26}$ kg, the mass of a spherical drop is $m_{dr} = m_w \cdot N_{wi} = 5.7 \cdot 10^{-15}$ kg, and its volume $V_{dr} = 5.7 \cdot 10^{-18}$ m^3. Drop radius $R_{dr} = (3V_{dr}/4\pi)^{1/3} = 1.1 \cdot 10^{-6}$ m. Thus, the release of radon atoms can lead to a noticeable decrease in air humidity. However, when substantiating the hypothesis of the participation of radon in changing the state of the atmosphere, it is necessary to give an answer to some details of this phenomenon. The place where the ACP value anomaly is observed covers an area of more than 10^{12} m^2 [2]. Taking into account the limited length of transport of a radon atom after exiting a crack, we must assume that this entire area is riddled with cracks. This is unlikely. The process of radon release lasts about a day. After this it stops for several days. Does this mean that all cracks are hermetically sealed at the same time? These and other questions suggest that other processes may also be involved in the phenomenon of ACP growth before an earthquake.

Multicharged clusters. During earthquakes, air glow is often observed due to electrical discharges in the ground. Matsumoto [4] discovered traces of particles on photographic films, which, in his opinion, are compact formations of a large number of electrons. We assumed that these particles are multiply charged clusters consisting of a group of ions located in a shell of polarized water molecules [3]. The Coulomb repulsion of ions is compensated by the force acting on the dipole moment of a water molecule located in a non-uniform electric field. Such clusters can appear when a strong ionic current passes through an electrolyte. Near the cathode there will be an increased concentration of positive ions, and near the anode - negative ions. These ions are surrounded by a layer of water. Thanks to the polarization of water molecules, an object can arise consisting of a cavity of radius R, inside which there is a certain number of ions of the same sign, and a shell of polarized water molecules with thickness a. Let us assume that inside this cavity there are $n_1 = 100$ ions with a total charge $Q_1 = 1.6 \cdot 10^{-17}$ C. Let's imagine the ion as a ball with a diameter $d_i = 4 \cdot 10^{-10}$ m. Let the ions be on the inner surface of the spherical cavity. Each ion occupies an area $s_i = 16 \cdot 10^{-20}$ m^2. Area of the sphere $S_1 = 4\pi R_1^2 = s_i \cdot n_1 = 16 \cdot 10^{-18}$ m^2. From here we find the radius of the sphere $R_1 = 11 \cdot 10^{-10}$ m. Let us place a water molecule on the outer surface of this sphere. We will consider it a ball with a diameter $d_w = 4 \cdot 10^{-10}$ m. The center of the ball is at a distance $R_{1w} = (11+2) \cdot 10^{-10}$ m from the center of the cavity in the electric field $E = Q_1/4\pi\varepsilon_0 R_{1w}^2 = 8.5 \cdot 10^{10}$ V/m. According to the Langevin criterion, complete polarization of water molecules occurs in an electric field whose intensity is higher than $E_{min} = 3k_B T/p_w$ (k_B is Boltzmann's constant, T is temperature). At T = 300 K $E_{min} = 2 \cdot 10^9$ V/m. A water molecule is attracted to the center of the sphere with a force

$$F_a = p_w \cdot \text{grad}\,(Q_1/4\pi\varepsilon_0 R_{1w}^2) = -\,p_w \cdot Q_1/2\pi\varepsilon_0 R_{1w}^3. \qquad (2)$$

Here $p_w = 6.327 \cdot 10^{-30}$ C·m is dipole moment of water molecule. Substituting into (3) $Q_1 = 1.6 \cdot 10^{-17}$ C and $R_{1w} = 13 \cdot 10^{-10}$ m, we find $F_a = 8.287 \cdot 10^{-10}$ N.

If the surface of the sphere is covered with a layer of water molecules, a force will appear that pushes the molecule out. The magnitude of this force [3]:

$$F_{rep} = 2.69 \cdot 10^{-9} (R_{1w} - R_0)^{-1.3}. \quad (3)$$

Here R_{1w} – in angstroms (10^{-10} m) – is the distance from the center of the sphere to the center of the water molecule, and the parameter $R_0 = -4.5$. At $R_{1w} = 13 \cdot 10^{-10}$ m $F_{rep} = 6.51 \cdot 10^{-11}$ N. The total force of attraction of a water molecule is equal to $F_{res} = F_a - F_{rep} = 7.64 \cdot 10^{-10}$ N. On the surface of a sphere with a radius $R_1 = 13 \cdot 10^{-10}$ m $N_w = 4\pi R_1^2/d_w^2 = 133$ water molecules can accommodate. The total force of their attraction to the center of the sphere is equal to $F_{w1} = F_{res} \cdot N_w = 1.015 \cdot 10^{-7}$ N. Ions with a total charge $Q_1 = 1.6 \cdot 10^{-17}$ C stretch the shell of the sphere with a force

$$F_{Q1} = Q_1^2/8\pi\varepsilon_0(R_1 - d_i/2)^2 = 9.51\ 10^{-7}\ \text{N}. \quad (4)$$

The repulsion force of ions in $F_{Q1}/F_{w1} = 9$ times greater than the compression force of the shell, consisting of one layer of water molecules. The force of Coulomb repulsion of ions can be compensated by increasing the thickness of the shell by 9 times. In this case, the thickness of the shell will be equal to $a_1 = 9\ d_w = 36 \cdot 10^{-10}$ m, and the radius of the cluster with a charge $Q_1 = 1.6 \cdot 10^{-17}$ C will be equal to $R_{c11} = R_1 + a_1 = 47 \cdot 10^{-10}$ m. Electric field strength on the surface of such a cluster is equal to $E_{sur} = 6.5 \cdot 10^9$ V/m. Once in humid air, this cluster will attract water molecules. Let's estimate the size to which such a cluster can grow. In this case, we will only take into account the effect of its electric field on the environment. Let us assume that the growth of the cluster will stop when the work A of removing a water molecule from its surface becomes equal to the average kinetic energy of an air molecule $E_c = k_B T$, i.e.

$$A = \int_R^\infty F_a(R)dR = \frac{p_w Q}{2\pi\varepsilon_0}\int_R^\infty \frac{dR}{R^3} = \frac{p_w Q}{4\pi\varepsilon_0 R^2}. \quad (5)$$

Considering $T = 300$ K and equating A to $k_B T$, for $Q = Q_1 = 1.6 \cdot 10^{-17}$ C we find that

$$R = \left(\frac{p_w Q}{4\pi\varepsilon_0 k_B T}\right)^{1/2} = 1.48 \cdot 10^{-8}\ \text{m}. \quad (6)$$

Thus, a cluster with a charge $Q_1 = 1.6 \cdot 10^{-17}$ C with a radius $R_{c11} = 47 \cdot 10^{-10}$ m, once in a humid environment, can increase its radius to $R_{lim1} = 148 \cdot 10^{-10}$ m. The volume of collected water $V_{w1} = 4\pi(R_{lim1}^3 - R_{cl1}^3)/3 = 1.314 \cdot 10^{-23}$ m^3. The density of water is $\rho_w = 10^3$ kg/m^3, the mass of water collected by the cluster is $m_{w1} = V_{w1} \cdot \rho_w = 1.314 \cdot 10^{-20}$ kg. Mass of a water molecule $m_m = 18 \cdot 10^{-3}$ kg/ $6.023 \cdot 10^{23} = 2.9885 \cdot 10^{-26}$ kg. The number of adsorbed water molecules $n_{ads1} = m_{w1}/m_m = 9.396 \cdot 10^5$. To collect one mole of water molecules, the presence of $6.41 \cdot 10^{17}$ clusters with a charge of $1.6 \cdot 10^{-17}$ C in 1 m^3 of air is necessary. The total charge of the clusters is $Q_{\Sigma 1} = 10.256$ C. If this charge accumulated for 100 seconds, then the average current of this process was about 0.1 A. Let us carry out the calculation using the scheme used for clusters with a charge $Q_2 = 1.6 \cdot 10^{-15}$ C. The diameter of the ion is $d_i = 4 \cdot 10^{-10}$ m, the area on which 10^4 ions can be placed is $S_2 = d_i^2 \cdot 10^4 = 16 \cdot 10^{-16}$ m^2. The radius of the sphere occupied by one layer of ions is $R_2 = (S_2/4\pi)^{1/2} = 113 \cdot 10^{-10}$ m. In this case, the radius at which the centers of the ions are located is equal to $R_{ci2} = 111 \cdot 10^{-10}$ m, and the center of the water molecule (a ball with a diameter $d_w = 4 \cdot 10^{-10}$ m) is located at a distance $R_{w2} = 115 \cdot 10^{-10}$ m. The electric field at the location of the water molecules is $E_{Rw2} = 10^{11}$ V/m. The force of attraction of a water molecule to the center of the sphere

$$F_{a2} = p_w Q_2/2\pi\varepsilon_0 R_{w2}^3 = 1.197 \cdot 10^{-10}\ \text{N}. \quad (7)$$

At $R_{w2} = 115 \cdot 10^{-10}$ m, the force of mutual pushing of water molecules can be neglected. The number of molecules in a layer with radius R_{w2} is equal to $N_{w2} = 4\pi R_{w2}^2/d_w^2 = 1.038 \cdot 10^4$. The force of

compression of the shell by one layer of water molecules is $F_{sh2} = F_{a2} \cdot N_{w2} = 1.243 \cdot 10^{-6}$ N. The force of Coulomb repulsion of charges

$$F_{Q2} = Q_2^2/8\pi\varepsilon_0(R_2 - d_i/2)^2 = 9.33 \cdot 10^{-5} \text{ N}. \quad (8)$$

The repulsion force of ions can be compensated by a shell consisting of $F_Q/F_{sh} = 75$ layers of water molecules. Shell thickness $a_2 = 75 \times 4 \cdot 10^{-10}$ m $= 300 \cdot 10^{-10}$ m, and cluster radius $R_{cl2} = R_2 + a_2 = 413 \cdot 10^{-10}$ m. The maximum radius of a cluster capable of holding water molecules on its surface is

$$R_{lim2} = (p_w Q_2/4\pi\varepsilon_0 k_B T)^{1/2} = 1.483 \cdot 10^{-7} \text{ m}. \quad (9)$$

The volume of water collected by the cluster is $V_{w2} = 4\pi(R_{lim2}^3 - R_{cl2}^3)/3 = 10^{-20}$ m^3. The mass of water is 10^{-17} kg, which corresponds to $3.3 \cdot 10^8$ water molecules. To remove $6 \cdot 10^{23}$ water molecules from one cubic meter of air, one will need $1.8 \cdot 10^{15}$ clusters with a charge of $1.6 \cdot 10^{-15}$ C. The total charge of these clusters is $Q_{\Sigma 2} = 2.88$ C. This is almost 8 times less than for clusters with a charge of $1.6 \cdot 10^{-17}$ C. Calculations show that the total charge of clusters with charge $Q_3 = 1.6 \cdot 10^{-13}$ C, which can adsorb one mole of water, is $Q_{\Sigma 3} = 0.215$ C, and the total charge of clusters with charge $Q_4 = 1.6 \cdot 10^{-11}$ C, which are necessary for this work, is $Q_{\Sigma 4} = 2.15 \cdot 10^{-2}$ C.

As we see, as the cluster charge increases, its "work" of collecting water molecules becomes more and more efficient. When the cluster charge increases by 100 times, the required total charge of the clusters decreases by 10 times.

1. S. Pulinets, D. Ouzounov, A. Karelin, K. Boyarchuk, *Earthquakes Precursors in the Atmosphere and Ionosphere. New Concepts,* Springer Nature, 2022.
2. Pulinets S.A., Budnikov P.A., Karelin A.V., Žalonar J. Thermodynamic instability of the atmospheric boundary layer stimulated by tectonic and seismic activity // *J. Atmos. Sol.-Terr. Phys.* 2023. V. 246. 106050. DOI: 10.1016/j.jastp.2023.106050.
3. Nikitin A.I., Nikitin V.A., Velichko A.M., Nikitina T.F. "Strange" particles and micro-sized ball lightning in some electric discharges // *J. Atmos. Sol.-Terr. Phys.* 2021. V. 218. 105525. DOI: 10.1016/j.jastp.2020.105525.
4. T. Matsumoto, Ball lightning during underwater spark discharges and the Matsumae earthquakes. In: *Proceeding 5th International Symposium on Ball Lightning (ISBL-97).* 1997. Tsugawa-Town, Niigata, Japan, pp. 193-201.

THE REASON FOR THE FORMATION OF SYMMETRICAL TRACES OF MULTI-CHARGED WATER CLUSTERS

Anatoly I. Nikitin, Vadim A. Nikitin, Alexander M. Velichko, and Tamara F. Nikitina

Semenov Federal Research Center for Chemical Physics, Russian Academy of Sciences, Moscow, Russia

In experiments on studying electrical discharges in electrolytes, the formation of "strange particles" was discovered, which leave continuous or dotted traces several microns wide on photographic films and on the surface of solids [1]. A large number of hypotheses has been proposed about nature of these particles: it is assumed that they are magnetic monopoles, electron pairs bound by magnetic attraction, particles of "dark matter", etc. [2]. As a rule, the authors of these hypotheses limit themselves to the formulation of their idea and do not make any attempts to explain the subtle details of the behavior of the "strange" particles. In particular, the reason for the simultaneous registration of a large number of traces of absolutely identical shape has not been studied at all. We assumed that the "strange particles" are objects consisting of a certain number of ions of the same sign, located in a shell of polarized water

molecules. To create these objects, it is natural to use an electric discharge in an electrolyte in which the current is carried by ions. To create a high volume density of ions of the same sign, one of the electrodes should be as small as possible.

We conducted a study of the properties of objects that appear when an electric current passes through an electrolyte. A capacitor bank with a capacity of 1.2 mF charged to a voltage of U_b = 1.7 kV served as an accumulator of electric energy. Using a switch consisting of three PME-213 magnetic starters connected in parallel, the positive voltage of the capacitor was applied to the electrode - a steel needle with a diameter of 1.2 mm, the tip of which was lowered into a saturated solution of sodium bicarbonate to a depth of 2 mm. A nickel plate with a thickness of 1 mm and a width of 10 mm served as the cathode, lowered into the liquid to a depth of 2 mm. The distance between the electrodes was 20 mm. The solution was poured into a rectangular glass cuvette measuring 10 × 15 × 5 cm. The duration of the current pulse was t_c = 15 ms. The resistance between the electrodes measured before the discharge was about R_c = 1 kOhm. It was not possible to determine the current value during the discharge due to strong interference on the measuring circuit. When the current passed through the liquid, an area of yellow glow about 3 cm in size appeared in it. A bright white dot about 1 mm in size was observed near the tip of the needle. Based on the given parameters, it can be assumed that the discharge current was not less than $I_c = U_b/R_c$ = 1.7 A. During the existence of the current, a charge of $Q_c = I_c \cdot t_c$ = 0.0255 C ($1.59 \cdot 10^{17}$ ions) passed through the solution. If we assume that the ions were in a volume of 1 mm^3 near the tip of the needle, their density was $1.59 \cdot 10^{26}$ pcs/m^3, and the charge density was $\rho_q = 2.55 \cdot 10^7$ C/m^3. It is possible that the discharge current was greater than the accepted value, and therefore the charge density near the needle was greater. It is important that the discharge occurred deep in the liquid and the ions were surrounded by a layer of water. In this zone, energy-intensive objects were formed, which, in our opinion, are charged aerosol particles. To register these particles, we used detectors made of DVD discs. Aerosol particles (multiple-charged water clusters), having hit the detector, moved along its surface, leaving traces [1]. To weaken the effect of external electric fields, the detectors were placed in metal screens. One side of the screen was made in the form of a metal mesh with a cell size of 5 × 5 mm. The detectors were located at a distance of about 1 m from the discharge zone and "irradiated" for 10-15 hours with pulses following with a period of 60 s. To protect against electrolyte splashes, the detectors were placed in envelopes made of 25 μm thick polyethylene film. Experiments have shown that the screens were not effective enough to protect the detectors from the strong electric fields generated by the setup during an electric discharge. Dotted or continuous traces of a straight or curved shape were recorded. In our papers [1, 2] an explanation is given of the formation process of such traces by the action of the energy of charged water clusters.

When such a cluster approaches the surface of a solid, polarization of the surface material occurs and a force arises that attracts the cluster to the surface. At some distance from the surface, some of the ions separate from the cluster, which, having hit the surface, leave a trace on it. The cluster, having received a recoil momentum, "flies up" above the surface, but under the action of the force of attraction, approaches it again.

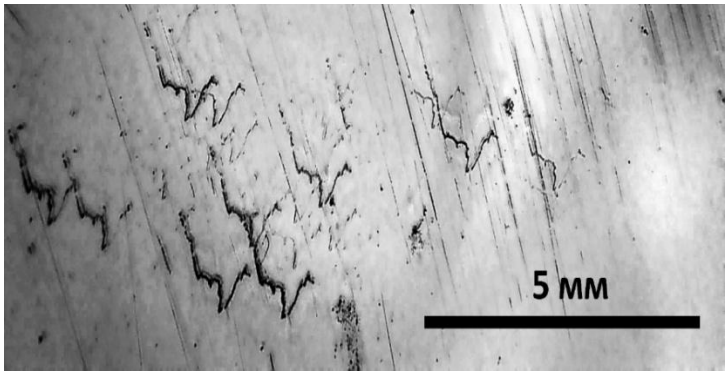


FIGURE 1. A group of 14 such traces.

The process is repeated. Under the action of the electric field vector parallel to the surface, the cluster moves along it, leaving a dotted trace. The process of "draining" the cluster charge can be continuous, in this case a solid trace will appear on the detector. The most interesting case of the action of clusters on the surface is the appearance of a group of traces of the same shape, figuratively called "twin traces".

It can be seen that the thickness of the traces varies, but the shape of the traces – both intense and weak – is the same. It can be assumed that all the traces were formed simultaneously, and the particles that made them moved synchronously under the action of a changing electric field. The magnitude of the field strength was the same in an area of about 1 cm. Let us discuss whether it is possible to find the properties of the clusters that left these traces based on the analysis of the obtained picture. Let us determine what the relationship between the cluster charge Q and its radius R can be. Let us assume that the cluster contains $n_1 = 2.8 \cdot 10^7$ $(OH)^-$ ions with a total charge of $Q_1 = 4.5 \cdot 10^{-12}$ C. We will consider the ion as a ball with a diameter of $4 \cdot 10^{-10}$ m. The area occupied by one ion is $s_i = 16 \cdot 10^{-20}$ m^2, n_1 ions can be placed on a sphere with an area of $S_1 = n_1 \cdot s_i = 4\pi r_1^2$, where $r_1 = 6 \cdot 10^{-7}$ m. The ions will stretch the sphere with a force

$$F_{Q1} = Q_1^2/8\pi\varepsilon_0 r_1^2 = 2.529 \cdot 10^{-1} \text{ N}. \quad (1)$$

On the outer surface of the sphere one can place $n_{w1} = 2.82 \cdot 10^7$ water molecules (we imagine a water molecule as a ball with a diameter of $4 \cdot 10^{-10}$ m, occupying an area of $s_w = 16 \cdot 10^{-20}$ m^2). The compression force of the sphere by one layer of water molecules is equal to

$$F_{1w} = p_w Q_1 n_{w1}/2\pi\varepsilon_0 r_1^3 = 6.685 \cdot 10^{-5} \text{ N}. \quad (2)$$

Here $p_w = 6.327 \cdot 10^{-30}$ C·m is the dipole moment of water molecule. The force F_{1w} is 3783 times less than the force F_{Q1}. The force F_{Q1} can be compensated if the shell consists of 3783 layers of water molecules. In this case, its thickness will be equal to $a_1 = 1.5132 \cdot 10^{-6}$ m, and the cluster radius will be equal to $R_{c1} = r_1 + a_1 = 2.113 \cdot 10^{-6}$ m. For this cluster, the ratio $A = Q_1/R_{c1}^2 = 4.5 \cdot 10^{-12}/4.4648 \cdot 10^{-12} = 1.008$ C/m^2. Interestingly, the ratio $Q/R_c^2 = 1$ C/m^2 is preserved for all clusters constructed according to the described scheme. For a cluster with charge $Q_2 = 4.5 \cdot 10^{-11}$ C, the radius of the sphere containing ions is $r_2 = 1.893 \cdot 10^{-6}$ m, the shell thickness is $a_2 = 4.786 \cdot 10^{-6}$ m, the radius is $R_{c2} = 6.679 \cdot 10^{-6}$ m, and the ratio is $A = 4.5 \cdot 10^{-11}$ C/$4.4612 \cdot 10^{-11}$ m^2 = 1.009 C/m^2. For a cluster with charge $Q_3 = 4.5 \cdot 10^{-10}$ C, the radius of the sphere is $r_3 = 5.986 \cdot 10^{-6}$ m, $a_3 = 15.1364 \cdot 10^{-6}$ m, the radius is $R_{c3} = 21.1223 \cdot 10^{-6}$ m, and $A = 4.5 \cdot 10^{-10}$ C/$4.4615 \cdot 10^{-10}$ m^2 = 1.0086 C/m^2. Above we found the possible value of the ions charge density in the region of their formation as $\rho_q = 2.77 \cdot 10^7$ C/m^3. The charge density in a cluster with charge Q, located inside a sphere of radius r, is $\rho_{qn} = 3Q/4\pi r^3$. For a cluster with $Q_1 = 4.5 \cdot 10^{-12}$ C $\rho_{q1} = 4.976 \cdot 10^6$ C/m^3, for a cluster with $Q_2 = 4.5 \cdot 10^{-11}$ C $\rho_{q2} = 1.585 \cdot 10^6$ C/m^3, and for $Q_3 = 4.5 \cdot 10^{-10}$ C $\rho_{q3} = 5 \cdot 10^5$ C/m^3. As we can see, the value of the charge density ρ_q, accumulated over time $t_c = 15 \cdot 10^{-3}$ s, is an order of magnitude greater than ρ_{qn}. It can be assumed that the cluster formation time was no more than $\tau_{cl} = t_c/(\rho_q/\rho_{qn}) = 1.5 \cdot 10^{-3}$ s. When a spherical cluster of radius R moves in air, two forces act on it. The first force F_Q is the action of the electric field E on the cluster charge, $F_Q = QE$. Opposite to this force, the friction force [3] acts on the cluster:

$$F_f = (\pi C_D \rho_a R^2 v^2)/2. \quad (3)$$

Here $\rho_a = 1.205$ kg/m^3 is the air density, and C_D is the coefficient of friction of the medium. As a result of these forces, the cluster moves in air at a constant speed

$$v = \left(\frac{2QE}{\pi C_D \rho_a R^2} \right)^{1/2}. \quad (4)$$

Assuming that the value of the coefficient C_D is the same for a group of clusters of different sizes, we come to the conclusion that clusters with the same value of the parameter $A = Q/R^2$ in an electric field E move with the same speed. This can explain the appearance of traces of the same shape shown in the figure. The particle that left a wide trace moved and made turns in its trajectory simultaneously with the particle that left a thin trace. The complete identity of the tracks allows us to assume that all the particles that left these tracks reached the detector simultaneously. The place of their formation - an electric discharge in a liquid - is at a distance of 1 m from the detector. The particles moved along the surface of the detector during the period of the presence of a rapidly changing electric field, which existed during the passage of a strong discharge current lasting 15 ms. During this time, the particles should have reached the detector. Let us assume that as a result of the discharge, a large cluster with a charge Q was formed, which, having begun to move towards the detector, under the action of an external electric field, divided into n identical fragments. During the flight to the detector, lasting $t = 5 \cdot 10^{-3}$ s, these fragments, due to the Coulomb repulsion of charges, moved away from the center of their formation to a distance of $x = 1$ cm. The average velocity of the fragments was $v_{av} = x/t = 2$ m/s. It can be assumed that the size of the fragment was close to the thickness of its trace. According to the figure, the thickness of the particle traces on the detectors was from 1 to 10 microns. Let us take the diameter D of the spherical fragment equal to $2 \cdot 10^{-6}$ m. For such a body, the Reynolds number $\mathbf{Re} = v_{av} D/ \boldsymbol{\nu} = 0.26$. Here $\boldsymbol{\nu} = 0.152$ cm^2/s is the kinematic viscosity of air. This value of **Re** corresponds to $C_D = 240$ [3]. Let us consider the symmetrical expansion of n spherical clusters of radius R_b with charge q from one center. The force stretching the sphere of radius x on which the clusters are located is equal to

$$F_{sp} = (nq)^2/8\pi\varepsilon_0 x^2. \quad (5)$$

Suppose that the same force acts on n clusters, each of which has a charge q. The force acting on one cluster is

$$F_q = nq^2/8\pi\varepsilon_0 x^2. \quad (6)$$

This force causes the cluster to fly with a speed $v = dx/dt$ in the direction from the point of departure. Moving in the air, each cluster is slowed down by the force of friction

$$F_{fr} = 0.5 \cdot C_D \pi R_b^2 (dx/dt)^2. \quad (7)$$

Equating F_q to F_{fr} and integrating, we obtain

$$x = 2^{1/2}(1/4\pi^2 C_D \rho_a \varepsilon_0)^{1/4} \cdot n^{1/4} \cdot (q \cdot t/R_b)^{1/2}. \quad (8)$$

Substituting into formula (8) $n = 16$, $C_D = 240$, $\rho_a = 1.205$ kg/m^3, $x = 10^{-2}$ m and $t = 5 \cdot 10^{-3}$ s, we obtain $q/R_b = [(4\pi^2 C_D \rho_a \varepsilon_0)^{1/2} \cdot x^2]/2n^{1/2} \cdot t = 7.944 \cdot 10^{-7}$ C/m. Earlier we found that for clusters constructed according to the scheme described above, the relationship $q = R_b^2$ is valid. From the analysis of the process of scattering of cluster fragments, the second relationship $q = 7.944 \cdot 10^{-7} R_b$ follows. Solving the system of equations, we find $R_b = 7.944 \cdot 10^{-7}$ m and $q = 6.31 \cdot 10^{-13}$ C. When analyzing the process of cluster dispersal, we assumed that the "parent" cluster split into n fragments with the same charge. In fact, the fragment charges may be different. In addition, there is a difficulty in determining the coefficient C_D. Spherical particles fly in the vertical direction with a speed of $v_v = 200$ m/s and simultaneously move horizontally with a speed of $v = 2$ m/s. They can rotate. Therefore, the obtained result should be treated as an estimate of the average charge and size of the "daughter" clusters.

1. Nikitin A.I., Nikitin V.A., Velichko A.M., Nikitina T.F. "Strange" particles and micro-sized ball lightning in some electric discharges // *Journ. Atm. Solar-Terr. Phys*. 2021. V. 218. 105525. DOI: 10.1016/j.jastp.2020.105525.

2. Nikitin A.I., Nikitin V.A., Velichko A.M., Nikitina T.F. Strange traces of a “strange” radiation // *RENSIT, Radioelectronics. Nanosystems. Information technologies*.2022. V. 14. No 3. P. 249-268. DOI: 10.17725/rensit.2022.14.249.
3. P.C. Reist, *Introduction to Aerosol Science*, Macmillan Publishing Company, New York/London, 1984.

THE EFFECT OF CORONA DISCHARGE PLASMA OF NEGATIVE POLARITY ON REDOX PROCESSES IN SOIL

Vladimir L. Bychkov, Aleksandr P. Shvarov, Ilya G. Stepanov, Pavel A. Goryachkin, and Dmitry N. Vaulin

Faculty of Physics, Lomonosov Moscow State University, Moscow, Russia

As is known [1], the redox potential indicates the level of activity of redox reactions, i.e. reactions in which the transfer or addition of electrons is carried out. In general, the oxidation-reduction reaction can be represented as follows: Ox + ne –⟶ Red, where Ox is the oxidizer; n is the number of electrons involved in the reaction; e is the electrons; Red is the reducing agent. Some substances lose electrons and are oxidized (oxidation reaction), others acquire electrons and are restored (reduction reaction). Most of the oxidation reactions of organic substances are irreversible.

One of the goals of this work was to conduct experiments to assess the effects of a negative polarity corona discharge on redox processes in the soil.

Objects of research. The object of the study was samples of lowland peat (capillarily saturated with water) and pure quartz sand (air-dry) in pure form and in mixtures with different ratios of peat and sand.

1. Pure peat (100%) by weight of the sample, the ash content is 10.5% (89.5% organic matter, 10.5% mineral part.
2. Peat + sand (78.6 +21.4)% by weight of the sample (70.3% organic matter, 29.7% mineral part.
3. Peat + sand (50+50)% by weight of the sample(44.25% organic matter, 55.75% mineral part.
4. Peat +sand (21.4+ 78.6)% by weight of the sample (19.2% organic matter, 80.8% mineral part.
5. 100% pure sand (100% mineral part).

Research methods. Samples weighing 70 grams were treated by corona discharge plasma - negative corona for 60 minutes. The choice of the corona discharge was made based on data on ion-rich air plasma and known corona discharge properties, which are used in practice to produce ozone [2].

Experimental setup. The effect of a corona electric discharge of negative polarity on soil properties was studied in laboratory conditions. The scheme of the experimental device is shown in Fig.1. The installation consists of a cell filled with soil samples and an electrical circuit. The upper electrode was a multi-needle system (29 needles) with a needle tip radius of -0.4 mm. The needles were placed at a height of 5-15 mm above the surface of the samples.

The electrodes were under negative potential. The cuvettes were made of metal or dielectric. The current in the discharge was measured by a milliammeter A1, the voltage was measured by a circuit consisting of a resistance R1 and a milliammeter A2. The volt-ampere characteristics of the discharge over the soil surface and grain crops were measured.



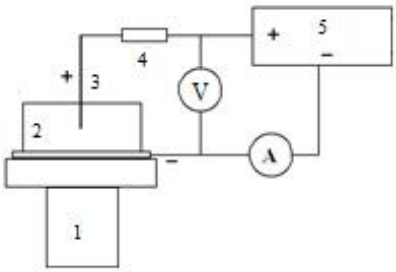




FIGURE 1. Photos and installation diagram for soil processing. Circuit designations: 1 – power supply, 1 2 – electric motor that creates vibrations, 2 3– cuvettes, 3 4 – multielectrode composition, 4 5 – ballast resistance, 5 6– high voltage source.

A direct current source (5) was used, the voltage in the experiment varied within U = 5-25 kV, the current varied within I = 20-200 mcA. The current (mcA) in the circuit was measured using a milliammeter A, the voltage (kV) was measured using an internal voltmeter V. Discharge Parameters: peat 100% (Uav=7.7, I av =38); peat +sand 50%+50% (Uav=7.2, Iav =160); peat +sand 78,6%+21,4% (Uav=9.3, I av =100); peat +sand 21,0 %+79,0% (Uav=10.0, I av =157).

After processing, the samples were brought to a paste-like state in which the parameter of specific electrical conductivity was determined.

The other part of the samples was placed in flasks with the addition of distilled water in a soil-water ratio of 1:5. Stirring was performed for 10 minutes and the suspension was filtered through a paper filter. In the filtered samples of water extract from soils, the parameters of specific electrical conductivity and ORP (redox potential) values were determined.

TABLE 1. Specific electrical conductivity of soil paste

Sample	EU control (without treatment), McSm/cm	EU treatment, McSm/cm	Δ EU, McSm/cm (with respect to the control)
peat 100%	1174	1300	126
peat +sand 78,6%+21,4%	972	1055	83
peat +sand 50%+50%	605	750	55
peat +sand 21,6%+78,6%	450	485	35
sand 100%	68	120	52

The organogenic sample shows a maximum electrical conductivity of 1174 Mc Sm/cm. With an increase in the mineral component of the samples, the electrical conductivity decreases. In pure sand, it is minimal and amounts to 68 Mc Sm/cm.

Corona discharge treatment of samples leads to an increase in electrical conductivity (Table 1). With a decrease in the proportion of the organic component in the samples, the effect of processing on electrical conductivity decreases. However, the effect of sample processing on the relative increase in electrical conductivity was recorded in pure sand.

A similar pattern in the effect of corona discharge treatment of samples was noted when measuring the electrical conductivity of an aqueous extract (Table 2). A more significant effect of corona discharge treatment of the samples was obtained in relation to the index of redox (ORR) conditions. In all control samples, this indicator was low and ranged from +38 mV on pure peat and +94 mV on pure sand. These

ORR values indicate the predominance of restoration conditions, which is typical from the point of view of the genesis of objects. Peat is a hydromorphic formation, the genesis of which is dominated by restorative processes.

TABLE 2. ORR and specific electrical conductivity of the water extract

Sample	Electrical conductivity, McSm/cm		ORR, mV	
	control	treatment	control	treatment
peat 100%	465	544	+38	+815
peat +sand 78,6+21,4	390	360	+65	+665
peat +sand 50+50	270	340	+72	+94
peat +sand 21,6+78,4	95	166	+81	+98
sand 100%	27	44	+94	+105

The effect of corona discharge treatment on the ORR index was very significant. This is especially evident in samples with a predominance of the organic component. The process of oxidation of organic matter is accelerated under the influence of several factors. The main oxidizing factor is the effect of ozone and negative ions, which are formed in the gas phase of the air during the plasma- electric action of a corona discharge on the air with the formation of negative ions and ozone in the air.

Because the active particles formed in the plasma move rapidly to the soil surface under the action of diffusion. The characteristic diffusion time $\tau \sim \frac{r^2}{6D}$, where r is the distance from the needle of the electrode to the soil surface (5-7 mm), D is the diffusion coefficient (the typical diffusion coefficient of O_2^- ions is 0.830 cm^2/s, O_3 - in oxygen, 0.056 cm^2/s in oxygen, and 0.182 cm^2/s in N_2-O_2 atoms). The diffusion time of particles formed in plasma to the soil surface is in the range of 0.3-1 s, which is much shorter than the time of soil treatment by the corona discharge plasma. Therefore, it can be assumed that the formation of active particles in the air by corona discharge, which affect ORR in the soil, is an important result of plasma exposure.

Conclusions. Experiments have been conducted to evaluate the effect of a negative polarity corona discharge on redox processes in the soil. A significant effect of corona discharge treatment of the samples was obtained in relation to the index of redox (ORR) conditions. In all control samples, this indicator was low and ranged from +38 mV on pure peat and +94 mV on pure sand. These ORR values indicate the predominance of restoration conditions, which is typical from the point of view of the genesis of objects. Peat is a hydromorphic formation in the genesis of which restoration processes dominate. The effect of corona discharge treatment of samples on the ORR index is very significant. This is especially evident in samples with a predominance of the organic component. The process of oxidation of organic matter is accelerated under the influence of several factors realized in the plasma of the corona discharge.

1. D.S. Orlov, L.K. Sadovnikova, N.I. Sukhanova, *Chemistry of soils*, Higher School, Moscow, 2005.
2. V.V. Lunin, V.G. Samoilovich, S.N. Tkachenko, I.S. Tkachenko, *Theory and practice of obtaining and applying ozone*, Publishing House of Moscow University, Moscow, 2023.

PENETRATION OF MULTI-CHARGED CLUSTERS INTO A SOLID BODY

Anatoly I. Nikitin, Vadim A. Nikitin, Alexander M. Velichko and Tamara F. Nikitina

Semenov Federal Research Center for Chemical Physics, Russian Academy of Sciences, Moscow, Russia

Usherenko Effect. In 1974, the Institute of Pulse Processes in Minsk discovered the phenomenon of penetration of particles moving at a speed of more than 500 m/s into a metal barrier to depths of tens and hundreds of millimeters (Usherenko Effect) [1]. Figure 1 shows a diagram of the setup for introducing fast powder particles into a metal matrix [2].

A portion of powder particles ranging in size from 10 to 200 μm and weighing 20-200 g was placed in a capsule located inside an explosive charge. When the explosion was initiated, the powder particles were accelerated by the explosion products to a speed of 1-3 km/s and hit the surface of a metal barrier.

At the moment of impact, the particle's pressure on the target reached 15 GPa. Calculations showed that the reserve of kinetic energy of a spherical particle could allow it to penetrate a solid body to a depth no greater than 5-6 times its diameter. Figure 2a shows such a particle. It can be seen that the embedded particle left a wide crater, and the resulting channel is filled with grains of the target material. Figure 2b shows a particle that managed to penetrate the target to a great depth [3].

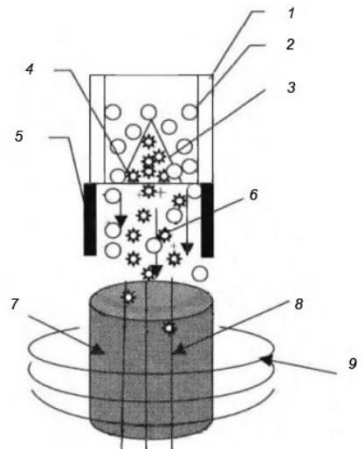


FIGURE 1. Scheme of the experiment to study the effect of a flow of SiC microparticles on a metal target. 1 - charge body; 2 - explosive substance; 3 - cumulative funnel; 4 - powder particles; 5 - control support; 6 - flow of powder particles and plasma; 7 - metal sample; 8 - electric field lines; 9 - magnetic field lines.

This picture is radically different from that shown in Fig. 2a. The embedded particle is in a channel, which is not filled with foreign inclusions behind it. This channel narrows behind the particle, and at some distance from it it collapses. The penetration depth depended on the particle size. Particles 60-70 μm in size penetrated to the maximum depth, and particles smaller than 5 μm and larger than 200 μm slowed down at shallow depths. It was found that the effect of ultra-deep penetration of particles occurs only when a bunch of particles collides with an obstacle. When individual particles collided with an obstacle, the effect of ultra-deep penetration was not found.

During the interaction of a stream of SiC microparticles with a cylindrical target made of steel-10, the appearance of an electromagnetic field pulse was detected [2]. The duration of the magnetic field pulse was $(5\text{-}12)\cdot10^{-6}$ s, and its induction was $B = (5\text{-}80)\cdot10^{-3}$ T. The induction value was maximum at a particle size of $r = 60$ μm and decreased to zero with an increase in size to $r = 220$ μm. During these studies, the surface of the cylindrical target was wrapped in X-ray film wrapped in several layers of black paper. After development, lines (tracks) with a length of $(10\text{-}15)\cdot10^{-3}$ m and a width of $(2\text{-}4)\cdot10^{-6}$ m were found on it [2]. The particles that left the tracks moved parallel to the plane of the film. The energy of these particles, estimated by the path length, was not less than 80-100 MeV. The same tracks were found on the surface of a silicon plate located next to a cylindrical target [2].

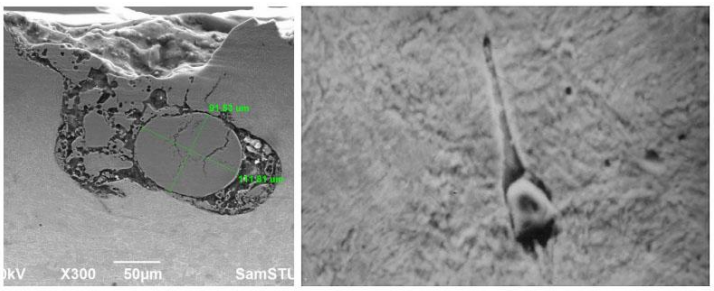


FIGURE 2. a) An iron particle embedded in the surface of an iron-nickel alloy target. b) A particle that penetrated steel to a great depth.

The hypothesis of the superdeep penetration. In [4] it was shown that the most suitable object capable of leaving the indicated traces are multiply charged clusters of water molecules. In these clusters, a certain ensemble of ions with a total charge Q is held inside a spherical shell of polarized water molecules. The Coulomb repulsion force of ions located on the surface of a sphere of radius r is equal to

$$F_Q = Q^2/8\pi\varepsilon_0 r^2. \quad (1)$$

This force is compensated by the pressure on the surface of the sphere of a layer of polarized water molecules of thickness a:

$$F_{pw} = \sigma a \cdot 4\pi R^2 \cdot \text{grad}\,(Q/4\pi\varepsilon_0 R^2) = \sigma a \cdot 4\pi R^2 \cdot (Q/4\pi\varepsilon_0)\cdot(2/R^3) = 2\,\sigma a Q/\,\varepsilon_0 R. \quad (2)$$

Here $\sigma = 1$ C/m^2 is the charge density of the ends of water dipoles on the surface of the sphere. The radius of such a cluster is $R = r + a$.

Let us assume that particles of metal powder flying at a speed of 1-3 km/s lose some electrons and acquire a positive charge upon collision with an obstacle. Let a spherical titanium ball collide with a target. Let us estimate what charge a titanium ball of radius $R = 30$ μm can acquire upon colliding with a steel target. The density of titanium is $4.5\cdot10^3$ kg/m^3. At $R = 3\cdot10^{-5}$ m, the volume of the ball is $V = 1.13\cdot10^{-13}$ m^3, and the mass is $M = 5\cdot10^{-10}$ kg. The kinetic energy of a ball flying at a speed of 3000 m/s is $E_c = 2.25\cdot10^{-3}$ J. Let us consider the process of electron transfer from the particle to the target. In this case, we will take into account that as part of the negative charge of the ball is removed, the value of the positive charge remaining on it increases and, consequently, the work on removing the next portion of the negative charge constantly increases. Let a portion of the negative charge Δq first pass into the target. The particle acquired a positive charge Δq. The work on separating the charges from the distance R to ∞ is equal to $\Delta A_1 = (\Delta q)^2/4\pi\varepsilon_0 R$. After this, the positive charge of the particle became equal to $2\Delta q$. When separating a negative charge of Δq from this particle, the work done will be $\Delta A_2 = (2\Delta q)\cdot(\Delta q)/4\pi\varepsilon_0 R$. When separating the n-th charge Δq, the work expended will be $\Delta A_n = (n\Delta q)\cdot(\Delta q)/4\pi\varepsilon_0 R$. The total work in performing n steps is $A = \Sigma\,(\Delta A_n) \approx (n^2/2)\cdot(\Delta q)^2/4\pi\varepsilon_0 R$. Let us equate it to the kinetic energy of the particle E_c.

$$(n^2)\cdot\,(\Delta q)^2 = E_c \cdot 8\pi\varepsilon_0 R. \quad (3)$$

The positive charge Q remaining on the particle is $n\Delta q$, so

$$Q = (E_c \cdot 8\pi\varepsilon_0 R)^{1/2}. \quad (4)$$

Substituting $R = 3\cdot10^{-5}$ m and $E_c = 2.25\cdot10^{-3}$ J into this formula, we find the charge acquired by the ball, $Q = 1.145\cdot10^{-9}$ C ($7.16\cdot10^9$ elementary charges).

Let us estimate the magnitude of the pressure exerted on the surface of the steel target by a titanium ball of radius $R = 3 \cdot 10^{-5}$ m, possessing a charge of $Q = 10^{-9}$ C. Let us consider the moment when it has just touched the surface. The force of attraction of the ball to the conducting plane is equal to:

$$F_{at} = Q^2/4\pi\varepsilon_0(2R)^2 = 2.498 \text{ N}. \quad (5)$$

The cross-sectional area of the ball is $s = \pi R^2 = 2.826 \cdot 10^{-9}$ m^2. The pressure of the ball on the surface is $P = F_{at}/s = 8.84 \cdot 10^8$ Pa = 884 MPa. The tensile strength of steel-10 is $P_t = 330$ MPa. Therefore, the ball must penetrate into the target material. Once inside the target, the charged ball will press on the walls of the formed channel. Let us estimate the magnitude of this pressure. Let us surround the charge $Q = 10^{-9}$ C with a sphere of radius $R = 3 \cdot 10^{-5}$ m. The charge will exert a pressure on this sphere

$$P_Q = (Q^2/8\pi\varepsilon_0 R^2)/(4\pi R^2) = 442 \text{ MPa}. \quad (6)$$

Let us consider how a ball with a positive electric charge Q_b will move inside the target material. Let the center of the ball go deeper into the target to a distance slightly greater than the radius of the ball $l = 4 \cdot 10^{-5}$ m. When the ball is introduced into the material of the steel target, positive charges will appear on its walls and a force will arise that repels the ball from these charges. This force takes on a maximum value when the ball is repelled from the nearest surface of the target. When the center of the ball is at a distance of $r_{in} = 4 \cdot 10^{-5}$ m from the surface of the target, a force directed into the target will act on it:

$$F_{pr} = Q_b^2/4\pi\varepsilon_0(2r_{in})^2. \quad (7)$$

If the charge of the ball Q_b remains equal to 10^{-9} C, then the force F_{pr} will be equal to 1.4 N. As the ball moves deeper into the target, the magnitude of the force F_{pr} will decrease. At $r_{in} = 5 \cdot 10^{-2}$ m $F_{pr} = 8.99 \cdot 10^{-7}$ N, and when the ball is at a point half the length of the target, it will be equal to zero. Now we need to understand how strongly a compressed metal ball, which is acted upon by a rather weak electric force, can move in a solid over a large distance. The only chance for it to do this is to reduce the friction force of the medium in the contact zone as much as possible. In this case, the introduced particle must have the ability to retain the acquired electric charge for a long time. For this, its shell (consisting of a dielectric, for example, oxides and water) must be a good insulator. At the end of the 20th century, scientists from the Institute of Chemical Physics of the USSR Academy of Sciences managed to show that if a solid subjected to high pressure undergoes shear deformation, then intensive chemical reactions begin to occur in it [5]. They discovered that the chemical reaction occurs precisely at the moment of deformation of the solid. In experiments demonstrating this effect, the test substance (for example, metal) was placed between two disks ("Bridgman anvils" [6]) and subjected to strong compression. At the moment of application of force, one of the "anvils" rotated at a certain angle around its axis. In this case, the bonds between the atoms in the crystal lattice were broken, and the metal acquired greater plasticity. The effective diffusion constant in the metal increased by 10 orders of magnitude and was 3-4 orders of magnitude greater than in liquid metal [7].The surface of a metal ball wedged into the metal is compressed by the deformed crystal lattice. At the moment of action of a force on the ball causing its displacement, the inter-atomic bonds between the surface of the ball and the surface of the target metal are broken. In this case, the friction force drops to almost zero. After the ball has been displaced a certain distance, the channel created by it is closed by the pressure force of the crystal lattice of the target metal. The movement of the charged ball inside the metal is determined by the action of forces arising from the polarization of nearby crystal grains.

Conclusion. This article proposes a new hypothesis to explain a set of phenomena accompanying the process of ultra-deep penetration of fast metal particles into a target: the appearance of intermittent traces on photographic films and the generation of a magnetic field pulse. We believe that the magnetic field is created by a flow of electrons that break away from a particle during deceleration, as a result of which it acquires a positive charge. This charge forces the particle to penetrate into the target. Once

inside a solid, the charged particle moves in it for some time, when the oscillations of the crystal lattice last, under the action of electric fields. Due to the combination of ultra-high pressure and shear effects, the viscosity of the metal is significantly reduced. Some of the charged particles come out of the target material and, interacting with the surface of the photographic film or solid plate, leave a chain of traces on it. The proposed hypothesis is described in more detail in the article [8].

1. S.M. Usherenko, *Superdeep penetration of particles into barriers and creation of composite materials*, Publishing house of the Research Institute of Pulse Processes, Minsk, 1998.
2. A.I. Belous, V.A. Solodukha and S.V. Shvedov, *Space electronics. In 2 books. Book 2*, Tekhnosfera, Moscow, 2015.
3. Sobolev V.V., Usherenko S.M.. Shock wave initiation of nuclear transmutation of chemical elements // *Journal de Physique IV (Proceedings)*. 2006. V. 134. P. 977–982.
4. Nikitin A.I., Nikitin V.A., Velichko A.M., Nikitina T.F. Tracks on films and multi-charged clusters // *RENSIT, Radioelectronics. Nanosystems. Information technologies*. 2021. V. 13. No 3. P. 355–356. DOI: 10.17725/rensit.2021.13.355.
5. Zhorin V.A., Zharov A.A., Kazakevich A.G., Enikolopov N.S. Motion of matter on Bridgman anvils at high pressures combined with shear deformation // *Solid State Physics*. 1975. V. 17. No 2. P. 393–396.
6. P.W. Bridgman, *Studies in large plastic flow and fracture. With special emphasis on the effects on hydrostatic pressure*, New York, Toronto, London, 1952.
7. N.S. Enikolopov, Solid-phase chemical reactions and new technologies. Report at the meeting of the Presidium of the USSR Academy of Sciences in October 1988. In: *Enikolopov N.S. Selected works. Memories*, ISMAN Publishing House, Chernogolovka, 1999, p. 102.
8. Nikitin A.I., Nikitin V.A., Velichko A.M., Nikitina T.F. The process of superdeep penetration of high-speed particles into a solid body // *Crystallography Reports*. 2024. V. 69. No 3. P. 682–691. DOI: 10.1134/S1063774524601783.

METHODS AND TECHNIQUES FOR REMOTE SENSING AND IDENTIFICATION OF HAZARDOUS CHEMICALS IN THE ATMOSPHERE AND DIFFERENT SURFACES

SAMPLING SYSTEM FOR GAS ANALYSIS BASED ON FTIR SPECTROSCOPY

Pavel P. Demkin, Viacheslav R. Bessonov, Igor S. Golyak, Ivan A. Karpov, Alisa P. Kosterova, Alexander D. Kuznetsov and Igor L. Fufurin

Bauman Moscow State Technical University, Moscow, Russia

Currently, the development of new screening technologies for high-quality spectra of gases and various gas mixtures, including human exhaled air and atmospheric air, is one of the most relevant areas in infrared (IR) spectroscopy [1]. Real-time analysis of such mixtures represents one of the modern approaches to solving this problem. Proper preparation of gas mixtures ensures the most accurate results during subsequent spectral processing [2].

This work examines a sampling system, particularly the procedures for sample drying, efficient cleaning of the optical cell, and target gas detection. Figure 1 shows the general functional diagram of the sampling system. Depending on the configuration of the needle valves, the sampling system can operate in different modes.

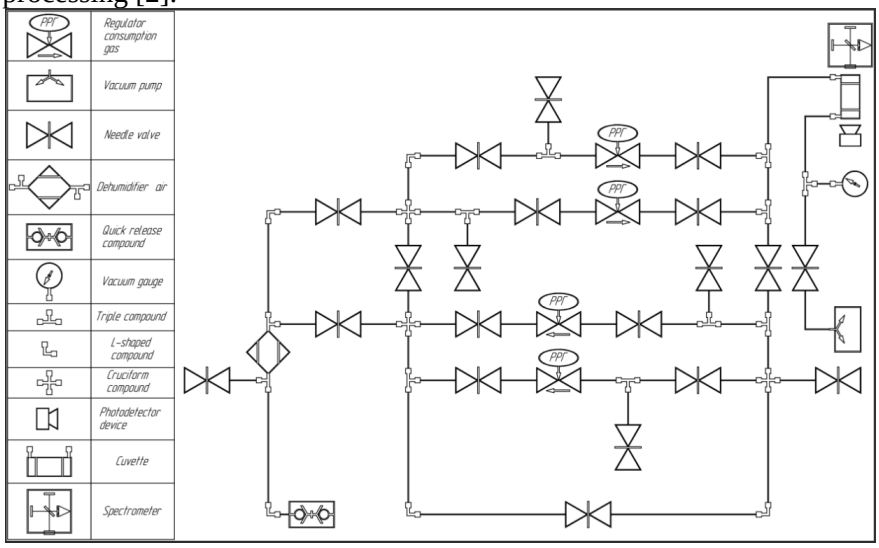


FIGURE 1. Functional diagram of the sampling system.

The main operating modes of the sampling system are: sample drying, cell cleaning, and working with calibration gas mixtures. Figure 2 shows the functional diagrams of the sampling system in the main operating modes, excluding unused elements of the general scheme for better clarity.

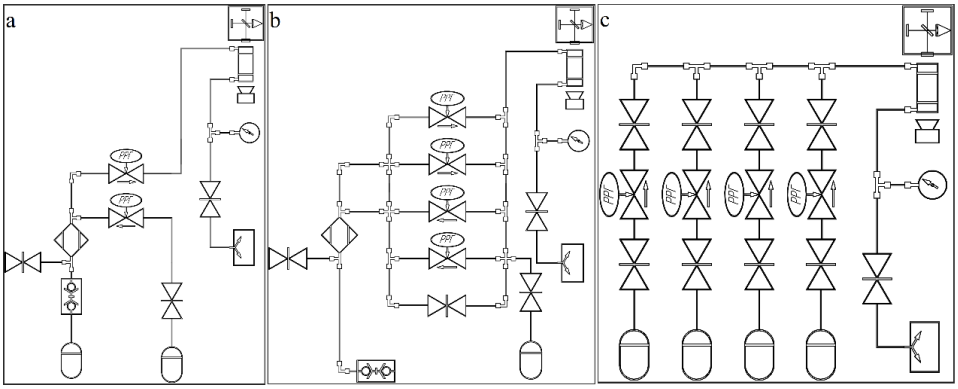


FIGURE 2. Options for assembling the sampling system: (a) a configuration that allows you to dry the sample, (b) a configuration that allows you to clean the system, and (c) a configuration that allows you to work with test gas mixtures.

Below is a sample preparation method that eliminates excess water vapor, which obscures the spectral lines of other substances in the approximate ranges of 1350 cm^{-1} to 1700 cm^{-1} and 3500 cm^{-1} to 4000 cm^{-1} [3]. Drying of the humid gas mixture is achieved by changing the ratio of the flow rates of the purge gas to the target gas mixture [4]. Table 1 presents comparative characteristics of drying quality, and Figure 3 shows the spectra of atmospheric air without drying and the spectra of atmospheric air with different drying options.

TABLE 1. Comparative characteristics of drying quality.

Consumption of wet gas mixture, SCCM	Purge gas flow rate, SCCM	Drying degree, %
100	300	89
100	400	92
200	800	91
250	500	58
250	1000	72
300	1200	87
300	1500	88

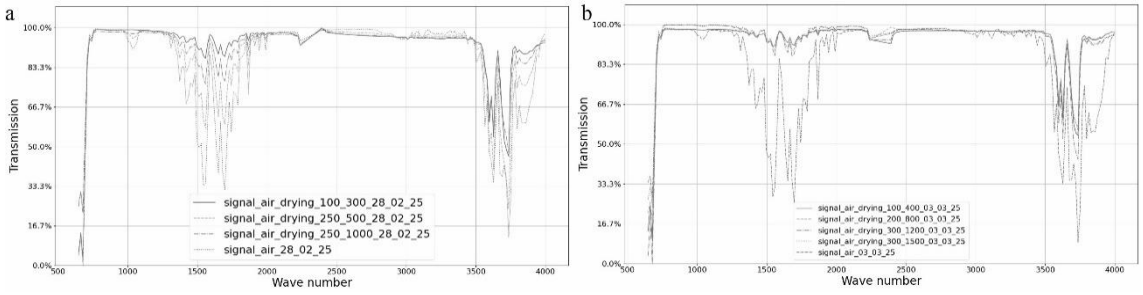


FIGURE 3. Spectra of atmospheric air with different degrees of humidity: (a) date of experiment 28.02.25, and (b) date of experiment 03.03.25.

From the obtained data, it is easy to see that the most effective drying is achieved at a ratio of 100 SCCM of the target gas to 400 SCCM of the dry purge gas. However, it is also worth noting the ratio of 200 to 800 SCCM, as it reduces drying time with minimal losses.

To test the efficiency of cleaning the gas cell, it was first filled with an IR-transparent gas, in this case nitrogen, and then a test gas, methanol, was introduced at a concentration of 1000 ppm through continuous purging. After that, the optimal nitrogen flow rate was selected for the fastest cleaning of the cell. Table 2 presents comparative characteristics of the cell cleaning efficiency (Fig. 4).

TABLE 2. Comparative characteristics of cleaning quality.

Purge gas flow rate, SCCM	Purge time, s	Drying of purification, %
500	300	93.2
500	600	97.0
500	900	99.2
500	1200	99.2
1000	300	96,6
1000	600	99,3
1000	900	99,3
1000	1200	99,7
2000	300	96.5
2000	600	99.3
2000	900	99.9
2000	1200	99.9

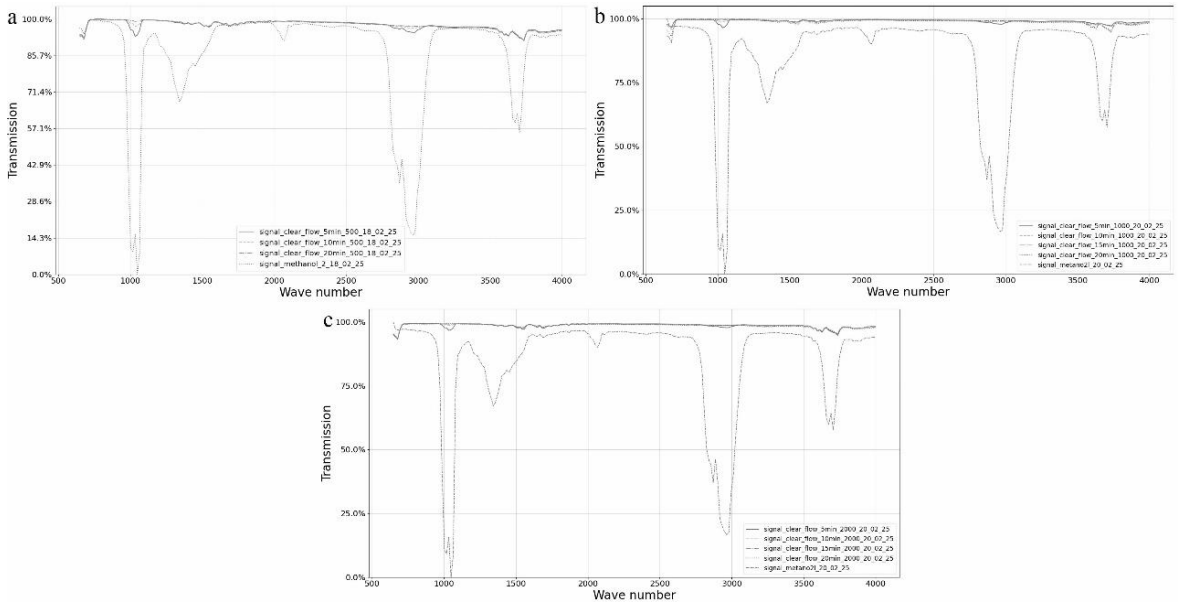


FIGURE 4. Spectra of the degree of purification of the cuvette from the test gas mixture of methanol with a concentration of 1000 ppm and nitrogen: (a) experiment date 02.18.25 and (b and c) experiment date 02.20.25

From this table, it is easy to see that the most thorough cleaning is achieved at a purge gas flow rate of 2000 SCCM, and such cleaning takes only 15 minutes.

The research results showed that the most effective drying is achieved at a ratio of target gas to dry purge gas flow rates of 100 SCCM to 400 SCCM, as well as at a ratio of 200 SCCM to 800 SCCM, which minimizes losses and reduces drying time. The optimal nitrogen flow rate for cleaning the cell was 2000 SCCM, ensuring thorough cleaning within 15 minutes. The obtained data, such as a drying efficiency of 91–92% and a cleaning efficiency of 99.9%, improve the accuracy of gas mixture analysis and enhance the quality of their spectra. The proposed system can be used for real-time monitoring of gas mixtures, making it promising for applications in environmental control, medicine, and other fields.

The work was carried out within the framework of the strategic academic leadership program «Priority 2030».

1. P. R. Griffiths and J. A. de Haseth, *Fourier Transform Infrared Spectrometry*, Wiley-Interscience, 2007. DOI: 10.1002/047010631X
2. Werle P., Mücke R., Slemr F. The Limits of Signal Averaging in Atmospheric Trace-Gas Monitoring by Tunable Diode-Laser Absorption Spectroscopy (TDLAS) // *Applied Physics B.* 1993. V. 57. No 2. P. 131–139. DOI: 10.1007/BF00325952.
3. A. N. Morozov and S. I. Svetlichnyi, *Fundamentals of Fourier Spectroradiometry*, Nauka, Moscow, 2014.
4. Zhao Y., Zhang L. Advanced Techniques for Gas Analysis in Environmental Monitoring // *Environmental Science & Technology*. 2016. V. 50. No 5. P. 2233–2245. DOI: 10.1021/acs.est.5b04999.

TECHNIQUES FOR METHANE LEAKS REMOTE DETECTION BY INFRARED NON-DISPERSIVE SPECTROSCOPY FROM AIRSPACE

Evgenii N. Zadorozhnyi, Dmitriy R. Anfimov, Ivan B. Vintaikin, Ilya S. Golyak, Igor L. Fufurin and Andrey N. Morozov

Bauman Moscow State Technical University, Moscow, Russia

Carbon dioxide (CO_2) is the most prevalent anthropogenic greenhouse gas, contributing to approximately 50% of global emissions. Methane (CH_4), the second most significant contributor, accounts for 20-30% of greenhouse gas emissions [1]. While carbon dioxide persists in the atmosphere for centuries, methane has a comparatively shorter atmospheric lifetime of approximately 12 years. Consequently, effective monitoring and mitigation of methane emissions present a critical opportunity to decelerate the rate of global warming and ameliorate the environmental impact of greenhouse gases [2].

Global methane emissions originate from both natural and anthropogenic sources. Natural sources, such as wetlands, termites, and geological seeps, contribute 35-40% of total emissions, whereas human activities, including agriculture, fossil fuel extraction, and waste management, are responsible for the remaining 60-65% [3]. Among these anthropogenic sources, methane leaks occurring during the extraction, transportation, and storage of natural gas represent a particularly pressing environmental and economic challenge. These leaks not only exacerbate climate change but also result in substantial economic losses due to the waste of a valuable energy resource.

Optical methods for gas leak detection are recognized as highly effective and widely utilized in various industrial and environmental applications [4, 5]. Among these, technologies employing highly sensitive thermal imaging cameras and tunable diode laser absorption spectroscopy (TDLAS) stand out due to their ability to accurately identify leaks over considerable distances [6]. These methods have proven particularly valuable for monitoring methane emissions, which are critical for both environmental protection and industrial safety.

This study focuses on the development and evaluation of a non-dispersive infrared (NDIR) methane sensor of the passive type, designed in both stationary and portable configurations. The research presents the design principles, operational characteristics, and experimental results of these sensors, highlighting their potential for reliable methane detection in diverse settings.

Figure 1 provides a detailed overview of the stationary version of the NDIR spectrometer, illustrating its design and key components.

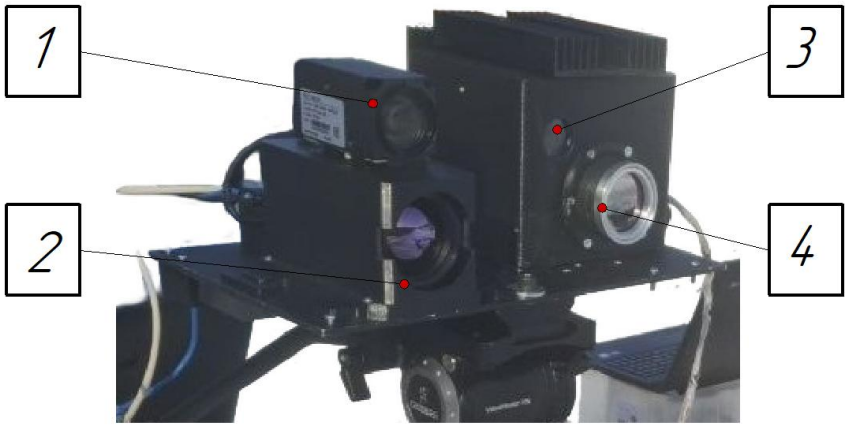


FIGURE 1. Stationary NDIR Spectrometer: 1- TV camera, 2 - Thermal camera, 3 - Photodetector (reference), 4 - Photodetector(signal)

The NDIR sensor incorporates two photodetector units: a signal channel and a reference channel. The signal channel is optimized to detect radiation filtered within the wavelength range corresponding to a specific methane absorption line, enabling targeted identification of methane. Simultaneously, the reference channel is calibrated to filter radiation in a spectral range devoid of absorption lines from typical atmospheric components, including methane. This design ensures that the reference channel provides a stable baseline, free from methane interference, which is critical for accurate differential measurement. By comparing the outputs of the signal and reference channels, the sensor achieves high sensitivity and specificity in detecting methane concentrations, even in complex environmental conditions.

The swift advancement of remote control technologies, in conjunction with the ongoing miniaturization of aerial platforms and the development of advanced sensor systems, has greatly broadened the scope of unmanned aerial vehicle (UAV) applications in environmental monitoring [7]. A particularly notable application is the use of UAVs for the detection and quantification of methane emissions [8]. Given the increasing reliance on UAVs for such monitoring tasks, the design and implementation of compact, portable spectrometer systems have become a crucial and timely research focus. These systems, when integrated into UAV platforms, hold the potential to significantly enhance the accuracy and operational efficiency of methane leak detection, especially in remote, inaccessible, or hazardous environments where human access is limited or poses significant risks.

Figure 2 shows a general view of the portable version of the NDIR spectrometer.

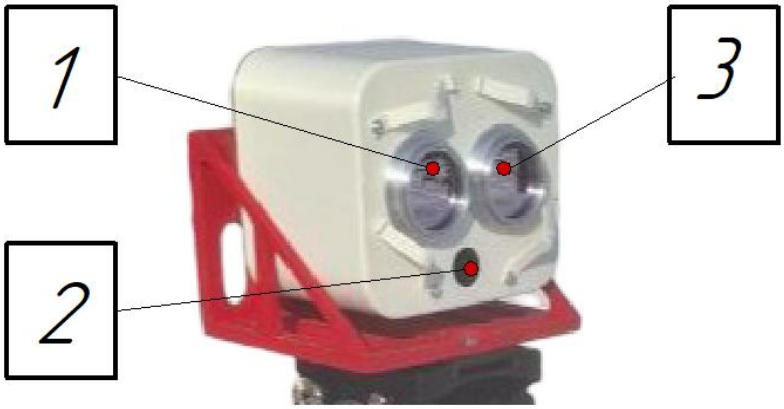


FIGURE 2. Portable NDIR Spectrometer: 1 – Photodetector(reference), 2 – Video camera, 3 – Photodetector(signal)

A series of experiments was conducted using the NDIR sensor to detect methane at distances of 60.8 meters and 90 meters. Four experimental trials were performed, each with varying gas supply durations for the devices at the specified distances. Detailed data on gas consumption, delivery time, and detection results are summarized in Table 1.

TABLE 1. Experimental results

The duration of the outflow of gas into the atmosphere, s	The rate of methane release from the cylinder, g/s	Detection, Stationary (60.8 m and 90 m)	Detection, Portable (60.8 m and 90 m)
30	1,6	clear identification	clear identification
10	2,3	clear identification	clear identification
60	0,9	clear identification	clear identification
66	1,5	clear identification	clear identification

The experimental results demonstrate that the developed NDIR sensors exhibit high reliability and efficiency in detecting methane at distances ranging from 60.8 to 90 meters. The minimum detection threshold corresponds to a leak rate of 1 to 2 grams per second. These findings confirm that the sensors are capable of providing accurate and stable methane detection even at considerable distances, making them a promising solution for leak monitoring in industrial and environmental applications.

Passive NDIR methane sensors have been engineered and validated through comprehensive testing. The stationary spectrometer model has a footprint of 250 x 420 x 230 mm (L x W x H) and a mass of 26 kg. On the other hand, the compact spectrometer is designed to facilitate methane leak detection within a 5 km radius from the operator of an aerial platform, operating at altitudes of up to 100 m. This lightweight device measures 180 x 155 x 160 mm (L x W x H) and weighs 1.8 kg. The experimental results confirm that the sensors are capable of reliably detecting methane at distances between 60 and 100 meters, with a minimum detectable leak rate of 1 g/s or greater.

The work was carried out within the framework of the strategic academic leadership program «Priority 2030».

1. Cain M., Jenkins S., Allen M. R., et al. Methane and the Paris Agreement temperature goals // *Philosophical Transactions of the Royal Society A: Mathematical, Physical and Engineering Sciences*. 2021. V. 380. No 2215. 20200456. DOI: 10.1098/rsta.2020.0456.
2. Saunois M., Stavert A.R., Poulter B., et al. The Global Methane Budget 2000–2017 // *Earth Syst. Sci. Data*. 2020. V. 12. No 3. P. 1561–1623. DOI: 10.5194/essd-12-1561-2020.
3. Jackson R.B., Saunois M., Bousquet P., et al. Increasing anthropogenic methane emissions arise equally from agricultural and fossil fuel sources // *Environmental Research Letters*. 2020. V. 15. No 7. 071002. DOI: 10.1088/1748-9326/ab9ed2.
4. Li X., et al. A comprehensive review of optical gas sensors for methane detection: From laboratory to field applications // *Journal of Natural Gas Science and Engineering*. 2021. V. 94. 104075. DOI: 10.1016/j.jngse.2021.104075.
5. Morozov A.N., Tabalin S.E., Anfimov D.R., et al. Estimation of Emissions From Metallurgical Plants Using Infrared Fourier Transform Spectroscopy // *Russian Journal of Physical Chemistry B*. 2024. V. 18. No 3. P. 763–772. DOI: 10.1134/S1990793124700234.
6. Wang L., et al. Recent advances in tunable diode laser absorption spectroscopy for gas sensing and leak detection // *Applied Spectroscopy Reviews*. 2022. V. 57. No 3. P. 231–256. DOI: 10.1080/05704928.2021.1920032.
7. Liu H., et al. Advances in drone-based gas leak detection using optical sensors: A review // *Drones*. 2023. V. 7. No 1. P. 12. DOI: 10.3390/drones7010012.
8. Smith T., et al. UAV-based methane emission monitoring: Challenges and opportunities // *Environmental Research Letters*. 2023. V. 18. No 3. 034012. DOI: 10.1088/1748-9326/acb5e3.

OPTICAL METHODS OF REMOTE SENSING OF THE EARTH FROM SPACE FOR THE STUDY OF ATMOSPHERIC GREENHOUSE GAS CONCENTRATION

Olga A. Nebritova, Andrey N. Morozov and Igor L. Fufurin

Bauman Moscow State Technical University, Moscow, Russia

In recent decades, the problem of climate change and its consequences has become one of the most pressing issues for the scientific community and society as a whole. One of the key factors contributing to global warming is the increase in the concentration of greenhouse gases in the atmosphere, such as carbon dioxide (CO_2) and methane (CH_4) [1]. Modern technologies are needed to effectively monitor and analyze these gases, and optical methods of remote sensing of the Earth from space are one of the most promising approaches [2].

The objective of the paper is to monitor the global distribution of carbon dioxide (CO_2) and methane (CH_4) using the GOSAT satellite equipped with the Thermal and Near Infrared Sensor for Carbon Observation Fourier-Transform Spectrometer (TANSO-FTS), which measures the absorption spectra of solar radiation and thermal infrared radiation. The object of the study is the Earth, and the hypothesis being tested is the possibility of long-term and accurate monitoring of greenhouse gases from space to assess sources and sinks of greenhouse gases.

The theoretical basis is the importance of accurate observations of CO_2 and CH_4 in the atmosphere to understand their long-term changes and assess sources and sinks. Satellite observations allow such

measurements to be made on a global scale. The study builds on previous work that has proven the usefulness of remote sensing of CO_2 concentrations for surface data analysis.

The methodology of the study includes the use of the GOSAT satellite with two instruments: TANSO-FTS and TANSO-CAI. TANSO-FTS measures three narrowband and one broadband spectral bands with a resolution of 0.2 cm^{-1}, while TANSO-CAI corrects cloud and aerosol data. The study was conducted in several stages, including model development, instrument testing, and calibration before launch and in orbit. The dependent variables are CO_2 and CH_4 concentrations, and the independent variables are spectral data obtained from GOSAT.

The the results of successful calibration and measurement of TANSO-FTS data. High signal-to-noise ratio (SNR) for spectral ranges was achieved, for example, SNR 345 for the 1P band. The instrument linearity and the effect of micro-vibrations on the data measured before launch and in orbit were also calibrated, confirming the high accuracy and stability of the measurements.

The conclusions of the study show a successful demonstration of methods for measuring CO_2 and CH_4 concentrations with high spectral resolution using a space platform. The novelty of the work lies in the application of a highly efficient Fourier spectrometer for wide ranges of IR and near IR radiation, as well as the adaptation of space calibration methods for long-term observation [3].

Optical satellites use spectroscopic methods to analyze light reflected from the Earth's surface and atmosphere. Each gas has a unique absorption spectrum, allowing researchers to determine its concentration based on spectral analysis. For example, carbon dioxide absorbs infrared radiation at specific wavelengths, making it possible to detect it using specialized sensors.

Modern satellites are equipped with various sensors, such as multispectral and hyperspectral cameras. These devices are capable of capturing data in a wide range of wavelengths, including visible and infrared light. For example, NASA's OCO-2 (Orbiting Carbon Observatory-2) satellite uses highly sensitive spectrometers to measure the concentration of CO_2 in the atmosphere, allowing for accurate data on its distribution and changes over time. Optical data allows us to create detailed maps of greenhouse gas distribution at the global level. These maps are an important tool for scientists and policymakers, as they help visualize gas concentrations in different regions and track changes due to human activity and natural processes. Comparison of data obtained at different points in time allows us to assess the effectiveness of measures to reduce greenhouse gas emissions and their impact on the climate.

Hyperspectral imaging: This technique involves capturing images in a large number of narrow spectral bands. Hyperspectral data can provide detailed analysis of the composition of materials and detect changes in the environment.

Optical interferometry: This technique uses light interference to measure small changes in distance or in the optical properties of materials. It can be used to monitor changes in the atmosphere and on the Earth's surface.

Ultraviolet and infrared spectroscopy: These techniques can examine molecules and atoms in different states, which is useful for analyzing gases in the atmosphere and their concentrations.

Ultraviolet and Infrared Spectroscopy: These techniques examine molecules and atoms in different states, which is useful for analyzing gases in the atmosphere and their concentrations.

NDIR (Non-Dispersive Infrared) is a method of measuring gas concentrations based on the principle of infrared absorption. It is widely used to monitor greenhouse gases and other gases in the atmosphere. Here are the main aspects related to NDIR sensors emit infrared light through a gas sample. Certain gas molecules absorb infrared radiation at specific wavelengths. For example, carbon dioxide (CO_2) absorbs light in a specific range of the infrared spectrum. After passing through a gas, the remaining light is recorded by a detector. By measuring the intensity of the light before and after passing through the gas, the concentration of the gas can be determined based on the level of absorption. NDIR methods can detect low concentrations of gases. Each gas has unique absorption spectra, which allows

its concentration to be accurately determined. The method allows for real-time measurements. Conditional dependence: Atmospheric conditions such as temperature and pressure can affect the accuracy of measurements.

Thus, NDIR is an important tool for gas analysis and environmental monitoring, especially in the context of combating climate change. In addition to NDIR, there are other infrared methods such as FTIR (Fourier Transform Infrared Spectroscopy), which can analyze gas mixtures and determine their concentrations.

There are several types of optical gas analyzers that can be used to measure greenhouse gas concentration dynamics. Here are some of them:

- Laser spectroscopy: This method uses lasers to accurately measure gas concentrations. Lasers can be tuned to specific wavelengths that correspond to the absorption spectra of different gases, allowing for highly sensitive measurements.
- FTIR (Fourier Transform Infrared Spectroscopy): This method analyzes gas mixtures by determining their concentrations based on infrared absorption. FTIR can measure multiple gases simultaneously, making it useful for monitoring greenhouse gases [4].
- Diffraction Spectroscopy: This technique uses the diffraction of light to analyze gases. It can be used to determine the concentrations of a variety of gases, including greenhouse gases.
- Fiber Optic Sensors: These devices use optical fibers to transmit light and can be used to measure gas concentrations. They can be compact and suitable for use in hard-to-reach locations.

Optical methods of remote sensing of the Earth from space are a powerful tool for studying the concentration of atmospheric greenhouse gases. Spectroscopy, modern sensors and mapping technologies allow scientists to obtain accurate and up-to-date data that are necessary for understanding climate change and developing effective strategies for its mitigation. In the context of global warming and increasing greenhouse gas emissions, such technologies are becoming an integral part of scientific research and decision-making at the level of states and international organizations.

1. Golyak I. S., Anfimov D. R., Vintaykin I. B., et al. Monitoring greenhouse gases in the open atmosphere by the Fourier spectroscopy method // *Russian Journal of Physical Chemistry B*. 2023. V. 17. No 2. P. 320-328. DOI: 10.1134/s1990793123020264.
2. Mayorova V., Morozov A., Golyak I., et al. Determination of greenhouse gas concentrations from the 16U cubesat spacecraft using fourier transform infrared spectroscopy // *Sensors*. 2023. V. 23. No 15. P. 6794. DOI: 10.3390/s23156794.
3. Fufurin I.L., Golyak I.S., Bashkin S.V., et al. FTIR spectroscopy based on a multipass gas cell and TE cooled HgCdTe sensors for environmental monitoring and defense applications // *Proc. SPIE 11775 – Integrated Optics: Design, Devices, Systems and Applications VI*. 2021. 1177512. DOI:10.1117/12.2588714.
4. Morozov A.N., Tabalin S.E., Anfimov D.R., et al. Estimation of Emissions From Metallurgical Plants Using Infrared Fourier Transform Spectroscopy // *Russian Journal of Physical Chemistry B*. 2024. V. 18. No 3. P. 763–772. DOI: 10.1134/S1990793124700234.

IDENTIFICATION OF SUBSTANCES BY CHARACTERISTIC LINES IN RAMAN SPECTRA

Roman A. Gylka, Yana R. Chubarkina, Dmitriy R. Anfimov, Pavel P. Demkin, Igor L. Fufurin, Ivan B. Vintaikin and Andrey N. Morozov

Bauman Moscow State Technical University, Moscow, Russian Federation

Various methods are utilized for substance analysis. The most common analytical methods for solids, powders, and liquids include methods of molecular spectroscopy [1].

Raman spectroscopy is one of the most effective methods for sample-free express analysis of substances [2]. The method allows the analysis of substances using a previously created spectral database in order to identify or classify them according to characteristic spectral features, such as characteristic lines of Raman spectra. Raman spectroscopy is highly sensitive to small differences in the chemical composition of a substance, which is especially relevant in the quality control of pharmaceuticals.

The use of the database of full Raman spectra is difficult due to the large volume, difficulties in replenishment and inaccessibility of data from open libraries.

Fig.1 shows a schematic of the experimental setup with a Ventana-785L-Raman diffraction spectrometer (800-940 nm) equipped with a stabilized laser 1 (785 nm, up to 120 mW, instability ≤1 %). The laser radiation passes through a beam splitter 2, is focused by a lens 3 on the sample 4, and then the scattered light passes through a notch filter 5, after reflection on a mirror 6 is dispersed by a diffraction grating 7, recorded on a photodetector 8 and transmitted to a computer 9 for analysis.

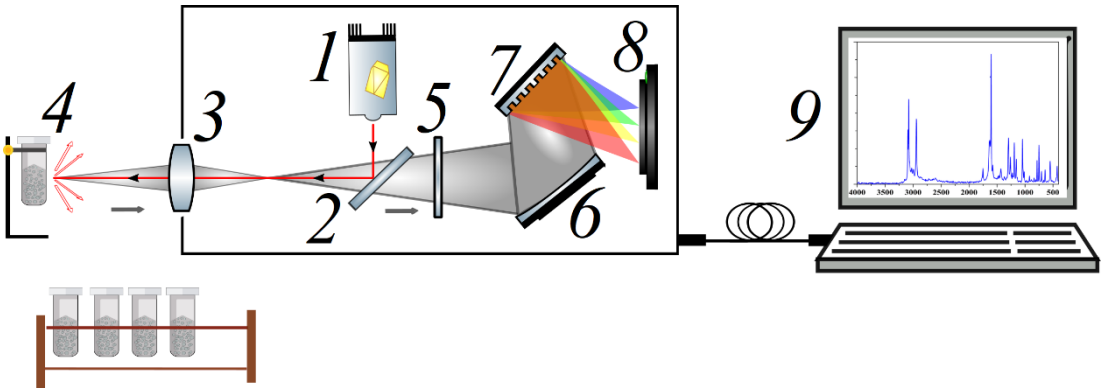


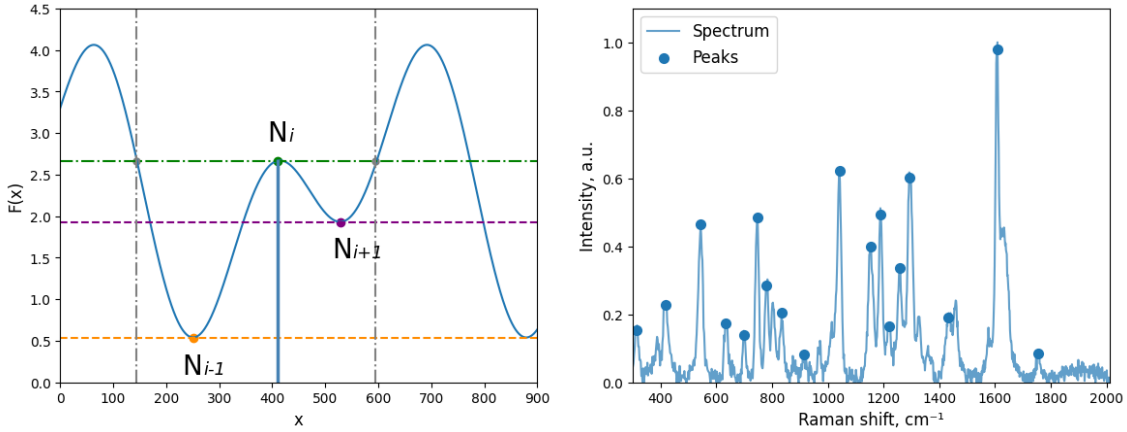
FIGURE 1. Schematic diagram of the experimental setup: 1 - laser source, 2 - beam splitter, 3 - focusing lens, 4 - sample, 5 - notch filter, 6 - reflecting mirror, 7 - diffraction grating, 8 - photodetector, 9 - computer.

A database of Raman spectra of 16 chemical compounds with defined positions of characteristic peaks used for the assessment of identification methods was registered for comparative analysis.

Before applying the identification methods, the measured Raman spectra are preprocessed. The least squares method is used to determine and subtract the baseline [3], after that the Raman spectra are normalized.

In this study, the reference method for comparing Raman spectra is the method using Pearson's correlation coefficient [4].

The function shown in Fig. 2. is utilized to find peaks using the average value, standard deviation for the segment of the spectrum without peaks, and signal-to-noise ratio (SNR) in the measured spectrum.



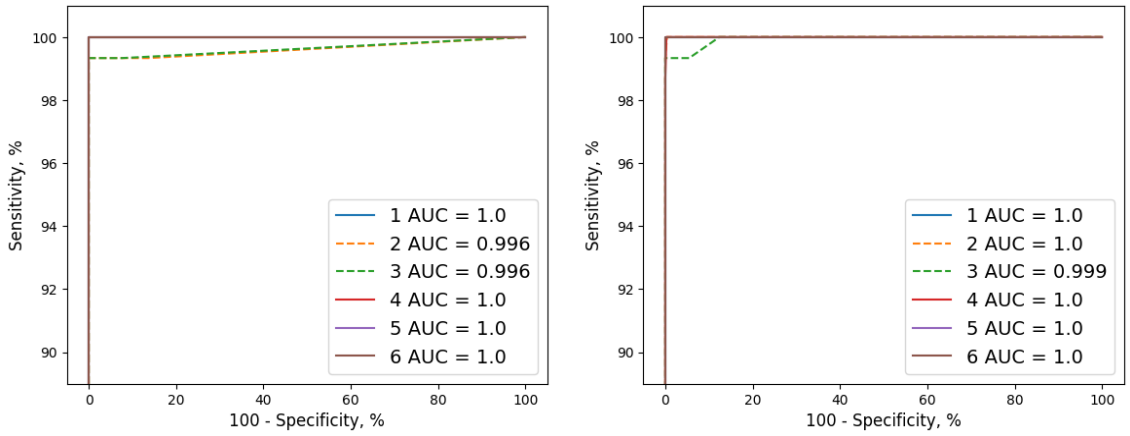
(a) (b)

FIGURE 2. The principle of peak search (a) in the function F(x)=sin(0.02x)+cos(0.01x) and (b) in the spectrum of aspirin (SNR=16).

To identify substances by peaks in the Raman spectrum, an algorithm has been developed that considers the intensity values and characteristic positions of peaks in the reference spectrum. The comparing method consists in calculating the residual for each of the substances in the database and determining the largest of a number of values.

In order to analyze the efficiency of substance identification of the developed algorithm, ROC-curves were constructed and AUC values were calculated for the reference and developed methods [5]. Fig. 3. shows the ROC curves for the reference (a) and developed (b) comparing methods.

The AUC of the developed method is different from the reference method, but high enough to indicate its high ability to separate classes of substances.



(a) (b)

FIGURE 3. ROC-curves for (a) reference and (b) developed comparing methods. 1 - Aspirin, 2 - Boric acid, 3 - Potassium chlorate, 4 - Glucose, 5 - Paracetamol, 6 - Soda.

Since the database of substance peaks contains information only on characteristic peaks, it occupies twice less memory than the database of full spectra, and the proposed comparing algorithm is about three times faster than the reference method algorithm.

This work was carried out with the support of the Foundation for Assistance to Small Innovative Enterprises in the Scientific and Technical Sphere and within the framework of the Student Start-Up V turn competition.

1. A.N. Morozov, S.I. Svetlichnyi, *Fundamentals of Fourier spectroscopy. 2nd ed.*, Nauka Publishing, Moscow, 2014.
2. Vintaykin I.B., Golyak Il.S., Golyak Ig.S., Morozov A.N., Tabalin S.E. Chemical physics and spectroscopy analysis methods of complex compounds in gas phase // *Chemical Physics*. 2020. V. 39. No 10. P. 20–26. DOI: 10.31857/S0207401X20100118.
3. Oller-Moreno S., Pardo A., Jimenez-Soto J.M., Samitier J. A novel approach to biosensing with nanomechanical resonators // *Biosensors and Bioelectronics*. 2018. V. 101. P. 1–8. DOI: 10.1016/j.bios.2017.10.002.
4. Pearson K. Contributions to the Mathematical Theory of Evolution // *Proceedings of the Royal Society of London*. 1895. V. 58. P. 240–242.
5. Wysoczanski A., Voigtman E. Evaluation of spectral interferences in atomic emission spectrometry using wavelet transform // *Spectrochimica Acta Part B: Atomic Spectroscopy*. 2014. V. 100. P. 70–78. DOI: 10.1016/j.sab.2014.07.001.

DEVELOPMENT OF NON-DISPERSIVE INFRARED GAS ANALYZER FOR MEASURING THE DYNAMICS OF GREENHOUSE GASES CONCENTRATIONS

Ivan A. Karpov, Igor L. Fufurin, Alisa P. Kosterova, Dmitriy R. Anfimov, Pavel P. Demkin, Vyacheslav R. Bessonov and Andrey N. Morozov

Bauman Moscow State Technical University, Moscow, Russia

Monitoring the concentrations and dynamics of greenhouse gases is a critical and essential task within the field of environmental monitoring. Gases such as water vapor, carbon dioxide, methane, and others are emitted into the atmosphere through both natural processes and human activities. The accumulation of these gases intensifies the greenhouse effect, leading to adverse effects on human health, agricultural productivity, and the broader environment. Consequently, the development of advanced devices capable of accurately measuring atmospheric greenhouse gas concentrations is of paramount importance. Optical measurement techniques, including nondispersive infrared (NDIR) spectroscopy, provide a non-contact and automated approach for analyzing the components of gaseous mixtures [1,2]. Figure 1 shows an explication scheme for detecting IR radiation using NDIR spectroscopy.

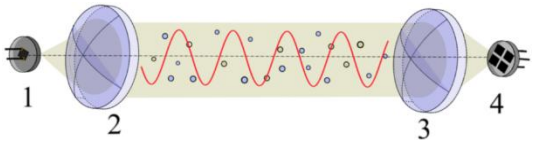


FIGURE 1. Schematic diagram of the developed gas analyzer. 1 – emitter; 2,3 – matching lenses; 4 – photodetector.

In accordance with the above scheme (Fig.1), an NDIR gas analyzer was developed. The device described in this study (Fig.2) detects radiation at a wavelength of 4.26 μm to quantify carbon dioxide concentration, with additional capability for water vapor detection. The acquired signal is normalized using a reference channel set at 3.95 μm. A mathematical model, developed using Python, processes the experimental data to determine atmospheric carbon dioxide and water vapor levels. The device is designed as an open-path gas analyzer, which allows for versatile deployment in various environments due to its low power consumption. This instrument is well-suited for applications such as environmental monitoring on carbon polygons and ensuring the quality control of low-Earth orbit satellites tasked with atmospheric greenhouse gas monitoring.

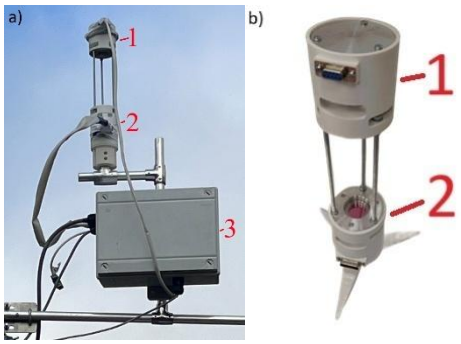


FIGURE 2. The appearance of the developed gas analyzer: a) during field measurement experiments; b) in off state. 1 – the IR emitter unit, 2 - photodetector unit, 3 - data collection unit.

The main technical characteristics of the presented device are shown in Table 1. A program code has been developed that controls the operation of the emitter and photodetector units. A rectangular signal with a 50% duty cycle and an amplitude from 0 to 5 V which is applied to the emitter to generate discrete IR radiation. The type of signal received from the data collection unit is shown in Fig. 3 [3]. Figure 4 shows an experiment on purging a constant flow of 600 ppm carbon dioxide in a calibration tube.

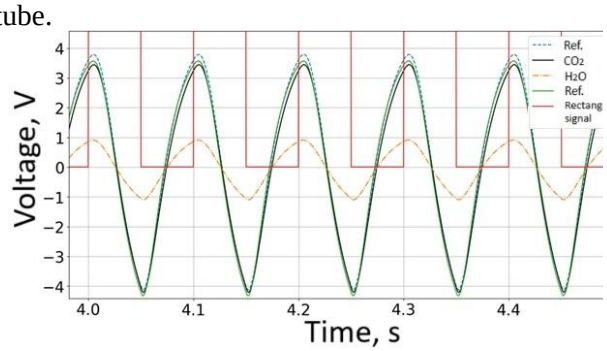


FIGURE 3. The type of signal from the photodetector.

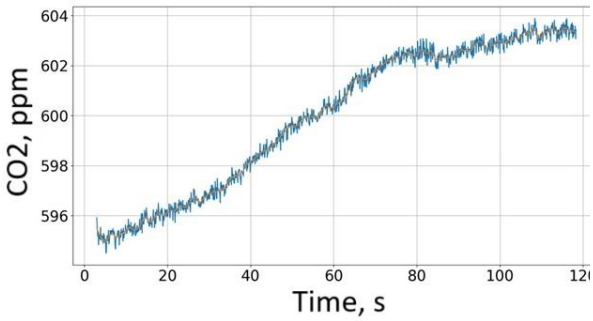


FIGURE 4. Graph of CO_2 concentration measurement.

TABLE 1. The main technical characteristics of the developed gas analyzer.

Parameter	Value
Emitter (JSIR 350-4)	
Spectral range, μm	2…15
Active area, mm^2	2,2 x 2,2
Peak power, mW	1200
Peak temperature of active area, °C	850

Photodetector (InfraTec LRM-244)			
Number of channels			4
Channel number	Function		
1	Reference	Installed bandpass filter, nm	3950±45
2	CO_2		4260±90
3	H_2O		5800±50
4	Reference		3950±45
Pyroelectric area of one channel, mm^2			2 x 2
Polarity			A negative signal with a positive change in the IR radiation flux
Electrical power supply, V			5,87
Other parameters			
Overall dimensions, mm			152 x 174 x 345
Mass, kg			1,1

The envelope was subtracted from the graph in Fig. 4 and the standard deviation was calculated. Thus, the sensitivity of the developed NDIR gas analyzer via the 2nd channel is 0.19 ppm for a gas mixture with a CO_2 concentration of 600 ppm.

The work was carried out within the framework of the strategic academic leadership program «Priority 2030».

1. Li Q., He Y., Zhao K., et al. Development and Testing of NDIR-Based Rapid Greenhouse Gas Detection Device for Dairy Farms // *Sustainability*. 2024. V. 16. No 5. P. 2131. DOI: 10.3390/su16052131.
2. Shah I.H., Manzoor M.A., Jinhui W., et al. Comprehensive review: Effects of climate change and greenhouse gases emission relevance to environmental stress on horticultural crops and management // *Journal of Environmental Management*. 2024. V. 351. 119978. DOI: 10.1016/j.jenvman.2023.119978.
3. Karpov I.A., Fufurin I.L., Vintaykin I.B., et al. Development of a non-dispersive infrared gas analyzer for measuring the dynamics of greenhouse gas concentrations // *Bulletin of the National Research Nuclear University "MEPhI"*. 2025. V. 14. No 1. P. 16-22. DOI: 10.26583/vestnik.2025.1.2.

ANALYSIS OF FIELD TEST DATASET OF WATER VAPOR AND CARBON DIOXIDE CONCENTRATIONS MEASUREMENT WITH USING METHODS OF INFRARED NON-DISPERSIVE SPECTROSCOPY

Alisa P. Kosterova[1], Igor L. Fufurin[1], Dmitriy R. Anfimov[1], Ivan A. Karpov[1], Ivan A. Seregin[2] and Alexey M. Yaroslavtsev[2]

[1]Bauman Moscow State Technical University, Moscow, Russia
[2]Russian State Agrarian University, Moscow, Russia

Environmental challenges are growing more urgent, making comprehensive monitoring of the environment increasingly important. Key focus is placed on gases like carbon dioxide, water vapor, and

methane, which play a significant role in Earth's climate. Their accumulation in the atmosphere enhances the greenhouse effect, causing negative impacts on ecosystems, human health, and agriculture.

On September 17, 2024, September 18, 2024, and October 17, 2024, comparative experiments were conducted in the village of Kamshilovka between the developed NDIR gas analyzer and its counterpart, the LI-COR LI-7500A.

The setup for monitoring greenhouse gas fluxes consisted of an open-path gas analyzer LI-7500A, an anemometer 1590-PK-020/W WindMaster, and the developed NDIR gas analyzer. The anemometer measured the speed of sound in the air, while the gas analyzers determined the concentrations of CO_2 and H_2O in the air.

This study focuses on analyzing field measurements of CO_2 and H_2O concentrations to apply the eddy covariance method. The eddy covariance method is a micrometeorological approach that directly measures the exchange of gases, such as CO_2, between the Earth's surface and the atmosphere. It is extensively employed to quantify CO_2 emissions from various ecosystems, including natural, urban, and agricultural environments. This method is increasingly being used to monitor large areas for potential CO_2 leakage from subsurface storage sites [1].

Figure 1 shows the signal from the NDIR gas analyzer.

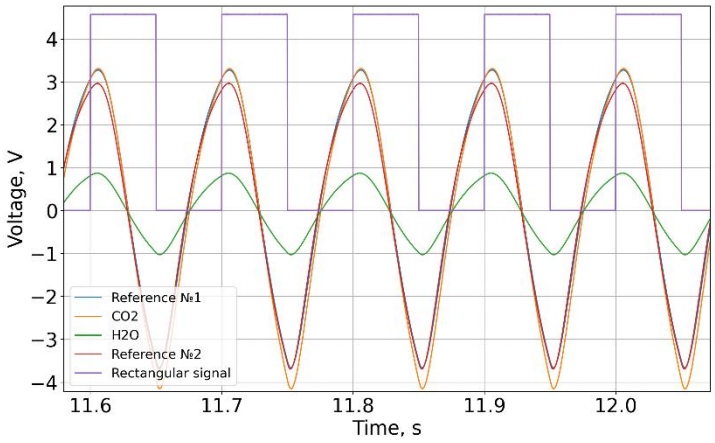


FIGURE 1. The type of signal from the photodetector.

For each of the four channels, the integral over each period of rectangular signal is calculated (after subtracting the offset voltage and taking the absolute value) and averaging is performed over the two reference channels (1):

$$< I_{ref} >= \frac{<I_{ref\ №1}> + <I_{ref\ №2}>}{2} \quad . \tag{1}$$

The quantity proportional to the optical density for carbon dioxide and water vapor is determined as follows (2):

$$Z = -\ln\frac{<I_{sig}>}{<I_{ref}>}, \tag{2}$$

where $<I_{sig}>$, $<I_{ref}>$ – the average intensities of the signal and reference channels, respectively.

After this, the value Z is compared with the calibration curve, which is established during the instrument calibration process [2]. Based on this comparison, the data obtained from the NDIR gas analyzer are converted into gas concentration values, expressed in ppm (Fig.2).

The flux from the area of interest can be represented as the product of the instantaneous deviation from the mean value of the vertical velocity and the instantaneous deviation from the mean value of the concentration of the substance of interest (3):

$$F = w'c', \tag{3}$$

where F – flux, w' – instantaneous deviation from the mean value of the vertical velocity, c'– instantaneous deviation from the mean value of the concentration of the substance [3].

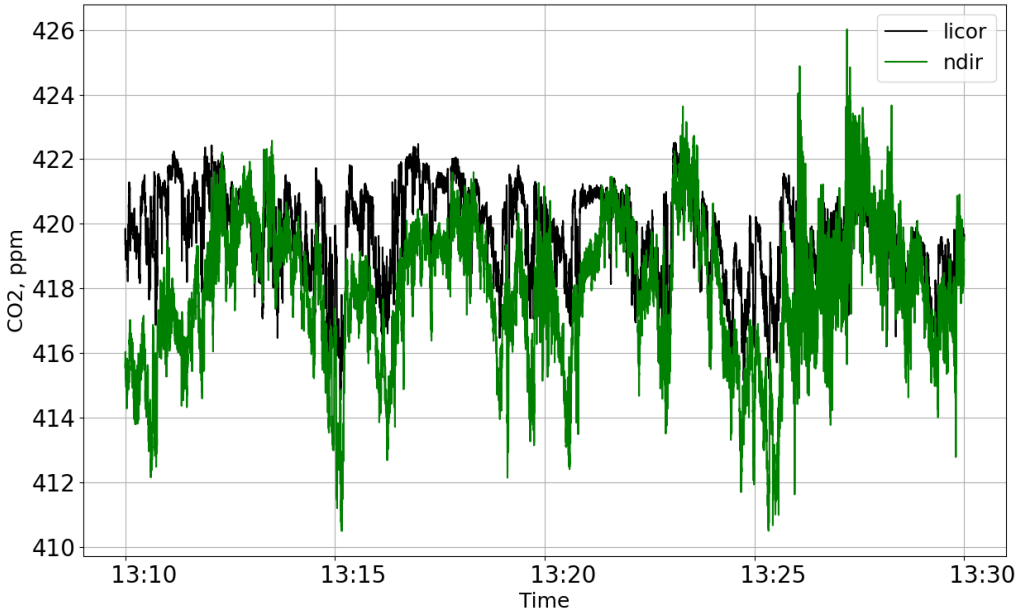


FIGURE 2. CO_2 concentration as a function of time for the experiment dated October 17 2024. Pearson correlation coefficient for CO_2 concentrations is 0.75.

Figures 3, 4 show the dependence of vertical velocity on time and the time dependences of CO_2 fluxes for the vertical component of wind velocity, measured using an NDIR gas analyzer and a LI-COR LI-7500A respectively.

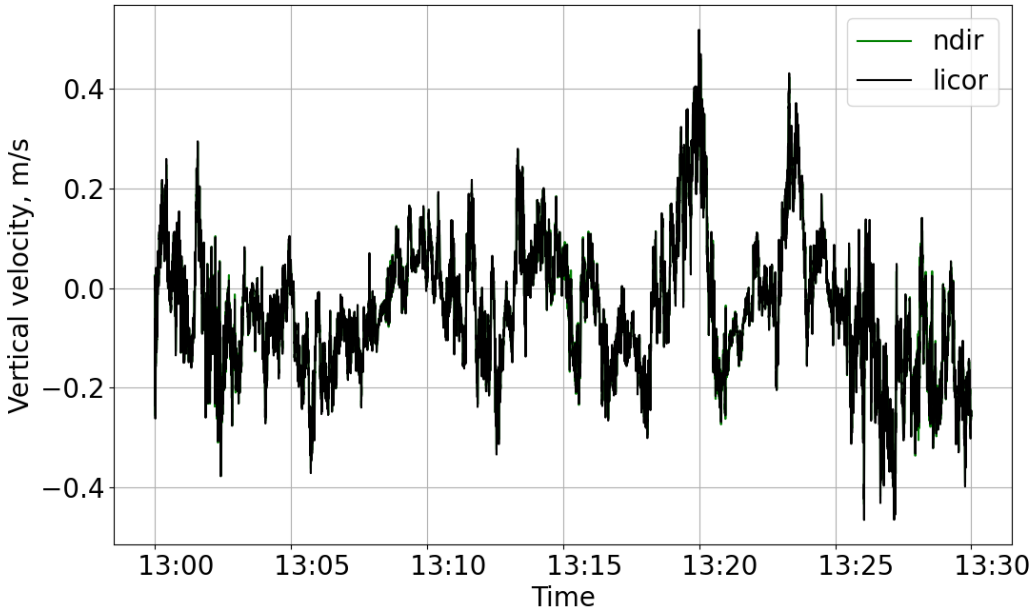


FIGURE 3. The vertical velocity as a function of time for the experiment dated October 17, 2024.

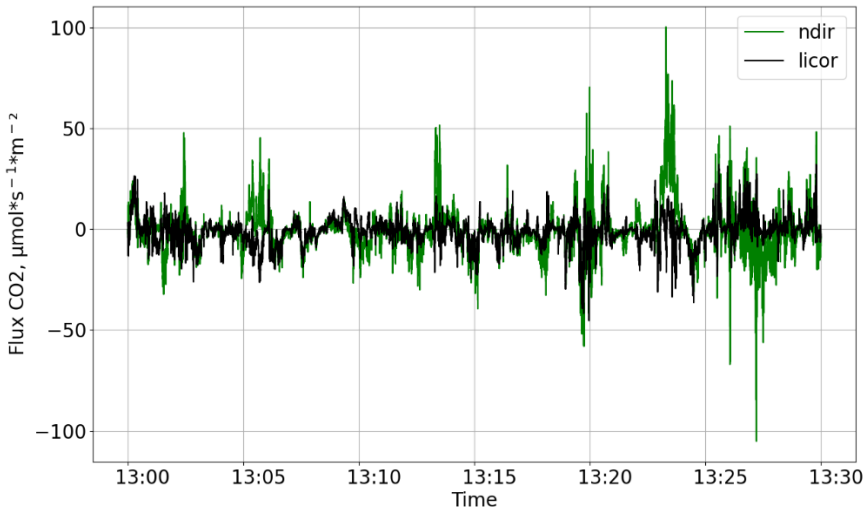


FIGURE 4. The CO_2 flux as a function of time for the experiment dated October 17 2024.

This paper presents the results of field measurements of CO_2 and H_2O concentrations obtained using the developed open-type non-dispersive infrared gas analyzer (NDIR) and the LI-7500A gas analyzer, and a comparison of the data obtained.

The work was carried out within the framework of the strategic academic leadership program «Priority 2030».

1 Burba G., Madsen R., Feese K. Eddy covariance method for CO_2 emission measurements in CCUS applications: principles, instrumentation and software // *Energy Procedia*. 2013. V. 40. P. 329-336. DOI: 10.1016/j.egypro.2013.08.038.

2 Karpov I.A., Fufurin I.L., Vintaykin I.B., et al. Development of a non-dispersive infrared gas analyzer for measuring the dynamics of greenhouse gas concentrations. // *Bulletin of the National Research Nuclear University "MEPhI"*. 2025. V. 14. No 1. P. 16-22. DOI: 10.26583/vestnik.2025.1.2.

3 G. Burba, J. Kurbatova., O. Kuricheva, et al., *The method of turbulent pulsations. A short practical guide*, IPEE named after A. N. Severtsova RAS, Moscow, 2016. DOI: 10.13140/rg.2.1.5109.5449.

EXPERIMENTAL BENCH FOR ANALYZING THE DYNAMICS OF CONCENTRATIONS OF WATER VAPOR AND CARBON DIOXIDE BY THE METHOD OF COVARIANCE OF TURBULENT PULSATIONS

Viacheslav R. Bessonov, Alexander I. Karpov, Alisa P. Kosterova, Dmitriy R. Anfimov, Pavel P. Demkin, Igor L. Fufurin and Andrei N. Morozov

Bauman Moscow State Technical University, Moscow, Russia

Accurate quantification of greenhouse gas fluxes is critical for assessing anthropogenic contributions to climate change. The turbulent pulsation covariance method, which calculates fluxes

using instantaneous deviations from mean vertical wind speed (ω') and gas concentration (c') requires precise synchronization of anemometric and gas concentration data at sampling rates ≥10 Hz. While commercial solutions such as the Li-Cor LI-7500 remain industry standards, their high cost has hindered widespread adoption. In this study, these limitations are addressed by developing a domestically produced NDIR gas analyzer. The modular architecture of the device combined with signal processing algorithms provides a cost-effective alternative for long-term environmental monitoring, especially at carbon landfills [1].

The theoretical foundation of this work lies in the covariance equation linking vertical gas flux F to wind speed fluctuations ω' and concentration deviations c':

$$F = \rho \cdot \overline{\omega' c'},$$

where ρ is air density, ω' represents instantaneous deviations in vertical wind speed, and c' denotes deviations in gas concentration. This method necessitates synchronous measurements at frequencies sufficient to capture turbulent eddies (≥10 Hz) [2-3].

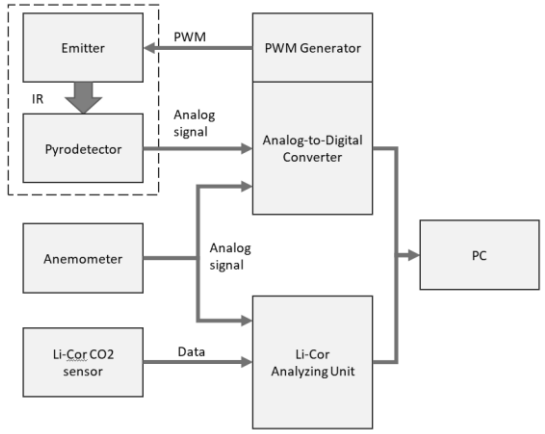


FIGURE 1. Functional diagram of the installation

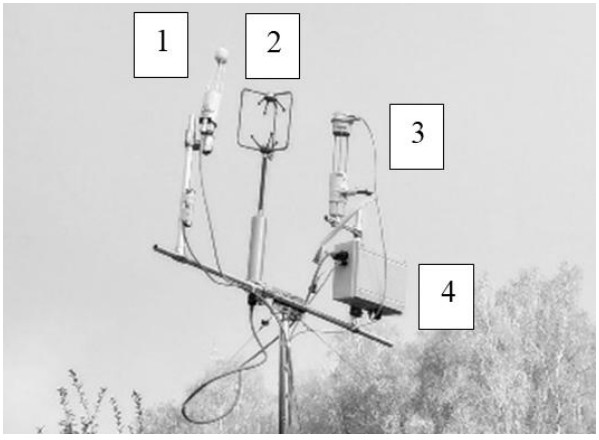


FIGURE 2. Installation at the training ground. 1 – Li-Cor gas analyzer, 2 – Three-axis anemometer, 3 – Developed NDIR gas analyzer, 4 – block with ADC/DAC and power supply.

The Gill WindMaster three-axis ultrasonic anemometer measures wind speeds ranging from 0 to 50 m/s with an accuracy of ±1% at a sampling rate of 32 Hz. The NDIR gas analyzer employs a four-channel InfraTec LRM-244 pyroelectric detector, which detects radiation in spectral bands corresponding to CO2 (4260 nm) and H2O (5800 nm) absorption. The optical subsystem integrates a broadband JSIR 350-4 infrared emitter, modulated at 10 Hz via pulse-width modulation (PWM) to synchronize with the anemometer's data acquisition cycle. The optical and electronic architecture of the NDIR gas analyzer is illustrated in Fig. 1, highlighting the synchronization between the PWM-modulated emitter and the pyroelectric detector. Laboratory calibration using certified gas mixtures demonstrated a sensitivity of 0.19 ppm for CO_2 at a reference concentration of 600 ppm, validated through spectral noise density analysis. Field trials conducted at the Kamshilovka carbon polygon (Fig. 2) revealed a strong correlation between the NDIR analyzer and the reference Li-Cor LI-7500. Pearson correlation coefficients for the three-dimensional wind velocity components (U, V, W) reached 0.982, 0.974, and 0.974, respectively, while the root mean square deviation (RMSD) for CO_2 concentrations between the two systems was 2.8 ppm. These results confirm the accuracy and reliability of the domestically developed NDIR gas analyzer under real-world operating conditions.

Prior to field deployment, the NDIR gas analyzer underwent rigorous calibration in a controlled environment using certified gas mixtures with precisely defined concentrations of CO_2 (600 ppm, 800 ppm, 1000 ppm) and H_2O (10 g/m^3, 20 g/m^3, 30 g/m^3). The optical subsystem — comprising a JSIR 350-4 broadband infrared emitter and a four-channel pyroelectric detector — was precisely aligned within a hermetically sealed calibration chamber. To simulate real-world operating conditions, a 10 Hz pulse-width modulation (PWM) signal was applied to the emitter, while the detector outputs were recorded via analog-to-digital converter (ADC) at 20 Hz. Signal processing algorithms were implemented to convert raw voltage measurements into gas concentration values by integrating the intensity of each PWM cycle and normalizing against reference channels (λ = 3950 nm) to account for optical path variations. Integrated temperature and humidity sensors provided real-time environmental data, enabling corrections for thermal drift in the detector and adsorption effects on optical surfaces, thereby ensuring measurement accuracy under variable laboratory conditions.

Field experiments were conducted at the Kamshilovka carbon monitoring site, characterized by heterogeneous terrain and dynamically shifting atmospheric conditions. To minimize spatial sampling errors, the NDIR gas analyzer and Gill WindMaster three-axis ultrasonic anemometer were co-located on a 3-meter meteorological tower. The anemometer, configured for 32 Hz sampling, provided high-resolution measurements of three-dimensional wind velocity components (U, V, W), while the NDIR analyzer recorded CO_2 and H_2O concentrations at 20 Hz. As shown in FIG. 2, the experimental setup included co-located NDIR and Li-Cor analyzers on a 3-meter tower to minimize spatial sampling errors.

For comparative validation, a Li-Cor LI-7500 open-path gas analyzer was deployed adjacent to the experimental setup, enabling simultaneous sampling of the same air column. Data streams from both systems were aggregated into a centralized logging unit equipped with redundant storage. Post-processing involved several key steps to ensure accurate data analysis. First, noise reduction was achieved by applying a 4th-order Butterworth low-pass filter with a cutoff frequency of 10 Hz, which effectively suppressed high-frequency artifacts. Next, temporal alignment was performed using cross-correlation analysis to compensate for inter-channel delays, ensuring synchronization within a range of $\pm$0.1 seconds. Following this, concentrations of CO_2 and H_2O were derived by calculating optical densities based on the Beer-Lambert-Bouguer law, with absorption coefficients dynamically adjusted for real-time ambient pressure and temperature fluctuations measured by onboard sensors. Finally, flux computation was carried out using Reynolds decomposition to isolate turbulent fluctuations (w', c') from 30-minute averaged values, and vertical fluxes were determined through covariance analysis. This comprehensive approach ensured robust and reliable results.

Data validation focused on quantifying systematic discrepancies between the NDIR and Li-Cor systems. Pearson correlation coefficients were computed for wind velocity components and gas concentrations. Long-term stability was assessed via Allan variance analysis, revealing a noise floor of 0.19 ppm for CO_2 and 0.05 g/m^3 for H_2O over 24-hour intervals. Residual analysis of linear regressions between NDIR and reference outputs further confirmed measurement consistency. Environmental challenges, including optical surface condensation at humidity levels >90%, were mitigated through periodic manual inspections and automated activation of thermoelectric coolers integrated into the detector housing [4].

The developed NDIR gas analyzer demonstrated accuracy and correlation with Li-Cor LI-7500 (Pearson up to 0.982). The modular design, synchronization with the anemometer and signal processing algorithms ensured the reliability of measurements. The device is promising for budget eco-monitoring, including carbon polygons.

The work was carried out within the framework of the strategic academic leadership program «Priority 2030».

1. *Molecular spectroscopy*, Moscow University Publishing, Moscow, 1980. 272 p.

2. Golyak I.S., Kareva E.R., Fufurin I.L., et al. Numerical methods for the analysis of multicomponent gas mixtures using infrared laser spectroscopy // *Computer Optics*. 2022. V. 46. No 4. P. 650-658. DOI: 10.18287/2412-6179-CO-1058.
3. Krivenok L.A., Suvorov G.G., Avilov V.K., Sirin A.A. Eddy covariance measurement of CO_2, CH_4, H_2O fluxes: Use of a mobile tower and taking into account the changing fetch // *Atmospheric and Oceanic Optics*. 2019. V. 32. No 11. P. 942–950. DOI: 10.15372/AOO20191111.
4. Karpov I.A., Fufurin I.L., Vintaykin I.B., et al. Development of a non-dispersive infrared gas analyzer for measuring the dynamics of greenhouse gas concentrations. // *Bulletin of the National Research Nuclear University "MEPhI"*. 2025. V. 14. No 1. P. 16-22. DOI: 10.26583/vestnik.2025.1.2.

DETECTION OF LINEAR EMISSION SPECTRUM SOURCES USING HYPERSPECTRAL IMAGE ANALYSIS

Bogdan V. Kolesnikov[1], Grigory A. Shvetsov[1], Alexey N. Vinogradov[1], Yulia A. Izmailova[1], Andrey A. Leontyev[1], Alexey I. Rodionov[1,2], Irina P. Rodionova[1,2], and Igor D. Rodionov[1,2]

[1]AO Scientific and Technical Center Reagent, Moscow, Russia
[2]Semenov Federal Research Center for Chemical Physics, Russian Academy of Sciences, Moscow, Russia

Remote sensing plays a crucial role in modern scientific and applied research, enabling the acquisition of valuable data about the surrounding environment. In recent years, hyperspectral imaging has been actively utilized in remote sensing. Unlike traditional three-channel images, hyperspectral images contain detailed spectral information spanning hundreds of narrow spectral channels. This allows for the identification of unique spectral signatures of objects and provides a significant advantage in the analysis of materials and their properties.

The problem of detecting linear emission radiation (“a line source”) can be considered as a problem of identifying spectral anomalies in hyperspectral data, because these sources have unique spectral features that differ from the background. Narrow spectral peaks are rare and atypical for natural objects such as vegetation, soil, or water. Examples of the objects under consideration include gas discharge lamps and open fire sources. Detection and identification of line sources can be used in the task of energy efficiency estimation of cities, in the elimination of fires at industrial facilities, in aircraft landing systems and assistance, etc.

Classical models for anomaly detection in the spectral feature space, such as the RX method (Reed-Xiaoli) described in [1], and its modifications, including Kernel-RX [2] and local-RX [3], are widely used in hyperspectral data analysis problems. There are also methods focused on object detection with known spectral signatures, such as Constrained Energy Minimization (CEM) [4] and Spectral Angle Mapper (SAM), Spectral Energy Minimization (SEM) [5]. However, these algorithms have limited applicability for this problem. For instance, RX-based algorithms show increased sensitivity to glares. CEM, SAM, SEM, and other similar algorithms require prior knowledge of the target object's spectral signature, which is often unavailable in practical scenarios.

In recent years, neural networks have been widely used in remote sensing and hyperspectral data analysis, as shown in many studies [6-8]. Unlike classical methods, neural networks are capable of automatic complex nonlinear feature extraction in data and are robust to noise, making them a promising tool for solving challenging hyperspectral data analysis problems.

Given the problem formulation, there is no need to create a labeled training dataset. Instead, the model is trained on "normal" background data. One of the most suitable approaches for solving this problem is the autoencoder [9], a neural network architecture that encodes input data into a lower-dimensional latent space and then decodes it to reconstruct the original data (Fig. 1). By comparing the reconstruction error between normal and anomalous data, autoencoders can efficiently identify outliers that do not conform to the learned patterns. Several studies [10-12] have demonstrated the reliability of autoencoders in solving anomaly detection problems.

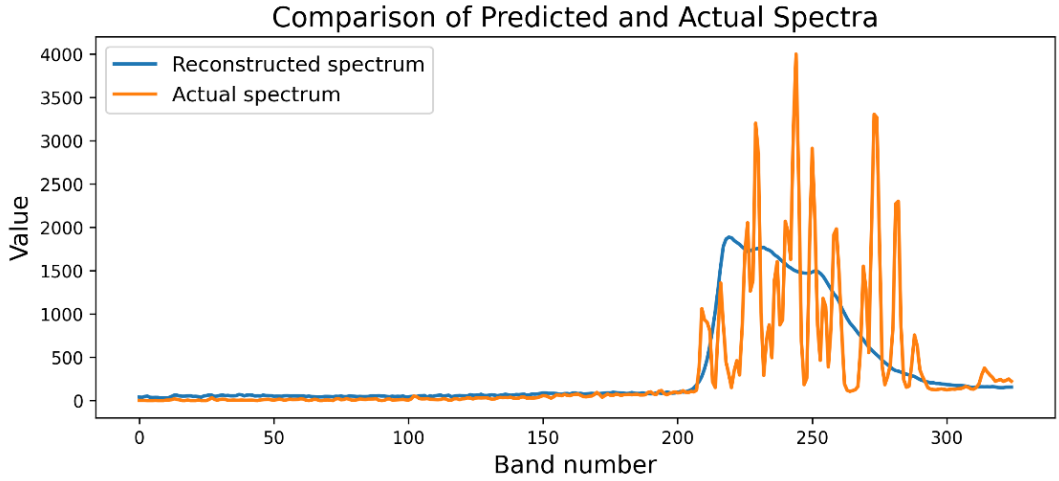


FIGURE 1. Comparison between the spectrum of a low-pressure neon lamp and the spectrum reconstructed by an autoencoder. Unlike the smooth reconstructed spectrum, the real spectrum from the neon lamp will be identified as anomalies.

To evaluate the detection robustness of the proposed autoencoder model, experimental images of target sources were captured using a hyperspectral camera developed by RDC “Reagent” (the specifications are provided in Table 1).

TABLE 1. Hyperspectral camera specifications.

Spectral Range (nm)	430 – 880
Number of spectral channels	>140
Spectral sampling (nm)	<4.5
Field of View (rad)	0.35
Ground Sampling Distance	0.5 m at a distance 1 km

An artificial scene was set to simulate various sources of radiation in the visible and near-infrared range, such as low-pressure neon lamp, colored lamps, sources with monochromatic spectra, and the combined interaction of these sources on various surfaces (Fig. 2). This setup was not merely a random arrangement but a carefully curated simulation intended to capture the complexity of real-world lighting conditions. The suggested scene is a dynamic and challenging environment for observation and analysis. Some areas of the scene were illuminated by soft diffuse light. In contrast, other regions are dominated by over-illuminated objects, where excessive light intensity led to a loss of detail, and a lot of glares. In Figure 2, bold text marks target objects for considered scene, while regular text denotes complex objects that could also introduce noise into the model's predictions, i.e., glares, colored lamps, color spots, multiple sharp edges, and so on.

The results of sources with line spectra and the low-pressure lamp detection are presented in Fig. 3 (a). It can be seen that the algorithm successfully detected all the investigated sources in the visible and infrared ranges. Figure 3(b) presents the detection results of low-pressure neon lamps only. Therefore, in the first case, the algorithm was trained to distinguish the spectra of sources with line spectra, while in the second

case, it was trained to search for specific lighting sources. This indicates that the algorithm can be trained and applied to various lighting sources as well as specific ones.

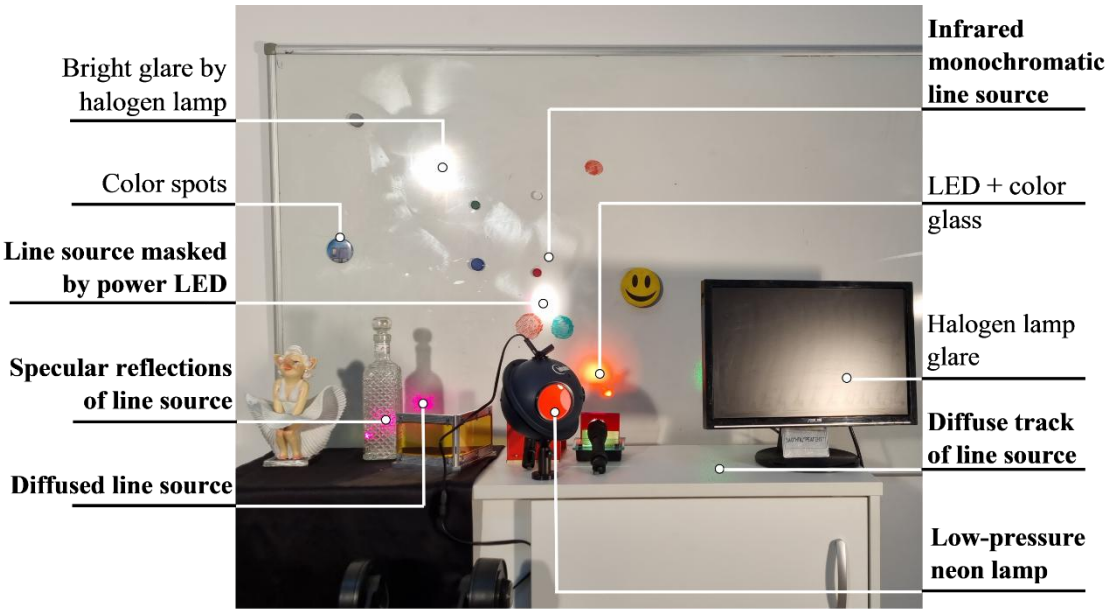


FIGURE 2. An artificial scene: bold text marks target objects, while regular text denotes complex objects that could lead to model instability.

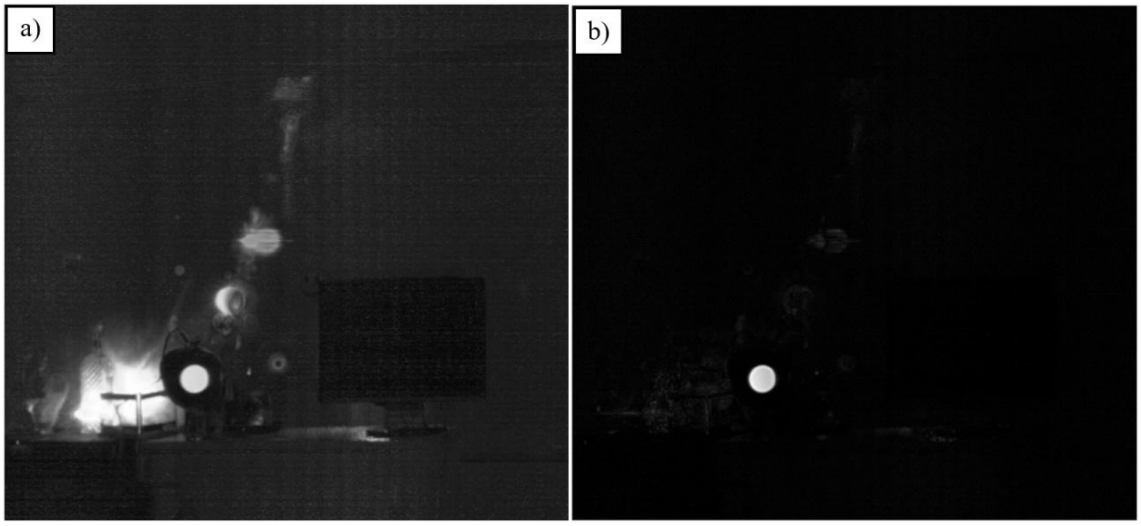


FIGURE 3. (a) Detection map of sources with line spectrum (overall), (b) Detection map of low-pressure neon lamp (specific).

To evaluate the performance quality, the ROC-AUC (Area Under the Receiver Operating Characteristic Curve) metric was selected. The final values of this metric on the validation set of images are presented in Table 2.

TABLE 2. ROC-AUC values on validation set.

Scene	ROC-AUC
Validation scene 1	0.8864
Validation scene 2	0.9144

Thus, the proposed autoencoder-based approach demonstrates high accuracy in detecting line spectrum radiation sources in hyperspectral images, achieving ROC-AUC values of 0.8864 and 0.9144 on the validation dataset. This confirms its potential for spectral anomaly analysis problems without the need for a priori knowledge about the target objects. The algorithm`s processing time for a data containing 1000 samples is 3 milliseconds, making it suitable for applications requiring high performance.

This study was carried out in the framework of State Assignment of the Ministry of Science and Higher Education of the Russian Federation (project No. 125012200611-5).

1. Molero J.M., Paz A., Garzón E.M. et al. Fast anomaly detection in hyperspectral images with RX method on heterogeneous clusters // *The Journal of Supercomputing.* 2011. V. 58. P. 411–419. DOI: 10.1007/s11227-011-0598-0.
2. Khazai S., Mojaradi B. A modified kernel-RX algorithm for anomaly detection in hyperspectral images // *Arabian Journal of Geosciences*. 2015. V. 8. P. 1487–1495. DOI: 10.1007/s12517-013-1218-5.
3. Rossi A., Acito N., Diani M., Corsini G. RX architectures for real-time anomaly detection in hyperspectral images // *Journal of Real-Time Image Processing.* 2014. V. 9. P. 503–517. DOI: 10.1007/s11554-012-0292-3.
4. Harsanyi J.C. *Detection and classification of subpixel spectral signatures in hyperspectral image sequences.* University of Maryland, Baltimore County, 1993, 116 p.
5. Zhao J., et al. SRA-CEM: An improved CEM target detection algorithm for hyperspectral images based on sub-region analysis // *IEEE Journal of Selected Topics in Applied Earth Observations and Remote Sensing*. 2023. V. 16. P. 6026–6037.
6. Zhao J., Wang G., Zhou B., Ying J., Liu J. Deep feature extraction and classification of hyperspectral images based on convolutional neural networks // *IEEE Transactions on Geoscience and Remote Sensing.* 2016. V. 54. No 10. P. 6232–6251. DOI: 10.1109/JSTARS.2023.3289943.
7. Zhong Z., Li J., Luo Z., Chapman M. Spectral–spatial residual network for hyperspectral image classification: A 3-D deep learning framework // *IEEE Transactions on Geoscience and Remote Sensing.* 2017. V. 56. No 2. P. 847–858. DOI: 10.1109/TGRS.2017.2755542.
8. Paoletti M. E., Haut J.M., Plaza J., Plaza A. Deep learning classifiers for hyperspectral imaging: A review // *ISPRS Journal of Photogrammetry and Remote Sensing.* 2019. V. 158. P. 279–317. DOI: 10.1016/j.isprsjprs.2019.09.006.
9. Sakurada M., Yairi T. Anomaly detection using autoencoders with nonlinear dimensionality reduction // *Proceedings of the MLSDA 2014 2nd workshop on machine learning for sensory data analysis.* 2014. P. 4-11. DOI: 10.1145/2689746.2689747.
10. Xiang P., Ali S., Jung S. K., Zhou H. Hyperspectral Anomaly Detection With Guided Autoencoder // *IEEE Transactions on Geoscience and Remote Sensing*. 2022. V. 60. P. 1–18. Art no. 5538818. DOI: 10.1109/TGRS.2022.3207165.
11. Müller K., Gogineni V.C., Orlandic M., Werner A. S.. Autoencoder-based hyperspectral anomaly detection using kernel principal component pre-processing // *31st European Signal Processing Conference (EUSIPCO), Helsinki, Finland*. 2023. P. 566–570. DOI: 10.23919/EUSIPCO58844.2023.10289889.
12. Chen S., Li X., Yan Y. Hyperspectral Anomaly Detection with Auto-Encoder and Independent Target // *Remote Sensing*. 2023. V. 15. P. 5266. DOI: 10.3390/rs15225266.

A ROBUST ALGORITHM FOR LOW-CONTRAST OBJECT DETECTION USING HYPERSPECTRAL IMAGING

Yulia A. Izmailova[1], Andrey A. Leontyev[1], Alexey N. Vinogradov[1], Maxim O. Shevchenko[1], Alexey I. Rodionov[1,2], Irina P. Rodionova[1,2], and Igor D. Rodionov[1,2]

[1]AO Scientific and Technical Center Reagent, Moscow, Russia
[2]Semenov Federal Research Center for Chemical Physics, Russian Academy of Sciences, Moscow, Russia

Hyperspectral imaging is a complex technology that captures and processes information across a wide range of wavelengths, enabling detailed analysis of materials and objects. This technology has a broad range of applications, including the detection of anthropogenic oil [1] and gas leaks [2,3], monitoring of natural resources [4], excavation of buried objects [5], detection of underwater objects including uncovering of the keel track [6]. It is also highly effective for detecting low-contrast objects [7], which can be extremely useful to identify hiker lost in the wilderness. These capabilities make hyperspectral imaging a valuable tool in problems requiring detailed object analysis.

Machine learning is essential in hyperspectral image analysis, as it enhances prediction accuracy by extracting features from complex data. Traditional methods include the naive Bayesian classifier, Support Vector Machines, Random Forests, and Matched Filter. Recently, Convolutional Neural Networks (CNNs) have become popular for hyperspectral classification because they handle challenges like lighting changes, observation angles, sensor errors, and varying SNR well.

In the present paper, we present the results on the detection of low-contrast objects, such as hiking wear, using an algorithm that combines a Siamese neural network with pseudo data generation, both of them are described in [8]. In addition, we examine the robustness and stability of this algorithm in challenging scenarios such as the SNR, lighting conditions change and distance between sensor and search object. The experiment was conducted using an hyperspectral camera developed by RDC Reagent (specifications are provided in Table 1). Fabrics typical for hiking wear were used as the objects of the current study: 1) single fabric clothes and 2) mixed fabric outfit. The search distance was 3.2 km. The surveys took place under clear weather conditions between 09:40 to 15:40. The characteristic spectra of search objects and the background (forest) were captured by the hyperspectral camera (Fig. 1).

To address the low-contrast objects detection, the algorithm proposed in [8] was considered. The core concept of this approach is to employ a Siamese neural network for hyperspectral object detection. In order to enhance detection accuracy, the authors suggested a pseudodata generation technique. This procedure helps to solve the problem related to the limited number of pixels representing the search class in hyperspectral images. Specifically, the authors proposed mixing the spectra with those of the object or background classes to create variations. This results in the creation of positive and negative spectral pairs, where the spectra correspond to different classes, such as object and background. The proposed method allows the model to account for distinctions between different classes.

TABLE 1. Characteristics of the hyperspectral camera.

Characteristics	**Value**
Type	push-broom
Spectral Range	430 – 910 nm
Number of spectral channels	228
Spectral Sampling	2.1 nm
Field of View	3°
Ground Sampling Distance (1 km distance)	0.12 m

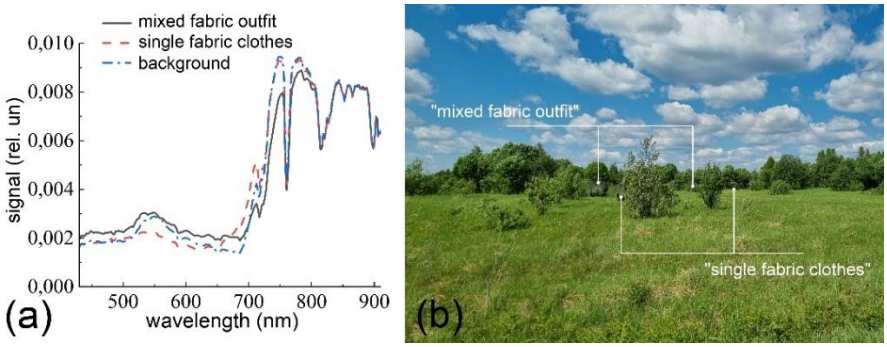


FIGURE 1. (a) Registered spectra of the search objects and background (forest), (b) scene.

The pseudodata generated through this process is essential for training either a single Siamese network or an ensemble of them. Such an ensemble consists of several independently trained networks, and their predictions are subsequently aggregated. The pseudodata generation technique increases the data volume, helps avoid overfitting, enhances the model's generalization capabilities, and improves its robustness under real-world conditions such as noise or variations in illumination, or different distances.

The training data for low-contrast object detection consisted of images captured during the first half of the day in winter, featuring nets located against snowy backgrounds and asphalt roads. Note that the algorithm's prediction performance was evaluated using images acquired in summer during daytime, featuring objects against vegetation backgrounds, which allows us to study the algorithm's robustness to varying weather conditions. All training and test spectra were normalized to their l_2 norm as part of the preprocessing of the captured data.

In the subsequent analysis, we will examine the robustness of the algorithm. The objects under consideration possess the properties and shooting details previously outlined. First, we monitor how the detection probability changes as a function of the signal-to-noise ratio (SNR).

Table 2 illustrates the variation in detection probability as a function of the maximum signal-to-noise ratio (SNR_{MAX}). Probability values were calculated as mean prediction probabilities for the search class. The magnitude of the signal-to-noise ratio was estimated based on the characteristics of a clear sky background. Signal-to-noise ratio adjustments were made by changing the exposure time. This enables estimation of the SNR's effect on detection probability.

TABLE 2. Experimental parameters and detection probabilities.

Exposure time, ms	SNR_{MAX}	Probability "mixed fabric outfit"	Probability "single fabric clothes"
10	70	0.9896	0.9583
15	88	0.9922	0.9706
20	90	0.9916	0.9682

Next, we explored how the detection probabilities of search objects change relative to the Sun's position. Table 3 shows detailed information, including the azimuth angle, the Sun's altitude, and the shooting time. The line of sight of the hyperspectral camera was pointed to the northwest. Table 3 also presents the resulting detection probabilities for the search objects.

TABLE 3. Shooting time, ΔΦ (the angle between line of sight and the Sun's azimuth), the Sun's altitude, and detection probabilities for the search objects.

Shooting time	ΔΦ, deg	Altitude, deg	Probability "mixed fabric outfit"	Probability "single fabric clothes"
9:37	198.06	41.5	0.9909	0.9469
15:39	71.7	41	0.9147	0.9604

Figure 2 shows examples of object detection using a Siamese neural network. Specifically, Figure 2 (a) demonstrates the detection results for "single fabric clothes" object. Meanwhile, Figure 2 (b) presents an example where the Siamese Neural Network has successfully detected the "mixed fabric outfit" object.

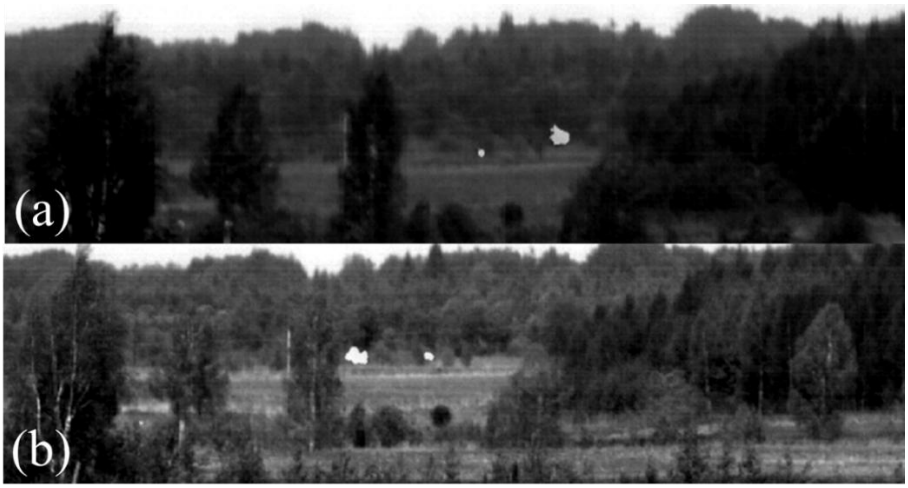


FIGURE 2. Detection maps for: (a) single fabric clothes; (b) mixed fabric outfit.

Detection map for "mixed fabric outfit" objects located at different distances is shown in Fig. 3. Table 4 provides "camera-object" distance data along with the corresponding detection probability.

TABLE 4. Detection probability for "mixed fabric outfit" objects located at different distances.

Distance, m	Detection probability
180	0.9916
3200	0.9730

It can be seen that the detection probability varies with distance to the object and the imaging time, but remains quite high. This denotes that the algorithm is robust to these parameters.

In conclusion, the algorithm based on a Siamese neural network combined with by a pseudodata generation procedure has demonstrated exceptional performance in the low-contrast objects detection using hyperspectral image analysis problem. The robustness of the algorithm is evident from its stability across varying signal-to-noise ratios (SNR), and different lighting conditions, and various distances. The results indicate that the detection probability remains rather high. This makes it a promising approach for applications requiring reliable detection capabilities under different observational conditions.



FIGURE 3. Example of object detection ("mixed fabric outfit") using Siamese neural network at different distances (180 m and 3200 m).

This study was carried out in the framework of State Assignment of the Ministry of Science and Higher Education of the Russian Federation (project No. 125012200611-5).

1. Zhu X., Li Y., Zhang Q., et al. Oil Film Classification Using Deep Learning-Based Hyperspectral Remote Sensing Technology // *ISPRS Int. J. Geo-Inf.* 2019. V. 8. P. 181. DOI: 10.3390/ijgi8040181.
2. Rodionov I.D., Gomorev M.A., Rodionova I.P., et al. Remote Detection of Emergency Emissions and Gas Leaks // *Russ. J. Phys. Chem. B.* 2024. V. 18. No 5. P. 1389–1395. DOI: 10.1134/S1990793124701124.
3. Xi L., Si F., Jiang Y., et al. The Ultraviolet Visible Hyperspectral Imaging Spectrometer (UVHIS), and high-resolution NO_2 mapping from its first airborne observation // *Atmos. Meas. Tech.* 2021. V. 14. P. 435–454. DOI: 10.5194/amt-2020-225.
4. Zhao Y., Zeng Y., Zheng Z., et al. Forest biodiversity mapping using airborne LiDAR and hyperspectral data // *Remote Sensing of Environment.* 2018. V. 213. P. 104–114. DOI: 10.1109/IGARSS.2016.7729922.
5. McFee J. E., Anger C., Achal S., et al. Landmine detection using passive hyperspectral imaging // *Proc. of SPIE.* 2007. V. 6554. P. 655404-1. DOI: 10.1117/12.722204.
6. Wright R., Deloatch J., Osgood S., et al. The spectral reflectance of ship wakes between 400 and 900 nanometers // *2012 IEEE International Geoscience and Remote Sensing Symposium, Munich, Germany.* 2012. P. 4186–4189. DOI: 10.1109/IGARSS.2012.6351746.
7. Zhao D., Liu S., Yang X., et al. Research on Camouflage Recognition in Simulated Operational Environment Based on Hyperspectral Imaging Technology // *Hindawi Journal of Spectroscopy.* 2021. V. 2021. P. 9. DOI: 10.1155/2021/6629661.
8. Zhang X., Gao K., Wang J., Hu Z., Wang H., Wang P. Siamese Network Ensembles for Hyperspectral Target Detection with Pseudo Data Generation // *Remote Sensing.* 2022. V. 14. P. 1260–1278. DOI: 10.3390/rs14051260.

FORMATION OF TWO-DIMENSIONAL GAS CONCENTRATION DISTRIBUTIONS IN THE OPEN ATMOSPHERE BASED ON REMOTE MEASUREMENTS FROM AN IR FOURIER SPECTROMETER

Igor S. Golyak, Dmitriy R. Anfimov, Ivan B. Vintaykin, Igor L. Fufurin and Andrey N. Morozov

Bauman Moscow State Technical University, Moscow, Russia

The growth of production in the energy, metallurgy and other industries has led to significant emissions of pollutants into the atmosphere [1]. Pollutants pose a high risk to human health [2–4]. Detection and identification of substances polluting the atmosphere plays an important role in environmental protection [5, 6]. Existing local monitoring sensors are installed at the emission source, which requires regular maintenance. At the same time, identification of pollutant emissions using remote monitoring sensors makes it possible to study mixtures emitted into the atmosphere by the source without installing local sensors on smoke stacks. Remote monitoring also makes it possible to monitor emissions without preparatory activities at the enterprise. Currently, there are various methods of active

pollution measurement and passive remote monitoring, which are used to analyze pollutants in the atmosphere. One of the promising methods of remote monitoring is infrared (IR) Fourier spectroscopy [7, 8].

Remote measurements of emissions of harmful substances from chimneys during the day were carried out of the sites of the working area of the Kolesnikov Nadezhda Metallurgical Plant of the PJSC “MMC ‘Norilsk Nickel's”, Polar Division in October 2024. The distance from the IR Fourier spectrometers to the top point of the chimneys was 250–760 m. During the measurement process, the Fourier spectrometers recorded the IR radiation of chimney emissions both on cross It can be seen that the sections and in the plumes of flue gases.

Most of the feedstock used to produce copper, nickel, and platinum group metals comes from the ore resources of the Norilsk industrial zone, which are rich in sulfide copper-nickel ores. Sulfur dioxide (SO_2) is the primary toxic material created during the oxidation of sulfide ores in the pyrometallurgical manufacturing process. [9]. Therefore, SO_2 is the most crucial element of chimney flue gases for the PJSC “MMC 'Norilsk Nickel's'” Polar Division to identify.

The methodology for determining the emission rate of SO_2 by scanning the flue gas plume is as follows:

1. A section of the plume is selected at least 50 meters away from the chimney, where the temperature of the flue gases has already decreased, and the radiation from hot water vapor and aerosols (dust) becomes less significant.
2. The scanning direction is chosen in such a way as to obtain a cross-section of the plume.
3. Knowing the distance from the monitoring station to the scanning point r and the angle of the scanning sector γ, the linear size of the plume cross-section l_1 is determined (Fig. 1).
4. Infrared spectra are recorded in the specified sector the integral concentrations C_{int} are determined.
5. The effective cross-sectional area of the plume in the specified scanning sector in the direction of the wind is calculated as:

$$S_{eff} = \frac{\pi}{4} l_1 l_2 \cos\alpha \,.$$

6. Taking into account the wind speed and the measured integral concentration, the flue gas emission rate is calculated as $Q = S_{eff} v C_{\text{int}} / l_2$. Considering the effective cross-sectional area of the plume, the emission rate can be expressed as:

$$Q = \frac{\pi}{4} l_1 \cos\alpha v C_{\text{int}}$$

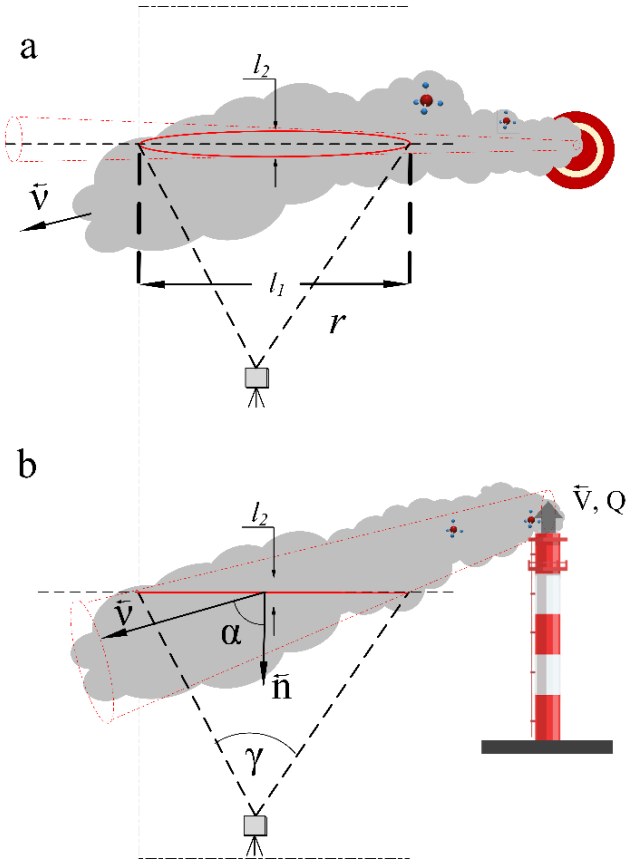
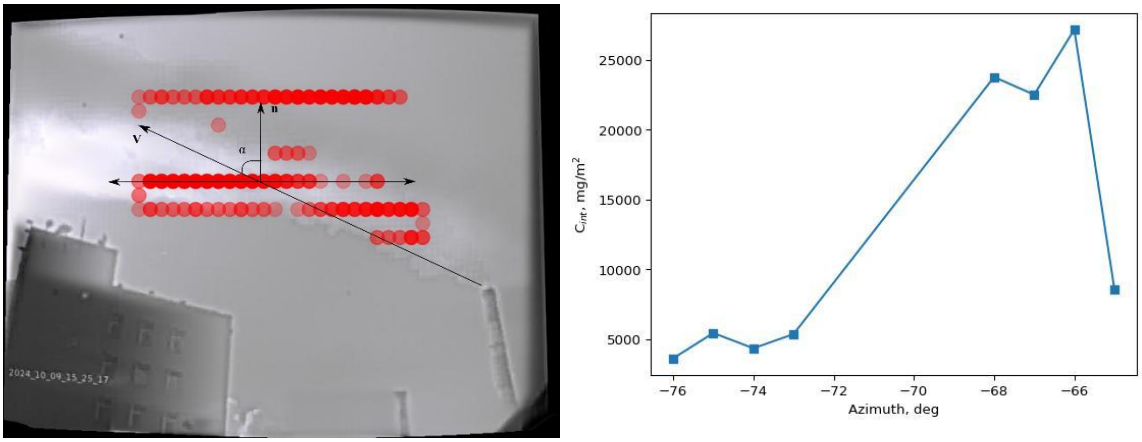


FIGURE 1. Diagram of flue gases from chimneys in top (a) and side views (b).

It is important to note that in this approach, the depth of the cloud l_2 is included in the structure of the integral concentration C_{int} and does not require measurement or estimation. However, for applying the proposed engineering model, it is necessary to know the values of wind speed v and the direction of the flue gas transport α. In this work, the wind speed is estimated based on data from the meteorological resource World Weather.

Figure 2 shows the result of using an engineering model to construct a two-dimensional distribution of sulfur dioxide concentration.



a b

FIGURE 2. A diagram of the device's position relative to the pipe and a section of the flue gas plume for a 31° elevation angle (a) and the concentration distribution in the plume for the 31° elevation angle (b).

Table 1 presents the calculated values of emission power for different elevation angles. The emission power correlates with data obtained from local sensors installed on the chimney.

TABLE 1. Emission power for different elevation angles.

№ p/p	Parameter	Unit	El. 27°	El. 29°	El. 31°
1	Distance to the plume, r	m	646.8	648.2	658.0
2	Sector angular size, γ	deg	4	18	6
3	Sector linear size, l_1	m	45.2	205.33	69.04
4	Wind velocity, v	m/s	3	3	3
5	Integral concentration, C_{int}	mg/m^2	30913.7	14453.5	32500.50
6	The angle between the wind speed and the plume cross-section, α	deg	65	65	65
7	**Emission power, Q**	kg/s	**1.3905**	**2.9555**	**2.2344**

An engineering model for determining the power of sulfur dioxide emissions has been developed based on experimental measurements of integral concentrations obtained using infrared Fourier spectrometers, as well as data on the direction of movement of the flue gas plume and its size, obtained from the results of analyzing the video sequence obtained from the television viewer of the Fourier spectrometer in the direction of the recording of the sulfur dioxide spectra. The emission power of flue gases was estimated using an engineering model.

The work was carried out within the framework of the strategic academic leadership program «Priority 2030».

1. Golyak I.S., Anfimov D.R., Vintaykin I.B., et al. Monitoring Greenhouse Gases in the Open Atmosphere by the Fourier Spectroscopy Method // *Russ. J. Phys. Chem. B*. 2023. No 17. P. 320–328. DOI: 10.1134/S1990793123020264.
2. Rossi R., Ciparisse J.F., Gelfusa M., et al. The project TELEMACO: detection, identification and concentration measurements of hazardous chemical agents // *J. Inst.* 2019. V. 14. No 3. P. C03004–C03004. DOI: 10.1088/1748-0221/14/03/C03004.
3. Donateo A., Villani M.G., Feudo T.L., Chianese E. Recent Advances of Air Pollution Studies in Italy // *Atmosphere*. 2020. V. 11. No 10. P. 1054. DOI: 10.3390/atmos11101054.
4. Morozov I.I., Vasiliev E.S., Volkov N.D., et al. Reactions of Benzyl- and Hydroxyethyl Radicals with Nitric Oxide // *Russ. J. Phys. Chem. B*. 2022. V. 16. No 5. P. 877–882. DOI: 10.1134/S1990793122050220.
5. Gaudio P., Gelfusa M., Malizia A., et al. Detection and monitoring of pollutant sources with Lidar/Dial techniques // *J. Phys.: Conf. Ser*. 2015. No 658. 012004. DOI: 10.1088/1742-6596/658/1/012004.
6. Gaudio P., Malizia A., Gelfusa M., et al. Lidar and Dial application for detection and identification: a proposal to improve safety and security // *J. Inst*. 2017. V. 12. No 1. P. C01054–C01054. DOI 10.1088/1748-0221/12/01/C01054.
7. Sung L.Y., Shie R.H., Lu C.J. Locating sources of hazardous gas emissions using dual pollution rose plots and open path Fourier transform infrared spectroscopy // *Journal of Hazardous Materials*. 2014. No 265. P. 30–40. DOI: 10.1016/j.jhazmat.2013.11.006.
8. Fufurin I.L., Shlygin P.E., Pozvonkov A.A. Temperature Dependence of the Sensitivity of an Infrared Fourier Spectrometer // *Russ. J. Phys. Chem. B*. 2021. V. 15. No 5. P. 911–918. DOI: 10.1134/S1990793121050146.
9. Tømmervik H., Johansen B.E., Pedersen J.P. Monitoring the effects of air pollution on terrestrial ecosystems in Varanger (Norway) and Nikel-Pechenga (Russia) using remote sensing // *Science of The Total Environment*. 1995. V. 160–161. P. 753–767. DOI: 10.1016/0048-9697(95)04409-T.

ESTIMATION OF INDUSTRIAL FLUE GAS EMISSION CAPACITY USING THE PASQUILL-BRIGGS MODEL

Vladimir L. Glushkov, Ivan B. Vintaikin, Igor S. Golyak, Roman A. Gylka, Igor L. Fufurin, and Andrei N. Morozov

Bauman Moscow State Technical University, Moscow, Russia

Recently, there has been an increasing interest in studying atmospheric diffusion and air pollution. The issue of maintaining the purity of the atmosphere has gone beyond scientific research and gained significant social and governmental importance. To address this issue, it is essential to adopt an integrated approach, and research in this field is an integral part of the broader goal of environmental protection and the conservation of natural resources. Despite significant efforts to protect the atmosphere from pollution, due to the growth of industry and motor transport, as well as the lack of effective anti-pollution measures, the concentrations of harmful impurities in the air of several cities still exceed acceptable levels. Of particular importance are developments in the meteorological aspects of air

pollution, which relate primarily to the study of atmospheric diffusion and the patterns of impurity spread, as well as the features of their spatial and temporal distribution. These are the basis for assessing the pollution status of the air and developing measures to ensure clean air [1].

The main goal of atmospheric air pollution modeling is to estimate the concentration of pollutants in the atmosphere from industrial facilities, emissions from stationary sources, and background concentrations from other sources. Modeling helps to determine the range of pollutant transport, as well as the degree of environmental impact from various sources and which sources contribute the most. Currently, there are numerous methods for calculating the spread of pollutants. Some of these methods focus on calculating a specific type of pollutant, while others are capable of performing complex calculations. These techniques have led to the development of models that predict the spread of pollutants in the atmosphere. Most of the models are based on distributed Gaussian (for example, ADM, ISC-3), less often based on the Euler or Navier-Stokes equations (Chensi, CAMx, PANACHE, REMSAD, WYNDVALLEY) [2].

In this study, we perform spatial modeling of sulfur dioxide emissions from the chimneys of metallurgical plants of the PJSC "MMC 'Norilsk Nickel's'," Polar Division. The Pasquill-Briggs model has been chosen as the one to use to describe the spread of impurities. This is because of its simplicity and flexibility in adapting to local conditions. The model is based on the assumption that the distribution of pollutants in the atmosphere follows a normal law, also known as the Gaussian distribution. This assumption is based on the turbulent diffusion equation with some simplifications [3]. There are several assumptions in this approach:

- scattering in the horizontal and vertical planes is described by a normal distribution with standard deviations of concentration σ_y and σ_z along the y and z axes;
- the average wind velocity, u, acting on the jet remains constant throughout the entire layer, and the wind direction does not change;
- the ejection power is constant;
- there is reflection of the jet on the earth's surface.

Considering these assumptions, the spatial distribution of the sulfur dioxide concentration, $c(x, y, z)$, from the described source, with a constant wind directed along the x-axis, can be represented by the following formula within the context of the Gaussian scattering model (Fig.1):

$$c(x,y,z)=\frac{q}{2\pi\sigma_y\sigma_z u}\exp\left(\frac{-y^2}{\sigma_y^2}\right)\left[\exp\left(\frac{-(z-h)^2}{\sigma_z^2}\right)+\exp\left(\frac{-(z+h)^2}{\sigma_z^2}\right)\right], \quad (1)$$

where q - source pollutant emission rate [kg/s]; h - height of emission plume centerline above ground level [m]; u - horizontal wind velocity along the plume centerline [m/s]. There are several Gaussian models with different scattering functions, such as the Pasquill-Briggs and Pasquill-Gifford models [3]. In the Pasquill-Briggs model, the values of the scattering function σ_y and σ_z are determined by the stability class of the atmosphere from 100 m to 10 km to the source. The stability class is determined by the wind speed, the degree of daytime insolation, and the number of night clouds.

Simulation of the dispersion of flue gas plumes in the Pasquill-Briggs model was used to estimate the emission rate of sulfur dioxide. The integral concentrations of harmful substances in the exhaust gas plume are calculated for those directions where experimental data are available. Minimizing the difference between the measured integrated concentration and the calculated value is the key to finding the variable parameters. Wind speed and direction, as well as the power of the pollutant emission source, have been chosen as variables to consider. With this algorithm, the theoretical concentration distribution matches the experimental concentration distribution of sulfur dioxide. The experimental data of integrated concentration in different directions was obtained based on remote optical monitoring of

chimney emissions using passive infrared Fourier spectrometers operating in the wavelength range of 7-13 microns with a spectral resolution of 4 cm^{-1} [4].

The results of one of the calculations for the exhaust plume are presented in Figure 2. The calculations were carried out for a pipe with a height of 150 meters and a wind speed of approximately 5 meters per second. The origin (black dot) corresponds to the location of the spectrometers, and the position of the pipe is indicated by a diagonal cross. The left graph illustrates the distribution of the volume concentration of SO_2 in a horizontal plane, while the right graph represents the concentration distribution perpendicular to the propagation direction of the plume at a distance of 200 meters from the pipe. Additionally, the graph includes lines indicating equal concentrations. Using the Pasquill-Briggs model, we can obtain a spatial distribution and estimate the total amount of sulfur dioxide emitted from pipes. This method can be used when there are multiple sources of emissions.

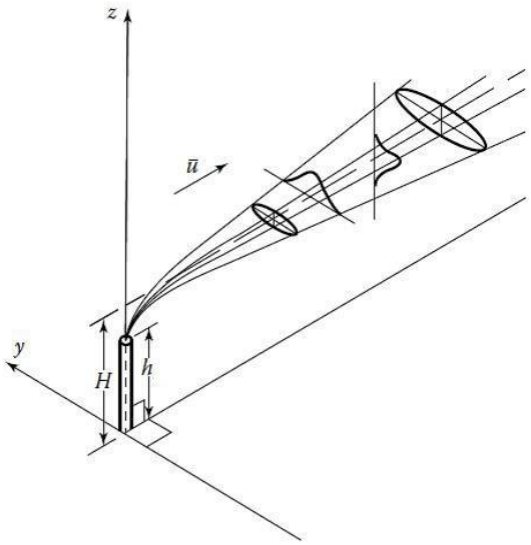


FIGURE 1. Visualization of a floating plume of sulfur dioxide dispersion in the Pasquill-Briggs model.

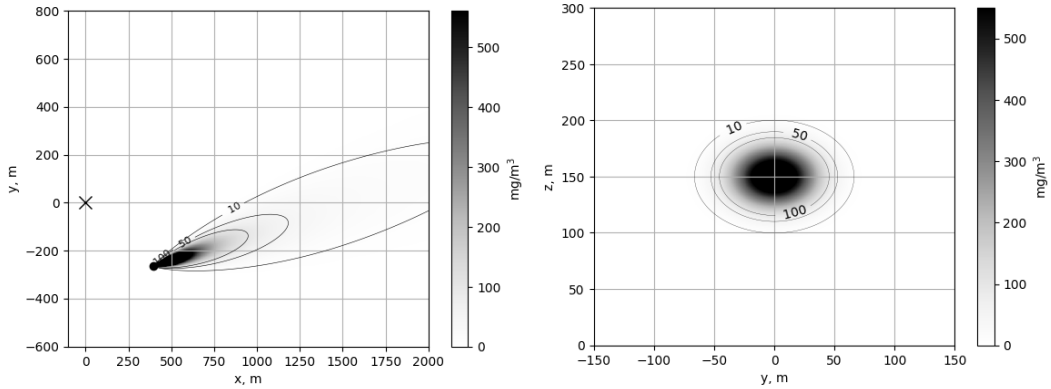


FIGURE 2. Distribution of the mass concentration of SO_2 in different sections for z=150 m. (left fig.), x=200 m. (right fig.).

The work was carried out within the framework of the strategic academic leadership program «Priority 2030».

1. Lukyanets A., Gura D., Savinova O., et al. Industrial emissions effect into atmospheric air quality: mathematical modeling // *Reviews on Environmental Health*. 2023. V. 38. No 2. P. 385–393. DOI: 10.1515/reveh-2022-0005.
2. Markiewicz M.T. A review of mathematical models for the atmospheric dispersion of heavy gases. Part I. A classification of models // *Ecological Chemistry and Engineering S*. 2012. V. 19. No 3. P. 297–314. DOI: 10.2478/v10216-011-0022-y.

3. Elsakov S.M., Drozin D.A., Herreinstein A.V., et al. Numerical Study of the Susuplume Air Pollution Model // *Bulletin of the South Ural State University. Series: Mathematical Modelling, Programming and Computer Software*. 2020. V. 13. No 4. P. 5–18. DOI: 10.14529/mmp200401.
4. Morozov A.N., Tabalin S.E., Anfimov D.R., et al. Estimation of Emissions From Metallurgical Plants Using Infrared Fourier Transform Spectroscopy // *Russian Journal of Physical Chemistry B*. 2024. V. 18. No 3. P. 763–772. DOI: 10.1134/S1990793124700234.

FTIR SPECTROMETER ONBOARD 16U CUBESAT SPACECRAFT FOR GREENHOUSE GASES MONITORING

Dmitriy R. Anfimov, Igor L. Fufurin, Ilya S. Golyak, Ivan B. Vintaikin, Dmitriy A. Rachkin, and Andrey N. Morozov

Bauman Moscow State Technical University, Moscow, Russia

The monitoring of greenhouse gases (GHGs), particularly carbon dioxide (CO_2) and methane (CH_4), from space has become a critical component of global efforts to understand and mitigate climate change. Fourier Transform Infrared (FTIR) spectroscopy has played a pivotal role in these efforts, enabling the detection and quantification of GHG concentrations with high precision.

The foundation for space-based GHG monitoring was laid by early missions such as SCIAMACHY (Scanning Imaging Absorption Spectrometer for Atmospheric Cartography) on board the ENVISAT satellite, launched in 2002. SCIAMACHY was one of the first instruments to retrieve column-averaged dry-air mole fractions of CO_2 and CH_4. These measurements were derived from spectra in the near-infrared and shortwave-infrared regions, with CO_2 retrieved from the 1.58 μm band and CH_4 from the 1.65 μm band. [1]. The launch of the Greenhouse Gases Observing Satellite (GOSAT) in 2009 marked another significant milestone. GOSAT was the first satellite dedicated to GHG monitoring, equipped with the Thermal and Near-Infrared Sensor for Carbon Observation Fourier-Transform Spectrometer (TANSO-FTS) and the TANSO Cloud and Aerosol Imager (TANSO-CAI).



FIGURE 1. Greenhouse gases observing satellite GOSAT "IBUKI".

TANSO-FTS measured absorption spectra in the shortwave-infrared (SWIR) and thermal-infrared (TIR) regions, enabling the retrieval of CO_2 and CH_4 concentrations with improved accuracy and spatial resolution compared to SCIAMACHY [2]. Figure 1 shows the "IBUKI" satellite of the GOSATS system. The successor to GOSAT, GOSAT-2, was launched in 2018 with enhanced capabilities.

The TANSO-FTS-2 instrument on board GOSAT-2 features improved spectral resolution and range, including measurements in the oxygen A band (0.76 μm), weak and strong CO_2 bands (1.6 and 2.0 μm), and methane bands (1.6 and 2.3 μm).

Additionally, TANSO-FTS-2 measures thermal-infrared radiation in the mid-wave (5.5–8.4 μm) and long-wave (8.4–14.3 μm) regions, allowing for better characterization of GHG sources and sinks [3].

The European Copernicus CO2M mission, scheduled for launch in 2026, represents the next generation of space-based GHG monitoring. The mission will utilize artificial neural networks (ANNs) for retrieving CO_2 and CH_4 from radiance measurements, with the goal of achieving spatio-temporal systematic errors below 0.5 ppm for CO_2 and 5 ppb for CH_4 [4].

The aim of this work is to modify the developed model of the dynamic Fourier spectrometer, placed on the 16U CubeSat spacecraft [5,6]. The model is designed to determine the concentrations of greenhouse gases in the Earth's atmosphere. Figure 2 shows the operation diagram of the passive Fourier spectrometer in space conditions.

The developed model of the dynamic Fourier spectrometer was modernized as follows:

1. the scanning system was modified, allowing to increase the frame movement speed and simultaneously the scanning frequency up to 2 scans per second;
2. replacement of the IR radiation receiver with an indium-gallium-arsenide photodetector IG26X1000T9 (Table 1) with an extended spectral range up to 2.6 μm. Expanding the spectral sensitivity range allows recording the absorption lines of CO_2 in the region of 2.05 μm (4878 cm^{-1}) and CH_4 in the region of 2.2 μm (4547 cm^{-1}), the absorption intensity of which is an order of magnitude greater than in the near IR region: CO_2 at 1.6 μm (6225 cm^{-1}) and CH_4 at 1.66 μm (6000 cm^{-1}).

Experiments were conducted on a mockup of a dynamic Fourier spectrometer to record the IR spectra of solar radiation passing through the Earth's atmosphere. Figure 3 shows the experimental setup. The objective of the dynamic Fourier spectrometer mockup is directed at the sky, the weather is cloudy. In this case, the spectrometer records the spectrum of solar radiation that has passed through the thickness of the Earth's atmosphere. Using a mockup of a dynamic Fourier spectrometer, a graph of the spectral transmittance coefficient of the atmosphere T(ν) was recorded, which is shown in Fig. 4. The spectrum recorded on the mockup shows intense absorption lines of greenhouse gases O_2, CO_2 and CH_4 in the near IR region. The spectral region in which the oxygen absorption line is shown in Fig. 5. The main absorption line of O2, corresponding to the wave number ν = 7880 cm^{-1}, is clearly expressed.

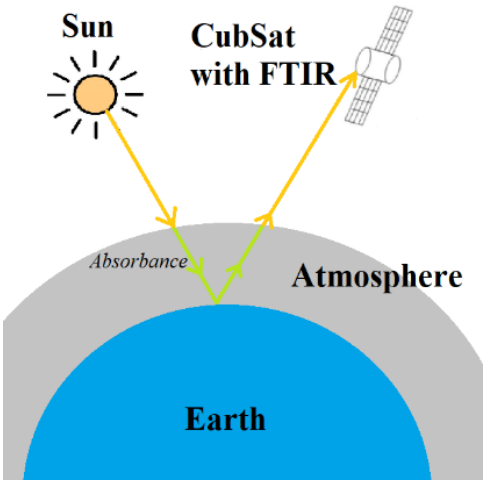


FIGURE 2. Obtaining a spectrum of solar radiation that has passed through the atmosphere.

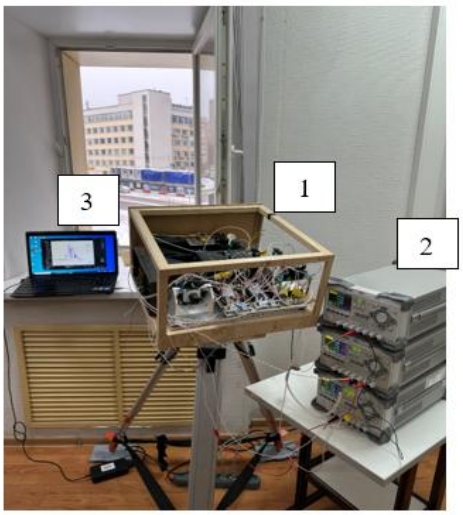


FIGURE 3. Registration of spectra on a mockup of a dynamic Fourier spectrometer. 1 – mockup, 2 – power supplies, 3 – PC.

TABLE 1. Shows the characteristics of the IG26X1000T9 photodetector.

Parameter	Unit	Value
Spectral range	µm	<2.45
Diameter	µm	2000
Operating Temperature	°C	-20
Shunt Impedance	kOhm	30
Peak Detectivity D*	cm $Hz^{1/2}$ / W	3.2 x 10^{11}
Peak NEP	W / $Hz^{1/2}$	5.5 x 10^{-13}
Capacitance	pF	1920

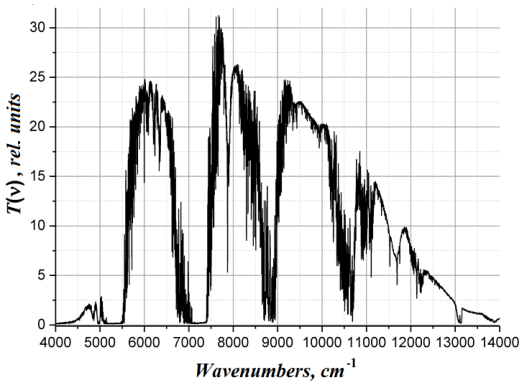


FIGURE 4. Spectral transmittance of the atmosphere recorded on a mockup in passive mode using an IG26 detector.

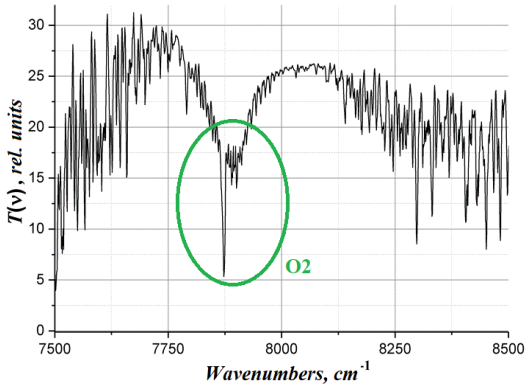


FIGURE 5. Spectral transmittance of the atmosphere recorded on a mockup in passive mode using an IG26 detector in range from 7500 - 8500 cm^{-1}.

The shape of the spectrum and the position of the main line coincide with the experimental and model spectra given in the literature and in the HITRAN spectral database. The obtained value of the spectral width of the main O_2 line is about 5 cm^{-1}.

The spectral region in which the absorption line of CO_2 and CH_4 is shown in Figure 6. In this region, the CO_2 lines are visible in the region of wave numbers 6150 and 6350 cm^{-1} and the CH_4 absorption line at 6000 cm^{-1}.

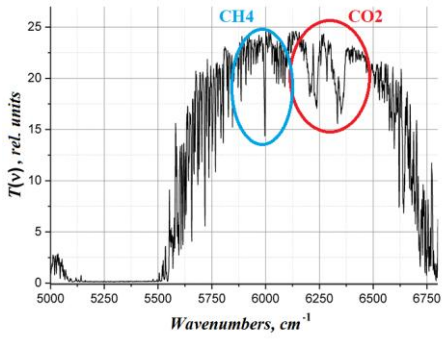


FIGURE 6. Spectral transmittance of the atmosphere recorded on a mockup in passive mode using an IG26 detector in range from 5000 to 6750 cm^{-1}.

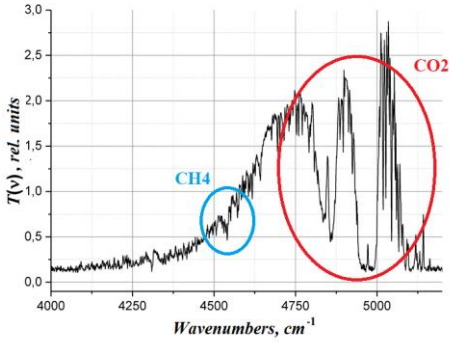


FIGURE 7. Spectral transmittance of the atmosphere recorded on a mockup in passive mode using an IG26 detector in range from 4000 to 5200 cm^{-1}.

The general shape and position of the absorption maxima of these gases here also coincide with their model spectra, which are given in the HITRAN spectral database. The lines corresponding to vibrational-rotational transitions of CO_2 and CH_4 molecules in the experimental spectrum, as in the case of recording spectra using the IG17 receiver, are not resolved.

The spectrum also contains weaker CO_2 gas lines in the region of 4750 - 5000 cm^{-1} and a weak CH_4 absorption line at 4547 cm^{-1} (Fig. 7).

The position of the lines and their shape coincide with the position of the absorption lines in the model spectra (HITRAN database).

Results of this work show that the expansion of the spectral range leads to a significant increase in the number of spectral lines. This can be used to improve the accuracy of calculating CO_2 and CH_4 concentrations in the earth's atmosphere from space.

1. Buchwitz M., Bovensmann H., Burrows J. P., Schneising O., Reuter M. Global mapping of methane and carbon dioxide: from SCIAMACHY to CarbonSat // *Proceedings ESA-iLEAPS-EGU conference on earth observation for land-atmosphere interaction science*, ESA Special Publications SP-688, ESRIN, Italy. 2010. P. 3-5.
2. Kuze A., Suto H., Nakajima M., Hamazaki T. Thermal and near infrared sensor for carbon observation Fourier-transform spectrometer on the Greenhouse Gases Observing Satellite for greenhouse gases monitoring // *Applied optics*. 2009. V. 48. No 35. P. 6716-6733. DOI: 10.1364/AO.48.006716.
3. Suto H., Kataoka F., Kikuchi N., Knuteson R. O. et al. Thermal and near-infrared sensor for carbon observation Fourier transform spectrometer-2 (TANSO-FTS-2) on the Greenhouse gases Observing SATellite-2 (GOSAT-2) during its first year in orbit // *Atmospheric Measurement Techniques*. 2021. V. 14. No 3. P. 2013-2039. DOI: 10.5194/amt-14-2013-2021.
4. Reuter M., Hilker M., Noël S., Di Noia A. et al. Retrieving the atmospheric concentrations of carbon dioxide and methane from the European Copernicus CO2M satellite mission using artificial neural networks // *EGUsphere*. 2024. V. 2024. P. 1-32. DOI: 10.5194/egusphere-2024-2365.
5. Mayorova V., Morozov A., Golyak I., Golyak I. et al. Determination of greenhouse gas concentrations from the 16U cubesat spacecraft using fourier transform infrared spectroscopy // *Sensors*. 2023. V. 23. No 15. P. 6794. DOI: 10.3390/s23156794.
6. Golyak I.S., Anfimov D. R., Vintaykin I. B., Golyak Ig. S. et al. Monitoring greenhouse gases in the open atmosphere by the Fourier spectroscopy method // *Russian Journal of Physical Chemistry B*. 2023. V. 17. No 2. P. 320-328. DOI: 10.1134/s1990793123020264.

EXPERIMENTAL SETUP FOR LEAK DETECTION WITH PASSIVE NDIR RADIOMETER AND INFRARED CAMERA

Dmitriy R. Anfimov, Ivan B. Vintaikin, Ilya S. Golyak, Igor L. Fufurin and Andrey N. Morozov

Bauman Moscow State Technical University, Moscow, Russia

Among the leak detection methods, remote leak detection methods are distinguished by their performance. Optical methods are very common among remote methods [1,2]. These include leak detection methods using highly sensitive thermal imaging cameras and tunable diode laser absorption

spectroscopy (TDLAS) [3]. However, the use of compact infrared OGI cameras [4] by personnel is limited by the security policy at hazardous facilities. Machine learning methods are used to detect leaks [5]. And the use of the TDLAS method for monitoring the production site is hampered by the need for constant space scanning.

This paper considers the creation of a complex, the components of which are: an infrared camera for an extended spectral range and a non-dispersive infrared (NDIR) sensor of a passive type and control software. The results of field tests of the complex's components are also described.

An infrared camera transmits an uncompressed video stream to a control computer, which performs statistical processing to evaluate fluctuations in the intensity of infrared radiation. Based on fluctuations, it is possible to make an assumption about the fact of leakage. The leak is clarified by the NDIR sensor. The NDIR sensor consists of two photodetector units: a signal and a reference. The signal unit senses radiation in the area on the gas absorption line, the reference unit senses the spectral region in which there will be no gas absorption lines under normal atmospheric conditions. The result of processing the video stream from the infrared camera during the leak is shown in Fig. 1.

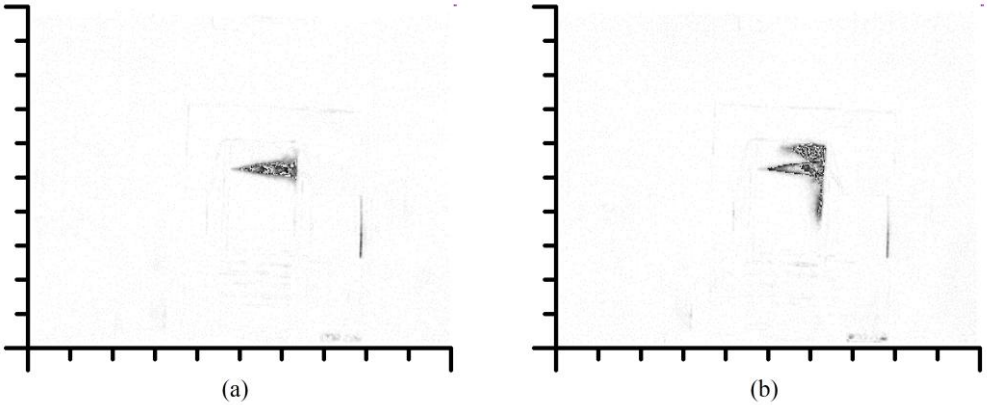


FIGURE 1. The result of processing a video stream from an infrared camera: a - at the beginning of a gas leak, b - during a gas leak.

The implemented video stream processing algorithm determines the expected location of the gas leak. At the same time, the OGI camera can control the angular field of 30 degrees horizontally and 20 degrees vertically. Thus, the analysis of only the areas of space suspected of leakage makes it possible to increase the efficiency of the industrial safety system.

Experiments were carried out separately with an NDIR sensor with a viewing sector of 1 by 1 degree. Experiments have shown its operability at distances up to 90 meters.

The combined use of the components listed above increases the speed of response to leakage and increases the reliability of its detection.

The work was carried out within the framework of the strategic academic leadership program «Priority 2030».

1. Korlapati N., Khan F., Noor Q., Mirza S., Vaddiraju S. Review and analysis of pipeline leak detection methods // *Journal of Pipeline Science and Engineering*. 2022. V. 2. No 4. P. 100074. DOI: 10.1016/j.jpse.2022.100074.
2. Boaz L., Kaijage S., Sinde R. An overview of pipeline leak detection and location systems // *Proceedings of the 2nd Pan African International Conference on Science, Computing and Telecommunications*. IEEE. 2014. P. 133-137. DOI: 10.1109/SCAT.2014.7055147.

3. Frish M.B., Wainner R.T., Green B.D., Laderer M.C., Allen M.G. Standoff gas leak detectors based on tunable diode laser absorption spectroscopy // *Infrared to Terahertz Technologies for Health and the Environment*. SPIE, 2005. V. 6010. 60100D. DOI: 10.1117/12.630599.
4. Maldague X. P. V., *Infrared Thermography: Errors and Uncertainties*, Wiley, 2009, pp. 52-58.
5. Golyak I.S., Anfimov D.R., Demkin P.P., Berezhanskiy P.V., Nebritova O.A., Morozov A.N., Fufurin I.L. A hybrid learning approach to better classify exhaled breath's infrared spectra: A noninvasive optical diagnosis for socially significant diseases // *Journal of Biophotonics*. 2024. e202400151. DOI: 10.1002/jbio.202400151.

FTIR SPECTROMETER FOR REMOTE MONITORING OF METALLURGICAL PLANT GAS EMISSIONS

Igor L. Fufurin[1], Maria A. Fufurina[2], Olga A. Yatsenko[2], Lidia A. Chertkova[2], Ivan B. Vintaikin[1], Roman A. Gylka[1] and Andrey N. Morozov[1]

[1] Bauman Moscow State Technical University, Moscow, Russia
[2] Center of Applied Physics Bauman Moscow State Technical University, Moscow, Russia

The modern environmental legislation of the Russian Federation is aimed at minimizing the impact of industrial emissions on the ecology of the relevant regions of the country.

All enterprises are required to carry out regular monitoring of industrial emissions into the atmosphere if there is at least one source of pollution on their territory, which includes ventilation shafts, deflectors, pipes, etc.

Deposits of the Krasnoyarsk region contain sulfide copper-nickel ores, which are particularly valuable polymetallic ore raw materials, since, in addition to nickel, copper and cobalt, it may contain platinoids, gold, silver, selenium, and tellurium. The combustion process of sulfide ores is endogenous, which is financially profitably, but is accompanied by the release of tons of sulfur dioxide into the atmosphere. Norilsk Nickel launched a sulfur program in 2022 and confirmed a 20% reduction in SO_2 by the end of 2024. With the project reaching full capacity in 2025-2026, emissions reduction at the Polar branch of Norilsk Nickel should amount to 45% compared to the base of 2015.

We performed measurements of SO_2 emissions in July 2023 and October 2024 in Norilsk Region (see Fig.1).

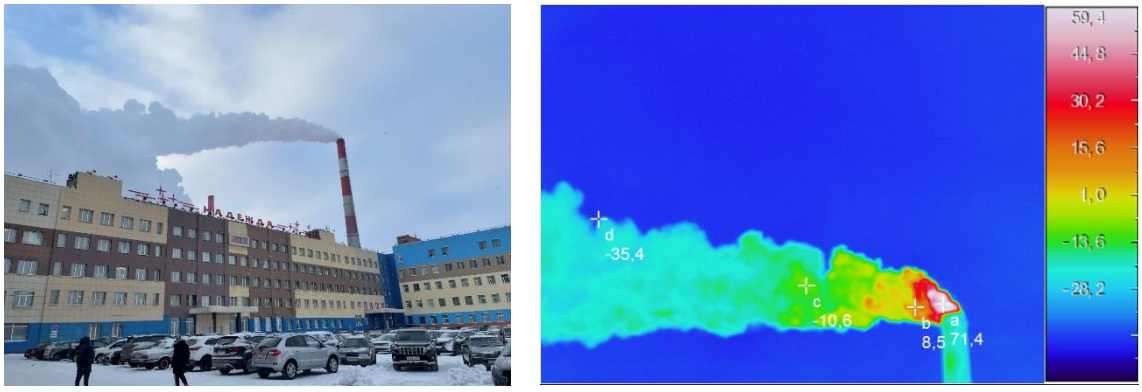


FIGURE 1. Chimney gas measurement conditions (view from the side of the device and thermogram)

For continuous monitoring of sulfur dioxide emissions by metallurgical factories, one of the remote sensing techniques is IR Fourier (FTIR) spectroscopy [1]. We used both a single-channel FTIR spectrometer with an FOV of 2x2 degrees, a spectral resolution of 4 cm^{-1}, a spectral range of 7-13 μm and a single measurement time of 1 s, and a multi-channel FTIR spectrometer with an angular field of view of an infrared channel of 20x3 degrees, a spectral resolution of 4 cm^{-1}, a spectral range of 7-13 μm and the time of one measurement is 1 s [2, 3].

Figure 2 shows a technique for remote measurement of emissions using FTIR spectrometers. The FTIR spectrometer targets the exhaust gases pos. 2 chimneys pos. 1, as a result of infrared radiation pos. 3 enters the Michelson two-beam interferometer pos. 4 and after modulation to the photodetector pos. 5.

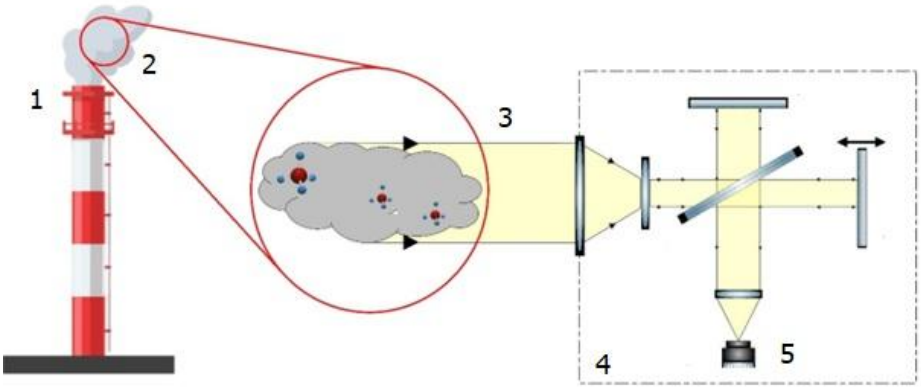


FIGURE 2. A technique for remote measurement of emissions using FTIR spectrometers

We used two methods to mathematically analysis of flue gas IR spectra. In the first method (engineering approach, see Fig. 3), we determined the cross-section of the plume using the video channel and then calculated the gas output power (kg/s of SO_2) based on the distribution of measured concentrations. The second approach is based on an approximation of the Pasquill-Briggs model (see Fig. 4).

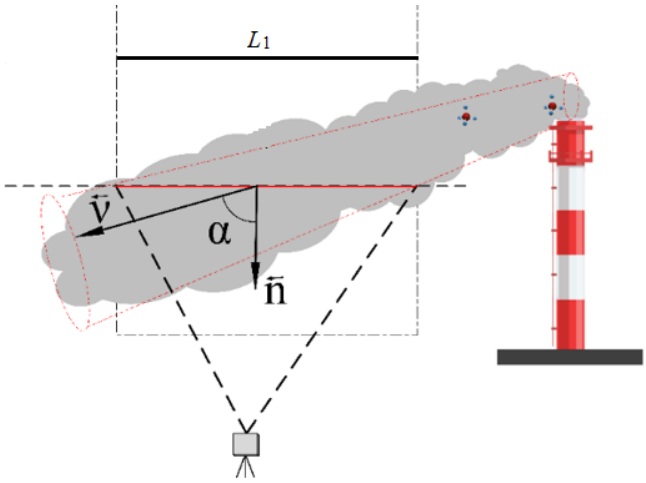


FIGURE 3. The engineering approach to determining the gas emission capacity

Taking into account the wind speed ***v*** and the measured integral concentration ***C*** (mg/m^2 or ppm·m), the gas emission power Q (kg/s) can be calculated as $Q = \pi/4 \cdot L_1 \cdot \cos\alpha \cdot v \cdot C$.

The Pasquill-Briggs model describes impurity transfer from a stationary point source. The model has limitations on the distance from the pipe and is applicable in the range from 100 m to 10 km to the pipe (source). A forbidden zone is introduced near the pipe, while the size of the simulated area is limited. Integral concentrations of sulfur dioxide in the flue gas plume are measured. The position of the observation post, the position of the chimney, the approximate parameters of the emission per unit of time, wind speed and direction, time of day, clouds, degree of insolation and type of terrain are set. The theoretical integral concentration is calculated for each of the observation directions.

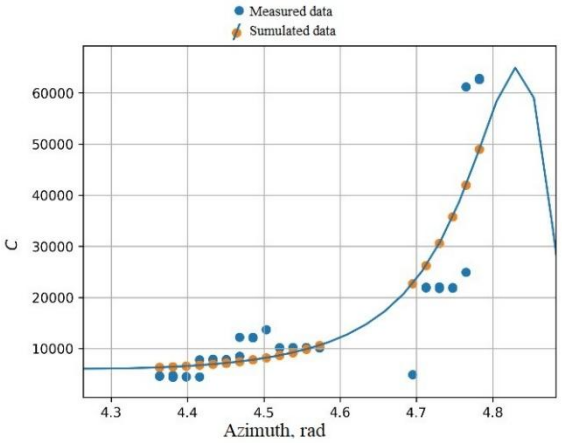


FIGURE 4. Simulation of the emission concentration using the Pasquill-Briggs model (Integral concentration C is given in mg/m^2)

The discrepancy between the measured and theoretical integral concentrations is determined, where the optimization parameters are wind speed and gas emission power (see Fig. 4).

Both engineering approach and Pasquill-Briggs models use remote measurements to obtain an estimation of the emission power of sulfur dioxide using infrared flue gas spectra using IR Fourier spectrometers.

The work was carried out within the framework of the strategic academic leadership program «Priority 2030».

1. Fufurin I.L., Golyak I.S., Bashkin S.V., et. al. FTIR spectroscopy based on a multipass gas cell and TE cooled HgCdTe sensors for environmental monitoring and defense applications // *Proc. SPIE 11775 – Integrated Optics: Design, Devices, Systems and Applications VI*. 2021. 1177512. DOI: 10.1117/12.2588714.
2. Morozov A.N., Svetlichnyi S.I., Fufurin I.L. Correction of wavenumbers in a FTIR imaging spectrometer // *Doklady Physics*. 2015. V. 60. No 9. P. 388–391. DOI: 10.1134/S1028335815090074.
3. Morozov A.N., Tabalin S.E., Anfimov D.R., et al. Estimation of Emissions From Metallurgical Plants Using Infrared Fourier Transform Spectroscopy // *Russian Journal of Physical Chemistry B*. 2024. V. 18. No 3. P. 763–772. DOI: 10.1134/S1990793124700234.
4. Kahl J.D.W., Chapman H.L. Atmospheric stability characterization using the Pasquill method: A critical evaluation // *Atmospheric Environment*. 2018. V. 187. P. 196–209. DOI: 10.1016/j.atmosenv.2018.05.058.

SPACE SYSTEM FOR MEASURING GREENHOUSE GAS CONCENTRATION

Ilya S. Golyak, Andrey N. Morozov and Larisa N. Timashova

Bauman Moscow State Technical University, Moscow, Russia

One of the most discussed problems in the world is climate change, including an increase in average annual temperature [1]. It is largely associated with increased concentrations of greenhouse gases in the

atmosphere. The main greenhouse gases in the atmosphere are follows: carbon dioxide (CO_2), methane (CH_4), ozone (O_3) and water vapor. Among them, the greatest impact on global warming is associated with an increase in CO_2.

Global monitoring of these gases is carried out from space. Various meteorological satellites are used for this: Sentinel-5P [2], GHGSat [3], OCO-2/3 [4] and others. Such systems allow a simultaneous capture of an area of up to 2500 km with a spatial resolution of 10 – 100 km. Such systems are based on dynamic or static Fourier spectrometers, Fabry-Perot interferometers or diffraction spectrometers [5, 6].

For measurements from near-Earth orbit several small CubeSat 16U spacecraft [7, 8] can also be considered. The dimensions of spacecraft are 226.3 x 226.3 x 454 mm and cost of such systems is much less.

The layout of a small system, which can be installed on one of these microsatellites for measurement of concentrations CO_2, O_2, are presented in this work.

The system is working in the infrared spectral wavelength range from 1.0 μm to 1.7 μm (10000 – 5880 cm^{-1}). According to the model and reference data [7, 8], in this spectral range there are CO_2 and O_2 absorption bands (Table 1). We are focused on measurement the CO_2 absorption lines in the 1.6 μm region and O_2 at a wavelength of 0.76 μm.

TABLE 1. Absorption lines of the gases of the atmosphere in the visible - near-IR range

greenhouse gases	Central wavelength, μm
CO_2	1,4, 1,6, 2,0, 2,7, 4,3
O_2	0,63, 0,69, 0,76, 1,06, 1,27, 1,58
CH_4	1,66, 2,2, 3,3

The O_2 absorption line is necessary to calculate the absolute concentration of CO_2 since the concentration of oxygen in the atmosphere varies little.

The system is designed for recording the absorption spectra of greenhouse gases in the Earth's atmosphere and monitoring the dynamics of their concentrations. The measurements are carried out in the passive mode by reflected solar radiation.

The main element of the system, that allows spectral decomposition, is tunable filter. The principle of the system's operation is to shift the filter's spectral transmission window along the wavelength depending on the angle of the incident radiation. Thus, the angles of the incident radiation determine the right and left boundaries of the gas absorption spectrum.

Layout spectrometer is shown in Fig. 1.

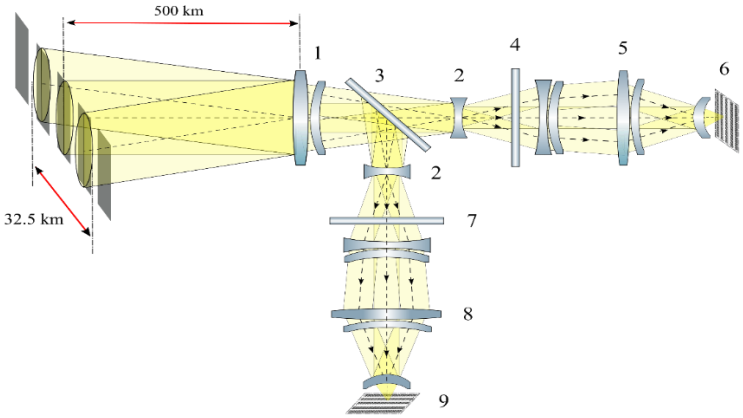


FIGURE 1. Layout of spectrometer: 1, 2 – entrance objective; 3 – beam splitter; 4 – NIR filter; 5 – NIR focusing objective; 6 – main channel detector; 7 – VIS filter; 8 – VIS focusing objective; 9 – reference channel detector.

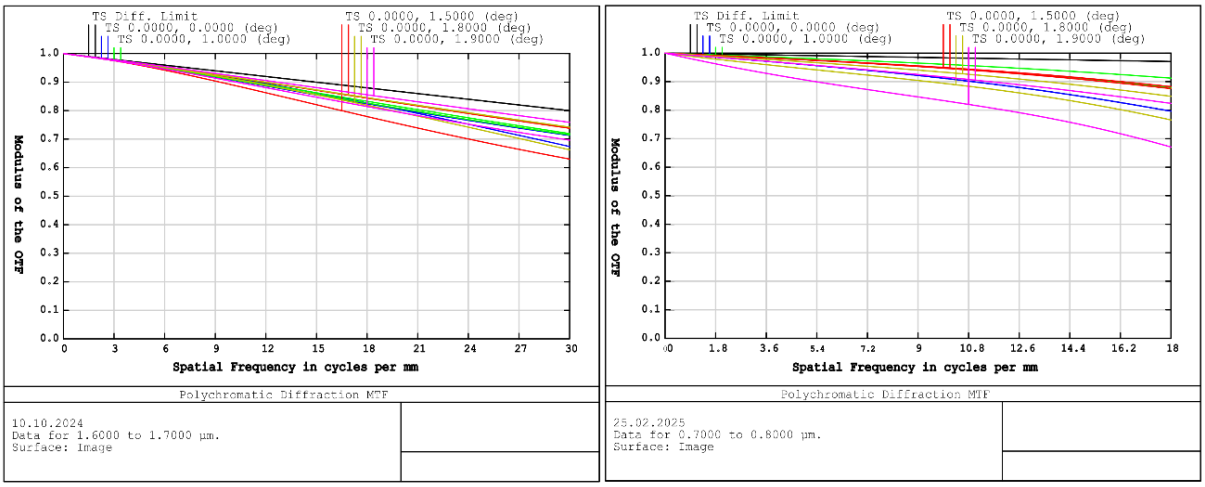
The spectrometer consists of two parts: a measuring channel (CO_2 channel) and reference channel (O_2 channel). To ensure good luminosity, a 100 mm diameter light flux is formed at the system input.

The angular field of view of the system being developed is 0.065 rad, which, when the system is located in low Earth orbit, 500 km, will give a viewing strip on Earth equal to 32.5 km.

A bandpass filters for the wavelength of methane (4) and oxygen (7) with a spectral bandwidth of 1 nm is used as the filters for the main and reference channels.

The radiation in the main channel is recorded by an InGaAs matrix with spectral sensitivity 1.0 – 1.9 μm. The matrix has 640 by 480 elements with element size of 15 μm. For registration radiation in the reference channel is used VIS matrix with 812 by 624 elements and element size of 9 μm.

The value of the modulation transfer function (MTF) for the calculated system is shown in the Figure 2. In Fig 2a for the main channel and Fig. 2b – reference channel. The resulting graphs show that the obtained value of the MPF is about 0.7 at a frequency of 30 lines/mm in the main channel (Fig. 2a) and 0.8 at a frequency of 18 lines/mm in the reference channel (Fig. 2b).



(a) (b)

FIGURE 2. MTF of the system: (a) – main channel, (b) – reference channel

These graphs show that this is enough to collect most of the incoming energy on one element of the matrix device in main and reference channel.

The work was carried out within the framework of the «BaumanGoGreen» strategic project of the «Priority-2030».

1. Manisalidis I., Stavropoulou E., Stavropoulos A., et al. Environmental and health impacts of air pollution. // *Front Public Health*. 2020. V. 8. No 14. DOI: 10.3389/fpubh.2020.00014
2. Tian Y., Hong X., Shan C., et al. Investigating the Performance of Carbon Monoxide and Methane Observations from Sentinel-5 Precursor in China // *Remote Sens*. 2022. V. 14. No 23. P. 6045. DOI: 10.3390/rs14236045
3. Jervis D., McKeever J., Durak B.O.A., et al. The GHGSat-D imaging spectrometer. // *Atmos. Meas. Tech*. 2021. V. 14. No 3. P. 2127–2140. DOI: 10.5194/amt-14-2127-2021
4. Chen Y., Cheng J., Song X., et al. Global-Scale Evaluation of XCO2 Products from GOSAT, OCO-2 and CarbonTracker Using Direct Comparison and Triple Collocation Method. // *Remote Sens*. 2022. V. 14. No 22. P. 5635. DOI: 10.3390/rs14225635
5. Vintaykin I.B., Golyak Il.S., Korolev P.A., et al. Application of a static IR Fourier spectrometer for recording chemical compounds in an open atmosphere // *Russian Journal of Physical Chemistry B*. 2021. V. 15. No 3. P. 413–419. DOI: 10.1134/S1990793121030131

6. Balashov A.A., Vagin V.A., Golyak Il.S., et al. Multichannel dynamic Fourier-Transform IR Spectrometer. // *Journal of Applied Spectroscopy*. 2017. V. 84. No 664. P. 664–667. DOI: 10.1007/s10812-017-0526-z
7. Golyak Il.S., Anfimov D.R., Vintaykin I.B., et al. Monitoring Greenhouse Gases in the Open Atmosphere by the Fourier Spectroscopy Method. // *Russian Journal of Physical Chemistry B*. 2023. V. 17. No 2. P. 320–328. DOI: 10.1134/S1990793123020264
8. Mayorova V., Morozov A., Golyak Il., et al. Determination of Greenhouse Gas Concentrations from the 16U CubeSat Spacecraft Using Fourier Transform Infrared Spectroscopy. // *Sensors*. 2023. V. 15. No 15. P. 6794. DOI: 10.3390/s23156794

ELEMENTARY PROCESSES IN THE UPPER ATMOSPHERE AND IONOSPHERE

CHANGE OF THE BORN-OPPENHEIMER PARADIGM IN THE ATOMIC COLLISION THEORY DURING THE HUNDRED-YEAR QUANTUM MECHANICS

Andrey K. Belyaev

Department of Theoretical Physics and Astronomy, Herzen University, St. Petersburg, Russia

Atomic collision theory has been under consideration practically since the very beginning of the quantum mechanics, which one-hundred-year foundation is celebrated this year. During that time, numerous quantum theoretical methods and approaches has been proposed and developed. The reason for this interest is two-fold: The processes in atomic and molecular collisions are of both (i) fundamental and (ii) practical importance. Former is due to the fact that even an atomic collision is a quantum few-body problem, which is important for many fields of physics, including atomic and molecular physics, nuclear physics, plasma physics, chemical physics, astrophysics, and so on. The latter is important because collision processes govern characteristics of gaseous and plasma media, including the Earth atmosphere, stellar atmospheres and IMS, and so on.

Many famous scientists have been working on the quantum atomic and molecular collision theory: V. A. Fock, L. D. Landau, L. D. Faddeev, Yu. N. Demkov, L. I. Ponomarev, E. E. Nikitin, S. Ya. Umansky, W. H. Miller, A. Dalgarno, D. R. Bates, R. McCarroll, to mention a few. Several theoretical approaches to the problem have been derived: the Faddeev equations, the hyperspherical adiabatic approach, the time-dependent wave packet approach, the semiclassical nonadiabatic approach, the surface hopping approach, and so on. These and other methods have been successfully adopted for studying inelastic collision processes. The stationary Born-Oppenheimer (BO) formalism [1] has been and still is the most widely used approach for theoretical studies of inelastic collision processes. The editors of their manuscript [2], W. Domcke et al., wrote: ”The Born-Oppenheimer adiabatic approximation represents one of the cornerstones of molecular physics and chemistry. The concept of adiabatic potential-energy surfaces, defined by the Born-Oppenheimer approximation, is fundamental to our understanding of molecular spectroscopy and chemical reaction dynamics.” According to the BO idea, the problem is treated into 2 steps, (1) the electronic structure calculation with the fixed-nuclei, and (2) the nonadiabatic nuclear treatment, based on the potentials obtained on the first step. The great progress in computer technology and software leading to more accurate electronic structure calculation, was expected to result in more accurate nonadiabatic nuclear dynamics study, and finally in more accurate cross sections and rate coefficients. Paradoxically, but it was not the case. In particular, some inelastic cross sections did not converge with respect to increasing internuclear distance and with respect to a number of partial waves included into consideration, that is, some cross sections increased unlimitedly. The cause is the molecular-state problem, the problem, which has been neglected in approximate or model studies, but which has been revealed in accurate calculations.

For the sake of simplicity, let us consider an atomic collision involving one electron and let us take into account only Σ molecular symmetry. In order to treat a fixed nuclei molecule, one should take the internuclear separation as one of the coordinates, and in order to have the nonadiabatic nuclear dynamical equations in the simplest form, one should choose the Jacobi coordinates. For a three-body system, there are three sets of the Jacobi coordinates: (i) the molecular-state Jacobi coordinates, which include the internuclear separation R and the electronic coordinate **r** measured from the center-of-nuclear mass; (ii) the scattering-channel Jacobi coordinates, which consist of the atomic coordinate $\mathbf{r}^{\mathbf{at}}$ for the electron measured from the nucleus and the interatomic separation $\mathbf{R}^{\mathbf{sc}}$ in the scattering channel A; and (iii) another scattering-channel Jacobi coordinates B. It is natural to use the molecular-state coordinates in the short- and intermedium-range region when electron actively interacts with both nuclei, so the conventional BO approach is formulated in the molecular-state representation over the whole interaction region assuming that all nonadiabatic couplings go to zero in the asymptotic region (R goes to infinity) and that the solutions of the Coupled Channel Equations (CCE's), including the asymptotic wave functions, obtained in the molecular-state representation are correct for extracting inelastic transition probabilities. Unfortunately, this interpretation of the nuclear dynamics is not correct.

It has been found out that within the formalism of the standard BO approach, some nonadiabatic couplings obtained in the molecular-state representation, remain non-zero in the asymptotic region up to the infinite separation of the nuclei. It was confirmed by both the accurate quantum chemical calculations and the analytical analysis. Moreover, it was derived [3], see also [4-11], that the nonadiabatic radial couplings $\left\langle \varphi_j \middle| \frac{\partial}{\partial R} \middle| \varphi_k \right\rangle$, which are responsible for nonadiabatic transitions between adiabatic molecular states *j* and *k*, have the following asymptotes:

$$\left\langle \varphi_j \middle| \frac{\partial}{\partial R} \middle| \varphi_k \right\rangle = \gamma_k \frac{m}{\hbar^2} \left[U_j(\infty) - U_k(\infty) \right] \left\langle \varphi_j \middle| z^{at} \middle| \varphi_k \right\rangle, \quad (1)$$

where $\left\langle \varphi_j \middle| z^{at} \middle| \varphi_k \right\rangle$ is the atomic transition dipole moment, γ_k is the scalar factor, *m* the mass of electron, $U_j(\infty)$ an asymptote of the adiabatic potential energy of the molecular state *j*. All values are taken at their asymptotic limits. One can see that for a collision process with asymptotes, for which the corresponding atomic transition dipole moment is not equal to zero and which are not degenerated, the asymptotic nonadiabatic coupling between these molecular states does not vanish in the asymptotic region. According to the standard BO interpretation, this means that nonadiabatic transitions between such molecular states exist at infinitely large internuclear separations. It is worth emphasizing that the non-zero asymptotic couplings between molecular states are the fundamental feature of the conventional BO approach. Such couplings cannot be removed by shifting the electron origin along the molecular axis, because corrections of the coupling due to this shifting are exactly compensated by additional operators which appear in the total Hamiltonian of the molecule. The presence of non-zero couplings in the asymptotical region makes a challenge for dynamical calculations and that is why this problem is called by "the molecular-state problem". It has been shown that the molecular-state problem is severe for rigorous calculations and exists for all dynamical methods developed within the BO approach. Usually, the non-zero asymptotic couplings are rather small as compared to maximal values of the couplings in the interaction regions and for this reason non-zero couplings are neglected, but (i) in the asymptotic region these couplings are expected to be equal to zero, so any non-zero value is not negligible in comparison to zero; (ii) they are equal to non-zero permanent values in the infinitively large region, so it must impact nuclear dynamics. It will be presented and discussed at the conference, how non-zero asymptotic couplings affect the nonadiabatic nuclear dynamics and finally the transition probabilities, inelastic cross sections and rate coefficients.

Actually, a part of the molecular-state problem has been known for a long time, since the article of Bates and McCarroll (1958) [12], and the problem has been called as the "electron translation" problem. Many methods have been proposed as a solution of this problem, see, e.g., [13-18], but no generally

accepted remedy has been appeared, and the problem has become considered as a general limitation of the BO approach [18].

However, the interest in the problem was renovated since 1999, after publication of the paper [3] with the quantum solution of the problem in the form of the reprojection method within the BO approach. It required to change the paradigm of the BO approach to the atomic collision theory [3-5]. The old paradigm assumed that a collision should be treated only in the molecular-state representation from zero and till a large enough internuclear distance, where all differential equations in the CCE's are uncoupled, and an inelastic transition probability current in the asymptotic region traverses completely from a molecular state into the corresponding scattering channel, so an inelastic transition probability should be calculated directly from the molecular state. In contrary, the reprojection method distinguishes a molecular state and the corresponding scattering channel, and hence, an inelastic probability should be calculated from the scattering channel probability currents, which are obtained after reprojecting the molecular-state wave functions onto the scattering-channel wave functions. According to new BO paradigm, the reprojection method treats a collision in different nuclear-coordinate regions, the interaction region and the asymptotic region(s), and uses different representations, the molecule-state representation and the scattering-channel ones [3-11]. Finally, nuclear dynamics in different regions is treated in different coordinates, which are better appropriate for different type of motion, a free motion in the asymptotic region (the scattering-channel Jacobi coordinates) and under a strong field in the interaction region (the molecular-state Jacobi coordinates). It turns out that the non-zero asymptotic couplings are needed for composing the correct wave functions in different regions. The detailed description and applications to realistic collisions will be presented at the conference.

The research was supported by the internal grant from the Herzen State Pedagogical University of Russia (project No. 46-VG).

1. Born M., Oppenheimer J.R. Zur Quantentheorie der Molekeln // *Ann. Phys*. 1927. V. 84. P. 457.
2. W. Domcke, D.R. Yarkony, H. Koppel (Eds.), *Conical Intersections. Advanced Series in Physical Chemistry V. 15*, World Scientific, NJ, Singapore, 2004.
3. Grosser J., Menzel T., Belyaev A.K. Approach to electron translation in low-energy atomic collisions // *Phys. Rev. A*. 1999. V. 59. P. 1309–1316. DOI: 10.1103/PhysRevA.59.1309
4. Belyaev A.K., Egorova D., Grosser J., Menzel T. Electron translation and asymptotic couplings in low-energy atomic collisions // *Phys. Rev. A*. 2001. V. 64. 052701. DOI: 10.1103/PhysRevA.64.052701
5. Belyaev A.K., Dalgarno A., McCarroll R. The dependence of nonadiabatic couplings on the origin of electron coordinates // *J. Chem. Phys*. 2002. V. 116. P. 5395–5400. DOI: 10.1063/1.1457443
6. Belyaev A.K. Revised Born-Oppenheimer approach and a reprojection method for inelastic collisions // *Phys. Rev. A*. 2010. V. 82. 060701(R). DOI: 10.1103/PhysRevA.82.060701
7. Belyaev A.K., Lebedev O.V. Nonadiabatic nuclear dynamics of atomic collisions based on branching classical trajectories // *Phys. Rev. A*. 2011. V. 84. 014701. DOI: 10.1103/PhysRevA.84.014701
8. Belyaev A.K. Model approach for low-energy inelastic atomic collisions and application to Al+H and $Al^{+}+H^{-}$ // *Phys. Rev. A*. 2013. V. 88. 052704. DOI: 10.1103/PhysRevA.88.052704
9. Belyaev A.K. Excitation cross sections in low-energy hydrogen-helium collisions // *Phys. Rev. A*. 2015. V. 91. 062709. DOI: 10.1103/PhysRevA.91.062709
10. Yakovlev S.L. Asymptotic solution of a Coulomb multichannel scattering problem with a nonadiabatic channel coupling // *Theor. Math. Phys*. 2020. V. 203. P. 664–672. DOI: 10.1134/S0040577920050086

11. Hedvall P., Hornquist J., Yakovlev S.L., Elander N.O., Larson A. Treatment of asymptotic non-adiabatic couplings with higher order reprojection method in the diabatic representation // *J. Chem. Phys*. 2024. V. 161. 054303. DOI: 10.1063/5.0213714
12. Bates D.R., McCarroll R. Electron capture in slow collisions // *Proc. R. Soc. A*. 1958. V. 245. P. 175. DOI: 10.1098/rspa.1958.0075
13. Thorson W.R., Delos J.B. Theory of near-adiabatic collisions. I. Electron translation factor method // *Phys. Rev. A*. 1978. V. 18. P. 117. DOI: 10.1103/PhysRevA.18.117
14. Schneiderman S.B., Russek A. Velocity-Dependent Orbitals in Proton-On-Hydrogen-Atom Collisions // *Phys. Rev*. 1969. V. 181. P. 311. DOI: 10.1103/PhysRev.181.311
15. Errea L.F., Mendez L., Riera A. On the choice of translation factors for approximate molecular wavefunctions // *J. Phys. B: Atom. Mol. Phys*. 1982. V. 15. No 1. P. 101. DOI: 10.1088/0022-3700/15/1/018
16. Thorson W.R., Delos J.B. Theory of near-adiabatic collisions. II. Scattering coordinate method // *Phys. Rev. A*. 1978. V. 18. P. 135. DOI: 10.1103/PhysRevA.18.135
17. Delos J.B. Theory of electronic transitions in slow atomic collisions // *Rev. Mod. Phys*. 1981. V. 53. P. 287. DOI: 10.1103/RevModPhys.53.287
18. McCarroll R., Crothers D.S.F. Adiabatic Expansions and Nonadiabatic Effects // *Adv. At. Mol. Opt. Phys*. 1994. V. 32. P. 253–278. DOI: 10.1016/S1049-250X(08)60019-1

PHYSICO-CHEMICAL SIGNIFICANCE OF QUANTUM ENTANGLEMENT AND SPIN SELECTION RULES

Vitaliy L. Berdinskiy, Marsel R. Arifullin and Alexandr R. Sadykov

Orenburg State University, Orenburg, Russia

Quantum entanglement [1,2] is the "mixing" of the quantum states of two or more particles, a property that currently does not have a strictly physical definition, such as a clear definition of the concepts of "energy", "momentum", "charge", "spin", etc. Instead of a clear definition, even the encyclopedic literature provides vague descriptions of a certain phenomenon such as «Quantum entanglement is the phenomenon of a group of particles being generated, interacting, or sharing spatial proximity in a manner such that the quantum state of each particle of the group cannot be described independently of the state of the others, including when the particles are separated by a large distance» [3]. The entanglement of the initial quantum states is illustrated by the spin state correlations of decay products in the Einstein–Podolsky–Rosen gedankenexperiments [4]. Despite the lack of a clear definition, the concept of "entanglement" is often used to describe various phenomena both in astrophysics [5, 6] and in particle physics [7, 8].

Mathematical definitions of entanglement of quantum states using physical formulas appear to be rigorous, but do not provide a physical interpretation of the "entanglement" concept. For example, in the language of wave functions $\Psi(\vec{r}_1,\vec{r}_2)$ or state vectors $\left|\Psi(\vec{r}_1,\vec{r}_2)\right\rangle$ of two particles. This concept can be illustrated as follows. If the state vector $\left|\Psi(\vec{r}_1,\vec{r}_2)\right\rangle$ of two particles can be represented as a product of individual particle state vectors

$$\left|\Psi(\vec{r}_1,\vec{r}_2)\right\rangle = \left|\varphi_i(\vec{r}_1)\right\rangle \otimes \left|\varphi_j(\vec{r}_2)\right\rangle, \quad (1)$$

then such a state is not "entangled". If such a simple representation is impossible and a more complex one is required, for example, a superposition of all possible paired tensor products of the state vectors

$$\left|\Psi(\vec{r}_1,\vec{r}_2)\right\rangle = \sum_{i,j}\left|\varphi_i(\vec{r}_1)\right\rangle \otimes \left|\varphi_j(\vec{r}_2)\right\rangle, \tag{2}$$

then such state is considered as "entangled" (if it cannot be transformed into the representation (1)).

If density matrix description is used, then the definition of "entanglement" is illustrated by the following formulas. A quantum state is considered "non-entangled" if the density matrix $\hat{\rho}(\vec{r}_1,\vec{r}_2)$ can be represented as a tensor product of density matrices $\hat{\rho}_1(\vec{r}_1)$ and $\hat{\rho}_2(\vec{r}_2)$ of independent particles

$$\hat{\rho}(\vec{r}_1,\vec{r}_2) = \hat{\rho}_1(\vec{r}_1) \otimes \hat{\rho}_2(\vec{r}_2). \tag{3}$$

An entangled state is a state of a complex system that cannot be represented as a tensor product or as a sum of tensor products of density matrices of independent particles.

Physical illustrations of correlated and entangled quantum mechanical states are the spin vectors of two-spin systems

$$\left|T_+\right\rangle = \left|\alpha_1\alpha_2\right\rangle = \left|\alpha_1\right\rangle \otimes \left|\alpha_2\right\rangle, \tag{4}$$

$$\left|T_-\right\rangle = \left|\beta_1\beta_2\right\rangle = \left|\beta_1\right\rangle \otimes \left|\beta_2\right\rangle, \tag{5}$$

$$\left|\Psi_3\right\rangle = \left|\alpha_1\beta_2\right\rangle = \left|\alpha_1\right\rangle \otimes \left|\beta_2\right\rangle, \tag{6}$$

$$\left|T_+\right\rangle = \left|\alpha_1\alpha_2\right\rangle = \left|\alpha_1\right\rangle \otimes \left|\alpha_2\right\rangle, \tag{7}$$

or vectors of triplet and singlet spin states

$$\left|T_0\right\rangle = 2^{-1/2}\left|\alpha_1\beta_2 + \beta_1\alpha_2\right\rangle, \tag{8}$$

$$\left|S\right\rangle = 2^{-1/2}\left|\alpha_1\beta_2 - \beta_1\alpha_2\right\rangle. \tag{9}$$

All spin states (4)–(7) are states with correlated spins. However, states (4) and (5) are correlated but not entangled, and states (6) and (7) are both correlated and entangled (the Bell states). Obviously, both entangled states (6) and (7) cannot be represented as a product of state vectors of individual particles

$$\left|\varphi_1\right\rangle = c_1\left|\alpha_1\right\rangle + c_2\left|\beta_1\right\rangle \text{ и } \left|\varphi_2\right\rangle = c'_1\left|\alpha_2\right\rangle + c'_2\left|\beta_2\right\rangle \tag{10}$$

with any choice of coefficients c_1, c_2, c'_1, and c'_2.

Unlike the physically meaningless general mathematical definitions, states (4) – (7) have a simple and clear physical meaning. The singlet state (7) is the spin state of two electrons forming a covalent chemical bond in diamagnetic molecules. The simplest examples of such naturally entangled and correlated spin states are two electrons in hydrogen molecules H_2 and in helium atoms He. The physical reason for this spin entanglement is the Pauli principle, which requires antisymmetry of the total wave function of indistinguishable femions.

It is well known [9,10] that spin selection rules operate in chemical reactions of radical recombination $R_1^* + R_2^*$, forming diamagnetic molecules $R_1 - R_2$. These rules allow the recombination of such radical pairs only, the spin state of which coincides with the singlet entangled state of the electron spins of the resulting molecules. Since neither the electron nor the nuclear spin can change their state (orientation) in the elementary acts of chemical reactions, recombination is strictly prohibited by the

spin conservation low. The spin state $\rho(1,2)$ of a pair of initial particles is described by formulas (1) or (4)–(7) and, by definition, is not entangled. These particles would be able to form a unified system, that is, to form an entangled singlet spin state, if their paired state $|\Psi(1,2)\rangle$ could be represented as a superposition containing an entangled state $|S\rangle$ only,

$$\begin{aligned}|\Psi(1,2)\rangle &= |\varphi_1\rangle \otimes |\varphi_1\rangle = \\ &= c_1c_1'|T_+\rangle + c_2c_2'|T_-\rangle + (c_1c_2' + c_2c_1')|T_-\rangle + (c_1c_2' - c_2c_1')|S\rangle.\end{aligned} \tag{11}$$

For random encounters of uncorrelated particles, the spin-dependent probability W of a singlet molecule formation is

$$\mathrm{W} = |c_1c_1' - c_1c_1'|^2. \tag{12}$$

These arguments can easily be generalized to the formation of multi-spin particles. In [11] multi-spin density matrices of indistinguishable fermions (electrons) are constructed and their spin states are proved to be entangled. These results, together with the above arguments, show the importance of the concept of "entanglement" for the analysis of "synthetic" processes of formation of multi-electron multi-spin particles, as well as to formulate multi-spin selection rules. A composite multielectron particle can be formed from independent particles only if their spin state contains a subset of entangled states. In spin-dependent chemical reactions and physical processes, the "entanglement" of multi-spin particles manifests itself as the conservation law of the total spin.

The spin-dependent probability of multielectron particle formation is proportional to the probability W of the initial particle entangled state

$$\mathrm{W} = Tr\left\{\hat{P}_{ent}(\rho_1 \otimes \rho_2)\hat{P}_{ent}\right\}, \tag{13}$$

where *Tr* is the operation of taking the trace of the matrix, $\hat{P}_{ent}$ is the projection operator on the subspace of entangled spin states of the resulting particle

$$\hat{P}_{ent} = \sum_i |\phi_i\rangle\langle\phi_i|. \tag{14}$$

In [11], examples of constructing density matrices $\rho(1,2,..,n)$ and projection operators $\hat{P}_{ent}$ in the form of a sum of nonorthogonal projectors are given. Those and similar considerations have been applied to the analysis of the role of entanglement of multi-spin states in nuclear reactions and in ion O_2^- formation reactions [12]. Those ions are formed in gas-phase reactions and in processes accompanying electron transfer in mitochondria.

1. Horodecki R., Horodecki P., Horodecki M., Horodecki K. Quantum entanglement. // *Rev. Mod. Phys.* 2009. V. 81. P. 865. DOI: 10.1103/RevModPhys.81.865.
2. Amico L., Rosario Fazio R., Andreas Osterloh A., Vlatko Vedral V. Entanglement in many-body systems // *Rev. Mod. Phys.* 2008. V. 80. P. 517. DOI: 10.1103/RevModPhys.80.517.
3. https://en.wikipedia.org/wiki/Quantum_entanglement
4. Reid M. D., Drummond P. D., Bowen W. P., Cavalcanti E. G., Lam P. K., Bachor H. A., Andersen U. L., Leuchs G. The Einstein-Podolsky-Rosen paradox // *Rev. Mod. Phys.* 2009. V. 81. P. 1727. DOI: 10.1103/RevModPhys.81.1727.
5. Boutivas K., Katsinis D, Pastras G., Tetradis N. Entanglement in cosmology // *J. Cosm. Astropart.* Phys. 2024. No 4. DOI: 10.1088/1475-7516/2024/04/017.

6. Gomez J., Peimbert A., Echevarría J. Optical Quantum Entanglement in Astrophysics. // *Revista Mexicana de Astronomía y Astrofísica*. 2009. V. 45. P. 179-189.
7. Particle Data Group Collaboration, Workman R. L., Burkert V. D., Crede V. et al. Review of Particle Physics // *Prog. Theor. Exp. Phys*. 2022. 083C01. DOI: https://doi.org/10.1093/ptep/ptac097.
8. Mahlon G., Parke S.J. Spin correlation effects in top quark pair production at the LHC // *Phys. Rev. D*. 2010. V. 81. 074024. DOI: 10.1103/PhysRevD.81.074024.
9. Buchachenko A.L., Molin Yu.N., Sagdeev R.Z., Salikhov K.M., Frankevich E.L. Magnetospin effects in chemical reactions // *Sov. Phys. Usp*. 1987. V. 30. P. 79. DOI 10.1070/PU1987v030n01ABEH002796.
10. Buchachenko. A.L. Second generation of magnetic effects in chemical reactions // *Rus. Chem. Rev*. 1993. V. 62. No 12. P. 1073-1082. DOI: 10.1070/RC1993v062n12ABEH000064.
11. Arifullin M., Berdinskiy V. Spin entanglement and nonlocality of multifermion systems. // *arXiv:1310.2863*. 2013. DOI: 10.48550/arXiv.1310.2863.
12. Arifullin M.R., Berdinskiy V.L. Spin states of multielectron systems and the action of multi-spin bans // *Rus. J. Phys. Chem. A*. 2013. V. 87. No 7. P. 1186–1190. DOI:10.1134/S0036024413070042.

THE WAVE PACKET METHOD FOR STUDYING OF CALCIUM-HYDROGEN INELASTIC PROCESSES

Maxim Yu. Yakovlev and Andrey K. Belyaev

Herzen State Pedagogical University of Russia, Saint Petersburg, Russia

The wave packet method is one of the efficient quantum approaches for studying nuclear dynamics. It allows one to solve the time-dependent Schrödinger equation within the framework of the Born-Oppenheimer approach:

$$i\hbar\frac{\partial\Psi(\vec{R},\vec{r},t)}{\partial t}=\hat{H}\Psi(\vec{R},\vec{r},t), \quad (1)$$

where $\vec{R}$ is the internuclear vector, $\vec{r}$ is a set of electronic coordinates, t is time, $\Psi(\vec{R},\vec{r},t)$ is a total wave function, $\hat{H}$ is the total Hamiltonian. In case of the Born-Oppenheimer approach the Hamiltonian can be written as:

$$\hat{H}=\hat{H}_e+\hat{T}_N, \quad (2)$$

$\hat{H}_e$ being the electronic Hamiltonian and $\hat{T}_N$ the nuclear kinetic energy operator. The total wave function can be expanded in terms of the basis of diabatic electronic wave functions $\varphi_j(\vec{r};R)$:

$$\Psi(\vec{R},\vec{r},t)=\sum_{J,M_J}\sum_j\frac{F_j(R,t)}{R}Y_{J,M_J}(\theta,\varphi)\varphi_j(\vec{r};R), \quad (3)$$

where J is a quantum number of a total angular momentum of the molecule, M_J a quantum number of a projection of a total angular momentum onto the internuclear axis, $F_j(R,t)$ is a radial nuclear wave function, $Y_{J,M_J}(\theta,\varphi)$ is the spherical nuclear wave function.

Using Eqs. (1)–(3), a set of differential equations reads:

$$i\hbar\frac{\partial F_k(R,t)}{\partial t}=\left(-\frac{\hbar^2}{2\mu}\frac{\partial^2}{\partial R^2}+\frac{\hbar^2}{2\mu}\frac{J(J+1)}{R^2}+H_{kk}\right)F_k(R,t)+\sum_{j\neq k}F_j(R,t)H_{kj}\,, \tag{4}$$

where $H_{kj}=\left\langle\varphi_k(\vec{r};R)\middle|\widehat{H}_e\middle|\varphi_j(\vec{r};R)\right\rangle$, μ is a reduced mass. The solution of these equations can be written as the matrix exponential:

$$\boldsymbol{F}=e^{(\boldsymbol{T}+\boldsymbol{U})t}\boldsymbol{F_0}, \tag{5}$$

where: $\boldsymbol{F}=\left(F_1(R,t),\dots,F_n(R,t)\right)^T$, $\boldsymbol{F_0}=\left(F_1(R,0),\dots,F_n(R,0)\right)^T$ is a vector of the initial radial nuclear wave functions,

$$[\boldsymbol{T}]_{kj}=\left(-\frac{i}{\hbar}\frac{\hbar^2\hat{k}^2}{2\mu}\right)\delta_{kj},\;\;[\boldsymbol{U}]_{kj}=-\frac{i}{\hbar}\left(\frac{\hbar^2}{2\mu}\frac{J(J+1)}{R^2}\right)\delta_{kj}-\frac{i}{\hbar}H_{kj}. \tag{6}$$

The split-operator method makes transfers between the momentum space and the coordinate space in order each operator in Eq. (5) acts in relevant spaces and finally represent actions in the following form:

$$\boldsymbol{F}=\left(e^{\frac{\boldsymbol{U}}{2}t}e^{\boldsymbol{T}t}e^{\frac{\boldsymbol{U}}{2}t}+O(t^3)\right)\boldsymbol{F_0}\approx e^{\frac{\boldsymbol{U}}{2}t}e^{\boldsymbol{T}t}e^{\frac{\boldsymbol{U}}{2}t}\boldsymbol{F_0}. \tag{7}$$

Thus, the set of differential equations (4) can be solved by the well-known algorithm which allows one to transfer from operator exponential to matrix exponential due to changing spaces [1].

1. $\boldsymbol{\xi}^{st.1}=e^{\frac{\boldsymbol{U}}{2}t}\boldsymbol{F_0}$,
2. $\boldsymbol{\xi}^{st.2}=FT[\boldsymbol{\xi}^{st.1}]$,
3. $\boldsymbol{\xi}^{st.3}=e^{\boldsymbol{T}t}\boldsymbol{\xi}^{st.2}$,
4. $\boldsymbol{\xi}^{st.4}=IFT[\boldsymbol{\xi}^{st.3}]$,
5. $\boldsymbol{F}=e^{\frac{\boldsymbol{U}}{2}t}\boldsymbol{\xi}^{st.4}$,

where $\boldsymbol{\xi}^{st.N}$ is a vector of the wave function on N-step, FT is the Fourier transform, IFT is the inverse Fourier transform. Calculation of matrix exponential can be done by using the Taylor series expansion or the Pade approximation or the hyperbolic matrix method, the method proposed by the present authors [2].

The vector of the asymptotic radial nuclear wave functions for the initial state should be set up as the wave packet:

$$W(R,0)=\left(\frac{1}{a\sqrt{\pi}}\right)^{1/2}e^{-\frac{1}{2}\left(\frac{R-R_0}{a}\right)^2+ik_0R}, \tag{8}$$

where a is a parameter, R_0 is a center of the wave function, k_0 is an average momentum of the wave packet. Wave packet is a superposition of the de Brough waves and describes motion of a single particle, but contains information about different collision energies. This property gets opportunity to take information about collisions with different collision energies in a single calculation.

Probabilities of non-adiabatic transitions from the j-state to the n-state can be obtained by computing the energy-resolved probability flux [1]:

$$P_{jn}=\frac{\hbar^2k}{\mu}\frac{1}{|B(k,0)|^2}\mathrm{Im}\left(F_n^*(R,E)\frac{\partial F_n(R,E)}{\partial x}\right)_{R=\tilde{R}}, \tag{9}$$

where

$$B(k)=\frac{1}{\sqrt{2\pi}}\int_{-\infty}^{+\infty}W(R,0)\,e^{-ikR}dR, \tag{10}$$

$$F_n(R,E)=\frac{1}{\sqrt{2\pi}}\int_{-\infty}^{+\infty}F_n(R,t)\,e^{\frac{i}{\hbar}Et}dt, \tag{11}$$

$\tilde{R}$ is a distant point in the asymptotic region.

The described method was used in the present study of mutual neutralization processes in calcium-hydrogen collisions. The investigation used the recent quantum chemical adiabatic potentials (Fig.1) and non-adiabatic radial matrix couplings [3].

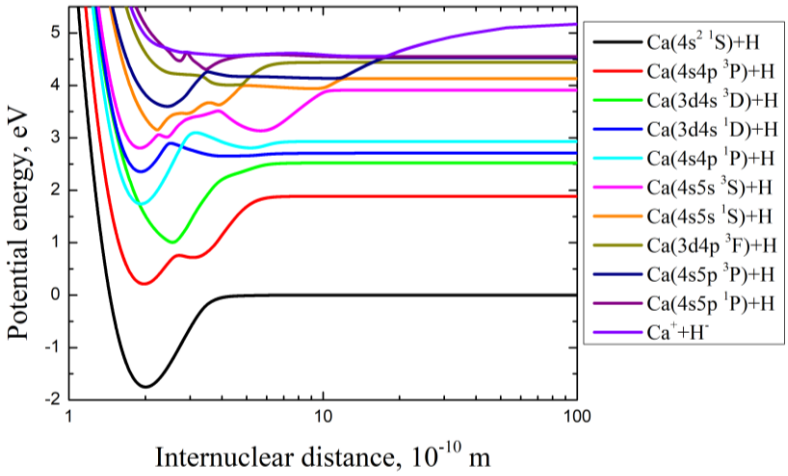


FIGURE 1. Adiabatic potentials of the CaH quasimolecule [3].

The wave packet method can be used in diabatic representation, so the quantum chemical adiabatic potentials were transformed to diabatic ones, see Fig. 2.

By the present paper we report the results of calculations of the non-adiabatic transition probabilities and the cross sections computed by the wave packet method for the collision energy from 0.1 eV to 20 eV. Fig.3 shows the present cross sections and their comparison with those obtained by means of other methods [4,5].

Figure 3 shows good agreement of the results of different theoretical methods for main part of the processes for the whole treated collision energy range. But the cross sections to the ground state and the first excited state obtained by the probability current method are overestimated, while the quantum time-dependent and time-independent methods demonstrate good agreement for these two processes.

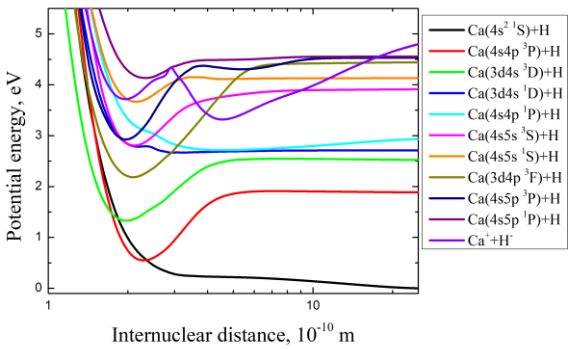


FIGURE 2. Diabatic potentials of the CaH quasimolecule obtained in the present work from the adiabatic potentials and couplings, see above.

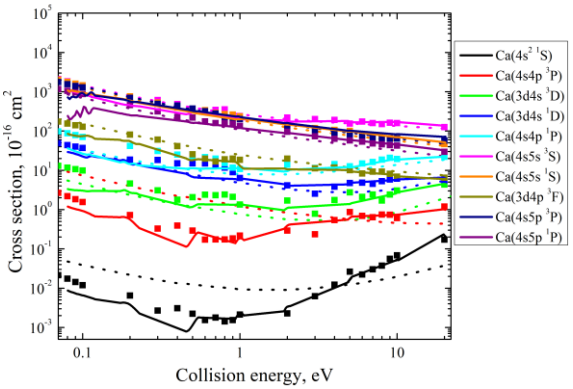


FIGURE 3. The neutralization cross sections. The solid lines are the wave packet method, the squares quantum calculation in time-independent problem [4], the dotted lines the probability current method [5].

Figure 3 shows good agreement of the results of different theoretical methods for main part of the processes for the whole treated collision energy range. But the cross sections to the ground state and the first excited state obtained by the probability current method are overestimated, while the quantum time-dependent and time-independent methods demonstrate good agreement for these two processes.

Since the data on the inelastic cross sections and rate coefficients are important in many fields of physics and chemistry, including physics of atmosphere, astrophysics, plasma physics, and so on, it is important to produce accurate data for numerous collisional processes, and the wave packet method is the efficient tool for required information.

The research was supported by an internal grant of the Herzen State Pedagogical University of Russia (project No. 46-VG).

1. Balakrishnan N., Kalyanaraman C., Sathyamurthy N. Time-dependent quantum mechanical approach to reactive scattering and related processes // *Physics reports*. 1997. V. 280. No. 2. P. 79-144. DOI: 10.1016/S0370-1573(96)00025-7.
2. Yakovlev M. Yu., Belyaev A. K. The hyperbolic matrix method for wave packet treatment of atomic and molecular dynamics // *Physics of Complex Systems*. 2024. V. 5. No. 1. P. 21-29. DOI: 10.33910/2687-153X-2024-5-1-21-29.
3. Mitrushchenkov A., Guitou M., Belyaev A. K., et al. Calcium-hydrogen interactions for collisional excitation and charge transfer // *The Journal of Chemical Physics*. 2017. V. 146. No. 1. 014304. DOI: 10.1063/1.4973457.
4. Belyaev A. K., Vlasov D. V., Mitrushchenkov A., Feautrier N. Quantum study of inelastic processes in low-energy calcium–hydrogen collisions // *Monthly Notices of the Royal Astronomical Society*. 2019. V. 490. No. 3. P. 3384–3391. DOI: 10.1093/mnras/stz2763.
5. Belyaev A. K., et. al. Atomic Data on Inelastic Processes in Calcium-Hydrogen Collisions // *The Astrophysical Journal*. 2017. V. 851. No. 1. P. 59. DOI: 10.3847/1538-4357/aa98da.

MODEL APPROACHES FOR TREATMENT OF INELASTIC PROCESSES IN LOW-ENERGY COLLISIONS WITH HYDROGEN

Svetlana A. Yakovleva and Andrey K. Belyaev

Herzen State Pedagogical University of Russia, Saint-Petersburg, Russia

Inelastic processes in collisions of different chemical elements with hydrogen atoms and negative ions are very important for correct non-LTE modelling of gaseous media, particularly for stellar and planetary atmospheres and interstellar medium. Such modeling requires the data for a large number of transitions between electronic states of the chemical element under consideration. In this work we describe collisional processes in molecular representation and use the Born-Oppenheimer approach to solve the problem in two steps: electronic structure calculations and nuclear dynamics treatment.

In the present work we discuss several model approaches that can be applied on both steps of the investigation, particularly if ab initio data on adiabatic potential energies and non-adiabatic coupling are scarce. Quantum approaches for non-adiabatic nuclear dynamics studies varies depending on the quantum-chemical data available for a particular quasimolecule: from a simplified model that requires only the data on atomic configurations and energy levels, multichannel Landau-Zener approaches that use analytical multichannel formula or a probability currents method, to wave-packet calculations and reprojection method for solving coupled-channel equations.

To include a larger number of higher-lying electronic states into account the asymptotic approach for electronic structure modelling within the Born-Oppenheimer approach was proposed in [1]. Further development of this approach allowed us to include fine structure levels in treatment of inelastic processes in collisions with hydrogen. Fine structure levels of a chemical element colliding with hydrogen are taken into account by expressing off-diagonal ionic-covalent matrix elements in the J-J representation via the same matrix elements in the L-S representation using Clebsch-Gordan coefficients. Modifications of non-adiabatic matrix elements lead to different parameters of non-adiabatic regions causing non-trivial changes in cross sections and rate coefficients of inelastic processes.

This research was supported by an internal grant of the Herzen State Pedagogical University of Russia (project No. 46-VG).

1. Belyaev A. K. Model approach for low-energy inelastic atomic collisions and application to Al+H and $Al^{+}+H^{-}$ // *Physical Review A—Atomic, Molecular, and Optical Physics.* 2013. V. 88. No 5. 052704. DOI: 10.1103/PhysRevA.88.052704.

ATOMIC DATA ON INELASTIC PROCESSES IN Ag-H COLLISIONS WITH THE ACCOUNT FOR THE FINE STRUCTURE OF Ag

Vera A. Vasil'eva and Svetlana A. Yakovleva

Herzen State Pedagogical University of Russia, Saint-Petersburg, Russia

The paper presents the results of a theoretical study of inelastic collisions of silver atoms and cations with hydrogen atoms and anions in the energy range from 10^{-4} to 100 eV. These processes play an important role in astrophysics, since accurate data on collisional transitions are necessary for correct modeling of stellar photospheric spectra, especially in conditions where deviations from local thermodynamic equilibrium (Non-LTE) are observed.

The electronic structure of AgH quasimolecule (Table 1) with the account of the fine structure of Ag is calculated using the asymptotic approach [1], for several low-energy states we used the data from [2] obtained by the MRCI method with scalar relativistic and spin-orbit corrections (Fig. 1). The nuclear dynamics is investigated by means of the multichannel Landau-Zener model.

TABLE 1. The AgH quasimolecule molecular channels, the corresponding asymptotic atomic states, the asymptotic energies with respect to the ground state, and total angular momentum number J for the Ag atom.

i	Scattering channels	Molecular symmetries	Asymptotic energies (eV)	J (Ag)
1	$Ag(4d^{10}5s\ ^2S) + H(1s\ ^2S)$	0 +	0.0000	1/2
2	$Ag(4d^{10}5p\ ^2P^\circ) + H(1s\ ^2S)$	0 +	0.1346	1/2
3	$Ag(4d^{9}5s^2\ ^2D) + H(1s\ ^2S)$	0 +	0.1378	5/2
4	$Ag(4d^{10}5p\ ^2P^\circ) + H(1s\ ^2S)$	0 +	0.1388	3/2
5	$Ag(4d^{9}5s^2\ ^2D) + H(1s\ ^2S)$	0 +	0.1582	3/2
6	$Ag(4d^{10}6s\ ^2S) + H(1s\ ^2S)$	0 +	0.1939	1/2
7	$Ag(4d^{10}6p\ ^2P^\circ) + H(1s\ ^2S)$	0 +	0.2201	1/2

8	$Ag(4d^{10}6p\ ^2P^\circ) + H(1s\ ^2S)$	0 +	0.2209	3/2
9	$Ag(4d^{10}5d\ ^2D) + H(1s\ ^2S)$	0 +	0.2220	3/2
10	$Ag(4d^{10}5d\ ^2D) + H(1s\ ^2S)$	0 +	0.2222	5/2
11	$Ag(4d^{10}7s\ ^2S) + H(1s\ ^2S)$	0 +	0.2364	1/2
ionic	$Ag^+(4d^{10}\ ^1S_0) + H^-(1s\ ^1S)$	0 +	0.2407	0

Particular attention is paid to the processes associated with the formation of resonant spectral lines of the Ag I doublet (328.6 nm and 338.3 nm), since these lines have high intensity and have a significant influence on the spectral characteristics of the stars.

The obtained data on collisional processes can be used for a more detailed analysis of the composition of stellar photospheres, as well as for modeling the processes of fast neutron capture (r-process) in the atmospheres of dwarf and giant stars.

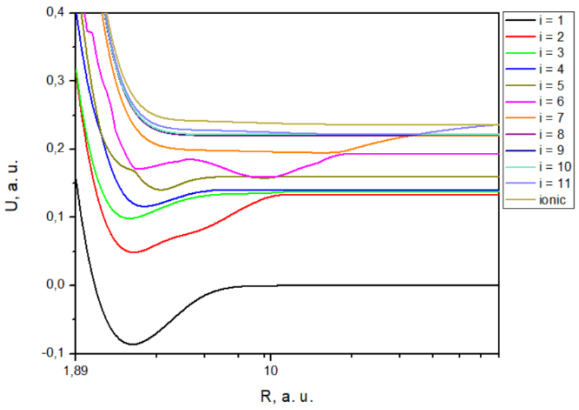


FIGURE 1. Adiabatic potential energies of quasimolecule AgH. Corresponding scattering channels are given in Table 1.

The research was supported by an internal grant of the Herzen State Pedagogical University of Russia (project No. 46-VG).

1. Belyaev A. K. Model approach for low-energy inelastic atomic collisions and application to Al+H and Al^++H^- // *Physical Review A—Atomic, Molecular, and Optical Physics.* 2013. V. 88. No. 5. 052704. DOI: 10.1103/PhysRevA.88.052704.
2. Mohammadian Z., Nourigheimasi F., Maghari A., Shayesteh A. (2024). Spin-orbit coupling in excited electronic states of AgH // *Chemical Physics Letters*. 2024. V. 849. 141418. DOI: 10.1016/j.cplett.2024.141418.

PROTON IMPACT IONIZATION CROSS SECTION FOR MOLECULAR TARGETS

Gleb I. Andreev and Vladimir L. Bychkov

Department of Physical Electronics, Faculty of Physics, Moscow State University, Moscow, Russia

In recent years, processes involving ionization of molecular targets by proton impact have garnered significant interest due to their relevance in various scientific and environmental contexts. These processes are particularly prevalent in the high atmosphere and the lower ionosphere, where interactions between protons and molecules play a crucial role in atmospheric chemistry and dynamics. Understanding these ionization mechanisms is essential for advancing our knowledge of space weather, atmospheric modeling, and the behavior of planetary atmospheres under the influence of solar radiation and cosmic rays. In this work, we focus on the ionization of specific diatomic and polyatomic molecules, like N_2, O_2, CO, and CO_2. These molecules were chosen due to their abundance in Earth's atmosphere and their importance in both natural and industrial processes.

In this work, it is demonstrated that the Born approximation approach can be effectively used for calculating ionization cross-sections resulting from proton impact on atomic targets. The Born approximation, a well-established method in quantum scattering theory, provides a reliable framework for describing high-energy collisions where the interaction between the projectile and the target can be treated as a perturbation. This approach is particularly suitable for proton-impact ionization due to its ability to simplify the complex dynamics of the collision process while maintaining a high degree of accuracy in the resulting cross-sections. To implement this methodology, the ATOM code [1] is employed, a computational tool specifically designed for atomic collision calculations. By using this code, we are able to systematically compute ionization cross-sections for a range of atomic targets, providing valuable data that can be compared with experimental results and other theoretical models.

For calculation molecular targets cross-section the Bragg additivity rule is applied. The Bragg additivity rule [2] assumes that the total cross-section of a molecule or a complex target can be approximated as the sum of the cross-sections of its constituent atoms. In other words, the interaction of the projectile with the molecule is treated as the sum of independent interactions with each atom in the molecule, neglecting any molecular bonding effects or intra-molecular interactions. Mathematically, for a molecule composed of atoms of type $i = 1 \ldots n$, the total cross-section for a specific process (e.g., ionization) is given by:

$$\sigma_{mol} \approx \sum_i n_i \sigma_i,$$

where n is the number of atoms of type i in the molecule, σ_i is the cross-section for the process involving the i-th type of atom. Using the ATOM code in conjunction with the Bragg additivity rule, the ionization cross-sections for several molecular targets were calculated. The calculated cross-sections were compared with available experimental data [3], as illustrated in Fig.1 and Fig.2.

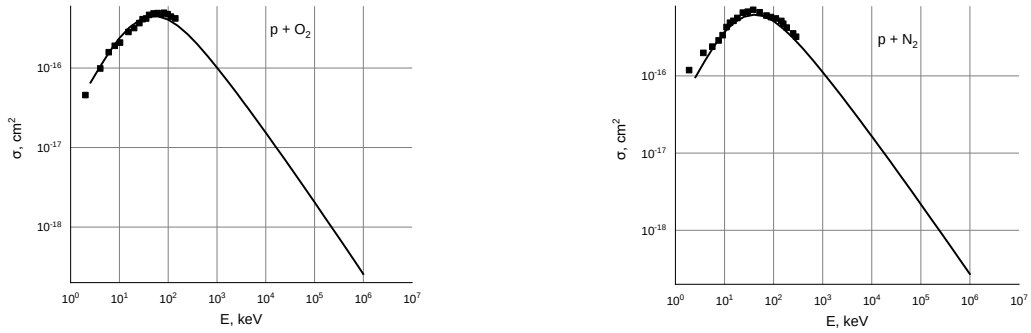


FIGURE 1. Ionization cross sections for molecular oxygen and nitrogen. Solid line - calculation with ATOM code [1], dots - experimental data [3].

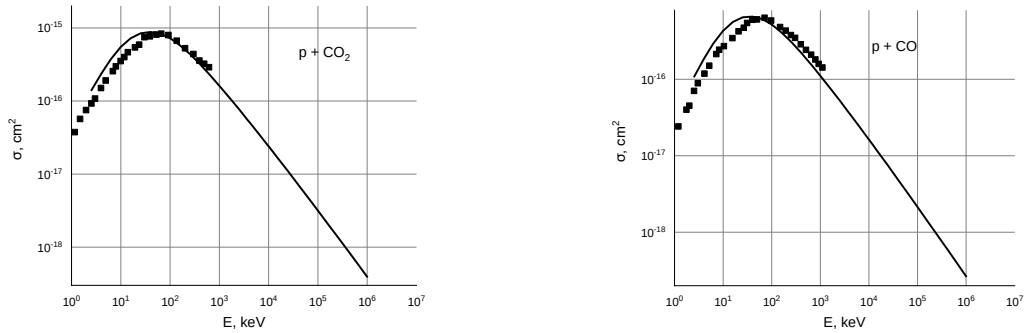


FIGURE 2. Ionization cross sections for carbon dioxide and carbon monoxide. Solid line - calculation with ATOM code [1], dots - experimental data [3].

The results demonstrate that the theoretical predictions align well with the experimental measurements. The agreement between the calculated and experimental data suggests that the combined use of the ATOM code and the Bragg additivity rule provides a robust framework for estimating ionization cross-sections for molecular targets.

This work highlights the utility of the Bragg additivity rule as a practical tool for estimating molecular ionization cross-sections, especially in cases where detailed molecular calculations are computationally prohibitive. The good agreement with experimental data validates the applicability of this approach for certain energy ranges and target molecules, while also underscoring the need for more sophisticated methods, such as molecular orbital calculations or density functional theory, to address cases where molecular effects cannot be neglected.

The authors are pleased to acknowledge helpful discussions with Shevelko V.P.

1. L.A. Vainshtein, V.P. Shevelko, *Atomic Physics for Hot Plasmas*, IOP, Bristol, 1993.
2. Bragg W. H. and Kleeman R. XXXIX. On the α particles of radium, and their loss of range in passing through various atoms and molecules // *The London, Edinburgh, and Dublin Philosophical Magazine and Journal of Science*. 1905. V. 10. No 57. P. 318–340. DOI: 10.1080/14786440509463378.
3. McNeal R.J. Production of Positive Ions and Electrons in Collisions of 1–25-keV Protons and Hydrogen Atoms with CO, CO_2, CH_4, and NH_3 // *J. Chem. Phys*. 1970. V. 53. No 11. P. 4308–4313. DOI: 10.1063/1.1673938.

ION FORMATION IN LOWER ATMOSPHERE UNDER THE ACTION OF COSMIC RAYS

Ilya G. Stepanov[1], Vladimir L. Bychkov[2], and Maxim G. Golubkov[1]

[1]Semenov Federal Research Center for Chemical Physics, Russian Academy of Sciences, Moscow, Russia
[2]Moscow State University, Moscow, Russia

The processes of ion formation in humid tropospheric air under the action of cosmic rays are considered. In this case, positive and negative cluster ions appear. For this analysis, a kinetic model was developed that includes 55 components and 161 reactions. The calculation was carried out using the KINET software package. It is shown that the ionization of air by cosmic rays at altitudes of 5-35 km leads to the formation of plasma consisting mainly of $NH_4^+ \cdot NH_3 \cdot H_2O$, $H^+ \cdot (H_2O)_4$ and $O_2^- \cdot (H_2O)_2$ ions. The maximum concentrations of ions under conditions of minimum magnetic rigidity are observed at altitudes from 10 to 18 km. These results differ sharply from the calculation results obtained for the dry air model.

The purpose of this paper is to determine the altitude dependence of the concentration of ions formed in the troposphere in calm geomagnetic conditions under the influence of cosmic rays and radioactive γ radiation from the soil surface in a humid atmosphere. The results obtained are necessary to control the formation of layered thunderstorm clouds and artificially stimulate precipitation [1].

In solving this problem, the KINET software package was used, designed to solve direct and inverse kinetic problems. As initial data, it sets the kinetic scheme of the process in the form of a set of basic reactions indicating the rate constants, and the reaction equations can be written in a form of conventional chemical designations. The initial concentrations of reagents and temperature, as well as the time interval at which a solution is required are indicated.

Atmospheric electricity in the lower atmosphere can be explained by the transfer of ions only. Thermal electrons are absent in the calm low atmosphere of the Earth due to their attachment to oxygen molecules, which occurs during three-particle collisions of slow electrons with nitrogen and oxygen molecules. The characteristic attachment time of electrons to oxygen molecules is $\tau \approx 10^{-8}$ s at a temperature of $T = 300$ K. Thus, the negative charge in the troposphere is presented in the form of negative ions only.

The main type of positive and negative ions in calm atmospheric conditions may be different depending on the content of impurities in a given area of the atmosphere, but the choice can be made from a limited number of the most stable ions. For ions in a dry atmosphere, these are negative NO_2^-, NO_3^-, CO_3^-, O_2^- and O^-, along with positive ones N_2^+, CO_2^+, N_2H^+, N_3^+, N_2O^+, N_4^+. In a humid atmosphere, negative ions $NO_2^- \cdot (H_2O)_n$, $NO_3^- \cdot (H_2O)_n$, $CO_3^- \cdot (H_2O)_n$ and $O_2^- \cdot (H_2O)_n$, and positive $H^+ \cdot (H_2O)_n$, $NH_4^+(NH_3)_m(H_2O)_k$ are the most stable.

As discussed in the article [2], the effect of fast particles of electric fields on the formation of ions in the lower atmosphere can be divided by height. Thus, in the lower layers of the atmosphere, the main role in the formation of singly charge ions is played by natural radioactive radiation from the soil surface [3]. However, this process takes place well below 500 m above the Earth surface, where the formed charged particles affect the distribution of the electric field. In the altitude range from 0 m to 6 km, the electric field of the Earth decreases from a value of about 130 V/m to 10-20 V/m and has little effect on the processes of electron-ion and ion-ion recombination, as well as the attachment of electrons to oxygen molecules involved in the formation of charged particles. At altitudes from 5 km to 25 km, the main process is the ionization of air by cosmic rays [1]. At the same time, the maximum altitude dependence of the total ionization rate *Q* is at an altitude of 12 km.

Considering that atmospheric air ionization is realized under the action of cosmic rays, the balance equation for the concentration of ions N_i in a quasi-neutral atmospheric plasma can be written as:

$$\frac{dN_i}{dt} = Q - \alpha N_i^2, \tag{1}$$

where *Q* is the ionization rate of atmospheric air, and α is the recombination coefficient of molecular ions in the air.

The Earth's magnetic field, which has the form of a magnetic dipole, has a significant effect on the penetration of charged particles or particles with a magnetic moment into the atmosphere. It prevents the free passage of charged low-energy particles into the Earth's atmosphere (with the exception of areas located near the magnetic poles). The magnetic rigidity *M*, which is proportional to the magnetic moment of the particle [1], is a measure of the effect of the magnetic field:

$$M = \frac{pc}{q} = BR, \tag{2}$$

where *q* and *p* are the charge and the projection of the particle momentum on the plane perpendicular to the direction of the magnetic induction vector **B**; *R* is the Larmor radius, *c* is the speed of light in vacuum.

An analysis of the elementary processes occurring in humid air shows that, after the production of electrons and ions by fast background particles $\hat{e}$, processes involving O_2, N_2, H_2O molecules and their molecular ions effectively take place. A kinetic scheme involving 55 components and 161 reactions was used to calculate ion concentrations [1].

Figure 1 shows the altitude dependences of the concentrations of main ions $H^+ \cdot (H_2O)_3$, $H^+ \cdot (H_2O)_4$, $H^+ \cdot (H_2O)_5$, $NH_4^+ \cdot NH_3 \cdot H_2O$, $NH_4^+ \cdot (H_2O)_2$, $NH_4^+ \cdot (H_2O)_3$ and $O_2^- \cdot (H_2O)_2$ in humid air at values of magnetic rigidity $M = 0.6 \cdot$GeV. The values of rate constants were taken from [4-7], and

the altitude dependence of temperature was taken from [8]. Calculations show that the concentrations of other ions in the troposphere are negligible. Their total contribution to the total concentration of charged particles does not exceed 1%. The data correspond to the moment of time t = 300 s, when the concentrations of the main ions reached a stationary value.

Note that positive ion reactions in humid air near the Earth's surface are significantly influenced by the presence of ammonia molecules with concentrations exceeding 10^{10} cm^{-3}. Ammonia has a high proton affinity, which is 40 kcal/mol more than that of water. Therefore, the reactions of ammonia with $H^+ \cdot (H_2O)_n$ clusters proceed quite rapidly with the release of a significant amount of energy:

$$H^+(H_2O)_n + NH_3 \rightarrow NH_4^+(H_2O)_{n-1} + H_2O, \qquad n=1–4. \tag{3}$$

$$NH_4^+(H_2O)_n + NH_3 \rightarrow NH_4^+ \cdot NH_3 \cdot (H_2O)_{n-1} + H_2O. \tag{4}$$

In the works [6,7] it was shown that the rate constants of reactions (3)–(4) are quite large (k ~ 10^{-9} cm^3/s). Consequently, it should be expected that the concentrations of positive $NH_4^+(NH_3)_m(H_2O)_k$ ions in the lower atmosphere will prevail over the concentrations of hydrated hydronium ions $H_3O^+ \cdot (H_2O)_n$. Our calculations show that this statement is true at altitudes from 0 to 15 km.

At altitudes above 15 km a significant contribution in ion concentration is made by association and dissociation reactions of $H^+ \cdot (H_2O)_4$ ions in the presence of molecular oxygen, i.e.

$$H^+ \cdot (H_2O)_4 + H_2O + O_2 \rightarrow H^+ \cdot (H_2O)_5 + O_2, \tag{5}$$

$$H^+ \cdot (H_2O)_4 + O_2 \rightarrow H^+ \cdot (H_2O)_3 + O_2 + H_2O. \tag{6}$$

As can be seen from Fig. 1, the heavier $H^+ \cdot (H_2O)_5$ ions are formed as a product of the reaction (5) at altitudes up to 10 km. The concentration of lighter $H^+ \cdot (H_2O)_3$ ions forming as a product of the reaction (6) has a maximum at altitudes of 30-35 km and is several times higher than the concentration of $H^+ \cdot (H_2O)_4$ ions here.

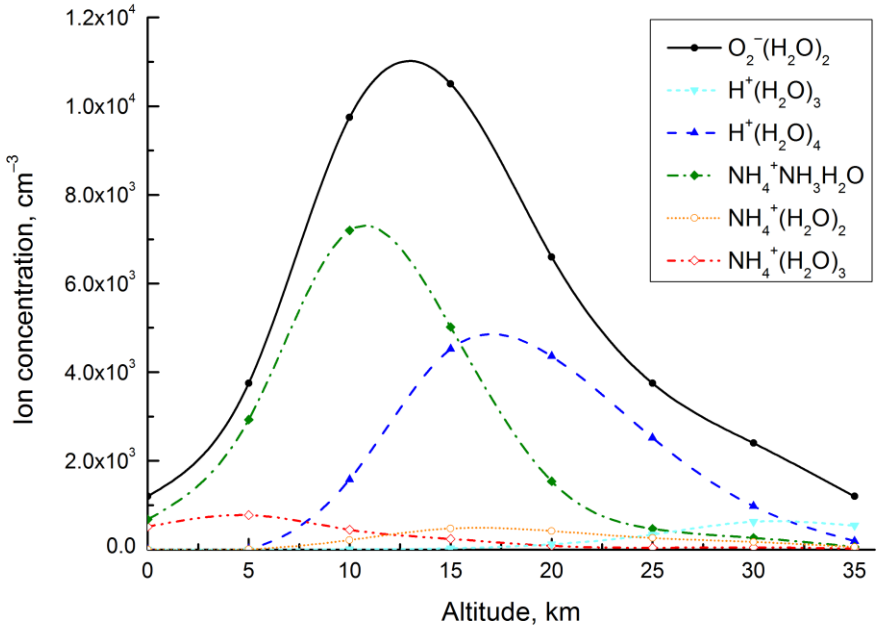


FIGURE 1. Altitude dependences of $H^+ \cdot (H_2O)_3$, $H^+ \cdot (H_2O)_4$, $NH_4^+ \cdot NH_3 \cdot H_2O$, $NH_4^+ \cdot (H_2O)_2$, $NH_4^+ \cdot (H_2O)_3$ and $O_2^- \cdot (H_2O)_2$ ion concentrations at magnetic rigidity M = 0.6 GeV.

The processes of ion formation in humid tropospheric air under the action of cosmic rays were considered. Positive and negative cluster ions appear in air when neutrals are exposed to cosmic rays. To calculate ion concentrations, a kinetic model was developed that includes 55 components and 161 reactions. For that purpose, the KINET software package was used. We show that the ionization of air by cosmic rays at altitudes from 5 to 35 km leads to the formation of plasma consisting mainly of $NH_4^+ \cdot NH_3 \cdot H_2O$, $H^+ \cdot (H_2O)_4$ and $O_2^- \cdot (H_2O)_2$ ions. Ion concentration maxima are observed at altitudes from 10 to 15 km for both $NH_4^+ \cdot NH_3 \cdot H_2O$ and $O_2^- \cdot (H_2O)_2$ ions. However, at altitudes above 15 km the largest contribution to the positive ion concentration is provided by ions $H^+ \cdot (H_2O)_3$ and $H^+ \cdot (H_2O)_4$. These results allow to create realistic models of cloud charging and complement the conclusions of [2] in which estimates were made for dry air. The obtained data on the distribution of ion concentrations in the troposphere allow to implement plasma regions for artificial stimulation of precipitation without the use of expensive chemical reagents. The processes considered in this paper can also influence the stability of global navigation satellite systems [9] and the formation of acoustic and internal gravity wave sources in the troposphere [10,11]. The obtained results can also be useful for correction of models used in the location and navigation of aircrafts during landing on coastal airfields [12].

This study was carried out in the framework of State Assignment of the Ministry of Science and Higher Education of the Russian Federation (project No. 125012200611-5).

1. Stepanov I.G., Bychkov V.L., Golubkov M.G. Formation of ions under the action of cosmic rays in humid air // *Journal of Atmospheric and Solar-Terrestrial Physics*. 2024. V. 262. No 106332. P. 1–4. DOI:10.1016/j.jastp.2024.106332.
2. Chengxun Y., Zhijian L., Bychkov V.L., et al. Distribution of positive and negative ion concentrations in the troposphere // *Russ. J. Phys. Chem. B*. 2022. V. 16. No 5. P. 955–964. DOI: 10.1134/S1990793122050189.
3. I.M. Blankson and J.E. Foster, in *Proceedings of the 11th International Conference on Plasma Assisted Technologies ICPAT-11*, Univ. Abu Dhabi, Abu Dhabi, 2018, p. 15.
4. Kossyi I.A., Kostinsky A.Y., Matveyev A.A., et al. Kinetic scheme of the non-equilibrium discharge in nitrogen-oxygen mixtures // *Plasma Source Sci. Technol*. 1992. V. 1. P. 207–220. DOI: 10.1088/0963-0252/1/3/011.
5. Good A., Durden D.A., Kebarle P. Mechanism and Rate Constants of Ion–Molecule Reactions Leading to Formation of $H^+(H_2O)_n$ in Moist Oxygen and Air // *J. Chem. Phys*. 1970. V. 52. P. 222–229. DOI: 10.1063/1.1672668.
6. Fehsenfeld F.C., Ferguson E.E. Thermal energy positive ion reactions in a wet atmosphere containing ammonia // *J. Chem. Phys*. 1973. V. 59. P. 6272–6276. DOI: 10.1063/1.1680006.
7. Bohme D.K., Mackay G.I., Tanner S.D. An experimental study of the gas-phase kinetics of reactions with hydrated H_3O^+ ions (n = 1-3) at 298 K // *J. Am. Chem. Soc*. 1978. V. 101. No 14. P. 3724–3730. DOI: 10.1021/ja00508a003.
8. G.P. Brassuer and S. Solomon, *Aeronomy of the middle atmosphere*, Reidel Publishing Company, 1986.
9. Golubkov G.V., Berlin A.A., Dyakov Y.A., et al. Growth of positioning errors with increasing signal power of Global Navigation Satellite Systems // *Russ. J. Phys. Chem. B*. 2023. V. 17. No 5. P. 1216–1227. DOI: 10.1134/S1990793123050214.
10. Kshevetskii S.P., Kurdyaeva Y.A., Gavrilov N.M. Coupled generation of acoustic and gravity waves by tropospheric heat sources // *Russ. J. Phys. Chem. B*. 2023. V. 17. No 5. P. 1228–1240. DOI: 10.1134/S1990793123050238.

11. Golubkov G.V., Adamson S.O., Borchevkina O.P., et al. Coupling of ionospheric disturbances with dynamic processes in the troposphere // *Russ. J. Phys. Chem. B.* 2022. V. 16. No 3. P. 508–530. DOI: 10.1134/S1990793122030058.
12. Rodionov A.I., Rodionov I.D. Rodionova I.P., et al. Heterogeneity accounting for the UV-C radiation propagation path over the sea // *Russ. J. Phys. Chem. B.* 2023. V. 17. No 5. P. 1246–1250. DOI: 10.1134/S1990793123050275.

INTEGRATED DENSITY OF STATE CALCULATION BY THE NUMERICAL INVERSION OF LAPLACE TRANSFORM

Sergey O. Adamson[1], Darja D. Kharlampidi[2,3] and Maxim G. Golubkov[1]

[1]Federal Research Center for Chemical Physics, Russian Academy of Sciences, Moscow, Russian Federation
[2]Moscow State Pedagogical University, Moscow, Russian Federation
[3]Peoples Friendship University of Russia, Moscow, Russian Federation

The using of quasi-equilibrium statistical theory (QET) to estimation of the rate constants it is necessary to calculate the densities of discrete vibrational states of activated molecules and transition complexes. As a rule, these calculations are carried out by differentiating with respect to energy of the $W(E)$ - integrated density function (IDS), which determines the number of states can be found below a given energy E ($E > 0$). In partial case, when the motion of nuclee replaced by a set of harmonic oscillators, this function can be estimated by the inequality

$$W(E) \leq CE^m, \quad (1)$$

where m is the number of degrees of freedom, and C is a constant [1-2]. Several methods have been proposed earlier for estimating the $W(E)$ function, but only the direct count method (DC) allows to perform its calculations with an accuracy of about 0.1%. The main disadvantage of this method is the sharp increase of computational cost with an increase in the number of populated states (1). Computational costs can be partially reduced by replacing the molecular states of close energies by effective degenerate states, but this technique leads to an increase in the systematic error of the method [3].

Later, the numerical inversion of the Laplace transform was proposed as a less expensive way to calculating IDS function [2]. In this approach IDS was calculating as a sum of integrals taken over short segments. The integral on each segment was calculated using the trapezoidal rule, using only the values of the integrand on the segment boundaries. The procedure was completed after summing on a sufficiently large (~ 2000) number of terms. Comparing the results [2] with reference (accurate) data, it can conclude that the absolute value of the relative calculation error depends on the energy of the system and ranges from 0.004 to 5% (Fig.1). Since the error value in this approach is close to the direct counting error, it can be considered as an alternative to the direct counting method.

One can point out at least three potential sources of errors in the procedure [2]. At the first, there is no check the convergence of the integral sum to the asymptotic limit, which does not provide the calculation accuracy even when a sufficiently large number of terms. Second, even for a small segment length ($\pi/2E_{max}$, where E_{max}>E is a scaling constant), integration over two points can lead to systematic error in the value of integral. In addition, the used by the authors intermediate coordinate transformation $y \rightarrow z=yE_{max}$ reduces the upper boundary of integration over the y coordinate to ~10π, which makes it unlikely that the sum of the integrals will approach the asymptotic limit. Taking into account these shortcomings,

a several improvements of the method [2] was proposed. The values of IDS, as in the original version, were calculated by summing the integrals taken over segments of finite length.

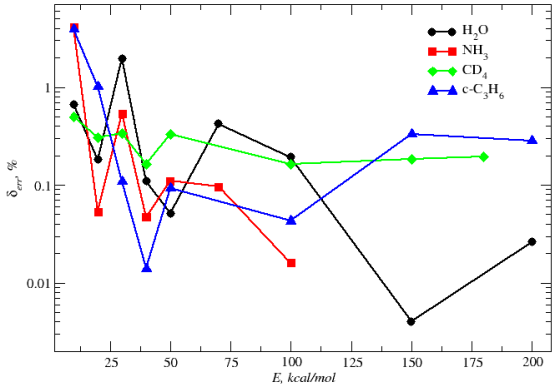


FIGURE 1. Absolute value of the relative error (δ_{err}) of the $W(E)$ function according to [2]. The results for the H_2O molecule are shown in black, NH_3 in red, CD_4 in green, and c-C_3H_6 in blue.

Integration over segments was carried out using the trapezoidal rule without the coordinate scaling. In the preliminarily calculations it was found that 800 nodes per segment of length 2π are sufficient to achieve a relative error of $\sim 10^{-5}$. Next, the found values of the integrals were transformed into an alternating sequence. The summation was completed by selecting from the sequence a monotonically converging subsequence, the maximum element of which did not exceed a certain small number (δ).

Using the H_2O molecule as an example, it was shown that this modification of the numerical inversion method allows to provide the accuracy of less than 0.1% for the energy range of 0 – 200 kcal/mol (Fig. 2, 3).

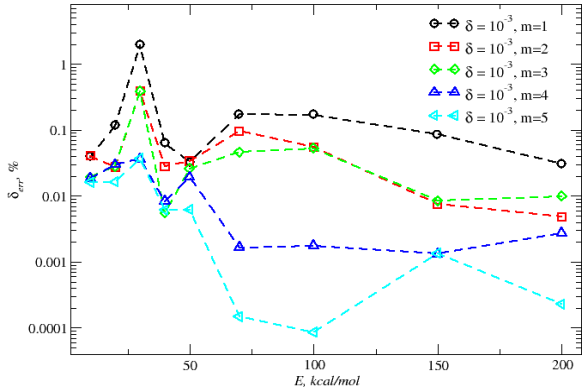


FIGURE 2. Dependence of the absolute value of the relative calculation error (δ_{err}) on the length of the subsequence. The number m corresponds to the number of elements of the monotonic sequence, δ is the maximal subsequence element.

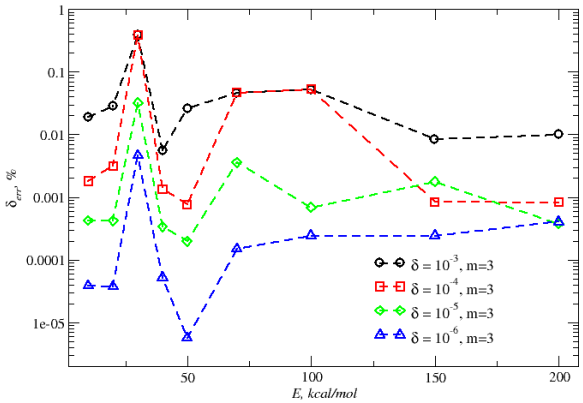


FIGURE 3. Dependence of the absolute value of the relative calculation error (δ_{err}) on the value of the subsequence element. The number m corresponds to the number of elements of the monotonic sequence, δ is the maximal subsequence element.

All the calculations were performed for 1200 integration nodes of the elementary interval. To increase the accuracy, the Euler transformation for alternating series can also be used [4].

This study was carried out in the framework of State Assignment of the Ministry of Science and Higher Education of the Russian Federation (project No. 125012200611-5).

1. Dubner H., Abate J. Numerical Inversion of Laplace Transforms by Relating Them to the Finite Fourier Cosine Transform // *J. of the A.C.M.* 1968. V. 15. No 1. P. 115–123. DOI: 10.1145/321439.321446.
2. Hoare M.R., Pal P. Densities of states and the complex partition function // *Molecular Physics*. 1971. V. 20. No 4. P. 695–704. DOI: 10.1080/00268977100100661.

3. Current J.H., Rabinovitch B.S. Decomposition of Chemically Activated Ethyl-d_3 Radicals. Primary Intramolecular Kinetic Isotope Effect in a Nonequilibrium System // *J. Chem. Phys.* 1963. V. 38. No 4. P. 783–795. DOI: 10.1063/1.1733764.
4. Longman I. M. A Method for the Numerical Evaluation of Finite Integrals of Oscillatory Functions // *Mathematics of Computation*. 1960. V. 14. No 69. P. 53–59. DOI: 10.2307/2002984.

COLLISIONAL-INDUCED REACTIONS BETWEEN METHANE AND SIMPLE CRIEGEE INTERMEDIATES CH_2OO, CH_3CHOO, AND $(CH_3)_2COO$

Yuri A. Dyakov and Maxim G. Golubkov

Semenov Federal Research Center for Chemical Physics, Russian Academy of Sciences, Moscow, Russia

Methane (CH_4), along with many other volatile components of the Earth's atmosphere (carbon dioxide (CO_2), water vapor, ozone (O_3), nitrous oxide (N_2O), etc.), is a one widely discussed active greenhouse gas that traps part of the infrared terrestrial radiation and contributes to the global warming. The greenhouse potential of methane is extremely high and far exceeds that of carbon dioxide. The reports of the World Meteorological Organization (WMO) indicate that CH_4 concentration in the atmosphere has already significantly surpassed significantly its preindustrial levels. Thus, methane can have a great impact on atmospheric chemistry and the climate of the Earth.

CH_4 emissions into the atmosphere can be from either anthropogenic activities such as agriculture, biogas release at waste disposal sites, coal mining, etc., or natural sources. Among the important natural sources are permafrost and gas hydrates on the seabed, both of which are being destroyed by releasing their methane into the atmosphere due to the global warming. The impact of methane and other greenhouse gases on the Earth's climate is not limited to the troposphere but also the stratosphere, mesosphere, and even ionosphere due to the upward transport of these gases. This means that the mechanisms of mixing of volatile atmosphere compounds (VACs), in particular, volatile organic compounds (VOCs) consisting from various unsaturated molecules like alkenes and polyaromatic unsaturated hydrocarbons (PAHs) between these layers, as well as chemical interactions occurring in the lower and upper atmospheres are of great scientific importance.

Methane can penetrate into the stratosphere via turbulent diffusion from the troposphere to the stratosphere, and sequentially to the mesosphere and ionosphere during tropical hurricanes, thunderstorms, and volcanic eruptions [1,2]. This transport process can be significantly enhanced by the propagation of internal and acoustic gravity waves (IGWs and AGWs) [3]. In the polar latitudes, troposphere gases can also be transported to the upper atmospheric layers through the polar vortex [4]. Since the polar region is also the largest reservoir of methane, this polar vortex transport is believed to have significantly contributed significantly to the increase of in methane concentration in the stratosphere in the last few decades.

PAHs are the main components of soot particles. Once formed in the lower atmosphere, they can be transported into the upper atmosphere layers through the same mechanisms described above for methane. Their major degradation pathways are reactions initiated with OH, O_3, NO_3, and halogens [5].

Carbonyl oxides, or Criegee intermediates (CIs), are form during the ozonolysis of alkenes, and their role in the atmosphere was first studied by Rudolf Criegee in the early 1950s [6]. Because of their extremely high instability, it is only recently that CIs are have been studied by direct experimental methods. Their high chemical activity is due to the presence of the biradical >C-O-O group, which readily interacts with various substances present in the atmosphere, such as and many other chemical

compounds. For example, their reactions with SO_2 and NO_2 molecules produce sulfuric and nitric acids [7].

The formation of CIs results in a significant energy release of about 40–50 kcal/mol [8]. In dense atmospheric layers, i.e., the tropo-sphere and lower stratosphere, this energy could quickly dissipate through collisions, and, as a result, the CI molecules would become thermodynamically stable, and then can react with water or other atmospheric compounds. In the upper stratosphere and mesosphere, however, the air density is very low and the concentration of molecules is rather small, intermolecular collisions are rare, and therefore CI molecules could retain a significant part of the internal energy obtained during the formation. Moreover, many molecules in the upper atmosphere can be electronically excited or ionized by the absorption of ultraviolet (UV) photons, which are present abundantly at high altitudes, and this certainly applies to CIs and methane molecules. The electronic spectroscopy and photochemistry of simple CIs like formaldehyde oxide, acetaldehyde oxide, and acetone oxide have been studied in the last two decades in detail and reviled that these CIs have strong transitions in the UV wavelength range of 300–400 nm, with a maximum at 320–340 nm depending on the specific molecule. The appropriate absorption cross section for the most of the studied CIs exceeds the value of 10−17 cm2 molecule^{-1}). Electronic excitations by UV photons are usually accompanied by a nonadiabatic transition to the underlying electronic state. The transition occurs through the conical intersection of electronic terms with simultaneous excitation of intramolecular vibrations. Ions could also be recombined into the highly excited neutral atoms and molecules through recombination with slow electrons. The internal vibrational energy of these molecules can then can be transferred into their kinetic energy through intermolecular collisions [9].

The reactions of CIs with other air compounds in the stratosphere and mesosphere produce a great variety of secondary products, such as acetaldehyde, formaldehyde, vinyl alcohol, acetone, acetic acid, etc. They are likely to contribute to the formation of high-altitude polar stratospheric and noctilucent clouds.

In this work, we investigate the chemical interaction between CIs and methane, induced by their collision. We choose three simple CI molecules, i.e., formaldehyde oxide CH_2OO, acetaldehyde oxide CH_3CHOO, and acetone oxide $(CH_3)_2COO$. They differ from each other in the replacement of hydrogen atoms with one or two methyl groups. The properties of some of these molecules have been studied earlier [10-12]. It was found that the interaction of CIs with various greenhouse gases strongly depends on the molecular kinetic energy and can leads either the formation of the van der Waals complex, which, in the case of methane, is likely to be unstable, or creation of relatively deep stable intermediate molecule, which, in its part, dissociate with producing a variety of secondary fragments. The third reaction pathway is the one-step formation of methanol and complementary fragments.

Calculations of the molecular potential energy surfaces (PES) along the reaction pathways has been performed by B3LYP/aug-cc-pVTZ DFT calculations. The energy valise in minima and maxima then have been improved by CCSD(T)/aug-cc-pVTZ method. The relative product's yield calculations then have been founded by the RRKM/VTST method. All *ab initio* calculations have been performed by the GAUSSIAN 09 package [13].

The relative products yield of reactions for reactions $CH_2OO + CH_4$, $CH_3CHOO + CH_4$, and $(CH_3)_2COO + CH_4$ are presented in Figure 1, 2, and 3. In these Figures we assume that reagents have quite enough kinetic energy to overcome the high entrance barriers and form energetically deep intermediates CH_3CH_2OOH, $(CH_3)_2CHOOH$, and $(CH_3)_3COOH$ without formation of weak Wan-der-Waals complexes. Direct formation of methanol is also one possible reaction routes.

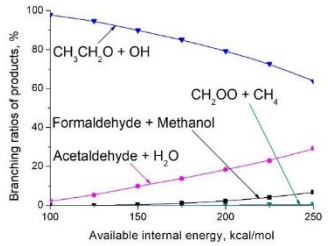


FIGURE 1. Relative product yields come from the dissociation of dissociation reaction initiated by collision of CH_2OO and methane. Energy values are measured from the energy of isomer CH_3CH_2OOH.

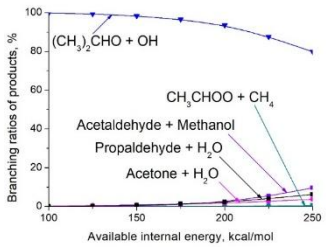


FIGURE 2. Relative product yields come from the dissociation of dissociation reaction initiated by collision of CH_3CHOO and methane ($(CH_3)_2CHOOH$) as a function of its internal energy.

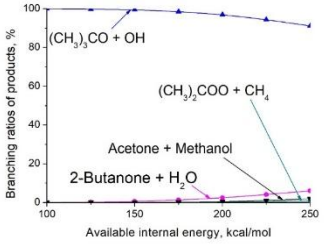


FIGURE 3. Relative product yields come from the dissociation of dissociation reaction initiated by collision of $(CH_3)_2COO$ and methane ($(CH_3)_3COOH$) as a function of its internal energy.

The short conclusion of this work is the chemical interaction between methane and simple Criegee intermediates CH_2OO, CH_3CHOO, and $(CH_3)_2COO$, initiated by collision, being occurs in the upper atmosphere, leads to various chemical reactions, which result in the formation of many radicals such as OH, CH_3, ethoxy, methyletoxy, and others, as well as atomic hydrogen, methanol, acetone, water, and various aldehydes. The processes studied in this work also indicate probable new sources of atomic hydrogen, methanol, acetone, and water creation in the mesosphere and ionosphere. They may modify the chemical physics of these layers and initiate the creation of high-altitude stratospheric and noctilucent clouds. In addition, we have shown that methylation of this class of molecules increases reaction barriers and generally slow down the rates of chemical processes. The high values of the entrance barriers of the collisional -induced reactions between methane and the simple CIs suggests that these reactions are most likely to occur in the rarefied layers of the upper atmosphere, where thermodynamic equilibrium is often disturbed and molecules with high kinetic energy are likely to be frequent.

This study was carried out in the framework of State Assignment of the Ministry of Science and Higher Education of the Russian Federation (project No. 125012200611-5).

1. Choi W., Kim S., Grant, W.B., et al. Transport of methane in the stratosphere associated with the breakdown of the Antarctic polar vortex // *J. Geophys. Res. Atmos*. 2002. V. 107. No D24. 8209. DOI: 10.1029/2001JD000644.
2. Nair P.R., Kavitha M. Stratospheric distribution of methane over a tropical region as observed by MIPAS on board ENVISAT // *Int. J. Remote Sens*. 2020. V. 41. P. 8380–8405. DOI: 10.1080/01431161.2020.1779376.
3. Golubkov G.V., Adamson S.O., Borchevkina O.P., et al. Coupling of ionospheric disturbances with dynamic processes in the troposphere // *Russ. J. Phys. Chem. B*. 2022. V. 16. No 3. P. 508–530. DOI: 10.1134/S1990793122030058.
4. Shinbori A., Otsuka Y., Sori T., et al. Electromagnetic conjugacy of ionospheric disturbances after the 2022 Hunga Tonga-Hunga Ha'apai volcanic eruption as seen in GNSS-TEC and SuperDARN Hokkaido pair of radars observations // *Earth, Planets Sp*. 2022. V. 74. No 106. P. 1–17. DOI: 10.1186/s40623-022-01665-8.
5. Lelieveld J., Dentener F.J., Peters W., Krol M.C. On the role of hydroxyl radicals in the self-cleansing capacity of the troposphere // *Atmos. Chem. Phys*. 2004. V. 4. P. 2337–2344. DOI: 10.5194/acp-4-2337-2004.

6. Criegee R., Wenner G. Die ozonisierung des 9,10-oktalins // *Justus Liebigs Annalen der Chemie*. 1949. V. 564. No 1. P. 9–15.
7. Kanakidou M., Seinfeld J.H., Pandis S.N., et al. Organic aerosol and global climate modelling: a review // *Atmos. Chem. Phys*. 2005. V. 5. P. 1053–1123. DOI: 10.5194/acp-5-1053-2005.
8. Herron J.T., Martinez R.I., Huie R.E. Kinetics and energetics of the Criegee intermediate in the gas phase. II. The Criegee intermediate in the photooxidation of formaldehyde, in alkyldioxy disproportionation and O + oxoalkane addition reactions // *Int. J. Chem. Kinet*. 1982. V. 14. P. 225–236. DOI: 10.1002/kin.550140303.
9. Hsu C.H., Tsai M.T., Dyakov Y.A., Ni C.K. Energy transfer of highly vibrationally excited molecules studied by crossed molecular beam/time-sliced velocity map ion imaging // *Int. Rev. Phys. Chem*. 2012. V. 31. P. 201–233. DOI: 10.1080/0144235X.2012.673282.
10. Kumar M., Francisco J.S. Reactions of Criegee intermediates with non-water greenhouse gases: implications for metal free chemical fixation of carbon dioxide // *J. Phys. Chem. Lett*. 2017. V. 8. P. 4206–4213. DOI: 10.1021/acs.jpclett.7b01762.
11. Xu K., Wang W., Wei W., et al. Insights into the reaction mechanism of Criegee intermediate CH_2OO with methane and implications for the formation of methanol // *J. Phys. Chem. A*. 2017. V. 121. No 38. P. 7236–7245. DOI: 10.1021/acs.jpca.7b05858.
12. Dyakov Y.A., Adamson S.O., Butkovskaya N.I., et al. Collisional-Induced Chemical Reactions between Methane and Simple Criegee Intermediates CH_2OO, CH_3CHOO, and $(CH_3)_2COO$: Theoretical Study // *Russ. J. Phys. Chem. B*. 2024. V. 18. No 3. P. 682–691. DOI: 10.1134/S1990793124700179.
13. Frisch M.J., Trucks G.W., Schlegel H.B., Scuseria G.E., Robb M.A., Cheeseman J.R., Scalmani G., Barone V., Mennucci B., Petersson G.A., et al. Gaussian 09, Revision A.02. Eds. Gaussian Inc.: Wallingford, CT, USA, 2009.

ATMOSPHERIC PROCESSES OF TOXIC CHLOROACETIC ACIDS

Igor I. Morozov[1], Eugenie S. Vasiliev[1], Nadezhda I. Butkovskaya[1], Polina S. Khomiakova[1], Aleksei G. Syromyatnikov[2] and Olga S. Morozova[1]

[1]Semenov Federal Research Center for Chemical Physics, Russian Academy of Sciences, Moscow, Russia
[2]Lomonosov Moscow State University, Faculty of Physics, Moscow, Russia

The paper summarizes the results of studies on reactions of atomic fluorine with toxic chloroacetic acids (CA).

The reactions of toxic anthropogenic pollutants in the atmosphere play an important role in influencing the ecology, air quality and water environment. Chlorine-containing compounds are mainly of anthropogenic origin, causing serious damage to the environment. Recent studies have shown that a large number of chlorine-containing compounds are formed in natural processes. Volatile organochlorine compounds, being photo-chemically oxidized in the atmosphere, are one of the sources of phytotoxic chloroacetic acids in the environment. Chloroacetic acids are produced in large quantities naturally by chlorination of organic matter, such as by soil microorganisms, marine algae, and salt lake bacteria, and show similar metabolic pathways. Understanding the origin and fate of these organohalogen compounds is essential to counteracting environmental problems caused by these compounds.

CA occupy a special place due to their wide application in modern technologies, agriculture, and everyday life. CA are found in atmospheric air, rainwater, surface and wastewater systems, and natural reservoirs [1-4]. Because of their low reactivity, chloroacetic acids can accumulate and their negative effects can spread over large areas. Monochloroacetic, dichloroacetic and trichloroacetic acids are extremely toxic substances. The hydration of chlorinated acids (monochloroacetic (MCA), dichloroacetic (DCA) and trichloroacetic (TCA)) was studied. DCA is widely used in the technology of organic synthesis. Trichloroacetic acid (TCA) belongs to a broad class of chlorinated organics, widespread in the surrounding nature. This is due to the fact that TCA is formed in the soil and in the atmosphere. It is a very active chemical compound that negatively affects environment and living organisms.

MCA plays a prominent role in fine organic synthesis. Monochloroacetic acid are formed in the atmosphere as a result of chemical reactions involving organochlorine compounds, mainly chloroethylene, tetrachloroethylene, chloroethane, oxidized in the presence of the main oxidizers of the atmosphere. Studies have shown that MCAs are formed in the atmosphere naturally. There is reason to believe that chloroacetic acids can be partially formed in plant tissues in a similar manner [5].

The present work is related to the determination of the subtleties of the reaction mechanism of radicals formed during the oxidation of MCA by hydroxyl radicals. These reactions with the OH radical have already been studied, but the problem of secondary radicals formed in these reactions with atmospheric molecular oxygen remains unstudied. This is due to the fact that it is very difficult to obtain high stable concentrations of OH radicals in the laboratory. Therefore, the work proposes to use the reaction of fluorine atoms with MCA as sources of C*HClCOOH radicals using the technique given in [**6**]. For this, it is necessary to study the kinetics of the primary reaction of free radical formation in the reaction of fluorine atoms with chloroacetic acids. The experimental setup was described in detail in our previous works [7]. The kinetics of the reaction of F-atoms with monochloroacetic acid was studied at 293 K using a low-pressure flow reactor. The concentrations of the reactants were monitored using mass spectrometry with molecular beam sampling. The rate constant was determined using the competing reactions method. Concentrations of the compound under study (MCA) and the reference compound (ref) were introduced into the reactor, where two parallel reactions took place:

$$F + CH_2ClC(O)OH \rightarrow Products\ (1),$$

$$F + ref \rightarrow Products\ (0),$$

The kinetic study of the reaction of MCA with fluorine atoms consisted of two series of experiments in which the k_1/k_{ref} ratio was measured for competing reactions of F-atoms with cyclohexane and 2-fluoroethanol.

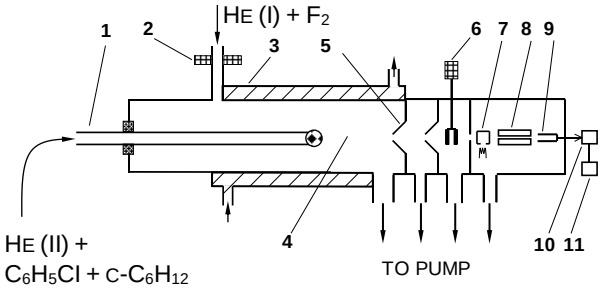


FIGURE 1. Scheme of the experimental setup. 1 – Inlet line for reagents mixed with helium, 2 – RF discharge on the supply line for molecular fluorine mixed with helium, 3 – Thermostatic jacket, 4 – Reaction zone, 5 – Nozzle – Separator, 6 - Beam modulator, 7 – Ion source, 8 – Electrodes of a quadrupole mass analyzer, 9 – Secondary electron multiplier (SEM), 10 – Synchronous detector, 11 – Computer.

$$CH_2ClC(O)OH + F \rightarrow Products, \quad (1)$$

$$c\text{-}C_6H_{12} + F \rightarrow C_6H_{11} + HF, \quad (2)$$
$$CH_2FCH_2OH + F \rightarrow \text{Products}, \quad (3)$$
$$CH_4 + F \rightarrow CH_3 + HF. \quad (4)$$

Experiment. Figure 2 shows a scheme of the experimental setup. The experiments were conducted using a low-pressure flow reactor connected to a mass spectrometer. The reactants and reaction products were analyzed in a mass spectrometer with molecular beam sampling. A low-pressure flow reactor connected to a mass spectrometer was used in the work. The choice of competing substances must meet two criteria:

1. The mass spectra of the substances under study must not overlap.
2. The reaction rate constants must not differ significantly.

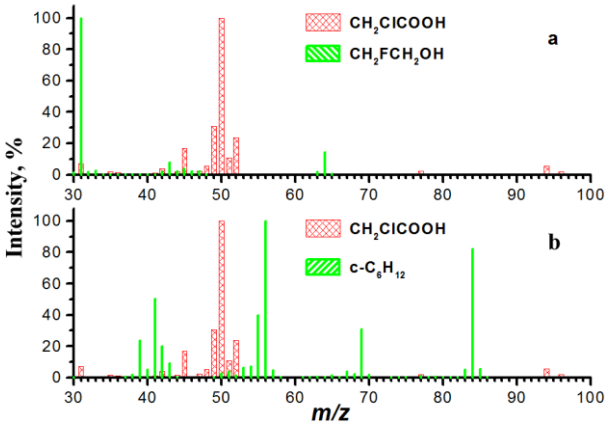


FIGURE 2. Fragment of the mass spectrum of monochloroacetic acid, 2-fluoroetalone (a) and cyclohexane (b) in the range m/z 30–100.

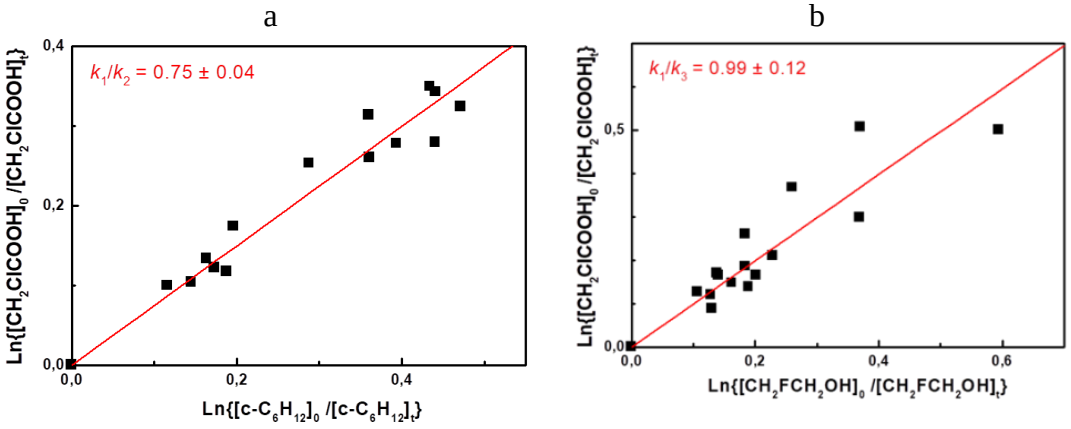


FIGURE 3. Plot of the relative rate of the reaction of F atoms with MCA using cyclohexane (a) and 2-fluoroethanol (b) as reference reagents.

Figure 3 shows the dependence of the relative reaction rate of F atoms with MCA using cyclohexane and 2-fluoroethanol (D), which were used as reference reagents. The rate constant for the reactions of fluorine atoms with monochloroacetic acid is $(0.96 \pm 0.38) \times 10^{-10}$ cm^3 molecules^{-1} s^{-1}.

The report will also present the studied mechanisms of reactions of fluorine atoms with DCA and TCA. The reaction mechanism and kinetics will be discussed.

This study was carried out in the framework of State Assignment of the Ministry of Science and Higher Education of the Russian Federation (project No. 125012200611-5).

1. Reimann S., Grob K., Frank H. Chloroacetic Acids in Rainwater // *Environ. Sci. Technol.* 1996. V. 30. No 7. P. 2340. DOI: 10.1021/es9507776.
2. Laniewski K., Boren H., Grimvall A. Fractionation of halogenated organic matter present in rain and snow // *Chemosphere*. 1999. V. 38. No 2. P. 393. DOI: 10.1016/S0045-6535(98)00181-7.
3. Nikolaou A.D., Golfinopoulos S.K, Lekkas T.D. Formation of organic by-products during chlorination of natural waters // *J. Environ. Monit*. 2002. V. 4. P. 910–916. DOI: 10.1039/B202965K.
4. Matucha M.,·Gryndler M.,·Forczek S. T., et al. Chloroacetic acids in environmental processes // *Environ. Chem. Lett*. 2003. V. 1. No 2. P. 127–130. DOI: 10.1007/s10311-003-0030-y.
5. Li J., Zhang Y., Zhou Y., et al. Haloacetic Acids in the Aquatic Environment // *Separation & Purification Reviews.* 2022. V. 53. P. 1–25. DOI: 10.1080/15422119.2022.2141649.
6. Vasiliev E.S, Morozov I.I., Karpov G.V. Rate constant for the reaction of F-atoms with trichloroacetic acid // *Intern. J. Chem. Kinet.* 2019. V. 51. No 12. P. 909–917. DOI: 10.1002/kin.21319.
7. Vasiliev E.S., Morozov I.I., Butkovskaya N.I., et al. Reactions of Halogenated Acetic and Propionic Acids with Fluorine Atoms // *Russ. J Phys. Chem. B.* 2023. V. 17. No 5. P. 1091–1097. DOI: 10.1134/S1990793123050251.
8. Vasiliev E.S., Karpov G.V., Shartava D.K., et al. Mass Spectrometric Study of the Reaction of a Fluorine Atom and Monocloroacetic Acid // *Russ. J. Phys. Chem. B.* 2022. V. 16. No 3. P. 388–394. DOI: 10.1134/S1990793122030113.

NOVEL METHODS FOR ENVIRONMENTAL CONTROL AND MONITORING

CONTROL OF STRUCTURAL PROPERTIES AND CHEMICAL COMPOSITION OF POROUS ANODIC ALUMINUM OXIDE

Elizaveta A. Konstantinova[1], Yulia.V. Nazarkina[1,2], Daria A. Dronova[1,2], and Ekaterina V. Kytina[1,3]

[1]Department of Physics, Lomonosov Moscow State University, Moscow, Russia
[2]National Research University of Electronic Technology – MIET, Zelenograd, Moscow, Russia
[3]Semenov Federal Research Center for Chemical Physics, Russian Academy of Sciences, Moscow, Russia

Due to its chemical and thermal inertness, refractoriness and accessible manufacturing technology, porous anodic aluminum oxide (PAAO) has found wide application in microelectronics and nanosensors. PAOA is characterized by a high degree of ordering: a small spread of pore diameters and a hexagonal-periodic arrangement of pores [1, 2]. By changing the technological parameters of anodic oxidation, it is possible to vary the size of pores and oxide cells of PAOA. It is possible to form porous aluminum oxide as both mesoporous (pore diameter from 2 to 50 nm) and microporous (pore diameter over 50 nm). In recent years, researchers have been attracted by the opportunity to study the optical properties of materials (analytes) deposited inside porous aluminum oxide in order to develop optical biosensors for diagnosing diseases at early stages, which allows for effective prediction, treatment and monitoring of their progress [3, 4]. Before introducing various analytes, it is necessary to obtain samples with reproducible geometric characteristics (length, pore diameter, porous cell diameter, porosity). The structural properties of porous aluminum oxide and the chemical composition of its surface can vary depending on the composition and concentration of the electrolyte in which it is formed, as well as the modes of its formation. Therefore, the aim of this work was to achieve control and reproducibility of the structural properties and chemical composition of PAOA.

To obtain micrographs of the samples, Helios NanoLab 650 and Supra 40 scanning electron microscopes were used. Statistical analysis of SEM images was performed using the Fiji software package [1].

The chemical composition was studied using a ZSX Rigaku Primus IV X-ray fluorescence spectrometer (Japan) with wavelength dispersion in vacuum. An RX40 diffraction crystal was used for the analysis of O, a PET crystal for Al, and a LiF200 crystal for Se. Analytical Kα lines were used for all elements. A PC detector was used to measure X-ray fluorescence radiation emitted by Al, O, and S.

X-ray diffraction analysis was performed on a Rigaku MiniFlex 600 instrument (Rigaku Corporation, Tokyo, Japan) with a Cu Kα radiation source (λ = 1.54 Å).

Let us discuss the effect of current density during sample formation on the geometric parameters of PAOA formed in H_2SeO_4 solutions. As an example, Fig.1 shows SEM images of the surface of PAOA formed at 5°C in 1 M H_2SeO_4 and in 1.5 M H_2SeO_4 at different current densities.

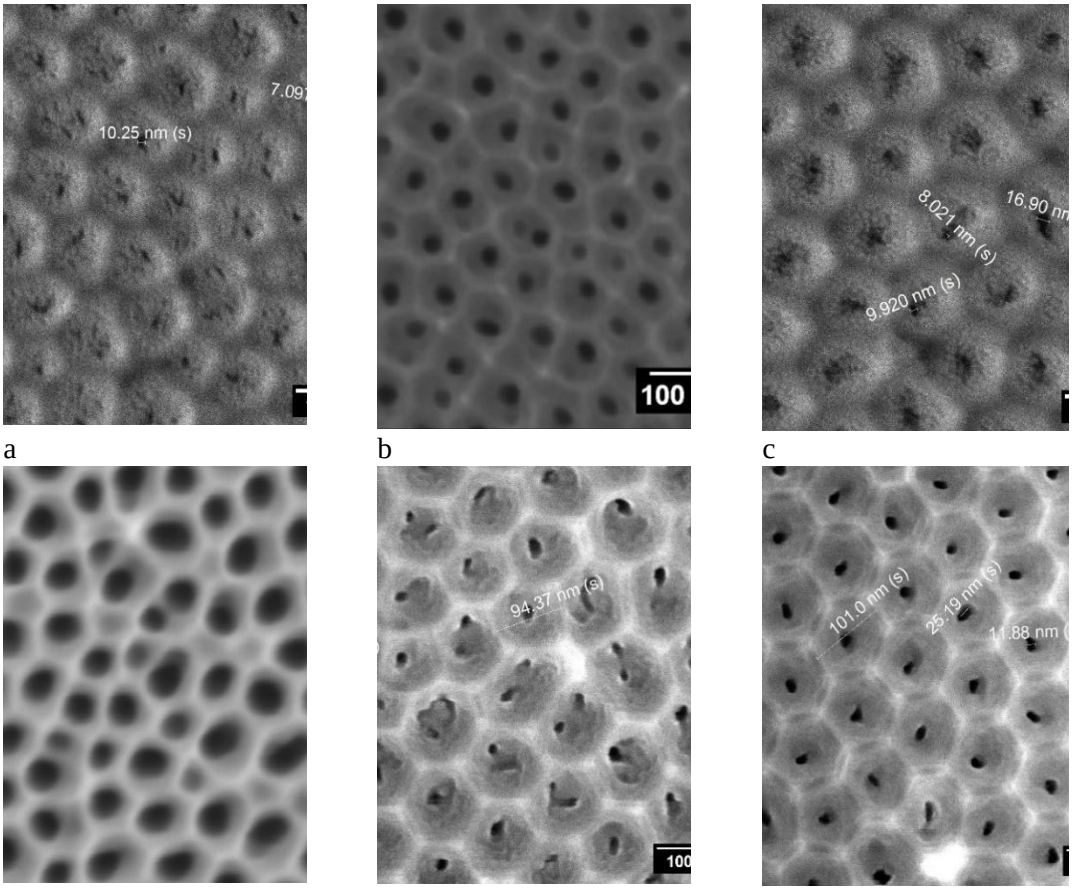


FIGURE 1. SEM images of the surface of PAOA formed at 5°C in 1.0 M H_2SeO_4 at a current density of: a) 2 mA/cm^2, b) 5 mA/cm^2, c) 10 mA/cm^2, and in 1.5 M H_2SeO_4 at a current density of d) 5 mA/cm^2, e) 10 mA/cm^2, f) 15 mA/cm^2.

At low current density values (up to 5 mA/cm^2), depending on the electrolyte concentration, two variants of the morphology of the porous structure are observed:

1) many small pores in one porous cell. Most of these pores are practically spherical, i.e. they only originate on the surface, but do not develop into a cylindrical porous structure (Fig. 1 a, b, such pores are also visible in Fig. 1e);

2) one pore of large diameter, which indicates significant etching of the pore walls (Fig. 1d). If at low current densities the formation of large pores with thin walls was observed, then an increase in current density leads to an increase in the thickness of the walls and a decrease in the diameter of the pores. It is also possible to increase the number of pores in one porous cell (Fig. 1d), however, with a further increase in current density, the porous structure comes to a self-ordered state (Fig. 1 c, f), in which one cell contains one pore, and the porous cells are smooth hexagons, the hexagonal symmetry of the porous structure has an extent of tens of cells. With a further increase in current density, defects in the formation of oxide "hot spots" are observed and the porous structure becomes non-uniform over the surface of the sample. The results of the study of the morphology of PAOA samples formed at various process parameters in H_2SeO_4 solutions are presented in Table 1.

TABLE 1. Values of the geometric parameters of oxides obtained at various process parameters of anodizing in H_2SeO_4 solutions.

Sample	Pore diameter, nm	Diameter of porous cells, nm	Porosity (analysis Fiji), %
Se-0.05M-5 ^{0}C-5mA/cm^2	16±8	147±15	1,2
Se-0.5M-5 ^{0}C-5mA/cm^2	15±6	114±10	1,6
Se-0.5M-5 ^{0}C-10mA/cm^2	25±7	106±13	3,4
Se-1.0M-5 ^{0}C-5mA/cm^2	15±5	80±11	3,5
Se-1.0M-5 ^{0}C-10mA/cm^2	16±5	78±10	2,2
Se-1.0M-5 ^{0}C-15mA/cm^2	12±4	65±6	3,5
Se-1.5M-5 ^{0}C-10mA/cm^2	14±4	82±8	1,7
Se-1.5M-5 ^{0}C-15mA/cm^2	17±4	84±7	2,0
Se-1.5M-5 ^{0}C-20mA/cm^2	20±4	86±7	3,0
Se-2.0M-5 ^{0}C-5mA/cm^2	37±9	67±7	25

The porosity of the oxide matrices obtained at 5°C varies from 1.5% to 25%. With increasing electrolyte temperature, the porosity increases significantly. When forming an oxide in 0.5 M H_2SeO_4, the porosity of the oxide increases from 1.6 to 16%. With increasing electrolyte concentration, the effect of increasing porosity (and therefore, enhancing chemical etching of the pore walls) increases significantly. The porosity changes from 1.7% to unmeasured values, since the porous structure in the upper part of the oxide is completely etched and the oxide disintegrates into fibers.

The chemical composition of the samples was studied using wavelength-dispersive X-ray spectroscopy (Table 2).

TABLE 2. Intensity maxima (in relative units) of the analyzed elements in samples with different concentrations of H_2SeO_4.

Element \ Sample	Se-0.5M-5C-10 mA	Se-1.0M-5C-10 mA	Se-1.5M-5C-10 mA
O (intensity)	2,40	2,4	2,4
Al (intensity)	119,9	118,9	116,0
Se (intensity)	51,3	48,7	46,5

The values of the intensity maxima of the main matrix of the substance (oxygen and aluminum) are almost identical, while the intensity of selenium decreases slightly with increasing concentration of H_2SeO_4. According to X-ray diffraction data, all obtained samples are amorphous.

Thus, PAOA samples with controlled and reproducible structural parameters were synthesized. The obtained data are of great importance for practical applications of PAOA in various fields, including biomedicine.

The study was supported by a grant from Russian Science Foundation № 24-19-00402, https://rscf.ru/en/project/24-19-00402/.

1. Jani A.M., Losic D., Voelcker N.H. Nanoporous anodic aluminium oxide: Advances in surface engineering and emerging applications // *Progress in Materials Science*. 2013. V. 58. No 5. P. 636-704. DOI: 10.1016/j.pmatsci.2013.01.002.

2. Brzózka A., Brudzisz A. Rajska D., et. al., Recent trends in synthesis of nanoporous anodic aluminum oxides. In *Micro and Nano Technologies, Nanostructured Anodic Metal Oxides*, Elsevier, 2020, pp. 35-88.

COMPARATIVE ANALYSIS OF PHOTOLUMINESCENT PROPERTIES OF POROUS ALUMINUM OXIDE FORMED IN ELECTROLYTES BASED ON SULFURIC AND SELENIC ACIDS

Ekaterina V. Kytina[1,2], Yulia V. Nazarkina[1,3], Elizaveta A. Konstantinova[1], and Alexander V. Pavlikov[1]

[1]Department of Physics, Lomonosov Moscow State University, Moscow, Russia
[2]Semenov Federal Research Center for Chemical Physics, Russian Academy of Sciences, Moscow, Russia
[3]National Research University of Electronic Technology – MIET, Zelenograd, Moscow, Russia

Porous anodic aluminum oxide (PAAO) is an array of ordered pores with a diameter in the range from units to several tens of nanometers. Therefore, it can be used to create nanocomposites; containers and templates for various substances; biosensors for tumor markers or other biological substances [1, 2]. In recent years, interest in the creation of biosensors for tumor markers has increased due to the growth of oncological diseases [1, 2]. Of greatest interest among them are optical sensors, since they do not require contacts and are characterized by a high response rate. One of the important examples of optical biosensors are photoluminescent sensors. Despite the large number of works devoted to studies of photoluminescence (PL) of individual PAAO matrices synthesized in a certain electrolyte. For example, in some works the origin of PL in PAAO films is explained by the presence of impurities in the form of electrolyte ions formed during anodization [1], in others - by different types of defects formed during anodization, which mainly include F centers (oxygen vacancies) and F+ centers (single-ionized oxygen vacancies). Some researchers argue in favor of one of the versions, some believe that luminescence is due to both impurities and vacancies. It is important to optimize the synthesis parameters to obtain non-luminescent PAAO samples. This will allow studying the PL of analytes in the pores of the PAAO, which will not be affected by the PL of the matrix itself. Therefore, the purpose of this work was to synthesize non-luminescent PAAO and study the PL of the test analyte in the pores of the samples. Rhodamine B was chosen as the analyte.

To obtain micrographs of the samples, Helios NanoLab 650 and Supra 40 scanning electron microscopes were used. Statistical analysis of SEM images was performed using the Fiji software package. To measure Raman and photoluminescence spectra, a Horiba Jobin Yvon HR800 micro-Raman setup was used. An argon laser with a wavelength of 488 nm served as the excitation source. The intensity of the exciting radiation was 20 W/cm^2. To study paramagnetic defects, a Bruker ELEXSYS-E500-10/12 electron paramagnetic resonance (EPR) spectrometer, located in the Collective Use Center of the Physics Department of Moscow State University, was used.

Aluminum foil (99.99% pure) was used for anodizing. Organic contaminants were removed from the surface by immersing the foil in acetone and placing it in an ultrasonic bath for 10 minutes. The surface roughness was reduced by polishing the aluminum substrates, which was carried out by electrochemical etching in a solution at a temperature of 5°C, containing 1:6 perchloric acid and ethyl alcohol, for 5 minutes at a voltage of 40 V, while stirring the electrolyte. After carrying out the described preliminary treatment of the surface of the aluminum substrates, they were thoroughly washed in

deionized water and dried in air. Anodizing was carried out in a dilute solution of sulfuric acid and selenium acid in a galvanostatic mode: in 1.5 M at a current density of 15 mA/cm^2 and at a temperature of 5°C. To obtain an ordered porous structure of aluminum oxide, a two-stage anodization technique was used. It should be noted that the synthesis parameters were chosen taking into account the literature data and based on our numerous experiments in order to obtain ordered arrays of nanopores in aluminum oxide. In addition, the parameters were selected in order to obtain non-luminescent samples. The first stage was carried out for 30 min, after which the resulting sacrificial oxide layer was selectively removed for 15 min in an aqueous solution of 0.4 M phosphoric acid and 0.2 M chromic acid at a temperature of 80 ºC. The second stage was carried out at the same process parameters as the first, but for an hour. The dye rhodamine B was dissolved in deionized water to obtain a solution with a concentration of 10^{-5}, 10^{-6}, 10^{-7} M. The samples were immersed in the dye for 30 minutes at a temperature of 40 °C, after which they were removed and dried in air. Thus, two series of samples were synthesized. The first series of PAAO was obtained in sulfuric acid, the second series of PAAO was synthesized in selenic acid. Each series of samples consisted of the original samples and 3 samples with different dye concentrations (see above).We will use the following designations for the samples, prepared in sulfuric acid: S5 (initial), S5-R1 (with Rhodamine B 10^{-5} M), S5-R2 (with Rhodamine B 10^{-6} M), S5-R3 (with Rhodamine B 10^{-7} M) and for the samples, prepared in selenium acid: Se5 (initial), Se5-R1 (with Rhodamine B 10^{-5} M), Se5-R2 (with Rhodamine B 10^{-6} M), Se5-R3 (with Rhodamine B 10^{-7} M).

Figure 1 shows SEM images of PAAO samples (initial and with applied dye) obtained in 1.5M H_2SO_4 and H_2SeO_4 at a current density of 15 mA/cm^2 and a temperature of 5°C.

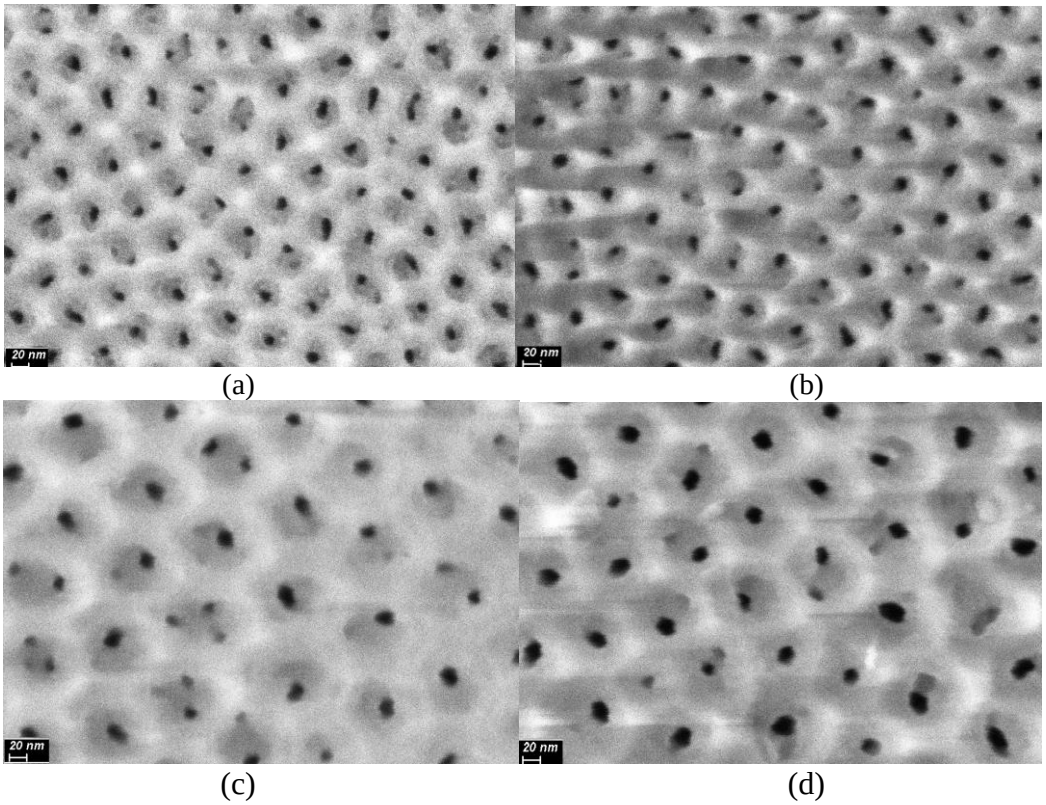


FIGURE 1. SEM images of the surface of S5 (a), S5-R1 (b), Se5 (c), Se5-R1 (d).

It is evident from Fig. 1 that the average pore diameter of the samples varies from 9 to 15 nm. Quite a large deviation in size can be explained by the elongated shape of some samples, probably due to the

merging of two "seed" pores into one during the formation of PAAO. The thickness of the porous layer is 7.5 μm. No structural changes are observed when the dye is applied (Fig. 1, b and d). Also, no large dye clusters or films are observed on the oxide surface, indicating that the dye was adsorbed exclusively on the sample surface. The samples acquire a stable pinkish tint that is not removed by washing.

Raman spectroscopy studies showed that the samples had an amorphous structure.

The initial PAAO (S5 and Se5) did not luminesce. Therefore, the obtained PAAO samples can be used for the analysis of the PL of the analyte (dye) in the pores of PAAO. S5-R1 and Se5-R1 samples demonstrated intense PL of rhodamine B in the range of 530-680 nm with a PL maximum at 573 nm (Fig. 2 and Fig.3, respectively).

The PL intensity of the dye increased sharply starting from the Rhodamine B concentration of 10^{-5} M in the samples synthesized both in sulfuric acid and in selenium acid (Figs. 2 and 3). At low dye concentrations (10^{-7}-10^{-6} M), the PL intensity was approximately the same for both types of samples. However, the PL intensity of the dye for the S5-R1 samples was more than 4 times higher than the PL intensity for the Se5-R1 samples. To identify the cause of such a significant difference, we studied the samples by EPR to identify the type of defects and determine their concentration. It was found that the main type of defects in the S5-R1 samples were oxygen vacancies with an unpaired electron (F+ centers, g=2.0020±0.0005) [3]. The concentration of F+ centers was $N_s=3\cdot10^{15}$ g^{-1}. In the Se5-R1 samples, paramagnetic complexes of the Al-SeO_3 type were found, which were built into the aluminum oxide structure from the electrolyte. F+ centers were also found in the Se5-R1 samples. The total defect concentration was $N_s=9.2\ 10^{16}$ g^{-1}. It can be assumed that the decrease in the dye PL intensity by several times in the Se5-R1 films compared to S5-R1 is due to an increase in the contribution of nonradiative recombination of photoexcited charge carriers on the detected paramagnetic defects, the concentration of which is more than an order of magnitude higher in the Se5-R1 films.

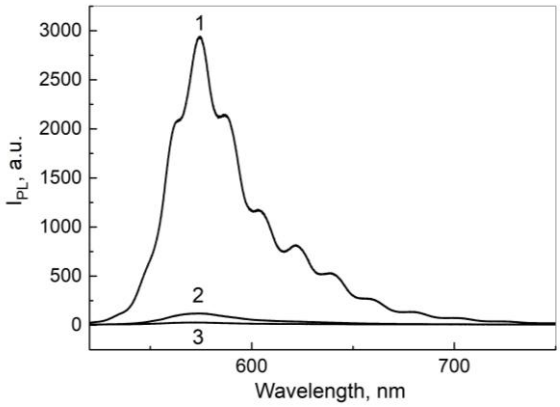


FIGURE 2. PL spectra of S5-R1 samples with different dye concentrations: 10^{-5} M (1), 10^{-6} M (2), 10^{-7} M (3).

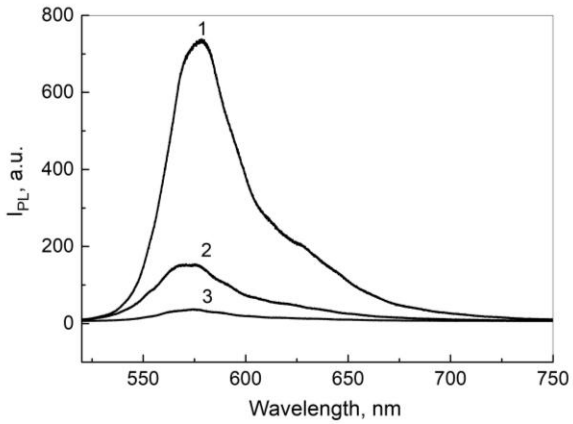


FIGURE 3. PL spectra of Se5-R1 samples with different dye concentrations: 10^{-5} M (1), 10^{-6} M (2), 10^{-7} M (3).

Thus, the exciting radiation is absorbed not only by the dye, but also by defects in the porous aluminum oxide structure.

These results are important for the creation of an optical sensor platform based on porous aluminum oxide.

The study was supported by a grant from Russian Science Foundation № 24-19-00402, https://rscf.ru/en/project/24-19-00402/.

1. Ku C.A., Yu C.Y., Hung C.W., et al. Advances in the Fabrication of Nanoporous Anodic Aluminum Oxide and Its Applications to Sensors: A Review // *Nanomaterials*. 2023. V. 13. P. 2853. DOI: 10.3390/nano13212853.
2. Eessaa A.K., El-Shamy A.M. Review on fabrication, characterization, and applications of porous anodic aluminum oxide films with tunable pore sizes for emerging technologies // *Microelectron. Eng*. 2023. V. 279. P. 112061. DOI: 10.1016/j.mee.2023.112061.
3. Khan G.G., Singh A.K., Mandal K. Structure dependent photoluminescence of nanoporous amorphous anodic aluminium oxide membranes: Role of F+ center defects // *J. Lumin.* 2013. V. 134. P. 772–777. DOI: 10.1016/j.jlumin.2012.06.050.

REDUCTION OF NITROUS OXIDE EMISSIONS IN NITRIC ACID PRODUCTION BY HIGH-TEMPERATURE CATALYTIC DECOMPOSITION ON PEROVSKITE-CONTAINING OXIDES $LaFe_{1-x}Me_xO_3$ (Me=Mn, Co, Ni)

Lyubov A. Isupova

Boreskov Institute of catalysis Russian Academy of Sciences, Novosibirsk, Russia

Among greenhouse gases, nitrous oxide has a significant global warming coefficient, about 310 times higher than that for CO_2, so reducing of N_2O emissions is an urgent task. One of the main sources of nitrous oxide entering the atmosphere is the production of nitric acid (global emissions of nitrous oxide in the production of nitric acid are about 300–400 kt/year), in which nitrous oxide is formed in the process of non-selective catalytic oxidation of ammonia on platinoid catalyst grids, as well as in secondary processes in the space after the grids during the interaction of the main product - nitric oxide - with ammonia that has slipped through the catalyst grids. Monitoring of the units has shown that in the Russian Federation the main sources of nitrous oxide emissions are the UKL-7 and AK-72M units equipped with low-temperature NOx purification based on the process of SCR NO with ammonia.

One of the ways to reduce nitrous oxide emissions in the production of nitric acid, which does not require significant modernization of the units, is the high-temperature catalytic decomposition of nitrous oxide on the catalyst layer, which is located after the platinoid grids (along the gas flow) in the ammonia oxidation reactor [1]. In this case, the catalyst must be active and stable under the conditions of the reaction environment formed after the platinoid grids (850-900°C, ~ 10% NO, 1000-2000 ppm N_2O, linear gas velocities ~ 3-6 m/s), decompose nitrous oxide and do not decompose the reaction product – nitric oxide, and are also characterized by low gas-dynamic resistance, which can be provided by using of honeycomb catalysts.

ABO_3 perovskites such as $LaFeO_3$, $LaCoO_3$, $LaMnO_3$ and $LaNiO_3$ are known to be active in the high-temperature decomposition reaction of nitrous oxide due to their physicochemical properties. The properties of ABO_3 perovskites can vary significantly depending on the nature of the A and B cations, their stoichiometric ratio, or when substituting cations are introduced into sublattices A and/or B. For example, the introduction of Sr into the La sublattice in the $La_{1-x}Sr_xMnO_3$ or $La_{1-x}Sr_xFeO_3$ systems leads to an increase in the activity of oxides, as does the introduction of Co into the Fe sublattice in the $LaFe_{1-x}Co_xO_3$ system, but up to a certain x [2-4]. Another factor influencing the activity of perovskites is the preparation method, which determines not only the size of the specific surface area, but also the features

of the microstructure of oxides [5]. One of the promising methods for obtaining honeycomb catalysts is the application of the active component to honeycomb carriers by impregnation from polymer-salt compositions [6]. After heat treatment, the method ensures the formation of a strong homogeneous catalytically active oxide layer on the the surface of channels. At the same time, there was no information in the literature on a systematic study of the effect of the degree of substitution and the nature of the replacement cation in sublattice B in $LaFe_{1-x}Me_xO_3$ (Me=Mn, Co, Ni) systems prepared from polymer-salt compositions.

Therefore, the object of this study is the perovskites $LaFe_{1-x}Me_xO_3$ Me = Mn, Co, Ni; x=0–1) prepared by the Pechini method, which were studied in the reaction of high-temperature decomposition of nitrous oxide, and their physicochemical properties were characterized by the methods of X-Ray, BET, EM, XPS, H_2-TPR. Oxides $LaFe_{1-x}Me_xO_3$ Me=Mn, Co, Ni; x=0–1) were prepared using solutions of a mixture of nitric acid and salts taken in a stoichiometric ratio, to which citric acid and ethylene glycol were added. After evaporation of solutions at 70-80°C, the resulting polymer-salt compositions burned during their drying, the resulting powders were then calcined at 900 ˚C.

The catalytic activity in the nitrous oxide decomposition reaction was determined in a flow-through reactor in the temperature range of 750-900 °C for a catalyst fraction of 0.25-0.5 mm at a contact time of 0.001 s using a reaction mixture of 0.15% N_2O, + 3% O_2 + 3% H_2O in helium. It was preliminarily established that there was no homogeneous process in the reactor, as well as the absence of intra- and external-diffusion restrictions.

It has been shown that the replacement of iron in lanthanum ferrite with cations Mn, Co, and Ni leads to the formation of single-phase $LaFe_{1-x}Me_xO_3$ perovskites, in which, with an increase in x, morphotropic phase transitions occur from orthorombic to rhombohedral modification at x ~ 0.6 for Mn and at x ~ 0.4 for Co and Ni cations. The introduction of substitute cations leads to a decrease in the cell parameters of $LaFe_{1-x}Me_xO_3$ oxides relative to $LaFeO_3$ in all cases due to the formation of homogeneous solid solutions, since the sizes of the substituting cations Co^{3+} and Ni^{3+} in the octahedral environment are smaller than the Fe^{3+} cation. For Mn^{3+} cation with an ionic radius close to Fe^{3+}, the decrease may be due to the formation of Mn^{4+} cations in $LaFe_{1-x}Mn_xO_3$ oxides, according to [7].

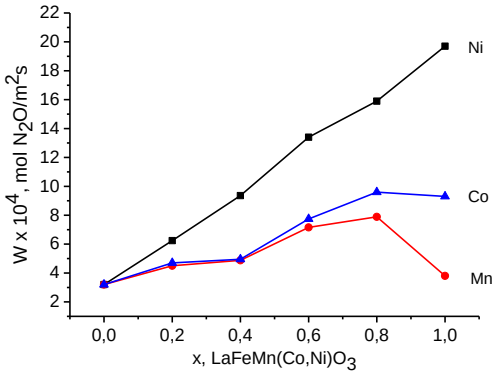


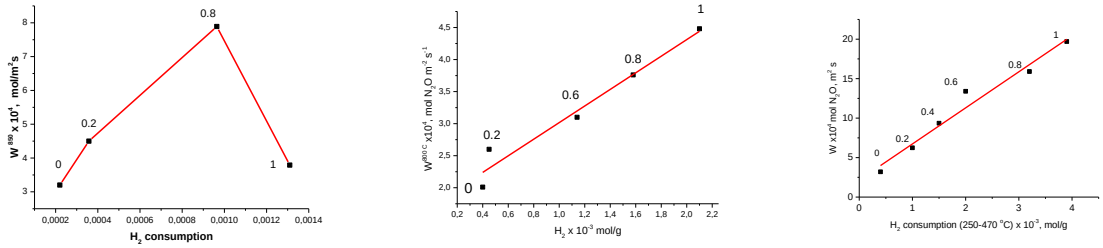
FIGURE 1. Dependence of the reaction rate of nitrous oxide decomposition at 850 °C on the composition of $LaFe_{1-x}Me_xO_3$ perovskites.

It has been established that an increase in the test temperature and the introduction of substituents lead to an increase in the conversion of nitrous oxide. Figure 1 shows the change in the rate of nitrous oxide decomposition reaction determined at 850 °C, depending on the composition of perovskites. It can be seen that the activity of $LaFe_{1-x}Me_xO_3$ oxides is higher than that of $LaFeO_3$. The largest increase, proportional to the degree of substitution, is observed in the $LaFe_{1-x}Ni_xO_3$ system. Although the activity increases with increasing x, the extreme terms – $LaMnO_3$, $LaCoO_3$ are not characterized by the highest activity in the corresponding $LaFe_{1-x}Me_xO_3$ oxides (Figure 1).

After longer tests at 900 °C, it was shown that the activity of $LaFe_{1-x}Ni_xO_3$ samples (x = 0.8 and 1) decreases and the maximum activity and stability is characterized by the $LaFe_{0.4}Ni_{0.6}O_3$ sample the activity (reaction rate) of which is 5 times higher than activity of $LaFeO_3$, while the activity of the most active $LaFe_{0.2}Mn_{O.8}O_3$ and $LaFe_{0.2}Co_{O.8}O_3$ oxides are ~2-3 times higher, respectively. These oxides in heating/cooling processes up to 900 ºC do not undergo polymorphic transitions, which is important for

the formation of strong active films on the surface of high-temperature honeycomb carriers (cordierite, corundum, silicon carbide, etc.).

According to H_2-TPR data, the introduction of substituents leads to an improvement in the reduction of oxides relative to $LaFeO_3$ (Figure 2). Linear correlations are observed between the rate of decomposition of N_2O for $LaFe_{1-x}Ni_xO_3$ (at a temperature of 850 °C) and $LaFe_{1-x}Co_xO_3$ (at a temperature of 800 °C) and the amount of hydrogen absorbed by the samples, which is consistent with the proposed reaction mechanism, according to which the limiting stage is the oxygen desorption step [8]. The deviation from this dependence at a process temperature of 900 °C for samples of $LaMnO_3$, $LaNiO_3$ and $LaCoO_3$ is due either to a change in the rate of the determining stage of the reaction ($LaMnO_3$) [9,10], or to the instability of the oxide in the reaction medium at high temperatures ($LaNiO_3$ and $LaCoO_3$) [11].



a b c

FIGURE 2. Dependence of the reaction rate on the amount of absorbed hydrogen up to ~ 450 °C for a - $LaFe_{1-x}Mn_xO_3$; b - for $LaFe_{1-x}Co_xO_3$; c - for $LaFe_{1-x}Ni_xO_3$.

Preliminary catalytic studies of block catalysts $LaFeO_3/\alpha\text{-}Al_2O_3$, $LaFe_{0.4}Ni_{0.6}O_3/\alpha\text{-}Al_2O_3$, $LaNiO_3/\alpha\text{-}Al_2O_3$prepared by impregnating block corundum carriers with solutions of polymer-salt compositions were carried out. The role of the carrier is revealed. The high activity of the $LaFe_{0.4}Ni_{0.6}O_3$ catalyst supported on the modified $\alpha\text{-}Al_2O_3$ carrier has been demonstrated. At a contact time of 0.06 s, the block catalyst provides a ~90% conversion rate.

The work was carried out with the financial support of the Ministry of Science and Higher Education of the Russian Federation as part of the state assignment of the Institute of Catalysis of the Siberian Branch of the Russian Academy of Sciences, project FWUR-2024-0038.

1. Pérez-Ramirez J., Kapteijn F., Schöffel K., Moulijn J.A. Formation and control of N_2O in nitric acid production: Where do we stand today? // *Applied Catalysis.* 2003. V. 44. P. 117–151. DOI:10.1016/S0926-3373(03)00026-2.
2. Ivanov D.V., Pinaeva L.G., Isupova L.A., Prosvirin I.P., Dovlitova L.S. Insights into the reactivity of $La_{1-x}Sr_xMnO_3$ (x = 0 ÷ 0.7) in high temperature N_2O decomposition // *Cat. Letters*. 2011. V. 141. P. 322–331. DOI: 10.1007/s10562-010-0503-0.
3. Ivanov D.V., Pinaeva L.G., Isupova L.A., et al. Effect of surface decoration with $LaSrFeO_4$ on oxygen mobility and catalytic activity of $La_{0.4}Sr_{0.6}FeO_{3-\delta}$ in high-temperature N_2O decomposition, methane combustion and ammonia oxidation // *Applied Catalysis A: General*. 2013. V. 457. P. 42–51. DOI: 10.1016/j.apcata.2013.03.007.
4. Wu Y., Cordier C., Berrier E., et al. Surface reconstructions of $LaCo_{1-x}Fe_xO_3$ at high temperature during N_2O decomposition in realistic exhaust gas composition: Impact on the catalytic properties // *Applied Catalysis B: Environmental.* 2013. V. 140–141. P. 151–163. DOI: 10.1016/j.apcatb.2013.04.002.
5. Bělina P., Sádovská G., Krejčíková V., Dohnalová Ž., Šulcová P. Preparation of $LaNiO_3$ perovskite by oxalate and carbonate precursor method for utilization as catalyst for high-temperature

decomposition of N_2O // *J. of Thermal analysis and Calorimetry*. 2019. V. 138. P. 4197–4202. DOI: 10973-019-08596-9.
6. Patent Ru 430781, 2011.
7. Tarjomannejad A., Farzi A., Gómez M.J.I., et al. Catalytic Reduction of NO by CO over $LaMn_{1-x}Fe_xO_3$ and $La_{0.8}A_{0.2}Mn_{0.3}Fe_{0.7}O_3$ (A = Sr, Cs, Ba, Ce) Perovskite Catalysts // *Catal. Lett*. 2016. V. 146. P. 2330–23.
8. Kaptein F., Rodriguez-Mirasol J., Moulijn J.A. Heterogeneous catalytic decomposition of nitrous oxide // *Applied Catalysis B: Environmental.* 1996. V. 9. P. 25–64. DOI: 10.1016/0926-3373(96)90072-7.
9. Ivanov D.V., Pinaeva L.G., Sadovskaya E.M., Isupova L.A. Isotopic transient kinetic study of N_2O decomposition on $LaMnO_{3+\delta}$ // *Journal of Molecular Catalysis A: Chemical*. 2016. V.412. P. 34–38. DOI: 10.1016/j.molcata.2015.11.018.
10. Isupova L.A., Rogov V.A., Gerasimov E.Y., Prosvirin I.P. Influence of the $LaMn_{1-x}Fe_xO_3$ (x = 0 - 1) Composition on Catalytic Activities in the Reactions Involving Oxygen // *Catalysts*. 2022. V.12. No 12. P. 1563. DOI:10.3390/catal12121563.
11. Isupova L.A., Ivanova Y.A., Prosvirin I.P., Gerasimov E.Y. $LaFe_{1-x}Ni_xO_3$ Perovskites in the Catalytic Reaction of High-Temperature Decomposition of Nitrous Oxide // *Dalton Transactions.* 2024. V. 53. P. 15273–15283. DOI: 10.1039/d4dt01897d.

SPIN PROBE STUDY OF POLYMER CHAIN COLLAPSE IN PNIPAM-b-PEG COPOLYMERS

Timofei D. Shatrov[1], Georgii A. Simenido[1], Elena A. Ivanova[1], Elena V. Chernikova[1] and and Elena N. Golubeva[1,2]

[1]Faculty of Chemistry, Lomonosov Moscow State University, Moscow, Russia
[2]Institute for Regenerative Medicine, Sechenov First Moscow State Medical University, Moscow, Russia

Thermoresponsive polymers remain attractive due to the ability to change solubility dramatically with temperature changes. Polymers with lower critical solution temperature (LCST) are soluble at low temperatures. When heated above LCST, they become unsoluble and undergo polymer chain collapse and phase separation. One of the most well-known thermoresponsive polymers is poly(N-isopropylacrylamide) (PNIPAM) [1]. The LCST of an aqueous solution of poly(N-isopropylacrylamide) (PNIPAM) is in the vicinity of the physiological range and is 32 °C, which determines its wide application in tissue engineering and selective drug delivery [2]. LCST can be altered by copolymerization (hydrophilic and hydrophobic comonomers increase and decrease LCST, respectively) [3] and solution composition (pH, ionic strength, etc.) [3].

The EPR spectroscopy method within the framework of the spin probe technique is actively used to study the dynamics of the phase transition of thermoresponsive polymers. The local probe environment affects the EPR spectrum lineshape and probe spin-Hamiltonian parameters (g-factor and hyperfine coupling constant), which allows us to estimate the micropolarity and microviscosity of the probe environment [4]. Earlier, using this approach, it was shown that the process of chain collapse in PNIPAM aqueous solutions begins with the formation of local inhomogeneities at temperatures below the LCST. These inhomogeneities are characterized by lower polarity and higher viscosity compared to bulk solution [5].

Objects of present study were PNIPAM (Mn = 13.2 kDa, PDI = 1.2) and its block copolymer with polyethyleneglycol (PNIPAM-*b*-PEG, Mn = 13.2 kDa, Mn(PEG) = 2.0 kDa, PDI = 2.0) [6] in 10wt% aqueous solutions. The dynamics of inhomogeneities was studied with nitroxyl radical TEMPO as a spin probe. Spectrum below LCST corresponds to fast isotropic motion of probe in bulk solution, its spin-Hamiltonian parameters correspond to TEMPO in pure water. This type of probe particles will be denoted as type **A** (Fig. 1, A). Spectra at temperatures above LCST consist of two types of particles: some probes are located in bulk solution (type **A**), and another are captured by forming polymer inhomogeneities (type **B**) (Fig. 1, A). Suppression of type **A** probes signal with Cu^{2+} ions [7,8] was used to obtain separate spectrum of type **B** particles (Fig. 1, B).

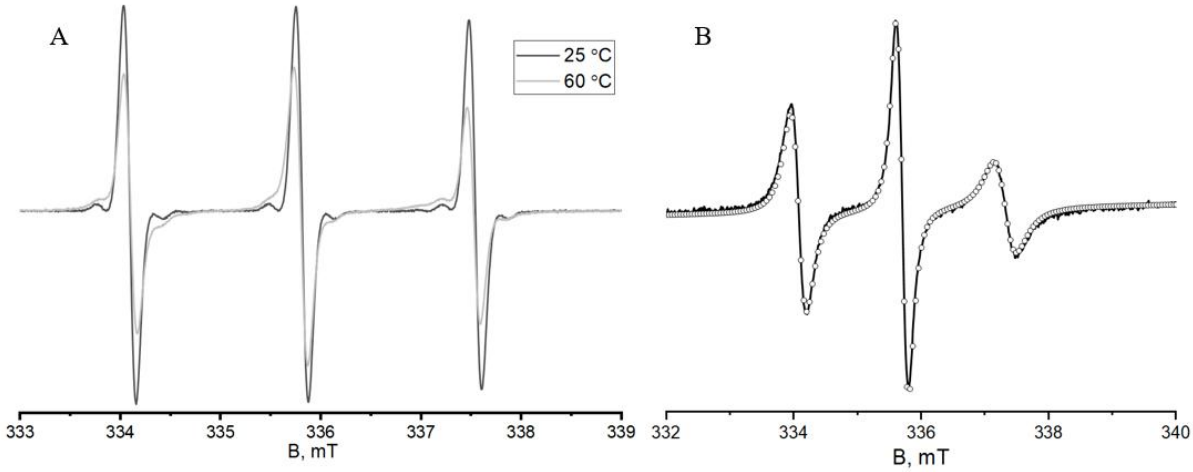


FIGURE 1. EPR spectra of TEMPO in 10wt% PNIPAM below and above LCST (A). EPR spectrum of TEMPO in 10wt% PNIPAM / 0.3M Cu^{2+} solution, t = 60 °C. (B). Experimental spectrum (solid line), simulated spectrum (circles).

This spectrum was successfully simulated with parameters a_{iso} = 1.62mT, t_{iso} = 2.6 ns, which is in agreement with previous results obtained for PNIPAM with higher molecular mass [8]. These parameters were used to simulate joint spectra of **A** and **B** particles, which resulted in temperature dependencies of type **B** probes fraction (Fig. 2, A) and hfc constant (Fig. 2, B).

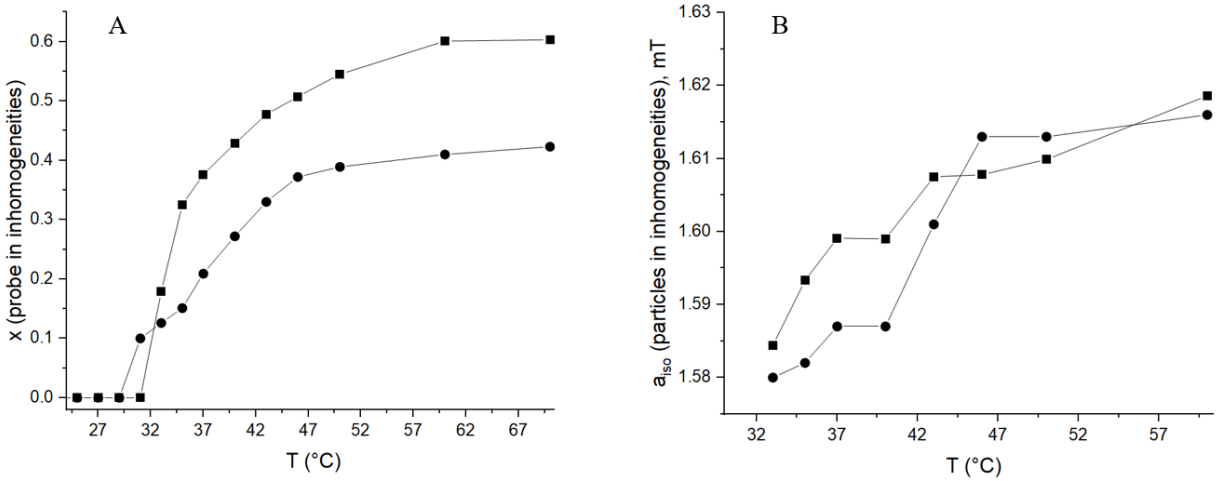


FIGURE 2. Temperature dependencies of type B probes fraction (A) and isotropic hfc constant (B). 10% PNIPAM solution (squares), 10% PNIPAM-b-PEG solution (circles).

According to the a_{iso} value of type **B** particles, the local polarity inside the polymer inhomogeneities is lower than in the bulk solution and is close to that in chloroform [4]; The increase in the hfc coupling constant of type **B** particles with temperature (Fig. 1 A) indicates the possibility of probe exchange between the inhomogeneities and the environment and the dynamic nature of the inhomogeneities [5]. In contrast, high molecular PNIPAM studied earlier possessed static inhomogeneities [ссылка], which indicates more dense globule structure in this case. Comparison of the temperature dependences of the fraction of probe particles in the inhomogeneities of PNIPAM and PNIPAM-*b*-PEG indicates that in the first case a wider temperature range of polymer chain collapse is observed.

1. Heskins M., Guillet J.E. Solution Properties of Poly(N-isopropylacrylamide) // *Journal of Macromolecular Science: Part A - Chemistry*. 1968. V. 2. No 8. P. 1441–1455.
2. Ward M.A., Georgiou T.K. Thermoresponsive polymers for biomedical applications // *Polymers*. 2011. V. 3. No 3. P. 1215–1242. DOI: 10.3390/polym3031215.
3. Hoogenboom R. 2-Temperature-Responsive Polymers: Properties, Synthesis, and Applications // *Smart Polymers and their Applications*. 2019. P. 13–44. DOI: 10.1533/9780857097026.1.15.
4. Hinderberger D. EPR spectroscopy in polymer science // *Top Curr Chem*. 2012. V. 321. P. 67–90. DOI: 10.1007/128_2011_236.
5. Kurzbach D., Junk M.J.N., Hinderberger D. Nanoscale inhomogeneities in thermoresponsive polymers // *Macromol Rapid Commun*. 2013. V. 34. No 2. P. 119–134. DOI: 10.1002/marc.201200617.
6. Ivanova E.A., Vlasov E.I., Bekanova M.Z., Simenido G.A. et al. Aqueous RAFT (co)polymerization of N-isopropylacrylamide above lower critical solution temperature of poly(N-isopropylacrylamide) and stimuli-responsive properties of the polymers formed // *Mendeleev Communications*. 2025. V. 35. No 1. P. 108–111. DOI: 10.71267/mencom.7545.
7. Caragheorgheopol A., Schlick S. Hydration in the various phases of the triblock copolymers EO13PO30EO13 (Pluronic L64) and EO6PO34EO6 (Pluronic L62), based on electron spin resonance spectra of cationic spin probes // *Macromolecules*. 1998. V. 31. No 22. P. 7736–7745. DOI: 10.1021/ma980982g.
8. Zubanova E.M., Kostjuk S.V., Timashev P.S., Rochev Y.A., Kokorin A.I., Melnikov M.Y., Golubeva E.N. Inhomogeneities in PNIPAM Aqueous Solutions: The Inside View by Spin Probe EPR Spectroscopy // *Polymers*. 2021. V. 13. No 21. P. 3829. DOI: 10.3390/polym13213829.

THEORETICAL FOUNDATION FOR OPTICAL DIAGNOSTICS METHODS TO MONITOR THE STATISTICAL STATE OF RANDOMLY NONUNIFORMED DISORDERED MEDIA

Yulia A. Chaikina, Anatolii I. Shushin and Maxim G. Golubkov

Semenov Federal Research Center for Chemical Physics, Russian Academy of Sciences, Moscow, Russia

Optical and spectral methods of diagnostics require theoretical approaches that allow us to bring the peculiarities of measurement data in line with the peculiarities of the state of media. The start of our work was set by experimental results obtained nearby critical point in 1980-2010: broadening of vibration bands and line shifts behavior in the Raman spectra of N_2, CO_2, O_2 and some other fluids and small-angle distribution of critical opalescence (anomalous Rayleigh light scattering) in critical CO_2.

All these effects are not in line with modern theory of critical fluids. So they were supposed to be right framework for optical diagnostics studies.

Besides, critical media possesses both phenomena of forming spatial nonuniformity in unordered media. The first is due to dynamics of molecules in small groups and it is described with the help of pair correlation function F_2. The second is due to thermal molecular movement and it is described in terms of density variance and density correlations. Note that the basic one is density nonuniformity formed by some physical phenomena such as density fluctuations in critical fluids or turbulence and transfer processes in atmosphere.

So we suggest in [1] next combined model for light scattering. Single scattering will be considered and the fact will be taken into account that before and after the scattering event light propagates in the dielectric medium with the refractive index that is randomly nonuniform. Therefore, geometrical path will be substituted by the optical one when evaluate the phases of the scattered light.

We started with Rayleigh light scattering measurements done in [2] with the results which fundamentally differs from the Ornstein–Zernike angle distributions. The estimation of the Poynting vector performed with the help of scattering model that is described above fit well the distinctive features of the experiment [2], see Fig.1.

In sum the proposed scattering model seemed to be supported, so we use it to run the first diagnostics for reduced density variance and density correlation length of critical fluid based on the optical measurements [2]. For the results see Fig.2. The ranges of values shown at Fig.2 were discussed in [3] and they were supposed to be realistic ones. The temperature behavior of these values differs strikingly from those dictated by the modern theory of the critical state. In particular, when passing from supercritical to subcritical temperatures through the critical point, a peculiar "step" in density variance is noticed rather than a power-law divergence. In [4] we used an integral equation well known in Dirac delta function theory to obtain a power-law dependence for density variance on temperature: $\sim|\tau|^{-0.05}$. This dependence becomes more complicated when approaching the critical point $|\tau| \sim 10^{-8}$, but does not demonstrate divergence, much less power divergence.

This made it possible to find the pair correlation function by solving "fluctuation theorem": the integral equation that expresses the relation between density variance and the pair correlation function. The first attempt was done in [4].

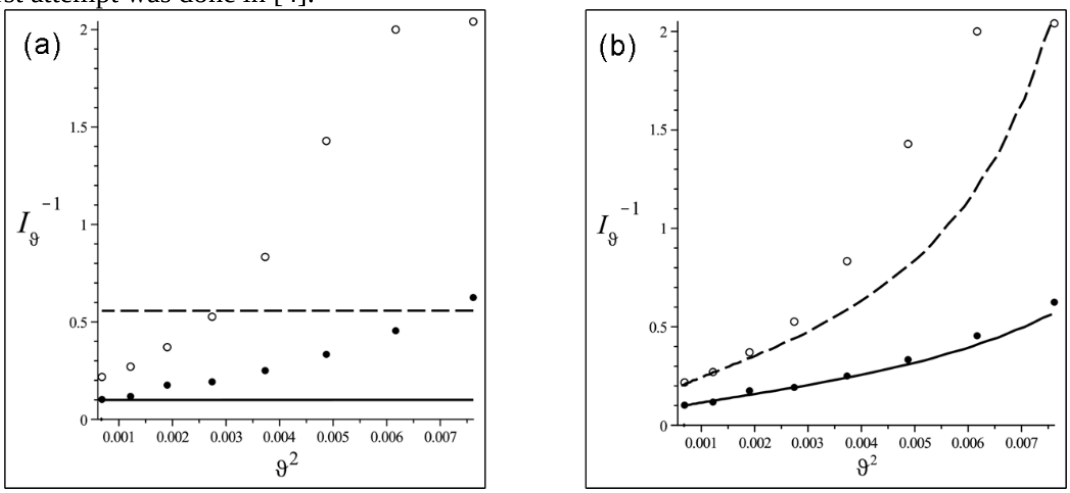


FIGURE 1. Ornstein-Zernike plots for data [2] (circles) as against theoretical data (lines). Note that experimental distributions in [2] are presented in relative units. To combine the curves, the Ornstein-Zernike plots are renormalized by one factor. Horizontal axe - squared scattering angle in rad. Vertical axe – inversed meanings of scattered light intensity (lines): (a) - for Ornstein - Zernike intensity distribution. It is seen that plots are practically flat. (b) - for estimations done in [1] with the help of combined scattering model. Open circles and dash line are

for temperature T=1.00001 T_{crit}, solid circles and solid line are for temperature T=0.99998 T_{crit}; T_{crit} is critical temperature, density is critical.

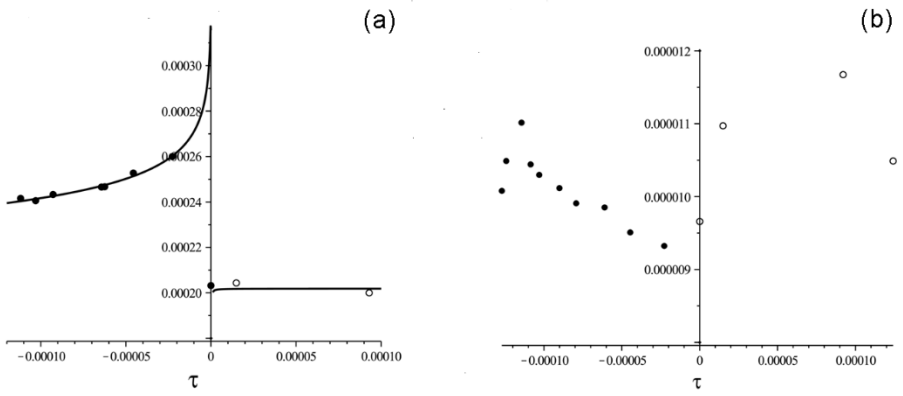


FIGURE 2. Temperature dependence for variance and correlation length of critical density fluctuations along the critical isochor; restored in [3,4] according to the data of [2]. Open circles are for $T>T_{crit}$, solid circles are for $T<T_{crit}$. Horizontal axe - $\tau = (T - T_{crit})/T_{ctit}$. (a) reduced density variance; line is for analytical approximation obtained in [4] (b) density correlation length (m).

The investigations were continued in [5] where we gave up the assumptions which makes the Ornstein – Zernike theory unusable for the needs of optical diagnostics, first of all we didn't consider the shape of the scattering light to be Lorentzian. The objective of the study is provided in [5] is to propose an approach to find the pair correlation function of the critical state assuming variance and correlation length of critical density fluctuations to be parameters of the problem and supposing these parameters can be detected by optical measurements. This will create a reliable theoretical basis for optical diagnostics of the critical state of fluid. In [5] we got the preliminary results, see Fig. 3. The studies are to be continued.

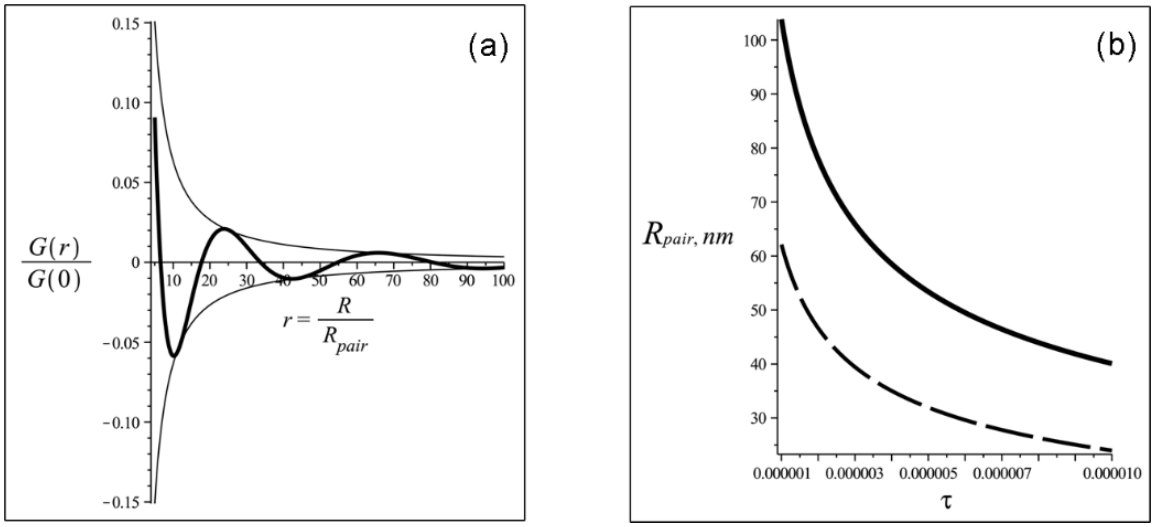


FIGURE 3. According to approach suggested in [2024]: (a) large-scale analytical asymptotic for normalized total correlation function $G=F_2$-1 (solid line). The thin solid line is the envelope of the correlation function $G \sim R^{-1.25}$.

Note that Ornstein – Zernike total correlation function is of $\sim R^{-1}$. R is intermolecular distance, R_{pair} is radius of pair correlations. (b) temperature dependence for R_{pair} (nm); $R_{pair} \sim |\tau|^{-\gamma/3}$, γ=1.24.

Let sum up the results. The analytics for pair correlation function allow us to continue the optical diagnostics of critical state based on the distinctive features of critical Raman spectra such as critical broadening of vibration bands and critical line shifts behavior. The combined model for light scattering proposed in [1] seems to be flexible and can be applied easily to any unordered nonuniform media including the atmosphere.

This study was carried out in the framework of State Assignment of the Ministry of Science and Higher Education of the Russian Federation (project № 125012200611-5).

1. Chaikina Y. A., Umanskii S. Y. Peculiarities of the small-angle scattering of laser radiation by critical CO_2 // *Chem. Phys.* 2020. V. 536. 110795. DOI: 10.1016/j.chemphys.2020.110795.
2. Zimnyakov D. A., Sviridov A. P., Konovalov A. N., Bagratashvili V. N. Small-Angle Light Scattering on Density Fluctuations of Supercritical Carbon Dioxide under the Conditions of Fast Cooling // *Sverkhkrit. Fluidy: Teor. Prakt.* 2008. V. 3. No 3. P. 30–38.
3. Chaikina Y. A., Umanskii S. Y. Diagnostics of the Critical State of Carbon Dioxide // *Russ. J. Phys. Chem. B.* 2021. V. 15. No 8. P. 1266–1272. DOI: 10.1134/S1990793121080029.
4. Lundin A. A., Chaikina Y. A., Shushin A. I., Umanskii S. Y. On the Capabilities of Optical Diagnostics Methods to Monitor the State of Supercritical Fluids near the Widom Line // *Russ. J. Phys. Chem. B.* 2022. V. 16. No 8. P. 1361–1370. DOI: 10.1134/S1990793122080115.
5. Chaikina Y. A., Vetchinkin A. S., Golubkov M. G., et al. Pair correlation function for equilibrium critical state of fluids on the mesoscopic space scale // *Sverkhkrit. Fluidy: Teor. Prakt.* 2024. V. 19. No 2. P. 59–81. DOI: 10.34984/SCFTP.2023.19.2.005.

POLYMERIZATION IN SUPERCRITICAL CARBON DIOXIDE: NOVEL APPROACH TO SYNTHESIS OF TERMORESPONSIVE POLYMERS

Anastasiia A. Popova[1,2], Valentina L. Lisina[1], Ekaterina A. Litmanovich[1] and Elena N. Golubeva[1,2]

[1]Department of Chemistry, Lomonosov Moscow State University, Russia
[2]Institute for Regenerative Medicine, Sechenov First Moscow State Medical University, Moscow, Russia

Supercritical carbon dioxide (SC CO_2) is a promising medium that allows for adjusting its properties (diffusivity, density, solvation capacity) simply by varying the system's parameters (T, P). Its lack of toxicity and comparatively low parameters of the critical point (31°C, 73.8 bar) make SC CO_2 a great substitute for organic solvents traditionally used in the synthesis of medical polymers, such as poly-N-isopropylacrylamide (PNIPAM) [1]. PNIPAM features thermoresponsive properties near physiological temperatures (lower critical solution temperature (LCST)~32 °C). In aqueous solutions PNIPAM undergoes coil to globule transition along with aggregation in response to an increase in temperature. That fact makes it a suitable material for use as carrier in drug delivery systems or as a substrate in tissue engineering [2]. However, latest data show that not only does the choice of medium affect such characteristics of PNIPAM as molecular weight and polydispersity, but it also alters the

lower critical solution temperature [3]. Therefore, there's a need for an alternative route of synthesis that minimizes traces of the solvent, and hence reduces their impact on polymer properties.

Advances have been made in the radical polymerization of vinyl monomers in SC CO_2. Evidence suggests that the mechanism of the reaction may differ from that of its organic counterpart. Shieh and Chen, for example, have shown that the polymerization of poly-N-isopropylacrylamide using SC CO_2 as a solvent yields a polymer with 4-5 times higher molecular mass than that in methanol, let along higher conversions of the monomer consumed in the given time period. Moreover, Ana A. C. Pacheco et al. reported that the performance of the RAFT agent, 2-(dodecylthiocarbonothioylthio)-2-methylpropionic acid (DDMAT), in the synthesis of polymethylmethacrylate is drastically affected by the substitution of the media from toluene to SC CO_2, resulting in control over polymer chain growth and, consequently, a narrower mass molecular mass distribution of the polymer.

Nevertheless, there's little information available in the literature on the reactivity of N-isopropylacrylamide (NIPAM) in either controlled or free radical polymerization in SC CO_2 up until this day. Therefore, the goal of this study is to establish kinetic patterns for NIPAM, as well as to reveal the relationship between parameters of SC CO_2 and the properties of the resulting PNIPAM.

Kinetics of the PNIPAM synthesis were obtained for both controlled (reversible addition-fragmentation chain transfer (RAFT)) and free radical polymerization (FRP) mechanisms within conditions' range T = 60-80 °C, P = 90-325 bar, C_{NIPAM} = 3.8 wt/vol%. So as to control growth of polymer chain following RAFT agents were introduced into reaction mixture DDMAT, S,S'-bis(α,α'-dimethyl-α''methyl acetate) trithiocarbonate (BDMMAT). The ratio of the reagents $[M]_0/([RAFT]_0)/[I]_0$ was set to 500/(3)/1 for either process.

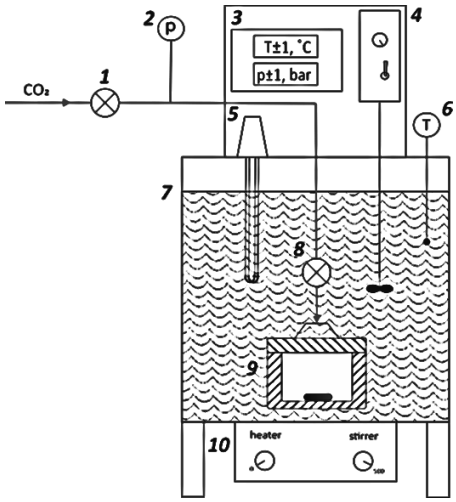


FIGURE 1. Schematic diagram of a high-pressure polymerization unit: (1, 8) valves; (2) pressure transducer; (3) PID regulator; (4) mechanical stirrer; (5) heater; (6) thermocouple; (7) polypropylene thermostat housing; (9) high-pressure cell; (10) magnetic stirrer.

NIPAM polymerization was carried out in a high-pressure reactor of 10.36 mL equipped with a magnetic stirrer, water thermostat, and pressure converter (Fig. 1). After the set time, the reactor was placed in an ice bath for 10 minutes until the system had completely cooled to 5°C. The CO2 was then removed from the system by passing it through a water trap. In some cases, purification of the monomer from the polymer solution was carried out by dialysis through a membrane with a molecular weight cut of 500 Da for a week. Then, PNIPAM was freeze-dried. The molecular characteristics of the PNIPAM were determined using gel-penetrating chromatography. To calculate the monomer conversion, the NMR signals corresponding to protons of the amide group (–CH2–NH–) were analyzed in the polymer (a widened signal at δ=3.9–4.0ppm) and the monomer (δ=4.15ppm). The ratio of the area under the proton signal at 3.9-4.0 to the sum of areas under peaks for both the polymer and the monomers was used as a measure of conversion. Aqueous solutions of RAFT and FRP PNIPAM samples were characterized using light scattering and EPR spectroscopy.

The LCST of the 6.7% mass solutions was determined by analyzing the temperature dependence of the reduced intensity of the high-field spectral component for the spin probe 2,2,6, 6-tetramethyl-piperidine-l-oxide (TEMPO). The cytotoxicity of SCF polymerization products was assessed by culturing mesenchymal stromal cells from human adipose tissue.

Polymerization of NIPAM under conditions of T = 60-80 °C and P = 325 bar, carried out in the absence of RAFT agent, corresponds to homogeneous precipitation polymerization. All kinetic curves corresponding to FRP process are characterized by a pronounced induction period. The duration of this period is 0.34, 2, and 3.5 hours at temperatures of 80°C, 70°C and 60°C, respectively (Fig. 2).

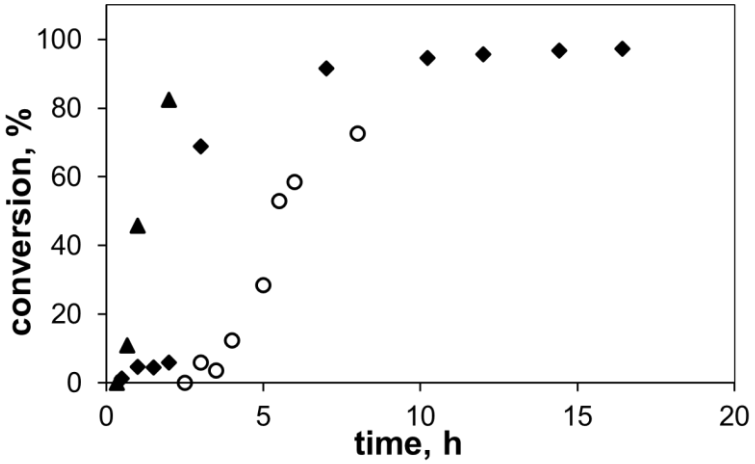


FIGURE 2. NIPAM conversion during polymerization at 325 bar and T: ○ 60 ℃, ♦ 70 ℃, ▲ 80 ℃.

Even with a low NIPAM conversion's level, the polydispersity coefficient (PD) exceeds 1.5 for each temperature within the studied range. The most significant increase in polydispersity occurs at conversions below 10%. The polydispersity remains relatively constant above 10% conversion at 60°C, reaching values of approximately 4.0±0.2. In contrast, at higher temperatures of 70°C and 80°C, the polydispersity increases continuously throughout the reaction time. According to the GPC data, the molecular mass distribution (MMR) is unimodal for conversions up to 10% NIPAM. The predominant masses of the growing chains were $1.15x10^6$, $1.5x10^5$, and $3.8x10^4$ at temperatures of 60, 70, and 80 °C, respectively. The end of the induction period was accompanied by a broadening of the MMR and a shift towards a bimodal weight distribution at each temperature. The higher MW shoulder occurs at 3.3×10^6 for 60 °C, 3.7×10^6 for 70 °C, and 3.2×10^6 for 80 °C.

Interestingly, the addition of either RAFT agent to the reaction mixture causes phase separation in the system. This results in two parallel radical polymerization reactions taking place: polymerization of NIPAM via FRP in the upper phase and polymerization via RAFT process in the lower phase. The reason for this is the affinity of the organic RAFT agents for the NIPAM-rich phase, which has a higher density. The kinetic curves of the NIPAM in such processes don't differ from those observed for FRP. Given that the initial concentrations of the reactants are relatively low, their faster diffusion in the SC CO_2 medium is not beneficial and results in products with high polydispersity indices ranging from 6 to 10. In fact, the use of RAFT agents to reduce the MMR of products is revealed under milder conditions, such as T and P, close to the critical point of CO_2. This approach allows one to minimize the solvation ability of a CO_2-enriched phase, which continuously increases with pressure at a constant temperature. As a result, the polydispersity indices of the PNIPAM samples obtained using this method vary from 1.18 to 2.7 for DDMAT, while remaining comparatively constant (1.35) throughout a reaction when BDMMAT is used as the RAFT agent.

The aqueous solutions of the polymers synthesized in similar conditions via FRP (70 °C and 325 bar, P1) and RAFT (70 °C and 229 bar, P2) polymerization were characterized by light scattering techniques. The particle size distribution of polymer P1 is unimodal (71 nm), whereas for P2 it is bimodal (10 and 45 nm) with average masses of 7.3×10^6 and 4.1×10^5 MM, respectively. The form

factor (R_g/R_h) of the polymer was 1.35 for P1 and 1.11 for P2, which is typical of branched (starlike) polymers (P1) and hyperbranched polymers (P2).

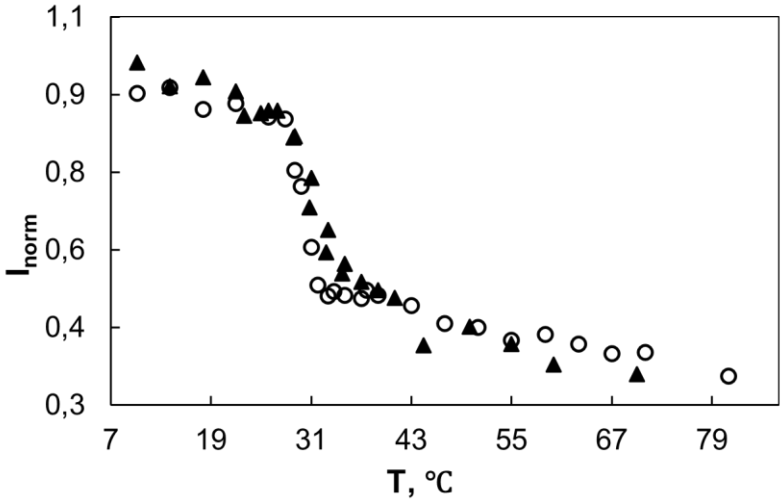


FIGURE 3. The temperature dependence of the normalized amplitude of the high-field component for polymers: ○ P1, ▲ P2.

LCSTs were determined for the polymers in question by means of EPR spectroscopy as a temperature where the sharp drop in intensity of the high field component is observed. The ratio of the intensities of the medium- and high-field components of the signal increases as temperature approaches the LCST. At a certain point, a new signal appears, corresponding to a spin probe localized in polymer globules with higher viscosity and lower polarity. This results in a shift and broadening of the lines compared to the spectrum of TEMPO in aqueous solution. The onset of the change in spectral shape corresponds to temperatures of 28 and 29 °C for samples P1 and P2, respectively. The range of temperatures over which the amplitude decreases is 3 °C for P1 and 14 °C for P2, due to the bimodal nature of the RAFT polymerization product (Fig. 3).

In terms of cytotoxicity, it has been shown that the metabolic activity of cells remains virtually unchanged (~100%) over the entire range of polymer concentrations (0.08 to 20 mg/ml). The dynamics in the amount of dsDNA with increasing polymer concentration has also revealed that the resulting polymer does not exhibit a toxic effect. Therefore, it was established that PNIPAM (conversion > 95%) obtained in the media of SC CO_2 can be used without further purification.

Thus, the study gives an outlook on the SC CO_2 use as promising media to the synthesis of thermoresponsive PNIPAM primarily taking into consideration both SC CO_2 tunable solvation capacity and diffusivity. On top of that, this work reveals the structure of the PNIPAM macromolecules and determines the way those features affect the LCST.

This investigation was performed with the financial support provided by the Russian Science Foundation (project no. 24-23-00196).

1. Kendall J.L., Canelas D.A., Young J.L., DeSimone J.M. Polymerizations in Supercritical Carbon Dioxide // Chem. Rev. 1999, V. 99. No 2. P. 543–564. DOI: 10.1021/cr9700336.
2. Doberenz F., Zeng K., Willems C., Zhang K., T. Groth. Thermoresponsive polymers and their biomedical application in tissue engineering – a review // *J. Mater. Chem*. B. 2020. V. 8. No 4. P. 607–628. DOI: 10.1039/C9TB02052G.
3. Halperin A., Kröger M., Winnik F.M. Poly(N-isopropylacrylamide) Phase Diagrams: Fifty Years of Research // *Angew. Chem. Int. Ed*. 2015. V. 54. No 51. P. 15342–15367. DOI: 10.1002/anie.201506663.

QUANTUM CHEMICAL CALCULATIONS OF $[Ln(PyrCOO)(acac)_2(H_2O)_2]$ (Ln = Dy, Er, Yb) – NEW SINGLE MOLECULE MAGNET

Natalia N. Breslavskaya[1], Elena N. Timokhina[2], Tatiana Yu. Astakhova[2], Andrey V. Gavrikov[1], Pavel N. Vasilyev1, Andrey B. Ilyukhin[1] and Nikolay N. Efimov[1]

[1]Kurnakov Institute of General and Inorganic Chemistry, Russian Academy of Sciences, Moscow, Russian Federation

[2]Emanuel Institute of Biochemical Physics, Russian Academy of Sciences, Moscow, Russian Federation

In recent years, there has been a growing research interest in Ln-based single molecular magnets (SMMs), the coordination compounds of Ln, which molecules exhibit properties characteristic of bulk ferromagnetic materials [1]. Like classical magnetic materials, such compounds have the potential to be applied as elements of high-density magnetic storage and in particular are the promising active components of information storage devices. The number of Ln carboxylate complexes exhibiting SMM properties that are currently known is significantly inferior to that of complexes with other ligands. The synthesis and comprehensive investigation of new carboxylate complexes of lantanides is of undoubted interest due to their important physico-chemical properties – photophysical, magnetic, sorptive, catalytic, etc. [2].

Previously [2] a series of isomorphic mononuclear complexes $[Ln(PyrCOO)(acac)_2(H_2O)_2]$ (Ln = Dy, Er, Yb); $acac^-$ – acetylacetonate (pentane-2,4-dionate) anion, PyrCOOH is pyrazine-2-carboxylic acid) were prepared and characterized by X-ray diffraction study and investigation of magnetic behavior. The molecular structure of isomorphic complexes was considered using Dy complex as the example (Fig. 1).

Slow magnetic relaxation indicating SMM behavior was found. The experimentally established magnetic relaxation paths are confirmed by *ab initio* calculations presented in this paper.

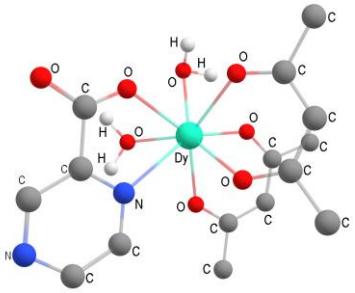


FIGURE 1. Molecular structure

All calculations were performed using ORCA 5.0.4 software [3, 4]. The atomic positions were extracted from the crystal structures obtained by X-ray diffraction. Only the positions of the hydrogen atoms were optimized at the DFT level, while other atomic positions were frozen. The calculations employed BP86 functional and def2-SVP basis set for all elements except Ln (Dy, Er and Yb), for which SARC2-DKH-QZVP basis set was used. The RI-JK accelerate approximation was used in combination with the segmented all-electron relativistically contracted auxiliary Coulomb fitting basis SARC/J. Complete active space self-consistent field (CASSCF) calculations were carried out with the SARC2-DKH-QZVP basis set for Ln and DKH-def2-TZVP basis set for other atoms. These calculations were accelerated through the RIJCOSX approximation in combination with AUTOAUX auxiliary basis. In all calculations the relativistic effects were modeled by the Douglas-Kroll-Hess (DKH) approximation.

The starting orbitals for the CASSCF calculations were taken from the restricted open-shell Hartree-Fock calculations. The CASSCF calculation has been performed by considering nine (Dy), eleven (Er), and thirteen (Yb) electrons in seven 4f orbitals, i.e., using CAS (n, 7) active space, where n = 9, 11 and 13, respectively. In these active spaces, we computed 21 sextets, 224 quartet and 490 doublets states for the Dy complex, 35 quartets and 112 doublets for the Er complex, and 7 doublets for the Yb complex. The spin-orbit coupling (SOC) Hamiltonian was then constructed and diagonalised using the basis of 21 sextets, 108 quartet and 32 doublets states for the Dy complex, 35 quartets and 73 doublets for the Er complex, and 7 doublets for the Yb complex. The SOC effects were incorporated by using quasi-degenerate perturbation theory (QDPT) to compute spin-orbit states. An atomic mean-field Hamiltonian (AMFI) was used to calculate the one-electron integrals.

The *ab initio* blocking barriers and magnetic properties were constructed using the SINGLE_ANISO program, which is incorporated into ORCA 5.0.4. The temperature dependence of the studied complex magnetic susceptibility was calculated for all complexes at a temperature range 2–300 K and under an applied DC field of 5000 Oe. The molar magnetization was calculated in the magnetic field range 0–5 T at 2, 4 and 6 K.

For identification of the most probable path for magnetic relaxation during the simulation/modeling of the magnetic relaxation pathways, Kramers doublets (KD) with increasing energies had been consistently taken involved until the set of following criteria was met:

(1) the transverse magnetic moment within currently considered KD was large ($\geq 10^{-2}$ μB).

(2) the components of the g-tensor corresponding to the currently considered KD ceased to meet the requirement for Ising systems ($g_x = g_y = 0$, or $g_x << g_z$ and $g_y << g_z$ for real systems).

In order to gain further insight into the relaxation pathways *ab initio* calculations were performed.

Corresponding approximations of the experimental DC magnetization curves are shown as solid lines in Fig. 2 while Fig. 3 and Tables 1-3 summarize calculated KDs.

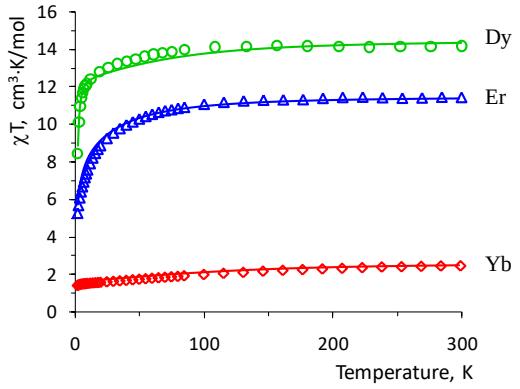


FIGURE 2. $\chi_m T$ *vs.* T dependencies for complexes under study in a 5000 Oe magnetic field. Solid lines represent *ab initio* calculations. Experimental data are shown in circles (Dy), triangle (Er) and diamonds (Yb)

The shapes of the obtained dependences are typical for the corresponding Ln^{3+} complexes, and the $\chi_m T$ (300 K) values are close to the theoretical ones for the corresponding non-interacting Ln^{3+} ions (Fig. 2). Thus, the magnetic behavior of complexes under study in the static mode is determined almost exclusively by the nature of Ln^{3+}. The $\chi_m T$ values for the Dy, Er, and Yb complexes remain virtually constant on cooling down to ~100 K, then decrease monotonically down to ~20 K and then drop sharply to a minimum value at T = 2 K. A low-temperature sharp decrease in $\chi_m T$ can be due to the depopulation of the m_J levels split by the crystal field, to the possible presence of weak antiferromagnetic intermolecular interactions between Ln^{3+} ions and/or to the influence of the Zeeman effect under the applied external magnetic field.

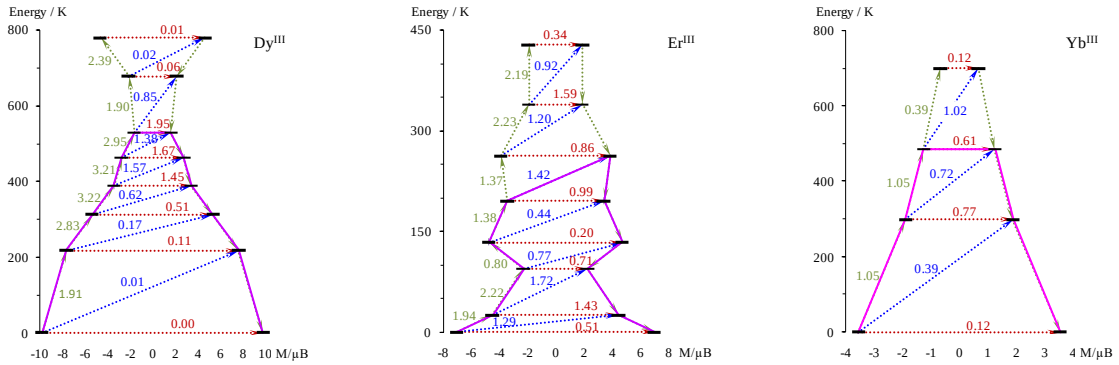


FIGURE 3. Calculated KDs and possible demagnetization pathways in complexes of Dy, Er and Yb. The thick black lines imply KDs as a function of their magnetic moment along the main anisotropy axis. The arrows indicate the considered magnetic relaxation path: QTM, TA-QTM (horizontal), possible Orbach relaxation. The most probable path of magnetic relaxation is highlighted with a bold line.The values near to the arrows indicate the matrix elements of the transverse magnetic moments (values greater than 0.15 imply a non-negligible contribution to the magnetic relaxation).

TABLE 1. CASSCF computed energy levels (K, Fig. 3), the composition of the effective g′-tensor (assuming a pseudospin S = 1/2) and major (>15%) components of the wave function for each m_J state of the lowest atomic multiplet J=15/2 of Dy^{3+}. KDs involved in magnetic relaxation are specified.

KD	Energy, K	g_x	g_y	g_z	Wave function, %
1	0	0.00	0.01	19.60	94|±15/2>
2	218.4	0.25	0.40	15.82	70|±13/2>+18|±9/2>
3	313	1.2	1.63	12.49	32|±11/2>+22|±7/2>
4	388.4	3.24	4.59	8.45	28|±11/2>18|±9/2>+22|±1/2>
5	462.5	1.26	4.54	8.53	31|±7/2>+24|±9/2>
6	529.4	1.59	3.76	13.44	39|±5/2>+26|±3/2>
7	678.1	0.06	0.14	16.70	24|±3/2>+38|±1/2>
8	780.1	0.00	0.03	18.85	19|±9/2>+20|±7/2>+18|±5/2>

TABLE 2. CASSCF computed energy levels (K, Fig. 3), the composition of the effective g′-tensor (assuming a pseudospin S = 1/2) and major (>15%) components of the wave function for each m_J state of the lowest atomic multiplet J=15/2 of Er^{3+}. KDs involved in magnetic relaxation are specified.

KD	Energy, K	g_x	g_y	g_z	Wave function, %
1	0.0	0.23	2.84	14.01	59|±15/2>
2	25.9	10.08	6.70	0.29	22|±15/2>+20|±9/2>
3	94.7	4.50	2.79	0.20	17|±11/2>+17|±1/2>
4	133.8	0.14	0.70	16.27	23|±11/2>+21|±9/2>+25|±7/2>
5	195.4	7.75	4.24	0.64	35|±13/2>+22|±3/2>
6	262.4	0.47	3.21	11.49	28|±11/2>+28|±5/2>
7	339.2	1.67	3.44	10.70	18|±9/2>+33|±3/2>+19|±1/2>
8	427.8	0.30	0.56	15.70	16|±3/2>+38|±1/2>

TABLE 3. CASSCF computed energy levels (K, Fig. 3), the composition of the effective g′-tensor (assuming a pseudospin S = 1/2) and major (>15%) components of the wave function for each m_J state of the lowest atomic multiplet J=7/2 of Yb^{3+}. KDs involved in magnetic relaxation are specified.

KD	Energy, K	g_x	g_y	g_z	Wave function, %
1	0.0	0.22	0.53	7.12	83|±7/2>
2	299.1	1.78	2.07	5.17	59|±5/2>+25|±1/2>
3	485.5	1.03	1.30	5.62	27|±5/2>+42|±3/2>+18|±1/2>
4	700.3	0.08	0.17	7.52	33|±3/2>+53|±1/2>

In the case of the Dy^{3+} complex, the transverse magnetic moment within the ground state shows non-negligible but non-decisive contribution of QTM to the demagnetization (Fig. 3). This fact agrees with the experimentally observed contribution of QTM in zero-field SMM behavior for the Dy complex and is additionally confirmed by the pronounced axial anisotropy of the corresponding g-tensor (Table 1). The results for both Er (Fig. 3 and Table 2) and Yb complexes (Fig. 3 and Table 3) indicate a pronounced contribution of QTM to the relaxation from the ground state of KD.

Thus, the studied complexes exhibit pronounced properties of field induced SMMs. Further development of such compounds seems promising in terms of achieving improved SMM characteristics combined with thermal and chemical stability.

This work was supported by the Ministry of Science and Higher Education of the Russian Federation as part of the State Assignment of the Kurnakov Institute of General and Inorganic Chemistry of the Russian Academy of Sciences (1021071612866-5-1.4.7)/

1. R. Sessoli and A. K. Powell. Strategies towards single molecule magnets based on lanthanide ions // *Coord. Chem. Rev*. 2009. V.253. No 19-20. P.2328-2341. DOI: 10.1016/j.ccr.2008.12.014
2. S. P. Petrosyants, K. A. Babeshkin, A. V. Gavrikov et al. Novel mononuclear Ln complexes with pyrazine2-carboxylate and acetylacetonate co-ligands: remarkable single molecule magnet behavior of a Yb derivative // *Dalton Trans*. 2017. V.46. No 35. P.11806-11816. DOI: 10.1039/c7dt02175e
3. F. Neese, F. Wennmohs, U. Becker, C. Riplinger. The ORCA quantum chemistry program package // *J. Chem. Phys.* 2020. V.152. P. 224108. DOI: 10.1063/5.0004608
4. F. Neese. Software update: The ORCA program system - Version 5.0. // *WIREs Comput. Mol. Sci.* 2022. V.12. No 5. P. e1606. DOI: 10.1002/wcms.1606

CARBON DIOXIDE CONVERSION OF METHANE ON $Mo_2C/CeZrO_2$ AS A METHOD OF GREENHOUSE GAS UTILIZATION

Natalya N. Gavrilova and Maria A. Myachina

Department of Colloid Chemistry,
D. Mendeleev University of Chemical Technology of Russia, Moscow, Russia

Carbon dioxide conversion of methane is not only a reaction that allows synthesis gas production but is also considered as an option for the utilization of two greenhouse gases – carbon dioxide and methane. That is why this reaction has received special attention in recent years by many researchers.

Among the promising catalysts that make it possible to obtain synthesis gas with a component ratio of $[H_2]/[CO] = 1$, molybdenum carbides are of the greatest interest. Molybdenum carbides exhibit high catalytic activity similar to activity of noble metals, have high mechanical and thermal stability, and are highly resistant to catalytic poisons [1, 2]. However, during the reaction, Mo_2C is oxidized to form inactive MoO_2. Oxidative stability can be improved by introducing promoters or using a carrier [3, 4]. Solid solutions of zirconium dioxide series can be used as a substrate for the Mo_2C catalyst.

Synthesis of $Mo_2C/Ce_xZr_{1-x}O_2$ catalytic systems was carried out by the sol-gel method. Solid solutions $Ce_xZr_{1-x}O_2$ with different composition (x = 0.9, 0.8, 0.5 and 0.2) were used as catalyst supports. The synthesized catalysts were characterized in terms of morphology, phase composition and porous structure. The TPR and TPO methods are also used for characterization. Catalytic activity and stability

were investigated in the reaction of carbon dioxide conversion of methane. The reaction was carried out in a reactor with a fixed bed of catalyst in the temperature range of 800-900°C.

A comparison of the specific catalytic activity showed that the samples deposited on solid solutions of cubic modification have the greatest catalytic activity, among them the best results were obtained on the sample $Mo_2C/Ce_{0.5}Zr_{0.5}O_2$. The reaction mechanism, which explains the high stability of this catalyst, was proposed.

It was shown that supported $Mo_2C/Ce_xZr_{1-x}O_2$ catalysts were more oxidative stable than unsupported Mo_2C, whose loss of activity was observed after a 60 min of experiment. Oxidation of supported $Mo_2C/Ce_xZr_{1-x}O_2$ was not observed under the reaction conditions.

The research was carried out within the state assignment of Ministry of Science and Higher Education of the Russian Federation (FSSM-2023-0004).

1. York A.P.E., Clarige J.B., Marquez-Alvarez C., Brungs A.J., Tsang S.C., Green M.L.H. Synthesis of early transition metal carbides and their application for the reforming of methane to synthesis gas // *Stud. Surf. Sci. Catal*. 1997. V.110. P. 711 - 720. DOI:10.1016/S0167-2991(97)81033-6.
2. Clarige J.B., York A.P.E., Brungs A.J., Marquez-Alvares C., Sloan J., Tsang S.C., Green M.L.H. New catalysts for conversion of methane to synthesis gas: molybdenum and tungsten carbide // *J. Catal*. 1998. V.180. № 1. P. 85 - 100. DOI:10.1006/jcat.1998.2260.
3. Darujati A. R.S., LaMont D.C., Thompson W.J. Oxidation stability of Mo_2C catalysts under fuel reforming conditions // *Appl.Catal. A: General*. 2003. V. 253. P. 397-407. DOI:10.1016/S0926-860X(03)00531-3.
4. Darujati A.D.S., Thompson W.J. Kinetic study of a ceria-promoted Mo_2C/γ-Al_2O_3 catalyst in dry-methane reforming // *Chem.Engi.Sci*. 2006. V.61. P. 4309-4315. DOI: 10.1016/j.ces.2006.02.007.

CONTENTS

ATMOSPHERE-IONOSPHERE COUPLING

Vargin P.N., Kostrykin S.V., Koval A.V., Rozanov E.V., Volodin E.M., Smyshlyev S.P., Mokhov I.I., Perminov V.I. Climate changes in stratosphere and mesosphere in observational and modeling data…..……..……..……. 3

Denisenko V.V., Rozanov E.V. The influence of clouds on the atmospheric conductivity…….……..…… 6

Nikolashkin S.V., Titov S.V., Evseev U. N., Sidorov N. E. Influence of solar and geomagnetic activity on temperature stratification of the middle atmosphere……...…….……. 10

Bakhmetieva N.V., Grigoriev G.I., Zhemiakov I.N., Kalinina E.E., Lisov A.A. Ionosphere between meso– and turbopause: ideas, experiments, new results……... 14

Didenko K.A., Koval A.V., Ermakova T.S., Fadeev A.S. Variations of atmospheric planetary waves under conditions of different combinations of natural tropical oscillations ……..……. 17

Zorkaltseva O.S., Saunkin A.V., Vasilyev R.V., Gavrilyeva G.A. Effects of sudden stratospheric warmings on airglow emission layers over Siberia…….. 20

Ryakhovsky I.A., Borchevkina O.P., Poklad J.V. The influence of atmospheric factors on the conditions of propagation of VLF signals ……..…..……... 24

Blagina A.P., Shatalina M.V. The electrical activity of clouds criteria based on field observations data ……..…….…..…….. 26

Yankovsky I.S., Nosikov I.A., Timchenko A.V., Klimenko M.V. Starvisor: a night sky optical monitoring project ……..……..……. 28

Smirnova E.S., Dobrokhotov S.Yu. On the three-dimensional modeling of the evolution of an acoustic atmospheric disturbance caused by the ground movement……...…….……..…. 31

Stupishina O.M., Golovina E.G., Noskov S. N., Eremin G. B. Space weather variations those can impact human health in diverse geographic points……..….. 34

Kostin V.M., Ovcharenko O.Ya., Trushkina E.P. Possible triggers of explosive changes in tropical cyclones parameters and strong earthquakes during the earth's passage through June meteor showers……...…….……..……..…….. 38

Denisenko V.V., Smirnov S.E. Distortions of the atmospheric electric field that occur during its measurement ……..……..…….. 41

Kostin V.M., Ovcharenko O.Ya., Truchkina E.P. Earthquake forecast up to 5 days based on tropical cyclone weather data ……...…….. 44

Shatalina M.V., Sarafanov F.G., Volkova A.V., Dolinin A.A., Shlyugaev Y.V. Variations of Schumann resonances characteristics in the upper Volga region: observations and analysis ……..…… 47

IONOSPHERIC-MAGNETOSPHERIC RELATIONS

Nosikov I. A., Klimenko M.V. On the direct approach for multi-hop ray path search … 51

Beletsky A.B., Syrenova T.E., Mikhalev A.V., Vasilyev R.V. Morphology and dynamics of mid-latitude auroral structures observed in the south of eastern Siberia ……..…..…. 52

Grach V.S., Demekhov A.G. The influence of amplitude and frequency variations of the chorus wave packet on the acceleration of energetic electrons ……..…..……. 55

Koltovskoi I.I., Ammosov P.P., Gavrilyeva G.A., Perminov V.I. Meridional net of infrared spectro-graphs and some results ……..…… 59

Dmitriev A.V., Suvorova A.V. Energetic protons and electrons under the earth radiation belt on the main phase of magnetic superstorm ……..……. 62

Ratovsky K.G., Klimenko M.V., Bessarab F.S., Klimenko V.V., Belyuchenko K.V., Shubin V.N. Ionospheric response to May 2024 geomagnetic storm: Irkutsk ionosonde data and modeling ……...…...……..…….……. 66

Sinevich A.A., Chernyshov A.A., Chugunin D.V., Mogilevsky M.M. Polarization jet/SAID occurrences during extreme geomagnetic storms …….……..…… 69

Myagkova I.N. Comparison of trapped and precipitating electron flux of the Earth's outer radiation belt according to data from the Meteor-M No. 2 satellite …….…….. 72

Abunina M.A., Maurchev E.A., Shlyk N.S., Abunin A.A., Belov A.V. Changes of geomagnetic activity for the period from 1932 to 2023…..…… 76

Klimenko M.V., Bessarab F.S., Klimenko V.V., Nosikov I.A., Borchevkina O.P., Timchenko A.V., Belyuchenko K.V., Efishov I.I., Yakimova G.A., Ratovsky K.G., Shubin V.N. Observation and modeling of upper atmosphere response to geomagnetic storms using WD IZMIRAN tools……. 79

Chernyshov A.A., Mogilevsky M.M., Shaposhnikov V.E., Chugunin D.V., Dorofeev D.A. Double plasma resonance as a possible mechanism for explaining non-thermal hectometric radiation ……..…..……. 83

Balabin Y.V., Germanenko A.V., Mikhalko E.A., Gvozdevsky B.B. Differential spectra of natural gamma-radiation in 0.1-5 MeV during precipitations……...… 86

Balabin Y.V., Germanenko A.V., Mikhalko E.A., Gvozdevsky B.B. Measurement of barometric coefficients for natural gamma radiation coming from the atmosphere in the range 0.1-5 MeV……..…….……..... 90

Belyuchenko K.V., Klimenko M.V., Klimenko V.V., Ratovsky K.G. Comparison of ionospheric disturbances for storms in March 2015 and May 2024 at mid-latitudes……..…….…... 93

Kurdyaeva Y.A., Borchevkina O.P., Padokhin A.M. Modeling of ionospheric disturbances variations caused by the passage of atmospheric waves from the troposphere ……..……..…… 97

Borchevkina O.P., Efishov I.I., Radievsky A.V., Tepenitsyna N.Y., Shagimuratov I.I., Yakimova G.A. Statistics of total electron content variations in the Kaliningrad station in 2023…….……..……..…….. 99

Buryak N.V., Vilutis A.R., Nosikov I.A. A new approach to modeling of vertical sounding ionograms. Comparison with observational data …….…….. 102

Vilutis A.R., Buryak N.V., Nosikov I.A. A new approach to modeling vertical sounding ionograms. Calculation technique …….…….…….…….. 103

Balabin Y.V., Germanenko A.V., Mikhalko E.A., Gvozdevsky B.B. Conducting spectral observations of natural gamma radiation in the range of 0.1-5 MeV in various geographical locations and comparing the spectra …… 105

Efishov I.I., Shagimuratov I.I. Longitudinal features of GPS signal scintillations development during the November 2021 storm ……. 108

Shagimuratov I.I., Klimenko M.V., Yakimova G.A., Efishov I.I. Signature of a polarization jet in TEC observations: case study……..…… 111

Shagimuratov I.I., Yakimova G.A., Tepenitsyna N.Yu., Efishov I.I. Occurrence of the polar tongue of ionization in the total electron content measurements during 14 January 2022 magnetic storm……. 115

Oinats A.V., Kurdyaeva Y.A., Tolstikov M.V., Syrenova T.E., Artamonov M.F. Multi-instrumental study of night mid-latitude traveling disturbances in the Earth's atmosphere ...……...…….. 119

Nosikova V.V., Timchenko A.V., Nosikov I.A. Ionospheric effects of the victory day geomagnetic storm based on ionosonde data at the WD IZMIRAN observatory …….. 123

Hamov I.V., Safianov K.R., Borchevkina O.P., Bessarab F.S. Search for anomalies in long series of measurements of the critical frequency of the ionospheric F2-layer at the WD IZMIRAN observatory…….. 125

Senyagin E.D., Timchenko A.V., Bessarab F.S. Seasonal features of the Es-layer characteristics over the Kaliningrad region during solar 24 and 25 cycles……. 127

Yahnina T.A., Demekhov A.G., Popova T.A. Dependence of the observation probability of relativistic electron precipitation with different formation mechanisms on the parameters of the solar wind and geomagnetic activity……..……. 131

Kolpak V.I., Mogilevsky M.M., Chugunin D.V., Chernyshov A.A., Moiseenko I.L. AKR spectrum modification as a result of propagation in inhomogeneous plasma…… 135

Demekhov A.G., Yahnina T.A., Popova T.A. Relationship between wave intensity in the magnetosphere and precipitating energetic particle fluxes……... 138

Popova T.A., Yahnina T.A., Demekhov A.G. Properties of relativistic electron precipitation in years of quiet (2017) and disturbed (2023) geomagnetic conditions….. 142

Shubin V.N. Global median model of the ionospheric e-layer based on radio occultation data…….. 145

ELECTROMAGNETIC AND OPTICAL PHENOMENA IN THE ATMOSPHERE INCLUDING LONG-LIVED AND PLASMA OBJECTS

Shaikhislamov I.F., Chibranov A.A., Berezutskii A.B., Posukh V.G., Rumenskikh M.S. Physics of expanding plasma clouds at ion gyroradius scale……..…… 148

Bychkov V.L., Logunov A.A., Bychkov D.V., Vaulin D.N. Special properties of ball lightning ……..……..…. 151

Klimov A.I. Study of electrophysical processes in an longitudinal heterogeneous plasma swirl flow……..…….……..…….. 155

Gorev V.V., Smyslov D.Yu. Evaluation of the effectiveness of using medium-energy heavy ions to generate linear lightning……..…….…… 158

Rumenskikh M.S., Chibranov A.A., Berezutsky A.G., Posukh V.G., Trushin P.A., Zakharov Y.P., Miroshnichenko I.B., Shaikhislamov I.F. Laser plasma spectroscopy and collisionless interaction in magnetized media ……. 162

Bychkov V.L., Sorokovykh D.E., Bychkov D.V., Logunov A.A. Long-lived luminous formations by the erosive plasma generator ……..……..…….……. 165

Nikitin A.I. Key observations of ball lightning as a basis for creating its model……..... 169

Nikitin A.I., Nikitin V.A., Velichko A.M., Nikitina T.F. Multiple-charged clusters as an agent reducing air humidity before an earthquake……...…….……. 172

Nikitin A.I., Nikitin V.A., Velichko A.M., Nikitina T.F. The reason for the formation of symmetrical traces of multi-charged water clusters …….…..……. 175

Bychkov V.L., Shvarov A.P., Stepanov I.G., Goryachkin P.A., Vaulin D.N. The effect of corona discharge plasma of negative polarity on redox processes in soil……..……..…..…… 179

Nikitin A.I., Nikitin V.A., Velichko A.M., Nikitina T.F. Penetration of multi-charged clusters into a solid body …… 182

METHODS AND TECHNIQUES FOR REMOTE SENSING AND IDENTIFICATION OF HAZARDOUS CHEMICALS IN THE ATMOSPHERE AND DIFFERENT SURFACES

Demkin P.P., Bessonov V.R., Golyak I.S., Karpov I.A., Kosterova A.P., Kuznetsov A.D., Fufurin I.L. Sampling system for gas analysis based on FTIR spectroscopy…….……...…….. 186

Zadorozhnyi E.N., Anfimov D.R., Vintaikin I.B., Golyak I.S., Fufurin I.L., Morozov A.N. Techniques for methane leaks remote detection by infrared non-dispersive spectroscopy from airspace……..……..…….... 189

Nebritova O.A., Morozov A.N., Fufurin I.L. Optical methods of remote sensing of the Earth from space for the study of atmospheric greenhouse gas concentration…….…….……..….. 192

Gylka R.A., Chubarkina Y.R., Anfimov D.R., Demkin P.P., Fufurin I.L., Vintaikin I.B., Morozov A.N. Identification of substances by characteristic lines in Raman spectra……..... 195

Karpov I.A., Fufurin I.L., Kosterova A.P., Anfimov D.R., Demkin P.P., Bessonov V.R., Morozov A.N. Development of non-dispersive infrared gas analyzer for measuring the dynamics of greenhouse gases concentrations ……...……..…….. 197

Kosterova A.P., Fufurin I.L., Anfimov D.R., Karpov I.A., Seregin I.A., Yaroslavtsev A.M. Analysis of field test dataset of water vapor and carbon dioxide concentrations measurement with using methods of infrared non-dispersive spectroscopy……..… 199

Bessonov V.R., Karpov A.I., Kosterova A.P., Anfimov D.R., Demkin P.P., Fufurin I.L., Morozov A.N. Experimental bench for analyzing the dynamics of concentrations of water vapor and carbon dioxide by the method of covariance of turbulent pulsations……...…….…….. 202

Kolesnikov B.V., Shvetsov G.A., Vinogradov A.N., Izmailova Y.A., Leontyev A.A., Rodionov A.I., Rodionova I.P., Rodionov I.D. Detection of linear emission spectrum sources using hyperspectral image analysis…….…….. 205

Izmailova Y.A., Leontyev A.A., Vinogradov A.N., Shevchenko M.O., Rodionov A.I., Rodionova I.P., Rodionov I.D. A robust algorithm for low-contrast object detection using hyperspectral imaging…….…...…….. 209

Golyak I.S., Anfimov D.R., Vintaykin I.B., Fufurin I.L., Morozov A.N. Formation of two-dimensional gas concentration distributions in the open atmosphere based on remote measurements from an IR fourier spectrometer……....……..…….. 212

Glushkov V.L., Vintaikin I.B., Golyak I.S., Gylka R.A., Fufurin I.L., Morozov A.N. Estimation of industrial flue gas emission capacity using the Pasquill-Briggs model... 215

Anfimov D.R., Fufurin I.L., Golyak I.S., Vintaikin I.B., Rachkin D.A., Morozov A.N. FTIR spectrometer onboard 16U cubesat spacecraft for greenhouse gases monitoring.. 218

Anfimov D.R., Vintaikin I.B., Golyak I.S., Fufurin I.L., Morozov A.N. Experimental setup for leak detection with passive NDIR radiometer and infrared camera……. 221

Fufurin1 I.L., Fufurina M.A., Yatsenko O.A., Chertkova L.A., Vintaikin I.B., Gylka R.A., Morozov A.N. FTIR spectrometer for remote monitoring of metallurgical plant gas emissions……...…….. 223

Golyak I.S., Morozov A.N., Timashova L.N. Space system for measuring greenhouse gas concentration……...…… 225

ELEMENTARY PROCESSES IN THE UPPER ATMOSPHERE AND IONOSPHERE

Belyaev A.K. Change of the Born-Oppenheimer paradigm in the atomic collision theory during the hundred-year quantum mechanics……...……... 229

Berdinskiy V.L., Arifullin M.R., Sadykov A.R. Physico-chemical significance of quantum entanglement and spin selection rules…….……..…….……... 232

Yakovlev M.Yu., Belyaev A.K. The wave packet method for studying of calcium-hydrogen inelastic processes…….. 235

Yakovleva S.A., Belyaev A.K. Model approaches for treatment of inelastic processes in low-energy collisions with hydrogen ……....…… 238

Vasil'eva V.A., Yakovleva S.A. Atomic data on inelastic processes in Ag-H collisions with the account for the fine structure of Ag ……..…...…….…… 239

Andreev G.I., Bychkov V. L. Proton impact ionization cross section for molecular targets…….…….……... 240

Stepanov I.G., Bychkov V.L., Golubkov M.G. Ion formation in lower atmosphere under the action of cosmic rays…...……...…….…...… 242

Adamson S.O., Kharlampidi D.D., Golubkov M.G. Integrated density of state calculation by the numerical inversion of Laplace transform……....…… 246

Dyakov Y.A., Golubkov M.G. Collisional-induced reactions between methane and simple Criegee intermediates CH_2OO, CH_3CHOO, and $(CH_3)_2COO$……...……. 248

Morozov I.I., Vasiliev E.S., Butkovskaya N.I., Khomiakova P.S., Syromyatnikov A.G., Morozova O.S. Atmospheric processes of toxic chloroacetic acids …….…….…. 251

NOVEL METHODS FOR ENVIRONMENTAL CONTROL AND MONITORING

Konstantinova E.A., Nazarkina Y.V., Dronova D.A., Kytina E.V. Control of structural properties and chemical composition of porous anodic aluminum oxide……...…… 255

Kytina E.V., Nazarkina Y.V., Konstantinova E.A., Pavlikov A.V. Comparative analysis of photoluminescent properties of porous aluminum oxide formed in electrolytes based on sulfuric and selenic acids…….…... 258

Isupova L.A. Reduction of nitrous oxide emissions in nitric acid production by high-temperature catalytic decomposition on perovskite-containing oxides $LaFe_{1-x}Me_xO_3$ (Me=Mn, Co, Ni) ……...… 261

Shatrov T.D., Simenido G.A., Ivanova E.A., Chernikova E.V., Golubeva E.N. Spin probe study of polymer chain collapse in PNIPAM-b-PEG copolymers…….……... 264

Chaikina Y.A., Shushin A.I., Golubkov M.G. Theoretical foundation for optical diagnostics methods to monitor the statistical state of randomly nonuniformed disordered media …….…..... 266

Popova A.A., Lisina V.L., Litmanovich E.A., Golubeva E.N. Polymerization in supercritical carbon dioxide: novel approach to synthesis of termoresponsive polymers……..….. 269

Breslavskaya N.N., Timokhina E.N., Astakhova T.Yu., Gavrikov A.V., Vasilyev P.N., Ilyukhin A.B., Efimov N.N. Quantum chemical calculations of $[Ln(PyrCOO)(acac)_2(H_2O)_2]$ (Ln = Dy, Er, Yb) – new single molecule magnet…..… 273

Gavrilova N.N., Myachina M.A. Carbon dioxide conversion of methane on $Mo_2C/CeZrO_2$ as a method of greenhouse gas utilization…….…….. 276

ATMOSPHERE, IONOSPHERE, SAFETY

Proceedings
of IX International conference

Компьютерная верстка В.А. Иванова

Подписано в печать 20.05.2025

Формат 70×100 1/16. Усл.печ.л. 17
Тираж 160 экз. Заказ 1

Издательство ООО «АЛГОМАТ»
238325, Калининградская область, Гурьевский р-н, п. М.Луговое, ул. Селецкая, 15

